GENETIC AND CHEMICAL CHARACTERISATION OF THE HOST SUCCESSION TO THE ARCHEAN JAGUAR VHMS DEPOSIT

Susan M. Belford

B.Sc.(Hons) University of Western Australia

M.Sc. University of Western Australia

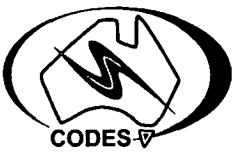

Submitted in fulfilment of the requirements
for the degree of Doctor of Philosophy
University of Tasmania

Hobart, Australia
October, 2010

STATEMENT AND AUTHORITY OF ACCESS

This thesis contains no material which has been accepted for a degree or diploma by the University or any other institution and, the best of my knowledge and belief, no material previously published or written by another person except where due acknowledgement is made in the text of this thesis.

This thesis is not to be made available for loan or copying for one year following the date this statement was signed. Following that time the thesis may be made available for loan and limited copying in accordance with the CopyrightAct 1968.

Date: 18 October 2010

Susan M. Belford

ABSTRACT

Jaguar, an Archean Cu-Zn-rich volcanic-hosted massive sulfide deposit, is situated in the Teutonic Bore volcanic complex in the Eastern Goldfields of the Yilgarn Craton, Western Australia. The Jaguar deposit is one of only three VHMS deposits that have been mined in the Eastern Goldfields. The deposit is hosted in a succession dominated by coherent facies and their associated volcaniclastic facies, with minor non-volcanic facies. The rocks (c. 2.69 Ga) have been affected by regional greenschist facies metamorphism and deformation, and hydrothermal alteration is intense around the massive sulfide orebody.

Using only drillcore across a 1 km x 1.6 km area, twenty-five principal lithofacies have been recognised in the study area and are organised into five groups: 1) coherent rhyolite, dacite, andesite, basalt and dolerite facies; 2) monomictic volcanic breccia and conglomerate; 3) polymictic volcanic breccia and conglomerate; 4) volcanic sandstone and mudstone; and 5) non-volcanic mudstone and chemical facies. The environment of deposition was submarine and below-storm-wave-base.

The stratigraphy at Jaguar has been reconstructed using observations and interpretations based on facies analyses and relationships, rock fabric and microstructure that are supported by the application of immobile element geochemistry. The succession is split into Footwall (FW), Mineralised Package (MP)and Hangingwall (HW) units. The FW is divided into four volcanic lithofacies having distinctive composition. It is marked by an absence of sedimentary units between the volcanic facies. The deepest footwall is andesite lava (DFA) which was succeeded by a rhyolite dome (FR). These units are overlain by coherent andesite (FA) and then pillow basalt (FB). The FW (DFA, FR, FA and FB) and the MP dacite magmas were closely related.

The MP is a complex assemblage of intercalated coherent, autoclastic, resedimented and non-volcanic lithofacies divided into six sub-units: 1) the Dacite MP (MPD) comprising coherent dacite, monomictic dacite breccia, and monomictic pumice-rich breccia facies; 2) the Conglomerate MP (MPC) comprising polymictic dacite breccia, polymictic conglomerate and pillow-fragment basalt breccia facies; 3) the Pumice-rich MP (MPP) comprising polymictic pumice-rich breccia and pumice granule sandstone facies; 4) the Laminated MP (MPS) comprising laminated volcanic mudstone, non-volcanic mudstone and black shale, polymictic conglomerate, volcanic sandstone and chert facies; 5) the Laminated Chert MP (MPH) comprising chert facies; and 6) the Sulfide ore (MPO).

The basal unit of much of the MP is laminated chert (MPH) (30–100 cm thick), which directly overlies the FB. Chemical deposition of the chert occurred on the sea floor as an exhalative precipitate immediately prior the eruption of the dacite (MPD). In places, plastic

deformation and brecciation occurred possibly during contemporaneous local seismic events (related to growth faulting) which locally exposed the FB.

The dacite (MPD) was erupted as a series of small domes or flows on to the seafloor in an unstable environment. The coherent centres of these domes pass through autoclastic margins into pumiceous carapace. Pumice formed by non-explosive, quench fragmentation of pumiceous carapace on the vesiculating dome. Spalling and debris flows of unstable primary breccias deposited the associated polymictic breccias (MPC) and incorporated plastically deformed clasts of seafloor chert. The polymetallic sulfide orebody was formed in this environment. Within the MPC, primary sulfide clasts indicate that the sulfide body was forming contemporaneously with the MP. Tectonic instability and growth faulting exposed the growing massive sulfide, creating local debris flows containing sulfide clasts. This instability caused elutriation of finer-grained particles into the water column where they were moved about by water and weak gravity currents, before settling out of suspension (MPS).

The HW comprises coherent and associated autoclastic lithofacies interbedded with laminated volcanic and non-volcanic mudstone facies. It is divided into four major volcanic units, defined by packages of associated volcanic lithofacies having distinctive composition. From the base of the hangingwall, these units are informally named: the Hangingwall Andesite (HA), the Hangingwall Basalt (HB), the Upper Porphyritic Andesite (HUA) and the Upper Quartz Rhyolite (HUR). The HA and the HB have been further subdivided into single mappable units, assisted in the case of the HA, by distinct geochemical characteristics. There was a profound change in composition from the FW to the HW magmas.

Volcanism resumed after the MP, more highly fractionated andesites (HA) interfingering with volcaniclastic and pelagic sediments. These units are overlain by a thick succession of compositionally monotonous basalts (HB), that includes facies dominated by fountain deposits (fluidal-clast breccia) to pillow lava. Transient growth faults caused episodic to gradual subsidence that formed wedge shaped thickening in the HA and lower HB units. Subsidence had ceased by the time the upper HB was erupted. Dolerite sills with the same composition as the HB were likely feeders to the HB lavas. They intruded the succession up to mid-level HB. At this time, evidence points to a change in the stress regime from extension to compression. The composition of the HB/D magmas was different from earlier magmas. The aggregate thickening of the succession from sill inflation was between 150 and 200 m. The inflation was probably not uniform; intrusion of more magma in the south of the area likely caused tilting to the north. The remainder of the hangingwall was deposited in an apparently seismically stable environment and each major volcanic event was followed by deposition of significant mudstone (plus sandstone and carbonaceous mudstone).

The lateral continuity of almost all units, and the lack of repetition of the sequence, does not support the presence of subtle thrust ramp repetitions, despite substantial evidence of shear related deformation in some sedimentary interbeds. All the sedimentary younging evidence unequivocally indicates younging to the west, implying no obvious major folds. The deformation of the sequence was not significant enough to influence stratigraphic reconstruction.

The dominant sulfide minerals are pyrite, pyrrhotite, sphalerite and chalcopyrite (and locally, magnetite). Galena and arsenopyrite are present as minor phases and trace amounts of tetrahedrite-tennantite and geochronite were identified. The majority of the ore minerals have been subject to varied amounts of strain. A low-strain window is the primary source of evidence that the deposit was syn-volcanic and formed predominantly beneath the seafloor. The evidence of the infill of open space textures, the colloform intergrowths of sulfide and chert, the sulfide replacement of spherulites plus replacement fronts within the dacite all support this conclusion. Where pyrite has been deformed, it has commonly failed in a brittle manner. Where there is interconnectivity of sulfide grains, most sulfides (excluding pyrite) show evidence of ductile flow deformation and durchbewegung textured bands. Relicts of undeformed colloform pyrite may remain within these ductile bands, and where pyrite has boudinaged or failed cataclastically, fine fractures perpendicular to the band have been filled with other sulfides. Where clasts of gangue have been dragged into the bands, typical durchbewegung texture is developed. Most bands appear to have been annealed post-deformation.

Multi-element and REE spidergrams suggest that the coherent rocks are similar to BABB, with Nb-Ta depletion indicative of a subduction-related arc signature. Discrimination diagrams (developed for Phanerozoic rocks) suggested a complex, early back-arc setting for Jaguar. This conclusion is consistent with an ensimatic rift environment where the rift was an early back-arc basin probably over a subducting slab, and coincided with a period of modest extension at local scales. Although only a small part of the whole succession was examined, ore formation appears to have been localised at a volcanic centre, during a transition in magma composition and productivity.

ACKNOWLEDGEMENTS

During the years that I have been working towards completion of my PhD I have enjoyed the assistance, encouragement and friendship of many people.

Foremost, I would like to thank my supervisors Garry Davidson, Jocelyn McPhie and Ross Large, without whom this study would not have been possible. I would like to thank them for their guidance, support, encouragement and reviews over the duration of the research. Thanks are extended to Tony Crawford whose discussion and reviews of my geochemistry chapter helped me immensely.

This research was sponsored by an Australian Post Graduate Research Award (Industry), supported by the ARC Centre of Excellence in Ore Deposits (CODES) at the University of Tasmania, and a Hugh McKinstry Grant from the Society of Economic Geologists Foundation. The IGCP National Committee are thanked for an Australian Government-sponsored grant-in-aid to attend a field trip to the Green Tuff belt in Japan. Jabiru Metals Limited are gratefully acknowledged for providing financial and logistical support.

Numerous people have helped me in various ways throughout this project and I would particularly like to thank Peter Cornish, Bruce Gemmell, Wally Herrmann, Christine Higgins, Nilar Hlaing, Katie McGoldrick, Karin Orth, June Pongratz, Phil Robinson, Helen Scott, Dianne Steffens and Simon Stephens from CODES who have provided encouragement and assistance and without which this project would not have been possible. Max Frater, Noel Marston, Neil Martin and the field staff from Jabiru Metals are thanked for their support, as well as the assistance they provided me while in the field. Thanks also go to my roommates in 200, along with past and present fellow PhD students, and I would particularly like to thank Andrea Agangi, Mathieu Ageneau, Darren Andrews, Martin Jutzeler, Teera Kamvong, Sarah Gordee, Joe Moye and Bronto Sutopo for their friendship and encouragement.

Special thanks are due to my family and my friends for their continued love and support over the years.

TABLE OF CONTENTS

APPENDICES

LIST OF FIGURES

LIST OF TABLES

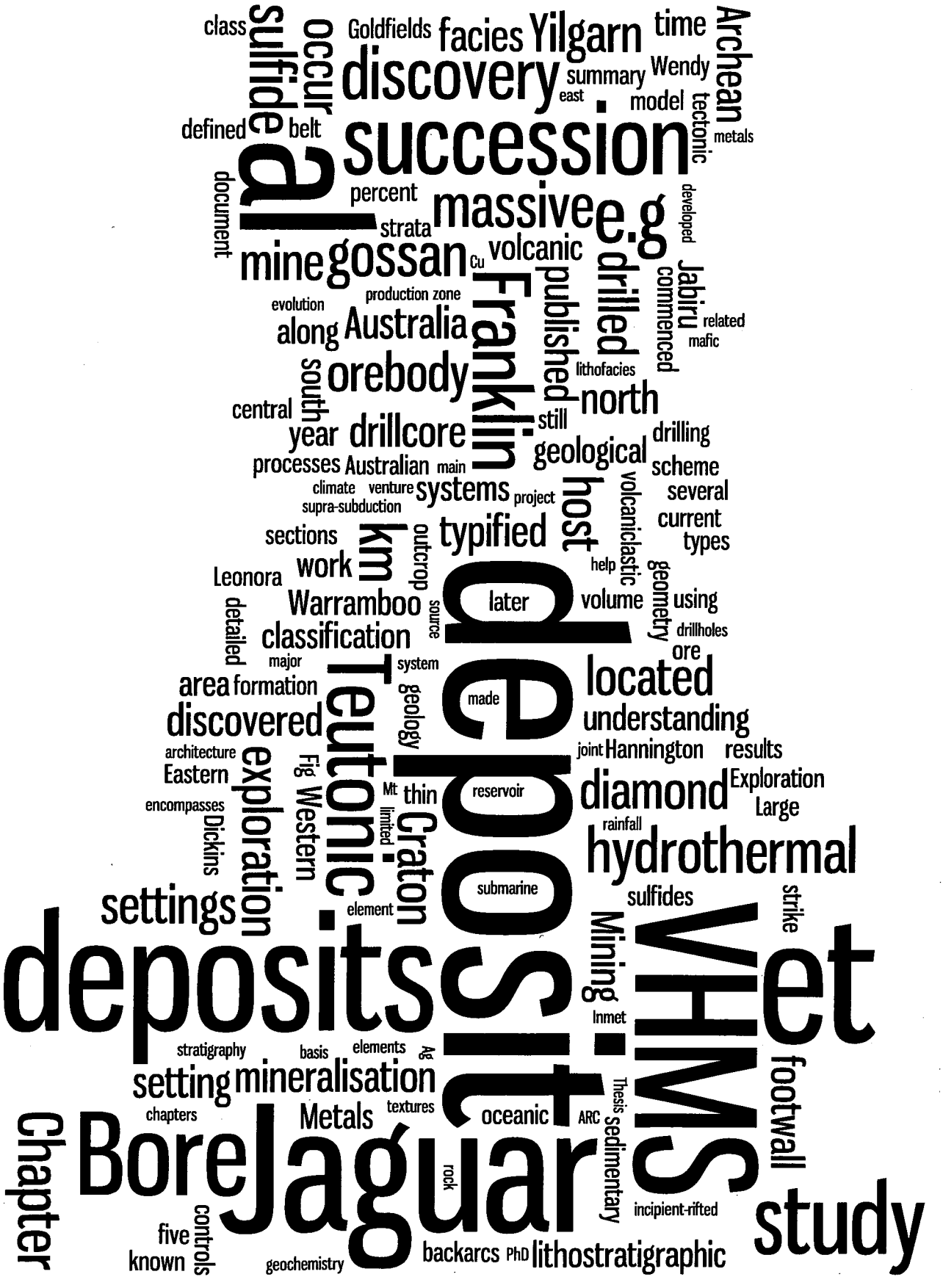
deposits
deposit
VHMS
et
Bore
Jaguar
Chapter
study
et al.
succession
discovery
Teutonic
Craton
Franklin
mineralisation
setting
settings
exploration
hydrothermal
diamond
located
host
typified
massive
gossan
orebody
drillcore
Australia
Yilgarn
facies
Archean
Goldfields
sulfide
occur
class
defined
belt
document
percent
strata
volcanic
Cu
mine
drilled
published
north
south
central
year
still
geological
drilling
scheme
several
current
types
processes
Australian
main
climate
venture
supra-subduction
systems
project
volcaniclastic
sections
km
work
outcrop
Leonora
Warramboo
source
later
volume
using
geometry
drillholes
detailed
classification
major
system
area
formation
geology
made
ore
discovered
understanding
architecture
joint
Hannington
results
Eastern
Fig
Western
Mt
thin
reservoir
Exploration
Large
encompasses
Dickins
limited
rainfall
submarine
sulfides
strike
Mining
Inmet
element
stratigraphy
basis
elements
Ag
textures
oceanic
ARC
Thesis
sedimentary
footwall
chapters
Metals
rock
incipient-rifted
five
known
controls
geochemistry
backarcs
PhD
lithostratigraphic
time
Wendy
summary
east
model
tectonic
metals
developed
Jabiru
commenced
related
mafic
lithofacies
evolution
production zone
along
Australia
Franklin
drilled
e.g.

1. INTRODUCTION

1.1 Preamble

Jaguar is a volcanic-hosted massive sulfide (VHMS) deposit discovered in 2002 and located in the Archean Yilgarn Craton of Western Australia. It is some four kilometres along strike from the Teutonic Bore VHMS deposit and only the fourth Yilgarn Craton VHMS deposit to be brought into production. Surprisingly few VHMS deposits are known in the Yilgarn Craton, when compared with the Canadian Archean. This is despite the large geographic expanse of the Yilgarn Craton and the submarine character of most of the volcanic sequences. This paucity remains an unexplained phenomena.

The deposit falls within the bimodal-mafic lithostratigraphic classification of VHMS deposits of Franklin et al. (2005). Its size and grade, of 1.6 Mt at of 3.1% Cu, 11.3% Zn, 0.7% Pb, 115g/t Ag (Jabiru Metals Annual Report, 2006), is greater and richer than the geometric mean for this class, being 1.4 Mt at 1.3% Cu, 2.5% Zn, 0.26% Pb, 23.97g/t Ag (Franklin, 2007).

The deposit does not outcrop. The top of the orebody extends upwards to an upper limit some 300 m below the surface and indeed the top 20 m of the overlying regolith consists of partially lithified, transported sediments with no outcrop of the up-dip position of the host unit. The nearest outcrop is in the footwall at a stratigraphic position interpreted to be greater than 200 m below the deposit. Zones of intense hydrothermal alteration occur in intimate association with the orebody footwall. The Neoarchean (ca 2.69 Ga) Jaguar host succession has experienced upper greenschist facies metamorphism with low strain except in very localised areas, where more ductile materials (graphite and some sulfides) document and preserve the record of this strain. Aside from these few exceptions, the original rock textures are generally well preserved and provide an excellent source of material for study.

1.1.1 Research significance

Background

The study and published literature on VHMS deposits is extensive and comprehensive. A summary review of the status of understanding of the deposit class compiled by Franklin et al. (2005), published in the Economic Geology 100th year Anniversary volume, is hard to better.

The existence of sea-floor hydrothermal discharge was postulated by Solomon and Walshe (1979), and proved later in that year with the discovery (Francheteau et al., 1979) of active hydrothermal systems. These manifested as black smokers actively discharging on the East

Pacific Rise spreading-centre and was soon followed by the discovery of black smokers in back-arc spreading centres (Lau Basin) (Fouquet et al., 1991). Since these discoveries, VHMS deposits as a class have been thoroughly researched with numerous individual papers, plus many summary volumes (e.g. Franklin et al., 1981; Large, 1992; Barrie and Hannington, 1999). In the Kuroko volume, Ohmoto and Skinner, (1983) (and references therein), established a model for the formation of VHMS deposits. This model was succinctly described by Lydon (1984, 1988) and refined by later researchers (Galley, 1993; Hannington et al., 1995; Galley et al., 2005). The model is summarised in Franklin et al. (2005) as having 6 main elements. These are: 1) a heat source to drive the hydrothermal system and possibly contribute some metals; 2) a high-temperature reaction zone that acts as a reservoir from which some metals are leached by interaction with evolved seawater; 3) synvolcanic faults that permit focused discharge from the reservoir; 4) footwall, and less commonly hangingwall, alteration zones produced by rock-fluid reaction involving the mixing of ascending hydrothermal fluid and ambient seawater; 5) the massive sulphide deposit itself, formed at or near the sea-floor; and 6) distal products which represent a hydrothermal contribution to background sedimentation, and in some places may reflect cooler satellite systems (e.g. Kalogeropoulas and Scott, 1983).

Some early researchers, (Hutchinson, 1973; Solomon, 1976; Franklin et al., 1981; Large, 1992) classified deposits on metal content (Cu/Pb/Zn) because such a scheme did not rely on interpretation (such as that of the tectonic environment), and could be used where only limited data was available. This scheme is still widely used. Franklin et al. (2005) group ancient VHMS deposits into five lithostratigraphic types, using sequence boundaries defined by major time-stratigraphic breaks, faults, or major (sub-volcanic) intrusions. This classification encompasses the scheme of Barrie and Hannington (1999) based on host-rock composition, as well as the deposit spectrum presented by Large et al. (2001). Franklin et al. (2005) describe the five types as: "(1) bimodal-mafic settings (e.g., Noranda, Urals) which occur in incipient-rifted supra-subduction oceanic arcs, typified by flows and <25 percent felsic strata; (2) mafic settings (e.g., Cyprus, Oman) which occur in primitive oceanic backarcs, typified by ophiolite sequences with <10 percent sediment; (3) pelite-mafic (e.g., Windy Craggy, Besshi) settings which occur in mature oceanic backarcs, typified by subequal amounts of pelite and basalt (including mafic sills); (4) bimodal-felsic (e.g., Skellefte, Tasmania) settings which occur in incipient-rifted supra-subduction epicontinental arcs, and typified by 35 to 70 percent felsic volcaniclastic strata; and (5) siliciclastic-felsic settings (e.g., Iberia, Bathurst) which occur in mature epicontinental backarcs, typified by continent-derived sedimentary and volcaniclastic strata". They further subdivide these five lithostratigraphic types on the basis of their occurrence in successions dominated by one of the three end-member lithofacies: flow, volcaniclastic, and sedimentary.

The shift over time from composition-based classification schemes to systems based on broadly defined geological settings reflects the better understanding of the processes that form VHMS deposits and their geological characteristics, which enable the formulation of meaningful exploration criteria. It is clear that there is still room for expansion of this classification, for instance to include ultramafic-hosted systems, which have recently been recognised in central eastern Russia (e.g. Ivanovka and Ishkinino deposits, southern Urals: Herrington et al., 2005; Nimis et al., 2008) and central western China (e.g, Derni deposit, Qinghai Province: Wang et al., 2000).

Questions Remaining

One of the important questions for exploration for VHMS deposits is how to improve the science of predicting their locations (Franklin et al., 2005). Why are these deposits located at specific time intervals during the evolution of submarine volcanic complexes? What does this time-stratigraphic restriction relate to? What processes are responsible? Is a specific phase in the evolution of an extensional rift required. How do we recognise these processes and can we establish predictive guidelines for them that could be useful for exploration?

Discussion

The discovery of the Jaguar deposit some 26 years after the initial discovery of VHMS mineralisation in the area suggests that there is huge potential for the discovery of additional deposits in the same belt, if successful tools can be developed to provide vectors to aid in the search. The belt encompasses many of the problems that have historically confounded Australian mineral discoveries: extensive cover, deep weathering, a lack of understanding of the nature of the geology, and insufficient understanding of the controls of formation. The results of my study are expected to help in the search for additional deposits in the greenstone belt by addressing some of these issues, in particular providing some lithogeochemical controls of the location of the Jaguar deposit, and to help to identify parts of the succession that may be prospective for as yet undiscovered ore deposits. The potential for such undiscovered massive sulfide deposits in the Teutonic Bore succession was a central motivator for the current study.

1.2 Aims of Thesis

The principal aims of this study were to:

- document the character and geometry of the volcanic and sedimentary facies;
- • develop a coherent lithological and compositional stratigraphy for the host succession;
- • document the relationship between volcanism and sulfide mineralisation using the
- mineralogy, textures, paragenesis, geometry and contact relationships;

- determine the geometry of the facies architecture of t • he Jaguar succession, and reconstruct the palaeovolcanological setting;
- determine if the deposit formed as a result of mound accumulation, sub-seafloor replacement, or some other mechanism;
- understand the temporal and spatial relationship between volcanism, sedimentation and the ore-forming hydrothermal system;
- establish the tectonic and paleovolcanic setting of depositional environment; and
- place the deposit and its immediate region in a global context.

1.3 Methods

At the start of this study the deposit was known only from diamond drillcore and the project has worked solely from that drillcore.

The objectives of this study were achieved through:

- detailed logging of 24 km of diamond drillcore with about 18 km of that concentrated in and around the Jaguar orebody, whereas the other 6 km of drillcore was from holes along strike and to the north;
- selected sampling of lithostratigraphic units;
- construction of twelve detailed geological cross-sections, graphic logs (at 1:200), facies analyses and interpretative facies architecture diagrams;
- detailed petrographic and textural studies on rocks of the host succession and massive sulfides using thin sections, polished thin sections and doubly polished thin sections; and
- whole rock, trace element and rare earth element geochemistry of least altered (and to lesser extent altered) host succession units.

1.4 Location, Access and Climate

The Jaguar VHMS deposit is located at latitude 28°26' south, 121°09' east, in the Leonora District of the north Eastern Goldfields, approximately 255 km north of Kalgoorlie, Western Australia (Fig. 1.1). Access is by way of Leonora, about 60 km north along the sealed Leonora - Leinster Highway, then about 2.5 km west by dirt road to the Jaguar mine site.

The topography is subdued and dominated by an outwash plain with minor low hills and ridges. The climate is described by the Australian Bureau of Meteorology (BOM) as desert, that is, hot and persistently dry, with hot dry summers and cold winters. The annual rainfall statistics from the BOM show an average of 235 mm, averaging 30 days per year that have ≥ 1 mm of rainfall, (<http://www.bom.gov.au/climate/averages/tables/cw_012046.shtm>).

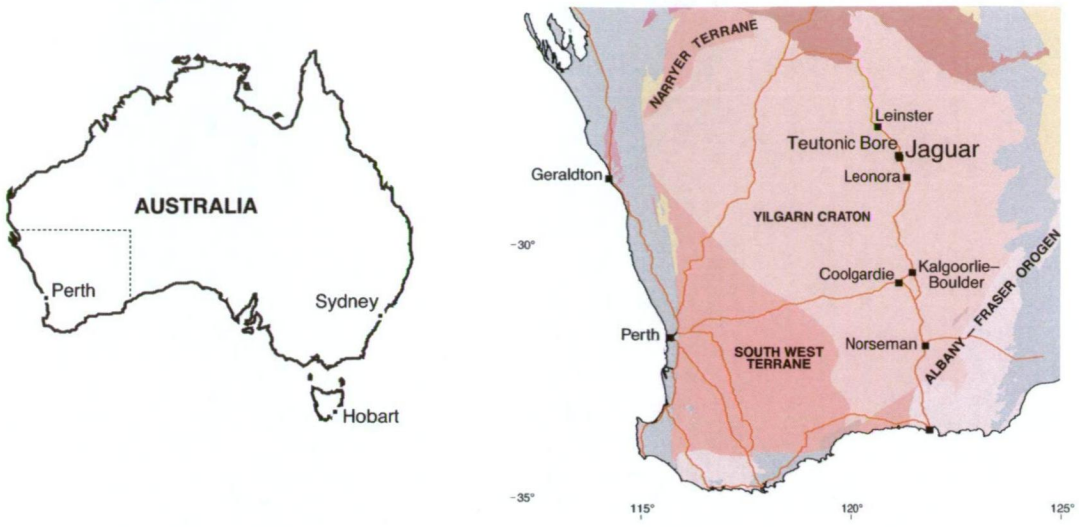

Figure 1.1 Location of the Jaguar VHMS deposit, and the large scale tectonic elements of the Yilgarn Craton.

1.5 Exploration History and Mining Status

In the early 1970s exploration for VHMS deposits commenced in the Eastern Goldfields region of the Archean Yilgarn Craton following the discovery of the Gossan Hill deposit at Golden Grove (Murchison District, Yilgarn Craton). Prospecting by Amax in 1973 in the general area located several pyritic gossans to the east in the footwall of the still to be discovered Teutonic Bore mine, and a stringer gossan (later the Warramboo gossan) was located to the south of Teutonic Bore, in an area to the north of Wendy Bore (Fig. 1.2). Warramboo Mining NL acquired the Wendy Bore property and promptly optioned the ground to Esso Exploration and Production Australia Incorporated which drilled several drillholes in 1975. Hole DDHWB-9 drilled into felsic volcanic units with minor sulfide mineralisation in an area now known to be the deep footwall to the Jaguar deposit.

The sub-cropping gossan over the Teutonic Bore VHMS deposit was discovered in 1975 by a joint venture between Carpentaria Exploration Company and Australian Selection during a program of reconnaissance mapping and surface sampling. Shallow percussion drilling in 1976 located a massive gossan which was then diamond drilled (Greig, 1984). The Teutonic Bore mine was developed as an open pit in 1979 and ceased production in 1984.

In 1979 Aquitaine acquired and drilled the Wendy Bore property and discovered zinc and copper sulfide mineralisation beneath the renamed Warramboo gossan. By the mid eighties the economic climate had changed and exploration for VHMS style mineralisation virtually stopped.

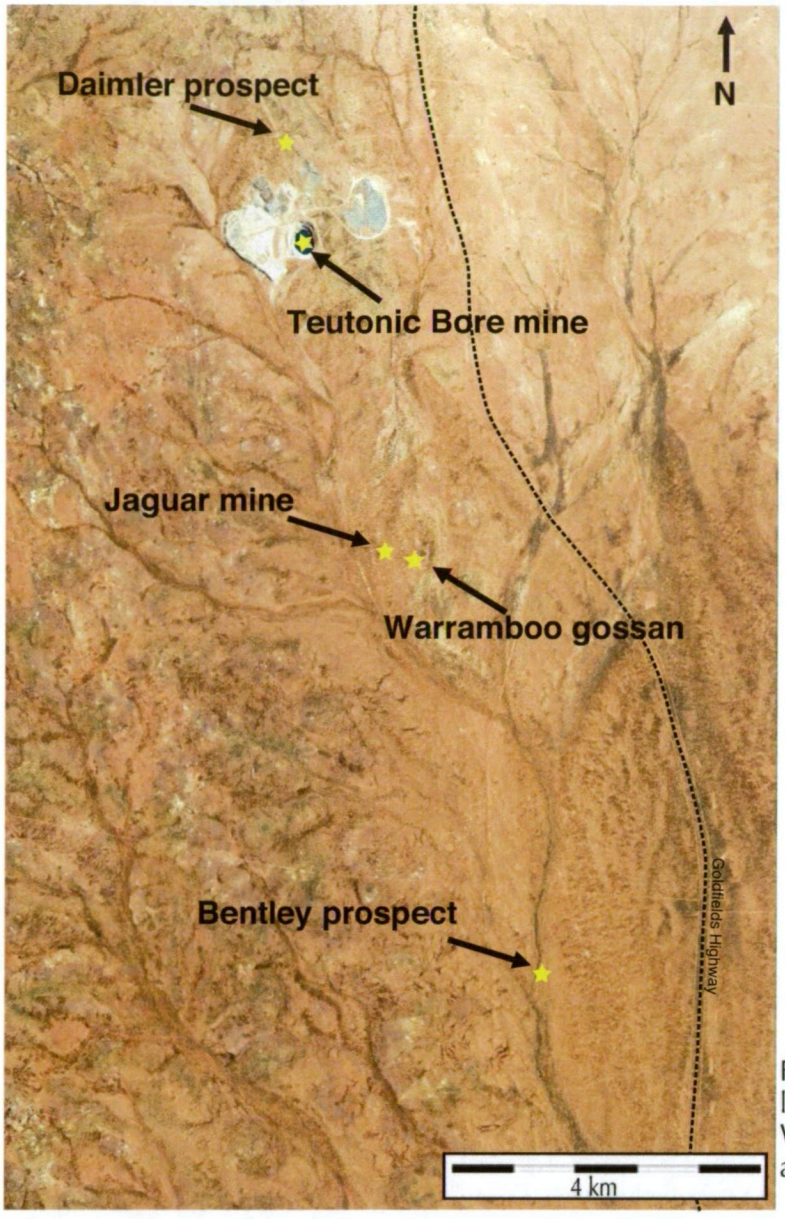

Figure 1.2 Mine and prospect locations in the vicinity of the Jaguar VHMS deposit. Based on 2005 aerial photograph.

1.5.1 Discovery

The Jaguar VHMS deposit is a blind geophysical discovery made by Inmet Mining Corporation, a Canadian company, in joint venture with the tenement holder, Jabiru Metals Ltd (then Pilbara Mining).

In 2001, Inmet carried out a fixed-loop transient electromagnetic (Deep EM) survey along strike and to the south of the Teutonic Bore mine. A strongly conductive zone was identified just west of the Warramboo gossan. In 2002, the second diamond drillhole that was drilled into this anomaly intersected massive sulfide. Follow-up drilling in the same year, defined the Jaguar VHMS deposit. At about this time Dr Garry Davidson (CODES) collaborated with Mr Peter Ellis (Pilbara Mining) to successfully apply for an ARC Linkage Grant which became the basis of support for this PhD research.

By the start of 2007, about 60 diamond drillholes, several with wedge intercepts had been drilled into the deposit and a Joint Ore Reserves Committee (JORC) compliant, probable reserve had been published (Jabiru Metals, 2006). The decline was commenced in 2006, mine development started in 2007 and first concentrate produced in mid-2007. No new mineralisation has been discovered in the immediate Jaguar environs since this time. In 2009 Jabiru Metals made a discovery at the Bentley prospect about 4 km south of Jaguar (Fig. 1.2). This is the focus of current exploration drilling.

1.6 Previous Studies

This study is the first work on the Jaguar orebody and the enclosing rocks.

Previous work that is directly related to the same succession is limited. It comprises published work on the Teutonic Bore orebody and gossan (Greig, 1984; Nickel, 1984; Vaasjoki, 1985), the geological setting of the Teutonic Bore deposit (Hallberg and Thompson, 1985; Hallberg and Giles, 1986). A rhyolite sample collected from diamond drillcore in the vicinity of the Teutonic Bore mine, provided a U-Pb SHRIMP age for the succession (2692 ±4 Ma; Nelson, 1995). A CSIRO compilation volume "Copper-zinc massive sulfide deposits in Western Australia" (McConachy and McInnes, 2004) included a summary of the geology of the Jaguar deposit (Ellis, 2004). A study on the vegetation and soil expression of the Jaguar deposit looked at the redistribution and transport of trace elements in the regolith above the deposit (Anand and Cornelius, 2004).

Current related work at the University of Western Australia includes a PhD study on the Geochemistry and petrogenesis of the Gindalbie Terrane, Eastern Goldfields, WA, from which some preliminary results have been published (Dickins et al., 2004; Dickins et al., 2006a; Dickins et al., 2006b). An ARC Discovery Project on The Early Evolution of the Earth System from Multiple Sulfur Isotope Records of Sediments and Seafloor Mineral Systems, commenced in 2008 supervised by Professor Mark Barley. Jaguar ore samples have been provided for inclusion in this study. The stratigraphic succession at the Jaguar VHMS deposit, was presented as a poster (Belford et al., 2010) at the 5th International Archean Symposium in Perth (September, 2010).

1.7 Thesis Organisation

This thesis comprises seven chapters. Chapter 1 introduces the main aims of the project and establishes a background for the subsequent chapters. Chapter 2 provides a synopsis of the regional geology and outlines the current interpretation of the tectono-stratigraphic setting and terrane boundaries. Chapter 3 is a descriptive analysis of individual lithofacies.

Chapter 4 documents the volcanic stratigraphy. Chapter 5 discusses the geochemistry of the host succession and the implications for the tectonic setting. Chapter 6 describes the sulfide mineralogy of the Jaguar orebody. Chapter 7 is a synthesis of the results and addresses the ore genesis and controls on formation plus makes a global comparison of Jaguar with other Archean deposits and districts.

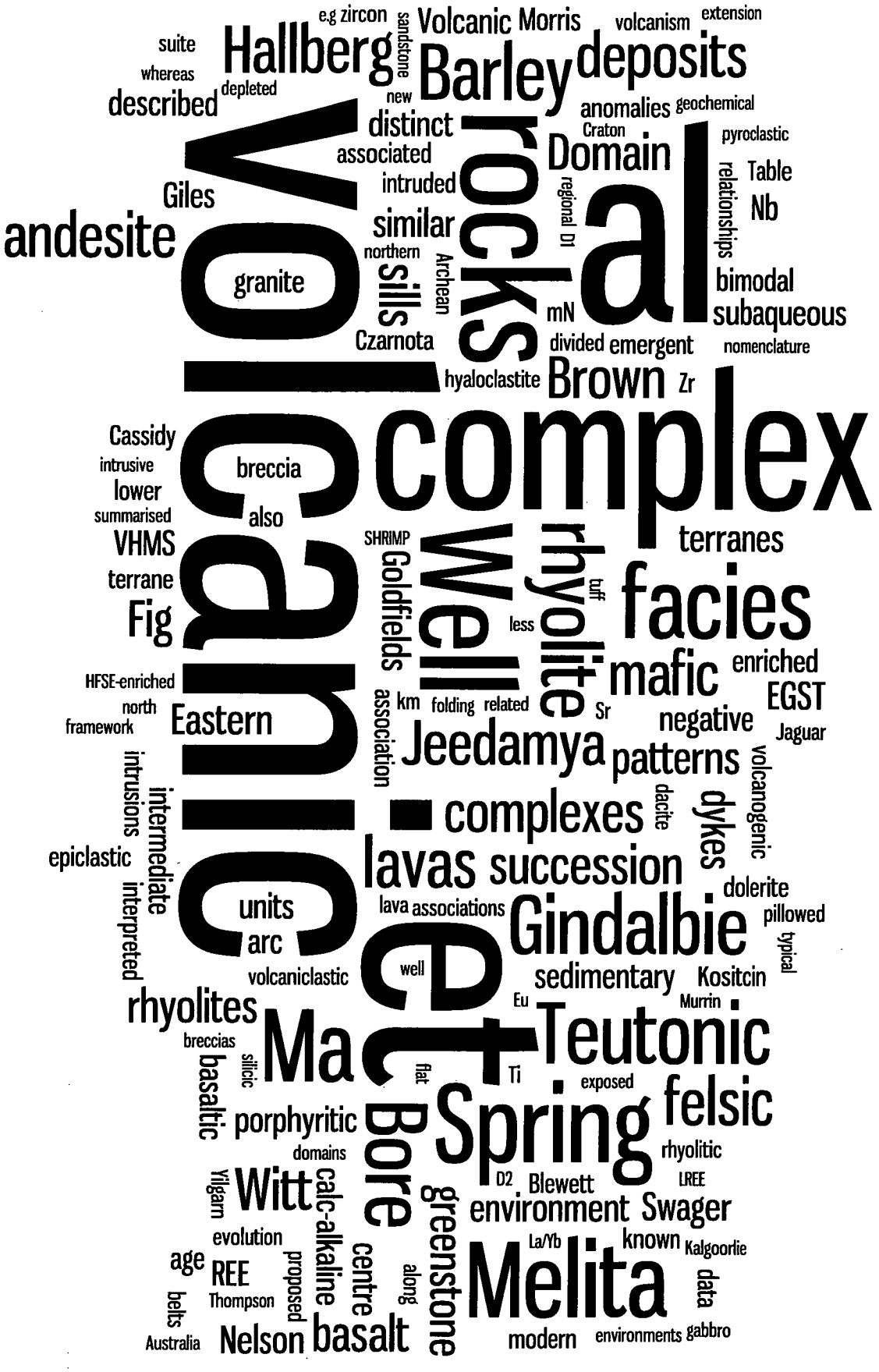
Volcanic
complex
Volcanic
Well
facies
Eastern
Jeedamya
complexes
lavas
succession
Gindalbie
Teutonic
Spring
Bore
Melita
Witt
Ma
Pt
rocks
al
Hallberg
Barley
deposits
Domain
andesite
Giles
granite
sills
Brown
rhyolite
mafic
Goldfields
Fig
VHMS
terrane
Cassidy
intrusive
lower
summarised
breccia
also
terranes
SHRIMP
tuff
less
enriched
EGST
Jaguar
negative
patterns
dykes
volcanogenic
dacite
km
folding
related
Sr
association
HFSE-enriched
north
framework
intrusions
intermediate
interpreted
epiclastic
units
arc
lava associations
dolerite
pillowed
typical
volcaniclastic
well
sedimentary
Kositcin
Murrin
Eu
rhyolites
breccias
basaltic
siliceous
porphyritic
domains
Ti
flat
exposed
felsic
rhyolitic
LREE
D2
Blewett
environment
Swager
greenstone
Yilgarn
calc-alkaline
evolution
La/Yb
known
Kalgoorlie
age
REE
Thompson
proposed
centre
along
data
belts
Australia
Nelson
basalt
modern
environments
gabbro
e.g zircon
sandstone
Volcanic Morris
volcanism
extension
suite
whereas
depleted
new
anomalies
geochemical
described
distinct
Craton
pyroclastic
associated
intruded
regional
D1
Table
relationships
Nb
similar
northern
Archean
bimodal
subaqueous
mN
Czarnota
divided
emergent
nomenclature
hyaloclastite
Zr

2. REGIONAL GEOLOGY

2.1 Introduction

In this chapter the establishment of geological framework of the Eastern Goldfields Superterrane is discussed. The greenstone belt geology is summarised, and the metamorphic evolution and the deformation history are outlined. The volcanic complexes of the northern Gindalbie Domain (Spring Well, Teutonic Bore, Melita and Jeedamya) are described and their chemistry is summarised. The Jaguar deposit is located in the Teutonic Bore volcanic complex. Lastly, the prospectivity of the Gindalbie Domain for VHMS is discussed, and known deposits are commented on.

2.2 Overview of the framework of the Eastern Goldfields Superterrane

The geological framework of the Eastern Goldfields region of Western Australia has undergone continuous reassessment since the initial subdivision of the Archean Yilgarn Craton into terranes[1] by Gee et al. (1981). The Yilgarn Craton was divided into two parts, an older gneiss terrain to the west and large areas of younger granite-greenstone terrain to the east. The granite-greenstone terrain was further subdivided into three provinces on the basis of lithostructural criteria. The recognition and division of distinct greenstone belts into stratigraphic associations (Hallberg 1985) was followed by the work of Swager et al. (1992) who divided the Kalgoorlie region into a number of terranes and further subdivided those terranes into domains. Subsequent mapping, combined with regional scale, U-Pb zircon geochronology by the Geological Survey of Western Australia, led to the recognition of fault-bounded terranes and domains in the greenstone belts of the Southern Eastern Goldfields, and the adoption of terrane and domain nomenclature (Swager, 1997).

A revised geological framework embracing the whole Yilgarn Craton, and incorporating new geophysical, geochemical, isotopic, and geochronological data (Cassidy et al., 2006), subdivided the craton into six terranes, the three easternmost of which form the Eastern Goldfields Superterrane (EGST)(Fig. 2.1).

The EGST comprises three tectono-stratigraphic terranes (Cassidy et al., 2006) defined on the basis of distinct volcanic facies, geochemistry, and age of volcanism. From southwest to northeast, these are the Kalgoorlie, Kurnalpi, and Burtville Terranes. Each terrane is divided into structurally bound domains that preserve dismembered parts of the succession,

1 As defined in Glossary of Geology (5th edition: Neuendorf et al., 2005). A terrane is a fault-bounded body of rock of regional extent, characterised by a geological history different from that of adjacent terranes. A domain is defined as a fault-bounded, geologically contiguous blocks within a terrane. A superterrane is defined as a grouping of related, adjacent terranes.

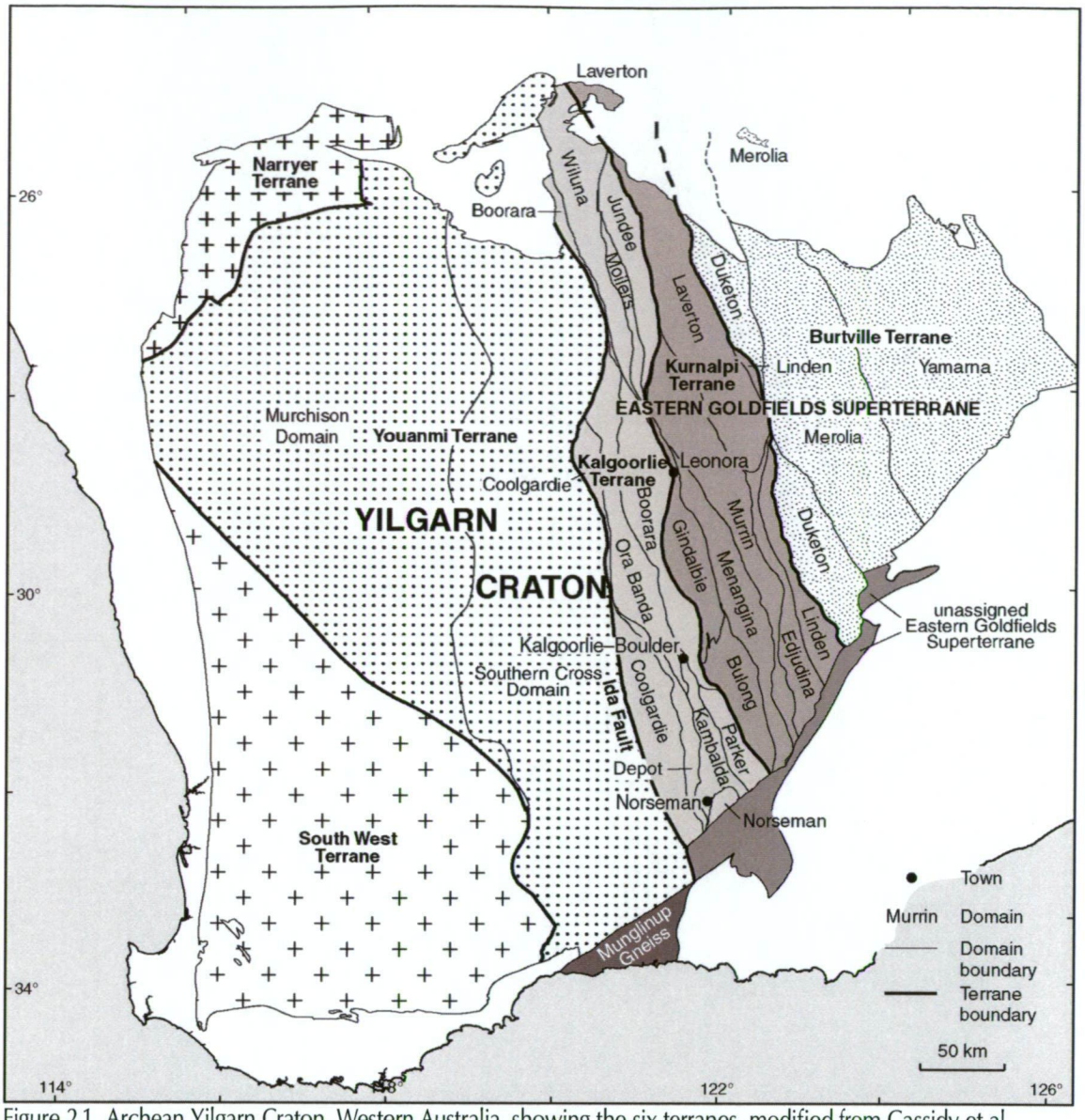

Figure 2.1 Archean Yilgarn Craton, Western Australia, showing the six terranes, modified from Cassidy et al. (2006).

and have locally distinct volcanic facies relationships. These terranes and domains are bound by interconnected fault systems which are defined by mapping and aeromagnetic and seismic data (Cassidy, 2004).

Archean greenstone evolution is a contentious field, and workers studying the Precambrian have yet to reach a consensus on the time of commencement, and nature of Archean plate tectonics (Rollinson, 2007). Recent workers in the Neoarchean greenstones of Western Australia belong to the group of greenstone belt researchers who tend to look for similarities between Archean greenstones and rocks in modern geotectonic settings, and use these similarities to construct a model for the evolution of the belts (Gee and Swager, 2008).

Recent work by Krapez and Barley (2008), Barley et al. (2008) and Krapez et al. (2008) presented an overall development model for the Eastern Goldfields greenstone terranes based on volcanological, geochemical and, in particular, detailed sedimentological

data. They proposed collision and accretion of different fragments of a volcanic arc to a continental margin that is today exposed as the eastern Yilgarn Craton. Whereas the major fault-system terrane boundaries of Cassidy et al. (2006) were accepted by Barley et al. (2008) and Krapez et al. (2008), the position of some boundaries, along with the change of status of some terranes to domains, was not. In contention were the positions of the Kalgoorlie and Kurnalpie terrane boundaries, and the existence of the Gindalbie Terrane as a distinct terrane. Barley et al. (2008) proposed a Gindalbie Domain that contained a number of felsic volcanic complexes that included the Spring Well complex (Fig. 2.2). Cassidy et al. (2006) included the Spring Well complex in their Murrin Domain.

For the purposes of this thesis, the boundaries and succession of the Gindalbie Domain are accepted as those of Barley et al. (2008) which are supported by recently published geochronology (Kositcin et al., 2008).

2.2.1 Greenstone Geology

The Meso- to Neoarchean EGST comprises elongate greenstone belts (Fig. 2.3) of deformed and metamorphosed volcanic and sedimentary rocks, intruded by granite batholiths (Barley et al., 2008). The separate greenstone terranes comprise volcanic and sedimentary rocks that were deposited between ca 2930 and ca 2650 Ma (Swager et al., 1992; Nelson, 1997; Cassidy et al., 2002), and were multiply folded, metamorphosed to low or medium greenschist facies, and intruded by granitoids at about 2680 – 2660 Ma (Champion and Cassidy, 2002). Towards the end of this history, they were subjected to major faulting along northerly to north-northwesterly trends (Swager, 1997; Blewett and Czarnota, 2007).

In the north Eastern Goldfields greenstone belts, there have been volcanological studies of the Spring Well complex (Giles, 1982), the Welcome Well volcanic complex (Giles and Hallberg, 1982), the Teutonic Bore volcanic complex (Hallberg and Thompson, 1985), and the Melita volcanic complex (Brown et al., 2002)(Fig. 2.2). Other studies concentrating on aspects of lithogeochemistry and geochronology, and comparisons of the complexes include Hallberg (1985), Hallberg and Giles (1986), Hallberg et al. (1993), Witt (1994), Morris and Witt (1997), Morris (1998), Brown et al. (2001), Messenger (2000), Brown et al. (2002), Groenewald et al. (2006), Barley et al. (2008) and Kositcin et al. (2008).

The Malcolm greenstone belt hosts three significant volcanic complexes, the Teutonic Bore volcanic complex (Hallberg and Thompson, 1985), the Jeedamya volcanic complex (Witt, 1994), and the Melita volcanic complex (Brown et al., 2002)(Fig. 2.2). Lack of outcrop separates these complexes, so the nature of the contact between them is unclear (Painter et al., 2003).

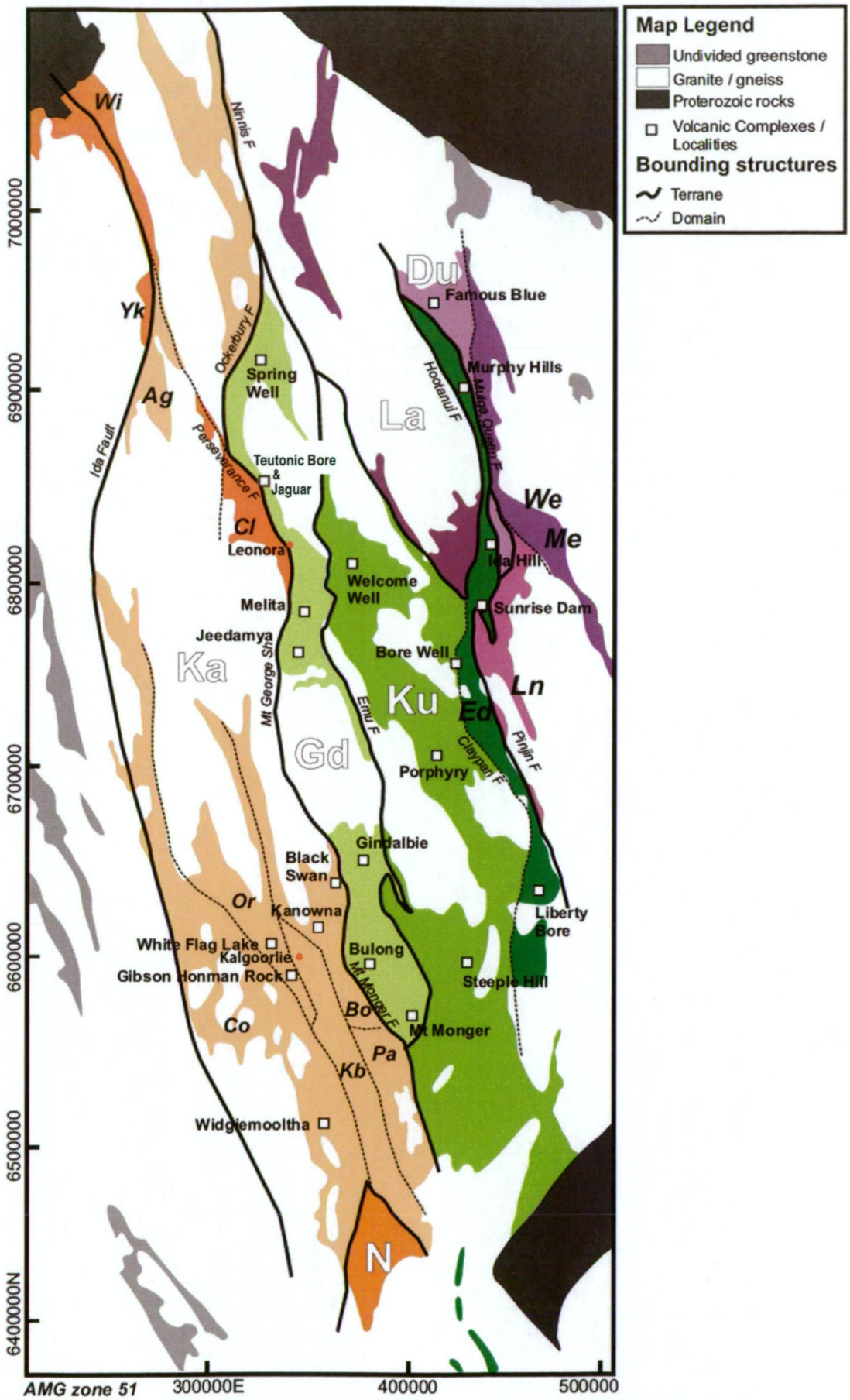

Figure 2.2 Eastern Goldfields Superterrane showing Gindalbie and adjacent terranes, modified from Barley et al. (2008). Terranes: Ka = Kalgoorlie, N = Norseman, Gd = Gindalbie, Ku = Kurnalpi, La = Laverton, Du = Duketon. Domains: Or = Ora Banda, Kb = Kambalda, Co = Coolgardie, Bo = Boorara, Pa = Parker, Ed = Edjudina, Ln = Linden, Me = Merola, We = Mt Weld, Cl = Clifford, Ag = Agnew, Wi = Wiluna

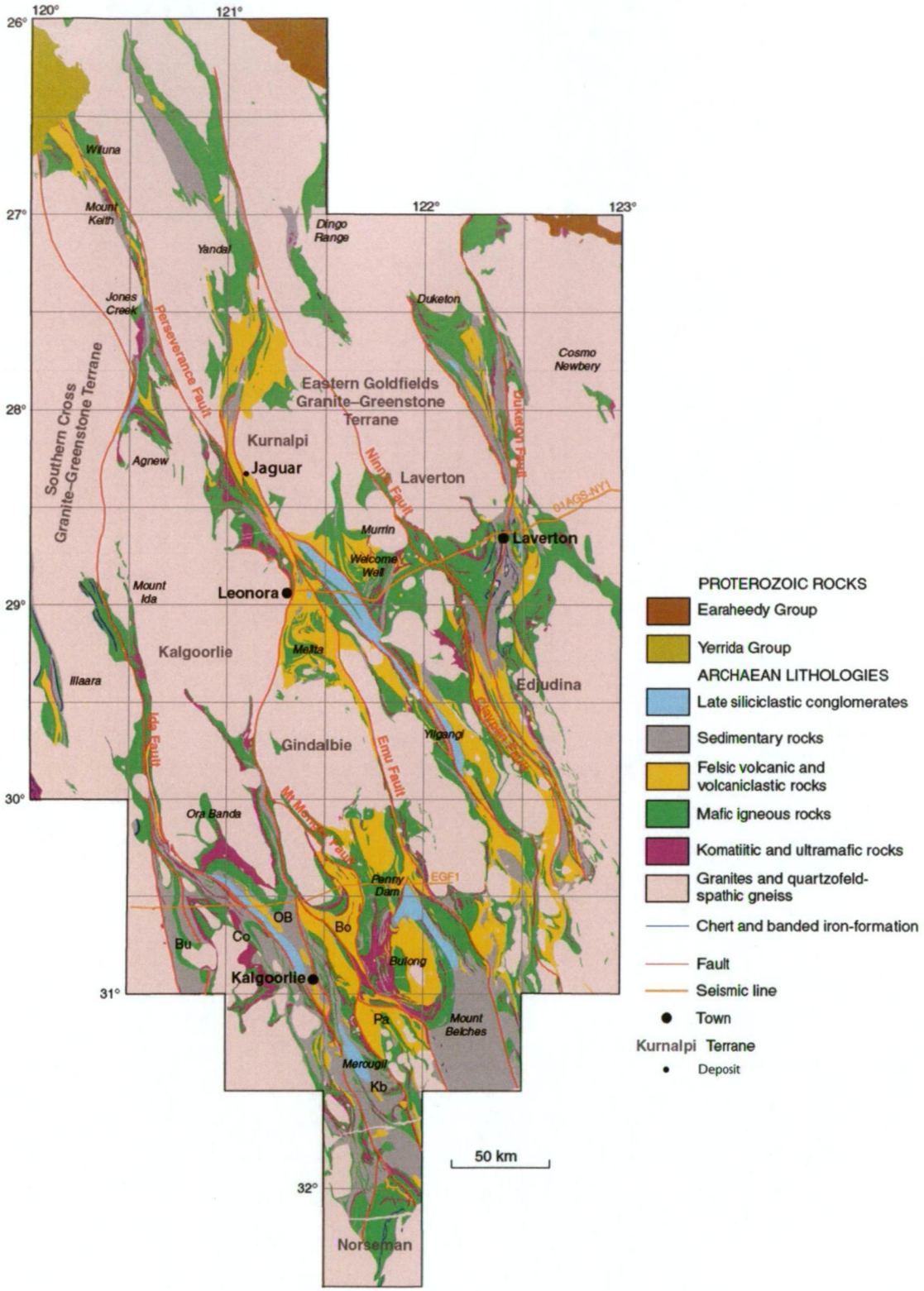

Figure 2.3 Eastern Goldfields, granite-greenstone terrane lithology map, after GSWA (2004).

2.2.2 Metamorphism

The metamorphic evolution of the EGST is constrained by geological relationships, relative garnet Lu-Hf chronology, absolute P-T calculations and a spatial database of metamorphic parameters (Goscombe et al., 2007). The post-2720 Ma thermo-barometric evolution is divided into 5 broad periods of contrasting metamorphic style, conditions, and possible mechanical/tectonic setting (Fig. 2.4). Goscombe et al. (2007) contended that unlike stress fields, thermal event switching involves slow rates, conductive delays, and a more continuous history than the structural evolution, necessitating broad thermal events and continuums between them.

The five periods can be summarised as follows (Goscombe et al., 2007):

Ma = rare, high-T, high-G (G= geothermal gradient), arc related metamorphism (2720-2685 Ma)
M1 = discrete, medium-P, low-G metamorphism (2720-2685 Ma)
M2 = granite pervaded, moderate-G, regional metamorphism (2685-2665 Ma)
M3a = extension related, high-G metamorphism (2665-2650 Ma)
M3b = fault kinematics, high-G alteration and Au-mineralisation (2650-2620 Ma)

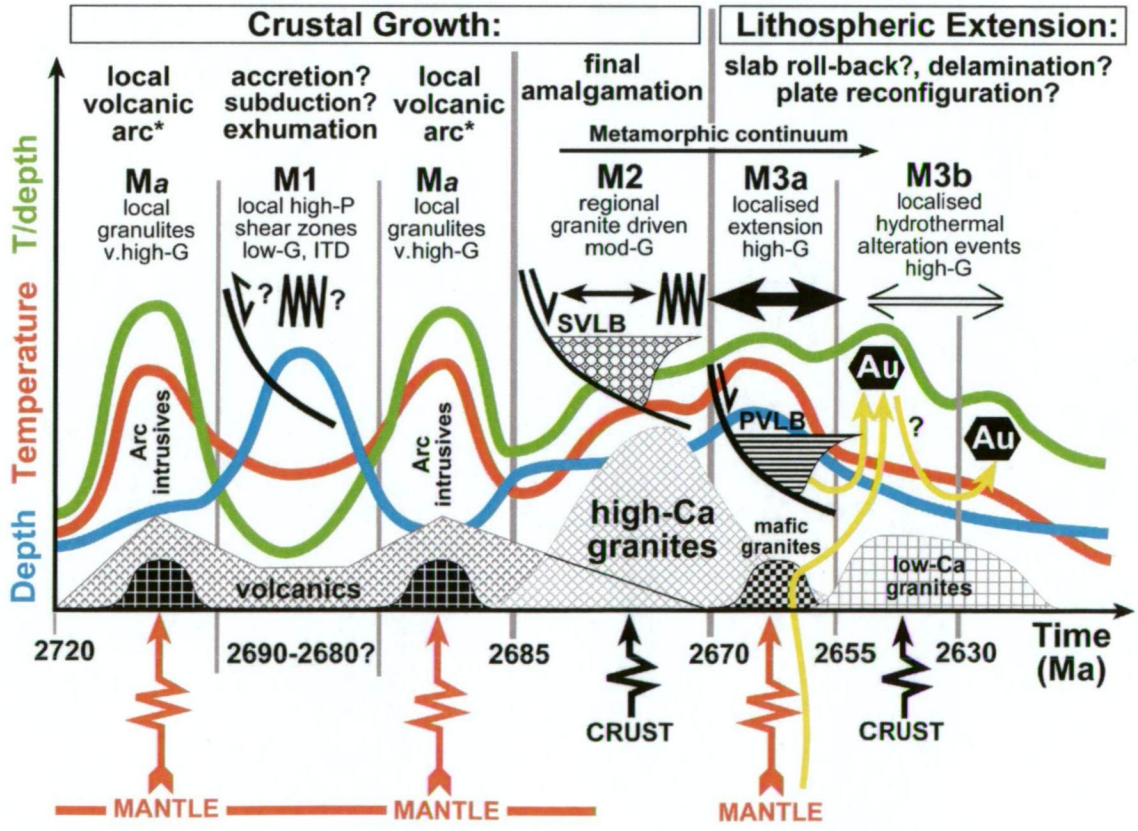

Figure 2.4 The post-2720 Ma thermo-barometric evolution of the EGST, after Goscombe et al.(2007). SVLB - syn-volcanic late basins, PVLB - post-volcanic late basins. G = geothermal gradient.

2.2.3 Deformation

Swager (1997) described a 'D1' to 'D4' nomenclature for the EGST based on 10 years of extensive mapping and the recognition of structural repetition in greenstones by workers such as Archibald et al. (1978). This deformation terminology is summarised as: 1) early 'D1' recumbent folding and thrusting during north-south shortening, followed by 2) east-west shortening through large-scale upright 'D2' folding and thrusting, then 3) sinistral strike-slip 'D3' faulting along north-northwest oriented structures with associated folding, followed by 4) continued regional 'D4' transpressive dextral oblique and reverse faulting along north to north-northeast oriented faults. This scheme acknowledged the likely existence of extensional events as proposed by some workers (e.g. Hammond and Nisbet, 1992).

A new, sevenfold (D1 to D7) deformation nomenclature based on kinematic analysis and cross cutting relationships was developed by Blewett and Czarnota (2007) and built on the early work of Swager (1997):

D1: long-lived extension and granite-greenstone formation
D2: termination of an arc and ENE-WSW contraction
D3: extensional granite doming, mafic granites and late basin formation (2 stages)
D4: Sinistral transpression
D5: dextral transtension and crustal melting
D6: low-strain systemic collapse
D7: Proterozoic contractional events

Table 2.1 shows the correlation between the long-used nomenclature of Swager (1997) and that proposed by Blewett and Czarnota (2007).

Table 2.1 The correlation between the nomenclature of Swager (1997) and Blewett and Czarnota (2007)

Deformation correlation from central Eastern Yilgarn			
		Blewett & Czarnota, 2007	Swager, 1997
Minor extension		D6	Collapse
Dextral strike-slip		D5	D4
Sinistral	NW-SE local compression	D4b	D3
Transpression	Late Basin upright folding	D4a	D2
Extensional	Stage 2 Late Basins	D3b	DE
doming	Stage 1 Late Basins	D3a	
Upright folding and reverse faulting		D2	D2
Extension with intermittent compression		D1	DE

2.2.4 An Integrated Tectonic Framework

A new integrated tectonic framework for the EGST was proposed by Blewett and Czarnota (2007) and incorporated a decade of new geochronology, geochemistry, isotope studies, stratigraphy, deep seismic profiles, 3D models and structural mapping from various Geoscience Australia, Geological Survey of Western Australia, AMIRA and pmd*CRC projects. This integration was summarised in a figure reproduced here as Figure 2.5.

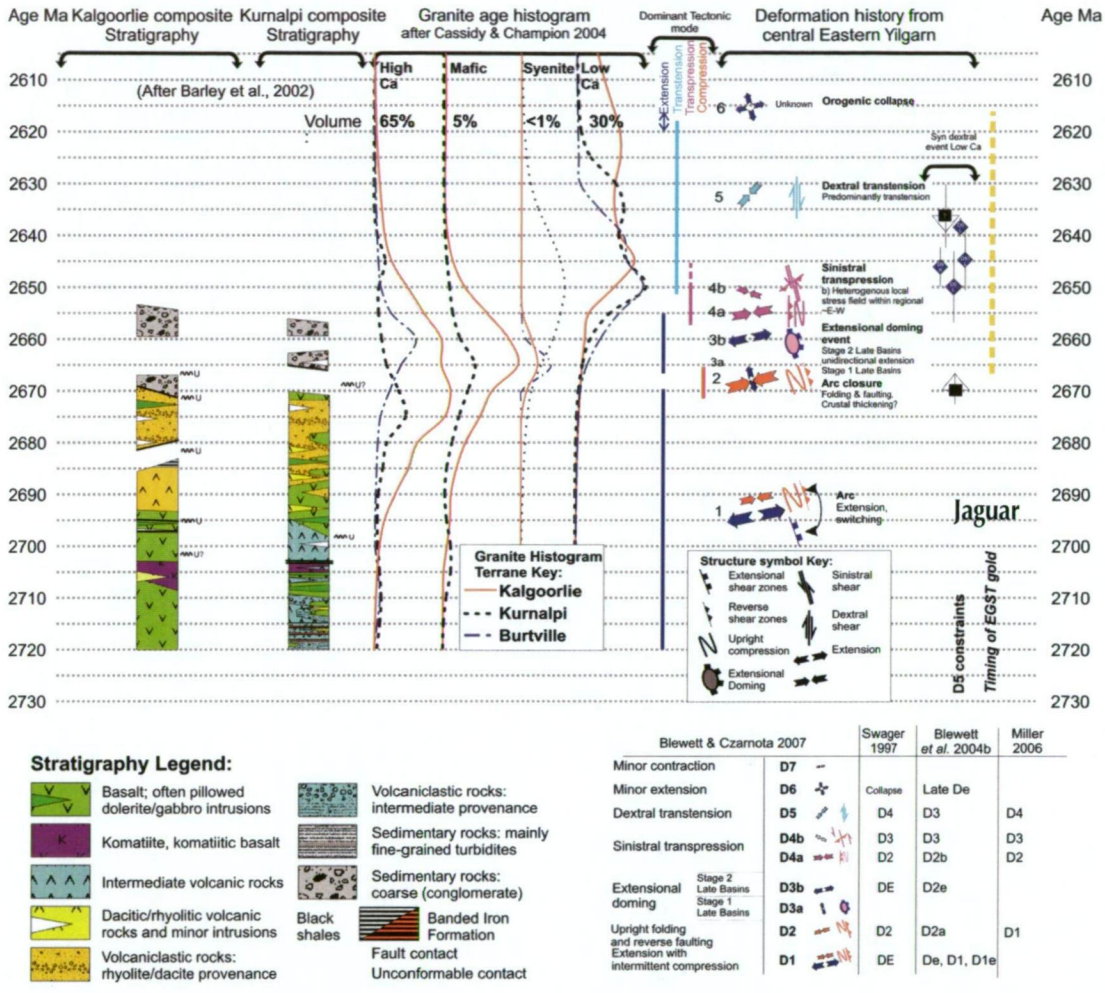

Figure 2.5 Geodynamic synthesis of the Eastern Goldfields Superterrane, after Blewett and Czarnota (2007)

The regional geodynamic synthesis for the central EGST (Fig. 2.5) (Blewett and Czarnota, 2007) implies that deposition of the Jaguar succession at ca 2690 Ma, took place in a period of arc building in a east-northeasterly directed extension-dominated regime. The first significant contraction terminated volcanism, and involved shortening oriented east-northeast, perpendicular to the grain of the earlier extensional orogen. This shortening was followed by significant granite doming accompanied by the development of high-strain shear zones around the major granite-dome margins.

The EGST was subsequently deformed by a series of long-lived extensional stages associated with granite emplacement, interspersed with short-lived contractional events.

2.3 Gindalbie Domain

The Gindalbie Domain (Fig. 2.2) is defined by High Field Strength Element (HFSE)-enriched bimodal (basalt–rhyolite) volcanic complexes (Melita and Teutonic Bore) and calc-alkaline intermediate–silicic volcanic rocks (Spring Well and Jeedamya), both associated with quartz-rich sedimentary rocks, mafic sills and layered mafic complexes (Barley et al., 2002a; Barley et al., 2002b; Barley et al., 2008), that range in age from 2694 ± 4 Ma to 2676 ± 5 Ma (Nelson, 1995; Nelson, 1996; Nelson, 1997a; Nelson, 1997b; Brown et al., 2002; Kositcin et al., 2008). Collectively, the volcanic and sedimentary rocks that make up the Gindalbie Sequence (Barley et al., 2008) are shown in Table 2.2. More detailed descriptions of the Spring Well, Teutonic Bore, Melita and Jeedamya volcanic complexes in the northern section of the Gindalbie Domain follow. The Spider Well and Garden Well intrusive complexes are not described in any published literature and the volcanic complexes in the southern half of the terrane are not considered here.

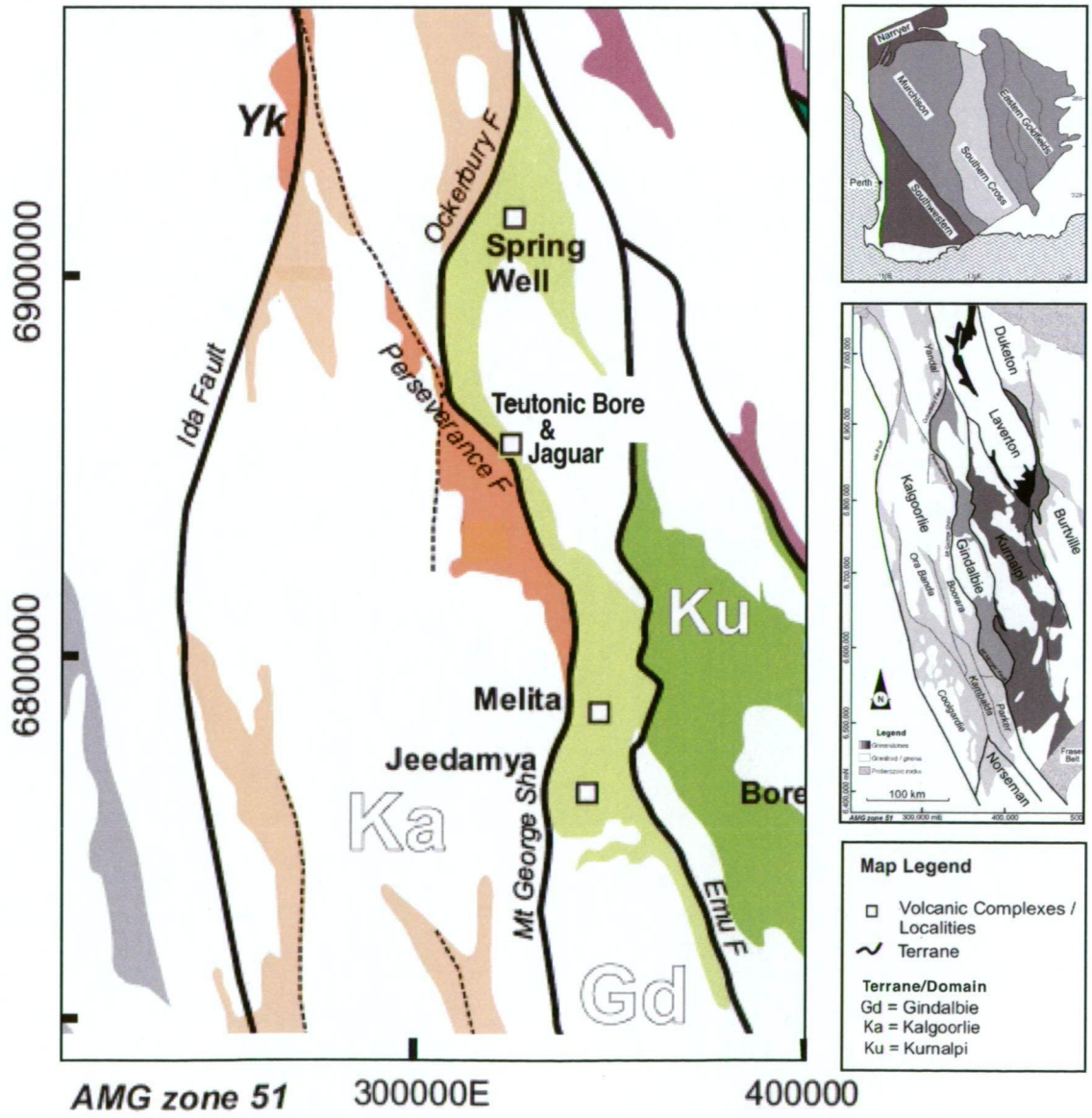

Figure 2.6 The Gindalbie Domain showing the centres of the volcanic complexes, after Barley et al. (2008).

The Gindalbie Domain is bounded to the west by structures associated with the Ockerbury Fault, the Mt George Shear, the Moriarty Shear, and the Mt Monger Fault. The eastern boundary is less well-defined due to structural overprinting, but probably coincides with sections of the Emu and Keith-Kilkenny Faults (Barley et al., 2008).

Table 2.2 Summary of volcanic and sedimentary facies of the Gindalbie Sequence; from Barley et al. (2008). Table superscripts: a Giles (1982); b Barley et al.(1998); c Crozier (1999); d Kositcin et al.(2008); e Nelson (1997a); f Brown et al.(2002); g Hallberg and Thompson (1985); h Nelson (1995)

Volcanic Complex/ locality	1:100,000 Map-Sheet (MGA)	Major Lithologies	Volcanic facies and environment
Spring Well [a-c] 2694 ± 4 Ma [d] 2690 ± 6 Ma [e]	Darlot 318,880 mE 6,911,230 mN	Calc-alkaline basaltic andesite to andesite, and dacite-rhyolite lavas, associated breccias; abundant microdioritic sills and dykes; subordinate volcanogenic conglomerate, sandstone, and shale; high Sr/Y andesite and lamprophyre dykes.	*Coherent facies*: andesite, dacite and rhyolite lavas; subordinate basalt; microdiorite sills, dolerite, porphyritic andesite dykes. *Volcaniclastic facies*: coarse-grained intermediate hyaloclastite and autobreccia, volcanogenic mass-flow breccia, cross-bedded sandstone, bedded tuff, locally pillow breccia. *Volcanic environment*: proximal-medial facies of a subaqueous to emergent felsic calc-alkaline volcanic centre; possibly marginal intra-arc or backarc environment.
Melita Complex [b] 2683 ± 3 Ma [b,f]	Melita 348,840 mE 6,784,860 mN	Tholeiitic basalt and basaltic andesite lavas, pillowed basalt, mafic hyaloclastite, porphyritic quartz-feldspar phyric rhyolite, rhyolite breccia, felsic and mafic volcanogenic sandstone, chert, dolerite and gabbro sills.	*Coherent facies*: pillowed to massive basalts, flow-banded rhyolite lavas, domes and shallow intrusions, dolerite and gabbro sills, lamprophyre dykes *Volcaniclastic facies*: mafic and felsic hyaloclastite, autobreccia and resedimented breccia (debris-flow deposits); resedimented volcanogenic sandstone and vitric tuff (debris-flow deposits, turbidite, water-lain tuff). *Volcanic environment*: proximal-medial facies of a subaqueous to emergent bimodal volcanic centre; similar facies to modern intra-arc and rifted-arc environments.
Jeedamya Rhyolite 2681 ± 5 Ma [e]	Melita 336,140 mE 6,752,460 mN	Porphyritic rhyolite and rhyodacite, felsic volcanogenic sandstone and breccia, basalt, dolerite.	*Volcanic environment*: proximal to medial facies of a subaqueous to emergent calc-alkaline volcanic centre.
Teutonic Bore [g] 2692 ± 5 Ma [h]	Weebo 318,440 mE 6,856,160 mN	Andesite, pillowed basalt, volcaniclastic rocks, porphyritic rhyolite, and dolerite sills.	*Volcanic environment*: proximal-medial facies of a subaqueous to emergent bimodal volcanic centre. Similar facies to modern intra-arc and rifted arc environments.
Garden Well (intrusive ages only)	Weebo 317,040 mE 6,867,860 mN	Porphyritic rhyolite, alkali-feldspar granite, diorite, gabbro	*Intrusive complex*: subvolcanic igneous intrusions, fine-grained and granophyric phases indicate shallow emplacement.
Spider Well ~ 2690 Ma	Weebo 310,140 mE 6,880,560 mN	Poorly exposed; porphyritic rhyolite and medium-grained granitoids.	*Intrusive complex*: subvolcanic intrusions, fine-grained and granophyric phases indicate shallow emplacement, and possible extrusive equivalents.
Gindalbie 2680 ± 4 Ma [d] 2676 ± 4 Ma [d]	Gindalbie 379,440 mE 6,643,860 mN	Weathered and schistose basaltic, intermediate and felsic volcanic rocks; polymictic conglomerate containing basalt and porphyry clasts.	*Volcanic environment*: proximal-medial facies of a subaqueous to emergent bimodal volcanic centre; exposure is not sufficient for detailed facies analysis.

The contact relationships between the volcanic complexes, all of which developed over an 18 million-year period, have not been observed and the relationships among them are not well understood. Witt (1994) interpreted the Jeedamya rhyolite to represent a more distal volcanic association compared to that represented by the Melita volcanic complex without implying that the rocks were derived from the same volcanic centre.

A summary of the Gindalbie sequence based on Barley et al. (2008) follows. Proximal volcanic facies comprise intermediate to silicic lavas and high-level intrusions, coarse-grained volcanic breccias and subaqueously deposited volcanogenic sandstones, commonly intruded by mafic to intermediate sills and dykes. Mafic volcanic rocks also include

massive to pillowed lavas and coarse-grained hyaloclastite, and are intercalated with felsic volcanic rocks in the Melita volcanic complex. More distal environments are indicated by cm- to mm-bedded volcanogenic turbidites interbedded with black shale. Volcanic and sedimentary facies indicate subaqueous to emergent conditions during volcanism. However, the observed successions include only subaqueously erupted or subsequently deposited facies preserved. HFSE-enriched granite and porphyries are spatially associated with bimodal and subalkaline volcanic complexes (e.g. Kookynie Granite), and have been interpreted as coeval plutons (Hallberg, 1985; Champion and Sheraton, 1997).

2.3.1 *Spring Well volcanic complex*

The Spring Well volcanic complex (Fig. 2.6) was described by Giles (1982) as a relatively unaltered and well exposed Archean felsic volcanic centre that is preserved in a synclinal structure at the top of the local greenstone succession. Subaerial silicic ignimbrites and subordinate lavas, intruded by anastomosing intermediate-silicic dykes and sills, comprise the near-vent facies. Away from the centre, subaqueous crystal tuff and other tuff units are intercalated with epiclastic sedimentary rocks. Giles (1982) interpreted the complex to be within the core of a tight north-plunging syncline, the axis of which passes through a folded layered mafic sill 8 km north of Spring Well. The recognition of finely laminated black shale interbeds and rhyolitic hyaloclastite (Messenger, 2000) suggests that the succession was at least partly submarine.

Barley et al. (2008) described the Spring Well volcanic complex as dominated by andesite and basaltic andesite lavas and sills, and epiclastic rocks. East of Spring Well, exposures are entirely made up of those lithologies, whereas to the west and southwest, rhyolitic and dacitic lavas and related epiclastic rocks intruded by basaltic-andesite sills are dominant. Sedimentary structures in epiclastic units indicate that the succession youngs toward the west. There is an overall progression from andesite lavas and breccias at the base, to more silicic volcanic rocks and epiclastic rocks in the upper half of the succession. Facies associations vary markedly in thickness along strike. Coarse-grained andesite breccia units thicken from 150 m (north of Spring Well) to more than 600 m (south of Spring Well). Thick rhyolite and dacite lavas and monomictic breccias pinch out over short distances (hundreds of metres or less) along strike, either representing fault contacts or constructional lava domes that included thick aprons of autoclastic debris. Massive microdiorite may represent a subvolcanic intrusion, whereas aphyric andesite and bifurcating microdiorite sills are common throughout the complex and intrude all associations. The estimated stratigraphic thickness is about 3 km. Barley et al. (2008) interpreted these volcanic facies associations and environments as typical of the central (proximal) facies of an emergent arc volcanic complex.

A crystal-rich rhyolite from the Spring Well volcanic complex produced a SHRIMP zircon age of 2690 ± 6 Ma (Nelson, 1997a). This rock was interpreted by Kositcin et al. (2008) as either a sub-volcanic sill or lava. A separate sample of porphyritic rhyolite has given a SHRIMP zircon age of 2694 ± 4 Ma (Kositcin et al., 2008). A sample from one of the porphyritic andesite dykes that produced an age of 2666 ± 7 Ma, indicating that the dykes were intruded at least 20 million-years after volcanism at Spring Well.

2.3.2 Teutonic Bore volcanic complex

The Teutonic Bore volcanic complex (Fig. 2.6), which hosts the Jaguar and Teutonic Bore massive sulfide deposits, comprises pillowed basalt, overlain by and interlayered with quartz-rich volcaniclastic units and coherent rhyolite. All units are intruded by sills and dykes of dolerite and gabbro that locally contain xenoliths of felsic volcanic rock. The succession is spatially and temporally associated with high-level intrusions of syenogranite and alkali-feldspar granite, which are also compositionally similar to the rhyolites (Hallberg and Thompson, 1985). Rhyolitic volcanic rocks are both underlain and overlain by mafic pillow lavas and interdigitate with them, forming a distinct bimodal basalt-rhyolite association (Hallberg and Giles, 1986).

Hallberg and Thompson (1985) described the oldest rocks in the succession as porphyritic, amygdaloidal andesite lavas and breccias. Although contact relationships cannot be observed, these calc-alkalic intermediate rocks that form the base to the bimodal volcanic succession at Teutonic Bore are interpreted to correlate with the Spring Well complex to the north, an inference supported by petrographic and compositional similarity. No estimation of the stratigraphic thickness in the Teutonic Bore area was attempted because of the presence of major structures and the voluminous amount of intrusions present.

Porphyritic dacite from the Teutonic Bore volcanic complex has a SHRIMP zircon age of 2692 ± 4 Ma (Nelson, 1995).

2.3.3 Melita volcanic complex

The Melita volcanic complex (Fig. 2.6), regarded as the best preserved volcanic eruption centre in the Eastern Goldfields (Witt, 1994; Morris and Witt, 1997) comprises rhyolitic pyroclastic units, and minor amounts of dacite lavas. Felsic rocks are interleaved with basalt. Poorly sorted, massive deposits were attributed to pyroclastic flows. Well-bedded, accretionary lapilli tuffs represent fall deposits, some of which have been subaqueously reworked (Morris and Witt, 1997).

A redefinition of the Melita volcanic complex (Brown et al., 2002) included the intercalated volcanic, and intrusive mafic units previously excluded by Witt (1994) and Hallberg (1985).

Approximately 3 km of stratigraphy is exposed in the Melita area (Brown et al., 2002) which can be divided into a lower, mafic-dominated (1-1.5 km) and upper, felsic-dominated succession. The lower mafic succession is dominated by basaltic to basaltic andesite lavas (locally pillowed), hyaloclastite and pillow breccia; minor rhyolite/rhyodacite lava are also present. The upper 1-1.5 km is dominated by felsic volcaniclastic rocks, epiclastic rocks including mudstone, and rhyolite lava, interlayered with mafic lavas. No primary subaerial pyroclastic deposits were identified, although subaerial explosive activity is indicated by the occurrence of accretionary lapilli and the abundance of relict shards and pumice fragments in resedimented deposits. Dolerite and gabbro sills and dykes, which intrude throughout, comprise between a quarter and a third of the succession.

Basalt lavas occur throughout the Melita volcanic complex and are interbedded with all other units, indicating that basaltic volcanism continued throughout the development of the volcanic complex. Interflow sedimentary rocks comprising mm- to cm-thick, bedded siltstone, form planar to wedge-shaped units, and locally separate lava lobes up to tens of metres thick. Brown et al. (2002) divided the volcanic succession into four facies associations: 1) a mafic to intermediate lava association; 2) a resedimented felsic volcaniclastic association; 3) coherent rhyolite; and 4) a fine-grained sedimentary association.

Three rhyolite samples from the Melita volcanic complex dated by SHRIMP zircon produced a weighted mean age of 2683 ± 3 Ma (Brown et al., 2002).

2.3.4 *Jeedamya volcanic complex*

The Jeedamya volcanic complex, south of the Melita volcanic complex, is less well exposed than the Melita volcanic complex. According to Witt (1994), it consists of rhyolitic to rhyodacitic pyroclastic rocks, related epiclastic rocks, and minor amounts of felsic porphyry, basalt, and dolerite. Hallberg (1985) maintained that many of these felsic rocks were intrusive, but Witt (1994) recorded widespread m-scale compositional and textural banding (bedding) and fragmental textures. Brown et al. (2001) described the Jeedamya volcanic complex (Fig. 2.2) as a calc-alkaline intermediate-silicic complex consisting predominantly of rhyolitic to rhyodacitic pyroclastic and volcaniclastic rocks.

A sample of porphyritic dacite from the Jeedamya volcanic complex has a SHRIMP zircon age of 2681 ± 5 Ma (Nelson, 1997a).

2.4 Geochemistry of the northern Gindalbie Domain

Although it is desirable to present equivalent geochemical data from the volcanic complexes that make up the northern portion of the Gindalbie terrane, the limited published research data precludes this. Comparisons among volcanic complexes and with the Teutonic Bore data presented in this thesis are discussed here later in Chapter 5.

2.4.1 Spring Well volcanic complex

The Spring Well basaltic andesites show geochemical patterns that are typical of modern calc-alkaline island arc basalts, such as decoupling between Light Ion Lithophile Elements (LILE) and HFSE, enrichment of LILE relative to normal MORB, peaks at Ce–P and Sm, and troughs at Ta–Nb and Zr (Messenger, 2000). Chondrite-normalised REE patterns are also typical of modern calc-alkaline island-arcs and Light Rare Earth Element (LREE) are enriched up to 100 x chondrite. The degree of enrichment in Sr, Ba, K and LREE is more similar to modern high-K island-arc basalts.

The Spring Well suite shows systematic variations from basaltic andesite to high-silica rhyolite, suggesting a cogenetic differentiation trend. The Spring Well andesites and microdiorite sills have elevated LILE relative to HFSE, and moderate negative Nb, Ta, Sr and Ti anomalies. Spring Well rhyolites have similar MORB and chondrite-normalised patterns to Spring Well andesites and are generally more enriched in LILE, LREE, Zr and Y, and have more pronounced negative Eu and Ti anomalies. The rhyolites have low Sr/Y and relatively flat REE patterns [(La/Yb)N = 4.2–5.0].

Kositcin et al. (2008) concluded that a series of porphyritic andesite dykes were distinct from the calc-alkaline Spring Well lavas. They displayed a Heavy Rare Earth Element (HREE) depletion, more typical of the high-Ca (± mafic) granitoid series, (see also Fig. 2.4).

2.3.2 Teutonic Bore volcanic complex

Hallberg and Giles (1986) compared the rhyolites and dacites from the Teutonic Bore complex with those of the Spring Well volcanic complex. The Teutonic Bore rocks are enriched[2] in Nb, Y, Zr, K, Rb and REE, and tend to be lower in Al and Ca, whereas Ba, Fe, Mg and Sr contents are similar. REE patterns exhibit a distinct negative Eu anomaly (Hallberg and Giles, 1986; Hallberg et al., 1993).

Geochemical studies of the dolerites, gabbros, basalts and felsic volcanic rocks in the Teutonic Bore volcanic complex (Dickins et al., 2006) identified two distinct groups: a group with LREE enrichment (the HFSE-enriched suite) and an older group characterised

2 No absolute values are given in the paper.

by flat REE patterns (the tholeiitic suite). The HFSE-enriched felsic volcanic rocks also display a large negative Ti anomaly on primitive mantle-normalised multi-element plots and are highly enriched in all incompatible elements, whereas the tholeiitic group does not display a negative Ti anomaly and is not enriched in incompatible elements. The raw data are yet to be published (Cathy Dickens, Univ. of WA PhD project). Sm-Nd isotope analysis of the HFSE-enriched suite yields εNdT values of -0.59 to +1.55, indicating a less depleted source. The tholeiitic suite yielded εNdT values of +1.09 to +3.27, indicating a more depleted source. Dickins et al. (2006) suggest the HFSE-enriched suite represents magmatism during a period of renewed extension, and are probably the result of melting of upwelling mantle that has been enriched by a previous episode of subduction, whereas the older tholeiitic rocks have come from a depleted mantle source.

2.4.3 Melita volcanic complex

Melita rhyolites have flat REE patterns ((La/Yb)cn = 4), and well developed negative Eu anomalies (Eu/Eu* 0.4–0.6), high Zr, Nb, Y, and low Sr (hence lower Sr/Y) (Morris and Witt, 1997).

Brown et al. (2002) classified the felsic volcanic rocks at Melita as dacite to high-silica rhyolite. They are enriched in HREE and HFSE (Zr, Nb and Y) and have positive Th and U anomalies, flat REE patterns, and moderate negative Nb, Ta and Eu anomalies where normalised to primordial mantle; Ti and Sr are strongly depleted.

On chemical grounds, the mafic rocks are genetically unrelated to the felsic volcanic rocks (Morris and Witt, 1997). The andesites have LREE-enriched patterns ((La/Yb)cn = 4-11) and La up to 100 x chondrite. When normalised to primordial mantle, basalt samples from Melita yield relatively flat trace element patterns, they show slightly to moderately negative Nb and Ta anomalies and little or no Ti depletion (Brown et al., 2002). The gabbros and dolerites are geochemically similar to the extrusive rocks and have similar primordial mantle-normalised patterns, suggesting the intrusive and extrusive rocks are co-genetic.

2.4.4 Jeedamya volcanic complex

Witt (1994) reported rhyolites at Jeedamya to be more plagioclase- and hornblende-rich and quartz-poor than rhyolites from the Melita complex. Jeedamya REE patterns are steeper than those of Melita rhyolites, ((La/Yb)cn from 7-8). They have lower HREE, well developed negative Eu anomalies (Eu/Eu* 0.4–0.6), high Zr, Nb, Y, and low Sr (hence lower Sr/Y) (Morris and Witt, 1997). Brown et al. (2002) concluded that the Jeedamya rhyolites are compositionally distinct from Melita rhyolites, being typically less evolved, and with lower concentrations of incompatible elements (Zr, Nb, La, Ce and Y). Barley et al.

(2008) described them as similar to rhyolites from the calc-alkaline Spring Well volcanic complex.

Jeedamya basalt is LREE depleted ((La/Yb)cn from 0.7-1.1) (Morris and Witt, 1997).

2.5 Tectonic Setting

The Spring Well volcanic complex is interpreted to occupy the northern preserved portion of the primary arc, remnants of which now extend south through Teutonic Bore to the Melita and Jeedamya volcanic centres (Messenger, 2000). South of Spring Well, volcanic sequences become distinctly bimodal (basalt and high-silica rhyolite) suggesting an increasing influence of arc extension toward the south.

The following interpretation of the tectonic setting of the Gindalbie Sequence was proposed by Brown et al. (2002) and suported by Barley et al. (2008): "The compositional range, eruptive style, abundant mass-flow deposits and association with late-stage mafic sill complexes is typical of intra-arc rift settings, such as the Sumisu Rift in the Isu-Bonin Arc of Japan (Marsaglia, 1995). Bimodal basalt-rhyolite volcanism, involving voluminous explosive rhyolitic eruptions and rapid resedimentation into a subaqueous environment, are characteristic of active rifting in marginal-arc (e.g. Taupo Volcanic Zone, New Zealand; Cole, 1990), and marginal backarc (e.g. Green Tuff Belt, Japan; Ohmoto et al., 1983) environments." A close spatial and temporal association with calc-alkaline intermediate to silicic volcanic rocks on local and regional scales (Barley et al., 1998; 2008) strongly supports a convergent margin environment: "Volcanism in the Gindalbie Terrane therefore records rifting of a marginal-arc system, perhaps related to the initiation of backarc spreading."

2.6 VHMS Deposits of the Eastern Goldfields

2.6.1 Prospectivity of the Gindalbie Domain

The inferred backarc setting, proximal subaqueous volcanic environment, abundance of originally permeable, coarse-grained volcaniclastic facies, and proximity to coeval subvolcanic intrusions are important attributes of both modern and ancient volcanic-hosted massive sulfide (VHMS) mineralising systems (e.g. Cas, 1992; Large, 1992; Fouquet et al., 1993; Allen et al., 1996). The REE and immobile element geochemistry of Melita and Teutonic Bore rhyolites are also similar to Archean felsic-volcanic associations which host VHMS deposits in the Superior Province of Canada (Kamiskotia, Kidd Creek, Noranda mining districts; Lesher et al., 1986; Barrie et al., 1993). The Gindalbie Domain

can therefore be considered a prospective VHMS target on the basis of its volcanic facies architecture, geochemical attributes and tectonic setting.

2.6.2 *Known Deposits*

Figure 2.7 shows the locations of known VHMS deposits (Table 2.3) and other deposits which are considered likely to be VHMS deposits in the EGST. Although at craton scale, the EGST in the eastern Yilgarn Craton is one of Earths largest and most intensely mineralised greenstone belts, the poor VHMS endowment is noted.

Table 2.3 VHMS deposits in the Eastern Goldfields Superterrane

Deposit	Host Rocks	Grade, tonnage	Status	Age
Teutonic Bore	Basalt and rhyolite.	1.5 Mt @ 3.6% Cu, 11.4% Zn, 167g/t Ag	Past Mine	2.69 Ga
Jaguar	As described in this thesis	1.6 Mt @ of 3.1% Cu, 11.3 Zn, 0.7% Pb, 115g/t Ag	Current Mine	2.69 Ga
Bentley	Rhyolite and andesite	2.3 Mt @ 1.8% Cu, 9.8 Zn, 1.0% Pb, 121g/t Ag, 0.06g/t Au.	Exploration prospect	2.69 Ga
Murrin Murrin	Pyritic, feldspathic greywacke, siltstone and shale	4595 t, contained Cu	Historic occurence copper oxide	-
Nimbus	Felsic volcanics and sediments	892,000 t @ 228 g/t Ag	Past Mine for silver oxide	-
Erayinya	Not known	Not known	Exploration prospect	-

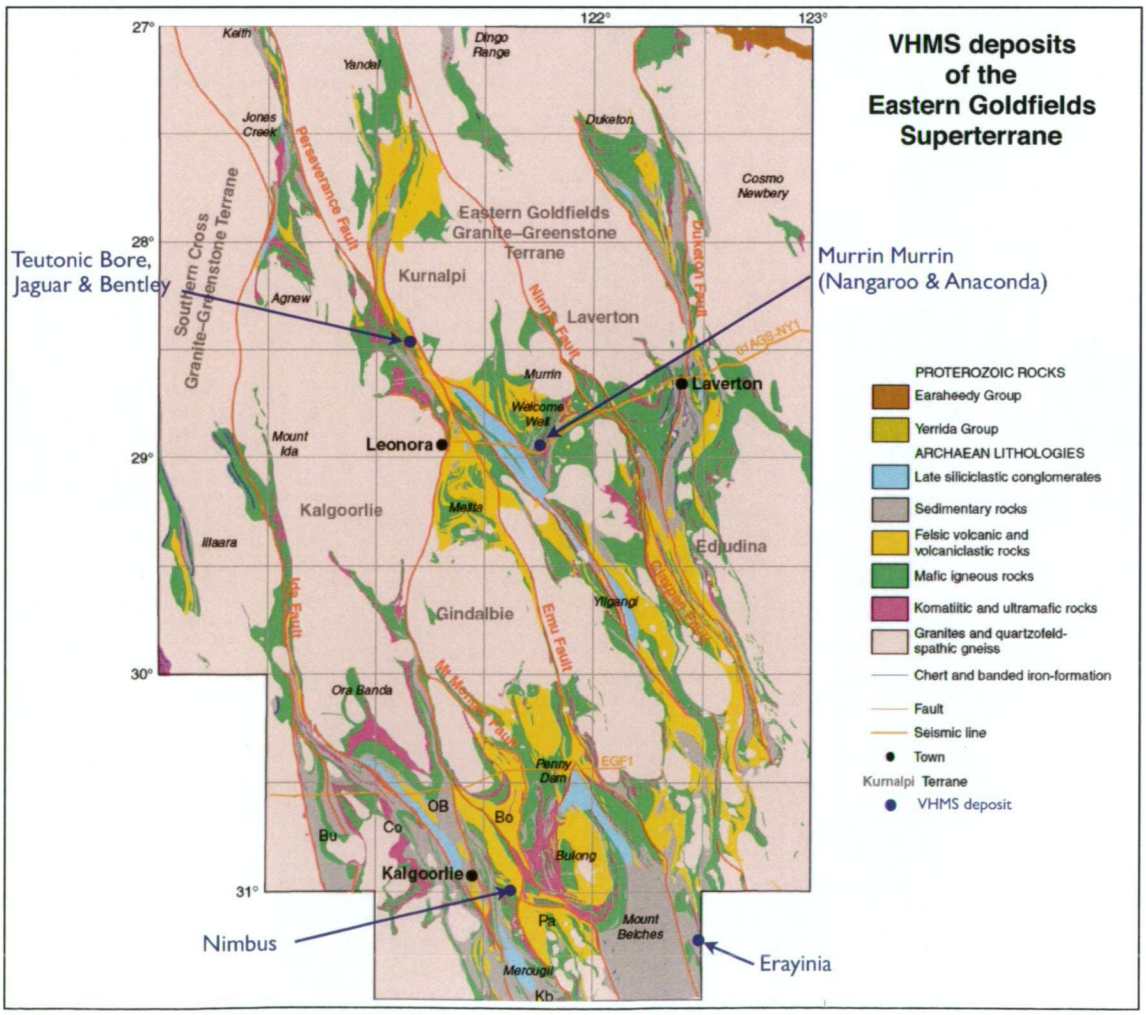

Figure 2.7 The VHMS deposits of the Eastern Goldfields Superterrane.

Known deposits include the Teutonic Bore, Jaguar and the recently discovered Bentley (Jabiru Metals, 2009) deposits in the Gindalbie Domain, the Nimbus deposit (Mulholland et al., 1998) in the Kalgoorlie Terrane and the Murrin Murrin occurrences (Marston, 1979) in the Kurnalpi Terrane. Little is known about a new discovery, reported in 2007 at Erayinia (Great Gold Mines, 2007), located about 150 km southeast of Kalgoorlie.

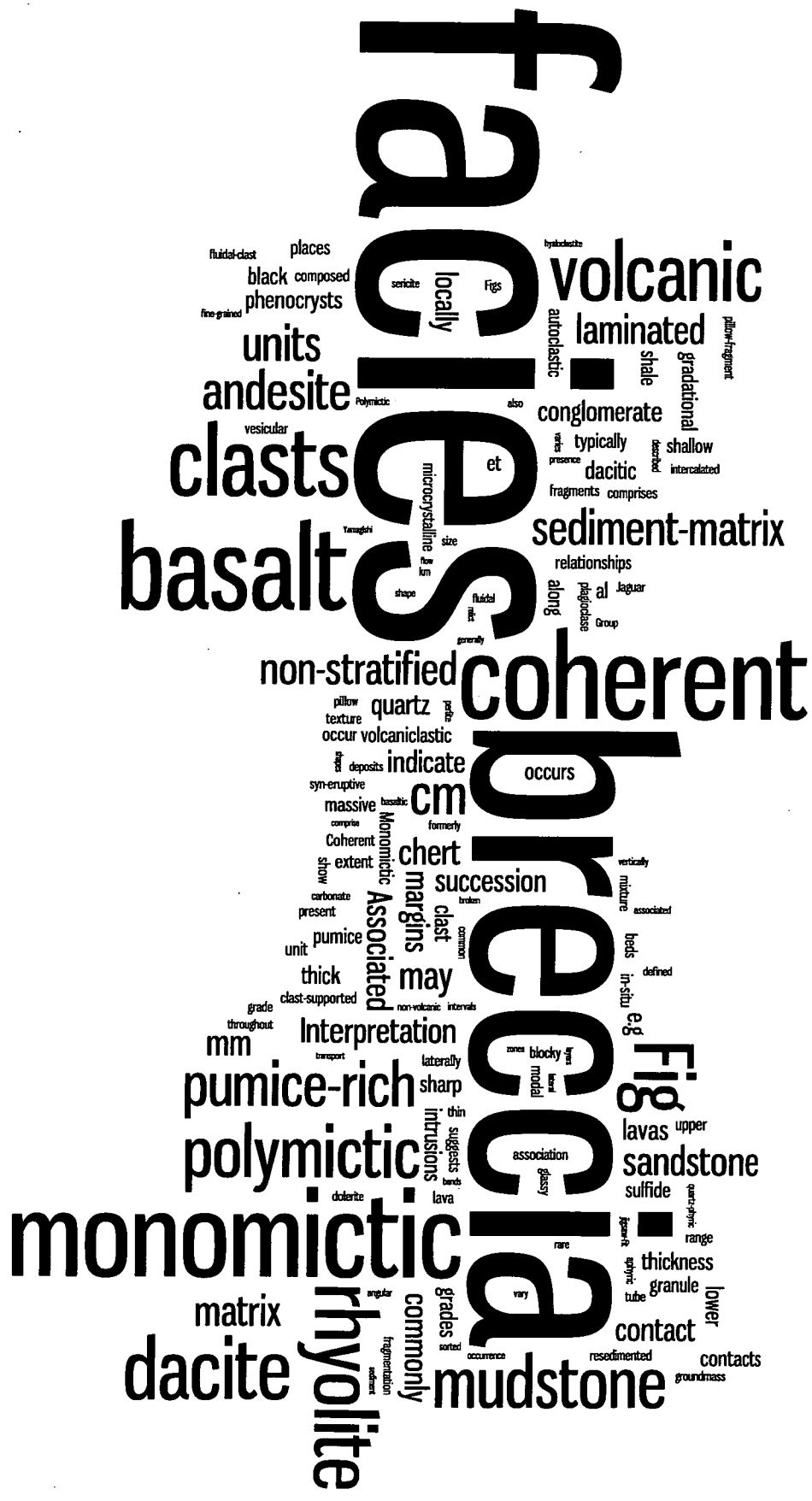
fragmental
clasts
basalt
andesite
units
phenocrysts
black
composed
places
fluidal-clast
fine-grained
locally
sericite
Figs
volcanic
laminated
autoclastic
shale
gradational
pillow-fragment
hyaloclastite
conglomerate
typically
dacitic
shallow
intercalated
described
fragments
comprises
sediment-matrix
relationships
along
plagioclase
al
Jaguar
Group
Polymictic
also
vesicular
et
microcrystalline
size
flow
km
shape
fluidal
clots
generally
Yamaguchi
non-stratified
coherent
quartz
pillow
texture
occur
volcaniclastic
deposits
indicate
occurs
cm
massive
basaltic
Monomictic
formerly
comprise
Coherent
extent
show
chert
succession
vertically
mixture
associated
broken
carbonate
present
Associated
margins
clast
pumice
unit
common
beds
in-situ
defined
thick
may
clast-supported
grade
throughout
non-volcanic
intervals
mm
Interpretation
transport
laterally
sharp
blocky
modal
pumice-rich
thin
intrusions
suggests
bands
lavas
upper
polymictic
association
glassy
sandstone
sulfide
lava
dolerite
monomictic
rare
range
thickness
granule
lower
tube
matrix
angular
grades
commonly
contact
dacite
rhyolite
sorted
occurrence
resedimented
contacts
groundmass
mudstone
fragmentation
sediment
Fig
e.g.
zones
types
lens
quartz-phyric
aphyric
vary

3. LITHOFACIES OF THE JAGUAR HOST SUCCESSION

3.1 Introduction

The succession at Jaguar is dominated by volcanic rocks, mainly intercalated coherent, and volcaniclastic facies, and minor non-volcanic sedimentary rocks. Various levels of the succession are inflated by voluminous mafic intrusions. In this chapter, the major lithofacies are described and brief first-order interpretations are given. These data provide constraints on eruptive style, emplacement processes and depositional setting discussed in later chapters. The stratigraphy of the succession (Chapter 4) was defined after identifying the lithofacies and determining their extent and geometry on drillhole cross-sections.

3.1.1 Methods and limitations

This study uses facies analyses as described in McPhie et al. (1993). The volcanic terminology used throughout follows that of Cas and Wright (1987) and McPhie et al. (1993). The facies were distinguished using textural criteria and other characteristics that included composition, contact relationships, depositional structures, and interpreted geometry. Primary volcanic textures have been preserved in most rocks despite the greenschist-facies regional metamorphism. However, the hydrothermal alteration associated with the sulfide mineralisation has commonly been mineralogically destructive and primary textures have also been destroyed by hydrothermal alteration in proximity to ore. In addition, there is no glass preserved, even though many facies were partly glassy originally.

All data come from diamond drillcore through, and along strike from the Jaguar deposit. Not all drillholes were logged. The orebody had been drilled out on an approximate 50 x 50 m spacing and drillholes across selected sections were chosen to represent the orebody and the enclosing host succession. Figure 3.1 presents an isometric projection along the Jaguar mine grid showing stacked cross-sections. The highlighted zones of the drillholes represent the intervals logged (total length logged 20.9 km). The grid coordinates and other details of the drillholes logged are tabulated in Appendix I. The extent of the area studied is about 1600 m (along strike 55350N to 56800N) by about 1000 m (across section) and extends to 900 m below the surface. The area of detailed drilling and interpretation is confined to a 500 x 500 x 900 m area. The choice of drillcore was dictated by a mix of geological and artificial constraints. On sections at the end and middle of the detailed zone, the upper level of logging was determined by the depth of surface weathering. The depth of logging was artificially constrained, because drilling usually stopped in a thick dolerite in the orebody footwall. The few drillholes that drilled through this unit were logged in their entirety. On other sections, zones through and around the orebody were logged. During the logging

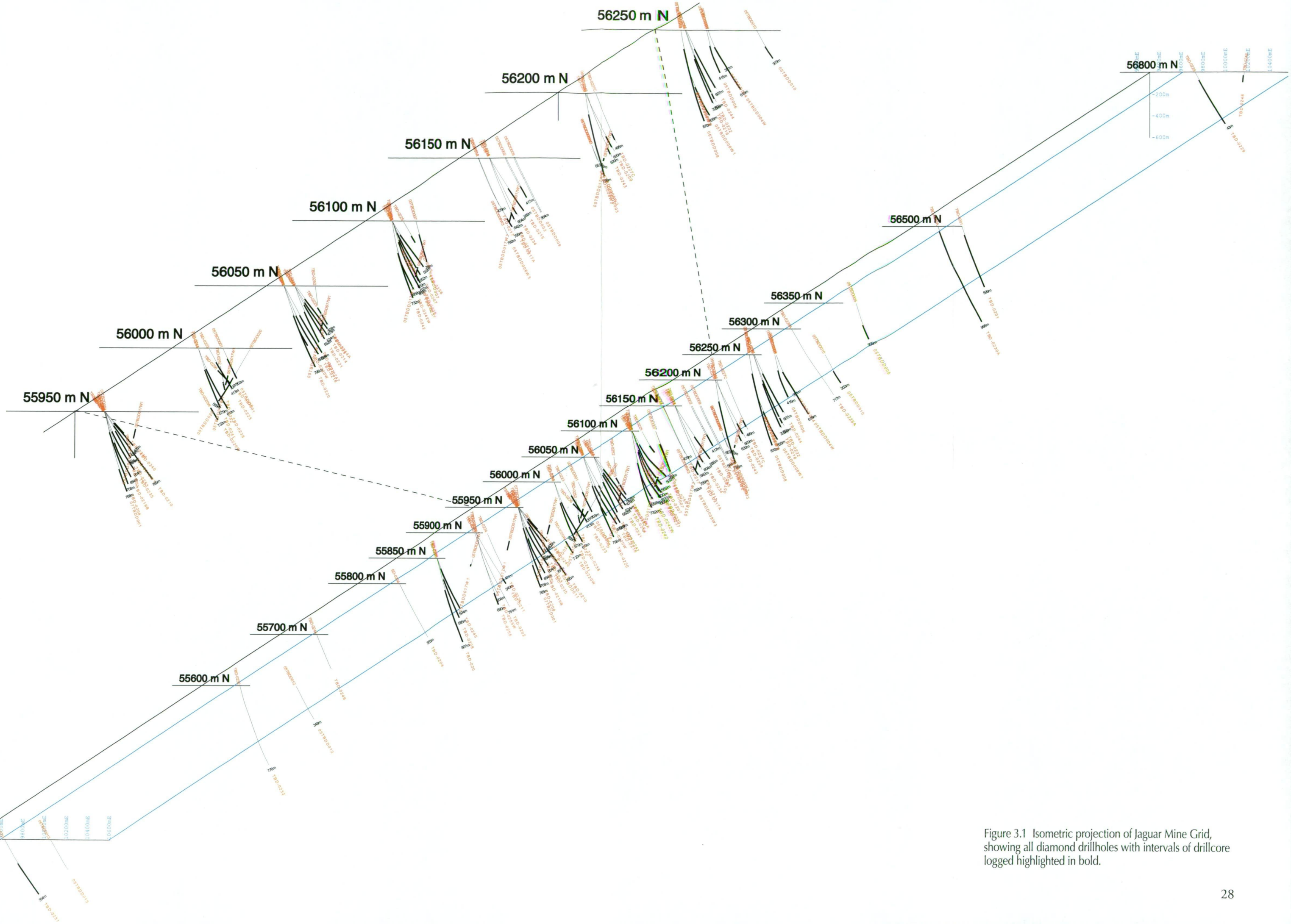

Figure 3.1 Isometric projection of Jaguar Mine Grid, showing all diamond drillholes with intervals of drillcore logged highlighted in bold.

process, other intersections were selected to add information where necessary.

The drillcore was mostly continuous, commonly having a diameter of about 50 mm. Rarely drillcore had a diameter of about 60 mm. Recovery was generally good but, in some places, contact relationships were lost or obscured by broken or missing drillcore and, in a few instances, whole coretrays were missing. All ore intersections had previously been halved for sampling purposes. In some instances only quarter core remained. Dependence on drillcore means that decimetre-scale and smaller lithofacies features and textures, and the vertical changes within the succession and single lithofacies, are well documented. The major disadvantage is the limited extent of any contact relationship exposed. The succession dips to the west at about 75°, so that the true thickness of the succession examined is less than 1000 m. Several drillholes outside this area were also logged to provide some indication of the strike extent of the major units but unfortunately these did not transect the entire section. Also, the distances between these holes, combined with the lack of surface geology and limited trace-element geochemical sampling, precluded confident correlation.

As part of the interpretation, all drillhole intervals were converted mathematically to true thickness using the downhole survey data for each drillhole and the dip (-75°) and strike (-360° Grid) of the strata. In this thesis, all unit thicknesses mentioned in the descriptions of the lithostratigraphy are true thicknesses. The grid used is the Jaguar mine grid and, in 2005 when the data were collected, Grid N = 336.5° Mag and True N = 358.9° Mag.

3.2 Facies of the Host Succession

The 25 lithofacies defined in the study area have been organised into five groups: 1) coherent volcanic facies; 2) monomictic volcanic breccia and conglomerate; 3) polymictic volcanic breccia and conglomerate; 4) volcanic sandstone and mudstone; and 5) non-volcanic facies. These groups do not represent facies associations, defined by Cas and Wright (1987) as a collection of facies that are spatially, mineralogically, compositionally or texturally related, and that may also be genetically related. The groups described here are collections of similar but unrelated (in most cases) facies. Several facies have been subdivided into sub-facies. Within each facies description is a list of other facies that have a spatial association with the described facies. Twenty-two of the facies are volcanic and three facies are non-volcanic. The volcanic facies include primary volcanic facies, syn-eruptive volcaniclastic facies, resedimented volcaniclastic facies, and post-eruptive resedimented facies. The non-volcanic facies have no direct link to volcanic processes. These five groups are summarised in Tables 3.1 to 3.5. Some of the facies are repeated in the succession whereas others occur only once.

Table 3.1 Lithofacies from the Jaguar host succession, Group 1: Coherent facies

Facies (sub-facies)	**Geometry** (thickness x lateral extent)	**Associated facies**	**Interpretation**
Coherent rhyolite *(quartz-phyric)* *(quartz-poor)*	10–>100 m x >1.6 km 10–>100 m x >1.6 km	monomictic rhyolite breccia polymictic rhyolite breccia non-stratified, sediment-matrix rhyolite breccia monomictic rhyolite breccia polymictic rhyolite breccia non-stratified, sediment-matrix rhyolite breccia	coherent facies of lavas and shallow intrusions coherent facies of lavas and shallow intrusions
Coherent dacite *(aphyric)* *(quartz-feldspar-phyric)*	1–>10 m x <50 m 1–>10 m x <50 m	monomictic dacite breccia monomictic dacitic pumice-rich breccia polymictic dacite breccia monomictic dacite breccia monomictic dacitic pumice-rich breccia polymictic dacite breccia	coherent facies of lavas and shallow intrusions coherent facies of lavas and shallow intrusions
Coherent andesite *(feldspar-phyric)* *(aphyric)*	1–>50 m x 0.5–>1.6 km 1–>50 m x 0.5–>1.6 km	monomictic andesite breccia non-stratified, sediment-matrix andesite breccia monomictic andesite breccia non-stratified, sediment-matrix andesite breccia	coherent facies of lavas and shallow intrusions coherent facies of lavas and shallow intrusions
Coherent basalt	1–30 m x >1.6 km	monomictic basalt breccia monomictic fluidal-clast breccia monomictic pillow-fragment basalt breccia non-stratified, sediment-matrix basalt breccia	coherent facies of lavas and shallow intrusions
Coherent dolerite	<1–140 m x <1–>1.6 km	coherent basalt	coherent facies of dykes and sills

Table 3.2 Lithofacies from the Jaguar host succession, Group 2: Monomictic volcanic breccia facies

Facies	**Geometry** (thickness x lateral extent)	**Associated facies**	**Interpretation**
Monomictic rhyolite breccia	<1–10 x ?	coherent rhyolite polymictic rhyolite breccia	autoclastic breccias (hyaloclastite, autobreccia) related to lavas and shallow intrusions
Non-stratified, sediment-matrix rhyolite breccia	<50 cm x ?	coherent rhyolite laminated volcanic mudstone	peperite: in-situ fragmentation of lava or magma intruding into wet, unconsolidated sediment
Monomictic dacite breccia	<1–10 m x ?	coherent dacite monomictic dacitic pumice-rich breccia polymictic dacite breccia polymictic conglomerate	autoclastic breccias (hyaloclastite, autobreccia) related to lavas and shallow intrusions
Monomictic dacitic pumice-rich breccia	<1 m x ?	coherent dacite monomictic dacite breccia polymictic pumice-rich breccia pumice-rich granule breccia	autoclastic breccias (hyaloclastite, autobreccia) related to lavas and shallow intrusions
Pumice-rich granule breccia	<50 cm x ?	monomictic dacitic pumice-rich breccia polymictic pumice-rich breccia volcanic sandstone	syn-eruptive and post-eruptive resedimented volcaniclastic deposits
Monomictic andesite breccia	<5–10 m x ?	coherent andesite	autoclastic breccias (hyaloclastite, autobreccia) related to lavas and shallow intrusions
Non-stratified, sediment-matrix andesite breccia	<2 m x ?	coherent andesite laminated volcanic mudstone	peperite: in-situ fragmentation of lava or magma intruding into wet, unconsolidated sediment
Monomictic basalt breccia	1–20 m x >1000 m	coherent basalt monomictic fluidal-clast breccia monomictic pillow-fragment basalt breccia	autoclastic breccias (hyaloclastite, autobreccia) related to lavas and shallow intrusions
Monomictic fluidal-clast breccia	1–15 m x >200 m	coherent basalt monomictic basalt breccia	syn-eruptive fountain deposit
Monomictic pillow-fragment basalt breccia	1–10 m x >1000 m	coherent basalt monomictic basalt breccia	resedimented, not in-situ
Non-stratified, sediment-matrix basalt breccia	<2 m x ?	coherent basalt laminated volcanic mudstone	peperite: in-situ fragmentation of lava or magma intruding into wet, unconsolidated sediment

Table 3.3 Lithofacies from the Jaguar host succession, Group 3: Polymictic volcanic breccia and conglomerate facies

Facies	Geometry (thickness x lateral extent)	Associated facies	Interpretation
Polymictic rhyolite breccia	10 m x ?	coherent rhyolite monomictic rhyolite breccia	syn-eruptive volcaniclastic gravity flow deposits, syn-eruptive resedimented volcaniclastic deposits
Polymictic dacite breccia	1–5 m x ?	monomictic dacite breccia polymictic conglomerate	syn-eruptive volcaniclastic gravity flow deposits, syn-eruptive resedimented volcaniclastic deposits
Polymictic conglomerate	5 cm -15 m x ?	polymictic dacite breccia polymictic dacite pumice-rich breccia volcanic sandstone laminated volcanic mudstone	syn-eruptive and post-eruptive resedimented volcaniclastic deposits
Polymictic pumice-rich breccia	<50 cm x ?	monomictic dacitic pumice-rich breccia pumice-rich granule breccia polymictic conglomerate chert	syn-eruptive volcaniclastic gravity flow deposits, syn-eruptive resedimented volcaniclastic deposits

Table 3.4 Lithofacies from the Jaguar host succession, Group 4: Volcanic sandstone and mudstone facies

Facies	Geometry (thickness x lateral extent)	Associated facies	Interpretation
volcanic sandstone	1–10 m x >1.6 km	pumice-rich granule breccia laminated volcanic mudstone polymictic dacite breccia polymictic conglomerate	syn-eruptive and post-eruptive resedimented volcaniclastic deposits
laminated volcanic mudstone	1–10 m x >1.6 km	non-stratified, sediment-matrix rhyolite breccia non-stratified, sediment-matrix andesite breccia non-stratified, sediment-matrix basalt breccia volcanic sandstone laminated non-volcanic mudstone and black shale	syn-eruptive and post-eruptive resedimented volcaniclastic deposits

Table 3.5 Lithofacies from the Jaguar host succession, Group 5: Non-volcanic facies

Facies	Geometry (thickness x lateral extent)	Associated facies	Interpretation
laminated mudstone and black shale	1–10 m x >1.6 km	laminated volcanic mudstone non-stratified, sediment-matrix rhyolite breccia non-stratified, sediment-matrix andesite breccia non-stratified, sediment-matrix basalt breccia	pelagic sediment and mud turbidites
chert	1–50 cm x ?	sulfide	chemical precipitate
sulfide	<1–15 m x <300 m	chert	chemical precipitate

The compositional criteria used for rock classification and to name the coherent facies are based on high field strength element (HFSE) ratios developed by Winchester and Floyd (1977), Hallberg (1984), and Pearce (1996). This approach was required because element mobility caused by alteration effects ruled out modal mineralogical or whole-rock geochemical schemes such as TAS (Le Maitre et al., 1898). The classification is further discussed in Chapter 4 (Stratigraphy) and the criteria are described in detail in Chapter 5 (Geochemistry).

3.3 Group 1: Coherent volcanic facies

3.3.1 Coherent rhyolite facies

The coherent rhyolite facies (Fig. 3.2a) comprises pale coloured, extremely hard, siliceous, variably porphyritic units that can be flow-banded or massive (Fig. 3.2b). This facies has two distinctive sub-facies which are distinguished on phenocryst abundance. One is the highly quartz-phyric rhyolite and the other is the sparsely quartz-phyric rhyolite. Flow-bands are locally defined by subparallel, sub-mm bands of chlorite-sericite intergrowth. Flow-banded rhyolite locally grades to monomictic rhyolite breccia.

This facies occurs at several levels throughout the succession and ranges from tens of metres to greater than 100 m thick. Few contacts were observed because the upper contacts were not intersected in drilling and the lower contacts are obscured by broken drillcore or younger dolerite intrusions. Where observed, the contacts are marked by intervals of non-stratified sediment-matrix rhyolite breccia, or monomictic or polymictic rhyolite breccia.

Sparsely quartz-phyric rhyolite has <5 modal % quartz phenocrysts (<1-2 mm) and no feldspar phenocrysts. Highly quartz-phyric rhyolite has common quartz phenocrysts (Fig. 3.2c) and plagioclase phenocrysts. The concentration of euhedral, bi-pyramidal quartz phenocrysts ranges within this facies to a maximum of about 25 modal % and phenocrysts range up to 3 mm in size. Quartz phenocrysts are embayed and clear. Some phenocrysts are broken, but remain as clusters. These clusters, along with aggregates of small anhedral quartz grains, occur in a groundmass of microcrystalline quartz, sericite (white mica) and chlorite.

Possible relict perlite showing the classical delicate arcuate fractures is preserved (Fig. 3.2c). The now devitrified, formerly glassy groundmass is commonly represented by a mixture of microcrystalline quartz, sericite, and chlorite. Other areas show a roughly rectilinear network of cracks that are oblique within a subparallel microstructure. This texture may be banded perlite.

Associated facies

- monomictic rhyolite breccia
- polymictic rhyolite breccia
- non-stratified sediment-matrix rhyolite breccia facies

Interpretation

The associated facies, contact relationships and textures (e.g. Ross and Smith, 1955; Pichler, 1965; Hanson, 1991) indicate the coherent rhyolite facies are the coherent parts of lavas and shallow intrusions (e.g. De Rosen-Spence et al., 1980; Yamagishi, 1987; Cas et al., 1990).

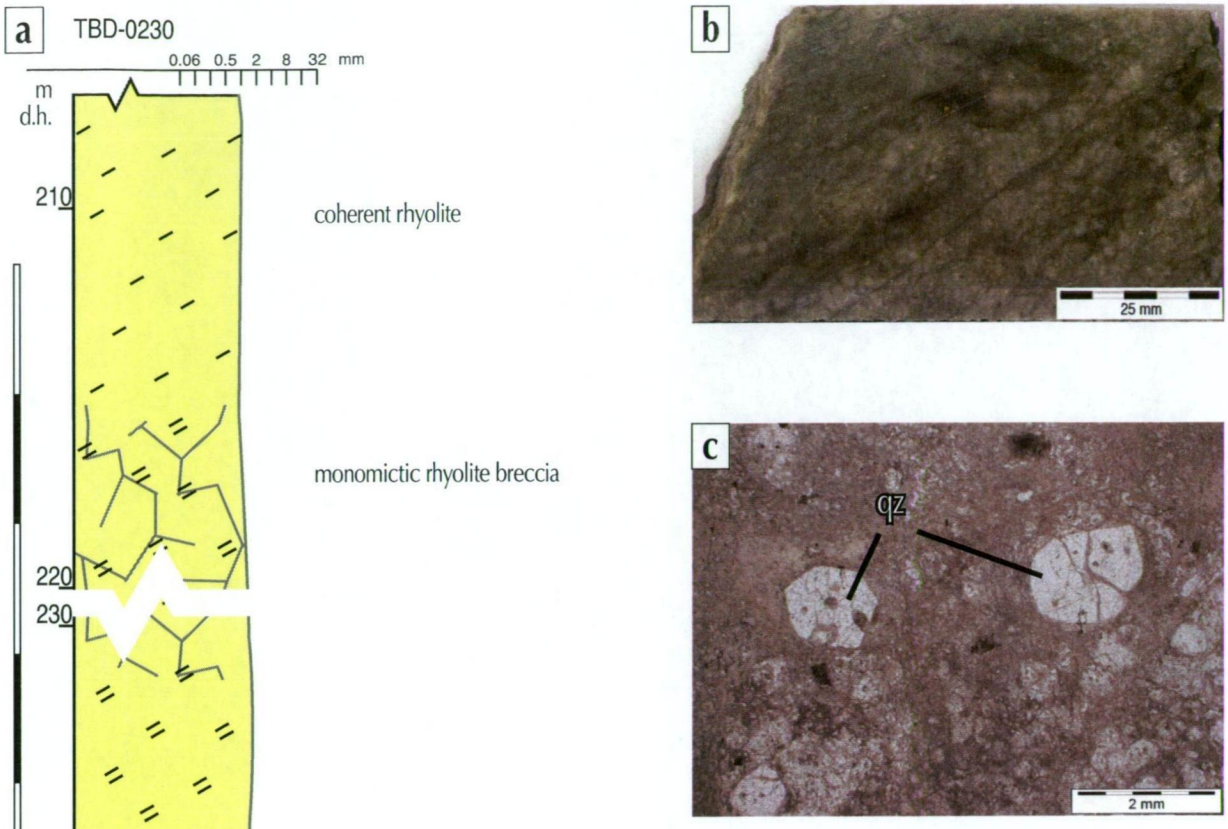

Figure 3.2 Coherent rhyolite facies:
a) graphic log of TBD0230, showing relationships and variations in facies;
b) flow-bands in coherent rhyolite, drillcore photograph, 05TB010 173.9 m;
c) quartz phenocrysts in coherent rhyolite, photomicrograph, plain-polarised light, 05TB010 173.9 m.

For Legend and anotations used see Figure 3.2d

Graphic logs

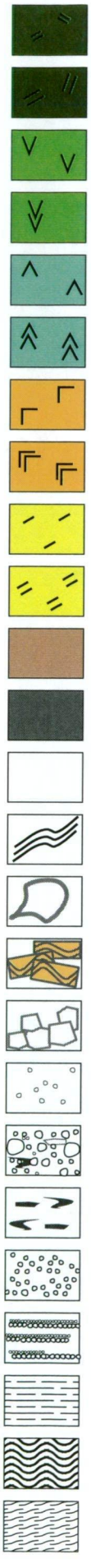

Photographs

rhy	rhyolite
dac	dacite
and	andesite
bas	basalt
cht	chert
bks	black shale
mds	mudstone
pum	pumice
qz	quartz
ch	chlorite
py	pyrite
plag	plagioclase

Figure 3.2 contined: d) Legend figures 3.2 to 3 26

3.3.2 Coherent dacite facies

The coherent dacite facies (Fig. 3.3a) comprises cream to dark grey, hard siliceous units that can be flow-banded or massive (Fig. 3.3b). There are two distinctive sub-facies that are distinguished by the presence or absence of phenocrysts. In both aphyric and porphyritic varieties, the groundmass can be microcrystalline, or more rarely show relict perlite in hand specimen. Flow bands (Fig. 3.3c) are locally defined by subparallel, sub-mm thick bands of chlorite-sericite intergrowth. The dacite is locally amygdaloidal and in places amygdales can comprise up to 50 modal %. The vesicles are generally spherical but may locally be ovoid and show a preferred orientation (Fig. 3.3c).

The porphyritic facies has plagioclase phenocrysts (<0.5-2 mm) (<5 modal %) and locally present euhedral quartz phenocrysts. Subparallel alignment of phenocrysts is common, and there are rare imbricated, broken crystals (Fig. 3.3d). The microcrystalline groundmass is composed of quartz, sericite and carbonate, with variable chlorite. The aphyric facies is generally more altered than the porphyritic varieties, but perlitic texture (Fig. 3.3e) is present, and spherulites are common. The perlite kernels are now a microcrystalline quartz - sericite mixture.

The dacite facies units are confined to a single interval in the succession. They occur as discontinuous lenses or are wedge shaped. Unit thickness ranges from a few metres to several tens of metres and they have lateral extents greater than 50 m. The margins of the coherent facies are commonly marked by intervals of monomictic dacite breccia, or locally by polymictic dacite breccia. Contacts between the facies are gradational. There are rare instances where the coherent facies grades into the monomictic dacitic pumice-rich breccia facies.

Associated facies

- monomictic dacite breccia
- polymictic dacite breccia
- monomictic dacitic pumice-rich breccia

Interpretation

The associated facies, contact relationships and textures (e.g. Ross and Smith, 1955; Pichler, 1965; Hanson, 1991) indicate the coherent dacite facies are the coherent parts of lavas and shallow intrusions (e.g. De Rosen-Spence et al., 1980, Cas et al., 1990)

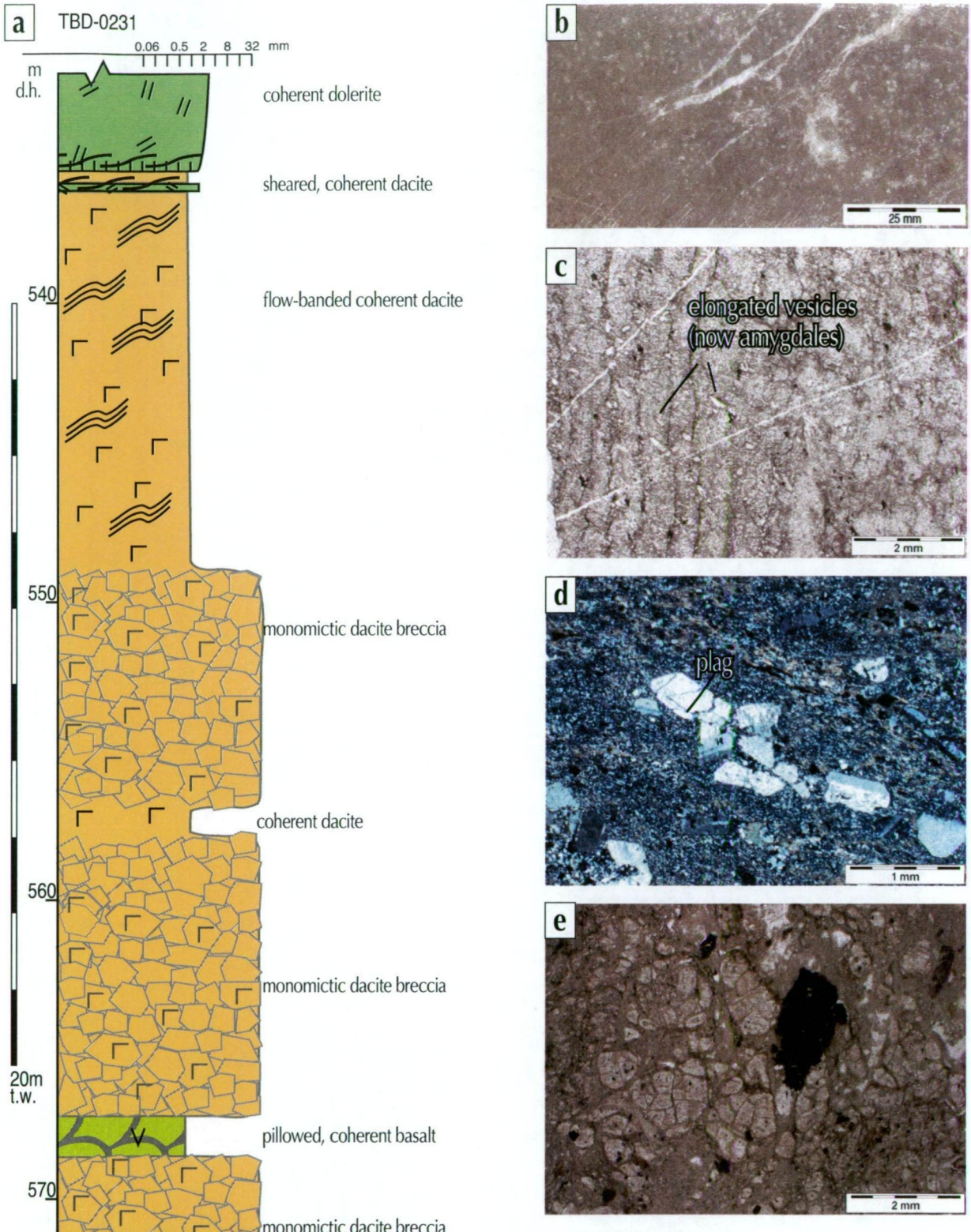

Figure 3.3 Coherent dacite facies:
a) graphic log of TBD0231, showing relationships and variations in facies;
b) felspar-phyric dacite, drillcore photograph, TBD0206 712.5 m;
c) flow bands and developing vesicles (now amygdales) in coherent dacite, photomicrograph, plain-polarised light, TBD0223 352.6 m;
d) alignment and imbrication of feldspar phenocrysts, photomicrograph, polarised light, 05TB008 810.4 m;
e) perlite in coherent dacite, photomicrograph, plain-polarised light, TBD0210 420.4 m.

For Legend and anotations used see Figure 3.2d

3.3.3 Coherent andesite facies

The coherent andesite facies (Fig. 3.4a) comprises two texturally distinct sub-facies: aphyric and feldspar-phyric (with rare quartz phenocrysts) coherent andesite. The colour varies from light blue-grey to dark green. The andesite is dominantly massive and is typically amygdaloidal (Fig. 3.4b). Flow bands occur locally. The modal % of amygdales commonly increases towards the margins of the units. Some units are pillowed (Fig. 3.4c). Small, loosely packed pillows range from 10 to 50 cm across, and have thin (5 mm), fine-grained, aphyric margins. The interpillow matrix mainly comprises fine (<2-4 mm) andesite fragments.

This facies is repeated throughout the succession. It occurs as extensive units, up to 70 m thick and extending throughout the area studied (>1600 m), and as layers, lenses and apophyses from centimetres to several metres thick.

The margins of the coherent facies can be sharp or gradational. The units may grade from massive into flow-banded and then to monomictic andesite breccia. Both upper and lower margins are observed to locally grade into non-stratified, sediment-matrix andesite breccia . Some lower contacts are sharp and irregular, and crosscut laminated mudstone (Fig. 3.4d). A thin halo (<10 cm) of silicification is common in the mudstone at these contacts. Some upper margins have sharp contacts and are overlain conformably by undisturbed mudstone.

The central zones show plagioclase phenocrysts in a felted or trachytic, microlite-rich groundmass. The size of the phenocrysts is variable within, and among units. Overall the average size of the plagioclase laths is in the range of 1–3 mm although in some units the average ranges from 3 to 6 mm. Single plagioclase range up to 8 mm. Plagioclase phenocrysts may be as abundant as 20 modal %. Rare subhedral quartz grains occur locally. In places the plagioclase phenocrysts and groundmass are altered to sericite, carbonate and chlorite. Numerous fine (~0.05 mm) pink leucoxene grains dominate in some hand-specimens. Round and oval amygdales (~1 to ~8 mm) filled by quartz or carbonate are common. In places, the margins of these units show trails of opaque minerals which may represent a variety of flow bands. In some cases the upper margins have a devitrified, formerly glassy groundmass that contains spherulites and perlite.

Associated facies

- monomictic andesite breccia
- non-stratified, sediment-matrix andesite breccia

Interpretation

Textures, associated facies, and their relationships (e.g. Yamagishi and Dimroth, 1985; Batiza and White, 2000) indicate that this facies is the coherent facies of lavas and intrusions. The presence of pillows in some units indicate that lavas are locally present, and that the depositional setting was subaqueous (e.g. McBirney, 1963; Appelgate and Embley, 1992).

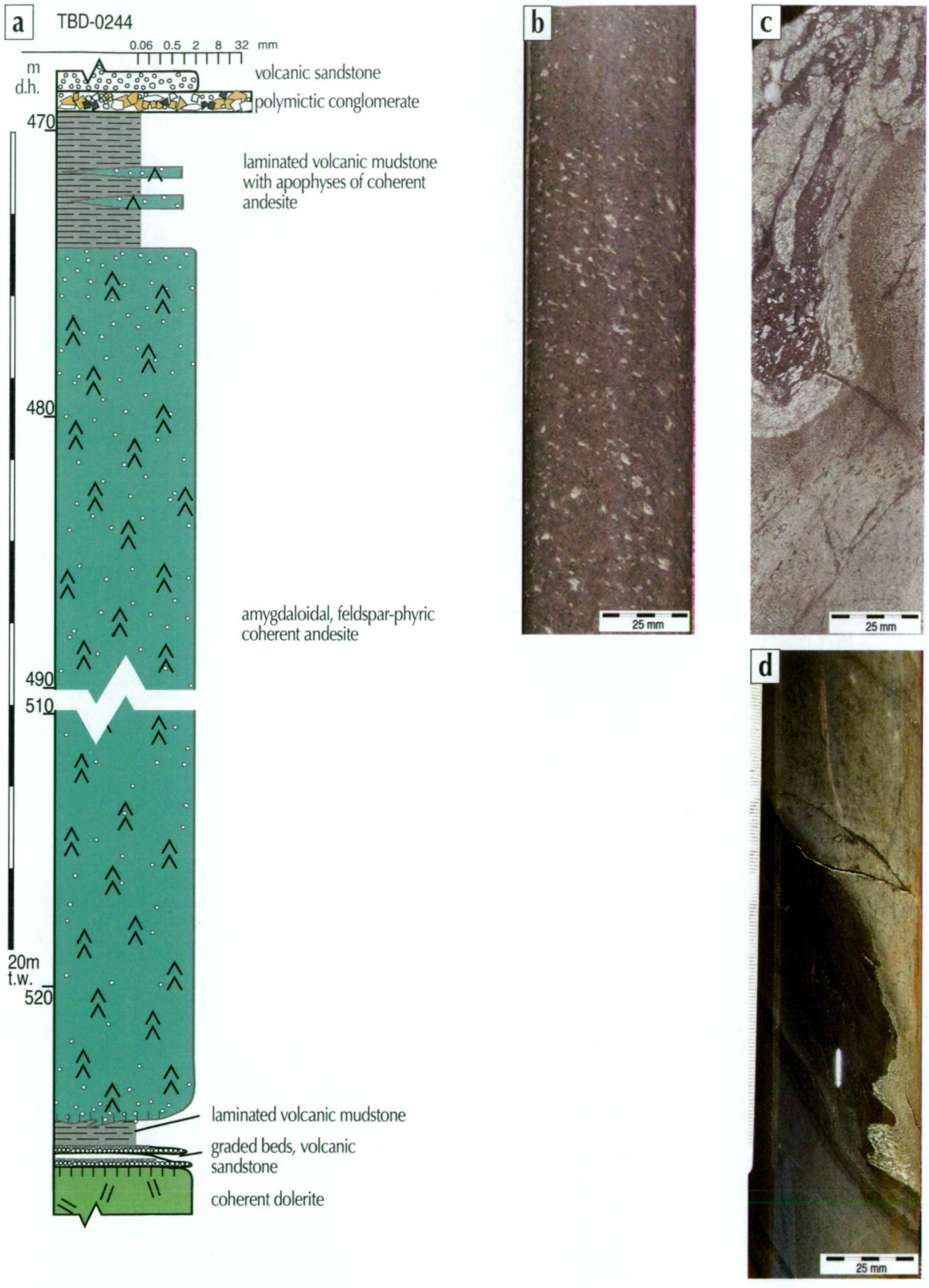

Figure 3.4 Coherent andesite facies:
a) graphic log of TBD0244, showing relationships and variations in facies;
b) massive, feldspar-phyric andesite, drillcore photograph, TBD0218 637 m;
c) pillow margin, and interpillow hyaloclstite, drillcore photograph, TBD0222 500.3 m;
d) chilled lower contact of coherent andesite, drillcore photograph, TBD0244 524.75 m.

For Legend and anotations used see Figure 3.2d

3.3.4 Coherent basalt facies

Coherent basalt (Fig. 3.5a) occurs throughout the succession and is dominantly aphyric, ranging from pale blue-green to dark green. Single intervals of coherent basalt facies may be as narrow as 1 m, and locally intercalated with monomictic basalt breccia, non-stratified, sediment-matrix basalt breccia, or rare, thin (<20 cm) occurrences of mudstone and black shale. Intervals of alternating coherent basalt and monomictic basalt breccia with minor non-stratified, sediment-matrix basalt breccia are up to 180 m thick.

The dominant lithofacies is pillow basalt (Fig. 3.5b). Massive basalt is also present and grades laterally and vertically into the pillow facies. Pillows range from 20 cm to >1 m across. The packing of the pillows varies from tight (interpillow matrix <10 mm) to dispersed (interpillow matrix width of 100–300 mm). The average interpillow thickness is around 10–40 mm. Commonly, the pillows towards the top of the single units are more loosely packed and separated by interpillow matrix up to 200 mm thick, than the pillows towards the base of units. The interpillow matrix comprises sand-granule hyaloclastite (<2 mm) (Fig. 3.5c) or mudstone. Formerly glassy pillow rims are commonly moderately to strongly amygdaloidal. The vesicles may be round, but commonly occur as a linear array of vesicles aligned along an axis normal to the pillow margin. The vesicles are filled by a mixture of quartz and carbonate.

The upper margins of this facies commonly grade over a short distance (<50 cm) into monomictic basalt breccia or fluidal-clast basalt breccia. In places, lower margins grade over a very short distance (<20 cm) into non-stratified, sediment-matrix basalt breccia.

Microtextures vary from sub-ophitic texture, composed of plagioclase laths in now-altered pyroxene, to trachytic (Figs 3.5d), showing variable alignment of microlites. Pillow rims are fractured (Fig. 3.5e), and may be perlitic (Fig. 3.5f) and variolitic. In places, relict plagioclase phenocrysts are preserved in a palagonite groundmass.

Associated facies

- monomictic basalt breccia
- monomictic fluidal-clast basalt breccia
- monomictic pillow-fragment basalt breccia
- non-stratified, sediment-matrix basalt breccia
- coherent dolerite

Interpretation

The common presence of pillows and associated monomictic basalt breccia (interpreted as in-situ hyaloclastite) indicate that this facies is most likely the coherent part of subaqueous basalt lavas (e.g. McBirney, 1963; Yamagishi, 1991; Appelgate and Embley, 1992, Batiza and White, 2000). Thinner intervals of massive basalt are interpreted as endogenous growth by inflation.

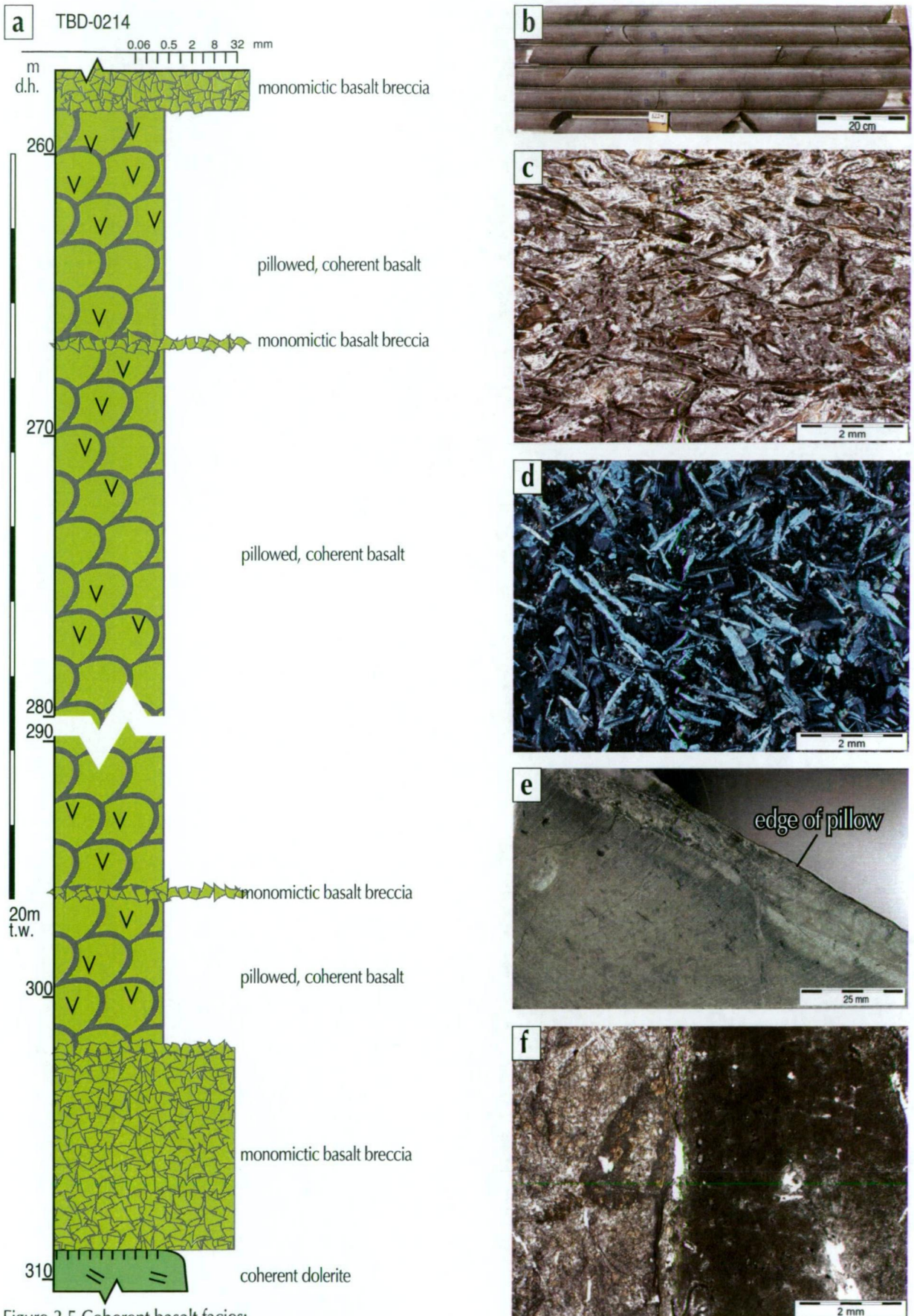

Figure 3.5 Coherent basalt facies:
a) graphic log of TBD0224, showing relationships and variations in facies;
b) pillow basalt, drillcore photograph, 05TBD008W1 ~520 m;
c) basalt hyaloclastite in interpillow zone, photomicrograph, polarised light, TBD0210 489m;
d) trachytic texture in coherent basalt, photomicrograph, polarised light, TBD0210 478.7 m;
e) pillow rim, drillcore photograph, TBD0208 539.8 m;
f) perlite and microlites in formerly-glassy pillow rim, photomicrograph, plain-polarised light, TBD0208 539.8 m.

For Legend and anotations used see Figure 3.

3.3.5 Coherent dolerite facies

The coherent dolerite facies (Fig. 3.6a) is typically massive, pale to dark green and equigranular, ranging from 0.05 to 4 mm in grainsize (Fig. 3.6b). This facies occurs as multiple lenses, both conformable and crosscutting lenses that range in thickness from <1 m to >140 m. The margins are commonly aphanitic and amydaloidal (Fig. 3.6c). The adjacent facies is typically chlorite-carbonate altered for up to 10 cm from the contact. Thin (10 cm to 1 m thick) apophyses are present locally (Fig. 3.6d). In addition, the thickest units of this facies comprise very coarse-grained zones cut by internal units with sharp contacts and aphanitic margins which, in turn, grade to coarse-grained centres (Fig. 3.6e). No breccia was observed on the margins. Contact relationships between this facies, and all volcaniclastic, sedimentary, felsic and andesitic facies are everywhere sharp, locally irregular and crosscutting (Fig. 3.6f). Contact relationships between coherent basalt units and this facies differ in upper versus lower parts of the succession. Lower in the succession, the dolerite margins are fine-grained and similar in style to those already described. Higher in the succession, the contacts with basaltic facies are not everywhere well defined and, in some instances, appear gradational over a width of up to 5 m. In these cases, an alteration halo, dominated by carbonate, may extend for up to 10 m into the coherent basalt facies.

This facies typically has an ophitic texture comprising plagioclase, clinopyroxene and minor quartz, with variable amounts of iron oxides (ilmenite-leucoxene and magnetite). It is variably altered. The major alteration minerals are epidote, chlorite and carbonate.

Associated facies

- coherent basalt

Interpretation

The sharp contacts and distinct chilled margins, plus the conformable and crosscutting nature relationships with other facies, indicate that the majority of the coherent dolerite units are sills and dykes. Higher in the succession, the gradational contacts between coherent dolerite units and coherent basalt may indicate that some units of this facies represent feeder dykes or sills for the basalt lavas.

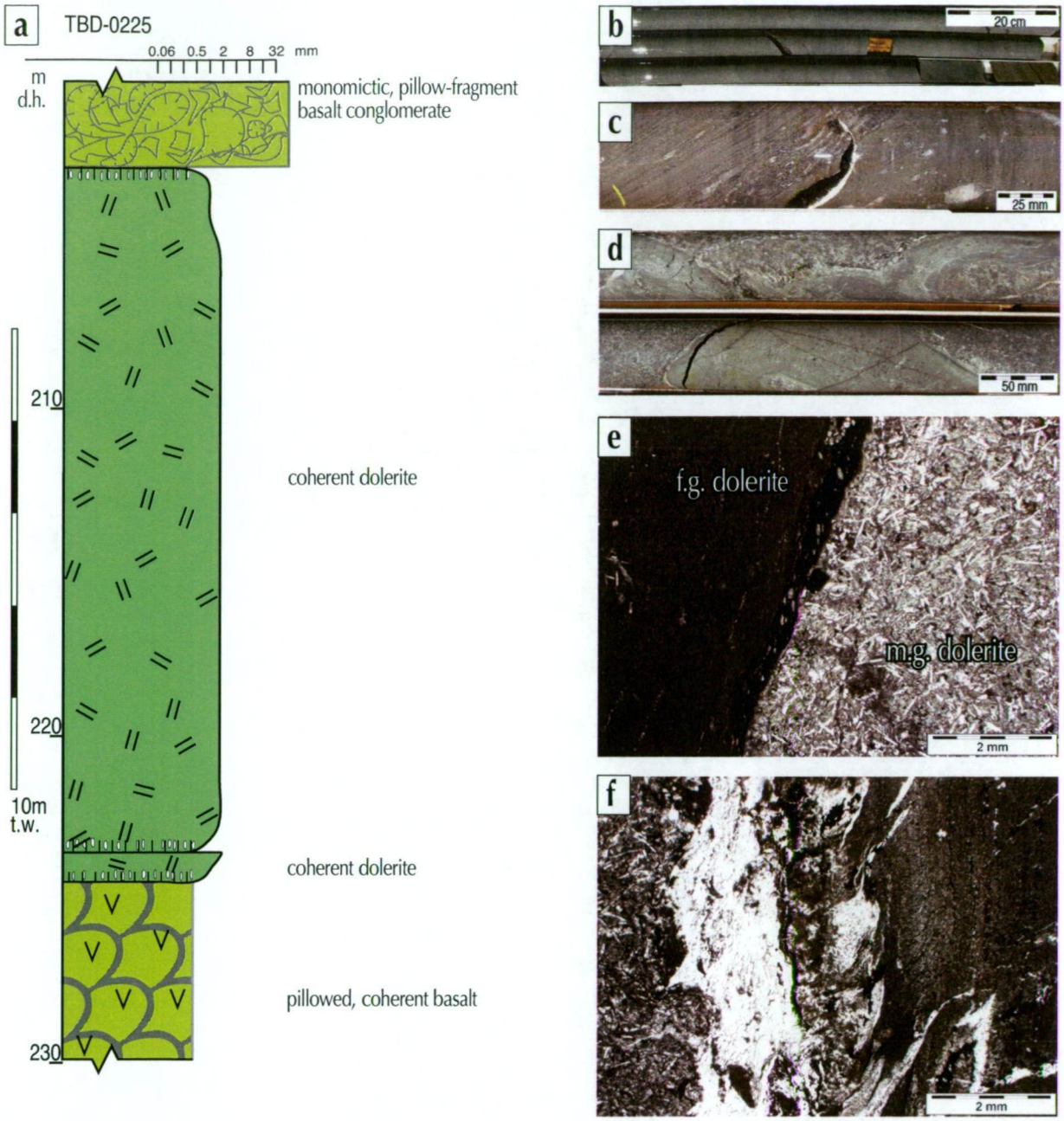

Figure 3.6 Coherent dolerite facies:
a) graphic log of TBD0225, showing relationships and variations in facies;
b) coherent dolerite, grainsize change from coarse (upper left) to very fine grained (lower right) in a chilled margin, drillcore photograph, TBD0221 492 m;
c) chilled, margin with quartz-carbonate filled amygdales, drillcore photograph, TBD0216 619 m;
d) very coarse grained dolerite intruded by very fine grained dolerite apophysis, drillcore photograph, TBD0218 667 m;
e) fine grained dolerite with sharp contact against the chilled margin of another dolerite, photomicrograph, plain-polarised light, TBD0242w 638.9 m;
f) carbonate vein along the edge of chilled dolerite, that intruded andesite, photomicrograph, plain-polarised light, TBD0216 545.7 m.

For Legend and anotations used see Figure 3.2d

3.4 Group 2: Monomictic volcanic breccia and conglomerate

3.4.1 Monomictic rhyolite breccia facies

The monomictic rhyolite breccia facies (Fig. 3.7a) is clast-supported and composed of angular and ragged rhyolite clasts. Jigsaw-fit clast domains grade to clast-rotated domains (Figs 3.7b and 3.7c). This facies typically occurs at the margins of, and within, coherent rhyolite. Contacts between the monomictic rhyolite breccia facies and coherent rhyolite facies are commonly gradational, from massive through flow-banded coherent rhyolite to monomictic rhyolite breccia. This facies has gradational contacts with polymictic rhyolite breccia.

The extent of monomictic rhyolite breccia units is not known, and they range from tens of centimetres to a few metres in thickness. The clasts range from <1 to >10 cm and have the same phenocryst populations as described for the coherent rhyolite. The monomictic rhyolite breccia is matrix poor and the matrix is typically a crypto- microcrystalline mixture of sericite and quartz.

Associated facies

- coherent rhyolite facies
- polymictic rhyolite breccia

Interpretation

The monomictic composition, the jigsaw-fit texture, and the association and contact relationships with the coherent rhyolite indicate that the monomictic rhyolite breccia facies are the in-situ autoclastic facies of lavas and shallow intrusions (e.g. Pichler, 1965; De Rosen-Spence, et al., 1980; Yamagishi and Dimroth, 1985; Hanson, 1991, McPhie et al., 1993).

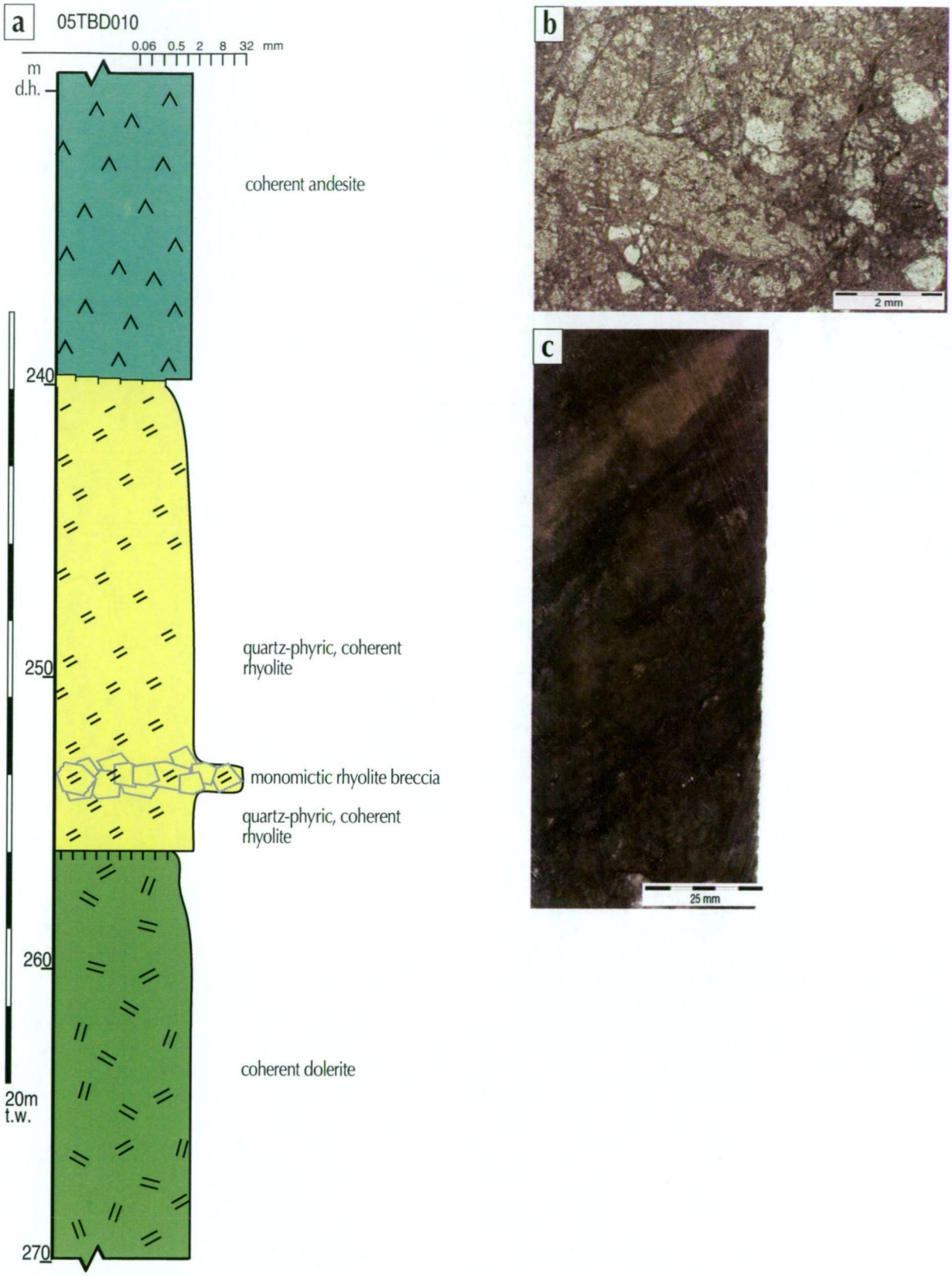

Figure 3.7 Monomictic rhyolite breccia facies:
a) graphic log of 05TBD010, showing relationships and variations in facies;
b) micro-clasts of rhyolite showing jigsaw-fit texture, photomicrograph, plain-polarised light, 05TBD010 253.3 m;
c) ragged clasts of rhyolite, drillcore photograph, 05TBD010 253.3 m.

For Legend and anotations used see Figure 3.2d

3.4.2 Non-stratified sediment-matrix rhyolite breccia facies

The non-stratified, sediment-matrix rhyolite breccia (Fig. 3.8) is composed of clasts of quartz-phyric rhyolite in a matrix of mudstone or sandstone. The facies is poorly sorted and dominantly clast-supported. The clasts are ragged to blocky in shape, and the rhyolite clast texture and mineralogy are identical to those of the coherent rhyolite facies. The mudstone matrix may show contorted or disrupted bedding.

Occurrences of this facies are uncommon and are located along margins of the coherent rhyolite facies. Thicknesses are typically less than 50 cm and grade into coherent rhyolite in one direction, and into laminated volcanic mudstone or sandstone the other.

Associated facies

- coherent rhyolite facies
- laminated volcanic mudstone
- volcanic sandstone

Interpretation

The combination of sedimentary and rhyolitic components, and association and contact relationships with the coherent rhyolite facies indicate that this non-stratified, sediment-matrix rhyolite breccia facies is peperite, formed by the in-situ fragmentation of the molten rhyolite intruding into wet, unconsolidated sediment (e.g. Kokelaar, 1982; Busby-Spera and White, 1987; Skilling et al., 2002).

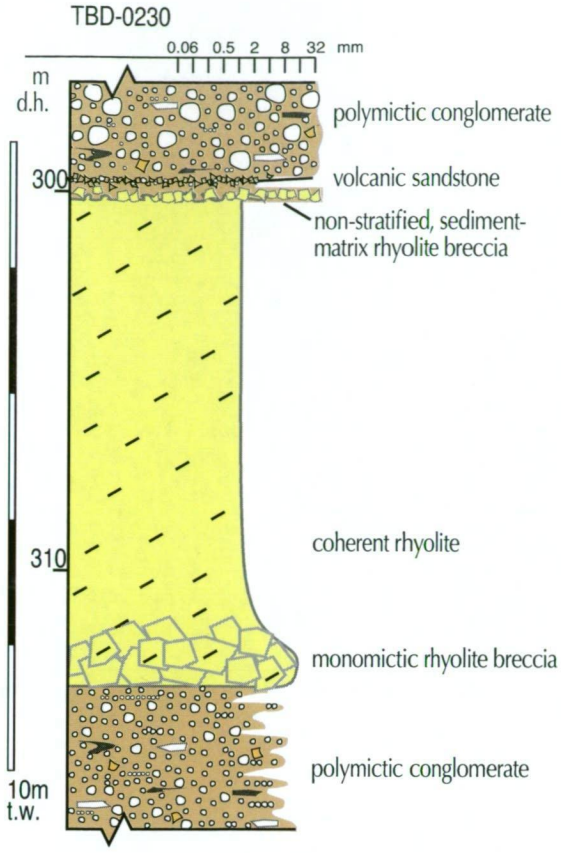

Figure 3.8 Non-stratified, sediment-matrix rhyolite breccia facies: graphic log of TBD0230, showing relationships and variations in facies.

For Legend and anotations used see Figure 3.2d

3.4.3 *Monomictic dacite breccia facies*

Monomictic dacite breccia (Fig. 3.9a) typically occurs along the margins of coherent dacite units. The breccia is non-stratified, and is everywhere clast-supported. Clasts (2 mm to 10 cm) are blocky to ragged, and show jigsaw-fit to clast-rotated texture (Fig. 3.9b). Clasts can be aphyric, quartz- or feldspar-phyric, or highly vesicular as described for the coherent dacite facies. Some clasts are flow banded. The matrix contains abundant <2 mm sized dacite fragments composed of microcrystalline quartz, sericite and chlorite (Fig. 3.9c).

The contacts between monomictic dacite breccia and coherent dacite are sharp to gradational. Coherent dacite passes into in-situ jigsaw-fit, then clast-rotated monomictic dacite breccia. In turn, the monomictic dacite breccia commonly grades laterally and vertically into the polymictic dacite breccia or polymictic conglomerate. Rarely, the monomictic dacite breccia grades into the monomictic dacitic pumice-rich breccia. Units of monomictic dacite breccia facies are typically limited in extent (<50 m) and range from <1 to 10 m in thickness. The clasts have the same microtexture as the coherent dacite although perlite is more common, as are spherulites.

Associated facies

- coherent dacite
- monomictic dacitic pumice-rich breccia
- polymictic dacite breccia
- polymictic conglomerate

Interpretation

The monomictic composition, the jigsaw-fit texture, and the association and contact relationships with the coherent dacite indicate that the monomictic dacite breccia facies are the in-situ autoclastic facies of lavas and shallow intrusions. A likely explanation is that this facies is an in-situ hyaloclastite that resulted from quench fragmentation of the carapace of a lava (e.g. Pichler, 1965; De Rosen-Spence, et al., 1980; Yamagishi and Dimroth, 1985; Hanson, 1991, McPhie et al., 1993).

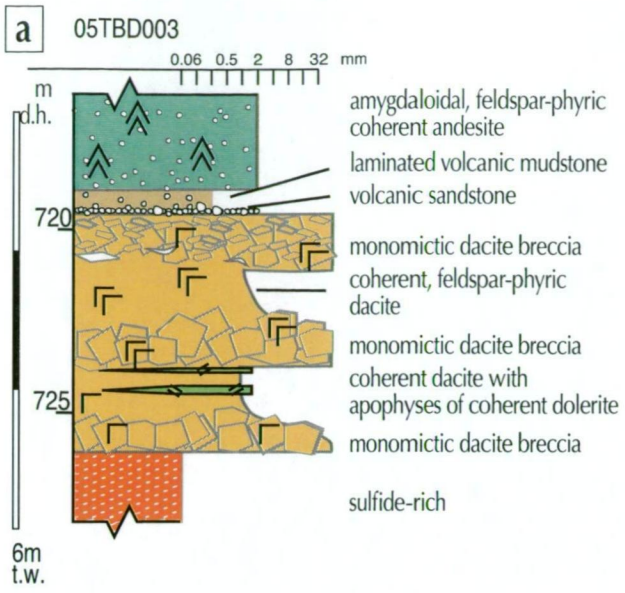

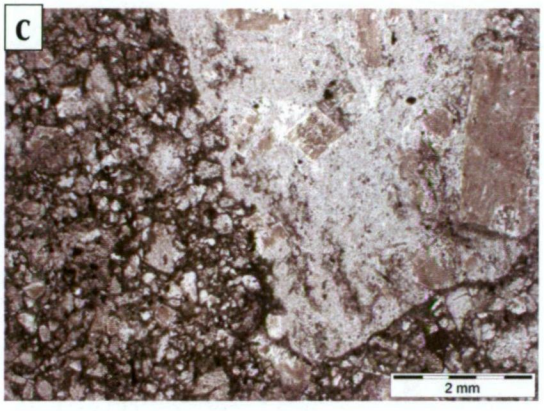

Figure 3.9 Monomictic dacite breccia facies:
a) graphic log of 05TBD003, showing relationships and variations in facies;
b) jigsaw-fit and clast-rotated dacite breccia , drillcore photograph, 05TBD003 720 m;
c) large dacite clast, in matrix of broken crystals and micro-clasts of dacite, photomicrograph, plain-polarised light, 05TBD001 236.5 m.

For Legend and anotations used see Figure 3.2d

3.4.4 *Monomictic dacitic pumice-rich breccia facies*

The monomictic dacitic pumice-rich breccia facies (Fig. 3.10a) is clast-supported and comprises clasts of relict tube pumice (up to 10 cm) and clasts of highly vesicular feldspar-phyric dacite in a microcrystalline siliceous matrix (Fig. 3.10b). Clasts are ragged to blocky to elongate, variably oriented, uncompacted to partly collapsed or bent, and moderately to densely packed. The clasts show jigsaw-fit to clast-rotated texture. Locally some domains of clasts preserve the transition from vesicular dacite to tube pumice (Fig. 3.10c). The colour of the facies ranges from grey-green to creamy white.

This facies is non-stratified and occurs as thin (<1 m) units adjacent and gradational to coherent dacite, and locally gradational to monomictic dacite breccia. In places, it grades into the pumice-rich granule breccia or polymictic pumice-rich breccia.

Associated facies

- coherent dacite
- monomictic dacite breccia
- pumice-rich granule breccia
- polymictic pumice-rich breccia

Interpretation

The association and contact relationships of this facies with the coherent dacite and monomictic dacite breccia indicate that the monomictic dacitic pumice-rich breccia is a variety of autoclastic facies. The mixture of domains of clasts of tube pumice, highly vesicular dacite clasts and clasts showing the transition from highly vesicular quartz-phyric dacite to tube pumice clasts indicates that the pumice clasts most likely formed by non-explosive, quench fragmentation of the pumiceous carapace of a dacite lava or dome, in a manner that has been modelled for this general scenario by Allen and McPhie (2009).

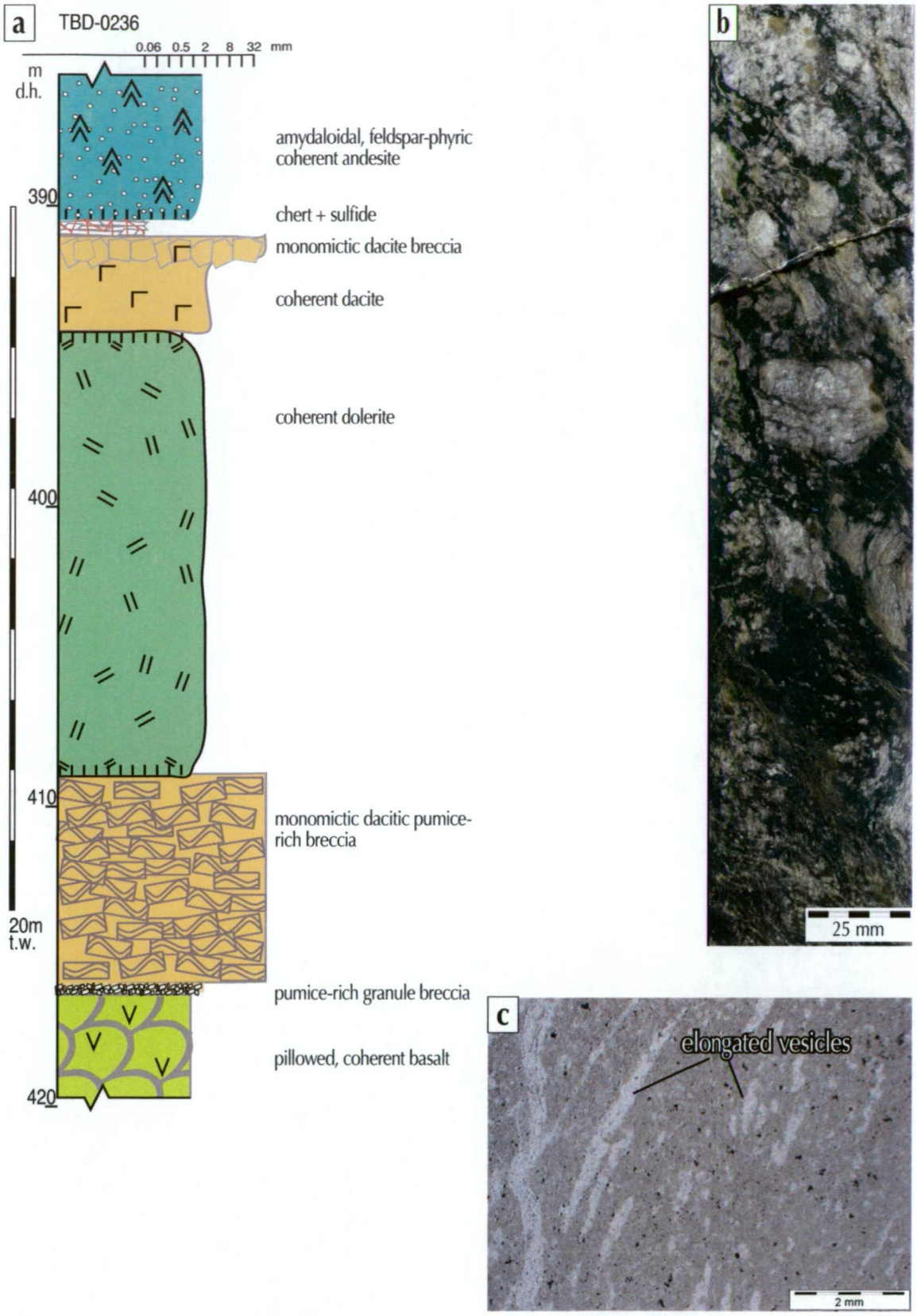

Figure 3.10 Monomictic dacitic pumice-rich breccia facies:
a) graphic log of TBD0236, showing relationships and variations in facies;
b) clasts of pumiceous dacite in silic-matrix, drillcore photograph, TBD0231 562.8 m;
c) dacite, showing development of elongated vesicles (now amygdales), photomicrograph, plain-polarised light, TBD0252 375.1 m.

For Legend and anotations used see Figure 3.2d

3.4.5 *Pumice-rich granule breccia facies*

The pumice-rich granule breccia facies (Fig. 3.11a) occurs in massive or normally graded, thin (3–10 cm) beds and lenses, up to 30 cm thick. It is monomictic and comprises well sorted, angular clasts of relict tube pumice (1–3 mm). The pumice granules are densely packed, uncompacted, and clast-supported, in a very fine-grained siliceous matrix (Fig. 3.11b). The overall colour of the facies is creamy white. The facies is not voluminous or extensive; occurrences are confined to the lowermost part of the Mineralised Package stratigraphic unit. This facies grades laterally and vertically into volcanic sandstone. In places, it grades upward into the monomictic dacitic pumice-rich breccia and drillhole correlation suggests it may grade laterally into the polymictic pumice-rich breccia. In places where this facies forms the basal layer of the Mineralised Package stratigraphic unit, isolated clusters of tube pumice fragments occur up to 15 cm into the underlying monomictic pillow-fragment basalt breccia facies. Where this facies overlies the chert facies (which more commonly forms the basal layer of the Mineralised Package stratigraphic unit), the lower contact is conformable and sharp (Fig. 3.11c).

Associated facies

- monomictic dacitic pumice-rich breccia
- polymictic pumice-rich breccia
- volcanic sandstone

Interpretation

The association and relationship of this facies with the monomictic dacitic pumice-rich breccia and the polymictic pumice-rich breccia, along with the angular granule shape, and the well sorted nature of the facies, indicate that the pumice-rich granule breccia is mainly composed of resedimented deposit of small juvenile fragments of pumice. The well-sorted mixture of granules of tube pumice indicate that some transport was involved. It is most likely derived by syn- or post-eruptive resedimentation of the monomictic dacitic pumice-rich breccia by grain-flow or other mass-flow processes and may be a more distal, finer-grained, and better sorted equivalent of the polymictic pumice-rich breccia.

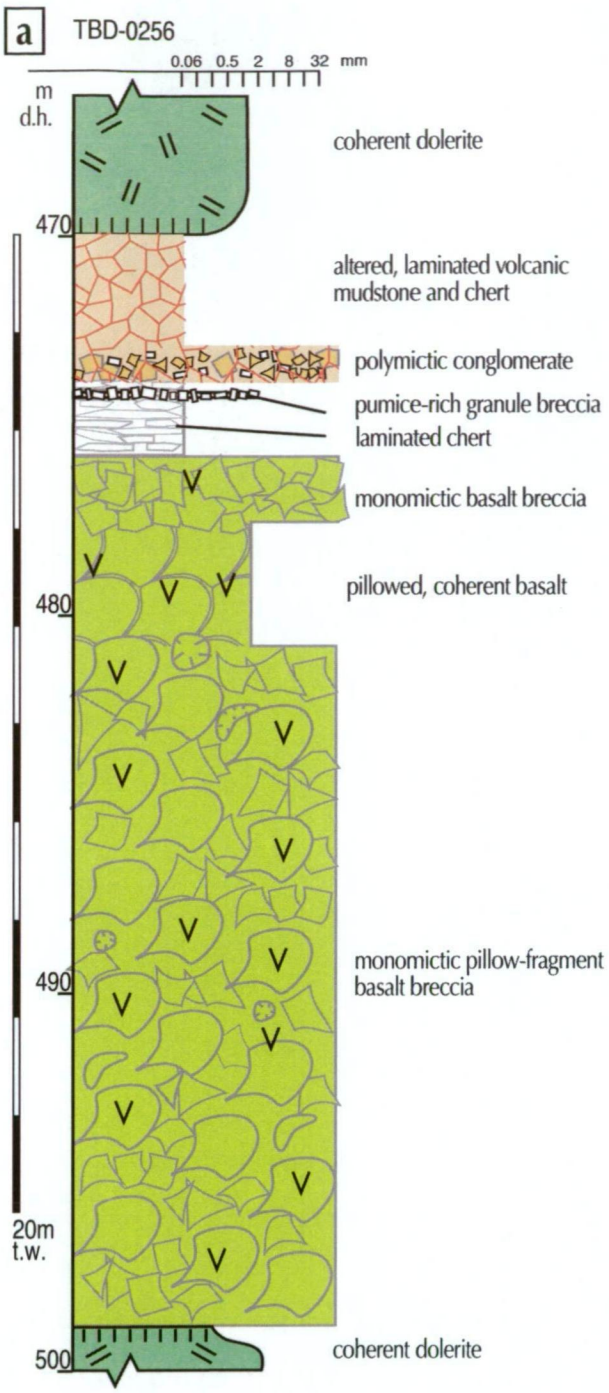

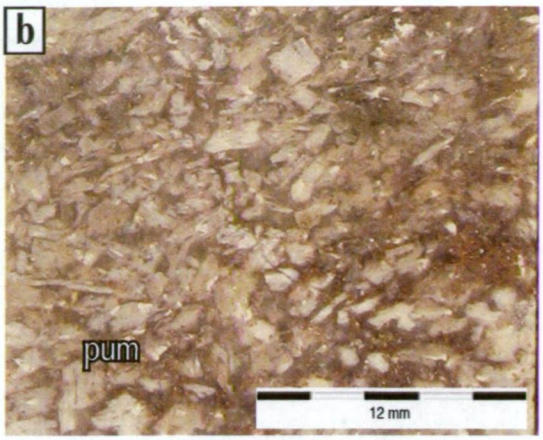

Figure 3.11 Pumice-rich granule breccia facies:
a) graphic log of TBD0256, showing relationships and variations in facies;
b) close up of angular, 1- 3 mm grains of tube pumice, drillcore photograph, TBD0256 474.2 m;
c) granular tube pumice overlying laminated chert, drillcore photograph, TBD0256 474.2 m.

For Legend and anotations used see Figure 3.2d

3.4.6 Monomictic andesite breccia facies

The monomictic andesite breccia facies (Fig. 3.12a) comprises monomictic, blocky and curviplanar-sided, splintery to ragged andesite clasts in a jigsaw-fit or clast-rotated arrangement (Figs. 3.12b) in a now-altered matrix of microcrystalline phyllosilicates. The clasts in the breccia are mostly 1 to 5 cm, but range up to 15 cm and vary in texture from formerly glassy, now-devitrified perlite comprising microcrystalline phyllosilicates (Figs 3.12c and 3.12d) to trachytic. In clasts with trachytic texture rare, small (<2 mm) amygdales are filled with a carbonate-quartz mixture and typically, carbonate and sericite have totally replaced feldspar.

This facies is unstratified and grades downwards over a short distance into vesicular, massive coherent andesite. It typically occurs at the margins of coherent andesite. Contacts between the monomictic andesite breccia facies and coherent andesite facies range from gradational to sharp. Units of the monomictic andesite breccia facies are typically limited in extent (<50–500 m) and range from tens of centimetres up to 10 m in thickness.

Associated facies

- coherent andesite

Interpretation

The monomictic composition, the jigsaw-fit texture, and the association and contact relationships with the coherent andesite indicate that the monomictic andesite breccia facies is the in-situ autoclastic facies of andesitic lavas and shallow intrusions (e.g. Pichler, 1965; Yamagishi and Dimroth, 1985; Kokelaar et al., 1985; Hanson, 1991; Batiza and White, 2000).

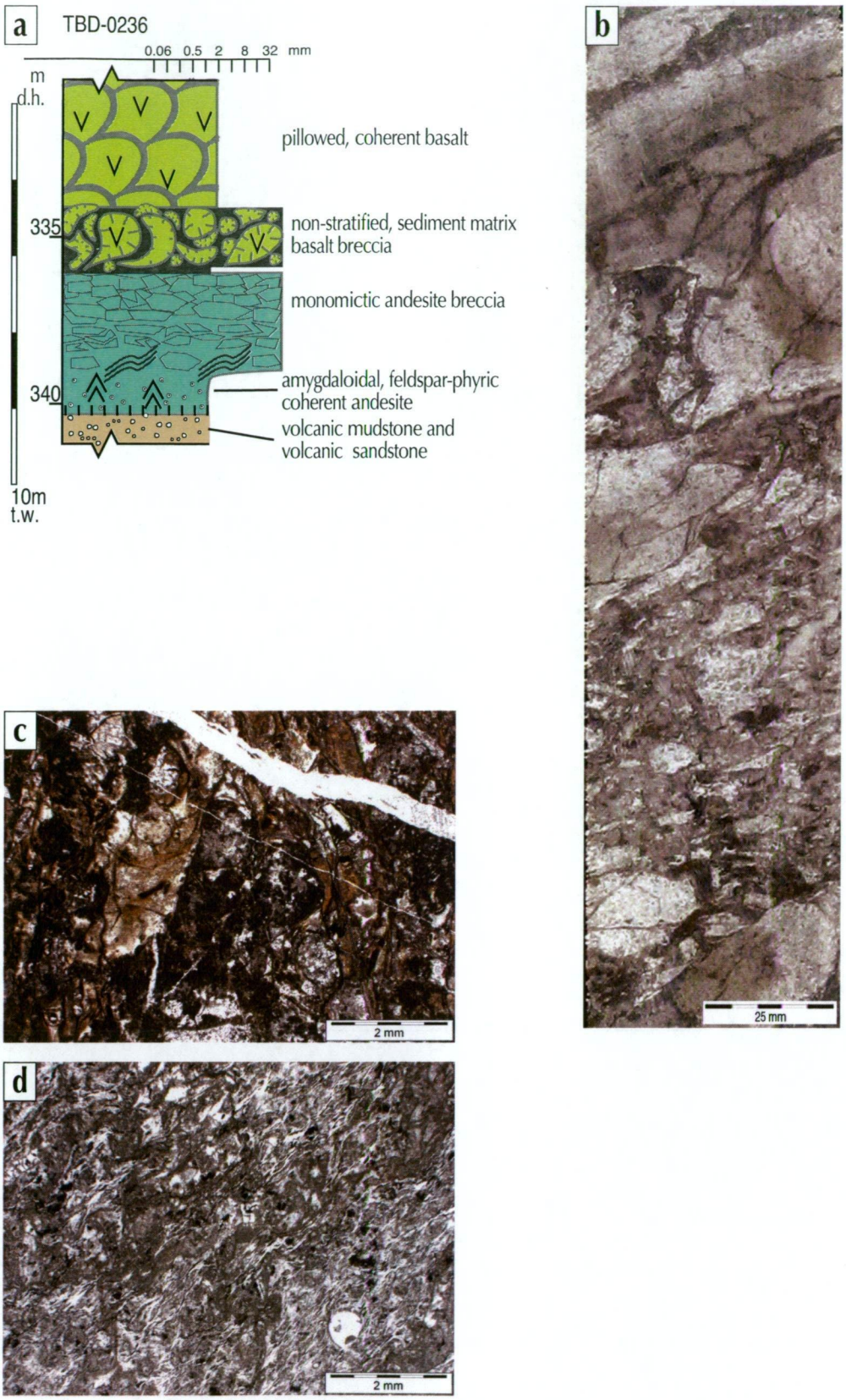

Figure 3.12 Monomictic andesite breccia facies:
a) graphic log of TBD0236, showing relationships and variations in facies;
b) mostly jigsaw-fit andesite breccia , drillcore photograph, TBD0236 37.4 m;
c) andesite showing perlite, cut by carbonate vein, photomicrograph, plain-polarised light, TBD0207 458.1 m;
d) formerly-glassy andesite with perlite texture and microlites, 0.5mm carbonate filled amygdale in lower right, photomicrograph, plain-polarised light, TBD0210 710 m.

For Legend and anotations used see Figure 3.2d

3.4.7 Non-stratified sediment-matrix andesite breccia facies

The non-stratified, sediment-matrix andesite breccia facies (Fig. 3.13a) is composed of andesite clasts (<2–20 cm) in a matrix of volcanic mudstone or black shale (Figs 3.13b and 3.13c). The breccia can be clast– or matrix–supported. In the clast–supported variant, the matrix is typically confined to irregular, fluidal to wispy lenses among clasts. Clasts may be blocky with curviplanar margins or small globular (<20 cm) clasts of andesite (Fig. 3.13d). Where the breccia is matrix–supported, the clasts are smaller (<1–10 cm) and blocky with curviplanar margins, and may show jigsaw fit (Fig. 3.13e), and the mudstone matrix may be featureless or show contorted or disrupted bedding.

Units of this facies range in thickness from 10 cm to >1 m, and typically occur along the lower margins of coherent andesite. Rarely, they occur along the upper margins of coherent andesite. The contact between the coherent andesite and this facies is generally gradational. As the distance from the coherent andesite increases, the clast to matrix ratio decreases (i.e. the matrix becomes more abundant).

Many clasts have a groundmass of relict perlite (Fig. 3.13f), indicating that they were formerly glassy. These clasts are now-devitrified and comprise microcrystalline phyllosilicates. Some clasts are porphyritic with plagioclase phenocrysts, and others show a trachytic texture in which carbonate and sericite have totally replaced feldspar.

Associated facies

- coherent andesite

Interpretation

The association and contact relationships with the coherent andesite facies indicate that the non-stratified, sediment-matrix andesite breccia facies is peperite resulting from the in-situ disintegration of the andesite magma as it intruded into, or flowed over wet, unconsolidated sediment (e.g. Kokelaar, 1982; Busby-Spera and White, 1987; Skilling et al., 2002).

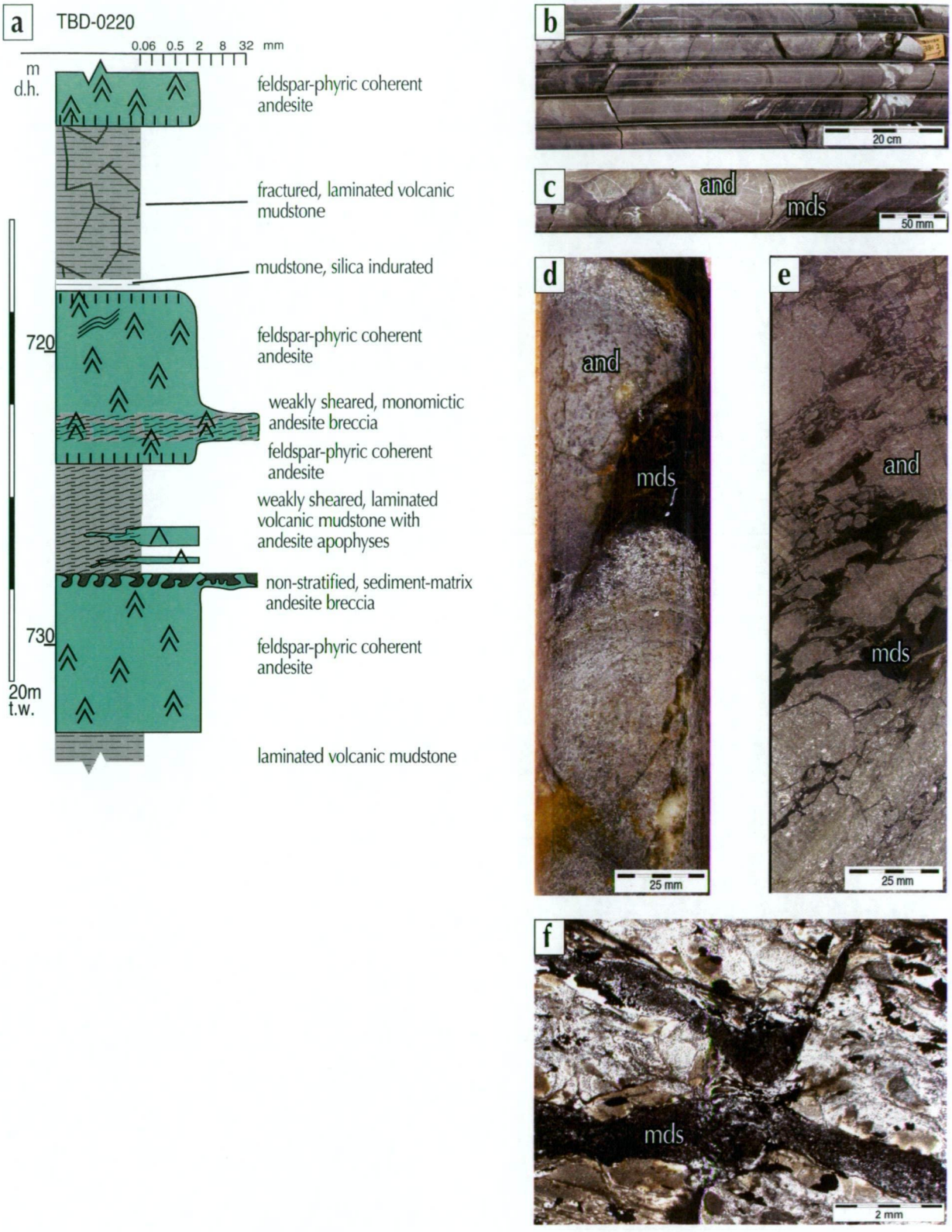

Figure 3.13 Non-stratified, sediment-matrix andesite breccia facies:
a) graphic log of TBD0220, showing relationships and variations in facies;
b) breccia of detached pillows, broken pillows and formerly-glassy clasts, in mudstone matrix, drillcore photograph, TBD0210 ~382 m;
c) andesite clasts in mudstone matrix, drillcore photograph, TBD0218 626.6 m;
d) brecciated andesite pillow in mudstone matrix, drillcore photograph, TBD0220 728.05 m;
e) jigsaw-fit andesite breccia in mudstone matrix, drillcore photograph, TBD0239 485.6 m;
f) perlitic andesite shards in mudstone matrix, note stretching bridge between shards in centre, photomicrograph, plain-polarised light, TBD0239 485.6 m.

For Legend and anotations used see Figure 3.2d

3.4.8 Monomictic basalt breccia facies

The monomictic basalt breccia (Fig. 3.14a) is clast-supported and comprises a mixture of clast sizes (2–25 cm) and shapes. The basalt clast shapes vary from blocky, to splinter with curviplanar sides, to fluidal, and different clast shapes dominate locally. The facies is non-stratified, but the local dominance of clasts with different sizes and shapes may reflect the presence of subtle thick beds (>50 cm). In places there are domains of jigsaw-fit clasts. The matrix comprises <2 mm angular basalt fragments. Where fluidal clasts comprise more than 10 modal %, the unit is defined as monomictic, fluidal-clast, basalt breccia facies. The facies occurs as lenses and laterally continuous layers up to 20 m thick.

The breccia units commonly grade downwards into coherent basalt that is either massive or pillowed. In places, this facies grades laterally or vertically into monomictic fluidal-clast basalt breccia or monomictic pillow-fragment basalt breccia.

The groundmass of the clasts is commonly variolitic, and in places is microcrystalline with plagioclase phenocrysts (Fig. 3.14b). Some clasts have a trachytic microtexture, whereas others have relict perlite. These formerly glassy clasts, now comprise microcrystalline phylosillicates.

Associated facies

- coherent basalt
- monomictic fluidal-clast basalt breccia
- monomictic pillow-fragment basalt breccia

Interpretation

The monomictic composition, the coarse grain size, the clast shape, and the associated facies indicate that this breccia facies is a variety of autoclastic breccia forming the carapace of lavas. The dominance of blocky or splintery clasts that were formerly glassy suggests that quench fragmentation was an important clast-forming mechanism. The clast variety, and weakly defined bedding indicate that local transport may have been involved and that not all clasts are in-situ (e.g. Yamagishi and Dimroth, 1985; Kokelaar et al., 1985; Batiza and White, 2000).

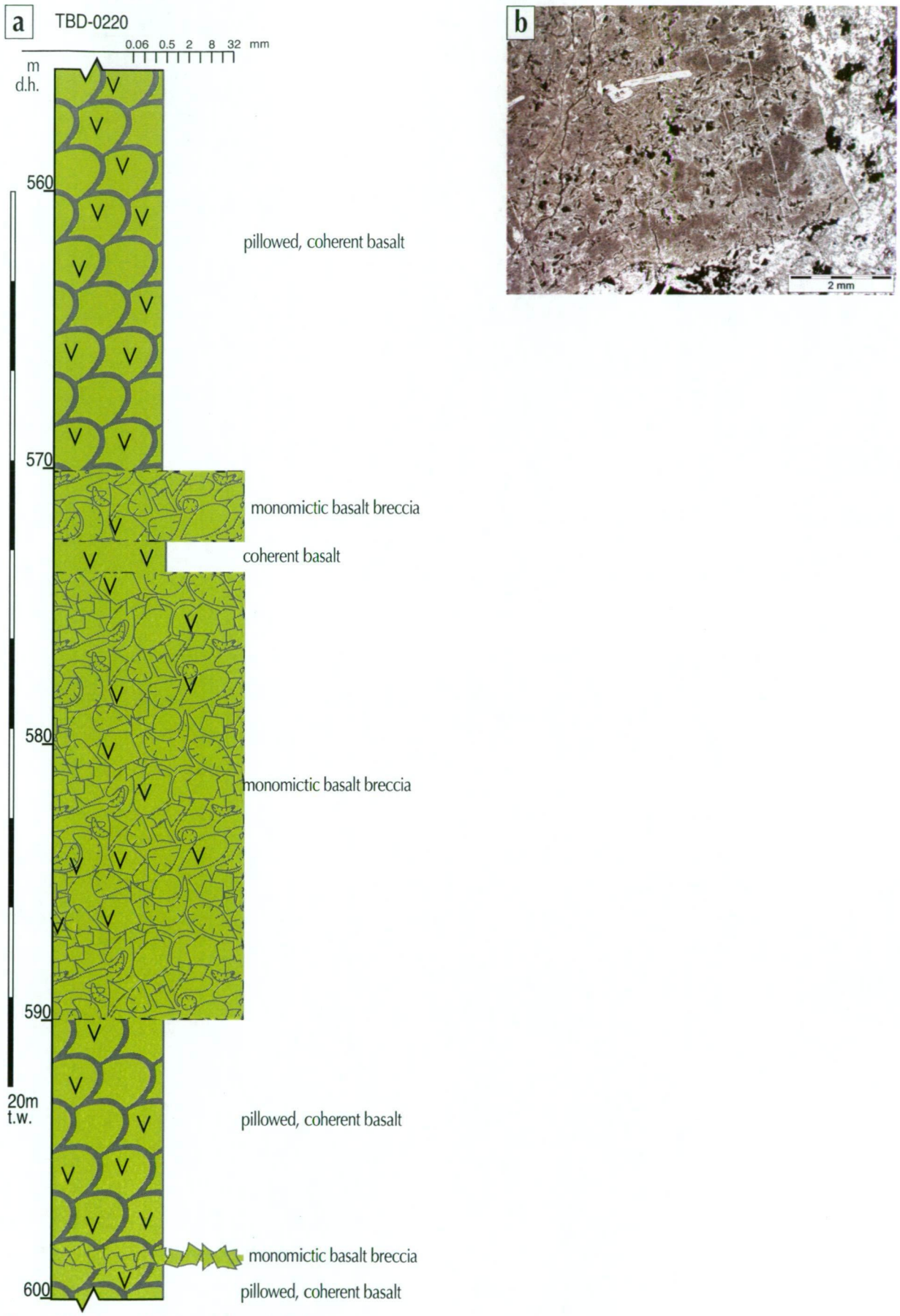

Figure 3.14 Monomictic basalt breccia facies:
a) graphic log of TBD0220, showing relationships and variations in facies;
b) clast margin, formerly-glassy basalt with variolites and microlites, note very sharp corner of clast in lower right, photomicrograph, plain-polarised light, TBD0253 470.7 m.

For Legend and anotations used see Figure 3.2d

3.4.9 Monomictic fluidal-clast basalt breccia facies

There is a single, albeit extensive, occurrence of monomictic fluidal-clast basalt breccia facies (Fig. 3.15a). This facies is clast-supported and composed of a poorly sorted assemblage of clasts that range in shape and size from fluidally shaped (2–25 cm), basalt clasts, to blocky to splintery (2–20 cm), angular basalt clasts in a matrix of <2 mm basaltic fragments. All fluidial clasts are aphyric. The fluidal clasts are typically elongate and have amygdaloidal (1–15 mm) cores . The margins are commonly up to 1 cm thick with smaller amygdales (0.5–1 mm) (Figs 3.15b, 3.15c and 3.15d). The intricately fractured, formerly glassy rims now comprise microcrystalline phyllosilicates) (Fig. 3.15d). The facies is defined by the presence of the fluidal clasts in excess of 10 modal %, and is otherwise the same as the monomictic basalt breccia into which it grades laterally and vertically.

The monomictic fluidal-clast basalt breccia facies is lens shaped and seen to extend at least 200 m along strike and about 150 m across strike. In the centre of its distribution it is up to 15 m thick. It extends laterally as lenses and wedge-shaped intercalations, ranging from <1 to 5 m thick, with the monomictic basalt breccia facies. As with the monomictic basalt breccia, the local dominance of different clast size and shape may reflect the presence of thick beds (>50 cm).

Associated facies

- monomictic basalt breccia
- coherent basalt

Interpretation

The monomictic composition, the very distinctive bimodality in clast shape and the associated facies indicate that this is a basalt breccia composed of both quench-fragmented debris and fluidal bombs. The clast shape of the blocky or splintery clasts that were formerly glassy, suggests that quench fragmentation was an important clast-forming mechanism. The fluidal clasts resemble bombs formed by tearing apart low viscosity lava ribbons (MacDonald, 1972). The fluidal shapes were partly controlled by surface tension and hydrodynamic forces on the still-molten fragments. The formerly glassy, outer margins were probable generated by quenching on contact with seawater. This facies formed by submarine fountaining of low-viscosity basaltic lava (e.g MacDonald, 1972, Wilson and Head, 1981, Smith and Batiza, 1989, Simpson and MacPhie, 2001). Although lava fountaining (hawaiian-style) is generally associated with sub-aerial settings, Head and Wilson (2003) have suggested that submarine hawaiian-style is more common than previously suspected and that it can occur to depths of up to 3000m, and the runout distance of the collapsing column surrounding the fountain would be in the order of twice the height of the fountain.

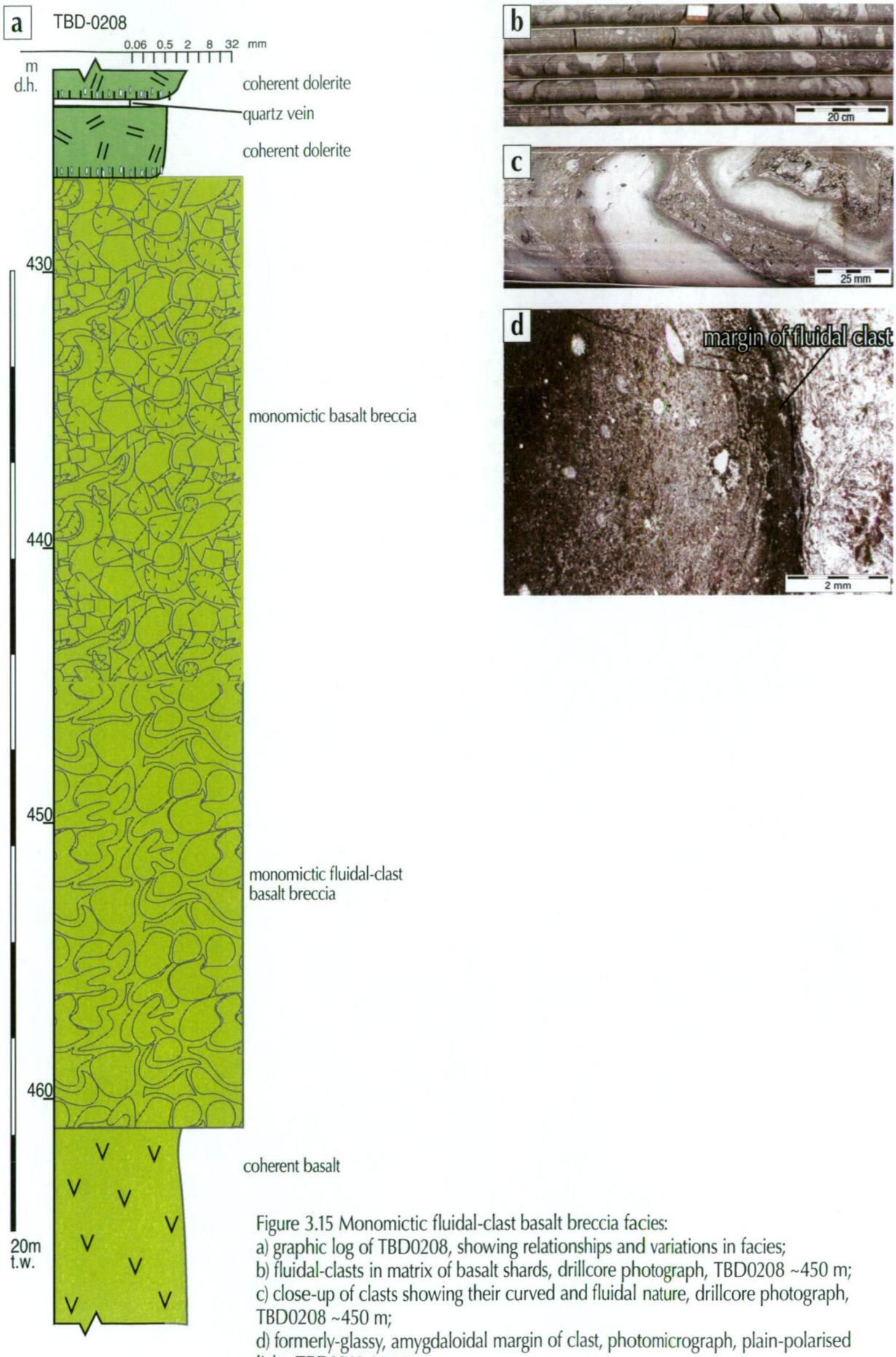

Figure 3.15 Monomictic fluidal-clast basalt breccia facies:
a) graphic log of TBD0208, showing relationships and variations in facies;
b) fluidal-clasts in matrix of basalt shards, drillcore photograph, TBD0208 ~450 m;
c) close-up of clasts showing their curved and fluidal nature, drillcore photograph, TBD0208 ~450 m;
d) formerly-glassy, amygdaloidal margin of clast, photomicrograph, plain-polarised light, TBD0210 284.7 m.

For Legend and anotations used see Figure 3.2d

3.4.10 Monomictic pillow-fragment basalt breccia facies

The clasts in the monomictic pillow-fragment basalt breccia facies (Fig. 3.16a) include basaltic pillow fragments, sub-angular to sub-rounded equant basalt clasts and blocky basalt clasts with curviplanar margins (Fig. 3.16b) in a matrix of <2 mm angular basalt fragments (Fig. 3.16c). The clasts comprise a mixture of formerly- glassy, amygdaloidal or non-amygdaloidal basalt and fine-grained amygdaloidal or non-amygdaloidal basalt (Figs 3.16c and 3.6d), with sizes that range from 2 mm to >20 cm (pillow fragments). The pillow fragments have margins that preserve partly chilled pillow rinds, and margins with straight truncations of the pillow rind, indicating that fragmentation occurred after solidification. Local domains of jigsaw-fit basalt clasts are also present (Fig. 3.16e). Clasts vary from poorly to moderately amygdaloidal.

This facies is intercalated with, and gradational to, the monomictic basalt breccia or coherent basalt, attains thicknesses of up to 20 m, and extends through out the study area (>1000 m). A single occurrence, less than 0.5 m thick, is intercalated between laminated mudstone layers. The pillow-fragment basalt breccia facies is dominantly monomictic, but rare polymictic occurances occur in some drillholes, where small (<2 mm) granules of tube pumice are seen in the top 15 cm of this facies, immediately below the Mineralised Package.

Bedding is not recognised but, as for the monomictic basalt breccia, the local dominance of different clast types and shapes may reflect the presence of thick beds (>50 cm) that are not recognisable in drill core.

Associated facies

- coherent basalt
- monomictic basalt breccia

Interpretation

The clasts of broken pillows were derived from the break-up of solidified pillow lava. The sub-rounding of some clasts, and mixture of clasts, indicate transport, whereas the angular nature of others, and poor sorting, suggest only minimal transport. The coarse grain size and lack of organisation are consistent with deposition from a high-concentration mass-flow, such as a grain flow. Such mass flows may be the result of seismically induced tectonic instability or local volcanic edifice collapse. The facies may be basaltic debris sourced from an unstable mound or ridge of basaltic lavas (e.g. McBirney, 1963; Kokelaar et al., 1985; Yamagishi, 1987; Batiza and White, 2000).

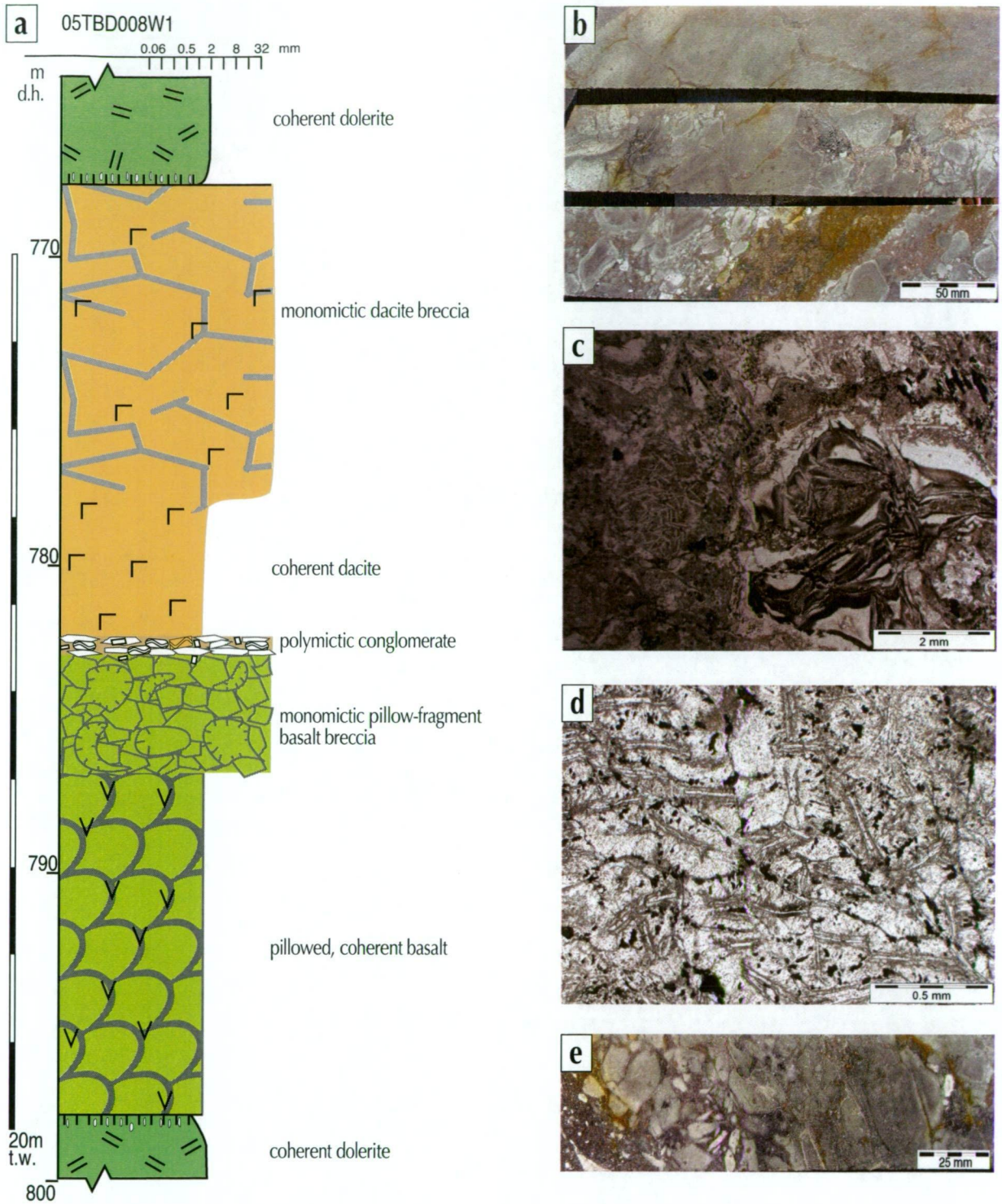

Figure 3.16 Monomictic pillow-fragment basalt breccia facies:
a) graphic log of 05TBD008w1, showing relationships and variations in facies;
b) three samples show variations in clast size, shape and packing, drillcore photograph, TBD0253 437-443 m;
c) matrix to larger clasts is a mixture of microclasts, showing shards (hyaloclastic clasts) mixed with m-grained trachytic clasts, photomicrograph, plain-polarised light, TBD0253 458.8 m;
d) varolites nucleating on microlites in a devitrified clast, photomicrograph, plain-polarised light, TBD0253 458.6 m;
e) jigsaw-fit transitioning to rotated clasts, drillcore photograph, TBD0253 479.7 m.

For Legend and anotations used see Figure 3.2d

3.4.11 Non-stratified sediment-matrix basalt breccia facies

The non-stratified, sediment-matrix basalt breccia facies (Fig. 3.17a) is composed of clasts of basalt (<2 mm –20 cm) in a matrix of black shale and volcanic mudstone (Figs 3.17b, 3.17c and 3.17d). The matrix commonly occurs as irregular fluidal to wispy lenses of mudstone or black shale among basalt clasts with ragged to curviplanar boundaries or among small globular (<20 cm) clasts of basalt. Intervals of this unit are non-stratified, poorly sorted and, in general, clast-supported. Relict laminae or disturbed beds can be seen in places in the matrix. Intervals of sediment-matrix basalt breccia facies are not common but, where they occur, they are typically located along the lower margin of coherent basalt. Units of this facies rarely exceed several metres thickness and are limited in extent (200–500 m). The contact between the coherent basalt and the sediment-matrix basalt breccia facies is gradational. The lower contact of this facies is either gradational to volcanic mudstone, or sharp and overlying coherent basalt.

The groundmass of the basalt clasts is commonly variolitic, and in places is microcrystalline with rare plagioclase phenocrysts. Some clasts have a trachytic microtexture.

Associated facies

- coherent basalt

Interpretation

The combination of sedimentary and basaltic components, and association and contact relationships with the coherent basalt facies indicate that this non-stratified, sediment-matrix basalt breccia facies is peperite, formed where basalt lava flowed over or invaded wet, unconsolidated sediment (e.g. Kokelaar, 1982; Busby-Spera and White, 1987; Skilling et al., 2002).

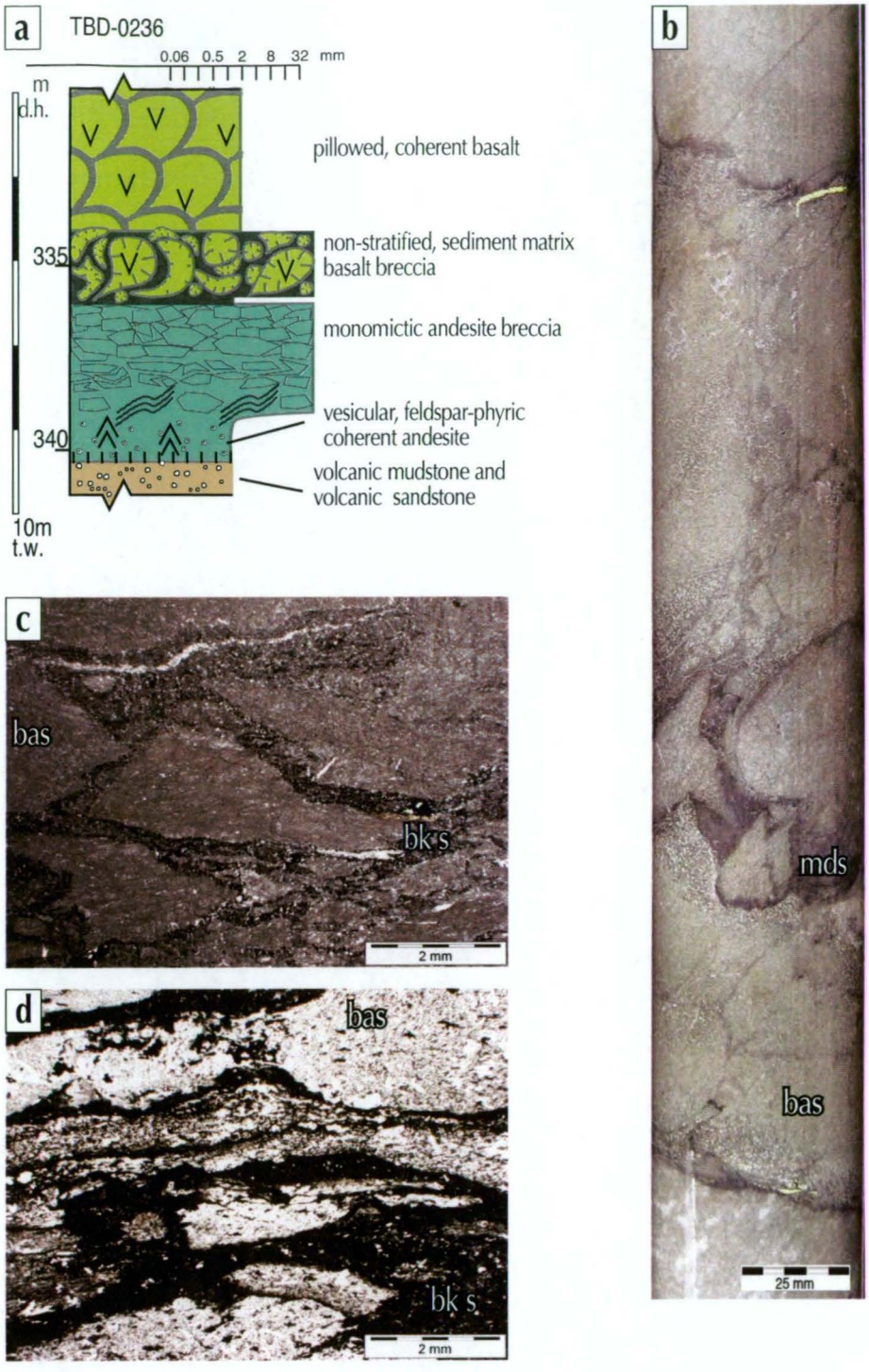

Figure 3.17 Non-stratified, sediment-matrix basalt breccia facies:
a) graphic log of TBD0236, showing relationships and variations in facies;
b) jigsaw-fit clasts of basalt in a mudstone matrix , drillcore photograph, TBD0220 680 m;
c) ragged, jigsaw-fit micro-clasts of basalt in a black shale matrix, photomicrograph, plain-polarised light, TBD010 692.2 m;
d) jigsaw-fit and rotated micro-clasts of basalt in a black shale matrix, photomicrograph, plain-polarised light, 05TBD006 228.5 m.

For Legend and anotations used see Figure 3.2d

3.5 Group 3: Polymictic volcanic breccia and conglomerate

3.5.1 Polymictic rhyolite breccia facies

The polymictic rhyolite breccia facies (Fig. 3.18a) is dominated by 2– to 10–cm, curviplanar-blocky clasts of quartz-phyric rhyolite (<75 modal %). Larger (>20 cm) curviplanar-blocky clasts of quartz-phyric rhyolite occur in places (Fig. 3.18b). The facies is poorly sorted and clast-supported in a fine-grained siliceous matrix. The non-rhyolite clasts (5–10 modal %) reflect the adjacent facies.

Only two intervals of this facies are recognised. In one occurrence, sub-rounded clasts of amygdaloidal aphyric basalt comprising <5 modal % reflect the basaltic substrate. It is intercalated with, and grades vertically into, monomictic rhyolite breccia over a short interval (<1 m). This occurrence is in the lower part of the succession where it was intersected by one drillhole. It has a thickness of 10 m, but the lateral extent is not known. The lower contact of the polymictic rhyolite breccia with pillow basalt is sharp.

The second occurrence, in the upper part of the succession, occurs along the lower margin of a unit of coherent rhyolite unit that grades downwards into polymictic rhyolite breccia facies. Altered, angular clasts of mudstone reflect the underlying unit. This occurrence has a sharp lower contact with underlying laminated volcanic mudstone.

Associated facies

- coherent rhyolite
- monomictic rhyolite breccia

Interpretation

In the lower occurrence, the clast varieties and the relationship with monomictic rhyolite breccia facies suggests that this facies is a resedimented, autoclastic breccia, derived from a collapse of a rhyolite lava or dome carapace. Transport distance was probably very short, given the poor sorting, lack of bedding and lack of rounding. The basalt clasts were probably collected from loose basaltic rubble on the sea floor.

The transition of the upper occurrence of the facies to the coherent rhyolite and the sharp contact to the underlying laminated mudstone suggest the facies is an autoclastic breccia formed by the in-situ fragmentation in the flow base of a lava that incorporated clasts of the unconsolidated substrate.

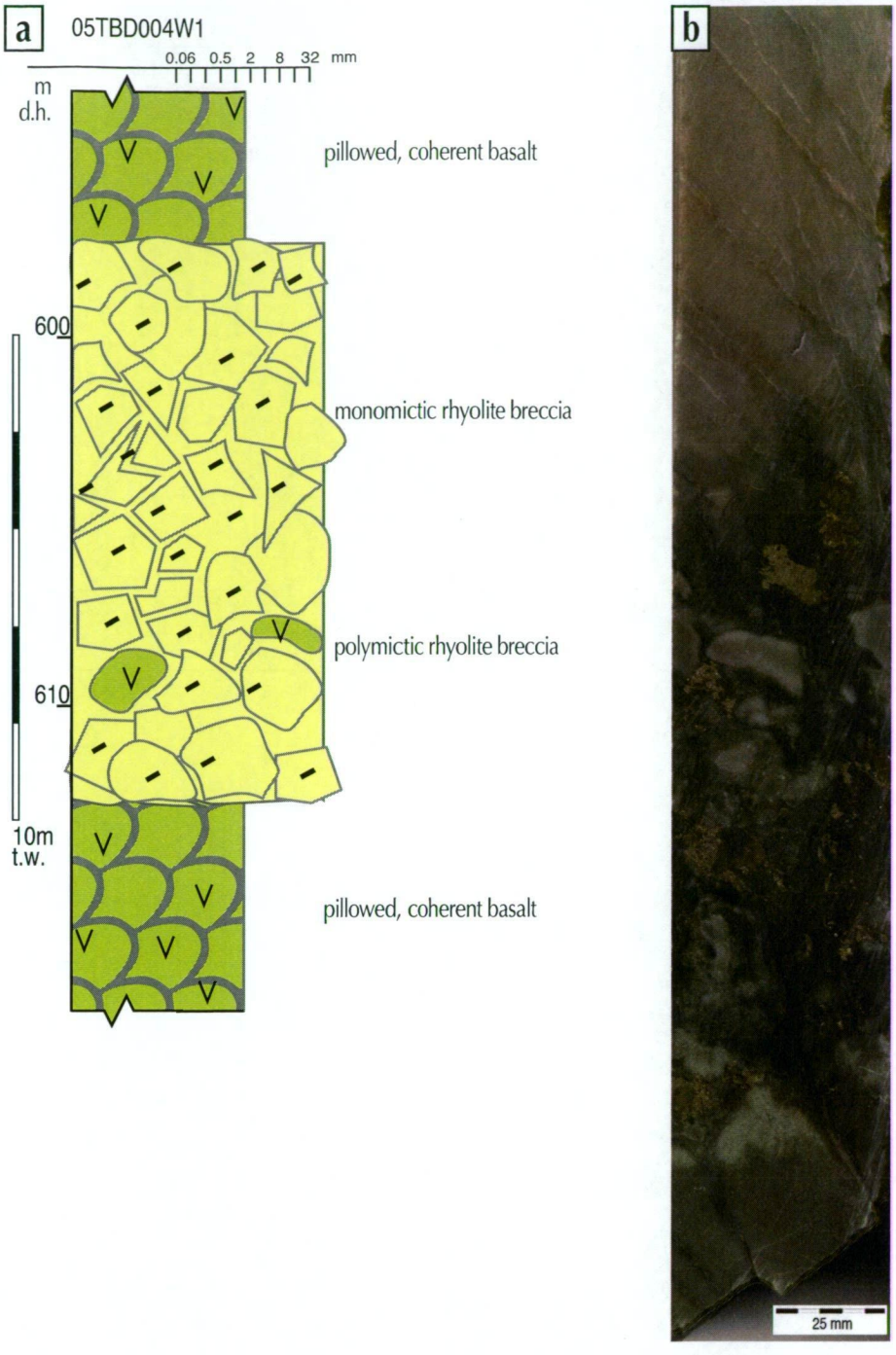

Figure 3.18 Polymictic rhyolite breccia facies:
a) graphic log of 05TBD004w1, showing relationships and variations in facies;
b) weakly chlorite altered and mineralised rhyolite breccia, clasts are curviplanar to blocky shape, drillcore photograph, 05TBD004w1 603 m.

For Legend and anotations used see Figure 3.2d

3.5.2 Polymictic dacite breccia facies

The polymictic dacite breccia facies (Fig. 3.19a) is composed of 2- mm to 20- cm clasts, commonly dacite with subordinate chert (<5-10 modal %). The dacite clasts are blocky to ragged or splintery (Figs 3.19b and 3.19c). The chert clasts are elongate and tabular or locally curved. This facies varies from clast-supported to matrix-supported. The matrix can be either a fine-grained siliceous sandstone or mudstone matrix. Where the facies is clast-supported the clasts are larger and the matrix is commonly a fine-grained siliceous sandstone, and where it is matrix-supported, the clasts are smaller (<10 cm) and the matrix is commonly mudstone.

This facies is confined to the mineralised package stratigraphic unit. It is not recognised as bedded and the thickness of units ranges from <1 to 5 m. The lateral extent is not known. Where present, it commonly grades laterally or vertically into the monomictic dacite breccia, or the polymictic conglomerate facies.

Associated facies

- monomictic dacite breccia
- polymictic conglomerate

Interpretation

The clast mixture and the gradational relationships with both the monomictic dacite breccia facies and polymictic conglomerate facies suggest that this facies is derived largely from a coherent dacite lava or dome, possibly by means of a collapse of an autoclastic carapace (e.g., Cas and Wright, 1987; McPhie et al., 1993; Fisher and Schmincke, 1994), and incorporation of a pre-existing semi-consolidated chert that covered the sea floor. The elongate and curved shapes of the chert clasts suggests they were still plastic at the time of incorporation and deposition.

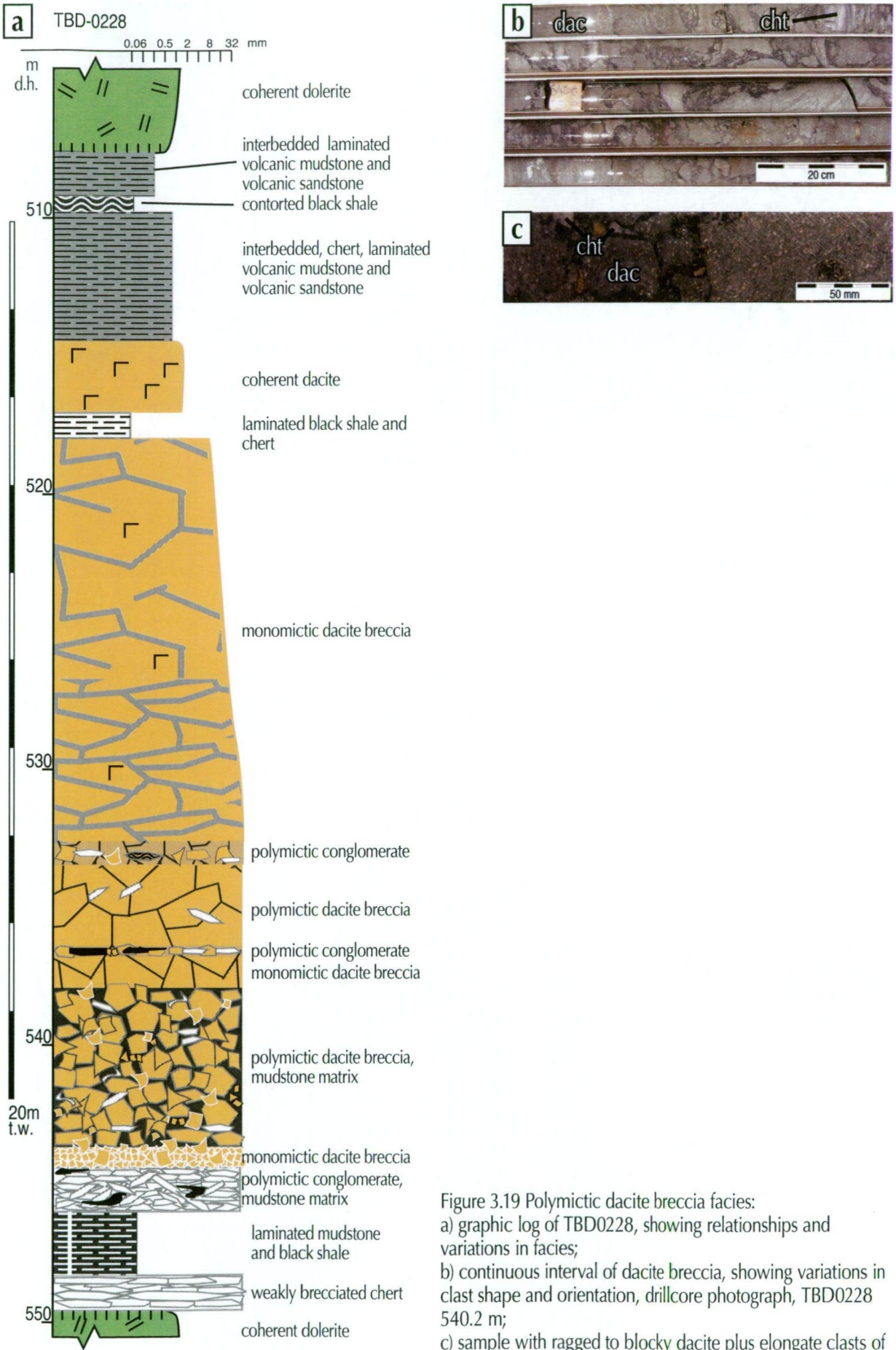

Figure 3.19 Polymictic dacite breccia facies:
a) graphic log of TBD0228, showing relationships and variations in facies;
b) continuous interval of dacite breccia, showing variations in clast shape and orientation, drillcore photograph, TBD0228 540.2 m;
c) sample with ragged to blocky dacite plus elongate clasts of chert, drillcore photograph, TBD0242 689.5 m.

For Legend and anotations used see Figure 3.2d

3.5.3 Graded or massive, polymictic conglomerate facies

The polymictic conglomerate facies (Fig. 3.20a) is composed of <20 cm-sized clasts. The clast population varies within beds, and throughout units. Clasts include dacite, andesite, pumice, chert, black shale, minor sulfide, and rare basalt in a matrix of volcanic sandstone to mudstone, or black shale (Figs 3.20b, 3.20c, 3.20d, 3.20e, 3.20f and 3.20g). The facies varies from clast-supported to matrix-supported. The dacite clasts (5–20 cm) are blocky, some with curviplanar faces to ragged edges. The chert clasts (1–2 x 5–15 cm) are elongate and tabular or locally curved, whereas the black shale clasts (<5 cm) are smaller and can be fluidal or have curved tabular shapes. The sulfide clasts (<1–2 cm) are commonly sub-rounded. The very rare basalt clasts (5–15 cm) are angular to sub-rounded. This facies is generally poorly sorted and normally graded where the facies grades upwards into the volcanic sandstone facies. The matrix is dominated by sandstone, but may be mudstone or black shale locally. The sandstone components also vary, and comprise variable amounts of volcanic clasts, pumice grains, and broken euhedral quartz and feldspar crystals.

Single beds may be as thin as 4 cm (Fig. 3.20h) and intercalated with sandstone and mudstone facies, or be tens of metres thick. Beds of this facies are medium to thick and either internally massive or graded. There are both sharp and gradational contacts. This facies grades laterally and vertically into the polymictic dacite breccia, polymictic pumice-rich breccia or volcanic sandstone facies.

Associated facies

- polymictic dacite breccia
- polymictic pumice-rich breccia
- pumice-rich granule breccia
- volcanic sandstone
- laminated volcanic mudstone

Interpretation

The massive or graded beds and the association with, or gradation into the polymictic dacite breccia facies suggests that transport and deposition was mainly from locally sourced sediment gravity flows, whereas the coarser more massive beds may reflect that transport was by debris flows (e.g. Lowe, 1982; Fisher and Schmincke, 1984; Cas and Wright, 1987; Fisher and Schmincke, 1994). Beds with a matrix of black shale could be debris-flow deposits, with the mud locally derived from unconsolidated mud substrate. The clast assemblage suggests the provenance included a dacite dome and/or lava. The elongated and curved shape of the chert clasts suggests they were still plastic at the time of incorporation and deposition, and the presence of minor sulfide clasts suggests that a sulfide deposit existed in the source, and/or outflow path.

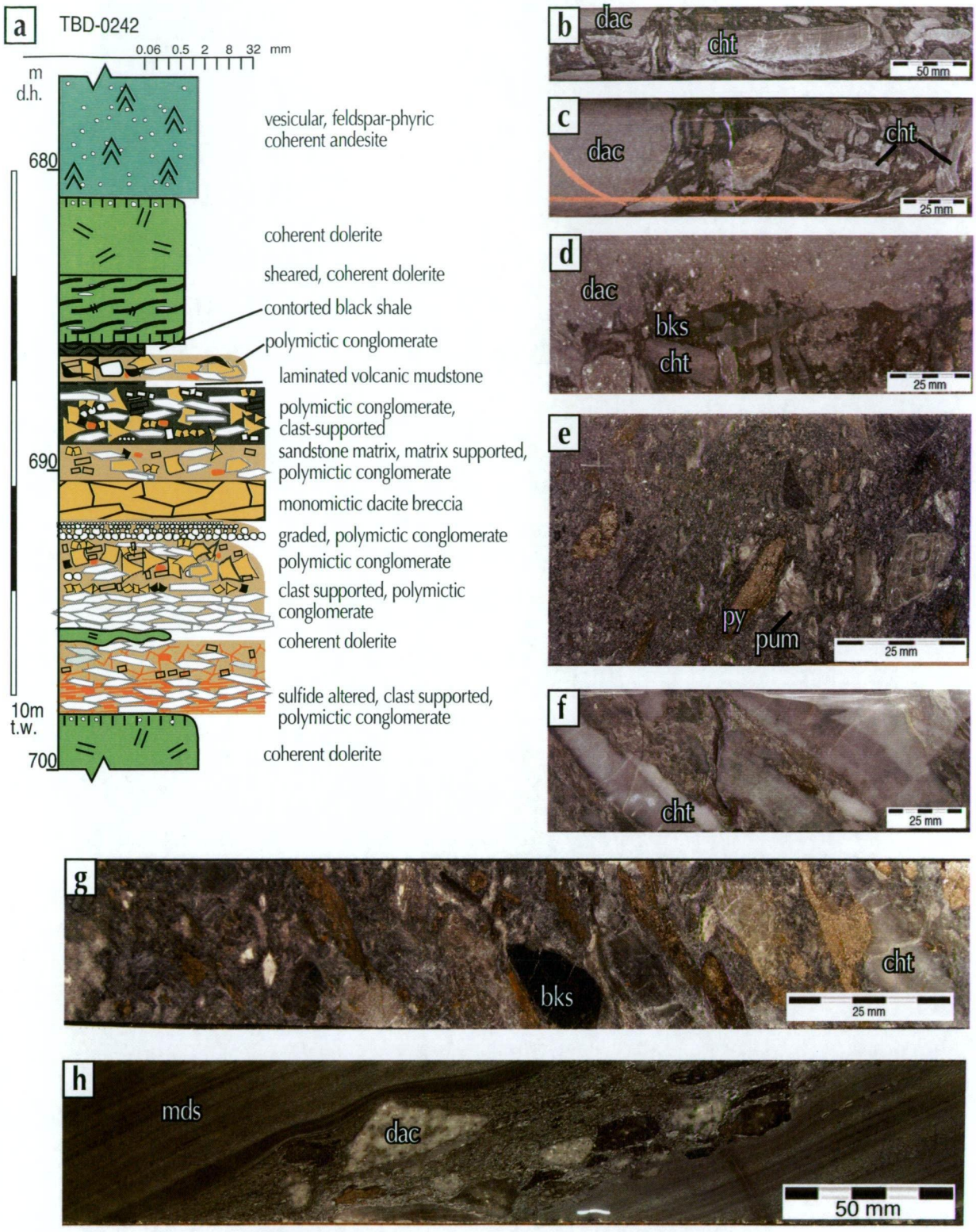

Figure 3.20 Polymictic conglomerate facies:
a) graphic log of TBD0242, showing relationships and variations in facies;
b) elongate clast of laminated chert among dacites clasts, drillcore photograph, 07TBD001 643.8 m;
c) chert and dacite clasts in black shale matrix, note plastic deformation of elongate chert clasts, drillcore photograph, 07TBD001 644 m;
d) mixed small clasts, pumice, dacite, chert and pyrite in sand sized matrix, drillcore photograph, TBD0242 691.8 m;
e) clast-supported, chert clasts mixed with collapsed pumice clasts, drillcore photograph, TBD0242 693 m;
f) ragged edge of dacite clast abuting randomly oriented chert clasts, drillcore photograph, TBD0242 689.8 m;
g) matrix-supported, mixed small clasts, tube pumice, dacite, chert, black shale and pyrite in sand sized matrix, overprinted sufide replacement, drillcore photograph, TBD0242 691.7 m;
g) 4 cm wide bed intercalated with laminated mudstone, drillcore photograph, TBD0216 617.85 m.

For Legend and anotations used see Figure 3.2d

3.5.4 *Polymictic pumice-rich breccia facies*

The polymictic pumice-rich breccia facies (Fig. 3.21a) is clast-supported and comprises clasts of partly compacted tube pumice, chert and rare dacite in a fine-grained siliceous matrix. The pumice clasts commonly 'wrap' around chert clasts (Fig. 3.21b) and there is very little matrix. The colour of the facies is grey to creamy white.

This facies occurs as thin units (<1 m) adjacent and gradational to the monomictic dacitic pumice-rich breccia facies and or the polymictic conglomerate facies. It also occurs as discrete lenses, up to 30 cm thick, overlying units of the chert facies, or bounded by sharp contacts with the sulfide facies. Drillhole correlation suggests it may grade laterally into the pumice-rich granule breccia.

Associated facies

- monomictic dacitic pumice-rich breccia
- graded or massive, polymictic conglomerate
- pumice-rich granule breccia
- chert
- sulfide

Interpretation

The association and relationship of this facies with other pumice-rich facies, along with the clast shapes and textures, indicate that the polymictic pumice-rich breccia is mainly composed of autoclastic debris. The mixture of clasts of tube pumice and chert indicate that some transport was involved, though the poor sorting suggests that the distance travelled may not be far. It is most likely to be derived from syn- or post-eruptive resedimentation of the monomictic dacitic pumice-rich breccia by grain-flow or other mass-flow processes, and incorporation of chert that was forming on the seafloor at the time (e.g., Cas and Wright, 1987; McPhie et al., 1993; Fisher and Schmincke, 1994).

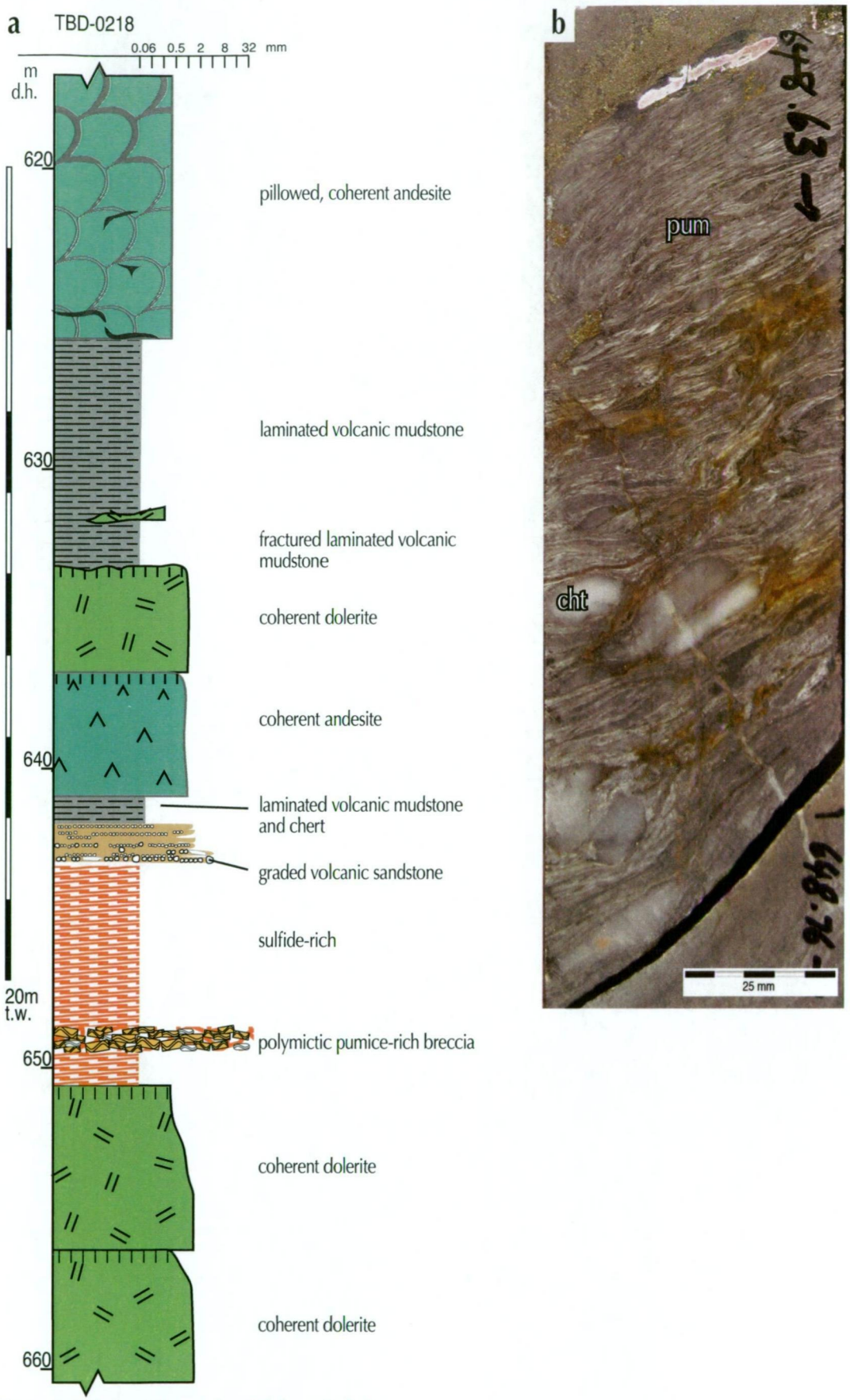

Figure 3.22 Polymictic pumice-rich breccia facies:
a) graphic log of TBD0218, showing relationships and variations in facies;
b) partly collapsed clasts of tube pumice 'wrapping' chert clasts showing a flattening foliation, drillcore photograph, TBD0218 648.6 m.

For Legend and anotations used see Figure 3.2d

3.6 Group 4: Volcanic sandstone and mudstone

3.6.1 Volcanic sandstone facies

The volcanic sandstone facies (Fig. 3.22a) comprises laminated and thinly bedded sandstone with a diverse grain population. Crystals of feldspar and clear volcanic quartz (euhedral crystals or sub-angular fragments), tube pumice and relict shards, and clasts of dacite or andesite are all present (Figs 3.22b and 3.22c). The grains are generally poorly sorted and not well rounded, although sparse, well-rounded, fine (<150 micron) quartz grains occur. Single beds are generally well-sorted. The grain size distribution and modal % of the grain types varies throughout the facies on a sub-centimetre scale.

The volcanic sandstone facies occurs as multiple stacked beds of sandstone, or is intercalated with beds of the laminated mudstone facies (Fig. 3.22d), or rarely black shale (locally graphitic) and beds of the polymictic conglomerate. In a gross sense, this facies commonly grades upwards into laminated volcanic mudstone. It grades laterally into polymictic conglomerate, pumice-rich granule breccia, laminated volcanic mudstone and, in places, downwards into polymictic dacite breccia facies or polymictic conglomerate facies. Bed thickness varies from <1 mm up to several centimetres. Beds display normal grading locally.

This facies is variably altered to assemblages of sericite, quartz, chlorite and carbonate, or a mixture of these minerals.

Associated facies

- polymictic conglomerate
- polymictic dacite breccia
- pumice-rich granule breccia
- laminated volcanic mudstone

Interpretation

The euhedral crystals and crystal fragments, tube pumice, and shards could have been produced originally by explosive or quench fragmentation and subsequently mixed with other clast types. Their unmodified state indicates little to no reworking, whereas the sparse well-rounded quartz grains indicate significant reworking. The polymictic composition and variation in roundness indicate mixing of particles from probably local and remote sources (e.g. Fisher and Schmincke, 1994). The graded bedding suggests deposition from dilute, water-supported gravity flows (essentially low-density turbidity currents) (e.g. Lowe, 1982). The association with, and gradation into, the laminated mudstone facies suggests that some of the finer intervals may have been deposited from suspension. The particle types indicate a strong link with adjacent coherent facies, indicating a likely local provenance of much of the material.

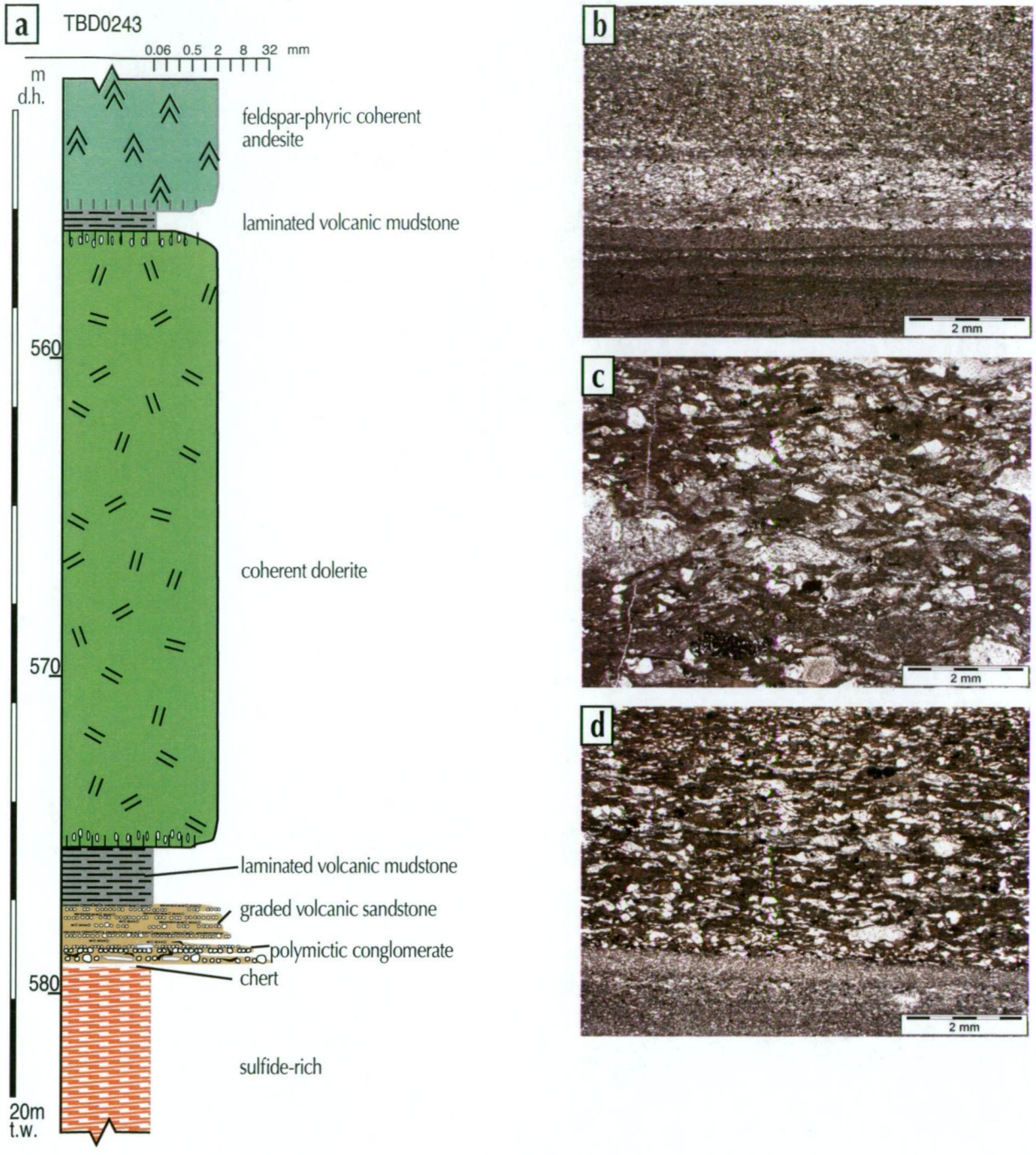

Figure 3.22 Volcanic sandstone facies:
a) graphic log of TBD0243, showing relationships and variations in facies;
b) bedded mudstone and sandstone, photomicrograph, plain-polarised light, TBD0256 409.5 m;
c) clasts of dacite, shards, pumice and broken crystals in sandstone, photomicrograph, plain-polarised light, TBD0216 618 m;
d) grains of collapsed pumice (showing a crude flattening foliation) and broken crystals overlying mudstone, photomicrograph, plain-polarised light, TBD0216 618 m.

For Legend and anotations used see Figure 3.2d

3.6.2 *Laminated volcanic mudstone facies*

The laminated volcanic mudstone facies (Fig. 3.23a) is pale to dark grey and locally black (Fig. 3.23b). Beds vary from <1 to 10 mm thick. This facies is difficult to distinguish from the non-volcanic mudstone and the criteria used in this study is the presence of broken crystals.

The facies is present throughout the succession. It can occur intercalated with coherent facies, and may make up the matrix in the non-stratified, sediment-hosted monomictic breccias that are locally present along some margins of the coherent units. It is also present in thicker units (1–5 m) intercalated with the volcanic sandstone facies. It commonly occurs gradationally at the top of units of bedded volcanic sandstone. The laminated volcanic mudstone facies grades also upward into the non-volcanic mudstone and black shale facies.

Passive contacts are seen where the mudstone overlies autoclastic tops of lavas. Elsewhere is a zone of non-stratified sediment-matrix breccia (peperite) between the mudstone and upper and lower contacts of a coherent facies. Non-conformable and irregular contacts occur at the base of coherent facies (Fig. 3.23b).

Associated facies

- volcanic sandstone
- non-stratified sediment-matrix rhyolite breccia
- non-stratified sediment-matrix andesite breccia
- non-stratified sediment-matrix basalt breccia
- laminated mudstone and black shale

Interpretation

The very fine grainsize and thinly bedded intervals suggest deposition from suspension sedimentation. Some laminated mudstone units that grade downwards into bedded volcanic sandstone and other volcaniclastic units could include a component of very dilute gravity current transport (e.g. Lowe, 1976; Lowe, 1982).

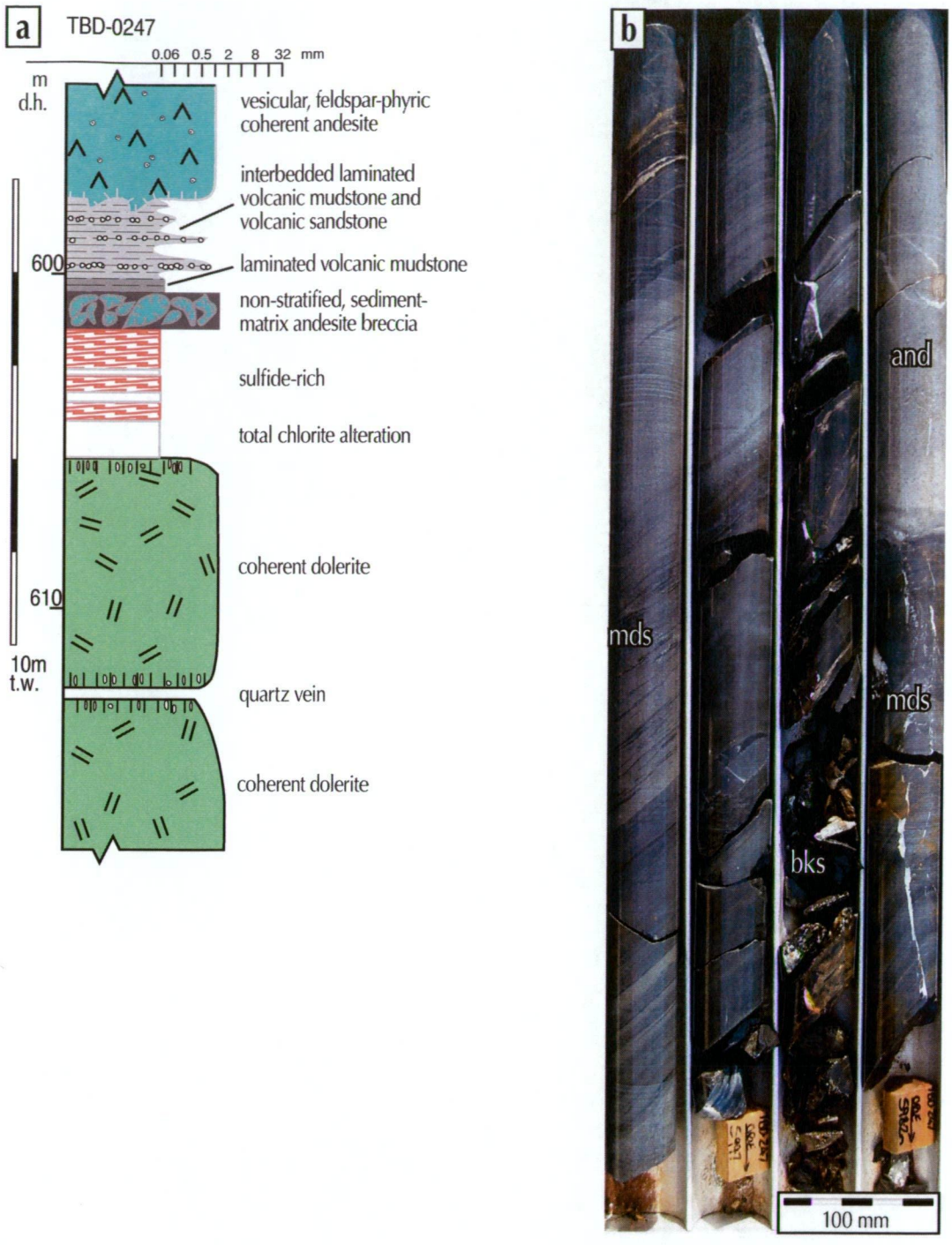

Figure 3.23 Laminated volcanic mudstone facies:
a) graphic log of TBD0247, showing relationships and variations in facies;
b) interval begins in top right corner - massive andesite with irregular, crosscutting intrusive contact against laminated light and dark grey mudstone intercalated with rare, narrow beds of sandstone and intervals of black shale, drillcore photograph, TBD0247 597.3-600.6 m.

For Legend and anotations used see Figure 3.2d

3.7 Group 5: Non-volcanic facies

3.7.1 Laminated mudstone and black shale facies

This facies comprises laminated mudstone and black shale (Fig. 3.24a) that occurs throughout the succession, either at the top of bedded volcaniclastic units, or as thin units (<2 m) among coherent and autoclastic volcanic facies. In this thesis, black shale refers a black, carbonaceous-rich mudstone. Beds vary from <1 to 10 mm in thickness (Fig. 3.24b). In all occurrences of this unit, concentration of carbonaceous material increases upward. This facies is difficult to distinguish from the laminated volcanic mudstone and the criteria used in this study is the absence of broken crystals.

Where this facies occurs at the top of bedded volcaniclastic units, the lower contact is gradational into laminated volcanic mudstone. Where the laminated mudstone is intercalated with coherent units, there is commonly a thin interval of non-stratified, sediment-matrix breccia along the upper contact between this facies and the coherent facies. The upper contact with the coherent facies may be sharp, non-conformable, and irregular, and may locally crosscut bedding. Where the upper contact is planar and sharp, it is commonly immediately underlain by deformed (sheared and contorted) black shale. Where observable, the lower contact may be passive, with the laminated facies overlying coherent or autoclastic facies, or there may be a thin interval of non-stratified, sediment-matrix breccia present along the lower contact between this facies and the coherent facies.

Associated facies

- laminated volcanic mudstone
- non-stratified sediment-matrix rhyolite breccia
- non-stratified sediment-matrix andesite breccia
- non-stratified sediment-matrix basalt breccia

Interpretation

The fine grain size and laminations indicate deposition from suspension. Some laminated mudstone units are the fine tops of bedded volcanic sandstone and other volcaniclastic units. This facies is interpreted to be largely non-volcanic, and composed of fine organic (pelagic) or organic and detrital (hemipelagic) particles.

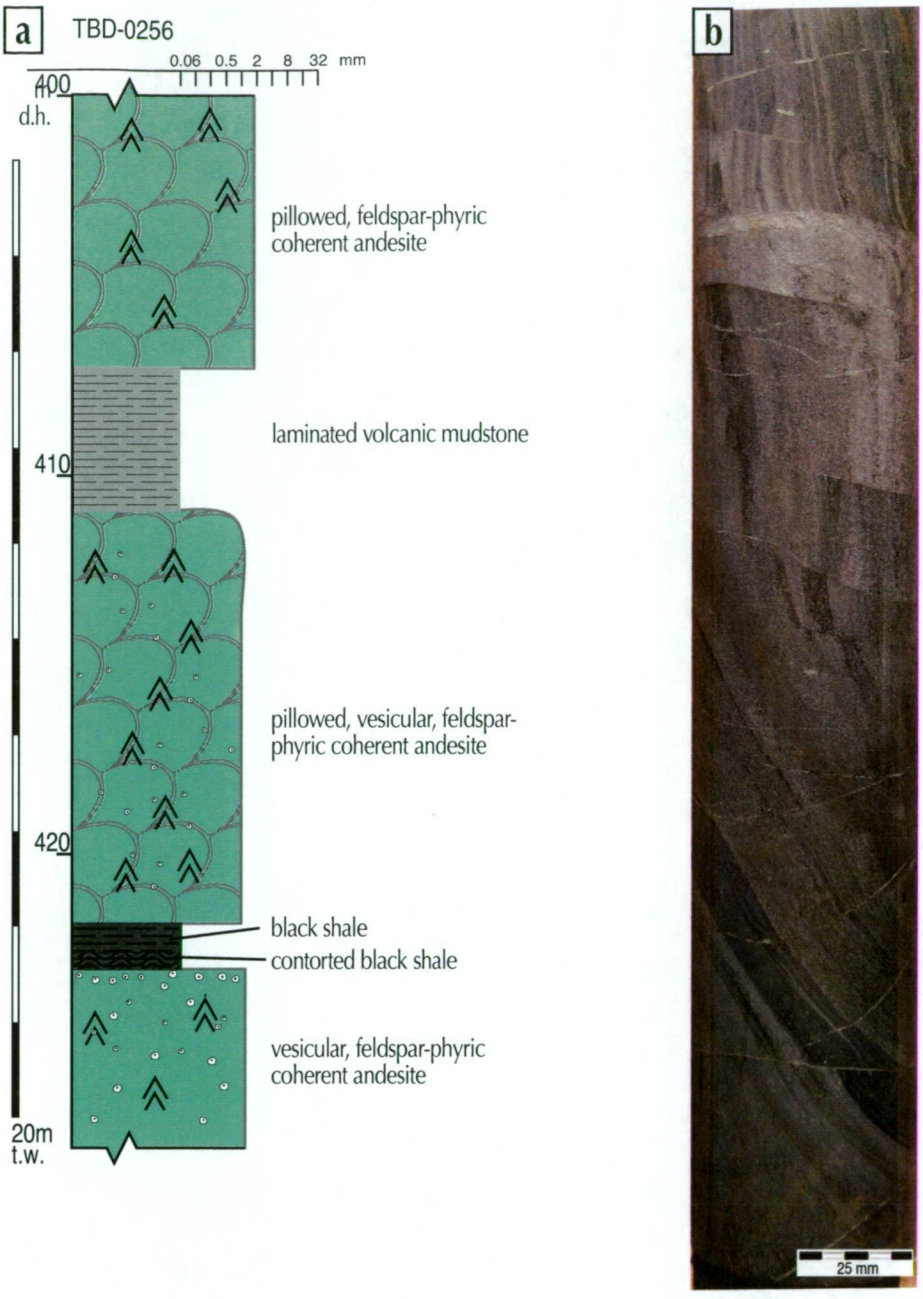

Figure 3.24 Laminated mudstone and black shale facies:
a) graphic log of TBD0243, showing relationships and variations in facies;
b) laminated mudstone, fractures are post-lithication, drillcore photograph, TBD0220 715 m.

For Legend and anotations used see Figure 3.2d

3.7.2 Chert facies

The chert facies (Fig. 3.25a) occurs as thin (2 to 30 cm) units throughout the mineralised package stratigraphic unit and does not occur at other levels within the succession. Milky white and dark grey-green bands or layers are common, especially close to the base of the mineralised package stratigraphic unit. At this level, many of the layers show soft-sediment deformation and disruption that locally grades to in-situ breccia and imbricate chert clasts (Fig. 3.25b). The chert facies and chert clasts in the polymictic dacite breccia, polymictic conglomerate and the polymictic pumice-rich breccia (Figs 3.18c, 3.20e and 3.20b) are identical. Thin (1–4 cm) milky-white to translucent chert layers, with or without disseminated sulfide, occur irregularly within the top part of the mineralised package stratigraphic unit where they are bounded by, or intercalated with, units of volcanic sandstone and mudstone and very fine, banded sulfide beds (Fig. 3.25c).

The upper and lower contacts are typically conformable and sharp. Locally, the chert facies may grade vertically into the sulfide facies. Where the chert facies occurs at the base of the mineralised package stratigraphic unit, it is commonly overlain by the pumice-rich granule breccia. In many instances the lower contact is planar and sharp against dolerite.

In thin section, the chert is a mosaic of fine-grained, intergranular quartz with straight or undulose extinction. The dark grey-green bands are enriched in chlorite and carbonate. In places, layers are defined by grain size variations within the quartz mosaic. Some layers show colloform intergrowth of chert and pyrite.

Associated facies

- volcanic sandstone
- pumice-rich granule breccia
- laminated volcanic mudstone
- sulfide-rich

Interpretation

The limited occurrence of the chert and its association with the sulfide facies (especially the colloform intergrowth of sulfide and quartz), suggests that the chert is a chemical sediment, precipitated from the mineralising hydrothermal fluids. Precipitation of hydrothermal chert requires low sedimentation rates and occurs at temperatures about 150° C (Kalogeropoulos and Scott, 1983). This facies is interpreted as a hydrothermal deposit that formed both on the sea floor as an exhalative precipitate, and possibly as a replacement of pre-existing units.

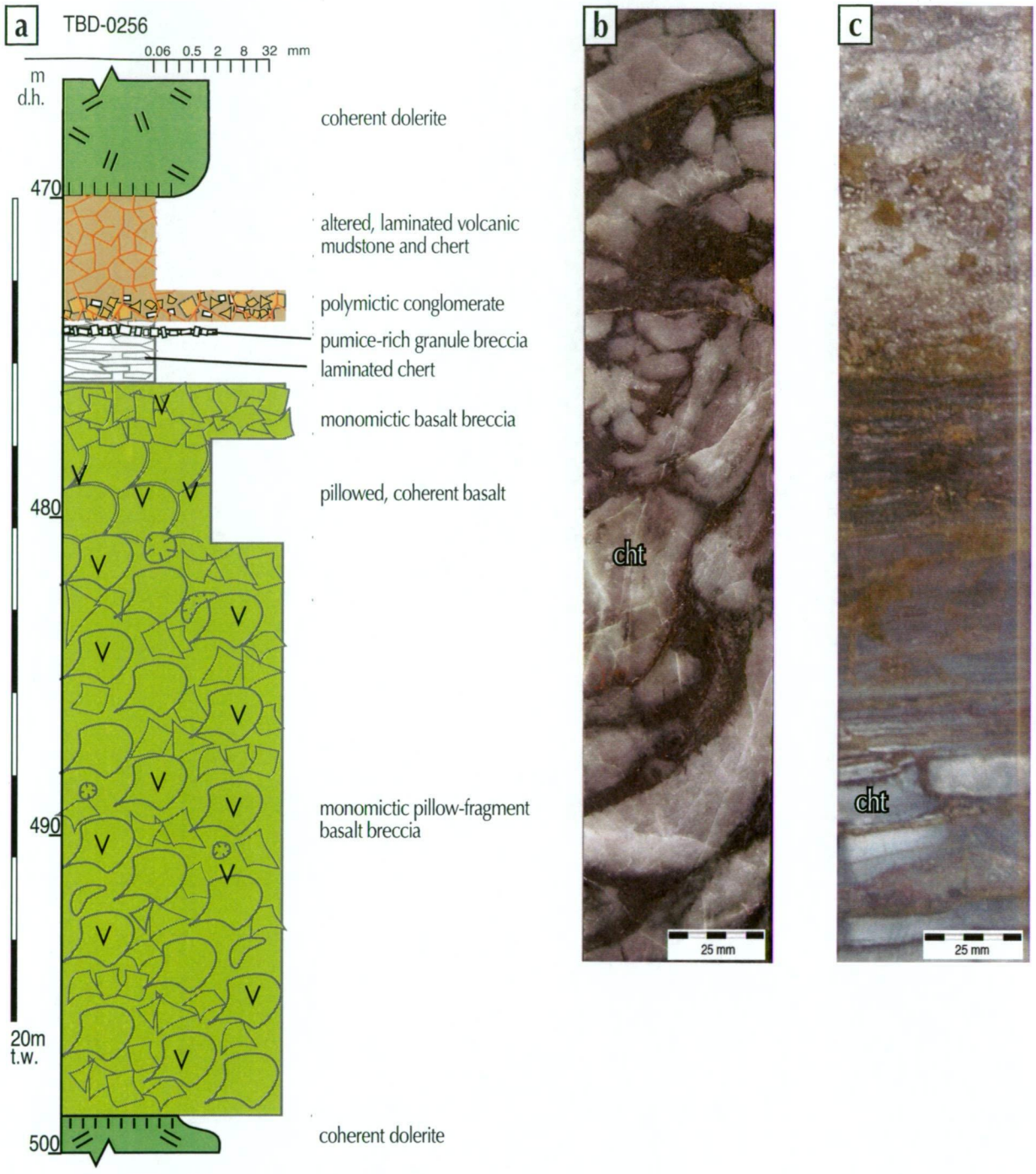

Figure 3.25 Chert facies:
a) graphic log of TBD0256, showing relationships and variations in facies;
b) soft-sediment disruption and brecciation of laminated chert, drillcore photograph, TBD0256 449.8 m;
c) weakly mineralised, tube pumice granule sandstone overlying laminated chert , drillcore photograph, TBD0256 473.9 m.

For Legend and anotations used see Figure 3.2d

3.7.3 Sulfide-rich facies

The sulfide-rich facies (Fig. 3.26a) that makes up the Jaguar orebody is a lens-shaped accumulation of polymetallic sulfide and gangue minerals. The main section of massive and semi-massive sulfide ore extends from 55900 N to 56200 N with a dip extent of roughly the same dimension (~300 m). The massive lens (Fig. 3.26b) is surrounded by a halo of disseminated or stringer sulfide that can extend laterally and stratigraphically below, up to an additional 100 m. The sulfide-rich facies is split by dolerite sills and the true thickness, prior to the intrusion is estimated to have been a maximum of 15 m (Fig. 3.26b).

The facies has mixed gradational and sharp contacts with the associated facies.

Associated facies

- chert
- laminated volcanic mudstone
- volcanic sandstone
- pumice-rich granule breccia
- monomictic dacitic pumice-rich breccia
- monomictic pillow-fragment basalt breccia

Interpretation

The sulfide-rich facies is interpreted as a chemical deposit which, along with the chert facies, precipitated from hydrothermal fluid. The sulfide minerals and their textures are discussed in detail in Chapter 6 on the ore body.

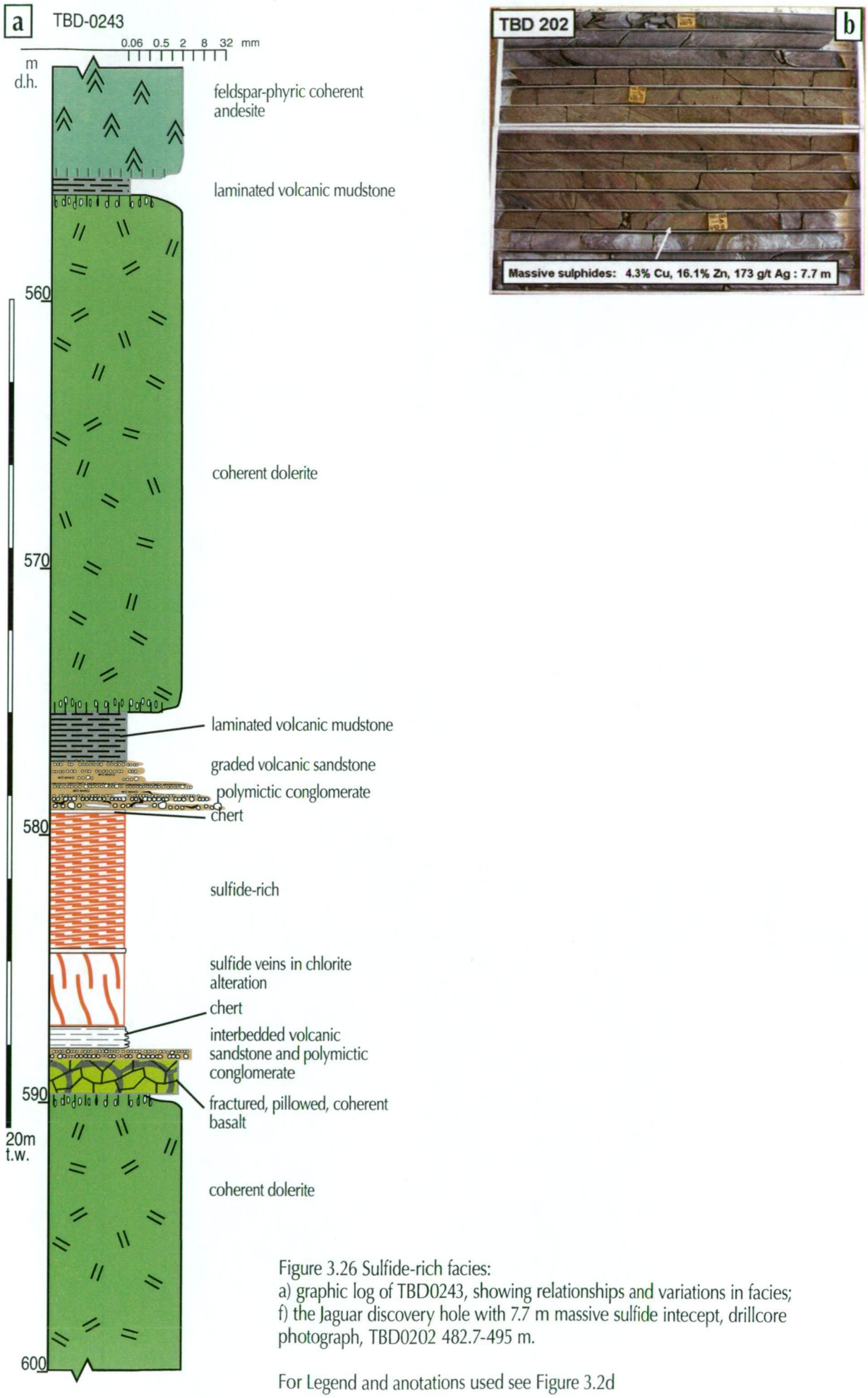

Figure 3.26 Sulfide-rich facies:
a) graphic log of TBD0243, showing relationships and variations in facies;
f) the Jaguar discovery hole with 7.7 m massive sulfide intecept, drillcore photograph, TBD0202 482.7-495 m.

For Legend and anotations used see Figure 3.2d

3.8 Summary

The Jaguar succession includes 25 major facies which have been combined into five groups. These groups are: coherent volcanic facies, monomictic volcanic facies, polymictic volcanic facies, volcanic mudstone and sandstone facies, and non-volcanic facies. These facies descriptions provide constraints on interpretations of eruption style, emplacement processes and setting, which are discussed in the following chapters.


facies
unit
breccia
andesite
coherent
basalt
rhyolite
succession
samples
lower
upper
laminated
mudstone
monomictic
Fig
contact
polymictic
dolerite
conglomerate
chert
area
units
dacite
volcanic
study
commonly
associated
sandstone
shale
clasts
MP
MPS
MPH
MPP
HA1
HB
base
HA2
HA3
HA
FA
FB
FR
Figs
beds
may
occurs
sharp
thick
lithofacies
black
across
stratigraphy
sills
Andesite
Footwall
shows
interpreted
Jaguar
occur
thickness
present
sulfide
overlying
throughout
sections
lavas
upwards
peperite
drillhole
Hangingwall
margin
within
Basalt
sediment-matrix
Barrett
places
footwall
top
diagram
sub-units
lava
alteration
stratigraphic
discussed
contacts
two
along
locally
Upper
seen
carapace
comprises
three composition
zones
DFA
HUS1
tholeiitic
Nb/Y
sedimentary
rare
data
Hallberg
Chapter
show
sub-unit
section
although
deformation
time
HB1
beneath
range
MacLean
plot
minor
Ti
Zr/Y
irregular
also
southern
HFSE
likely
vs
Zr
ore
underlying
HUS2
part
field
Mineralised
grades
comprising
dominated
drillholes
FA
Package
non-stratified
strike
analysed
Zr/TiO2
cm
overlies
structures
single
thin
whereas
collected
values
extent

4. THE LOCAL STRATIGRAPHY AND STRUCTURE AT JAGUAR

4.1 Introduction

The Jaguar and Teutonic Bore VHMS deposits are located within the Teutonic Bore volcanic complex (Fig. 2.6) which is part of the Malcolm greenstone belt. There is no formal stratigraphy in place and little is known about the volcanology and sedimentology of this volcanic complex, because systematic regional mapping concentrating on recognition of distinctive volcanic facies and facies associations has yet to be undertaken in this area. This chapter presents a new stratigraphic scheme for the Jaguar host succession in the immediate vicinity of the Jaguar orebody. The distribution of each unit is described along with its composition, textures, affecting structures and its relationship to adjacent units.

4.1.1 Implementation of a stratigraphic framework

An informal stratigraphy for the greenstone belt was established by Hallberg and Thompson (1985) for the area near the Teutonic Bore mine and extended along the greenstone belt (Fig. 4.1). The distance along strike between the Jaguar and Teutonic Bore deposits is about 4.5 km, but there is no clear understanding as to their relative stratigraphic levels; the Teutonic Bore mineralisation extended to the surface in sub-cropping rocks, whereas the top of the Jaguar orebody lies about 300 m beneath the surface and in an area covered by 20 m of transported sediment. The lack of outcrop above, and immediately along strike from the Jaguar deposit, means that no surface continuity can be established between the two deposits. In addition there is limited diamond drilling across the succession between the two deposits. Stratigraphic correlation, particularly geophysically based correlation is further complicated by the presence of extensive bodies of dolerite.

The mine stratigraphy for Teutonic Bore, as established by Greig (1984) and extended by Hallberg and Thompson (1985), cannot easily be correlated with the units seen at Jaguar in this study. At Teutonic Bore, the orebody is reported as occurring towards the base of a unit of tholeiitic basalts. In the vicinity of the open pit, the hangingwall is described as pillowed, vesicular basalt. Lava flow units are said to be 0.3 to >5 m thick, and interflow sediment is generally absent. A sedimentary unit, 13–28 m thick, lies at least 35 m above the orebody and consists mainly of chert, black shale and mudstone. A conglomerate with rounded felsic volcanic pebbles occurs in pockets within this unit. There are minor pyrite and pyrrhotite disseminations and veinfill in this unit, but base metal sulfides are generally absent and no relationship with the underlying mineralisation is recognised. The footwall to the massive sulfide lens is a basaltic pillowed lava, including minor flowtop breccias and thin layers of chert and black shale. As will be shown, this succession is compositionally different from the succession seen at Jaguar.

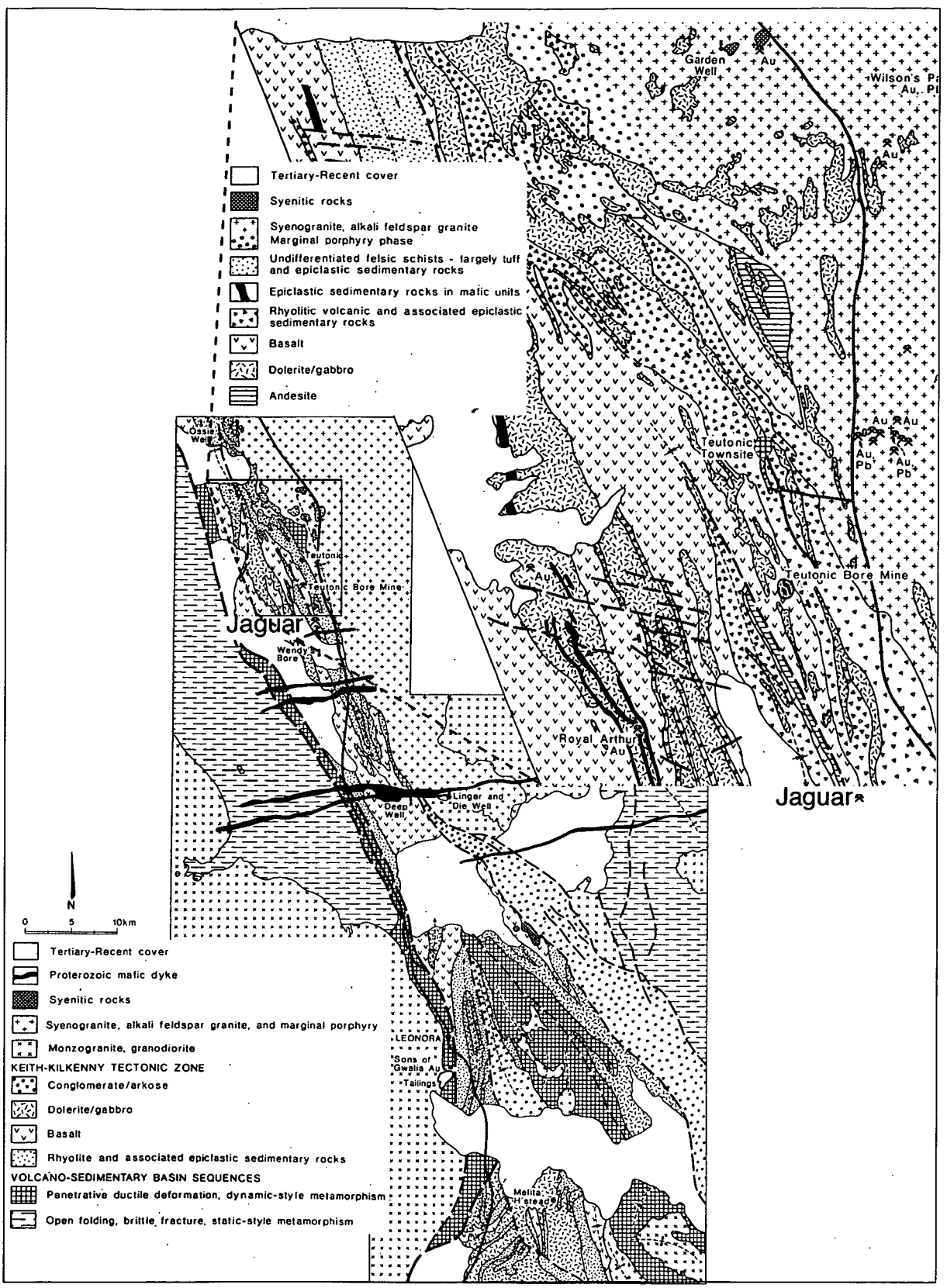

Figure 4.1 Local geology of Teutonic Bore - Jaguar area, after Hallberg and Thompson (1985). The location of the Jaguar deposit is just south of the boundary of the enlargement.

4.1.2 Approach

In this thesis the stratigraphic units have been named and classified on the basis of their pre-metamorphic character. High Field Strength Element (HFSE) data are used as a basis for rock classification, complimenting and refining the texture-based field classifications of the lithofacies. Hallberg (1984) used Ti/Zr ratios to define compositional fields for the major igneous rock types. This work was based on the analysis of >9000 samples all collected from Archean greenstone belts in the northeastern Yilgarn Craton, including the Malcolm greenstone belt which hosts the Jaguar deposit. Over 90% of these samples analysed were given primary names on the basis of megascopic and microscopic textures and known relationships. The resulting Ti/Zr criteria, rhyolite <4<dacite<12<andesite<60<basalt, have been adopted to classify the coherent facies, especially as alteration effects ruled out modal mineralogical or whole-rock geochemical techniques. Compositional data are further discussed in detail in Chapter 5. Appendix II contains compositional data, the original laboratory reports, comparisons between analytical and methods and histograms with error analysis for element ratios.

The stratigraphy was produced after identification of single lithofacies as described in Chapter 3, and through subsequent mapping on to drillhole cross-sections and lithostratigraphic correlation. Appendix III contains the cross-sections. Geochemical data were used to assist in defining these lithostratigraphic units. During the logging, samples were collected for geochemical analysis. The initial sampling strategy was to collect samples for geochemical analysis from selected drillholes at a regular spacing to sample across the stratigraphy. The recognition that the succession was considerably more complex than identified at the start of this study, lead to a reappraisal of, and increase in the amount of core logging necessary to adequately describe the succession. Financial constraints limited collection of further samples for geochemical analysis. The result is an irregular sampling density in which some units have been over sampled whereas others are under sampled. All samples were included during the development of the stratigraphy, so in the sections that follow, the numbers of samples for the units and sub-units may seem unbalanced.

I refer to each of the described stratigraphic intervals as a unit or sub-unit. Because there is no published regional stratigraphy, formal lithostratigraphic terms have not been used. A stratigraphic unit is not the same as a facies association.

Of the 25 facies recognised in the host succession, some appear only once in the succession, whereas others occur multiple times. Each stratigraphic unit may have one or more lithofacies, and may include multiple repeats of a single lithofacies. The event-sequence based stratigraphic units were defined by eruption sequences bounded or identified by major compositional changes or intervals of repose-period facies. In the description that follows

a combination of three techniques was found to produce the most robust stratigraphic succession: (1) recognition of typical associated lithofacies; (2) correlation of lithofacies; and (3) correlation of immobile element geochemistry (the immobile nature of the HFSE is discussed in detail in Chapter 5).

4.2 Local Stratigraphy of the Jaguar Host Succession

In this study the Jaguar host succession was divided into four obvious parts based on the position relative to the massive sulfide orebody: the footwall, the mineralised package, the hangingwall and intrusions. These intervals have been further subdivided into distinct units. Figure 4.2 shows an idealised graphic log of the stratigraphic succession. Table 4.1 summarises the stratigraphic succession and includes: compositional data, the distribution and geometry, relationships, and an interpretation for each of the units. The sections following describe the units from the base of the succession upwards.

These intervals are: (i) the footwall, comprising the Deep Andesite, the Footwall Rhyolite, the Footwall Andesite and the Footwall Basalt; (ii) the Mineralised Package, consisting of a complex succession of intercalated dacite, breccia, conglomerate, sandstone and mudstone; (iii) the hangingwall package of four distinct volcanic units of mixed lithofacies (the Hangingwall Andesite, the Hangingwall Basalt, the Upper Porphyritic Andesite and the Upper Quartz Rhyolite) intercalated with sedimentary facies; and (iv) dolerite sills which intrude all units below and including the Hangingwall Basalt.

Six cross-sections, showing interpreted solid geology extended along 750 m of strike, are presented as Figures 4.3 and 4.4. The area of study extended beyond this zone and covered 1600 m of strike. The sections show that there is both continuity and variation in different parts of the stratigraphic succession. The logged geology is shadowed behind the solid geology on the trace of the drillholes, to give an indication of the data distribution used. These drillholes can be identified using the table in Appendix III.

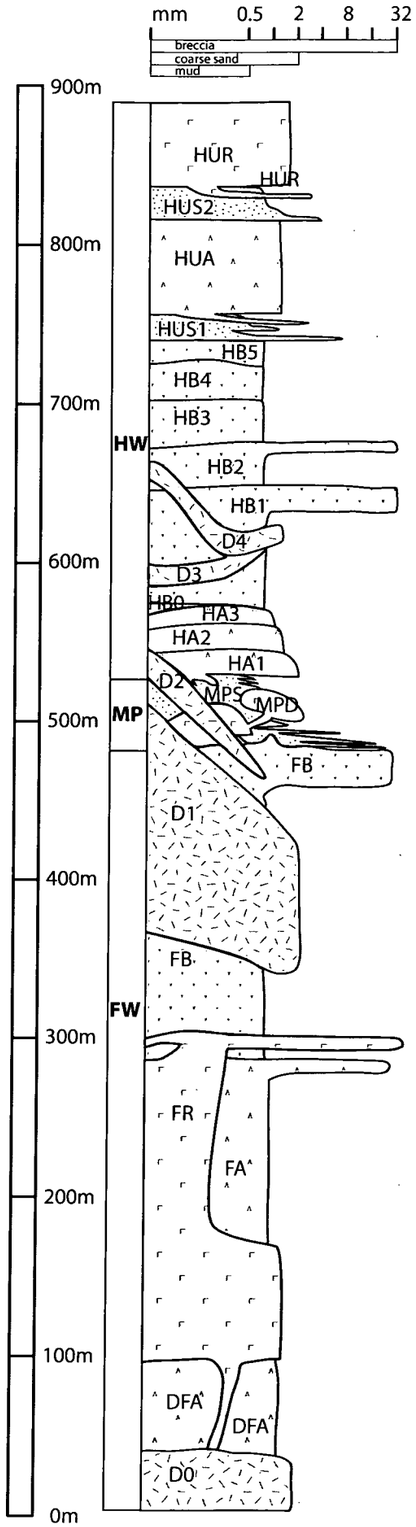

Figure 4.2 Idealised graphic stratigraphic section.

Table 4.1 The stratigraphic succession at Jaguar.

	Unit (abrev.) Subunits	Magmatic/igneous affinity	Lithofacies	Distribution and Geometry	Relationships	Interpretation
INT	Dolerite (D) D4 D3 D2 D1 D0	Tholeiitic, Zr/Y 2.6-4 Ti/Zr 55 - 98	Coherent dolerite	Throughout the sequence from HB2 downwards. Sills are sub-parallel to stratigraphy. Thickness from 10-20 to140 m. Numerous apophyses from < m to m's	Intrusive, contacts of lower sills always chilled. Contacts of the upper sills can be gradational into the HB	Later intrusions, possibly contemporaneous with and feeders to the HB; the D1 sill has multiple internal sills with chilled margins representing multiple magma pulses
HW	Upper Quartz Rhyolite (HUR)	Zr/Y 7.2 Ti/Zr 3.3	Coherent rhyolite Monomictic rhyolite breccia Polymictic rhyolite breccia Non-stratified sediment-matrix rhyolite breccia	Top of sequence, seen in one hole at north of area studied >100m thick	Upper contact not seen, flow base on lower contact with peperitic apophyses into lower sediment	Coherent, flow-banded lava with peperitic flow base with sub-volcanic apophyses extending into underlying sedimentary unit
	Upper Sediment 2 (HUS2)		Polymictic conglomerate Laminated volcanic mudstone Non-volcanic laminated mudstone and black shale	Complete unit seen only in one hole in N of study area study area ~ 30 m thick	Passive lower contact, overlying andesite, sharp upper contact where sub-volcanic rhyolite has flowed and burrowed	Hiatus in volcanic activity, mass-flows of volcanic material to deposit polymictic conglomerate beds
	Upper Porphyritic Andesite (HUA)	Strongly calk-alkaline Zr/Y 9.1 - 28 Ti/Zr 17 - 25	Coherent andesite Monomictic andesite breccia Non-stratiffied sediment-matrix andesite breccia	Unit seen throughout study area. Full profile only seen in N of study area ~70 m thick. Numerous feldspar phyric apophyses into underlying sediment	Upper contact passive, flow banded, vesicular andesite overlain by laminated mudstone, lower contact, peperitic interaction and apophyses into underlying sediment	Flow banded coherent lava, auto-brecciated flow base over a debris flow breccia of andesite clasts and reworked sediment
	Upper Sediment 1 (HUS1)		Volcanic sandstone Laminated volcanic mudstone Non-volcanic laminated mudstone and black shale	Unit seen throughout study area. Thin in south <5m to >30m thick in north	Passive lower contact overlying basalt hyaloclastite flowtop at top of HB	Hiatus in volcanic activity, pelagic deposition and resedimentation of volcanic components
	Hangingwall Basalt (HB) HB5 HB4 HB3 HB2 HB1 HB0	Tholeiitic Zr/Y 2.6 - 4 Ti/Zr 52 - 80	Coherent basalt Monomictic basalt breccia Fluidal-clast basalt breccia Monomictic pillow-fragment basalt breccia; Laminated volcanic mudstone Non-volcanic laminated mudstone and black shale	Unit 150 - 180 m thick; single flows; 0.5 to 30 m; up to 6 main episodes with HB1 & HB2 developing thick hyaloclastic breccia carapaces; rare black shale interflows pillows; 30 cm to 5 m, packed loosely to tightly; interpillow; <10 mm to >100 mm, commonly 10-40 mm	Likely to be associated with dolerite sills conformably overlies ha, where HB0 developed, lower contact is peperitic into sediment	Voluminous outflow of basalt as pillowed and massive flows throughput of magma sufficient to develop a sustained fire-fountain resulting in a breccia of at least 0.04 sq. km surface extent
	Hangingwall Andesite (HA) HA3S HA3 HA2S HA2 HA1S HA1	Each successive lava less calk-alkaline, and more basaltic HA1 Zr/Y 5.6 - 10 Ti/Zr 26 - 32 HA2 Zr/Y 5.3 - 9 Ti/Zr 43 - 56 HA3 Zr/Y 3.9 - 6.1 Ti/Zr 47 - 64	coherent andesite Monomictic andesite breccia Non-stratiffied sediment-matrix andesite breccia volcanic sandstone Laminated volcanic mudstone Non-volcanic laminated mudstone and black shale	Unit 10 - 60 m three lavas, total volume of each flow increases to the N HA1 does not extend to the S end of area studied, at its southern extent it exists only as a sub-volcanic unit HA2 and HA3 occur throughout area as surface flows	Ha1 lower contact is peperitic into partly consolidated sediment or intrusive into consolidated sediment of the mp, the upper contact has both peperities and hyaloclastite flow breccia margins HA2 and HA3 have peperitic lower contacts and both peperitic and hyaloclastite breccia upper-contacts	Pelagic sedimentation continued, interrupted by three andesite lava flows with minor associated hyaloclastic breccia and volcaniclastic sedimentation
MP	Mineralised Package (MP) MPS MPC MPP MPD MPO MPH	Two distinct dacites: tholeiite group Zr/Y 3.4 - 4.2 Ti/Zr 4 - 6.4 calk-alkaline group Zr/Y 6.1 - 7.9 Ti/Zr 3.7 - 7.3	coherent dacite Monomictic dacite breccia Polymictic dacite breccia Monomictic dacitic pumice-rich breccia Pumice granule breccia Volcanic sandstone Laminated mudstone and black shale Chert; sulphide	Unit 20 -40 m thick; dolerites obscure and dislocate relationships; dacites occur as domes with monomictic breccia aprons which grade into polymictic breccias; polymictic breccias exist as thick wedges, are better developed to the south and deeper in section	Lower contact, small clasts filtered down into top 20 cm of basalt breccia; top contact varied; intruded by andesite, over lain by andesite or dislocated by shearing gradational contacts between all lithofacies in unit, conformably overlies FB	
FW	Footwall Basalt (FB)	Tholeiitic Zr/Y 2.8 - 4.9 Ti/Zr 39 - 74	Coherent basalt Monomictic basalt breccia Monomictic pillow-fragment basalt breccia	About 65 m thick; occurs throughout the study area although limited because of dolerite sills	Upper contact passive, basalt breccia, some infiltration of pumice granules into matrix space from overlying MP	Series of basalt lavas, dominantly pillowed with hyaloclastic breccia carapaces
	Footwall Andesite (FA)	Transitional Zr/Y 4.7 - 6.9 Ti/Zr 43 - 56	Coherent andesite Monomictic andesite breccia	Occurs in one hole at southern end of study area, 50 m intersected	Upper contact passive, overlain by basalt flow. lower contact not seen	Coherent lava with autoclastic flow top carapace
	Footwall Rhyolite (FR)	Calk-alkaline Zr/Y 5.2 - 9.6 Ti/Zr 3.6 - 5	Coherent rhyolite Monomictic rhyolite breccia Polymictic rhyolite breccia	Occurs in northern part of study area. Inferred thickness of 200 m, limited amount of unit intersected due to gap in drilling	Upper contact of coherent rhyolite not seen, upper contact of polymictic breccia; sharp, irregular, overlain by pillow basalt, lower contact sharp and overlying pillow basalt, a dyke of FR intrudes the DFA	Lava dome with associated hyaloclastic spall and debris flows, feeder dyke cutting unit below
	Deep Footwall Andesite (DFA)	Calk-alkaline Zr/Y 6.2 - 7.9 Ti/Zr 25 - 29	Coherent andesite	50 m of section intersected in one hole in the northern part of study area, distribution not known	Upper contact, sharp, chilled and amygdaloidal, overlain by coherent rhyolite lava; lower contact not seen	Coherent lava flow

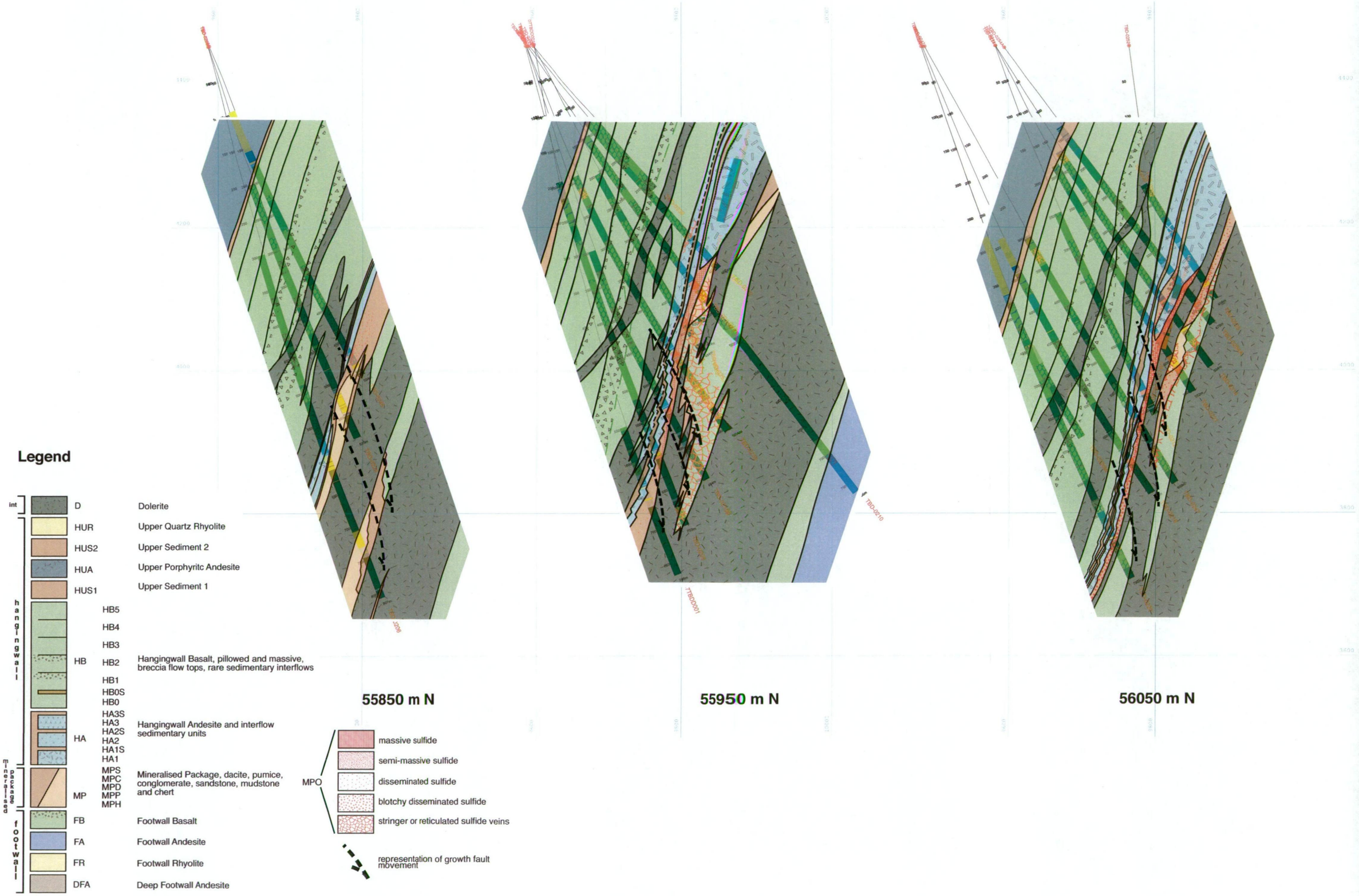

Figure 4.3 Cross-sections of 55850N, 55950N and 56000N showing a solid geology interpretation overlying the drillholes traces and logged geology.

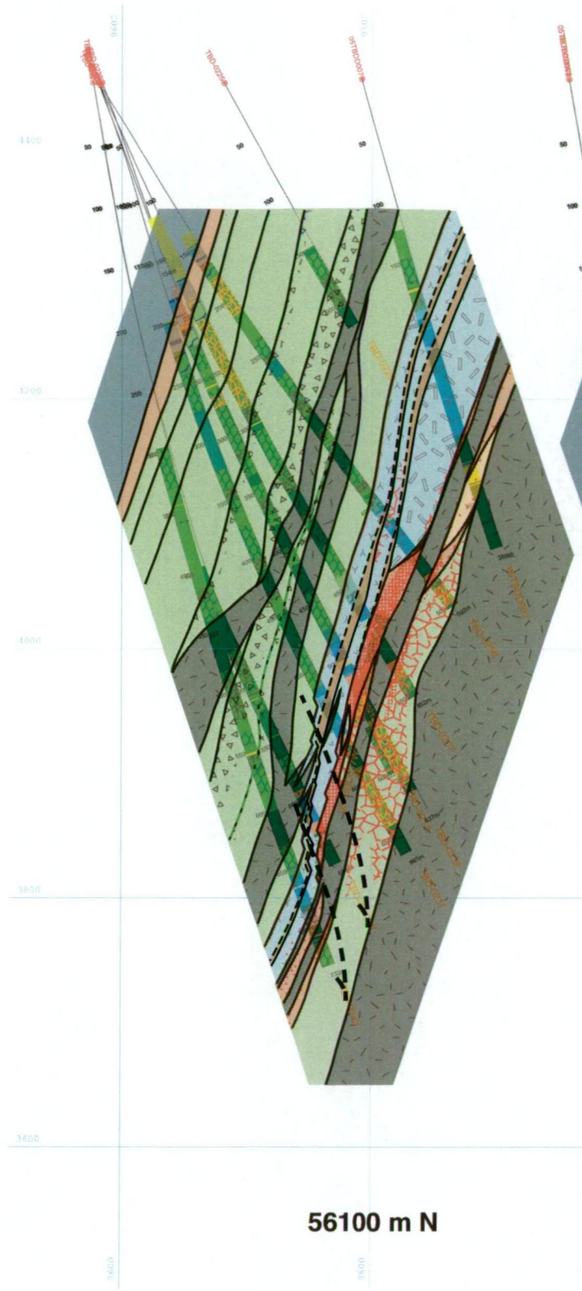

56100 m N

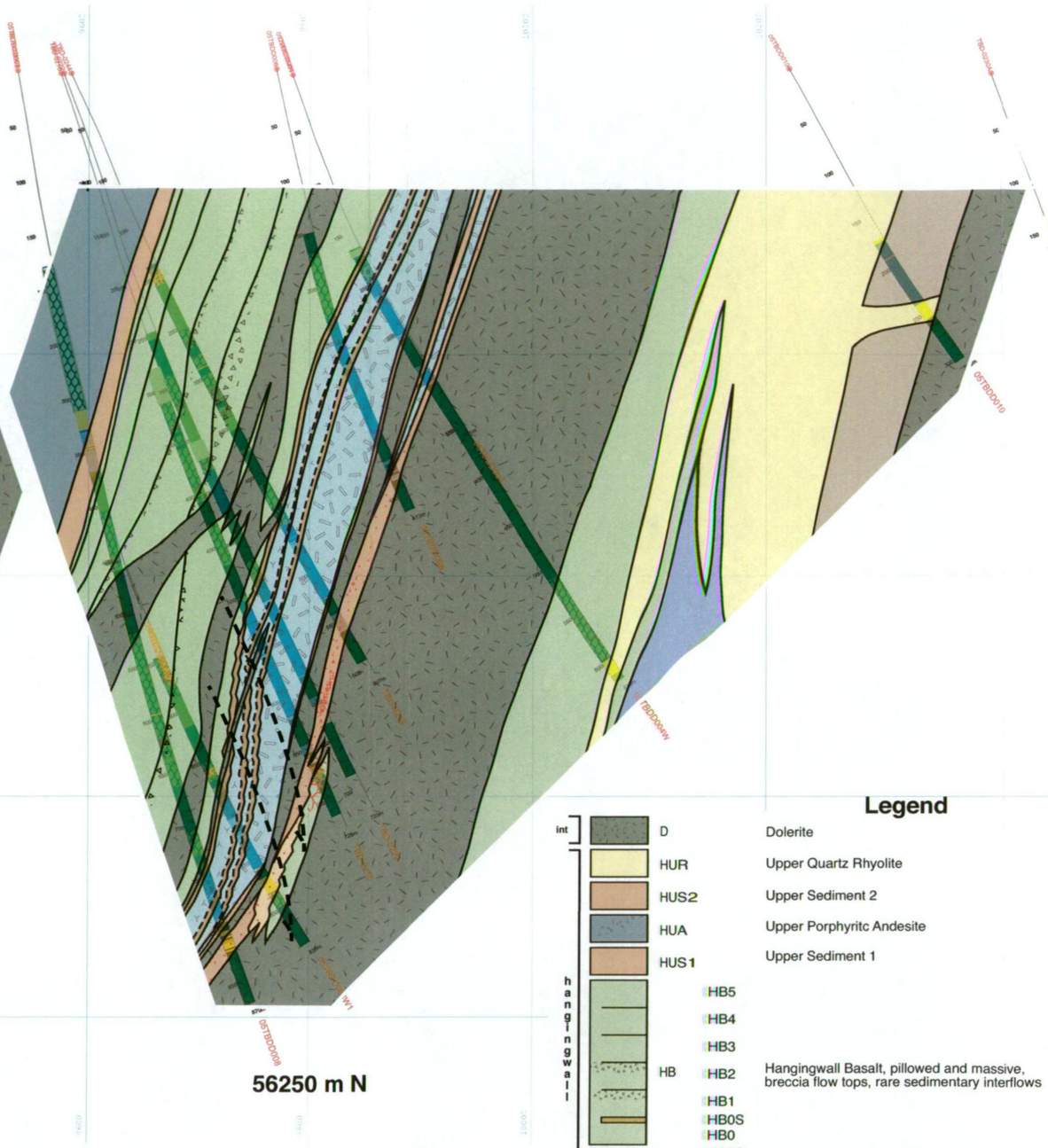

56250 m N

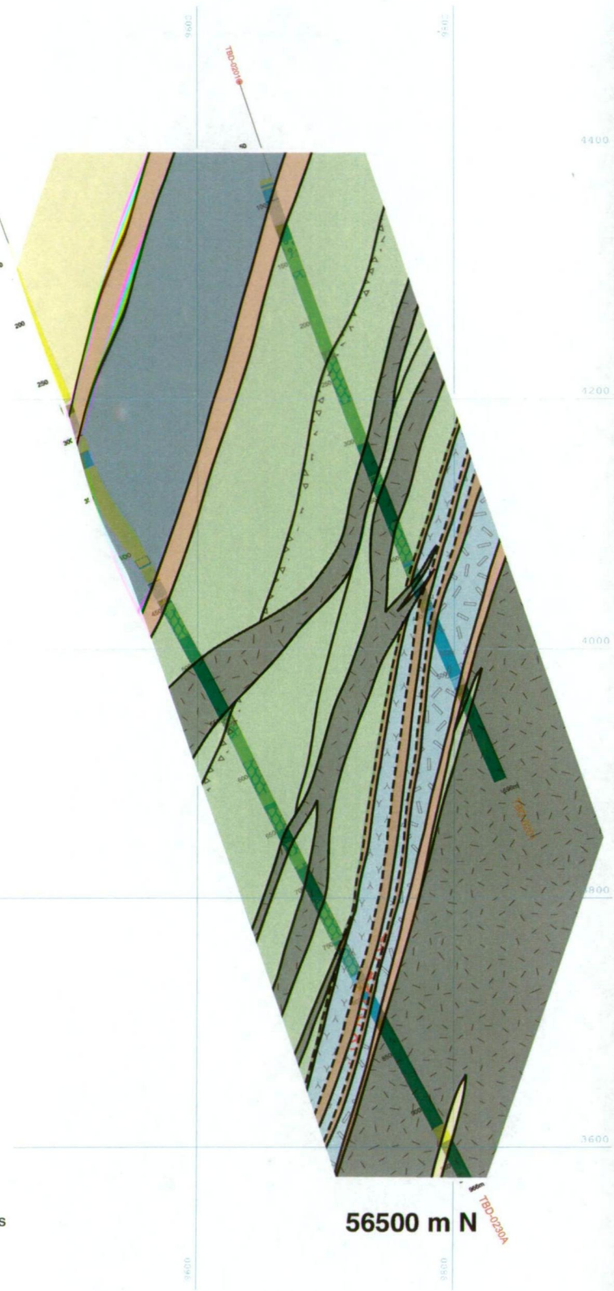

56500 m N

Legend

int	D	Dolerite
hangingwall	HUR	Upper Quartz Rhyolite
	HUS2	Upper Sediment 2
	HUA	Upper Porphyritc Andesite
	HUS1	Upper Sediment 1
	HB	HB5, HB4, HB3, HB2, HB1, HB0S, HB0 — Hangingwall Basalt, pillowed and massive, breccia flow tops, rare sedimentary interflows
	HA	HA3S, HA3, HA2S, HA2, HA1S, HA1 — Hangingwall Andesite and interflow sedimentary units
mineralised package	MP	MPS, MPC, MPD, MPP, MPH — Mineralised Package, dacite, pumice, conglomerate, sandstone, mudstone and chert
footwall	FB	Footwall Basalt
	FA	Footwall Andesite
	FR	Footwall Rhyolite
	DFA	Deep Footwall Andesite

MPO
- massive sulfide
- semi-massive sulfide
- disseminated sulfide
- blotchy disseminated sulfide
- stringer or reticulated sulfide veins

representation of growth fault movement

Figure 4.4 Cross-sections of 56050N, 56250N and 56500N showing a solid geology interpretation overlying the drillholes traces and logged geology.

4.3 The Footwall (FW)

The amount of footwall logged was limited, because the lower stratigraphy is extensively intruded by dolerite sills (Figs 4.3 and 4.4) and the drilling generally terminated in the coarse grained dolerite beneath the orebody. Where seen, the footwall comprises a succession of lavas and associated volcaniclastic facies. Basalt (FB) occurs immediately beneath the Mineralised Package unit, whereas deeper in the footwall, andesite (FA), rhyolite (FR) and another andesite (DFA) occur. The areal extent of these three units is not known and their contact relationships are unclear. The limited data available suggests that the order is DFA succeeded by FR succeeded by FA. Although the deepest unit seen in the footwall is dolerite, the descriptions start with the Deep Footwall Andesite, and the dolerite intrusions are discussed later in the chapter.

Only a few samples were collected from these deep footwall units, and only immobile element abundance is available (Chapter 5 documents which elements were determined to be immobile). More samples were collected from the Footwall Basalt and whole rock analyses are available for these.

4.3.1 Deep Footwall Andesite (DFA)

The Deep Footwall Andesite (DFA) occurs in one drillhole (05TBD010) on section 56250N in the northern part of the deposit (Fig. 4.4b). The width of the unit in the drillhole is about 48 m. It consists of a single lithofacies – coherent andesite (Sec. 3.3.3 and Fig. 3.4).

It is dark green, has a massive texture and is variably feldspar-phyric. The feldspar phenocrysts are most abundant in the upper third of the unit. Amygdales are also common in the top third. The lower third of the unit has numerous fine (~0.05 mm), pink leucoxene grains that are distinctive in hand-specimen.

The upper contact of the DFA is sharp, but is difficult to interpret because the drillcore is shattered. The colour becomes paler towards the upper margin and the grain size decreases, and the volume and size of amygdales increases, consistent with a lava top. The lower margin of the unit shows a zone of silica-induration cutting across a sharp, step-defined contact against rhyolite.

Two samples from this unit were analysed for HFSE (Fig. 4.5). On a Nb/Y vs Zr/TiO_2 diagram the samples lie within the andesite field (Winchester and Floyd, 1977). The Ti/Zr values vary from 25 to 29 plotting in the andesite field (Hallberg, 1984) whereas the Zr/Y range of 6.2 - 7.9 resembles those of Phanerozoic transitional to calc-alkaline magmatic suites (Barrett and MacLean, 1994).

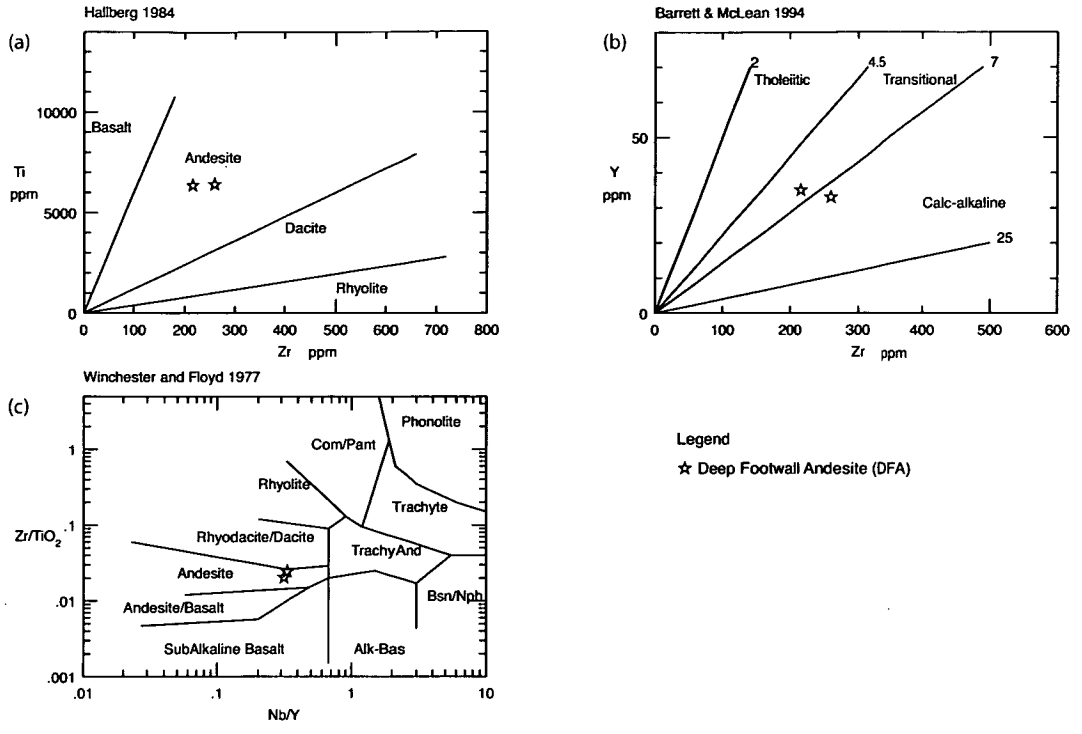

Figure 4.5 HFSE data for the Deep Footwall Andesite, (a) after Hallberg, (1984), (b) after Barrett and McLean, (1994), and (c) after Winchester and Floyd, (1977).

4.3.2 *Footwall Rhyolite (FR)*

The Footwall Rhyolite (FR) occurs in the northern part of the study area where it comprises three lithofacies: coherent rhyolite, monomictic rhyolite breccia and polymictic rhyolite breccia (Figs 3.2, 3.7 and 3.17).

The unit occurs towards the bottom of a drillhole (05TBD004W1) that penetrates beneath the dolerite sill (D1) on section 56250N (Fig. 4.4b). Another drillhole (05TBD010) collared within the footwall on the same section, intersects a rhyolite that is likely to correlate with this unit but a gap in the drilled succession precludes a definitive statement on this matter. The actual depth in the footwall is not known because the presence of two major dolerite sills complicates the stratigraphy. If the dolerites are assumed to have inflated normal to their strike and this thickness is simply subtracted from the calculated true width of the succession, then the depth beneath the Mineralised Package unit at this position is estimated to be about 65 m.

In hole 05TBDD010 the thin interval of FR at the top of the hole is a quartz-phyric, flow-banded, rhyolite. The upper contact is not intersected in this drillhole. The lower contact with the underlying DFA is sharp, but its nature is unknown due to shattered core. There is 12 m thick interval of flow-banded, quartz-phyric rhyolite with a central zone of monomictic rhyolite breccia about 48 m below the lower contact with the DFA. The upper

contact between this rhyolite and the andesite shows chilled, fine-grained rhyolite alongside a sharp, stepped, intrusive contact with silica-induration extending into the andesite. The lower contact of this interval is with a dolerite which has a sharp, chilled, amygdaloidal margin.

In hole 05TBDD004W the FR unit is about 11 m thick and comprises a mixture of monomictic rhyolite breccia and polymictic rhyolite breccia dominated by clasts of quartz-phyric rhyolite with rare sub-rounded clasts of vesicular basalt. The contacts between these facies are gradational. The upper contact with the overlying pillow basalt is irregular and sharp. The lower contact is sharp and marked by polymictic rhyolite breccia overlying pillow basalt.

Three samples were analysed for HFSE, one from each of the coherent rhyolite, the polymictic conglomerate and monomictic breccia rhyolite facies (Fig. 4.6). On a Nb/Y vs Zr/TiO_2 diagram (Winchester and Floyd, 1977) the samples plot in a group within the rhyolite field. On a Ti vs Zr diagram (Hallberg, 1984), they plot along the dacite-rhyolite boundary and range from 3.6–5. The Zr/Y values from 5.2–9.6 broadly indicate a transitional to calc-alkaline magmatic affinity (Barrett and MacLean, 1994), although the data are scattered.

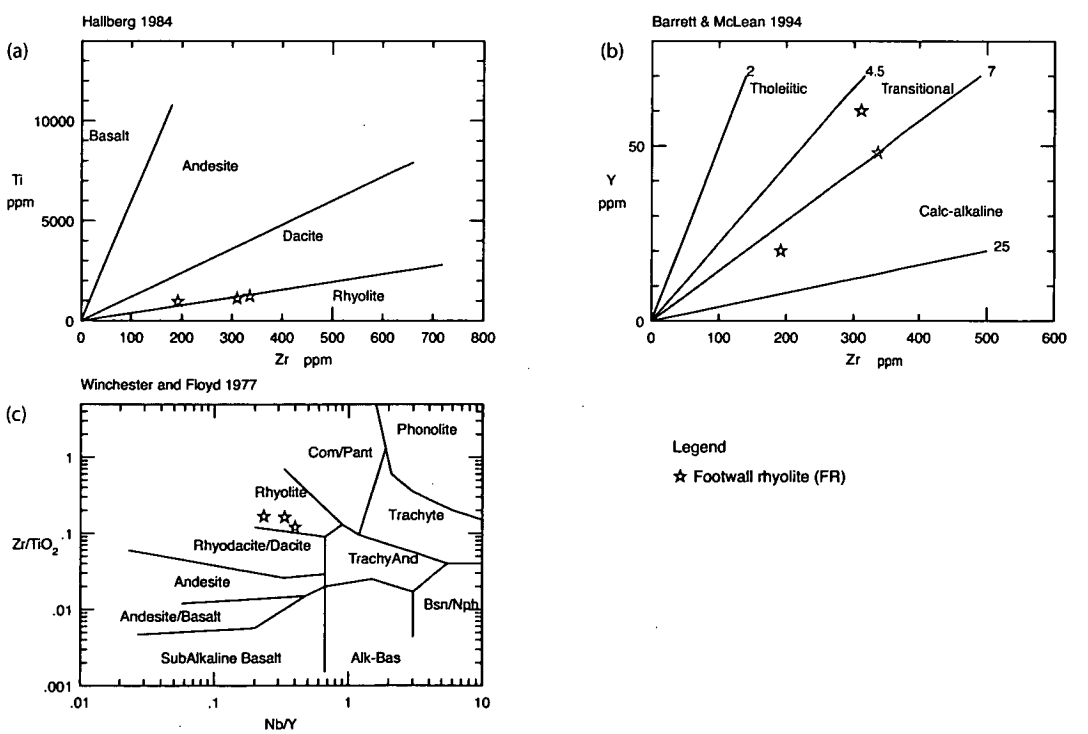

Figure 4.6 HFSE data for the Footwall Rhyolite, (a) after Hallberg, (1984), (b) after Barrett and McLean, (1994), and (c) after Winchester and Floyd, (1977).

4.3.3 Footwall Andesite (FA)

The Footwall Andesite (FA) is intersected at the base of two drillholes (TBD0210 and TBD0231) that penetrate beneath the dolerite sill in the southern part of the orebody on sections 55950N (Fig. 4.3b) and section 55300N (not shown) respectively. The top of this unit is estimated to lie some 65 m beneath the Mineralised Package unit. About 52 m of the FA is intersected. The FA comprises two lithofacies: coherent andesite and monomictic andesite breccia (Figs 3.4 and 3.11).

The upper contact with the overlying Footwall Basalt is sharp but otherwise unremarkable. The top quarter of the unit, about 12 m thick, is hyaloclastite (monomictic andesite breccia) that grades downwards into coherent andesite. The upper margin of the coherent andesite shows fractured perltic texture. A few metres from the margin, samples typically have trachytic texture. The upper half of the unit is khaki coloured (intense carbonate-sericite-pyrite alteration). The intensity of the alteration decreases proportionally with the distance from the upper margin of the coherent facies. Deeper in the unit, samples are less altered and preserve clear trachytic texture.

Ten samples collected from the FA were analysed for HFSE (Fig. 4.7). On a Nb/Y vs Zr/TiO_2 diagram (Winchester and Floyd, 1977), they plot in a tight group in the basalt/andesite field. On a Ti vs Zr diagram (Hallberg, 1984), they plot just within the andesite - basalt boundary in a tight range from 43–56. The Zr/Y values range from 3.6–6.9 broadly consistent with a transitional magma source (Barrett and MacLean, 1994). The sample on the Zr vs Y diagram that lies in the tholeiitic field and has the lowest Ti on the Ti vs Zr diagram. This sample was collected from the hyaloclastite top 5–8 cm beneath the contact with the overlying tholeiitic Footwall Basalt.

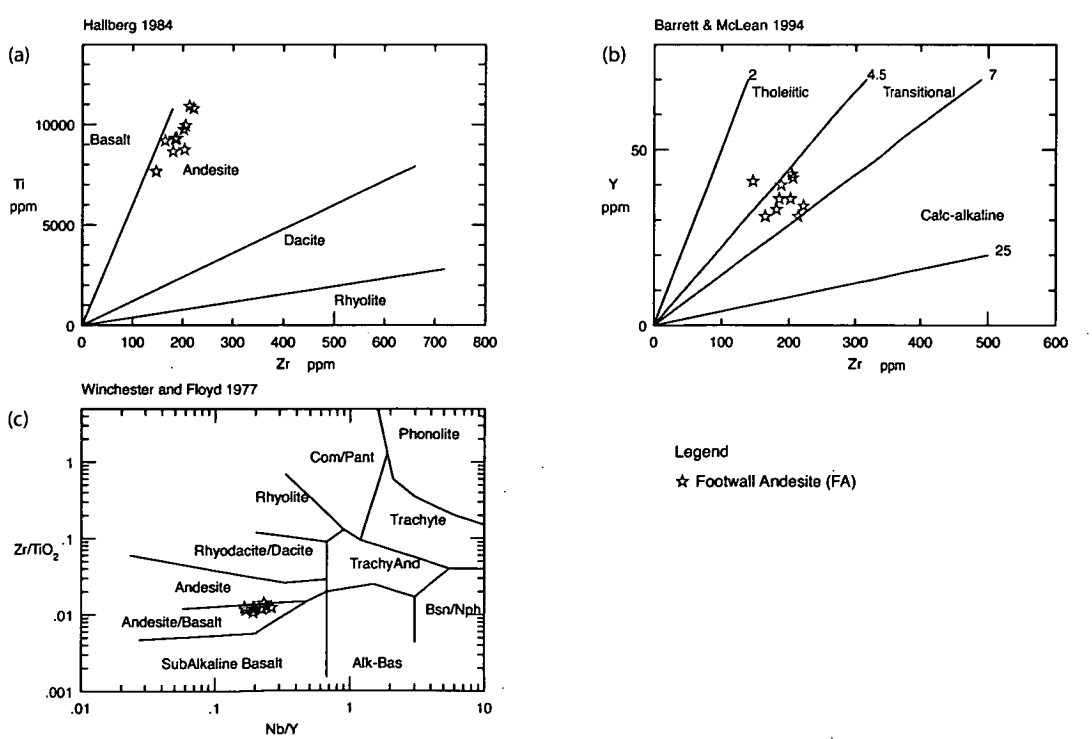

Figure 4.7 HFSE data for the Footwall Andesite, (a) after Hallberg, (1984), (b) after Barrett and McLean, (1994), and (c) after Winchester and Floyd, (1977).

4.3.4 Footwall Basalt (FB)

The Footwall Basalt (FB) extends across the study area and is intersected on all logged sections (Figs 4.3 and 4.4). It is the top unit of the footwall succession and is dominated by three lithofacies: coherent basalt (dominantly pillowed), monomictic basalt breccia and monomictic pillow-fragment basalt breccia (Figs 3.5, 3.13 and 3.15). Rare, thin (<20 cm) occurrences of laminated volcanic mudstone are also present. The FB is extensively intruded by dolerite and is not preserved as a physically continuous entity anywhere in the study area. The thickness without the dolerite sills is about 65 m, assuming the dolerite sills have inflated perpendicular to their lower contacts. The transgression of the lower dolerite sills upwards through the succession from south to north (Figs 4.3 and 4.4) results in a diminishing volume of observable FB in the northern part of the study area compared with the southern part.

The coherent and breccia facies are gradational within the unit. The monomictic pillow-fragment basalt breccia lithofacies is commonly seen at the top of the unit and extends downwards where it grades into monomictic basalt breccia. Both breccia facies are intercalated locally. The monomictic basalt breccia commonly grades downwards into coherent basalt which is commonly pillowed. The interpillow matrix is sand-granule hyaloclastite.

This unit was variably altered by mineralising hydrothermal fluids. In some drillholes, particularly where the sulfide orebody is thick, the FB is totally recrystallised and primary microstructure and original mineralogy have been obliterated (Fig. 4.8a). The dominant alteration minerals are chlorite, silica and sulfide. In other areas, sulfide veins and their associated alteration halos have generated a pseudo-breccia texture.

The upper contact of the FB with the sedimentary and volcanic facies of the Mineralised Package is sharp and commonly irregularly undulating (Fig. 4.8b). The lower contact of the FB on both the Footwall Andesite and the Footwall Rhyolite is sharp but irregular and interpreted as a lava flow base.

Twenty five samples collected from the FB coherent and breccia facies were analysed for HFSE (Fig. 4.9). On a Nb/Y vs Zr/TiO_2 diagram (Winchester and Floyd, 1977), the samples plot within the basalt/andesite field although consistently more mafic than the FA. On a Ti vs Zr diagram (Hallberg, 1984), they plot close to the andesite - basalt boundary ranging from 39–74. The Zr/Y values range from 3.5–5.7, and the samples cluster across the tholeiite - transitional magmatic affinity (Barrett and MacLean, 1994) and the majority lie within the tholeiitic field.

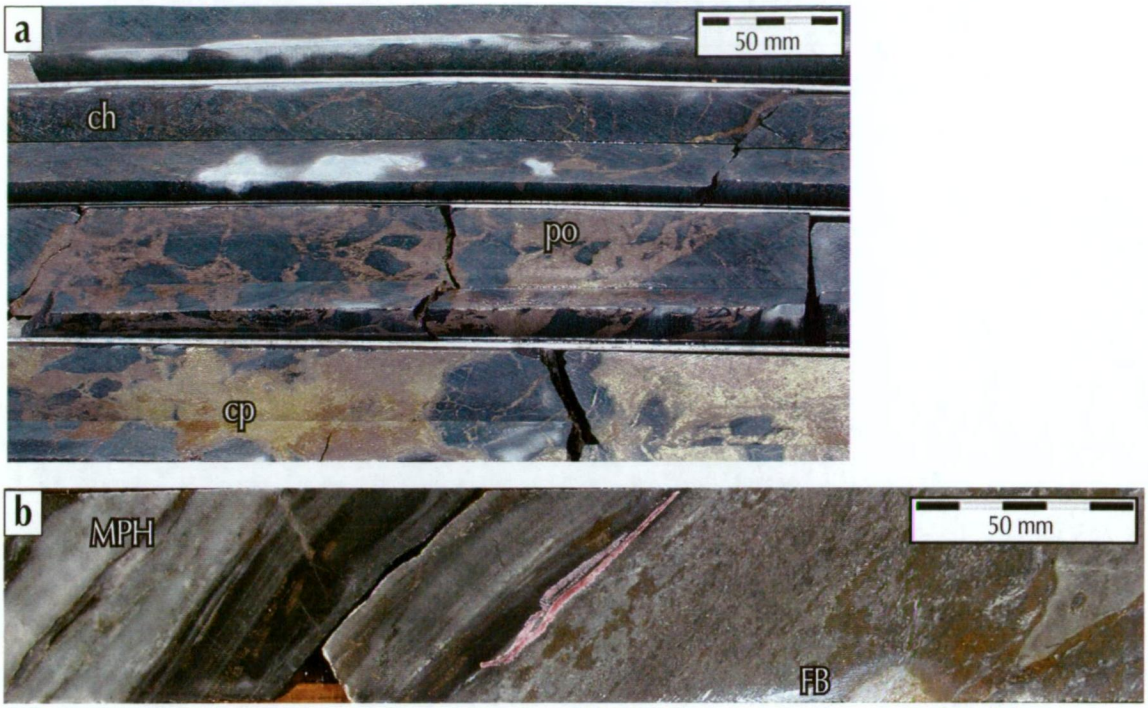

Figure 4.8 Footwall Basalt examples. a. Stringer pyrrhotite (po) and chalcopyrite (cp) mineralisation in massive chlorite (ch), an example of total obliteration of primary microstructure and mineralogy by hydrothermal chlorite in the Footwall Basalt. TBD0256, ~490 m; b. Conformable contact between chert (MPH) at the base of the Mineralised Package and intensely altered basalt breccia at the top of the footwall (FB). TBD0216, 667.25 m.

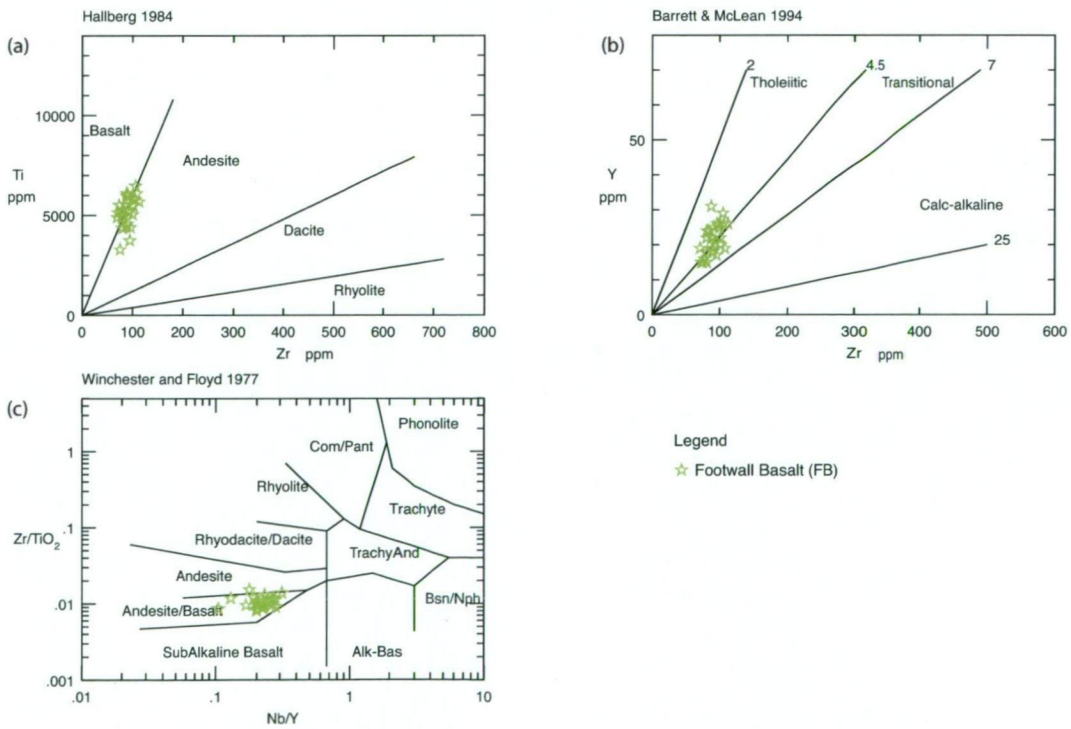

Figure 4.9 HFSE data for the Footwall Basalt, (a) after Hallberg, (1984), (b) after Barrett and McLean, (1994), and (c) after Winchester and Floyd, (1977).

4.3.5 Discussion

The limited exposure of the lower footwall units, and a lack of detail on the contacts means that the interpreted relationships as discussed here are not tightly constrained. The footwall comprises a succession of subaqueous lavas, comprising coherent and associated autoclastic facies. Essentially no sedimentary lithofacies occur. HFSE data (Fig. 4.10) show that all units have immobile Zr/Y element ratios typical of tholeiitic to transitional affinity (Barrett and MacLean, 1994).

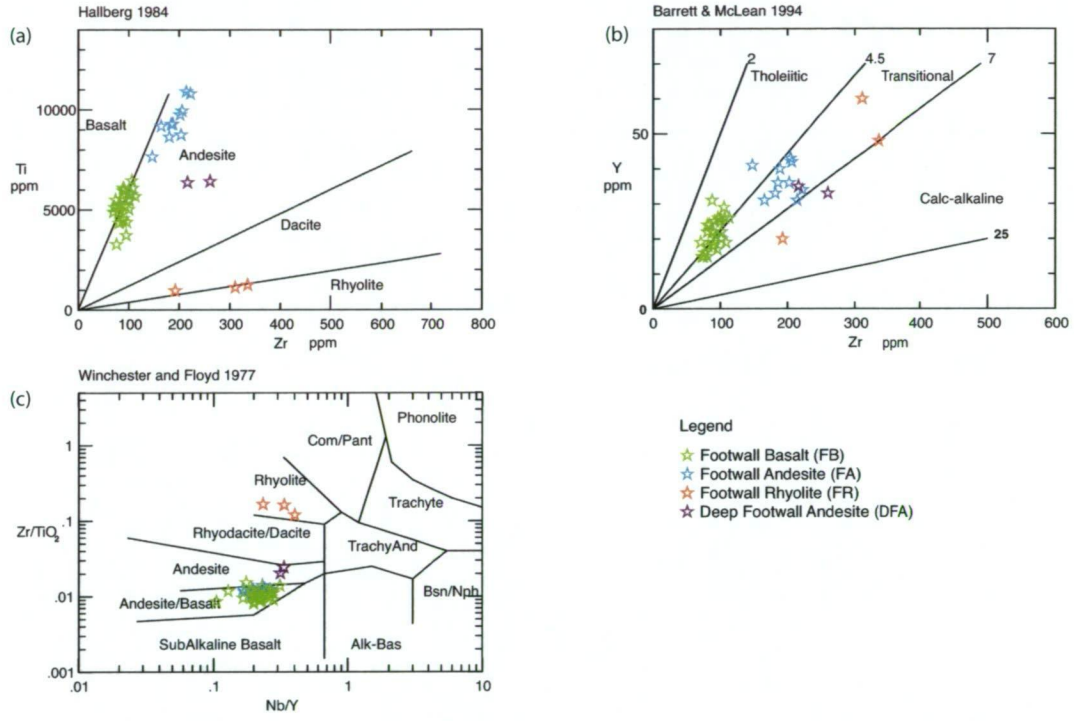

Figure 4.10 HFSE data for the footwall volcanic units, (a) after Hallberg, (1984), (b) after Barrett and McLean, (1994), and (c) after Winchester and Floyd, (1977).

The oldest unit, the DFA, is a thick (>50 m) body of massive coherent andesite interpreted as an lava or sub-volcanic sill. The lack of a preserved upper contact precludes distinction between those two alternatives. If it is intrusive, it may be coeval with, or older than the FR, but not younger because the FR is clearly intruding the DFA. The difference in geochemical composition between the DFA and the FA (Fig. 4.10 and further discussed in Chapter 5) indicates that they are not the same unit and the preferred interpretation is that the DFA predates the FA.

The physical characteristics of the rhyolite facies of the FR suggest that the logged drillcores intersected part of a lava dome (Figs 4.11a and 4.11b). The interval of monomictic rhyolite breccia and coherent rhyolite that intrude the DFA is interpreted as part of a feeder conduit to the overlying rhyolite dome. The outlier of intercalated monomictic rhyolite breccia and polymictic rhyolite breccia down-dip of the rhyolite dome (Fig. 4.4b) conformably overlies pillow basalt, and is interpreted as resedimented autoclastic debris from the dome

carapace. The basalt clasts within the polymictic breccia facies are interpreted to have been incorporated from the substrate by a mass flow originating on the dome. In turn this outlier of FR was conformably overlain by pillow basalts of the FB.

South of the interpreted position of the rhyolite dome, and most likely while the rhyolite dome was still building, andesite lava (FA) was erupted on the seafloor. In the study area, both the FA and FR units lie about 65 m beneath the top of the footwall and each unit occurs on only one cross-section. These sections are 300 m apart and there are no logged holes between them at this level of the stratigraphy. Hence, the FA and FR may be time equivalents in the lower footwall and have been interpreted as such. The lower contact of the FA was not intersected, so what lies beneath the FA is unknown. It is likely to be the FR although it is possible that it is the DFA.

The FB conformably overlies the FA. There was no interflow sediment deposited prior to the basalt eruption which suggests that only a short time interval occurred between the emplacement of the FA and the FB. The FB is interpreted as a series of submarine pillow lavas and mounds. As discussed above, in the northern part of the study area where the FB overlies the FR, the base of the FB inter-fingered with the FR. The top of the unit was likely to have been topographically irregular (Fig 4.11b).

The lack of sedimentary facies in the footwall could reflect a high rate of volcanic accumulation and/or the constructional morphology of the volcanic facies.

In summary, at the cessation of the volcanic activity of the footwall, FB formed the seafloor and had an irregular topography comprising unstable mounds of pillow basalts surrounded by talus aprons formed by a combination of autoclastic processes and local collapse due to tectonic/gravitational instability.

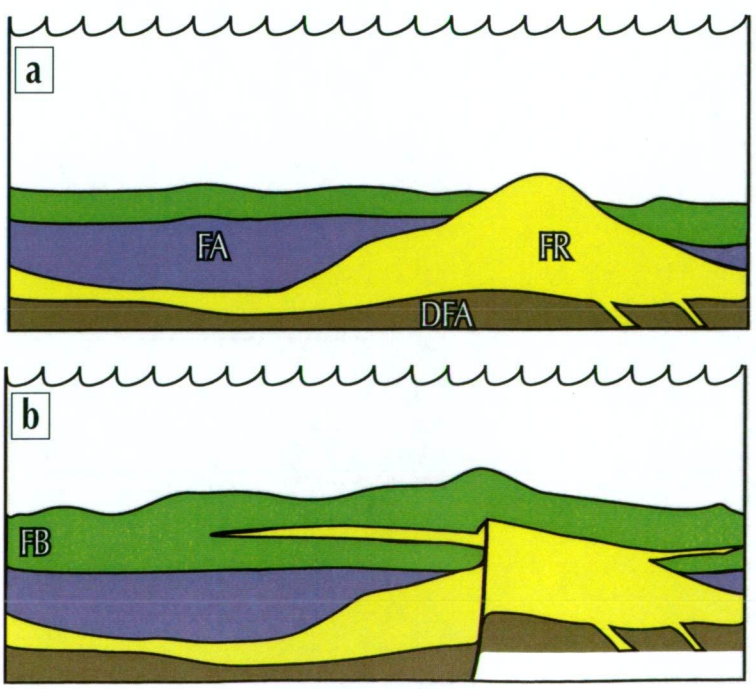

a) early in FB times showing the rhyolite dome before collapse of dome carapace and resulting mass-flow

b) end of FW times with irregular seafloor topography of basalt ridges and mounds

Figure 4.11 Construction of the late Footwall. [Figure is not to scale, and narrow units are vertically exaggerated to better show the process].

4.4 The Mineralised Package (MP)

The Mineralised Package (MP) is a complex assemblage of intercalated coherent, autoclastic, resedimented and non-volcanic lithofacies divided into six sub-units: 1) the Dacite MP (MPD) comprising coherent dacite; monomictic dacite breccia and monomictic dacite pumice-rich breccia facies; 2) the Conglomerate MP (MPC) comprising polymictic dacite breccia, polymictic conglomerate and pillow-fragment basalt breccia facies; 3) the Pumice-rich MP (MPP) comprising polymictic pumice-rich breccia and pumice-rich granule breccia facies; 4) the Laminated MP (MPS) comprising laminated volcanic mudstone, non-volcanic mudstone and black shale, polymictic conglomerate, volcanic sandstone and chert facies; 5) the Laminated Chert MP (MPH) comprising chert facies; and 6) the Sulfide ore (MPO) which is discussed in detail in Chapter 6. The sub-units commonly have gradational boundaries with other sub-units both laterally and vertically, with the exception of the chert (MPH), which has sharp contacts.

Intense alteration associated with the sulfide ore hinders the identification of the lithologies, but this is still possible by scrutiny of windows in the alteration intensity, and by the use of HFSE analysis. This alteration, locally to the point of obliteration of primary lithology and microstructure, makes rock identification extremely difficult, especially when close to ore. The dominant alteration minerals are quartz, chlorite, white mica, carbonate and sulfide.

The lowest unit of the MP is commonly either the MPH or the MPP, and in places, the MPD (Fig. 4.12). Where the MPP occurs at the base, pumice granules locally occur in the top 15 cm of the matrix of the underlying basalt conglomerate facies (top of the FB). Where the MPH occurs at the base of the MP, the contact with the FB is sharp (Fig. 4.8b).

The upper contact of the MP is locally gradational or sharp and discordant or marked by a narrow zone of sheared and deformed black shale.

The MP is dominated by the MPS sub-unit which is nearly always seen at the top of the unit. Although the MP is distributed throughout the study area (Figs 4.3 and 4.4), not all sub-units are mappable at the section scale, and are not separately identified on the cross-sections. The overall thickness of the MP varies from 20 to 40 m.

4.4.1 Laminated Chert MP (MPH)

The MPH (Fig. 3.25) is a distinct sub-unit (30 to <50 cm thick) that consists solely of the chert facies and that commonly occurs at, or close to the base of the MP. It is not mappable at the scale of the cross-sections (Figs 4.3 and 4.4).

The chert is commonly banded at sub-centimetre scale, and locally shows soft-sediment

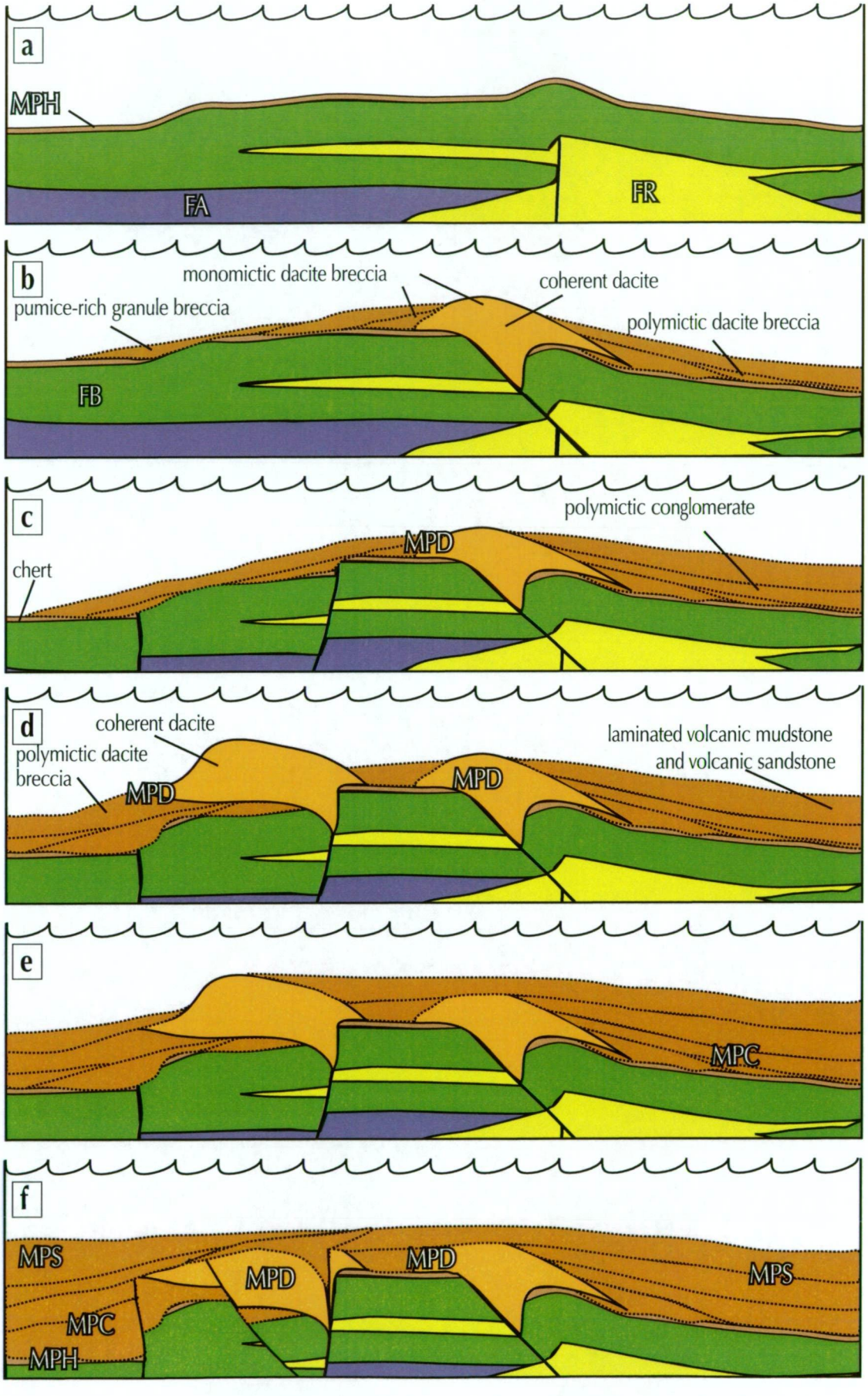

Figure 4.12 Construction of Mineralised Package unit from a) to f). Showing some lithofacies and stratigraphic sub-units. [Figure is not to scale, and narrow units are vertically exaggerated to better show the process].

deformation and slumping that in places transitions to local brecciation and imbrication of clasts. These brecciated clasts are identical to the chert clasts in the polymictic conglomerate. Where the MPH occurs the base of the MP, the contact with the Footwall Basalt is sharp (Fig. 4.8b). The relationship of the MPH to the sulfide ore is discussed in Chapter 6.

4.4.2 Dacite MP (MPD)

The MPD comprises coherent dacite, monomictic dacite breccia and monomictic dacite pumice-rich breccia facies (Figs 3.3, 3.9 and 3.10) and occurs on most sections (Figs 4.3 and 4.4) but is not present in every drillhole logged. During logging it was given the field names of rhyolite to dacite, depending on the colour, which varied respectively from cream to dark grey. The rock is commonly porphyritic with a groundmass varying from perlitic, formerly-glassy to microcrystalline. Both aphyric and crystal-phyric varieties vary from massive to flow banded, and the autoclastic facies comprise both autobreccia and hyaloclastite breccia with variable vesiculation to pumice-rich varieties. The breccia is composed of clasts (2 mm to 10 cm) which are blocky to ragged, jigsaw-fit to rotated, in a highly siliceous matrix.

Twenty-one samples representing the coherent and breccia facies were analysed for HFSE (Fig. 4.13). On a Nb/Y vs Zr/TiO_2 diagram (Winchester and Floyd, 1977) the data are clustered and fall across the rhyolite/dacite field. On a Ti vs Zr diagram (Hallberg, 1984), they describe a broad trend ranging from 3.7–9.2, falling dominantly within the dacite

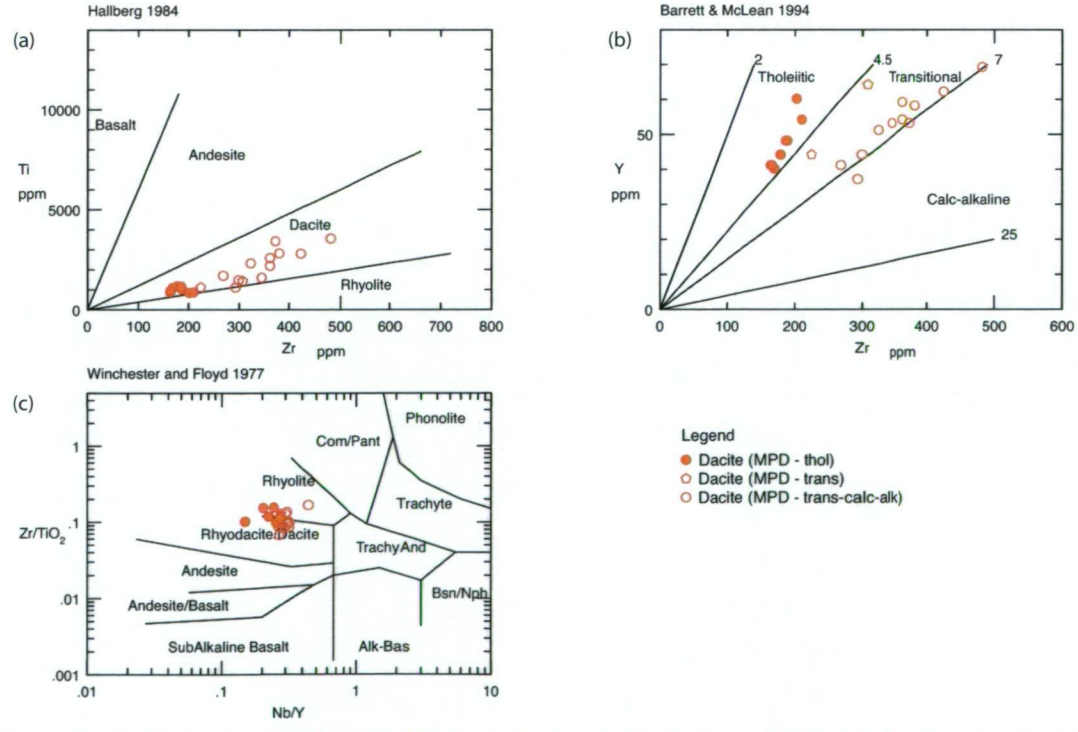

Figure 4.13 HFSE data for the Mineralised Package Dacite, (a) after Hallberg, (1984), (b) after Barrett and McLean, (1994), and (c) after Winchester and Floyd, (1977). Plots are coloured to reflect the Zr/Y trends.

field. The Zr vs Y diagram (Barrett and MacLean, 1994) shows two distinct trends, with values ranging from 3.4–4.2 (tholeiitic) and 6.1–7.9 (transitional - calc-alkaline) trend. There are two samples which do not fall on either trend.

The Zr vs Y data trends suggest that there are two distinct dacites. All the quartz-phyric dacite samples are transitional to calc-alkaline, whereas the aphyric dacite samples are tholeiitic. The two samples that fall on neither trend are aphyric dacite. As the two groups show fundamental sub-divisions, the implication is that the magmas may originate from two sources.

4.4.3 Pumiceous MP (MPP)

The MPP sub-unit comprises two pumice-rich facies: the polymictic pumice-rich breccia and the pumice-rich granule breccia facies (Figs 3.20 and 3.21). It is distributed sporadically throughout the study area close to the base of the Mineralised Package (Figs 4.3 and 4.4) and is not mappable at the scale shown on the cross sections. It is thin (<30 cm) and the continuity is not known.

The MPP grades laterally and vertically into the MPC, MPS, MPH and MPO. Where it overlies the MPH, the contact is conformable and sharp. Where the MPP is the basal layer of the Mineralised Package, it locally infiltrates downwards (up to 15 cm) into the monomictic pillow-fragment basalt breccia facies at the top of the FB.

4.4.4 Conglomerate MP (MPC)

The MPC comprises intercalated polymictic dacite breccia and polymictic conglomerate plus a single interval of monomictic pillow-fragment basalt breccia facies (Figs 3.18, 3.19 and 3.15). It commonly occurs in the lower half of the Mineralised Package unit (Figs 4.3 and 4.4) and it may appear as a single interval or multiple intervals intercalated with MPS. It is not shown separately on the cross-sections due to scale.

Intersections of the MPC are thicker in the southern end of the study area, and overall, the sub-unit has a pronounced wedge shaped geometry, being thicker (up to 20 m) down-dip and thinner (<5 m) closer to the surface. Commonly within the MPC, single beds are defined by subtle changes in clast populations and sizes, and more rarely matrix composition. The facies are as described in Chapter 3 and the clasts are locally sourced and dominated by dacite and chert, and in places sulfide. The sulfide clasts have a variable distribution. The sole intersection of pillow-fragment basalt breccia is <1 m thick (drillhole TBD0208) at the southern end of the study area, and deep in the section, where the sub-unit is thickest. Internal and external contacts are commonly gradational, but locally sharp. The facies that comprise this sub-unit grade laterally and vertically into each other, and into

the MPD, MPP and MPS sub-units.

4.4.5 Laminated MP (MPS)

The MPS sub-unit makes up the bulk of the MP and is distributed throughout the study area (Figs 4.3 and 4.4). The MPS comprises intercalated laminated volcanic mudstone facies, volcanic sandstone facies, local polymictic granule to pebble conglomerate facies, thin beds of the chert facies and minor occurrences of the laminated mudstone and black shale facies (Figs 3.23, 3.22, 3.19, 3.25 and 3.24).

The MPS grades laterally and downwards into the Laminated Chert (MPH), MPC and MPP. Beds range from <1 mm up to several centimetres and, very rarely decimetres thick. Normal grading of beds is common and everywhere display upwards younging. Load casts at the base of some gravel beds indicate upwards younging. Flame structures occur in places along boundaries between sandstone and mudstone beds, and always young uphole. The grain population is diverse and dominated by quartz and feldspar, but pumice and shards are common (Fig. 4.14a). Grains are angular to sub-angular with the larger grains sub-angular to sub-rounded (Fig. 4.14b). The tube pumice population is concentrated in the lower third of the unit. The clasts in the conglomerate beds comprise locally sourced dacite and less commonly chert (Fig. 4.14c). Thin beds of chert (<2 cm) occur irregularly in the upper part of the sub-unit. At the top of the unit, some translucent chert layers show colloform intergrowth of sulfide and chert (discussed in Chapter 6).

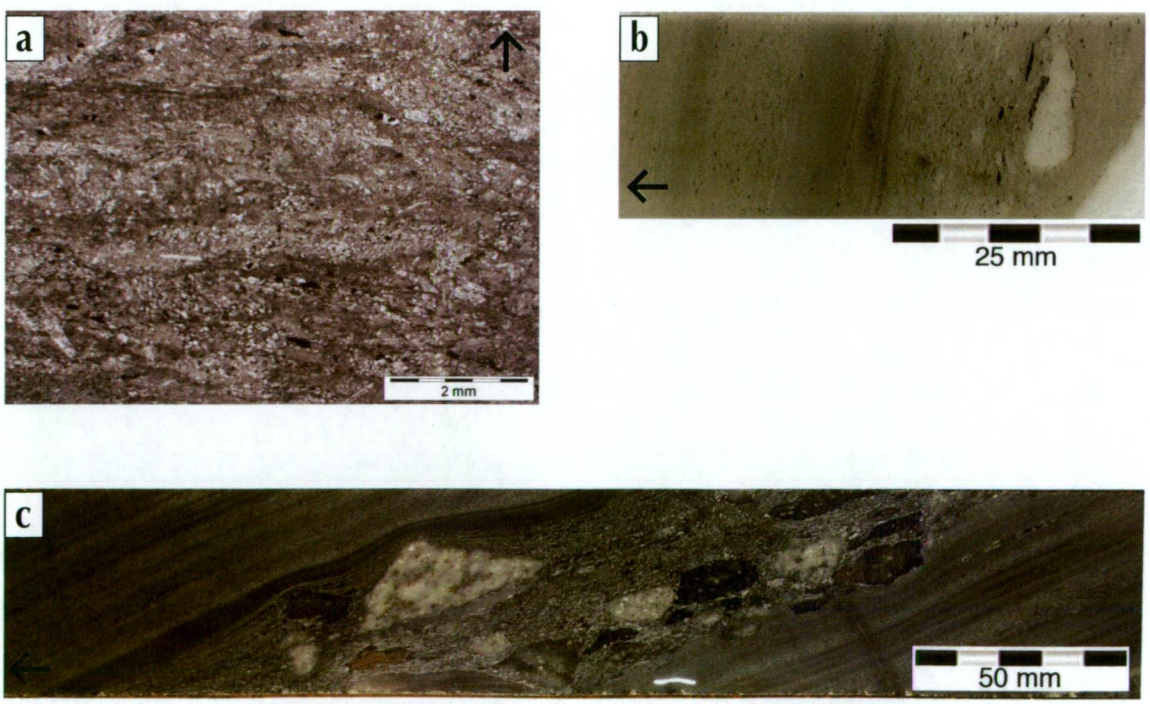

Figure 4.14 Grain forms and textures in the MPS. a. Photomicrograph in plane-polarised light showing pumice grains, TBD0242 710.3 m ; b. Scan of thin section showing bedding and rounding of large grain (dacite clast) TBD0216 618 m c. Photograph of drillcore showing a 50 mm conglomerate bed in laminated mudstone. Arrows show direction up-hole and direction of facing.

The MPS is commonly altered to sericite, silica, chlorite, carbonate, and pyrite, or a mixture of these minerals.

4.4.6 Geochemistry of the Mineralised Package

Along with the 21 samples collected from the MPD, 33 samples from volcaniclastic facies were collected within the MP. The samples were predominantly laminated volcanic mudstone, but included samples of polymictic conglomerate. One sample was from the pumice-rich granule breccia, and two were volcanic sandstone. The conglomerate samples include matrix and clasts. Most samples were altered, some to a significant extent.

Figure 4.15 shows the relationship of these samples to the MPD samples. The Zr vs Ti graph shows that these samples form three loose clusters in the basalt, andesite and dacite fields. Most of the MPC samples plot in the dacite field. The two that do not are a sample from the pillow-fragment basalt breccia which plots in the basalt field and a sample from the polymictic conglomerate facies in drillhole TBD0242 which plots in the andesite field. The MPS samples plot across all fields, and two samples of volcanic sandstone that contain minor pumice, plot in the andesite field. The MPP sample plots in the dacite field. The Zr vs Y graph shows distinct trends, whereas the Nb/Y vs Zr/TiO_2 graph is less definitive. The value of these samples is not specifically in how they relate to the coherent rocks but in possible correlation of the volcaniclastic facies of the MP on a wider-than prospect scale.

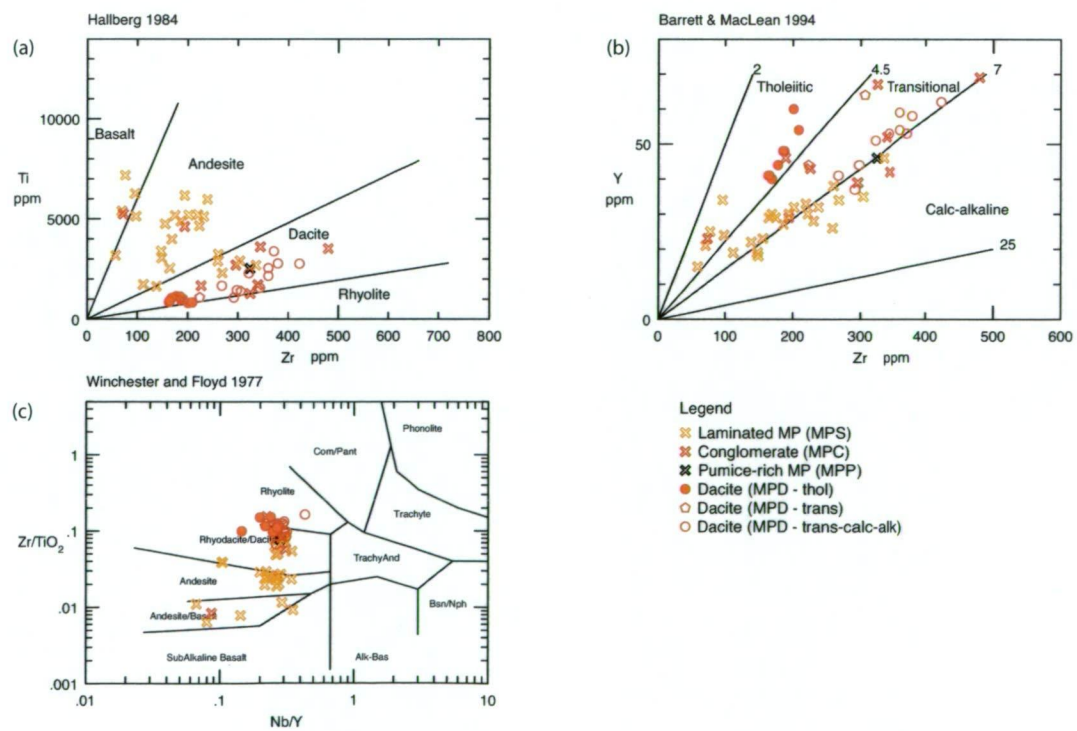

Figure 4.15 HFSE data for the Mineralised Package Dacite and volcaniclastic facies, (a) after Hallberg, (1984), (b) after Barrett and McLean, (1994), and (c) after Winchester and Floyd, (1977).

4.4.7 Discussion

The MP is a complex assemblage of lithofacies that can be presented in six sub-units dominated by volcaniclastic facies associated with the coherent dacite. Figure 4.12 shows the evolution of the MP.

In the study area the basal unit of much of the MP is the MPH (laminated chert) which directly overlies the FB (Fig. 4.12a). This is interpreted as a hydrothermal deposit that formed on the sea floor as an exhalative precipitate. This would suggest that a circulating hydrothermal system was developing in the footwall and that little sediment input was otherwise occurring at this time. The plastic deformation and brecciation that occur in places in this unit are interpreted to result from contemporaneous local seismic events. Conformably overlying this unit is the MPP, comprising the pumice rich facies. In places the MPH is missing and the MPP directly overlies the FB (Fig. 4.12b). Where this occurs, pumice granules were locally observed in the top 15 cm of the FB and are interpreted to have filtered downwards at the time of formation into the matrix of the basalt breccia.

The coherent dacite, monomictic dacite breccia and polymictic dacite breccia facies are closely associated. The emplacement setting is interpreted as a dacite dome or a series of small domes or lavas extruded onto the sea floor in an actively unstable environment (Figs 4.12b and 4.12c). Spalling, and mass-flows of the unstable carapace breccias have created the associated polymictic breccias and conglomerates which have locally incorporated plastically deformed clasts of the seafloor chert. The chert is interpreted to have still been in a plastic state at the time of incorporation because some clasts locally show greater deformation than most layers still in-situ. The wedge-like shapes of the conglomerate units suggest that growth faults may have been active at this stage. Within the conglomerates, many of the sulfide clasts are interpreted as of primary origin rather than replacement, which suggests that the sulfide body was forming contemporaneously with the MP and that the tectonic instability may have been the cause of the sulfide clast input. The polymetallic sulfide orebody was formed in the MP environment. Descriptions of the ore, its textures, and its relationship to the enclosing facies will be discussed in Chapter 6.

The MPS sub-unit dominates the upper part of the Mineralised Package. Towards the very top of the MPS, above the massive sulfide MPO sub-unit, thin beds of translucent chert showing colloform intergrowth of chert and sulfide, intercalated with laminated mudstone occur.

4.5 The Hangingwall

The hangingwall to the Jaguar deposit is a succession of coherent and associated volcaniclastic lithofacies interbedded with laminated volcanic mudstone and non-volcanic mudstone facies. In the area studied, the succession is divided into four units informally named: the Hangingwall Andesite (HA), the Hangingwall Basalt (HB), the Upper Porphyritic Andesite (HUA) and the Upper Quartz Rhyolite (HUR). These units are bounded by sedimentary intervals (units HUS1 and HUS2).

The HA and the HB have been further subdivided into single mappable units, assisted in the case of the HA, by distinct geochemical composition.

4.5.1 Hangingwall Andesite (HA)

The HA comprises coherent andesite, monomictic andesite breccia, non-stratified sediment-matrix andesite breccia, and laminated volcanic mudstone and sandstone facies and rare beds of polymictic conglomerate facies (Figs 3.4, 3.11, 3.12, 3.23, 3.22 and 3.19). The HA is distributed across the entire area studied (Figs 4.3 and 4.4). The unit is thickest in the north and the lateral extent and thickness of flows decreases to the south. In the southern end of the studied area the unit has an average thickness of 10–12 m whereas in the north the average thickness is 50–60 m. There are up to three emplacement units, identified here as HA1, HA2 and HA3, from the lowest upwards, that are either lavas or shallow intrusions. The three emplacement units are separated by intervals of interbedded mudstone and sandstone, named HA1S, HA2S and HA3S. The lowermost sub-unit (HA1), is about twice the thickness of the HA2 and HA3, and is less extensive; it does not appear to extend to the southern part of the studied area.

The HA1, HA2 and HA3 mainly consist of coherent feldspar-phyric andesite. This facies forms the core of the HA1, HA2 and HA3 lavas. Pillows are common in HA3 and occur locally in HA2. Monomictic andesite breccia forms the topmost (<5 m) of HA3 and is also locally present in HA2. Non-stratified sediment-matrix andesite breccia occurs along some lower contacts of the HA2 and HA3 lavas and also along the upper margins of HA1 and HA2.

The sedimentary sub-units (HA1S, HA2S and HA3S) consist of well laminated volcanic mudstone and volcanic sandstone, and minor laminated mudstone and black shale and rare beds of polymictic conglomerate. HA1S is dominated by laminated volcanic mudstone and volcanic sandstone with minor black shale, and rare polymictic conglomerate beds are also present. The sand and granules in the volcaniclastic beds in HA1S comprise devitrified shards, andesite clasts, broken crystals of quartz and feldspar, and minor (<1–3% modal) disseminated pyrite. HA2S and HA3S are dominated by laminated volcanic mudstone, and

laminated mudstone and black shale. In places minor post-consolidation micro-faulting in HA2S and HA3S has displacements from millimetre to centimetre scale.

The lower contact of HA1 is in places sheared and the original relationship is unclear. In instances where the contact is weakly to moderately sheared, graphitic black shale (in places contorted and bearing deformed quartz-carbonate veins), and durchbewegung-textured sulfides occur along the margin (discussed in Chapter 6). Where it is not sheared, the contact is sharp and cross-cutting, or peperite (non-stratified, sediment-matrix, andesite breccia) is present indicating the andesite intruded the laminated mud of the MPS. Where HA1 is absent, MPS grades into HA1S with no contact point identified. The lower contacts of both HA2 and HA3 are generally irregular and locally peperitic.

The upper primary contacts of HA1 show that in places this unit was extrusive and in other places it was intrusive. The extrusive contacts are marked by hyaloclastite (monomictic andesite breccia) passively overlain by laminated mudstone. The intrusive andesite has peperite (non-stratified, sediment-matrix, andesite breccia) on the top contacts. In nearly all occurrences of HA2 and HA3 the upper contacts are passive, and laminated mudstone (HA2S and HA3S, respectively) conformably overlies massive or pillowed, fine-grained vesicular andesite or hyaloclastite (monomictic andesite breccia).

Forty-nine samples were collected from the HA and analysed for HFSE (Fig. 4.16). Of these samples, 43 were collected from the andesite sub-units and six from the mudstone intervals (HA1S, HA2S, HA3S). Table 4.2 shows a summary of the element ratios for the three sub-units.

Table 4.2 Hangingwall Andesite HFSE composition, showing ranges of values

Flow	Ti/Zr range	Zr/Y range
HA (all)	24–64	4.9–10
HA1	24–32	5.6–10
HA2	43–61	5.3–9
HA3	47–64	4.9–7.3

The data show that, overall, the source magma had a transitional to calc-alkaline affinity (Fig. 4.16b), and that although visually there is little difference between the coherent andesite facies of HA1, HA2 and HA3, they each have a distinct geochemical composition. HA1 forms a discrete group on the lithology plots (Ti vs Zr and Zr/TiO_2 vs Nb/Y) whereas HA2 and HA3 group into tight clusters that overlap. The similarity in the geochemical composition of HA1 and HA1S (three samples) reflects the comparable nature of the grains and clasts observed in thin-section and indicates that the grains are most likely locally sourced from the hyaloclastic fragmentation of the extruded HA1 lava. The range in the values of the HA2S and HA3S, which are dominantly black shale, indicates that their provenance is wider than their immediate environment, as would be expected. HA2S in

particular, shows evidence of an input of components of similar chemical composition to the MPD dacite unit, and the single sample from the HA3S is also more felsic than the underlying sub-unit. It is also possible that the composition has been affected by processes of sedimentary fractionation during diagenesis or inclusion of an organic component, which may alter the ratios of HFSE. Successive sub-units (HA1 -> HA3) are slightly more mafic and tholeiitic in character, as shown by the increasing Ti/Zr and decreasing Zr/Y valves.

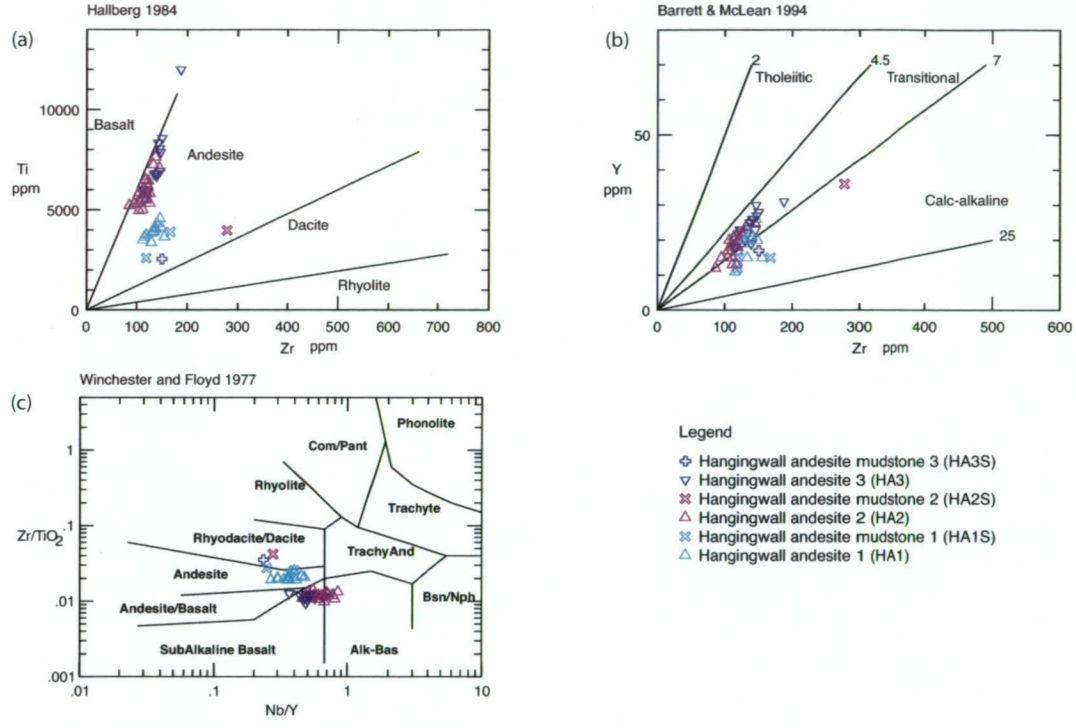

Figure 4.16 HFSE data for the Hangingwall Andesite sub-units, plus a few samples from the interbedded mudstone sub-units, (a) after Hallberg, (1984), (b) after Barrett and McLean, (1994), and (c) after Winchester and Floyd, (1977).

4.5.2 *Hangingwall Basalt (HB)*

The Hangingwall Basalt (HB) is 150 to 180 m thick and occurs throughout the study area (Figs 4.3 and 4.4). It comprises coherent basalt, monomictic basalt breccia, monomictic fluidal-clast basalt breccia, monomictic pillow-fragment basalt breccia, non-stratified sediment-matrix basalt breccia and rare laminated volcanic mudstone facies (Figs 3.5, 3.13, 3.14, 3.15, 3.16 and 3.23). Six mappable sub-units have been identified, HB0, HB1, HB2, HB3, HB4 and HB5 named from the base of the unit upwards, not all of which are continuous throughout the study area. The upper sub-units display relatively consistent thicknesses whereas the three lowest sub-units (HB0, HB1 and HB3) are wedge-shaped, being thickest in the down-dip areas of the cross-sections. HB0 is the least extensive, generally only occurring in the down-dip area, and invariably overlain by a thin interval (<1 m) of black laminated mudstone (HB0S). HB1 to HB5 extend throughout the study area, although HB5 is not present in at least two drillholes (TBD0254A and TBD0214) and is

thin (<5.5 m) in an adjacent drillhole. Rare, discontinuous black mudstone beds also are present throughout the HB unit and are not separately named.

The dominant lithofacies of the Hangingwall Basalt is coherent pillow basalt. Massive basalt is also present and grades laterally and along strike into the pillow facies. The next most common lithofacies is the monomictic basalt breccia which occurs as an autoclastic flow carapace overlying coherent basalt facies in sub-units HB1, HB2, HB3, HB3, HB4 and HB5. In the HB1 and HB2 sub-units, the autoclastic carapace can be up to 35 m thick. In the other sub-units the distribution is irregular and it may be missing or range up to 5 m thick. The monomictic fluidal-clast basalt breccia facies occurs towards to top of HB1, (as part of the carapace), and extends for at least 200 m along strike and about 150 m across strike. The full strike extent of this facies is unknown as the logging at this level in the hangingwall was limited. It is the main breccia facies in the centre of its distribution, and extends laterally in fingers and wedge-shaped intercalations through the monomictic basalt breccia facies. The sub-unit HB5 is distinctive in comprising pale green pillows showing semi-concentric bands defined by very pale green <1 mm bands at a 1–2 cm spacing.

The HB, either HB0 or HB1, conformably overlies the upper sedimentary layer (HA3S) of the HA. The lower contact of the HB0 is marked by up to a metre of peperite (non-stratified sediment-matrix basalt breccia facies) that indicates that the underlying sediments were semi-consolidated at the time of emplacement. HB1 always has a pillowed base, overlying black shale and mudstone. The lower contacts of HB2, HB3, HB4 and HB5 are similar and commonly sharp where coherent basalt overlies monomictic basalt breccia. More rarely, a thin (<1 m) zone of peperite (non-stratified sediment-matrix basalt breccia facies) occurs along the basal contact and this has a sharp lower contact overlying coherent basalt.

Forty-two samples collected from monomictic basalt breccia and coherent basalt facies from all sub-units, were analysed for HFSE (Fig. 4.17). On a Nb/Y vs Zr/TiO_2 diagram (Winchester and Floyd, 1977), the samples plot in a cluster in the andesite/basalt field. On a Ti vs Zr diagram (Hallberg, 1984), they describe a line astride the andesite - basalt boundary ranging from 52–80, whereas the Zr/Y (Barrett and MacLean, 1994) values range from 2.6–4, plot in the tholeiitic field. The HB is more tholeiitic and has a higher Ti/Zr ratio than the FB (Fig. 4.9).

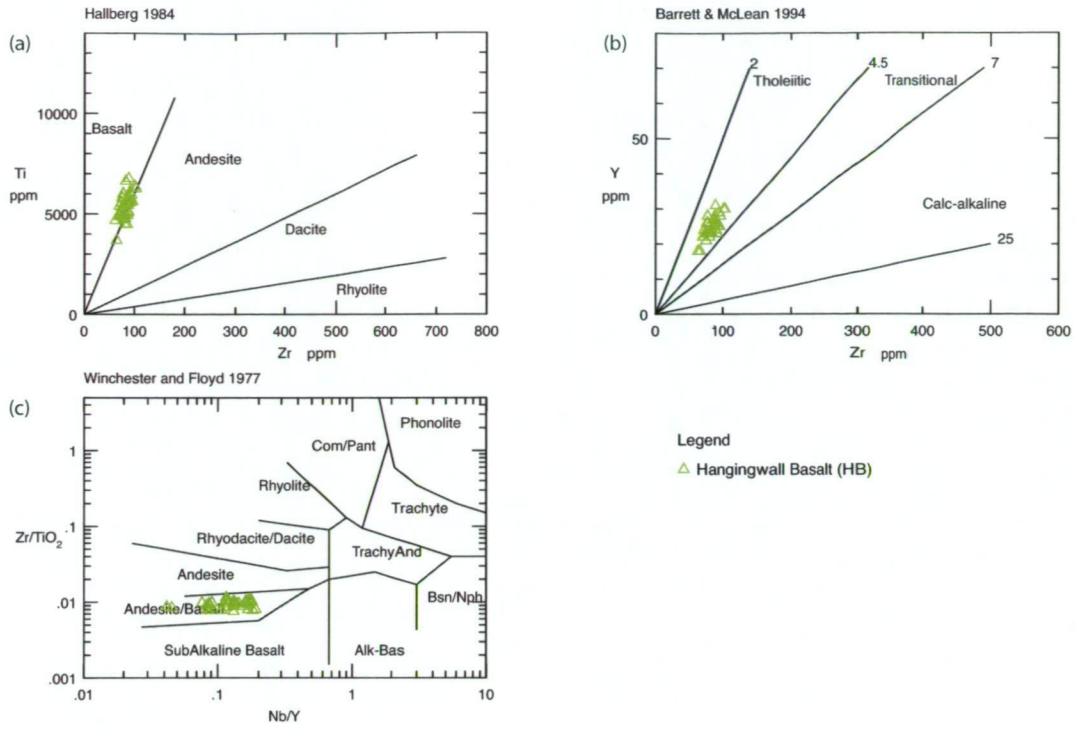

Figure 4.17 HFSE data for the Hangingwall Basalt, (a) after Hallberg, (1984), (b) after Barrett and McLean, (1994), and (c) after Winchester and Floyd, (1977).

4.5.3 *Upper Sediment 1 (HUS1)*

The HUS1 occurs throughout the area and varies in thickness from several metres up to about 30 m thick (Figs 4.3 and 4.4). The thinnest intersections are in the southern part and the thickest in the northern part of the study area. The HUS1 comprises intercalations of the volcanic sandstone, the laminated volcanic mudstone and the laminated mudstone and black shale facies (Figs 3.22, 3.23 and 3.24). The unit is bedded, and dominated by laminated mudstone, with minor black shale (locally graphitic), sandstone beds and rare conglomerate beds. The beds are commonly located at the base of the unit. Beds are locally normally graded and always display upwards younging. Similarly, load casts at the base of some beds always indicate upwards younging. Flame structures are seen in places along boundaries between sandstone and mudstone and these also always face uphole. In a very general sense the entire unit fines upwards, and the coarser sandstone and conglomerate units predominate lower in the unit.

The lower contact with the HB unit is passive. The contact is always sharp and may be irregular. The unit is overlain by the Upper Porphyritic Andesite, and in nearly all instances, the upper contact is immediately underlain by sheared and contorted black shale. The deformation obscures the nature of the relationship although numerous apophyses of the overlying Upper Porphyritic Andesite have intruded throughout the upper half of the unit, commonly within tens of centimetres of the upper contact. In most instances, these apophyses have peperite margins (non-stratified sediment-matrix andesite breccia) (<1 m thick).

4.5.4 Upper Porphyritic Andesite (HUA)

This unit is present across the area studied, although in most drillholes only the lower part of the unit is present. The entire unit was intersected in only two northern drillholes (TBD0230A and 05TBD008) and has an average thickness of about 60 m (Figs 4.3 and 4.4).

This unit comprises coherent andesite, monomictic andesite breccia and non-stratified sediment-matrix andesite breccia facies (Figs 3.4, 3.11 and 3.12). Throughout the study area the basal zone is commonly but not always monomictic andesite breccia. Intervals of coherent andesite grade vertically or laterally into zones of autoclastic breccia (monomictic andesite breccia). There are numerous apophyses of the unit, which intrude the underlying HUS1 unit, peperite (non-stratified sediment-matrix andesite breccia facies) commonly occurs along their margins. These apophyses range from cm to >1 m in thickness.

The upper contact was only intersected twice and was sheared and equivocal. In both instances coherent andesite is overlain by a polymictic conglomerate. In hole 05TBD008 the andesite is pillowed and locally aphyric, whereas in TBD0230A the andesite is flow-banded and vesicular. Along the lower margin, the breccia may be monomictic andesite breccia in which fluidal black shale clasts are common. This facies grades into the basal peperite (non-stratified sediment-matrix andesite breccia). The underlying black shale is generally sheared and contorted.

Eight samples collected from the feldspar-rich and feldspar poor, coherent andesite facies were analysed for HFSE (Fig. 4.18). On a Nb/Y vs Zr/TiO_2 diagram (Winchester and Floyd, 1977), the samples plot in a cluster across the andesite - dacite boundary. On a Ti vs Zr diagram (Hallberg, 1984), they plot in a group in the centre of the andesite field with a Ti/Zr value ranging from 17–25. The Zr/Y (Barrett and MacLean, 1994), values ranges from 9.1–28; i.e. clearly calc-alkaline.

4.5.3 Upper Sediment 2 (HUS2)

The HUS2 occurs in only two of the drillholes logged. One intersection is incomplete and includes only the basal 1.5 m. A complete section of HUS2, about 35 m thick, occurs in TBD0230A (Fig. 4.4). The thickness is inflated by the presence of a thick apophysis or dyke of the quartz-phyric coherent rhyolite facies.

The unit is bedded and comprises a mixture of laminated volcanic mudstone and sandstone facies, polymictic conglomerate facies plus non-volcanic, laminated mudstone and black shale facies (Figs 3.23, 3.22, 3.19 and 3.24). Beds are locally normally graded. Good younging indicators occur at various levels throughout the unit with graded bedding, flame structures and load casts all younging up-hole, and to the west.

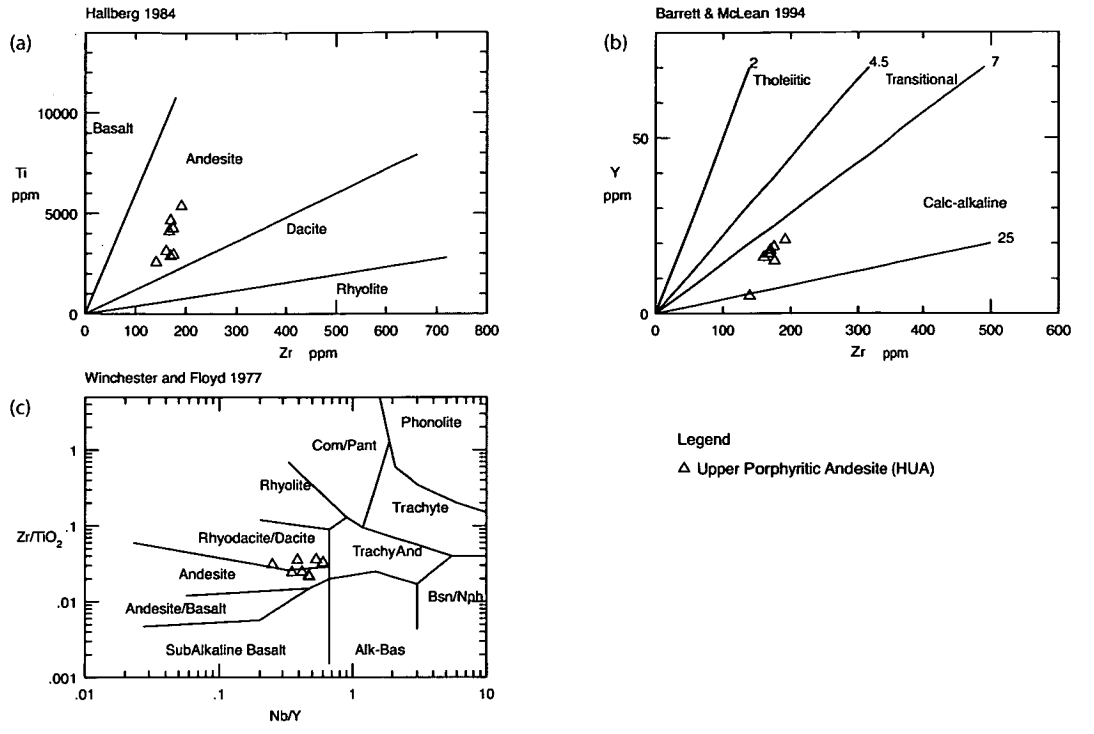

Figure 4.18 HFSE data for the Upper Porphyritic Andesite, (a) after Hallberg, (1984), (b) after Barrett and McLean, (1994), and (c) after Winchester and Floyd, (1977).

The upper contact is sharp. Polymictic rhyolite breccia (dominated by clasts of the quartz-rich rhyolite) overlies laminated mudstone. The lower contact, is sheared and marked by polymictic conglomerate passively overlying coherent andesite.

No samples from this unit were analysed for HFSE.

4.5.4 Upper Quartz Rhyolite (HUR)

Intersected in a single drillhole (TBD0230A) in the northern part of the study area (Fig. 4.4c), this is the top-most unit in the stratigraphic column for Jaguar. Although the full extent of the unit is not known, more than 100 m of section is intersected. The HUR comprises coherent rhyolite, monomictic rhyolite breccia, non-stratified sediment-matrix rhyolite breccia and polymictic rhyolite breccia facies (Figs 3.2, 3.7, 3.8 and 3.17).

The HUR is dominated by lithofacies of coherent quartz-phyric rhyolite, commonly massive but locally flow banded. At the base of the unit, a polymictic rhyolite breccia containing rare domains of semi- jigsaw-fit clasts of quartz-phyric rhyolite grades upwards into a coherent, flow-banded rhyolite. The concentration of bi-pyramidal euhedral quartz phenocrysts (maximum diameter up to 3 mm) varies throughout the unit. There are zones where the flow-banding grades to autobrecciation and becomes monomictic rhyolite breccia facies.

This unit has a style of alteration not occurring elsewhere in the stratigraphy. Large intervals

of pink - red hematite and K-feldspar alteration are associated with zones of brittle fracture and brecciation, and are accompanied by minor magnetite and rare pyrite.

In the single example of the lower contact, polymictic rhyolite breccia, with rare clasts of sandstone, overlies laminated sandstone of the HUS2. An apophysis or dyke of vesicular, quartz-phyric rhyolite with a peperitic upper margin intrudes the underlying HUS2, some 18 m beneath the lower contact. The peperitic nature of the contact indicates that the underlying sediment was semi-consolidated at the time of emplacement. The upper contact of the HUR is not seen.

A single sample was collected from this unit and analysed for HFSE (Fig. 4.19). On a Nb/Y vs Zr/TiO_2 diagram (Winchester and Floyd, 1977), the sample plots in the rhyolite field. On a Ti vs Zr diagram (Hallberg, 1984), it again plots in the rhyolite field with a Ti/Zr value of 3.3, whereas the Zr/Y (Barrett and MacLean, 1994) value is 7.2; it is clearly calc-alkaline.

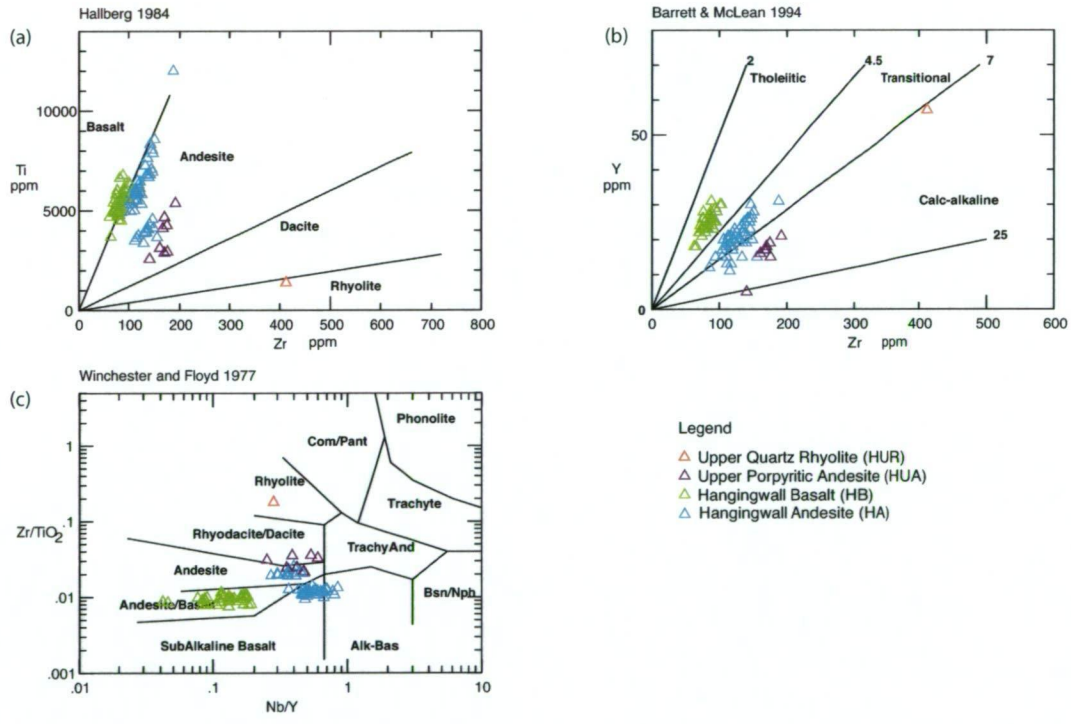

Figure 4.19 HFSE data for the hangingwall volcanic units, (a) after Hallberg, (1984), (b) after Barrett and McLean, (1994), and (c) after Winchester and Floyd, (1977).

4.5.5 *Discussion*

The onset of HW times was signalled by the emplacement of the HA1 lava. This andesite lava had predominantly a burrowing habit and was intruded into the slowly accumulating sedimentary interval that the MP had become. In some places, the lava burrowed deep enough to intrude consolidated mudstone and formed cross-cutting contacts. Less commonly the HA1 lava developed a hyaloclastic breccia carapace where it was erupted

locally on the seafloor. The HA1 lava has the form of a low aspect coulee and although twice the thickness of the HA2 and HA3 lavas, it has a more restricted areal extent than these lavas.

Sedimentation continued after eruption of HA1, depositing laminated mudstone intercalated with sandstone beds (HA1S). HA2 erupted onto the seafloor and partially burrowed into the unconsolidated sediments of HA1S that made up the sea floor at the time. All lower contacts of HA2 show peperite margins, whereas the upper contacts have either peperite margins, indicating where the lava burrowed, or have a hyaloclastite breccia carapace overlying coherent andesite. Sedimentation continued and the HA2S mudstone and black shale were laid down forming a passive conformable contact over the occurrences of HA2 carapace breccias. HA3, the last andesite, was then erupted onto the seafloor. The lower contacts of HA3 either show peperite or andesite conformably overlying mudstone, whereas the upper contacts are marked by hyaloclastite breccia carapace overlying coherent andesite or pillowed andesite, passively overlain by laminated mudstone (HA3S). The HA is thickest in the area between 56100 N and 56250 N and the vent source was probably close to this area.

The HB which followed is interpreted as having been formed by the voluminous outpouring of tholeiitic basalt in five major episodes. The initial lava HB0 was of low volume and limited in extent. It appears to have been restricted to the southern down-dip area and the likelihood is that this was a topographic low at the time. The HB1 lava which followed is the thickest and also appeared to have filled a topographic low in the southern down-dip area. The HB1 and HB2 were marked by pillow lavas with extensive hyaloclastite breccia carapaces (up to 20 m thick), whereas the later flows (HB3, HB4 and HB5) have thinner carapace breccias.

The widespread extent of the fluidal-clast breccia facies (a fire fountain spatter deposit with a surface extent of at least 0.04 sq. km) associated with the HB1 carapace indicates that there may have been several vents, most likely along a fissure. In the study area, the thickest development of the fluidal-clast breccia facies occurs on 56100 N but the limited logging on adjacent sections at this level of the stratigraphy may prejudice this selection. The greatest concentration of fluidal clasts is likely to be close to the vent, although local resedimentation of a rapidly accumulating pile would change the original distribution.

During this outpouring there was minimal deposition of sediment implying rapid accumulation. Only rare instances of black mudstone occur, and where present it is as a component of peperite at the base of coherent basalt. By the end of the formation of the HB, the gradual subsidence appears to have ceased, indicated by the relatively even thicknesses of the upper three HB units.

When the outflow that generated the hangingwall basalts had ceased, there was a period of sedimentation dominated by mudstone (HUS1). Rare conglomerate beds occur towards the base of the unit. Although the HUS1 extends throughout the study area, unlike all units lower in the succession, is thicker in the northern part of the area. This change in thickness across the study area, may reflect that the depositional surface was now elevated in the opposite fashion to that earlier, and that the southern part of the area was a topographic high when the unit was deposited.

This period of sedimentation was followed by the eruption of a major andesite unit HUA interpreted as a series of submarine lavas.

The HUS2 sedimentary unit passively overlies the HUA and the basal unit is conglomerate that contains clasts of andesite, similar to the HUA. These presence of the andesite clasts suggest that the upper surface of the HUA may have been irregular and that locally the lower contact may be erosive.

Immediately overlying the HUS2 is the HUR, a quartz-phyric rhyolite unit. Underlying the rhyolite and intruded into the HUS2 is a body of dominantly coherent rhyolite with peperite margins that is interpreted as either an apophysis or feeder dyke of the HUR. The HUR may represent a rhyolite dome and the dyke may be a feeder but there is insufficient evidence make any interpretation on the form and significance of this rhyolite.

The HW succession is dominantly a constructional sequence. There is wedge shaped thickening of the lower HW units in the southern down-dip area of the study area that may indicate infill of developing depressions was ongoing. However, it had ceased by the by the time the upper units of the HB were erupted. The remainder of the HW was deposited in an apparently seismically stable environment although there may have been some tilting associated with the dolerite intrusions.

4.6 Dolerite (D)

The Dolerite is composed solely of the coherent dolerite facies (Fig. 3.6). Samples are of a typical dolerite with an equigranular fabric, varying from fine to very coarse grained (gabbro) and from magnetic to non-magnetic.

Five major late-stage Dolerite sills have been identified at Jaguar (Figs 4.3 and 4.4). The sills are referred to as D0, D1, D2, D3 and D4 from the lowermost upwards (Fig. 4.2). They intrude all units beneath the lower units of the HB. Minor unassigned sills and apophyses are named 'D'. The lowest part of the Jaguar stratigraphy (Fig. 4.4b) is a dolerite (D0). There is a strong level of interconnectedness among the sills D1 to D4 (Figs 4.3 and 4.4)

and on some sections, the interconnecting shape of the dolerite intrusions is interpreted as arcuate. Numerous smaller apophyses are associated with these four sills. In cross section, different sills and different parts of sills dip both ways relative to the bedding. The changes in position along strike show that D1 and D2 gradually cut across the succession, climbing up through the stratigraphy to the north. Although the relative positions of D3 and D4 change, they do not appear to climb across the stratigraphy in a measurable way. The direction of opening of the sills is difficult to determine. Because all drillholes intersect the succession at angles between 35° and 50° the measurement of displacement in any possible markers is not possible. However, inter-hole correlation of HB1 relative to D4 suggests that, at least D4 was likely to have inflated normal to its orientation. The sills vary in thickness from <10 m to >140 m, and as a general rule, the lower the position in the stratigraphy, the thicker the sill.

Contacts between the dolerite and the FW units, the MP and the HA are everywhere sharp, and locally irregular. At the margin, the coherent dolerite is fine-grained and vesicular. Higher in the succession the contacts are not as well defined, and in some instances coherent dolerite appears to be gradational with the host basalt units over an interval of up to 5 m. A marginal zone of low intensity, pervasive, blotchy alteration is associated most commonly with D3, but locally with D2 and D4 and extends from the sill and into the host rock by as much as 10 m. This distinctive zone is associated with nearly all occurrences of D3 and consists predominantly of carbonate. Where the coherent dolerite intrudes the sulfide mineralised host rocks, the dolerite everywhere has a chilled margin and is not affected by the hydrothermal alteration that affects the host rock. Where the dolerite is in contact with sulfide ore, the grainsize within the sulfide shows no appreciable increase in grainsize or deformation towards the dolerite. In rare instances minor (<1 mm sized) veinlets of chalcopyrite pass <5 cm into the chilled margin. Although the Dolerite has not been affected by the hydrothermal alteration associated with the orebody, but the metamorphic minerals seen in thin section indicate that it has been metamorphosed to upper greenschist facies.

Forty-six samples collected from dolerite sills were analysed for HFSE (Fig. 4.20). The geochemical composition of the dolerite is almost indistinguishable from that of the HB. On a Nb/Y vs Zr/TiO_2 diagram (Winchester and Floyd, 1977), the samples plot in a cluster in the basalt/andesite field. On a Ti vs Zr diagram (Hallberg, 1984), the samples plot in a line along the andesite - basalt boundary, with values ranging from 55–98. The Zr/Y values range from 2.6–4, clear indications of a tholeiitic magma source (Barrett and MacLean, 1994).

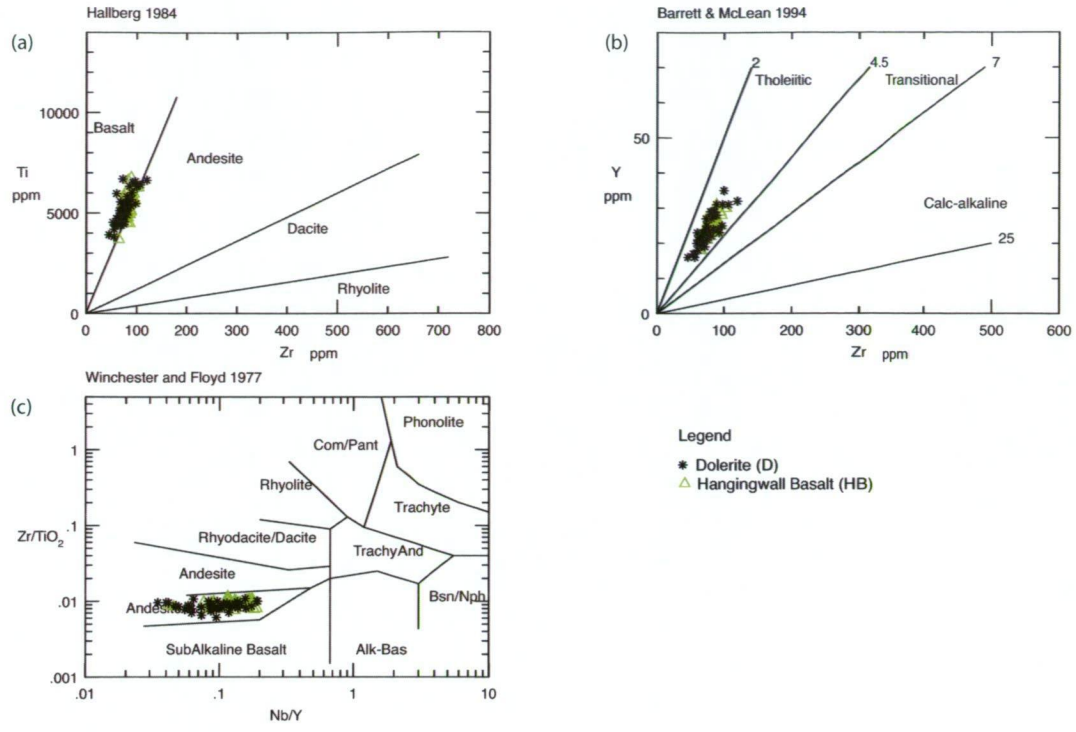

Figure 4.20 HFSE data for the Dolerite, overlain on the Hangingwall Basalt plot (Fig. 4.17), (Winchester and Floyd, 1977; Hallberg, 1984; Barrett and MacLean, 1994).

4.6.1 Discussion

The Dolerite intrusions post-date the mineralisation and deposition of the HA and lower units of the HB.

The striking similarity in the chemistry between the Dolerite and the HB (Fig. 4.17) suggests that the D and the HB basalts were comagmatic. The nature of the contacts of D3 and D4 with the upper units of the HB, suggests that as well as D being comagmatic, it was coeval with the HB; the upper flows of the HB unit were still forming as the dolerite sills were intruded lower in the succession. The arcuate shape of the interconnecting zones between dolerites seen on some sections may reflect where the dolerites have cut across the stratigraphy following existing planes of weakness, possibly the position of a listric growth fault. Most likely the dolerites were the feeders to the HB lavas. If this is the case, using the estimated cumulative thickness of the separate sills, the aggregate uplift to the succession by the dolerite was likely to have been between 150 and 200 metres. This inflation may not have been uniform across the study area. If more magma was intruded in the south of the area this may have caused the tilting to the north of the succession, which resulted in a thicker accumulation of the HUS1 unit in the northern part of the study area.

An alternative to this interpretation is that although the HB basalts and the D were comagmatic the sill emplacements may not have been contemporaneous with the basalt eruptions, instead originating from a later pulse from the same magma chamber. It is also

possible that the units were comagmatic and that one or all of the D1, D2, D3 and D4 sills were coeval with the HB, and the magma chamber remained in existence, and that, later on, further sills and dykes were intruded, including into higher levels of the sequence than examined in this study. The district geology as presented in Figure 4.1 shows that mafic intrusions are extensive throughout the succession and it is not known how these relate to the Dolerite unit.

4.7 Structure and Deformation

In this section the degree to which deformation has modified stratigraphic sub-division and reconstruction of volcanic facies architecture is assessed. The regional geodynamic synthesis for the central Eastern Goldfields Super Terrane (Fig. 2.5) (Blewett and Czarnota, 2007) indicates that deposition of the Jaguar succession occurred during a period of arc building within an east-northeasterly directed extension-dominated regime. It is not the intention in this thesis to place the deformation at Jaguar into the regional setting nor to attempt to relate any of the local structures to a specific deformation event.

The lateral continuity of almost all units, and the lack of repetition of the sequence, does not support the presence of subtle thrust ramp repetitions at the scale of the deposit. All the sedimentary younging evidence, (graded bedding, flame structures, load casts etc) unequivocally youngs to the west, indicating that no obvious major folds are present.

4.7.1 Bedding orientations

The Jaguar succession and the surrounding greenstone belt strike at ~ 337° Magnetic. At Jaguar, the succession dips steeply to the west at ~75°. All indicators show the succession youngs to the west. The younging indicators include, normally graded bedding, flame structures, load casts, chert desiccation cracks. There are also younging indicators associated with the sulfide ore (discussed in Chapter 6), the presence of well-developed stockwork mineralisation in the footwall to the massive sulfide ore and the presence of chert at the top of the massive ore. Bedding appears planar over the 1600 m strike extent of the study area, at least in the upper half of the succession that is uninterrupted by intrusions.

4.7.2 Syn-sedimentation deformation

Within the study area, structures produced by soft-sediment slumping have been observed only rarely in some of the fine grained laminated units, whereas the MPH shows local folds associated with breccia and in-situ imbrication of layers. Locally collapsed pumice clasts define a flattening foliation sub-parallel to bedding. Where soft-sediment slump products are present in the MPS, they are locally accompanied by discrete local pull-apart structures

in chert layers. In the fine-grained laminated layers, cm-scale listric pull-apart faults are present (Fig. 4.21).

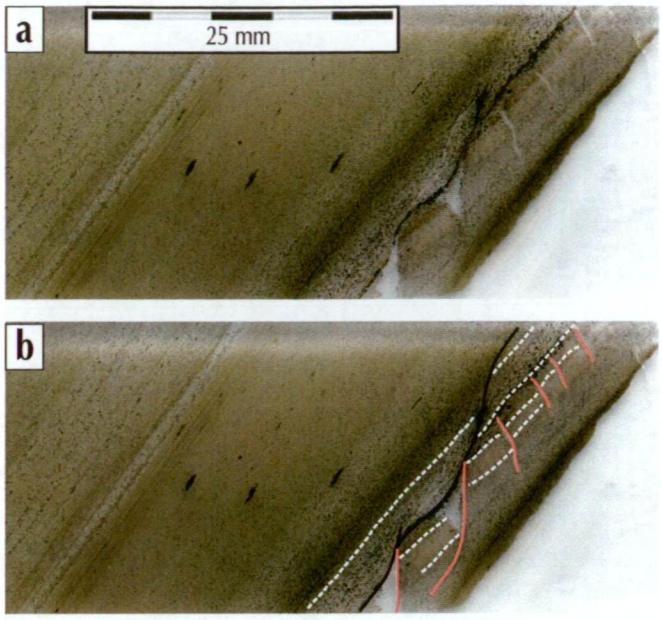

Figure 4.21 Example of syn-sedimentary development of micro-listric pull-apart faults in laminated mudstone. Facing is uphole, to the left. Scan of thin-section from hole TBD0256, 409.5 m

Thick (5–20 m), wedge-shaped beds of the MPC occur in the MP. The wedge-shape is present in the southern part of the study area, in the deepest parts of the sections (Fig. 4.22). This geometry is consistent with unequal subsidence occurring during the deposition and emplacement of these units. Wedge-shaped accumulations of monomictic basalt breccia and monomictic pillow-fragment basalt breccia in the upper zones of the HB1 and HB2 in the lower hangingwall are also present and these may also be related to subsidence. However, they could also be a volcanic constructional feature.

This subsidence was most likely the result of transient 'growth faults', being listric faults that typically develop as a response to extension (e.g. Pollard and Fletcher, 2006). Because it has not been possible to pinpoint the actual position of these growth faults, it is likely that they were transient and did not repeatedly propagate at the same location, and subsidence may have occurred incrementally without producing large fault scarps. The evidence is that these growth faults continued to be active at least until after HB2 was erupted, as HB2 is the highest unit in the succession that shows the wedge-shaped geometry.

Distortions of bedding that are related spatially to intrusions and apophyses occur in the upper part of the MPS, the HUS1 and HUS2.

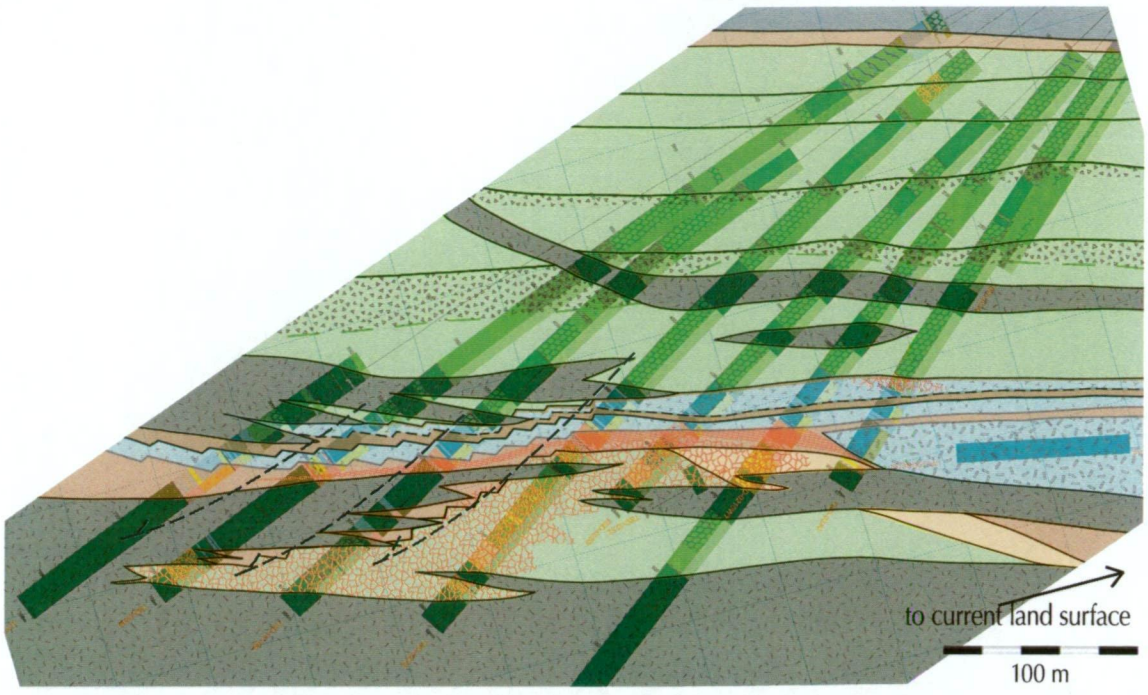

Figure 4.22 Enlargement of the section 55950 N (Fig. 4.3b) rotated to show interpreted position at the time of deposition of the upper hanging wall. The evidence for growth faults is indicated by the wedge shaped MP unit in the lower half of the succession. No actual fault positions have been identified and the dotted lines on this figure and on Figures 4.3 and 4.4 are solely schematic indications of movement and throw. It may be that some of the faults are intruded by the dolerite sills, because the interpreted shape of some of these sills reflects an apparent listric shape. Legend is as for Figures 4.3 and 4.4.

4.7.3 Brittle - ductile deformation

The top of the sulfide body (MPO) is in places marked by narrow zones (<30 cm) of moderately contorted, sheared graphitic black shale that contains boudinaged, irregular, quartz-carbonate veins. Similar zones are also present along the contact between the HUS1 and HUA units. These structures are interpreted as the result of competency contrasts between the two units and formed during simple shear. A sense of movement cannot be determined as the drillcore in these areas is commonly fractured and broken and furthermore, generally un-oriented.

Where present at the top of the MPO, these structures are commonly associated with underlying thin zones, generally <30 cm wide, of pyrrhotite-dominated, durchbewegung-textured (see Chapter 6) ore breccia. Narrow zones of durchbewegung-textured intra-ore breccia are locally present throughout the ore body (discussed further in Chapter 6).

4.7.4 Brittle deformation

In the laminated mudstone in the MP and HA, there are fractures and displacements on the millimetre to centimetre scale, commonly accompanied by pervasive, low-intensity carbonate alteration. In the ore body, cataclastic fracture occurs in pyrite grains (discussed further in Chapter 6).

Minor zones (30 – 100 cm) of jigsaw-fit breccia, commonly with a quartz-carbonate cement, occur throughout the succession cross-cutting a variety of rock types. The jigsaw-fit breccia passes outwards into a narrow envelope of fractures associated with quartz-carbonate veining. These zones are not associated with any obvious hydrothermal alteration. Intervals where this breccia is associated with a cataclastic zone or fault gouge are very rare. It has not been possible to correlate between these zones of fault breccia or gouge because of the absence of any kinematic indicators. Therefore the extent and the direction of movement, if any exists, is unknown. In the study area, fault movement is assumed to have been minor due to the planar nature of the succession as evident in the upper hangingwall and the ability to readily correlate the succession across these fault zones.

4.7.5 Metamorphism

The overall general level of metamorphism is upper greenschist facies as confirmed by the mineralogy of the dolerites. These show equilibrium assemblages that are comparable with the metamorphic grades seen in the ore (discussed later in Chapter 6).

4.8 Summary

The stratigraphy at Jaguar is built on a series of eruption events which were identified by observations and interpretations based on facies analyses and relationships, rock fabric, and microstructure, and are supported by the application of immobile element geochemistry.

The presence of growth faults is indicated although no actual positions have been identified and the dotted fault positions on Figs 4.3 and 4.4 are solely indications of the direction of movement. This wedge shaped thickening of the lower units in the southern part of the study area that indicates that infill of developing depressions was ongoing. However, this subsidence had ceased by the time the upper units of the HB were erupted. The remainder of the hangingwall was deposited in an apparently seismically stable environment. It may be that some of the faults are intruded by the dolerite sills, as the interpreted shape of some of these sills on section reflects a listric fault shape.

The large volume of the dolerite sills in the lower half of the succession causes some problems for the interpretation. The sill opening is assumed to have been perpendicular to the long axis which would cause little if any dislocation of stratigraphy. However, if the opening was orthogonal then the effect may have been some dislocation of the stratigraphy on either side of the sill. If this is the case then dislocation associated with the D1 dolerite (the thickest sill, up to 140 m thick) is unlikely to have been recognised due to the lack of data at this level in the footwall.

The deformation of the sequence is not significant enough to influence stratigraphic reconstruction.

Being at deposit scale, the lateral extent of the study area is quite small (~ 1600 m). This distance is only is slightly greater than one quarter of the distance between the Teutonic Bore and Jaguar deposits. The Jaguar succession is compositionally different from the succession described at Teutonic Bore (Greig, 1984; Hallberg and Thompson, 1986). Hence stratigraphic correlation between the two deposits remains uncertain, but comparing the description of the Teutonic Bore stratigraphy with that just described for Jaguar, it is suggested that Jaguar lies at a higher stratigraphic level than Teutonic Bore.

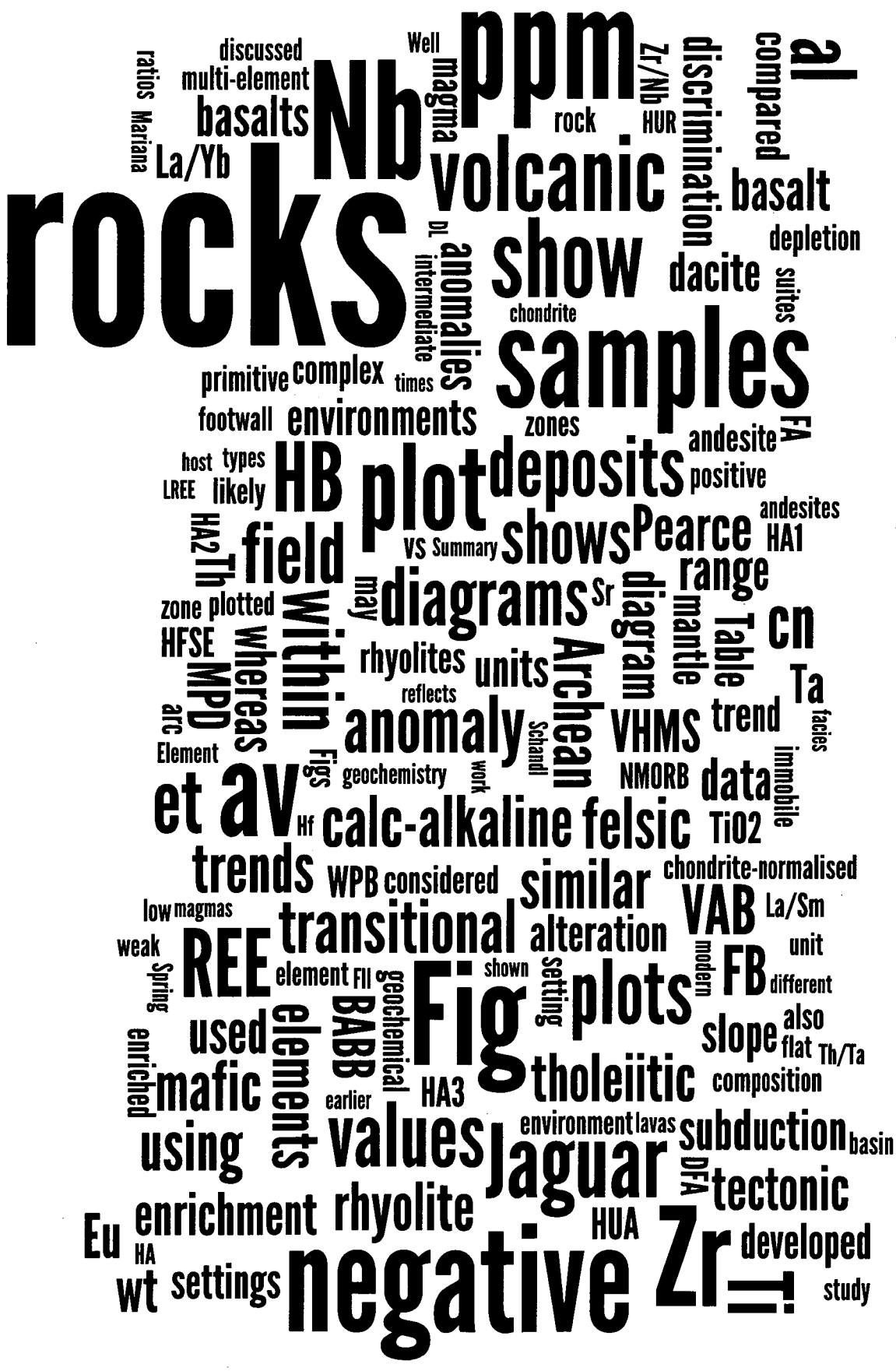
rocks
ppm
Nb
volcanic
Fig
samples
show
basalt
al
compared
discrimination
basalts
multi-element
discussed
ratios
Mariana
La/Yb
Well
magma
Zr/Nb
rock
HUR
depletion
dacite
suites
chondrite
anomalies
DL
intermediate
primitive
complex
times
footwall
environments
zones
andesite
FA
host
types
LREE
likely
HB
plot
deposits
positive
andesites
HA1
HA2
Th
field
VS
Summary
shows
Pearce
range
zone
plotted
diagrams
may
Sr
diagram
mantle
Table
cn
HFSE
MPD
whereas
within
rhyolites
units
Archean
Ta
arc
Element
reflects
anomaly
Schandl
VHMS
trend
facies
Figs
geochemistry
work
NMORB
data
immobile
et
av
Hf
calc-alkaline
felsic
TiO2
trends
WPB
considered
similar
chondrite-normalised
low
magmas
transitional
alteration
VAB
La/Sm
weak
REE
element
FII
geochemical
shown
setting
plots
modern
FB
unit
Spring
different
used
BABB
slope
also
flat
Th/Ta
enriched
elements
earlier
HA3
tholeiitic
composition
mafic
environment
lavas
subduction
basin
using
values
Jaguar
DFA
tectonic
enrichment
rhyolite
HUA
Eu
HA
wt
settings
negative
Zr
Ti
developed
study

5. GEOCHEMISTRY OF THE VOLCANIC ROCKS

5.1 Introduction

In this chapter the criteria used to classify the lithologies described in Chapters 3 and 4 (lithofacies and stratigraphy) is expanded and the use of immobile elements to characterise the volcanic rocks is explained. The immobile element geochemical composition is used to demonstrate that these rocks are sub-alkaline, and links to magmatic suites are further explored and discussed. Discrimination diagrams developed for modern rocks are used as a basis for characterising the Jaguar rocks. Normalised multi-element variation diagrams of REE and trace-elements are plotted against chondrite, primitive mantle, NMORB and BABB (back-arc basin basalt). The 'fertility' concept is discussed and comparisons drawn with other (Archean) VHMS camps (in Canada). The geochemical composition is compared with published geochemical data from other suites in the Eastern Goldfields Superterrane, in particular the Gindalbie and Kurnalpi suites, and comparisons are made and discussed. The chapter concludes with an evaluation of the possible tectonic setting using known data and discrimination diagrams, and published data from modern settings.

5.1.1 Element mobility and geochemical classification

As noted in earlier chapters, rocks within the study area have been affected by regional lower-greenschist facies metamorphism and locally intense hydrothermal alteration. All samples selected for this study have, therefore, undergone some degree of mineralogical and chemical change. As alkali elements can be mobile during metamorphism and hydrothermal alteration, classification schemes based on alkalis or total alkalis, such as the SiO_2 versus total alkalis (Cox et al., 1979; Le Maitre et al., 1989), are deemed unreliable for such rocks in this case. The suite of elements widely considered to remain chemically immobile under greenschist facies metamorphism and moderate to high degrees hydrothermal alteration are the HFSE: Ti, Zr, Y, Nb, Ga, P, REE, Hf, Ta and Th, and the transition metals: V, Cr and Sc (Pearce and Cann, 1973; Winchester and Floyd, 1977; Whitford et al., 1989).

Winchester and Floyd (1977) developed a an immobile element discrimination rock classification diagram, Zr/TiO_2 vs Nb/Y, that discriminated between magma series and their differentiation products. It is based on the knowledge that, although both ratios are indices of alkalinity, Zr/TiO_2 also represents a differentiation index and is an effective immobile proxy for SiO_2. In work on five VHMS deposits, Finlow-Bates and Stumpfl (1981) established that in sites of intense hydrothermal alteration, Y and particularly Sc and Nb may be extremely mobile, and that only Zr and TiO_2 may be used with any reliability

to identify the degree of magmatic differentiation in a hydrothermally altered rock. Pearce (1996) refined the boundaries of the 1977 Zr/TiO_2 vs Nb/Y diagram of Winchester and Floyd. Hallberg (1984) developed criteria using Ti/Zr values to define compositional fields for the major igneous rock types, based on the analysis of >9000 samples. Over 90% of these samples were given rock names on the basis of megascopic and microscopic textures and known relationships. These samples were all collected in the north-eastern Yilgarn Craton from Archean greenstone belts around Leonora, including the Malcolm greenstone belt which hosts the Jaguar deposit. At the Scuddles deposit, another Yilgarn, Archean VHMS deposit, the elements Ti, V, Zr, Nb and Y remained immobile through alteration (Whitford and Ashley, 1992). Work on many VHMS deposits around the world (e.g., MacLean and Barrett, 1993; Barrett and MacLean, 1994) has recognised that the heavy REE are essentially immobile under all conditions represented in VHMS deposits, whereas the light REE showed evidence of some mobility in proximal, intensely chlorite-altered zones.

MacLean and Barrett (1993) recognised that gradients of chemical trends also varied according to magmatic affinity, and that samples from different magmatic suites produce separate linear trends of magmatic enrichment. In particular, Zr vs Y plots can be used to separate magma affinities in altered volcanic rocks, with Y/Zr used as an index: i.e., tholeiite from 2 to 4.5, transitional from 4.5 to 7 and calc-alkaline from 7 to 25 (MacLean and Barrett, 1993; Barrett and MacLean, 1994).

5.1.2 Discrimination diagrams and tectonic setting

The idea that magmas could be fingerprinted to identify tectonic setting originated with Pearce and Cann (1973), who showed that it is possible to use geochemical composition to distinguish between modern basalts in different, known tectonic settings. Subsequent work (Floyd and Winchester, 1978; Wood, 1980; Meschede, 1986; Cabanis and Lecolle, 1989; Rollison, 1993; Pearce, 1996; Gorton and Schandl, 2000) included rocks from the Precambrian to the present time.

Pearce (1996) developed a protocol intended to reduce the ambiguities often seen in the results of the use of discrimination diagrams. A ternary diagram (Fig. 5.1) represents the tectonic classification of basalts. It is convenient to treat the end-members as three, tectonically defined basalt types: (1) mid-ocean ridge basalts (MORB), erupted at divergent plate margins; (2) volcanic-arc basalts (VAB), erupted at convergent plate margins; and (3) within-plate basalts (WPB), erupted away from any plate margin. Where the eruptive environment is a more complex tectonic setting, between the end-members, the geochemical signature is more complex and care must be taken in the analysis of the discrimination diagrams.

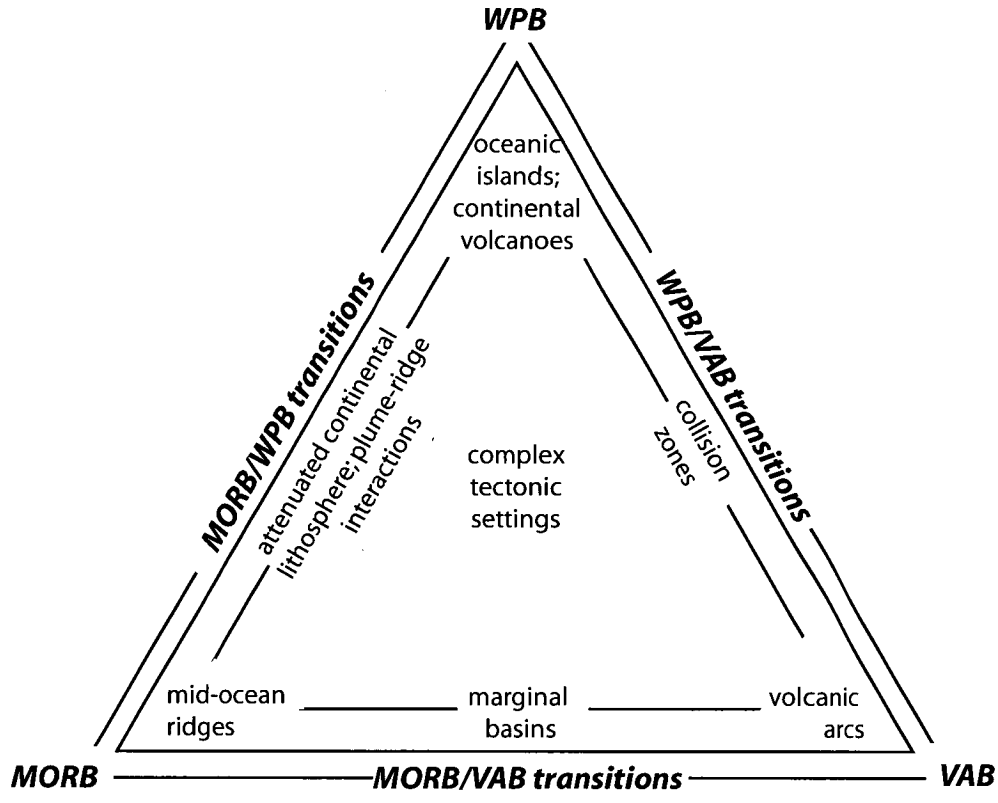

Figure 5.1 Graphic representation of the tectonic classification of basalts. The three major basalt types (MORB, VAB and WPB) are represented by the apices of the triangle and the common transitions between them by the edges of the triangle. Eruptive settings in which these magma types are located are shown inside the triangle. From Pearce (1996).

The applicability of this work in fingerprinting Archean tectonic settings is not yet demonstrated, as there is no consensus as to the timing of commencement of modern-style plate tectonics. Two strongly contrasting hypotheses place the start of plate tectonics in either the Neoproterozoic ca 1.0 Ga (Stern, 2005,), or the Hadean, ca 4.4–4.5 Ga (Harrison et al., 2005). Rollinson (2007a, 2007b) argued for a change from "ancient" to "modern" plate tectonics at about 2.5–3.0 Ga. Condie (2008) further argued that changes in the ratio of TTG to calc-alkaline granitoids after 2.5 Ga indicate that Archean subduction zones must have differed from younger subduction zones.

The problem of attempting to fingerprint Archean basalts is addressed by Pearce (1996), who noted that, although plots of Archean basalts on discrimination diagrams provide meaningful information about their magma genesis, the results do not necessarily have any tectonic significance. For the interpretation of discrimination diagrams developed using Phanerozoic rocks to be meaningfully applied to Archean rocks, there must be some confidence that the same tectonic mechanisms applied. This has particular consequence for discussions about the settings of Archean VHMS deposits. Although this issue is beyond the scope of this thesis, discrimination diagrams have been used in the analysis of the geochemical composition in order to compare with analogous Phanerozoic tectonic settings. By comparison of stratigraphic styles in Archean greenstone belts to those of modern and Phanerozoic depositional basins, Eriksson et al. (1994) defined seven dominant

lithological associations and determined that tectonic environments between 3.8 and 2.5 Ga were remarkably similar to those in the modern Earth. They emphasised that Archean greenstone belts do not represent a single geotectonic setting, but reflect a diverse range of tectonic environments. Many Archean VHMS researchers have used Phanerozoic-based discrimination diagrams in Archean settings (e.g. Lentz, 1998; Schandl and Gorton, 2002; Hathway et al., 2008).

Thorium is the most effective element for characterisation of VAB (Pearce, 1996). It is selectively enriched in this magma type but relatively immobile with respect to weathering and low-grade metamorphism. Gorton and Schandl (2000) developed Th/Yb vs Ta/Yb diagrams for use with felsic rocks, and defined three tectonic environments: oceanic arcs; active continental margins (ACM); and within-plate volcanic zones (WPVZ). These are distinct from the MORB and WPB fields on the Th/Yb vs Ta/Yb plot of Pearce (1983). The objective was to define tectonic settings of intermediate and felsic volcanic rocks on discrimination diagrams using trace elements from rocks in well known tectonic settings, and then apply them to rocks from ancient settings. Their work showed that felsic magmas erupting in WPVZ have the lowest Th/Ta values (1–6), ACM zones have intermediate values (>6–20), and the highest Th/Ta values occur in magmas erupting in oceanic arcs (>20–90). Gorton and Schandl (2000) suggested that the progressive enrichment in Th in the three sequential environments (WPVZ, ACM and oceanic arcs) reflected the increasing contribution of an arc component to the erupting lavas. These fields are not constrained and the WPVZ and the ACM have been interpreted to be transitional environments (in the sense of Pearce, 1996).

Felsic volcanic rocks from all the Archean VHMS deposits of the Superior Province plot within the WPVZ field, whereas younger deposits such as Bathurst, San Nicholas and Kuroko all plot within the ACM field (Schandl and Gorton, 2002). Thus, felsic rocks that host Archean deposits are characterised by very low Th/Ta (2–6) and a wide range of Yb concentrations (2–37 ppm), whereas volcanic rocks that host younger deposits have a wide range in Th/Ta (6–22), and a narrower range of Yb concentrations (1–10 ppm). They consider that this difference reflects a relative enrichment of Th in post-Archean deposit environments due to Th enrichment in younger volcanic rocks as a result of crustal evolution through subduction. Schandl and Gorton (2002) concluded that evidence of Th enrichment in post-Archean environments compared to Archean environments meant that, although the character of associated felsic volcanics has not changed significantly since the Archean (Lesher et al. 1986), the range of geotectonic settings of VHMS deposits probably has. They suggested that the Archean deposits of the Superior Province probably formed in an ensimatic rift environment, whereas the post-Archean deposits of Bathurst, San Nicholas and Kuroko formed in subduction-related rift zones within arc environments.

5.1.3 VHMS deposits and the 'fertility' concept

Early research to develop discrimination signatures and identify prospective rock suites focused on deposits in felsic volcanic-dominated environments (Lesher et al. 1986; Lesher and Campbell, 1987, 1990; Whitford and Cameron, 1987; Offler and Whitford, 1992; Whitford and Ashley, 1992; Barrie et al. 1993; Lentz, 1998), although Crowe et al. (1992) and Syme and Bailes (1993) worked in mafic terranes. These workers used discriminants based on ratios of compatible and incompatible elements. The work on Archean deposits concluded that VHMS deposits are typically associated with felsic volcanic rocks (dacites to high-silica rhyolites) with certain specific geochemical characteristics. Felsic volcanic rocks were classified (Table 5.1) as either FI, FII or FIII types, the FIV type was introduced by Hart et al. (2004) . The findings concluded that FI alkalic dacites and rhyodacites are typically barren, some FII calk-alkalic dacites and rhyodacites do host deposits, but most are barren. FIII tholeiitic and FIV depleted rhyolites and high-silica rhyolites most commonly host deposits and FIII rhyolites appear to host the largest deposits. The work on VHMS deposits in the Archean Superior province established that all of the deposits are associated with geochemically distinctive rhyodacites, rhyolites and high-silica rhyolites (Lesher et al. 1986; Lesher & Campbell, 1987, 1990; Barrie et al. 1993; Lentz, 1998). Subsequent work showed that discriminants developed for one terrane have not always been successful when applied in another terrane or in another era (Lentz, 1998).

Hart et al. (2004) reassessed the physical conditions responsible for producing the geochemistry of ore-associated FII and FIII-FIV felsic volcanic rocks. They also reviewed the compositions of felsic volcanic rocks associated with Mesoarchean to Cenozoic VHMS deposits to constraint models for VHMS-associated felsic volcanic rocks and their relationship to mineralisation. They suggested that compositional variations from FI through FII to FIII-FIV may be explained by low to moderate degrees of partial melting of mafic sources at a range of depths within rift environments where the mineralogy and composition of the source regions, modes, and degrees of partial melting, pressure and temperature of melting, and, to a lesser extent, subsequent fractionation processes account for the compositional variations. They concluded that favourable lithogeochemistry cannot be used in isolation as an exploration tool, and that other factors, including an assessment of tectonic setting, volcanic environment and the presence of subvolcanic intrusions, must be considered, because felsic rocks of favourable geochemistry may form in environments in which VHMS deposits may not form.

The general conclusions (Lesher et al., 1986; Lentz, 1998; Hart et al., 2004) were that Archean VHMS deposits are hosted mainly by FIII rhyolites, whereas most post-Archean VHMS deposits are hosted predominantly by FII rhyolites, and FI rhyolites are unfavorable for VHMS mineralisation in any time period. The discovery of the world-class, gold-rich

VHMS LaRonde deposit in FI and FII rhyolites (Mercier-Langevin et al., 2007a, b) raised doubts about the application of the rhyolite-fertility classification in VHMS exploration. Following this discovery, Gaboury and Pearson (2008) assessed the rhyolites of the Abitibi greenstone belt. They classified the rhyolites using the parameters of Hart et al. (2004) and compared them with VHMS tonnages, mineralisation type, and volcanic rock characteristics. They concluded that a combination of rhyolite geochemistry, volcanic facies, and style of the mineralisation may be more meaningfully applied in exploration than rhyolite type alone, particularly in the case of FI and FII rhyolites.

Table 5.1 Classification and parameters of FI, FII, FIII and FIV rocks (after Lesher et.al., 1986; Hart et.al.,2004; Mercier-Langevin et al., 2007a, b; Glaboury and Pearson, 2008)

	FI	FII	FIIIA	FIIIB	FIV
Lithology	dacite-rhyolite	dacite-rhyolite	rhyodacite- high Si rhyolite	rhyodacite- high Si rhyolite	rhyolite- high Si rhyolite
Si02 (wt%)	64 – 67	64 – 81	67 – 78	67 – 84	69 – 81
Ti02 (wt%)	0.16 – 0.65	0.16 – 0.89	0.21 – 0.99	0.09 – 0.73	0.09 – 0.57
Y (ppm)	6 – 31	11 – 73	25 – 96	72 – 238	18 – 36
Zr/Y	8.8 – 31	3.2 – 12.12	3.9 – 7.7	1.7 – 6.2	0.67 – 4.8
Yb (ppm)	0.43 – 3.8	1.3 – 7.9	3.4 – 9.3	5 – 32	1.5 – 8.4
[La/Yb]cn	5.8 – 3.4	1.7 – 8.8	1.5 – 3.5	1.1 – 4.9	0.22 – 2.1
Eu/Eu*	0.87 – 1.5	0.35 – 0.91	0.37 – 0.94	0.20-0.61	?
Affinity	alkaline – calc-alkaline	calc-alkaline	tholeiitic	tholeiitic	tholeiitic
Mineralisation style	Atypical Cu-Au veins, disseminations and replacement of permeable volcaniclastic rocks	Exhalative stratiform lenses High grade, low tonnage Cu-Zn ± Ag ± Au index Discrete alteration pipe and Cu-rich stringer zone or Atypical Cu-Au veins, disseminations and replacement of permeable volcaniclastic rocks	Exhalative stratiform lenses High grade, low tonnage Cu-Zn ± Ag ± Au index Discrete alteration pipe and Cu-rich stringer zone	Exhalative stratiform lenses High grade, low tonnage Cu-Zn ± Ag ± Au index Discrete alteration pipe and Cu-rich stringer zone	
Examples	LaRonde Bousquet 1 and 2	Sturgeon Lake, Kuroko, Rio Tinto, Bathurst, Myra Falls, Mt. Windsor, Tulsequah Chief, Mt. Chalmers, Thalanga, Boliden, Selbaie, Salt Creek, Murgul, Benambra	Noranda, Jerome, United Verde, Parys Mountain, Ambler, Avoca, Woodlawn, Buchans, Prieska, Fox Lake, Manitouwadge, Hood River, Sulphur Springs, Scuddles, Berslagen, Winston Lake	Kidd Creek, Kamiskotia, Eskay Creek, Neves Corvo, Shasta, Crandon, Mattagami Lake, Mons Cupri, South Bay	Stekenjokk, Snow Lake, Flin Flon, West Shasta, Kutcho Creek, Canatuan

Chondrite-normalising factors from Nakamura (1974); Eu* calculated by linear interpolation between chondrite-normalised Sm and Tb.

5.2 Sampling and Analytical Methods

In the initial stages of the study, representative samples were collected systematically from all the lithofacies within the study area. These samples included hydrothermally altered specimens from zones where alteration was pervasive and difficult to avoid. When the study area was expanded to include units higher in the Jaguar host succession, sampling was not as extensive due to financial limitations on additional analyses. Consequently, there is a skewed distribution in sample locations within lithofacies and unequal representation across units. A total of 252 samples from the various lithofacies were analysed from selected Jaguar drillholes. These samples included representative coherent, volcaniclastic and sedimentary facies.

All samples were crushed and ground by Genalysis Laboratories using a jaw crusher followed by a single-stage mix and grind in a low-chrome steel mill. Using the pulp samples, pressed powder disks were prepared by SGS laboratories in Perth, Western Australia, prior to X-ray Fluorescence (XRF) spectrometery, using a XuniqueII instrument made by Panalytical (previously Philips), with an Rh tube. These samples were spread over several batches and analysed in 2005 and 2006. Table 5.2 shows the elements assayed, and the detection limits. All 252 samples were analysed for Y, Ti, Nb and Zr, 222 were analysed for Rb and Sr and 44 were analysed for the remaining elements in Table 5.2.

Table 5.2 Elements measured at SGS using XRF, and their detection limits.

Pressed Powder Pills with Rh X-ray tube											
Element	Y	Ti	Nb	Zr							
DL (ppm)	2	4	2	3							
Element	As	Ba	Cr	Cu	Mo	Pb	Rb	Sb	Sn	Sr	Zn
DL (ppm)	3	10	5	2	3	5	2	3	3	2	2

A subset of 81 samples, chosen as least-altered on a visual basis, were selected for whole rock and selected trace-element determinations, and completed in several batches. XRF analysis was completed at the University of Tasmania (UTAS) facility under the supervision of analyst Philip Robinson, using a Philips PW1480 X-ray Fluorescence Spectrometer on fused and pressed powder disks. The fused glass and pressed powder disks were prepared at UTAS using the pulps prepared by Genalysis Laboratories. Table 5.3 shows the elements assayed, the tubes used, and the detection limits. Internal UTAS standards were used. Some repeat analyses of trace elements were carried out on samples assayed by Genalysis as an additional check.

Solution ICP-MS analysis on 41 samples was also carried out at UTAS using an Agilent 4500 ICP-MS machine. The sample solutions were prepared from the pulps prepared by Genalysis Laboratories. Several digestion methods were employed for the different rock types: for basalts and easily dissolved samples, an open vessel HF/HNO_3 digestion was used (with an additional aqua regia step when sulfides were present), and for samples with refractory minerals, a HF/H_2SO_4 digestion was used with the Pico-Trace high-pressure

digestion equipment. Table 5.4 shows the elements assayed, and the detection limits.

Table 5.3 Elements measured at UTAS using XRF, and their detection limits.

Fusion Discs with ScMo tube (ORE2 program)												
Element	SiO_2	TiO_2	Al_2O_3	Fe_2O_3	MnO	MgO	CaO	Na_2O	K_2O	P_2O_5		
DL (%)	0.002	0.006	0.008	0.0041	0.0035	0.011	0.0009	0.024	0.0004	0.0026		
Pressed Powder Pills with Au X-ray tube												
Element	Sb	Sn	Cd	Ag	Nb	Zr	Sr	Cr	Ba	La	Ce	Nd
DL (ppm)	2	2	1	2.5	1	1	1	1	4	2	4	2
Pressed Powder Pills with ScMo X-ray tube												
Element	Y	Rb	Pb	As	Bi	Zn	Cu	Tl	Se			
DL (ppm)	1	1	1.5	3	2	1	1	2	1			

Table 5.4 Elements measured at UTAS using ICP-MS analysis and their detection limits.

Element	Li	Be	Sc	Ti	V	Cr	Mn	Co	Ni	Cu	Zn	Ga
DL (ppm)	0.04	0.02	0.04	0.32	0.01	0.32	0.12	0.02	0.04	0.06	0.15	0.01
Element	As	Rb	Sr	Y	Zr	Nb	Mo	Ag	Cd	In	Sn	Sb
DL (ppm)	5	0.04	0.028	0.011	0.02	0.006	0.04	0.05	0.1	0	0.018	0.1
Element	Te	Cs	Ba	La	Ce	Pr	Nd	Sm	Eu	Gd	Tb	Dy
DL (ppm)	0.1	0.5	0.08	0.008	0.02	0.004	0.016	0.012	0.005	0.013	0.003	0.01
Element	Ho	Er	Tm	Tb	Lu	Hf	Ta	W	Re	Tl	Pb	Bi
DL (ppm)	0.003	0.007	0.003	0.008	0.003	0.009	0.003	0.08	0	0.05	0.03	0.05
Element	Th	U										
DL (ppm)	0.003	0.002										

Before being used for statistical and graphical analysis, the major element analyses were recalculated to 100% anhydrous to remove variations caused by differing loss on ignition values. All sample plots were generated using IGPET software (Carr, 2007). All sample locations, geochemical analyses, and associated data are located in Appendix II. In addition reports by UTAS analyst Phillip Robinson comparing the UTAS ICP-MS, XRF and SGS XFR results, with, plus original SGS laboratory reports are also located in Appendix II.

5.3 Geochemistry and Results

5.3.1 Rock classification: immobile element characterisation

As discussed earlier, immobile element characterisation was used to classify the coherent facies. In this study, in all but the most altered rocks the HFSE/REE ratios are consistent with immobile behaviour. In Chapter 4, bivariate plots for Ti–Zr (Figs 4.7a, 4.9a, 4.10a, 4.13a, 4.16a, 4.17a and 4.20a) show that trends for single coherent lithofacies, project through, or very close to, the origin. Furthermore, bivariate plots for Hf–Zr, Nd–Zr, Nb–Zr and La–Nb show trends that project through, or very close to, the origin in samples from across the entire volcano-sedimentary succession (Fig. 5.2). Correlation coefficients (r) and regression lines were calculated for these pairs of elements and all show $r>0.78$. This linear correlation of HFSE reflects the preservation of primary element ratios due to their immobility, and the regression to the origin in part reflects mass gain or mass loss (Finlow-Bates and Stumpfl, 1981). A total of five out of the 252 samples assayed for the HFSE suite

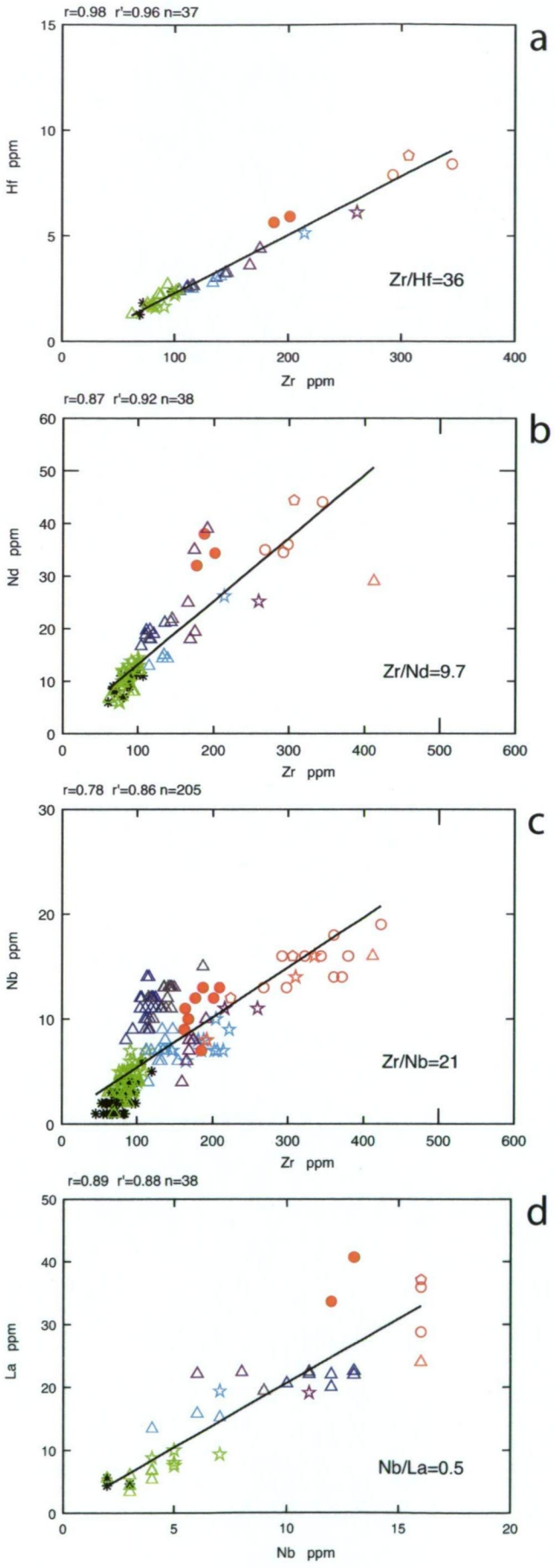

Figure 5.2 Bivariate plots of immobile elements (some scatter) with regression lines shown. (a, b and c) show Hf, Nd and Nb plotted against Zr. (d) shows La plotted against Nb. All show correlation indicating the immobility of the elements, with r (the correlation coefficient) ranging from 0.78 to 0.98. r' is the Spearman rank correlation.

were considered to show extreme mobility of one or more of the HFSE and were therefore excluded from the discussed data set.

The classic immobile element discrimination diagram, Zr/TiO_2 vs Nb/Y (Winchester and Floyd, 1977) was re-worked by Pearce (1996), using a significantly greater sample population. All samples are plotted on these diagrams (Figs 5.3a and 5.3b) and are clearly sub-alkaline (Nb/Y <0.7 = sub-alkaline).

For this study, the coherent facies relied on the Ti/Zr-based ratios bounding criteria of Hallberg (1984), which define compositional fields for the major igneous rock types (basalt, andesite, dacite and rhyolite). Magmatic affinities were identified using the criteria developed by Barrett and MacLean (1994) for sub-alkaline rocks using Y/Zr (Fig. 5.3d). Results show that the magma affinities range from tholeiitic through transitional to calc-alkaline. Most of the volcanic units plot in individual discrete clusters. The exception is the MPD unit from the MP stratigraphic unit, which forms two distinct trends, one tholeiitic and one transitional to calk-alkaline, clearly indicating that a number of different lithostratigraphic units constitute this stratigraphic entity. The Zr/Nb plot (Fig. 5.3e) shows a spread in values from <10 to >30, but that individual units form clusters. Some of these clusters show good linear regression, but generally with intercepts other than zero.

5.3.2 Alteration Effects

Whereas the HFSE are shown to be essentially immobile, this is not the case for the major oxides, SiO_2, FeO, MgO, MnO, CaO, Na_2O and K_2O, which are chemically mobile within hydrothermal alteration and greenschist facies metamorphism zones. This study, located in the immediate vicinity of a sulfide body, clearly accords with this. Although the subset of samples chosen for whole-rock analysis were selected on a least-altered basis, data analysis highlighted four samples that showed such extreme variation away from trends that they are shown separately on the plots. A series of bivariate plots of the major oxides (Fig. 5.4) shows the nature of the geochemical relationships. FeO–TiO_2 (Fig. 5.4a) and FeO, MgO and MnO versus SiO_2 (Figs 5.4b - 5.4d) show relatively good correlations, which are interpreted to closely approximate magmatic trends, except for the four strongly altered samples (shown as green and black dots), which instead show very anomalous values. The CaO, Na_2O and K_2O versus SiO_2 (Figs 5.4e - 5.4g) plots show a scatter of data points interpreted to result from their mobility during hydrothermal alteration, as does a TAS (Na_2O + K_2O versus SiO_2) plot (Fig. 5.4h).

As alteration effects are not a focus in this study, other than to highlight the obvious variations from primary trends in the samples in order to identify the least altered samples, no further comment will be made on the alteration chemistry.

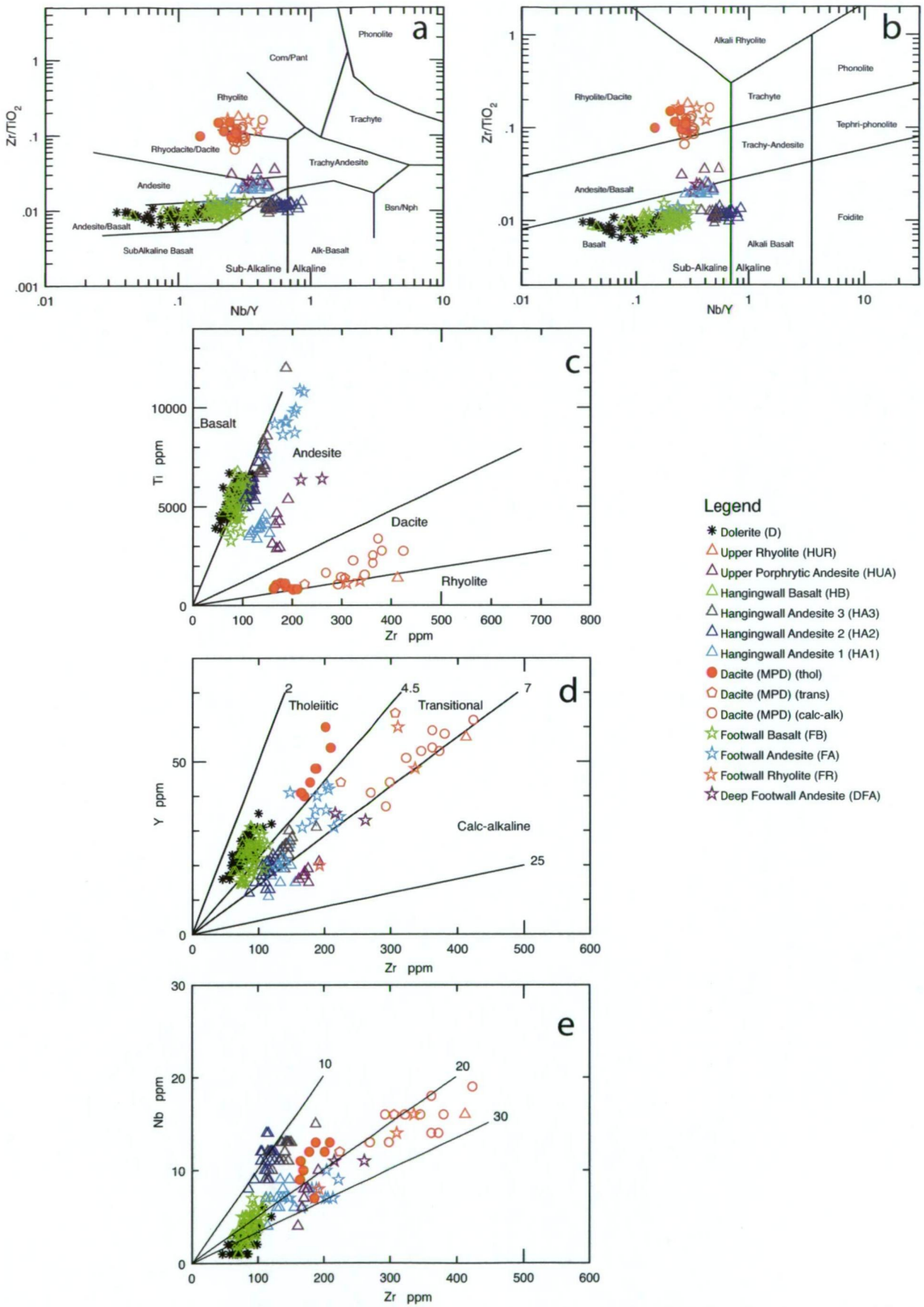

Figure 5.3 Rock classification for the Jaguar sequence. Nb/Y vs Zr/TiO_2 plot showing the volcanic rocks. The majority fall into the sub-alkaline field of the plot, (a) field boundaries from Winchester and Floyd (1977) and (b) field boundaries revised by Pearce (1996). (c) Zr vs Ti plot showing tight ranges in the Zr/Ti values for individual units, boundaries from Hallberg (1984). (d) Zr vs Y plot. The mafic rocks are generally tholeiitic, the intermediate rocks are predominantly transitional but range up to calc-alkaline, and the felsic rocks show two clear trends; one tholeiitic and a transitional to calc-alkaline trend, boundaries from Barrett and McLean (1994). (e) Zr vs Nb plot showing clustering of units, Zr/Nb ratios for comparison.

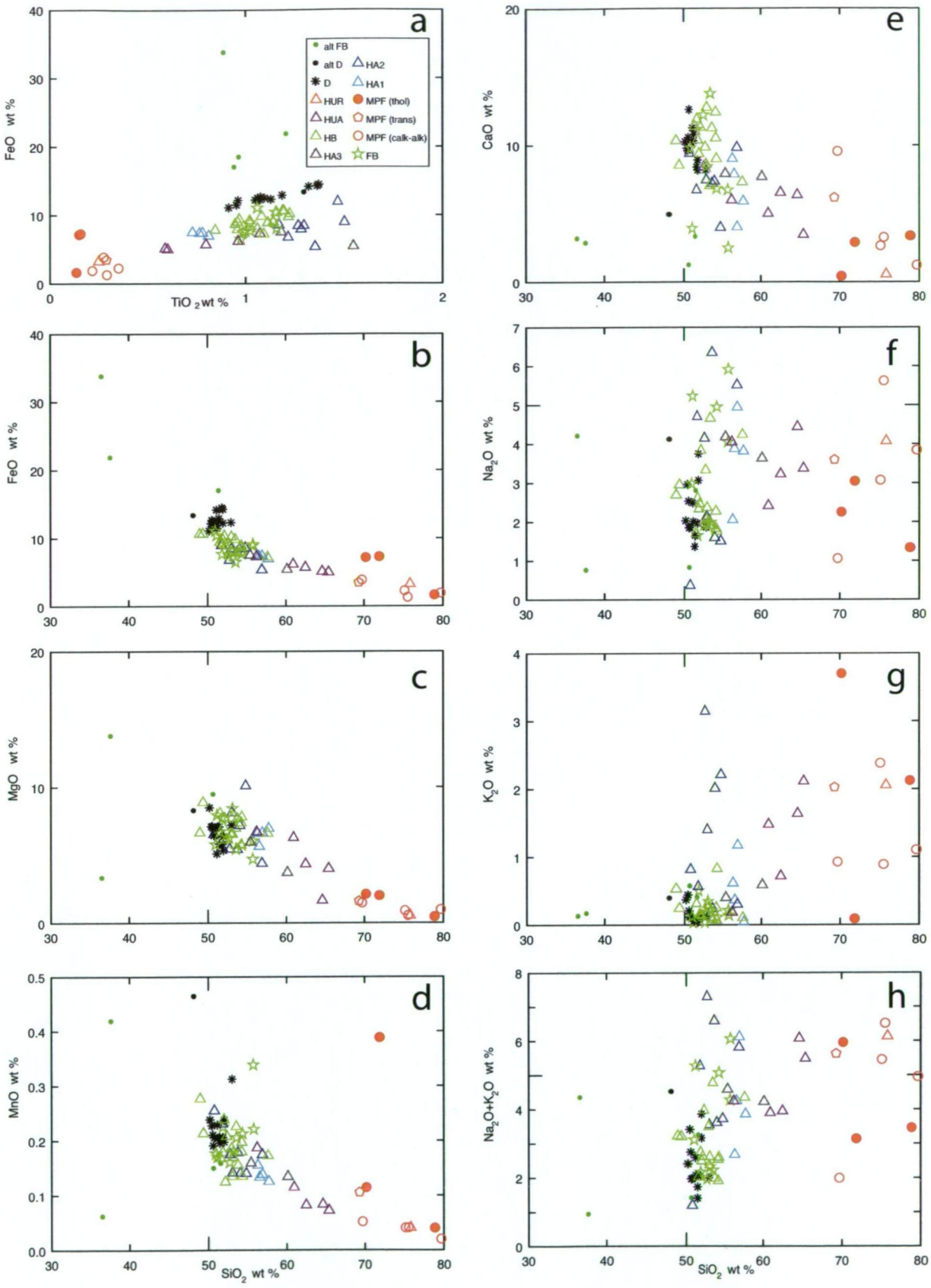

Figure 5.4 Bivariate plots for major oxides. (a) shows TiO_2 vs FeO which clearly identifies the four strongly chlorite-altered samples. (b,c and d) show SiO_2 vs FeO, MgO and MnO, all of which demonstrate the anomalous behaviour of these elements. (e,f and g) show anomalous behaviour of the alkali elements Ca, Na and K respectively, and (h) is the TAS plot showing the behaviour of SiO_2 vs $Na_2O + K_2O$.

5.3.3 Geochemistry of the mafic rocks

The mafic volcanic rocks in the study area include the basalts in the footwall (FB) and hangingwall (HB) and the dolerite intrusions (D) throughout the Jaguar succession. The bivariate plots of Zr vs Ti and Zr vs Y are shown for these units in Figures 4.9, and 4.18 respectively, and these units are plotted with all samples in Figures 5.3c and 5.3d. They show that the samples are tholeiitic basalts.

The HFSE contents of the FB (n=28, av. TiO_2=0.86 wt%, av. Nb=4.7 ppm, av. Zr=89.7 ppm, av. Y=21.4 ppm), the HB (n=39, av. TiO_2=0.89 wt%, av. Nb=3.1 ppm, av. Zr=82.6 ppm, av. Y=24.6 ppm) and the D (n=43, av. TiO_2=0.87 wt%, av. Nb=2.4 ppm, av. Zr=75.8 ppm, av. Y=23.7 ppm) are similar but the Zr/Nb ratios (Fig. 5.3e) show some variation (HB=26.8 and FB=19). The Mg number for all the mafic units is low (23–45 for FB, 33–41 for HB, 21–37 for D) indicating that they are not unmodified primary magmas.

Discrimination diagrams

The mafic rocks are plotted on a series of discrimination diagrams (Fig. 5.5) to compare their chemical signatures with those from known tectonic settings, following the protocol developed by Pearce (1996).

Since some of these diagrams (for instance, those of Pearce and Cann (1973) were developed prior to the recognition of environments such as back-arc basins, a plot using data from modern back-arc basins (Manus, Lau, east Scotia and Mariana Trough: http://www.petdb.org: Lehnert et al., 2000) is included alongside each Jaguar plot for comparison purposes (samples where SiO_2 was >58% were not included). Back-arc basin basalts (BABB) have lower TiO_2 and FeO contents relative to basalts from other ridges. In addition to a subduction component and wedge depletion, BABB reflect a prevalent enriched component akin to enriched ocean ridge basalts worldwide, despite the absence of mantle plumes (Langmuir, et al., 2006).

The triangular Ti–Zr–Y diagram (Fig. 5.5a) is used (Pearce and Cann, 1973) to distinguish WPB from other basalt types. This shows that the D and HB plot mainly within field B (MORB and calc-alkaline VAB) and the FB plots mainly within field C (VAB), identifying the mafic rocks as non-WPB. When considering transitional tectonic settings (Fig. 5.1), the plotted area could represent: attenuated continental lithosphere; plume-ridge interactions; collision zone; or a marginal basin. A different breakdown of the data is provided by a Nb–Zr–Y diagram (Meschede, 1986). This plot (Fig. 5.5b) is not as effective as Ti–Zr at WPB discrimination but the inclusion of Nb enables separation between NMORB and EMORB. However, this diagram is problematic in a complex setting involving subduction because Nb is depleted in subduction-related magmas. On Figure 5.5b, the FB cluster is separate from the HB and D, and plots mainly in field C (tholeiitic WPB and VAB), whereas the D

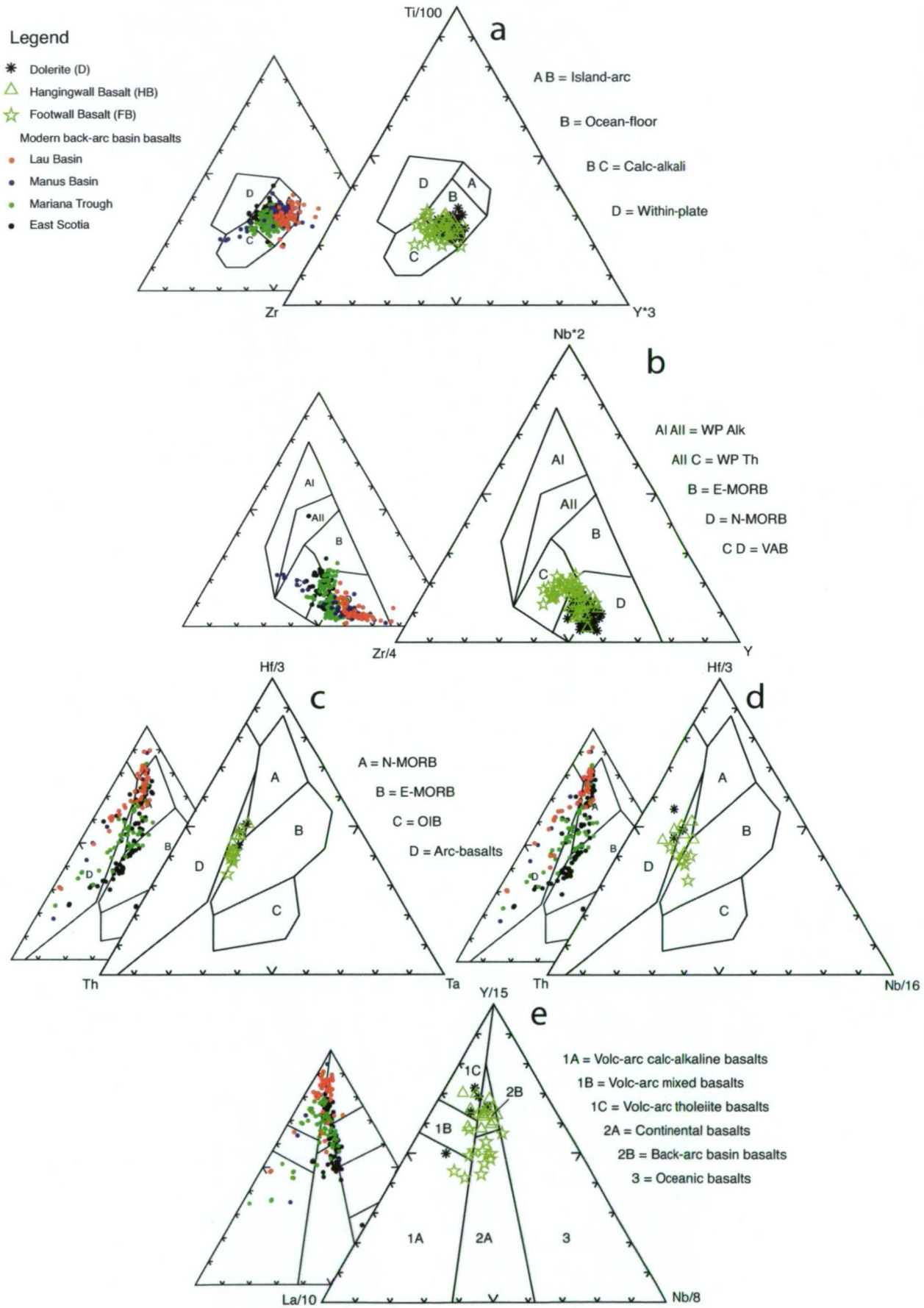

Figure 5.5 Discrimination diagrams for mafic rocks. (a) plot of Ti–Zr–Y developed by Pearce and Cann (1973) showing a single cluster external to the WPB field, the small plot shows modern back-arc basin basalts for comparison. (b) plot of Nb–Zr–Y developed by Meschede (1986) showing the separation of the FB from the HB+D, the small plot shows modern back-arc basin basalts for comparison. (c) plot of Hf–Th–Ta developed by Wood (1980) showing a tight cluster, the smaller plot shows modern back-arc basin basalts for comparison. (d) plot of Hf–Th–Nb developed by Wood (1980) showing a greater spread caused by a greater depletion in Nb in the HB+D, the small plot shows modern back-arc basin basalts for comparison. (e) La-Y-Nb plot of Cabanis and Lecolle (1989) showing the separation of the FB from the HB+D, the small plot shows modern back-arc basin basalts for comparison.

and HB plot mainly in field D (VAB and NMORB).

The Th–Hf–Ta diagram (Fig. 5.5c) is in common use as an indicator of subduction and used to distinguish VAB and MORB (Wood, 1980). Here, the mafic rocks plot across the boundary between EMORB and VAB. A variation on this diagram uses Nb rather than Ta (Fig. 5.5d). This shows a larger spread based on the Nb axis, separating the FB from the HB, with the FB plotting mostly within the EMORB field but extending to the VAB field, whereas the HB and D plot mainly within the VAB field. When transitional or complex settings are considered, the plot area is focused on the attenuated continental lithosphere field (MORB/WPB), marginal to the collision zone field (VAB/WPB), peripheral to plume-ridge interactions field, and external to the marginal basin field.

Figure 5.5e is the La–Y–Nb plot of Cabanis and Lecolle (1989) which seeks to discriminate between VAB, continental basalts, and oceanic basalts on the basis of the La/Nb ratio. This can be problematic if the La has been mobilised due to hydrothermal alteration (Rollinson, 1993), which may result in distortion depending on the Ta content. On this diagram, the mafic rocks plot across the VAB and continental basalt fields boundary, with the FB lying across the VAB/continental basalt field (WPB) boundary, and the HB and D predominantly within the back-arc basin basalt (BABB) field. Of particular interest here, is the plot of the modern BABB where they plot over a much wider area than the field defined by Cabanis and Lecolle (1989).

If the plots of the Jaguar data are compared with the plots of the modern BABB (Manus, Lau, East Scotia, Mariana Trough) it is obvious that there is a coincidence among the data, particularly for the Mariana Trough, which is the most Ta and Nb rich of the group.

In summary, the mafic rocks appear to have been erupted in a complex transitional environment. Solely WPB and MORB environments are excluded. For the FB, indications for VAB, MORB/WPB transitions, VAB/WPB transitions and MORB/VAB/WPB transitions exist, whereas the HB and D plots indicate MORB/WPB transitions, VAB/WPB transitions and possible MORB/VAB and MORB/VAB/WPB transitions. The data suggest that the HB was more transitional than the FB. The common thread across all plots is VAB and BABB.

Normalised multi-element plots

Figure 5.6 shows REE chondrite-normalised diagrams, along with plots showing values compared against primitive mantle and NMORB using values and element order from Sun and McDonough (1989) and compared against BABB using samples from the Mariana Trough (http://www.petdb.org).

These plots highlight the difference between the FB and the HB and reinforce the earlier

discussed similarities between the HB and the D. Compared to chondrite (Fig. 5.6a), the FB shows a marked LREE enrichment (La=20 to 45 times chondrite) with a pronounced positive Eu anomaly and a negative slope (i.e. decreasing abundance with increasing atomic no). The range of [La/Yb]cn is 3.6–4.2. The HB and D (Fig. 5.6b) together show a much flatter slope (La=14 to 20 times chondrite). The [La/Yb]cn range of the HB is 1.6–2.6, with a flat to negative Eu anomaly, and the [La/Yb]cn range of the D is 1.8–2. A negative slope is considered to reflect magma generation by hydrous fluid flux melting a mantle source overlying a downgoing lithospheric slab (Hawkesworth et al., 1993).

Where samples are normalised to primitive mantle, all elements are enriched, with positive Rb and Ba in all three units. As these elements are very sensitive to alteration, this is probably not meaningful. The trend is relatively flat for all three units, with a slight negative to neutral slope observed for the FB. Nb, Ta, Sr, Hf and Ti show negative anomalies in all three units (Figs 5.6c and 5.6d).

Compared to NMORB all three mafic units are moderately to strongly enriched in LILE, and have a moderate negative slope (Figs 5.6e and 5.6f). The FB is weakly enriched in LREE (<5 times) and is non- to weakly depleted in the HREE, whereas the HB is enriched up to 3 times in the LREE, and weakly depleted in the HREE. All units show negative anomalies in Nb, Sr, Hf and Ti. A weak positive anomaly is apparent in Eu in the FB but is not present in the HB.

Where the samples are normalised against BABB (Mariana Trough), the plots are typically flat to very gently sloping for all samples (Figs 5.6g and 5.6h). Cs shows some enrichment, Rb and Ba are erratic and there are negative anomalies with respect to Sr and Ti. Otherwise, the FB shows a slight enrichment in the LREE, with a positive Eu anomaly compared to BABB, and a flat trend. The plot for the HB and D shows erratic values in the alteration-susceptible elements Cs, Rb and Ba, negative depletion with respect to Sr, apositive value for Ta, with otherwise slightly depleted LILE, with an overall slight positive slope.

The strong depletion of Nb relative to Th and La is apparent in the primative mantle and NMORB plots. If the elements most susceptible to alteration are excluded from consideration, the mafic rocks show the most similarity to the Mariana Trough BABB as the slopes are almost flat and enrichment is very low. Nb and Ta have low solubility in hydrous fluids and the negative anomaly in these elements most likely reflects a lower solubility of these elements in migrating fluids overlying a downgoing lithospheric slab (Pearce and Peate, 1995). The major deviation from Mariana Trough BABB is small positive Nb and Ta anomalies. Ti is also conservative during subduction, so a negative Ti anomaly in mafic rocks is also considered indicative of a subduction-related arc signature (Pearce, 1996).

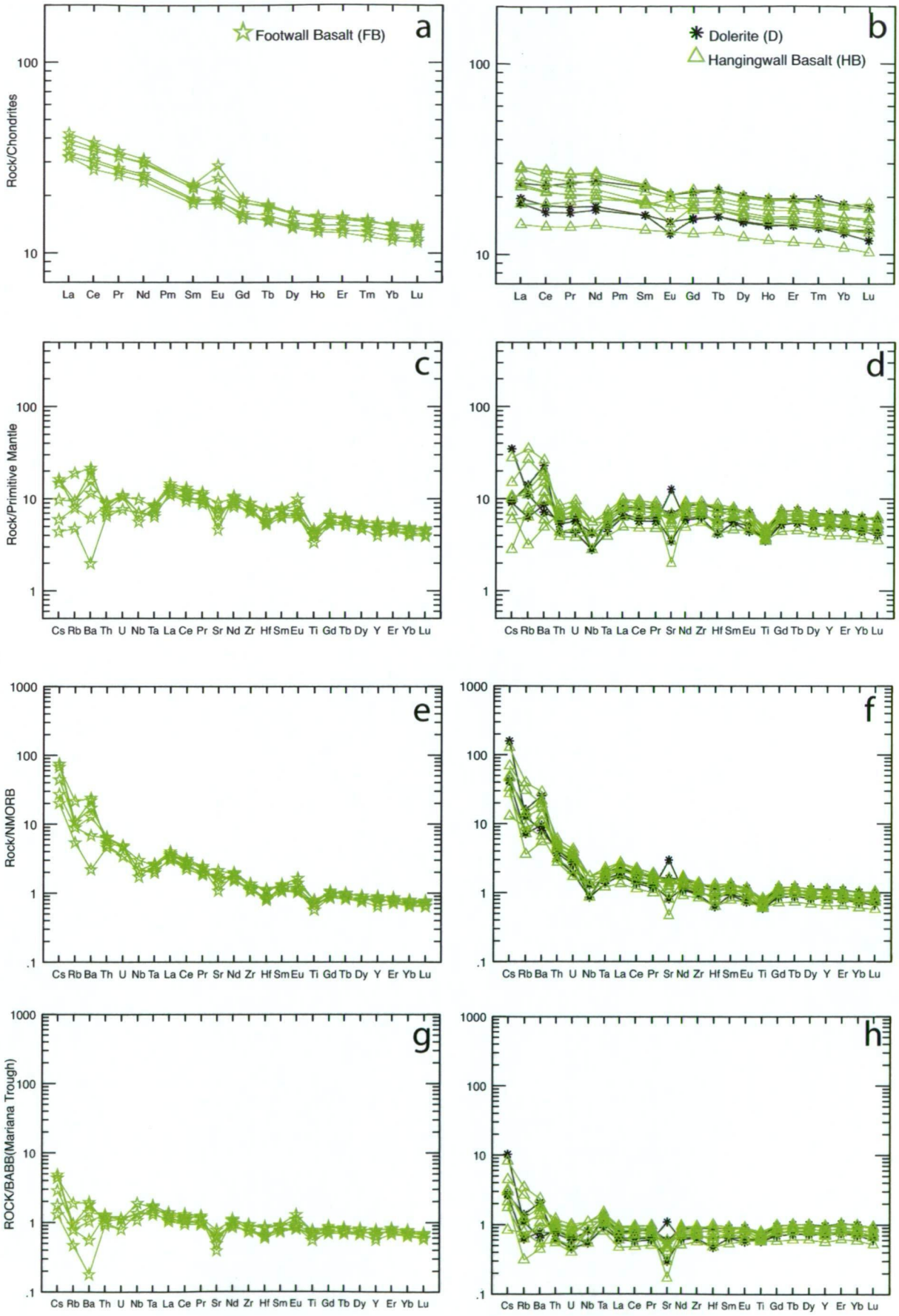

Figure 5.6 Normalised multi-element variation diagrams for the mafic rocks. The left column shows FB samples, whereas the right column shows samples from the HB and D. (a) and (b) are normalised for chondrite samples, (c) and (d) for primitive mantle, (e) and (f) for NMORB and (g) and (h) for BABB (Mariana Trough). (a)-(f) have normalising values and order from Sun and McDonough (1989), whereas (g) and (h) are normalised against an average of 51 samples from the Mariana Trough (http://www.petdb.org).

Summary

The chemical composition of the mafic rocks is summarised in Table 5.5. The key features are:

- similar to Mariana Trough BABB
- enriched about 4–6 times over primitive mantle
- Nb depletion, expressed as negative Nb anomalies (indicative of subduction)
- weak negative Ti anomaly which can be indicative of subduction but, more likely reflects strongly fractionated basalt
- weak negative Hf anomaly
- positive Eu in the FB

Table 5.5 Summary of the geochemistry of the mafic rocks

	FB	HB	D
Lithology	basalt	basalt	basalt
Affinity	tholeiitic	tholeiitic	tholeiitic
HFSE	n = 28	n = 39	n = 43
TiO_2 (wt%)	0.86	0.89	0.87
Nb (ppm)	4.7	3.1	2.4
Zr (ppm)	89.7	82.6	75.8
Y (ppm)	21.4	24.6	23.7
Zr/Nb	19	26.8	31.4
Zr/Y	3.5 – 5.7	2.6 – 4	2.6 – 4
Ti/Zr	39 – 74	52 – 80	55 – 98
	n = 10	n = 16	n = 13
Mg#	23 – 45	33 – 41	22 – 37
REE	n = 6	n = 8	n = 3
[La/Sm]cn	1.6 – 1.9	1.0 – 1.3	1.0 – 1.2
[La/Yb]cn	2.6 – 3.0	1.3 – 1.9	1.3 – 1.5
Eu/Eu*	1.09 – 1.37	0.79 – 1.11	0.82 – 0.94
Nb/Th	5.12 – 9.35	3.73 – 9.17	4.04 – 6.6

Chondrite normalising values from Sun and McDonough (1989). All ratios calculated using ppm.

5.3.4 *Geochemistry of the intermediate rocks*

The intermediate volcanic rocks in the study area include two andesite units in the footwall (DFA and FA) and two in the hangingwall (HA and HUA). The units have variable plagioclase phenocryst populations as discussed in Chapter 4. The bivariate plots of Zr–Ti and Zr–Y are shown individually for these units in Figures 4.5, 4.7, 4.14 and 4.16. They are also plotted with all the volcanic rocks (Fig. 5.3c and 5.3d), and are unambiguously andesites. They are mostly sub-alkaline (Fig. 5.3b), with each unit forming an identifiable cluster.

The HFSE contents of the two footwall andesites, the DFA (n=2, av. TiO_2=1.06 wt%, av.

Nb=11 ppm, av. Zr=238 ppm, av. Y=34 ppm) and the FA (n=10, av. TiO_2=1.57 wt%, av. Nb=7.6 ppm, av. Zr=191.4 ppm, av. Y=36.7 ppm) show Ti to be about 50% greater in the FA. The three hangingwall andesites (HA1, HA2 and HA3) show an upward increase in Ti but no other consistent trend. HFSE contents of the HA1 (n=13, av. TiO_2=0.65 wt%, av. Nb=6.9 ppm, av. Zr=133.3 ppm, av. Y=19.1 ppm), the HA2 (n=24, av. TiO_2=0.99 wt%, av. Nb=11.2 ppm, av. Zr=115.2 ppm, av. Y=18.8 ppm), and the HA3 (n=12, av. TiO_2=1.23 wt%, av. Nb=11.9 ppm, av. Zr=139.6 ppm, av. Y=24.4 ppm) result in distinct differences in element ratios. The HUA (n=7, av. TiO_2=0.65 wt%, av. Nb=7.3 ppm, av. Zr=172 ppm, av. Y=17.6 ppm) plots in a separate cluster. This is emphasised on the Zr–Nb plot which provides evidence of distinctly different Zr/Nb values (DFA=21.6, FA=25.2, HA1=19.3, HA2=10.2, HA3=11.7, HUA=23.6) (Fig. 5.3e).

Discrimination diagrams

Some of the basalt discrimination diagrams are considered valid for intermediate rocks with a specified Ca and Mg content (Rollinson, 1993). For this reason some of the intermediate rocks have been plotted on the same discrimination diagrams that were used for the mafic rocks (Fig. 5.7). As before, the protocols developed by Pearce (1996) are followed in the assessment. As discussed in the section on mafic rocks, some of these diagrams were developed prior to the recognition of environments such as back-arc basins, so this must be considered when interpreting the results.

The triangular Ti–Zr–Y diagram (Fig. 5.7a) is used (Pearce and Cann, 1973) to distinguish WPB from other types. The graph is suitable for rocks with the composition range 20 wt% > CaO + MgO > 12 wt% (Rollinson, 1993). This value is not known for all samples because of the limited whole-rock chemistry. However, all HA samples with known oxide chemistry lie within the specified range. Thus the HA samples are plotted whereas; HUA is not plotted, because the known HUA values fall outside this range. The CaO + MgO values for the FA and DFA are not known but, because these samples have a similar differentiation index (Zr/TiO_2) to the HA, these samples are included on the plot. The samples form two clusters– one comprising HA1 and DFA and the other comprising FA, HA2 and HA3. Both clusters plot mainly within field C (calc-alkaline) and could represent a volcanic arc environment (VAB). If more complex settings are considered, the cluster comprising HA1 and DFA shows characteristics of VAB/WPB collision zones, whereas the other cluster, comprising FA, HA2 and HA3, could be VAB/WPB collision zone or WPB attenuated continental lithosphere.

The chemical composition has also been plotted on a Nb–Zr–Y diagram (Fig. 5.7b) (Meschede, 1986), which is also suitable for rocks with the composition range 20 wt% > CaO + MgO > 12 wt% (Rollinson, 1993). This plot is not as effective as Ti–Zr–Y at WPB discrimination, but the inclusion of Nb enables separation between NMORB and

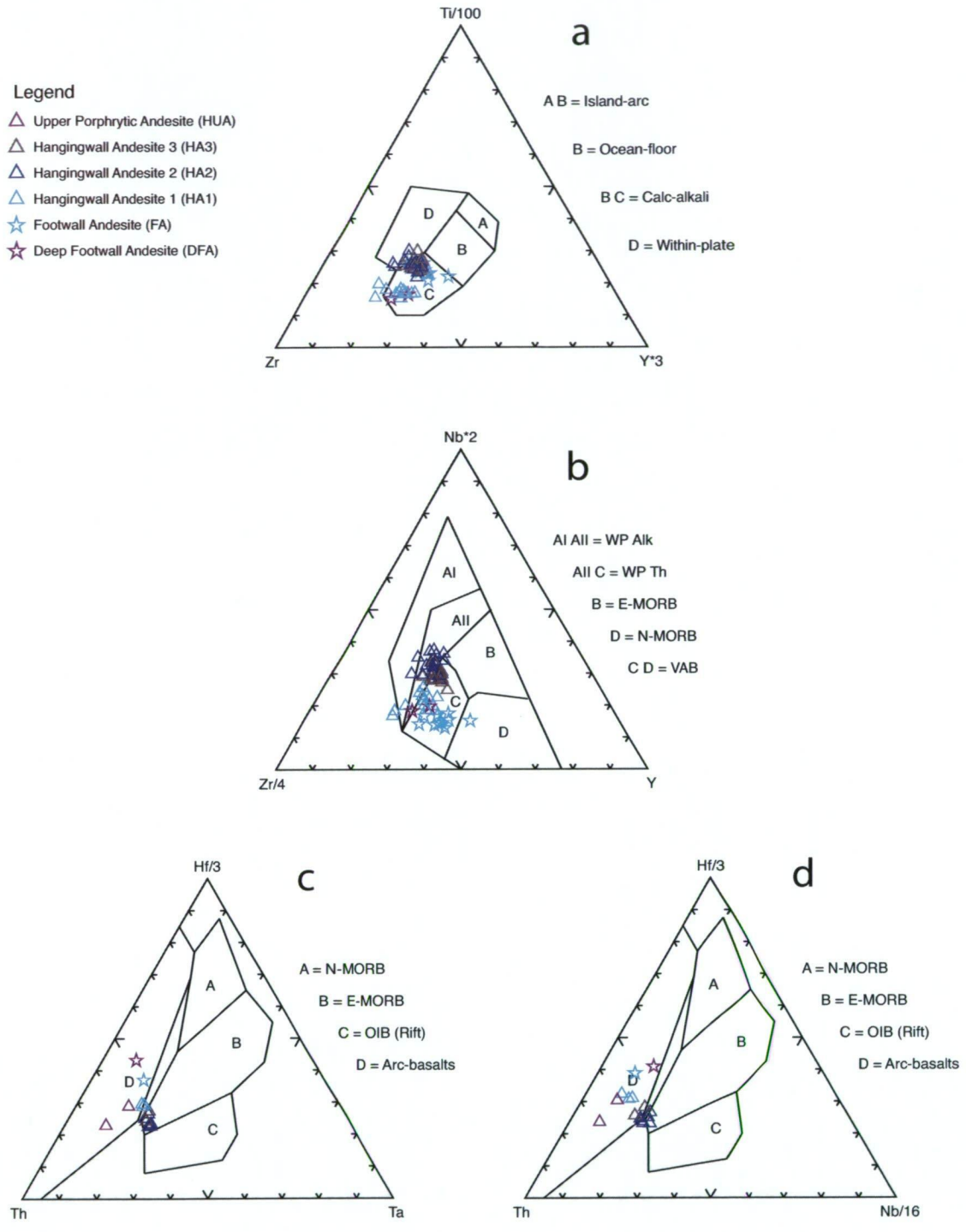

Figure 5.7 Discrimination diagrams for intermediate rocks. (a) plot of Ti-Zr-Y developed by Pearce and Cann (1973) showing separation into two clusters. (b) plot of Nb-Zr-Y developed by Meschede (1986) showing the HA2 and HA3 in a seperate cluster. (c) plot of Hf-Th-Ta developed by Wood (1980) showing the samples plot in the arc-volcanics field.volcanic zone.(d) plot of Hf-Th-Nb developed by Wood (1980) showing separation of the HA2 and HA3.

EMORB. This is not really an issue with andesite as it does not occur in oceanic crust. However, as mentioned earlier, application of this diagram is problematic in a complex setting involving subduction because Nb is depleted in any magma (Pearce and Norry, 1979). On this diagram HA1, FA and DFA plot mainly in field C (tholeiitic WPB and VAB) whereas HA2 and HA3 straddle the boundary between field AII (WPB) and field C (tholeiitic WPB and VAB).

The Th–Hf–Ta diagram (Fig. 5.7c) is used as an indicator of subduction, and can be useful to distinguish VAB and MORB, and is suitable for all rock types (Wood, 1980). The HUA, DFA and FA andesites plot within field D (VAB) and HA1, HA2 and HA3 plot across the boundary between field B (EMORB and tholeiitic WPB) and field D (VAB). The Th–Hf–Nb diagram is an equivalent diagram (Fig. 5.7d) (Wood, 1980) that shows a clear distinction between HA1, which plots within field D, and HA2 and HA3, which plot on the boundary between fields B and D. If transitional environments are considered, the eruptive environment could be in a VAB/WPB collision zone or WPB attenuated continental lithosphere (Fig. 5.1).

In summary, the andesites appear to have been erupted in a complex transitional environment. Solely WPB and MORB environments are excluded, and transitional environments that include VAB, VAB/WPB transitions, MORB/WPB transitions and MORB/VAB/WPB transitions are likely. As for the mafic rocks, the common thread is VAB.

Normalised multi-element plots

A series of multi-element variation diagrams (Fig. 5.8), show REE chondrite-normalised diagrams along with plots showing values compared against primitive mantle and NMORB using values and element order from Sun and McDonough (1989) and compared against BABB using samples from the Mariana Trough (http://www.petdb.org).

The chondrite-normalised REE plots show DFA and FA to have very similar trends; they show a marked LREE enrichment (La up to 85 times chondrite), and a negative Eu anomaly (Fig. 5.8a) and a negative slope that flattens in the HREE (at about 20 times chondrite enrichment). The [La/Yb]cn for the DFA and FA is 5.3 and 5.5.

The HA and HUA show steep negative slopes, starting at a similar enrichment level, with the trend continuing into the HREE through a weak positive Eu anomaly to moderate HREE enrichment of 9 to 14 times chondrite. Generally the slopes of the HA1, (HA2 and HA3) and HUA plots become progressively steeper, with each unit showing increasing enrichment in the LREE (Fig. 5.8b and Table 5.6). This change in the REE pattern is most likely to be a reflection of fractionation. HA2 and HA3 are grouped together for this

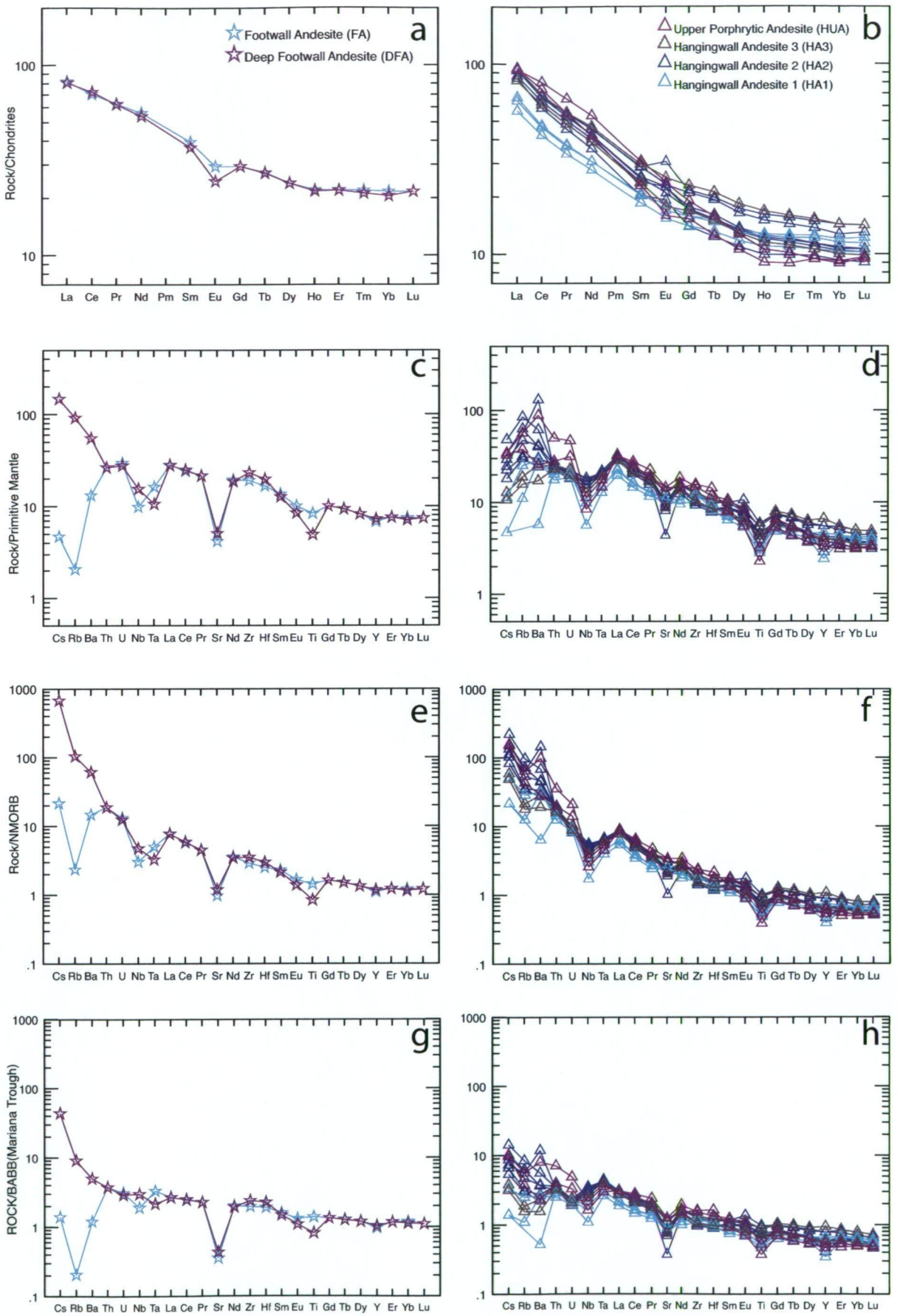

Figure 5.8 Normalised multi-element variation diagrams for the intermediate rocks. The left column has samples from the DFA and FA, whereas the right column has samples from the HA1, HA2, HA3 and HUA. (a) and (b) are normalised for chondrite samples, (c) and (d) for primitive mantle, (e) and (f) for NMORB and (g) and (h) for BABB (Mariana Trough). (a)-(f) have normalising values and order from Sun and McDonough (1989), whereas (g) and (h) are normalised against an average of 51 samples from the Mariana Trough (http://www.petdb.org).

interpretation as their HFSE ratios (Fig. 5.3) indicate they are closely related. The [La/Sm] cn ratio increases, HA1 is 3.1–3.3, HA2 is 3.2–4.2, HA3 is 3.2–3.5 and HUA is 3.0–4.2. The [La/Yb]cn ratio shows the same trend, HA1 is 5.4–5.8, HA2 is 7.5–9.1, HA3 is 6.6–8.2 and HUA is 10.16–10.57.

The primitive mantle-normalised plots show enrichment in all elements, and show a relatively flat trend with a slight negative slope. Nb, Sr and Ti all show negative anomalies in all units (Figs 5.8c and 5.8d). Erratic anomalous values with respect to Cs, Rb and Ba in all spidergrams are likely to be the result of alteration, as is the marked negative anomaly in Sr.

Compared to NMORB, all andesites are enriched in LILE, have a steep to moderate negative slope, and show negative anomalies in Nb, Ta, and Ti. The footwall andesites are only slightly enriched in the HREE whereas all the hangingwall andesites show depletion in the HREE (Figs 5.8e and 5.8f) relative to NMORB.

BABB normalised plots show a weak enrichment of up to 3 times LILE in the footwall, with flat to weak negative slopes and negative anomalies in Sr and Ti (Figs 5.8g and 5.8h). The hangingwall andesites have a weak negative slope and weak LILE and REE enrichment (except for a negative Sr anomaly), with slight depletion in the HREE.

If the elements most susceptible to alteration (Cs, Rb, Ba and Sr) are excluded from consideration, the trends of the andesites show the most similarity to BABB as the slopes of the patterns are almost flat. The major deviations from BABB are the small, negative Ti anomaly and the gentle downward slope. As suggested earlier, Nb and Ta have low solubility in hydrous fluids and the negative anomaly in these elements (with respect to NMORB and primitive mantle) most likely reflects a lower solubility of these elements in migrating fluids overlying a downgoing lithospheric slab (Pearce and Peate, 1995). A negative Ti anomaly can be considered indicative of a subduction-related arc signature (Pearce, 1996), but more likely reflects fractionation from a more Ti-rich basalt.

Summary

The chemical composition of the intermediate rocks is summarised in Table 5.6 and the key features are:

- similar to BABB Mariana Trough
- Zr/Nb ratio indicative of BABB (10–20) and most island-arc lavas
- enriched about 4–6 times over primitive mantle
- Nb depletion, expressed as negative Nb anomalies (indicative of subduction)
- weak negative Ti anomaly (can be indicative of subduction - or fractionation)

Table 5.6 Summary of the geochemistry of the intermediate rocks

	DFA	FA	HA1	HA2	HA3	HUA
Lithology	andesite	basaltic-andesite	andesite	basaltic-andesite	basaltic-andesite	andesite
Affinity	transitional - calc-alkaline	transitional	transitional - calc-alkaline	transitional	transitional	calc-alkaline
HFSE	n = 2	n = 10	n = 13	n = 23	n = 12	n = 7
TiO_2 (wt%)	1.06	1.57	0.65	0.99	1.23	0.65
Nb (ppm)	11	7.6	6.9	11.2	11.9	7.3
Zr (ppm)	238	191.4	133.3	115.2	139.6	172
Y (ppm)	34	36.7	19.1	18.8	24.4	17.6
Zr/Nb	21.6	25.2	19.3	10.2	11.7	23.6
Zr/Y	6.2 – 7.9	3.9 – 6.9	5.6 – 10	5.3 – 9	4.9 – 7.3	9.1 – 28
Ti/Zr	25 – 29	43 – 56	24 – 32	43 – 61	47 – 64	17 – 25
REE	n = 1	n = 1	n = 3	n = 6	n = 2	n = 2
[La/Sm]cn	2.2	2.1	3.1 – 3.3	3.2 – 4.2	3.2 – 3.5	3.0 – 4.2
[La/Yb]cn	3.9	3.8	5.4 – 5.8	7.5 – 9.1	6.6 – 8.2	10.16 – 10.57
Eu/Eu*	0.74	0.85	0.93 – 1.01	0.94 – 1.22	0.88 – 0.96	0.83 – 0.96
Nb/Th	4.9	3.11	2.68 – 3.79	5.2 – 6.33	4.59 – 5.31	1.89 – 2.52

Chondrite normalising values from Sun and McDonough (1989).

5.3.5 *Geochemistry of felsic volcanic rocks*

The felsic volcanic rocks in the study area include a rhyolite unit in the footwall (FR), a rhyolite unit in the hangingwall (HUR) and dacite (MPD) within the mineralised package (MP) stratigraphic unit. The felsic rocks have variable quartz and plagioclase phenocryst populations as discussed in Chapters 3 and 4. The Nb/Y vs Zr/TiO_2 plot (Fig. 5.3b) (after Pearce, 1996) shows the felsic rocks are unambiguously sub-alkaline. The bivariate plots of Zr–Ti and Zr–Y (Figs 5.3c and 5.3d) include all volcanic rocks. The Zr–Y plot shows a clear difference in the magma affinity among the dacite samples, indicating a distinct split between tholeiitic and calc-alkaline trends. These sub-units are shown separately on the plots as MPD (thol), MPD (trans) and MPD (calc-alk). There are no trace and REE analyses available for the FR rhyolite unit and limited trace and REE analyses (XRF only) available for the HUR rhyolite unit.

The HFSE contents of the dacite sub-units in the MPD unit are quite different from each section, with the tholeiitic MPD (n=8, av. TiO_2=0.16 wt%, av. Nb=10.9 ppm, av. Zr=181.8 ppm, av. Y=47 ppm) having twice the amount of Ti and Zr than the calc-alkaline MPD (n=10, av. TiO_2=0.36 wt%, av. Nb=15.5 ppm, av. Zr=342.1 ppm, av. Y=51.2 ppm). The Th/Ta values are also different, with tholeiitic MPD (n=2, Th/Ta=6.5–7.3) having no overlap with the calc-alkaline MPD (n=3, Th/Ta=3.3–3.9). The footwall rhyolite (FR) (n=3, av. TiO_2=0.18 wt%, av. Nb=12.7 ppm, av. Zr=279 ppm, av. Y=42.7 ppm) appears similar to the rhyolite (HUR) at the top of the succession (n=1, av. TiO_2=0.23 wt%, av. Nb=16 ppm, av. Zr=412 ppm, av. Y=57 ppm), but the lack of samples should be noted, and the absence of REE values for the rhyolites precludes any definitive conclusion.

Discrimination diagrams

There are few discrimination diagrams suitable for felsic rocks. However, the Th–Hf–Ta diagram is identified as suitable for all rock types (Wood, 1980) and is in common use as an indicator of subduction. On Figure 5.9a, the dacite samples plot within field D indicating a VAB environment and, if considered a transitional environment, within a VAB/WPB transition. There is a clear separation between the tholeiitic and calc-alkaline dacites.

Two plots using Ta, Th and Yb were developed by Gorton and Schandl (2000) for felsic and intermediate rocks to differentiate tectonic environments. The environments have been defined on the basis of differences in the degree of incompatibility between Th, Ta and Yb. The Ta/Yb vs Th/Yb plot is a revision of the work of Pearce (1983) and a new Th/Ta vs Yb plot has been developed. These plots have been used specifically to discriminate tectonic settings in Archean VHMS environments (Schandl and Gorton, 2002). As rocks suitable for inclusion are those with SiO_2 from 54 to < 63 wt %, and MgO from 3 to 4.5 wt %, the two HUA samples which fall within this range are considered here. On the Ta/Yb vs Th/Yb plot, the calc-alkaline dacite samples lie within the WPVZ whereas the tholeiitic dacite samples lie just within the ACM field (Fig. 5.9b). These relationships are reproduced on the Yb - Th/Ta plot (Fig. 5.9c).

In summary, the possible eruptive environments indicated by the felsic rocks are across the spectrum of VAB, and the transitional settings ACM and WPVZ.

Fertility Determination

The felsic rocks have been plotted on the fertility diagrams developed for Archean environments in the Superior Province. On the Zr/Y vs Y plot (Fig. 5.9d) the samples fall within the FII and the 'fertile' FIIIA field of Lesher et al. (1986). On the Hart et al. (2004) plot (a revision of Lesher et al., 1986) of chondrite-normalised La/Yb vs Yb the rocks fall into the 'fertile' FII field (Fig. 5.9e). A comparison with other parameters is shown in Table 5.7. Normalising factors are from Nakamura (1974).

Normalised multi-element plots

A series of multi-element variation diagrams (Fig. 5.10) show REE chondrite-normalised diagrams along with plots showing values compared against primitive mantle and NMORB using values and element order from Sun and McDonough (1989) and compared against BABB using samples from the Mariana Trough (http://www.petdb.org).

The chondrite-normalised plot of the MPD shows strong LREE enrichment and a negative Eu anomaly (Fig. 5.10a) with a negative slope and flat HREE. The [La/Yb]cn is 4.1–5.9and the [La/Sm]cn is 2.4–3.5. One sample shows a pronounced positive Eu anomaly in an

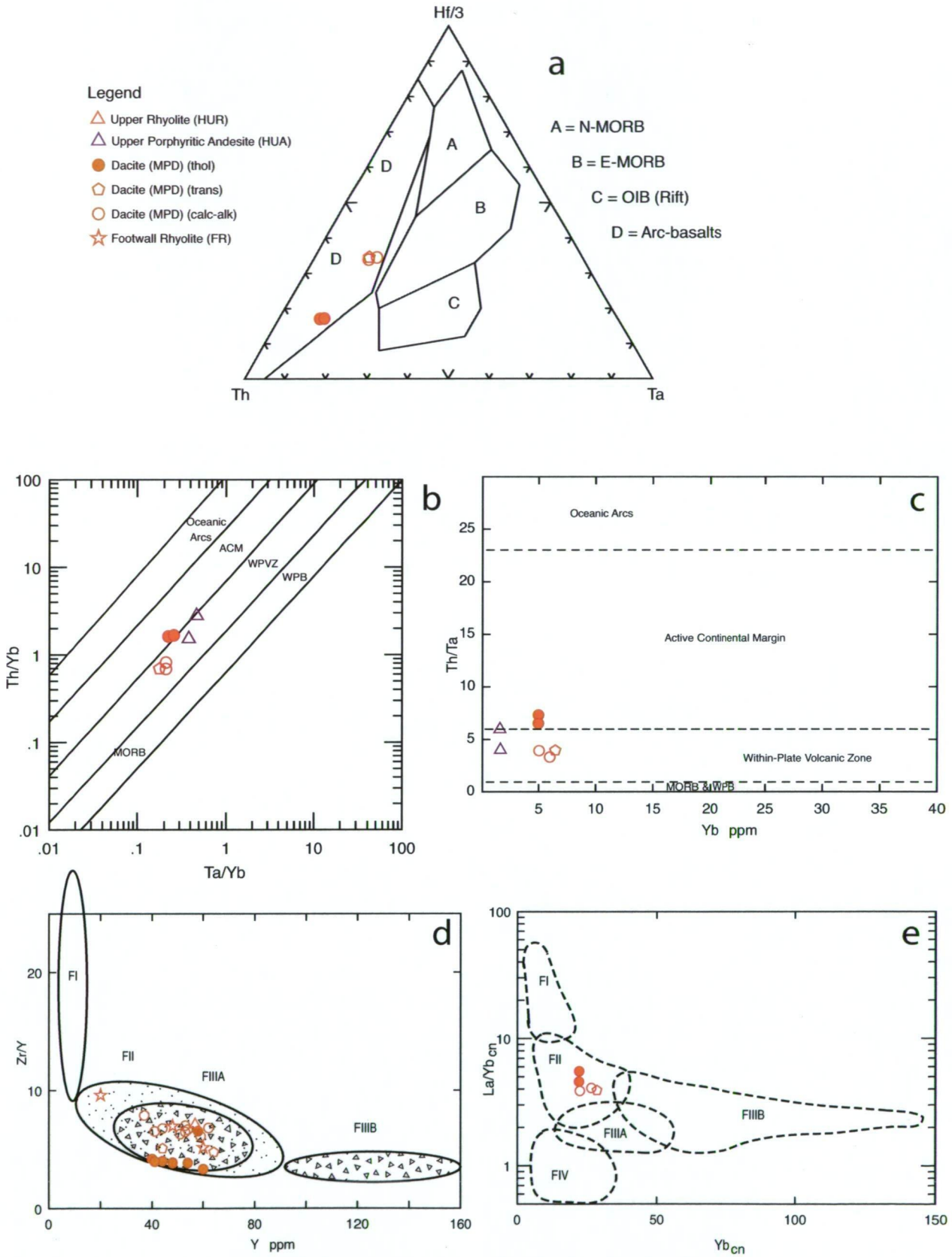

Figure 5.9 Discrimination diagrams for felsic rocks. (a) plot of Hf-Th-Ta developed by Wood (1980) showing the MPD samples plot in the arc-volcanics field. (b) plot of Ta/Yb vs Th/Yb with boundaries developed by Gorton and Schandl (2000), to define the tectonic setting, showing that samples of the tholeiitic MPD lie on the boundary between the active continental margin (ACM) and the within-plate volcanic zone (MPVZ) types, and the transitional to calc-alkaline MPD and HUA lie within the within-plate volcanic zone type. (c) plot of Th/Ta vs Yb (boundaries by Gorton and Schandl (2000)) showing the tholeiitic samples lie just within the active continental margin and the remainder of the samples lie in the within-plate volcanic zone. (d) plot of Y vs Zr/Y with fields from Lesher et al., (1986) shows that the FR, MPD and HUR all plot within the FIIIA field. (e) chondrite-normalised plot of Yb vs La/Yb, showing that the MPD samples lie within the FII field of Hart et al., (2004). Normalising factors from Nakamura (1974).

Table 5.7 Volcanic fertility assignment. Comparison of the Jaguar felsic rocks with FI, FII, FIII and FIV rocks (all data other than from Jaguar, from Lesher et al., 1986; Hart et al., 2004; Mercier-Langevin, 2007b; Gaboury & Pearson, 2008). For clarity Jaguar is shown as a separate column here; this is not meant to imply that Jaguar compositions represent a new chemical class of VHMS.

	FI	FII	**Jaguar (FII -FIIIA)**	FIIIA	FIIIB	FIV
Lithology	dacite-rhyolite	dacite-rhyolite	**rhyolite – dacite (MPD)**	rhyodacite-high Si rhyolite	rhyodacite-high Si rhyolite	rhyolite-high Si rhyolite
SiO_2 (wt%)	64 – 67	64 – 81	**69 – 80**	67 – 78	67 – 84	69 – 81
TiO_2 (wt%)	0.16 – 0.65	0.16 – 0.89	**0.16 – 0.26**	0.21 – 0.99	0.09 – 0.73	0.09 – 0.57
Y (ppm)	6 – 31	11 – 73	**37 – 64**	25 – 96	72 – 238	18 – 36
Zr/Y	8.8 – 31	3.2 – 12.12	**3.4 – 7.8**	3.9 – 7.7	1.7 – 6.2	0.67 – 4.8
Yb (ppm)	0.43 – 3.8	1.3 – 7.9	**4.9 – 6.4**	3.4 – 9.3	5 – 32	1.5 – 8.4
[La/Yb]cn	5.8 – 3.4	1.7 – 8.8	**3.4 – 5.5**	1.5 – 3.5	1.1 – 4.9	0.22 – 2.1
Eu/Eu*	0.87 – 1.5	0.35 – 0.91	**0.38 – 0.81 ****	0.37 – 0.94	0.20-0.61	?
Affinity	alkaline – calc-alkaline	calc-alkaline	**tholeiitic – calc-alkaline**	tholeiitic	tholeiitic	tholeiitic
Mineralisation style	Atypical Cu-Au veins, disseminations and replacement of permeable volcaniclastic rocks	Exhalative stratiform lenses High grade, low tonnage Cu-Zn ± Ag ± Au index Discrete alteration pipe and Cu-rich stringer zone or Atypical Cu-Au veins, disseminations and replacement of permeable volcaniclastic rocks	**Disseminations and replacement of permeable volcaniclastic rocks**	Exhalative stratiform lenses High grade, low tonnage Cu-Zn ± Ag ± Au index Discrete alteration pipe and Cu-rich stringer zone	Exhalative stratiform lenses High grade, low tonnage Cu-Zn ± Ag ± Au index Discrete alteration pipe and Cu-rich stringer zone	
Examples	LaRonde Bousquet 1 and 2	Sturgeon Lake, Kuroko, Rio Tinto, Bathurst, Myra Falls, Mt. Windsor, Tulsequah Chief, Mt. Chalmers, Thalanga, Boliden, Selbaie, Salt Creek, Murgul, Benambra	**Jaguar**	Noranda, Jerome, United Verde, Parys Mountain, Ambler, Avoca, Woodlawn, Buchans, Prieska, Fox Lake, Manitouwadge, Hood River, Sulphur Springs, Scuddles, Berslagen, Winston Lake	Kidd Creek, Kamiskotia, Eskay Creek, Neves Corvo, Shasta, Crandon, Mattagami Lake, Mons Cupri, South Bay	Stekenjokk, Snow Lake, Flin Flon, West Shasta, Kutcho Creek, Canatuan

Chondrite-normalising factors from Nakamura (1974); Eu* calculated by linear interpolation between chondrite-normalised Sm and Tb; ** single positive anomaly of Eu not considered.

otherwise consistent pattern. This value of 1.51 is difficult to explain as the sample has no phenochrysts of plagioclase, so the Eu is unlikely to reflect a cumulate phase. The sample has significant titanite which can concentrate the middle REE. However, it is unlikely that the Eu would fractionate from the other REE.

Where the MPD is normalised to primitive mantle, the MPD shows enrichment in all elements, with a slight negative slope. Erratic anomalous values in Cs, Rb and Ba in all spidergrams are likely to be the result of alteration, as is the pronounced negative Sr anomaly. Nb, Ta and Ti all show negative anomalies (Fig. 5.10b). Compared to NMORB, the MPD is strongly enriched in LILE, has a steep to moderate negative slope and shows negative anomalies with respect to Nb, Ta and Ti (Figs 5.10c). Ignoring the alteration affected Cs, Rb, Ba and Sr anomalies, the BABB-normalised plot shows moderate

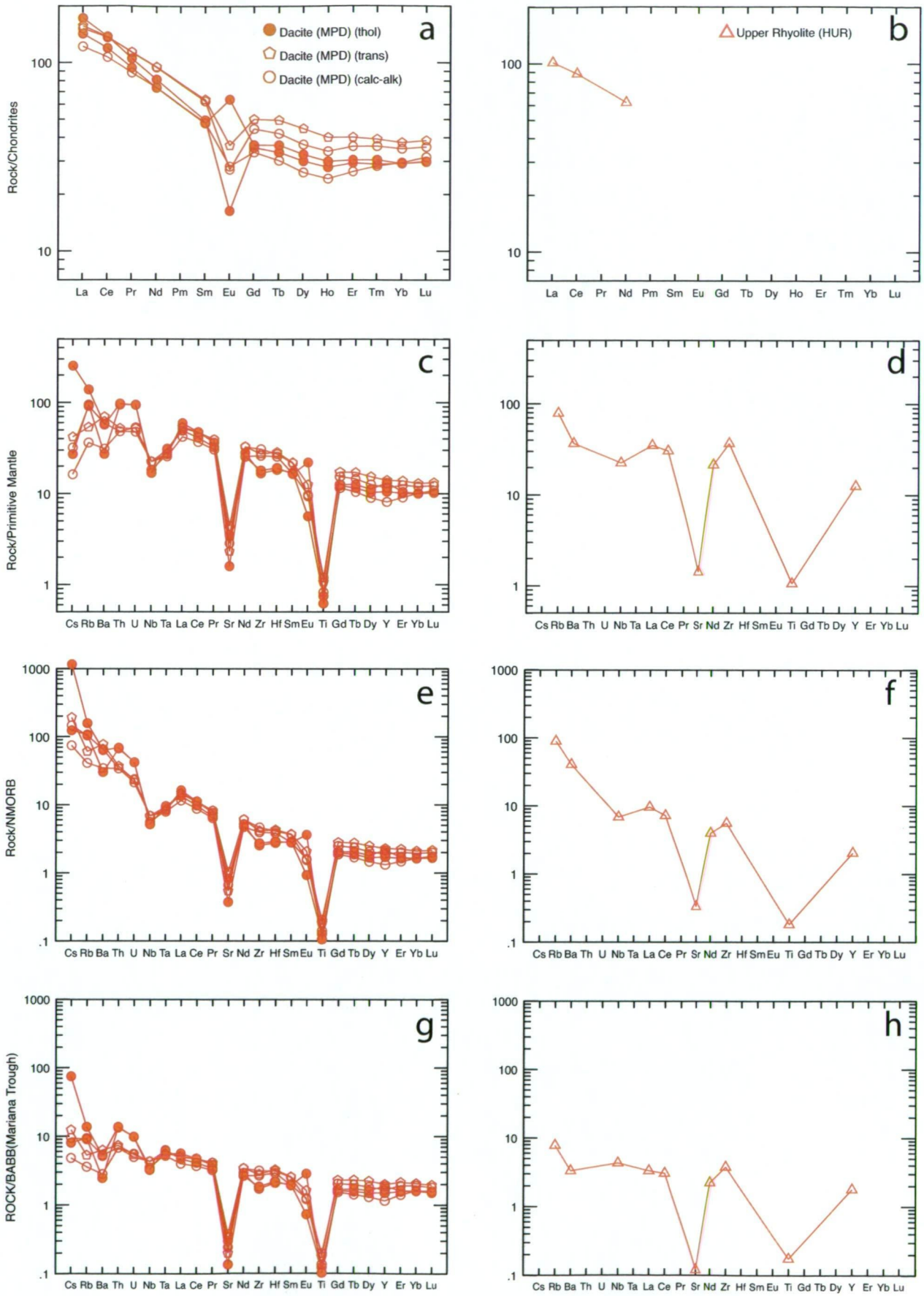

Figure 5.10 Normalised multi-element variation diagrams for the felsic rocks. (a) and (b) shows REE normalised for chondrite samples, whereas (c) and (d) shows elements normalised for primitive mantle, (e) and (f) for NMORB and (g) and (h) for BABB (Mariana Trough). (a)-(f) have normalising values and order from Sun and McDonough (1989), whereas (g) and (h) are normalised against an average of 51 samples from the Mariana Trough (http://www.petdb.org).

enrichment, a flat to weak negative slope, and negative anomalies with respect to Sr and Ti (Fig. 5.10d). The dacite pattern is most similar to the BABB pattern. As discussed earlier, Nb has low solubility in hydrous fluids and the negative anomaly in these elements shown in the NMORB and primative mantle spidergrams most likely reflects a lower solubility of these elements in migrating fluids overlying a downgoing lithospheric slab (Pearce and Peate, 1995). A negative Ti anomaly can be indicative of a subduction related arc signature (Pearce, 1996) but, in this case, it probably represents fractionation processes.

Summary

The chemical composition of the felsic rocks is summarised in Table 5.8 and the key features are:

- Nb depletion - implies subduction
- elevated HFSE
- similar to BABB Mariana trough

Table 5.8 Summary of geochemistry of the felsic rocks

	FR	MPD - all	MPD (thol)	MPD (calc-alk)	HUR
Lithology	rhyolite	dacite	rhyolite - dacite	rhyolite - dacite	rhyolite
Affinity	transitional - calc alkaline	mixed	tholeiite	calc-alkaline	calc-alkaline
HFSE	n = 3		n = 8	n = 10	n = 1
TiO_2 (wt%)	0.18		0.16	0.36	0.23
Nb (ppm)	12.7		10.9	15.5	16
Zr (ppm)	279		181.8	342.1	412
Y (ppm)	42.7		47	51.2	57
Zr/Nb	22		16.7	22.1	25.8
Zr/Y	5.2 – 9.6	3.4 – 7.9	3.4 – 4.2	6.1 – 7.9	7.2
Ti/Zr	3.6 – 5	3.7 – 9.2	3.9 – 6.4	4 – 9.1	3.3
REE	n = 0	n = 5	n = 2	n = 3	n = 0
[La/Sm]cn		2.4 – 3.5	3 – 3.5	2.4 – 2.5	
[La/Yb]cn		4.1 – 5.9	4.9 – 5.9	4.1 – 4.3	
Eu/Eu*		0.38 – 0.69 (1.51**)	0.38 (1.51**)	0.51 – 0.69	
Nb/Th		1.45 – 3.92	1.45 – 1.62	3.91 – 3.91	
Th/Ta		3.3 – 7.3	6.5 – 7.3	3.3 – 3.9	

** an extreme outlier of 1.51 exists; chondrite normalising values from Sun and McDonough (1989)

5.3.6 Regional geochemistry

The available published geochemistry from other volcanic complexes in the Gindalbie Terrane (Spring Well, Melita and Jeedamya) (Fig. 2.2) is compared here with the Jaguar geochemistry. As discussed in Chapter 2, there are no published geochemical data available from the Teutonic Bore volcanic complex, which contains the Jaguar deposit. The data for the Spring Well, Melita and Jeedamya volcanic complexes is taken from Morris and Witt (1997), Messenger (2000), Brown et al. (2002) and Barley et al. (2008). These data are provided in Appendix IV.

Bivariate element plots of Ti and Y versus Zr (used to discriminate and classify the Jaguar

rocks) are shown for the available published data from the other complexes, and compared with averages of the Jaguar rocks in Figure 5.11. REE diagrams normalised to chondrite (normalising factors of Sun and McDonough, 1989) and normalised multi-element variation primitive mantle (normalising factors of Anders and Grevesse, 1989) (Fig. 5.12) are shown for comparison with Jaguar.

At Spring Well the Zr-Ti plot shows that the volcanic rocks range from andesite through to dacite (Fig. 5.11c). These samples are described as basaltic andesite to andesite and dacite and rhyolite by Messenger (2000) and Barley et al. (2008). The Zr-Y plot shows they have calc-alkaline to transitional affinities (Fig. 5.11d). The primitive mantle normalised multi-element diagram (Fig. 5.12c) shows similar trends to Jaguar, with values of Nd and Zr being similar, but Y slightly higher in the Jaguar felsic rocks. A strong negative Nb anomaly is present in both suites. The Spring Well intermediate and felsic volcanic rocks have very similar chondrite-normalised REE trends (Fig. 5.12d) to the Jaguar rocks, with both suites showing a slight negative slope, although the slope is steeper in the Spring Well samples. The Jaguar mafic rocks have an almost flat REE pattern compared to the Spring Well 'basalt', which has a more andesitic trend. The felsic rocks from Spring Well show a depletion in the HREE compared to Jaguar. Both suites have similar negative Eu anomalies.

For the Melita samples, the Zr-Ti diagram (Fig. 5.11e) shows a distinct compositional gap, demonstrating the bimodal nature of this succession. The mafic volcanic rocks range from basalt to andesite and show two distinct affinity trends on the Zr-Y plot (Fig. 5.11f); tholeiitic and calc-alkaline. These samples are described as basalt by Morris and Witt (1997) and Brown (2002). The two dolerite samples plot within the transitional field. The felsic volcanic rocks range from dacite to rhyolite, and some of the rocks described as rhyolite by Morris and Witt (1997) and Brown (2002) plot well within the dacite field. The felsic rocks also show two distinct Zr/Y trends, one tholeiitic and one calc-alkaline. The true rhyolites (all with a Ti/Zr <3.6) are tholeiitic, whereas those that lie in the dacite field are calc-alkaline. The primitive mantle normalised multi-element diagram (Fig. 5.12e) shows similar trends to Jaguar, with similar values of Nd, Zr and Y. A strong negative Nb anomaly is present in both suites. The Melita rocks have very similar chondrite-normalised REE trends (Fig. 5.12f) to Jaguar if the Melita rhyolites are excluded (on the basis that REE are not available for Jaguar rhyolites). The mafic rocks from Jaguar have lower LILE and LREE than Melita. Both sets have similar negative Eu anomalies in the intermediate and felsic rocks, whereas the mafic rocks have no Eu anomalies compared to the Jaguar positive Eu anomaly in the FB and the absent to negative anomaly in the HB and D.

At Jeedamya the Zr-Ti plot of the volcanic rocks shows a range from basalt to dacite (Fig. 5.11g) on a small set of 4 samples, with a clear compositional gap. The mafic volcanic rocks

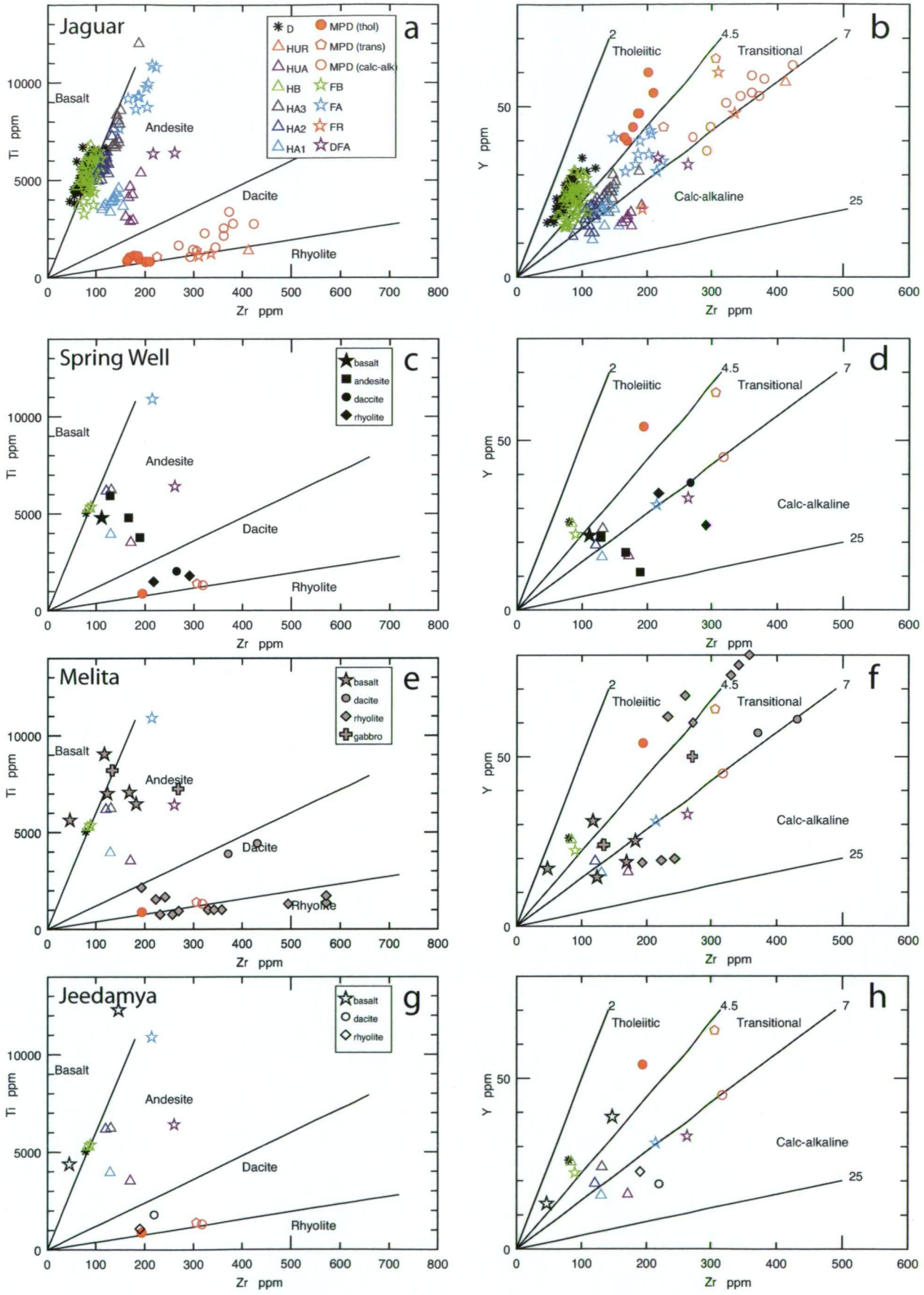

Figure 5.11 Bivariate element plots of Ti and Y vs Zr for Jaguar (averaged) and the Spring Well, Melita and Jeedamya volcanic complexes. (a) and (b) all samples from Jaguar; (c) and (d) Spring Well data plus average Jaguar samples; (e) and (f), Melita data plus average Jaguar samples; (g) and (h) Jeedamya data plus average Jaguar samples. The data, and rock names for the these complexes are from Morris and Witt (1997), Messenger (2000), Brown et al. (2002), and Barley et al. (2008).

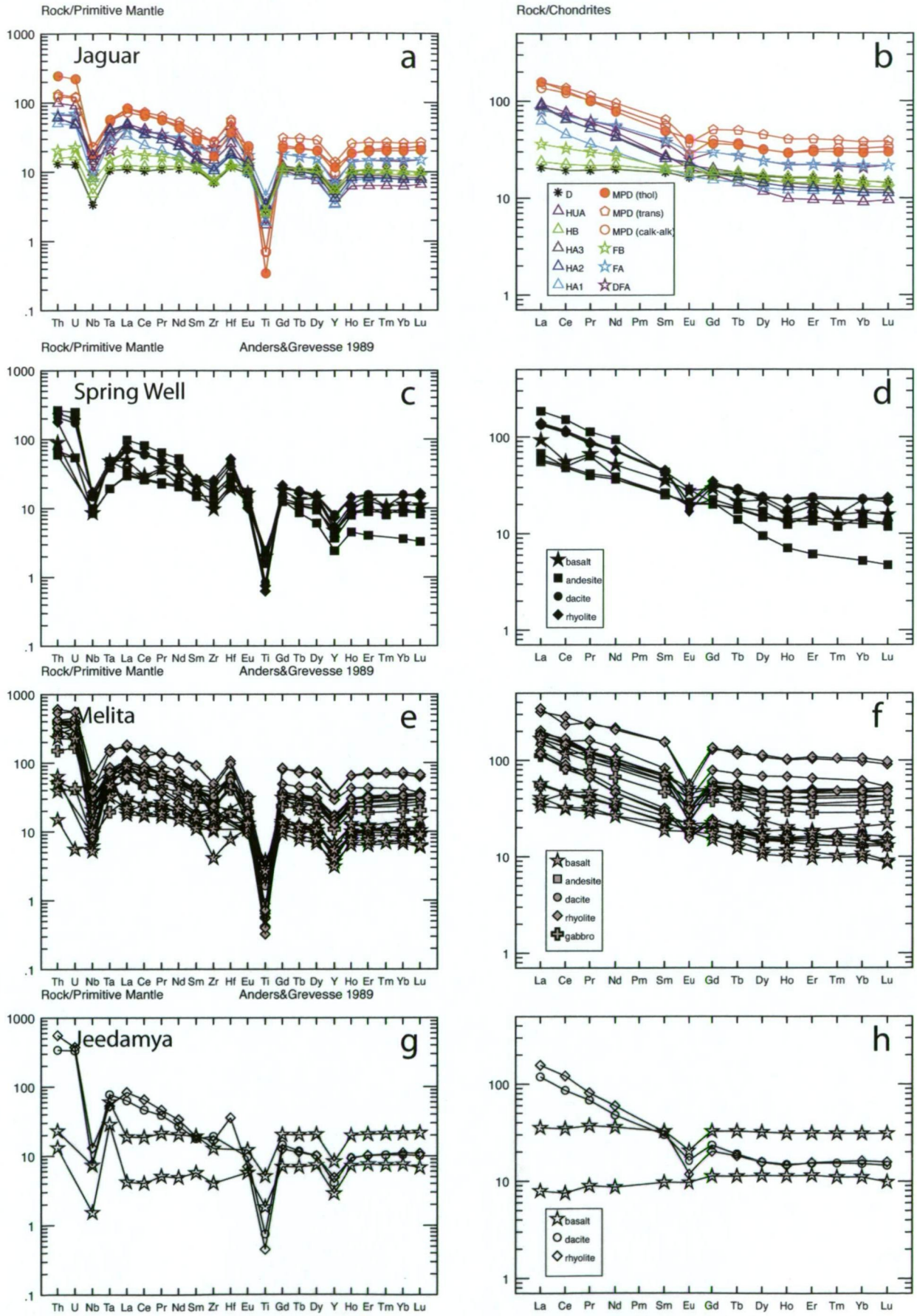

Figure 5.12 Normalised multi-element variation diagrams for Jaguar (averaged rocks) and the Spring Well, Melita and Jeedamya volcanic complexes. The data for the these complexes are from Morris and Witt (1997), Messenger (2000), Brown et al. (2002) and Barley et al. (2008). (a), (c), (e) and (g) show Primitive Mantle normalised multi-element variation diagrams. Normalising values from Anders and Grevesse (1989). (b), (d), (f), and (h) show chondrite normalised diagrams. Normalising values from Sun and McDonough (1989). Sample lithologies are as named in original papers.

show tholeiitic affinities whereas the felsic rocks show a calc-alkaline trend (Fig. 5.11h). For the mafic rocks the trend for the chondrite-normalised REE plot (Fig. 5.12h) shows a flat to positive slope whereas the Jaguar mafic rocks show a slight negative slope. Both sets have similar negative Eu anomalies in the intermediate and felsic rocks, whereas the mafic rocks show variable Eu. Overall, the Jaguar rocks show an enrichment in all REE compared to Jeedamya. The primitive-mantle-normalised multi-element diagram (Fig. 5.12g) shows comparable trends to Jaguar, with similar values of Nd, Zr and Y. A strong negative Nb anomaly is present in both suites.

Summary

In summary, a similar character is apparent among the spidergrams with all showing a strong negative Nb anomaly, and a subduction-related character for all four volcanic complexes.

5.4 Discussion and Interpretation

5.4.1 Relationships between units

The coherent volcanic rocks at Jaguar represent a suite from basalt to andesite to dacite to rhyolite and, unlike many successions that host VHMS deposits (MacGeehan and MacLean, 1980; Large, 1992; Barrett and MacLean, 1999), is not bimodal and does not have a large compositional gap. Figures 5.13a and 5.13b show BABB-normalised multi-element and chondrite-normalised REE trends for the coherent rocks (samples averaged), except the FR, for which there is no trace or REE data, and the HUR, which has only a small amount of XRF data. Although there are many similarities in the geochemical trends of the Jaguar rock suite, there are several marked changes in ratios across the mineralised package. The negative Nb, Ta and Ti anomalies are constant throughout, whereas the Eu anomaly varies, from positive in the FB to negative in most other rocks. The [La/Sm]cn and [La/Yb]cn values indicate a close relationship among some rocks but not others, as do the groupings and range in Zr/Nb. Although some conclusions can be drawn from this data about the magma type and its properties, it is beyond the scope of this thesis to determine in detail the source and origin of the magmas. No isotopic work was carried out, and the question as to whether the coherent rocks are truly co-genetic cannot be answered here. Future Nd isotope work may resolve this question.

The lavas stratigraphically beneath the massive sulfide mineralisation, to at least 450 m below ore, show a marked similarity, consistent with a constant source. With the exception of a single MPD sample, the DFA, FA, FB and MPD show near-identical trends and slopes in the BABB-normalised multielement and chondrite-normalised REE spidergrams (Figs

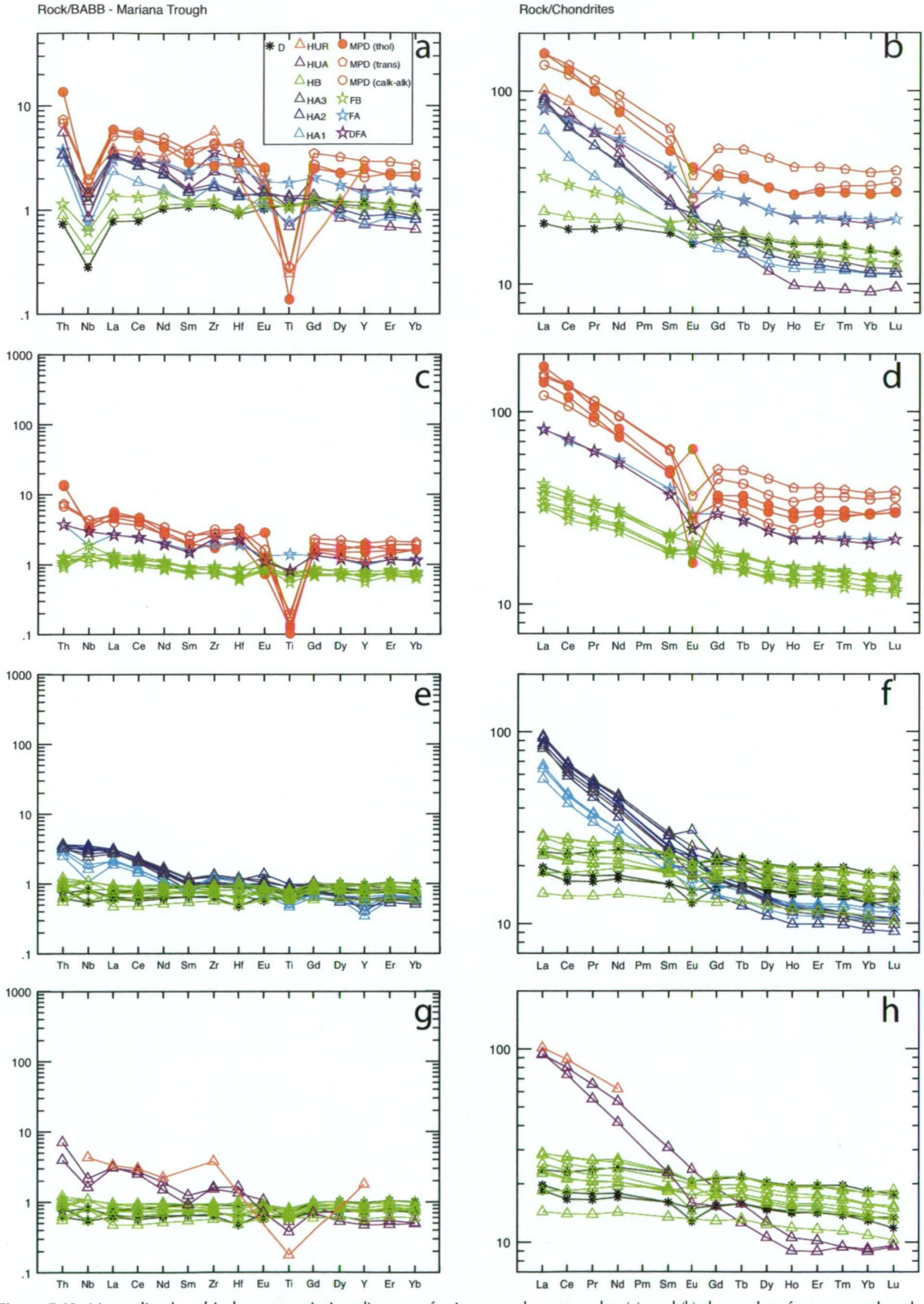

Figure 5.13 Normalised multi-element variation diagrams for Jaguar coherent rocks. (a) and (b) show plots for averaged rock samples, (a) shows an BABB-normalised spidergram, whereas (b) shows the same samples on a chondrite-normalised REE plot. (c) and (d) show footwall samples on a BABB-normalised spidergram and a chondrite-normalised REE plot which show the same trends. (e) and (f) show the HB plus D plotted together with the HA1, HA2 and HA3 lavas on samples on a BABB-normalised spidergram and a chondrite-normalised REE plot which show the dissimilarity in the trends. (g) and (h) show the HB plus D plotted together with the HUA and HUR lavas on samples on BABB-normalised and Chondrite-normalised plots. The HUA is most likely related to the HA lavas whereas the missing data in the HUR trends precludes confident recognition of an association. REE normalising values and order are from Sun and McDonough (1989) and values for BABB-normalisation are from the BABB PETDB (http://www.petdb.org).

5.13c and 5.13d). The range of [La/Sm]cn and [La/Yb]cn values reflect the sub-parallel slopes of the trend lines and have a weak negative slope. The rocks have similar Zr/Nb values, and show similar enrichment and depletion anomalies in other elements, with the exception of Eu (Table 5.9).

Table 5.9 Summary of geochemistry of footwall and mineralised package lavas.

	DFA	FR	FA	FB	MPD - all	MPD (thol)	MPD (calc-alk)
Lithology	andesite	rhyolite	basaltic-andesite	basalt	dacite	rhyolite - dacite	rhyolite - dacite
Affinity	transitional - calc-alkaline	transitional - calc alkaline	transitional	tholeiitic	mixed	tholeiite	calc-alkaline
HFSE	n = 2	n = 3	n = 10	n = 28	n = 20	n = 8	n = 10
Zr/Nb	21.6	22	25.2	19		16.7	22.1
Zr/Y	6.2 – 7.9	5.2 – 9.6	3.9 – 6.9	3.5 – 5.7	3.4 – 7.9	3.4 – 4.2	6.1 – 7.9
Ti/Zr	25 – 29	3.6 – 5	43 – 56	39 – 74	3.7 – 9.2	3.9 – 6.4	4 – 9.1
REE	n = 1	n = 0	n = 1	n = 6	n = 5	n = 2	n = 3
[La/Sm]cn	2.2		2.1	1.6 – 1.9	2.4 – 3.5	3 – 3.5	2.4 – 2.5
[La/Yb]cn	3.9		3.8	2.6 – 3.0	4.1 – 5.9	4.9 – 5.9	4.1 – 4.3
Eu/Eu*	0.74		0.85	1.09 – 1.37	0.38 – 0.69 (1.51**)	0.38 & (1.51**)	0.51 – 0.69

** an extreme outlier of 1.51 exists; chondrite normalising values from Sun and McDonough (1989).

There is no REE data for the FR so to include it among this group is speculative, although the Zr/Nb ratio puts it within the group range. The positive Eu anomaly in the FB trend may represent an emptying of the host magma chamber and a possible expulsion of residual plagioclase cumulates, as igneous plagioclase concentrates Eu (Rollinson, 1993).

Following the emplacement of the FW there was a hiatus in the volcanic pile development, marked by the deposition of volcaniclastic and sedimentary units that gradually became finer grained upwards. The orebody developed at this time.

When volcanism resumed, there was a change in the composition of the magmas. The first volcanics emplaced at Jaguar after the hiatus are the HA1, HA2 and HA3. The trends, slopes and ratios of these lavas do not match the trends in the footwall (Figs 5.13e and 5.13f). The ranges in [La/Sm]cn and [La/Yb]cn values indicate REE patterns with much steeper, negative slopes than recorded in the footwall rocks. The HA andesites become successively more mafic from HA1 to HA3, and change in affinity from calc-alkaline to transitional. In addition, Zr/Nb values decrease, with the group having a lower ratio than the footwall group. The Zr remains relatively constant, indicating an increase in Nb. This could be due to slightly decreasing amounts of partial melting of the same source, leading to increasing abundance of the very incompatible Nb relative to Zr, or involvement of a slightly more fertile (or less depleted) source compared to earlier melts. Alternatively, it may reflect an increased crustal contamination by something with no Nb depletion.

The HB lavas that follow the HA are distinctly different from the earlier (DFA, FR, FA, FB

and MPD) magmas, although the HUR lava, which follows later in the succession, does show a similar trend (Fig 5.13g and 5.13h). The D trend is nearly identical to the HB and is most likely the same magma. The HB remains relatively chemically constant through the HB1 to HB5 lavas and is represented singly as HB. The HB and D have the highest Zr/Nb values of all the units, which again reflects low Nb rather than an increase in Zr. This magma also has the flattest REE trends [La/Yb]cn (1.3–1.9) and [La/Sm]cn (1.0–1.3) and, unlike all other units, has virtually no slope on the BABB-normalised spidergram (Table 5.10). It is likely to have been a new pulse of magma, concomitant with a new heat pulse. The HB was a voluminous outpouring of lava, that produced high-flow eruption features such as fountain deposits (see Chapter 4).

Table 5.10 Summary of geochemistry of intrusions and hangingwall lavas

	HA1	HA2	HA3	HB	D	HUA	HUR
Lithology	andesite	basaltic-andesite	basaltic-andesite	basalt	basalt	andesite	rhyolite
Affinity	transitional - calc-alkaline	transitional	transitional	tholeiitic	tholeiitic	calc-alkaline	calc-alkaline
HFSE	n = 13	n = 23	n = 12	n = 39	n = 43	n = 7	n = 1
Zr/Nb	19.3	10.2	11.7	26.8	31.4	23.6	25.8
Zr/Y	5.6 – 10	5.3 – 9	4.9 – 7.3	2.6 – 4	2.6 – 4	9.1 – 28	7.2
Ti/Zr	24 – 32	43 – 61	47 – 64	52 – 80	55 – 98	17 – 25	3.3
REE	n = 3	n = 6	n = 2	n = 8	n = 3	n = 2	n = 0
[La/Sm]cn	3.1 – 3.3	3.2 – 4.2	3.2 – 3.5	1.0 – 1.3	1.0 – 1.2	3.0 – 4.2	
[La/Yb]cn	5.4 – 5.8	7.5 – 9.1	6.6 – 8.2	1.3 – 1.9	1.3 – 1.5	10.16 – 10.57	
Eu/Eu*	0.93 – 1.01	0.94 – 1.22	0.88 – 0.96	0.79 – 1.11	0.82 – 0.94	0.83 – 0.96	

Chondrite normalising values from Sun and McDonough (1989).

The HUA, which followed after another hiatus, shared the chemical trends of the HA lavas with a further steepening of the REE trends, a [La/Yb]cn ratio of 10.16–10.57 and a [La/Sm]cn ratio of 3.0–4.2. These features suggest that it may be related to the HA, but is not likely to be a differentiation product of the HB lava as the HUA trend cuts the HB trend (Fig. 5.13b), and fractionation within the basalt compositional range does not modify LREE ratios (i.e. change the [La/Sm]cn).

After the cessation of eruption of the HUA, there was another volcanic hiatus before the emplacement of the HUR. There are limited trace and REE assays available for the HUR and the limited number of data points (Figs 5.13g and 5.13h), preclude confident recognition of a co-magmatic relationship between the HUR and HUA or HB lavas. However, the Zr/Nb ratio of the HUR is closer to the HB and D group than any to other unit.

Summary

The footwall (DFA, FR, FA and FB) and the MPD magmas (which are closely related) were emplaced along with associated volcaniclastic facies with no interfingering sedimentary layers. They were followed by a hiatus in volcanism, during which time volcaniclastic

and volcano-sedimentary deposits dominated the sequence. The positive Eu anomaly in the basalt (FB) at the top of the footwall sequence may be evidence of the emptying of the magma chamber. Volcanism resumed with more highly fractionated andesites (HA) interfingering with volcaniclastic and pelagic sediments. This was succeeded by a sustained outpouring of chemically monotonous basalts (HB) that included facies dominated by fluidal-clasts, and pillow lavas. Dolerite sills (D) with the same chemical composition as the HB are considered to have the same source as the HB outpouring. These basaltic magmas were distinctly different from earlier magmas. A short hiatus was followed by the emplacement of the HUA andesite, which was related to the HA magma, and this in turn was succeeded by the HUR rhyolite.

5.4.2 Regional correlation to other suites in the EGST (Gindalbie/Kurnalpi)

Allowing for the local differences among the Jaguar rocks, the chondrite-normalised and primitive mantle-normalised patterns exhibited by the Jaguar sequence are similar to those from the other volcanic complexes in the Gindalbie Domain. However, unlike Jaguar and the andesitic Spring Well complex, which have a continuous spectrum of rock types, the Melita and Jeedamya sequences have a large compositional gap, and are more bimodal in nature.

Workers in the Eastern Goldfields Superterrane have generally included the Teutonic Bore volcanic complex in the Gindalbie tectonostratigraphic unit containing the Melita and Jeedamya volcanic complexes. Cassidy et al. (2006) regarded the Gindalbie association as a domain within the Kurnalpi Terrane, rather than a separate terrane. They placed the Spring Well complex in their Murrin Domain. However, Barley et al. (2008) and Kositcin (2008) placed the Spring Well complex in their Gindalbie association, based on its geochemical affinities.

The similarities illustrated in this thesis between the Jeedamya, Melita and Spring Well complexes and the Jaguar sequence suggest that they are all part of the same tectonostratigraphic component of the Eastern Goldfields Superterrane, here called the Gindalbie Domain after Cassidy et al. (2006).

5.4.3 Implications for tectonic setting

Establishing the tectonic setting in Archean rocks based upon discriminators developed using Phanerozoic rocks as modern analogues presents problems. However, as discussed earlier, it is common practice. If the geochemical signatures of modern rocks can be extrapolated back to the Archean in a meaningful way, then the main conclusions identified by their use as analogues in the discrimination diagrams are described below.

The multi-element and REE patterns all suggest that the coherent rocks have an enriched

component, but with anomalies indicative of a subduction-related arc signature. In summary, of the settings suggested by analysis of the discrimination diagrams, the types of volcanic rocks are interpreted as transitional between MORB and VAB (with possible WPB), all of which could occur an early back-arc basin setting. VAB compositions may be found in a backarc basin ridge systems during the early stages of backarc opening when the ascending asthenospheric mantle providing MORB to the embryonic backarc basin pirates melts from the adjacent arc magmatic system (Sinton and Fryer 1987; Stern et al. 1990; Sinton et al. 2003;). As the backarc basin widens, a transition from backarc basin basalts with an arc signature, to true N-MORB-type compositions occurs, as the ascending asthenospheric mantle is removed from the influence of the arc magmatic system (Crawford et al. 1981; Taylor and Martinez 2003). VAB/MORB/WPB transitions may include attenuated continental lithosphere above subduction zones (e.g. margins of the Japan Sea; Pouclet and Bellon, 1992).

Pearce (1996) recognised the following circumstances in complex tectonic settings that results in basalts that plot in a transition zone: (1) attenuated continental lithosphere resulting from back-arc basin development after collision, subduction and rollback; (2) attenuated lithosphere, but not associated with a subduction zone or; (3) a complex collision zone setting with regions of back-arc basalts and volcanic-arc basalts, therefore a within-plate volcanic zone. He suggested that early back-arc basalts display MORB patterns contaminated by slab-derived fluids, and may show weak LILE and LREE enrichment, best displayed by a negative Nb anomaly.

Comparison with settings of other Archean VHMS deposits

When the Jaguar data for all rock suites are plotted on a Ta/Yb vs. Th/Yb plot (Fig. 5.14) with the boundaries developed by Gorton and Schandl (2000), they lie within the field occupied by the deposits from the Superior Province, Canada. The Jaguar suite reflects the same relative depletion in Th as in the host rocks of the Superior Province deposits when compared to that present in the host rocks of most post-Archean deposits. However, despite this relative depletion, the Jaguar rocks still contain levels of Th that, when plotted on the Hf–Th–Ta discrimination diagram developed by Wood (1980) fall within the VAB field (Fig. 5.8a).

Schandl and Gordon (2002) interpreted this difference to reflect the addition of Th to younger volcanic rocks by the release of fluids from a subducting slab, and they suggest that the Archean deposits of the Superior Province probably formed in an ensimatic rift environment (non-arc), whereas the post-Archean deposits of Bathurst, Canada, San Nicholas, Mexico and Kuroko, Japan formed in subduction-related rift zones of an arc environment. However, Hawkesworth et al. (1997) suggested that, whereas Th is mobilised in fluids derived from the subducted slab, the variations in the Th contents of primary

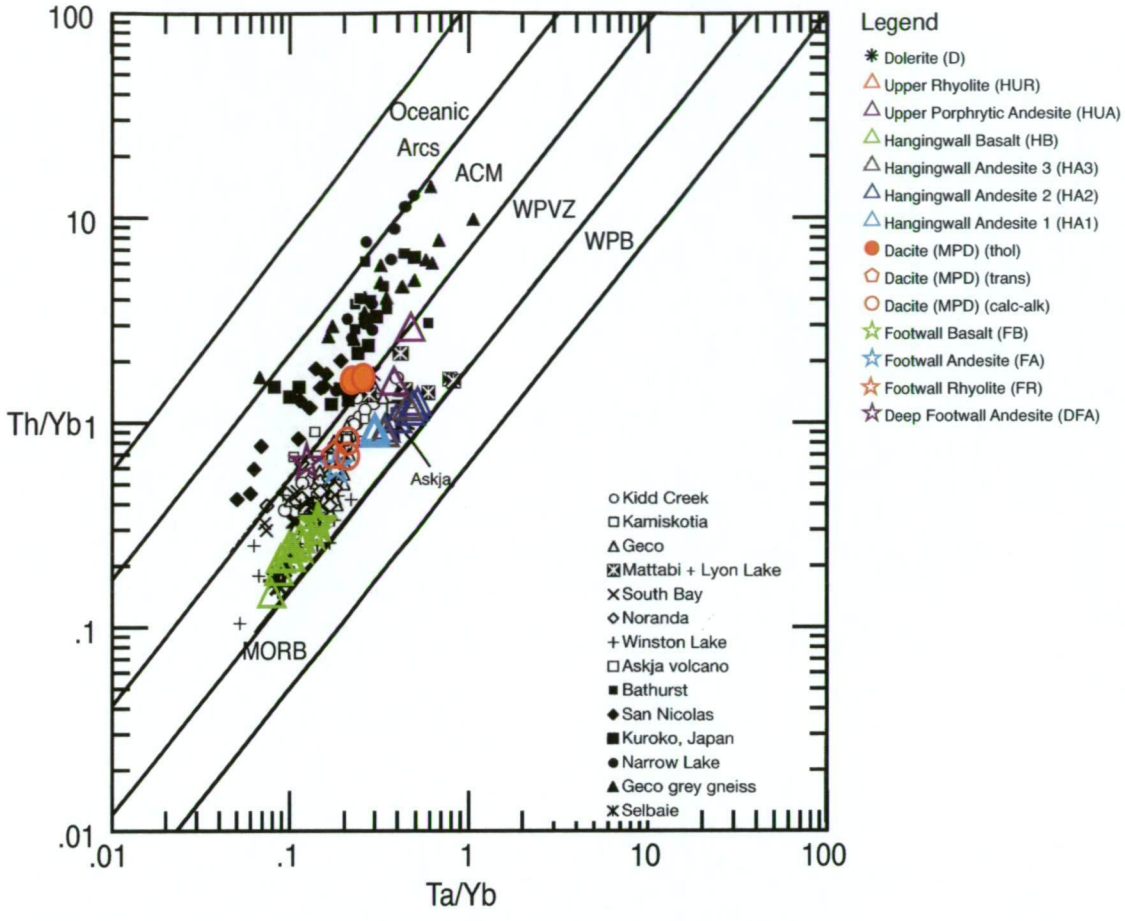

Figure 5.14 Jaguar data shown on plot of Ta/Yb vs Th/Yb with boundaries developed by Gorton and Schandl (2000) showing their data points. The Archean data almost all lie in the WPVZ field whereas the post-Archean data lie within the ACM field. [Data points: Kidd Ck, Kamiskotia, Gecco, Mattabi, South Bay, Noranda, Winston Lk and Selbaie are Archean VHMS deposits in the Superior province, Canada; Askja volcano is a modern rhyolite volcano in Iceland; Bathurst, San Nicolas and Kuroko are post-Archean VHMS deposits]

island arc magmas depend largely on the contribution from subducted sediments. This results in an explanatory impasse in that the relatively higher level of Th in post-Archean suites may be a function of the fact that post-Archean downgoing slabs have more sediment to recycle thus more Th. Thus a lower Th/Ta does not preclude a subduction-related rift zone within an arc environment.

5.4.4 Conclusion

An ensimatic rift environment scenario is possible for Jaguar as the multi-element and REE trends are similar to the BABB trends, and the Jaguar data also has a subduction signature in the form of the strong negative Nb and Ta anomalies. Most of the discrimination diagrams used suggest a complex, early back-arc setting for Jaguar. Langmuir et al. (2006) noted that in addition to a subduction component and wedge depletion, BABB reflect a prevalent enriched component akin to enriched ocean ridge basalts worldwide, despite the

absence of mantle plumes.

The geological constraints are that the Jaguar sequence is dominated by coherent volcanic rocks and their associated facies. There was local reworking and minor input from pelagic sources, but no terrigenous input, so it is probably was not close to an emergent arc, and was not surrounded by, or adjacent to, any higher ground, i.e. within a larger fault basin. The most likely tectonic setting for Jaguar is an extensional environment, adjacent to a subduction zone, but not close to an emergent arc.

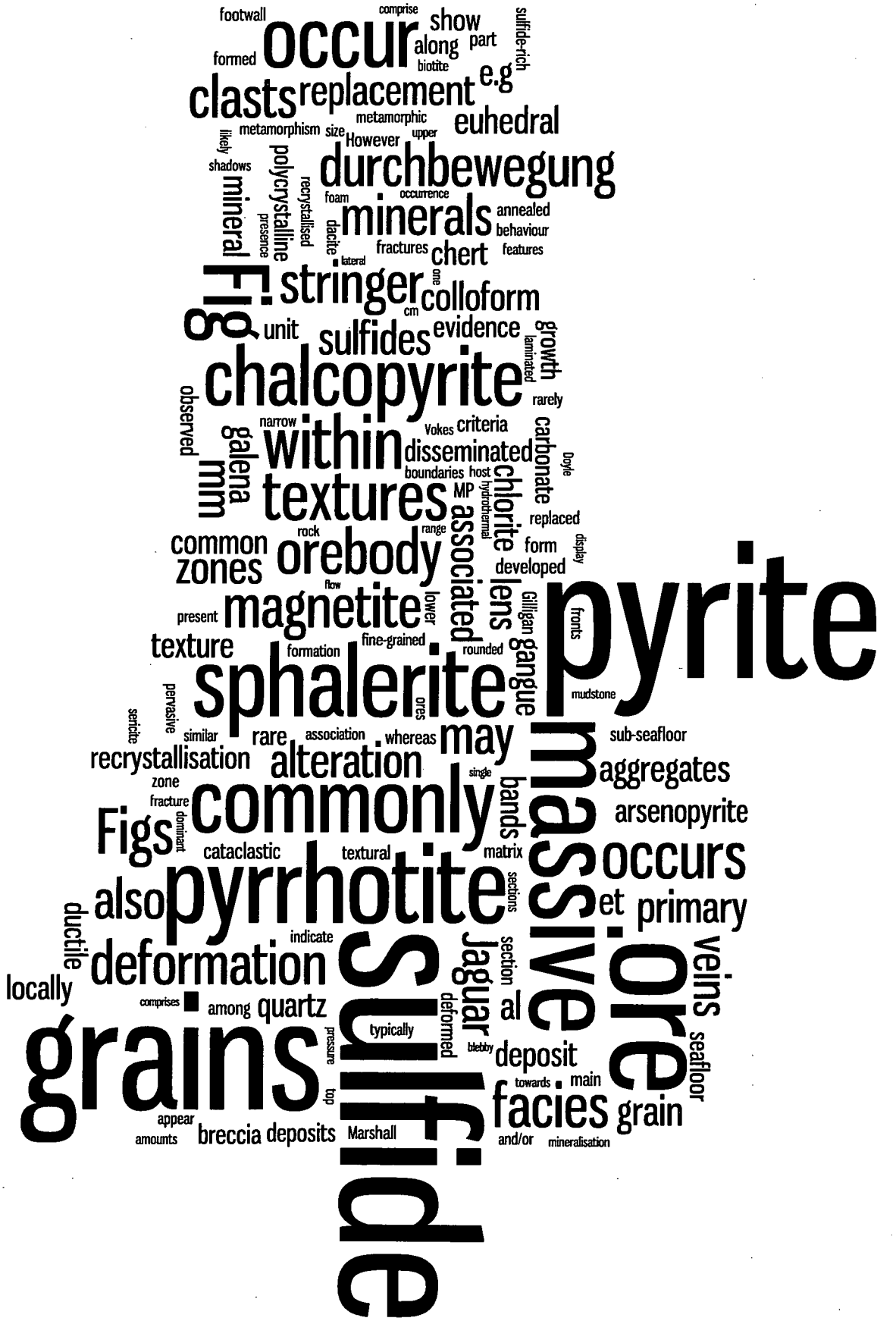
pyrite
sulfide
ore
massive
grains
pyrrhotite
chalcopyrite
commonly
sphalerite
occur
durchbewegung
minerals
stringer
Fig
Figs
within
textures
orebody
magnetite
deformation
occurs
aggregates
arsenopyrite
primary
veins
facies
grain
deposit
breccia deposits
quartz
alteration
recrystallisation
clasts
replacement
euhedral
colloform
sulfides
evidence
disseminated
associated
lens
gangue
zones
common
texture
also
locally
ductile
Jaguar
bands
matrix
cataclastic
textural
foliation
Gilligan
fronts
mudstone
sub-seafloor
seafloor
veins
footwall
formed
along
part
biotite
e.g
metamorphic
metamorphism
However
upper
shadows
polycrystalline
recrystallised
foam
occurrence
annealed
behaviour
mineral
presence
dacite
lateral
fractures
chert
features
cm
unit
laminated
growth
rarely
observed
narrow
Vokes
criteria
carbonate
galena
mm
boundaries
host
MP
hydrothermal
Doyle
replaced
rock
range
form
display
developed
present
flow
lower
fine-grained
rounded
formation
texture
pervasive
sericite
similar
rare
association
whereas
may
zone
fracture
dominant
single
aggregates
arsenopyrite
occurs
et
primary
indicate
section
sections
deformed
typically
pressure
top
blebby
towards
main
among
quartz
comprises
appear
amounts
Marshall
and/or
mineralisation
al
deposit
grain
comprise
show
sulfide-rich
likely
one
cm
Vokes
Doyle

6. ORE MINERALOGY AND TEXTURES

6.1 Introduction

This chapter examines the occurrence, mineralogy and textures of the base metal sulfides and minor magnetite at Jaguar. It is based entirely on core logging of 62 selected intersections that intersected the Mineralised Package unit, on selected cross-sections along the strike of the orebody, and examination of polished thin sections from samples collected during that logging. No mineral specific analyses were undertaken, nor has any mineral mapping within the ore zones been carried out. No underground mapping of the ore was carried out.

Few primary features remain in the sulfide body at Jaguar. As will be shown, most (but not all) features seen in the ore are the result of metamorphism and deformation The dominant sulfide minerals of the ore at Jaguar are pyrrhotite, pyrite, sphalerite and chalcopyrite. Pyrrhotite, pyrite and sphalerite appear to occur in equal amounts and each comprises about 30 vol. % of the sulfide mass. Magnetite is present as a minor constituent, and galena and arsenopyrite are present as accessory phases. Trace amounts of tetrahedrite-tennantite and geochronite have also been identified. The gangue minerals are quartz, chlorite, carbonate and sericite with lesser amounts of biotite, titanite, tremolite-actinolite, epidote, clinozoesite and rare prehnite. The main ore type is massive sulfide and in this thesis the term massive sulfide is used to denote abundances greater than 50 vol. %.

In review, sulfide deposits respond to metamorphism by recrystallisation and to tectonism by deformation. The more refractory or competent minerals, such as pyrite, arsenopyrite, magnetite and sphalerite, show little change with low grade metamorphism and retain their primary compositions (Vokes, 1969; Marshall and Gilligan, 1987; Marshall and Gilligan, 1993). As metamorphic grade increases they lose their zoning, and re-equilibrate compositionally; they coarsen in grain size, anneal and develop idioblastic or porphyroblastic texture or characteristic triple junctions. In response to stress they fracture rather than flow. However, less refractory or softer sulfides, such as pyrrhotite, chalcopyrite and galena, re-equilibrate compositionally under lesser degrees of metamorphism. They therefore have limited value in determining initial formation conditions. These minerals can deform by twinning and kink-banding, but primarily they flow, which commonly leads to mechanical break up of ore and country rock. This produces the diagnostic durchbewegung textures (Ramdohr, 1960, 1980; Volkes, 1969) and the presence of injected sulfides along cleavages and fractures within gangue and more competent ore minerals.

The alteration mineralogy and the distribution within the alteration halo that exists around VHMS bodies is well understood (Galley, 1993; Alt, 1999) and is well documented for

many deposits around the world (Gemmell and Herrmann, 2001; Hannington et al., 2003a, 2003b; Gifkins et al., 2005; Relvas et al., 2006; Dube et al., 2007). An in-depth analysis of the alteration associated with the Jaguar deposit is not a specific concern of this thesis and as such will not be discussed in any detail other than as mineral components of the gangue, and that to say the dominant alteration species are chlorite, sericite, quartz and carbonate. Chlorite, intense and pervasive, is predominant in the footwall and associated with the footwall stringer ore in the basalt facies beneath the ore, no alteration pipe was recognised in the drillcore logging. Within the orebody itself the alteration is not symmetric and a zoning or distribution pattern is not apparent. The massive sulfide was associated with quartz, sericite, carbonate and chlorite in varying intensities. Above the orebody, variable weak to moderate intensity alteration comprising pervasive carbonate, sericite and/or quartz persists up through the overlying mudstone and in some instances up to several metres into the Hangingwall Andesite. This hangingwall alteration is accompanied by disseminated pyrite and less common pyrrhotite, sphalerite and chalcopyrite. Locally, carbonate-pyrite±pyrrhotite stringer veins also occur above the orebody. A number of spectral readings were taken during the study both on drillcore samples and on thin section off-cuts using a PIMA instrument (a portable, infrared spectrometer that operates in the Short Wave InfraRed range of the electromagnetic spectrum). These data were processed by The Spectral Geologist software and are presented for completeness in Appendix V but they are not discussed within the thesis body.

The chapter starts with a description of the physical architecture of the deposit and then describes the main ore types and their relationships. A brief description of individual ore and gangue minerals is followed by a description and classification of the observed textures. This is followed by final summary and discussion where a paragenesis is attempted and the environment of formation of the orebody is considered.

6.2 Architecture of the orebody

At Jaguar the massive sulphide orebody is hosted within a sequence of bedded volcaniclastic and coherent rocks that comprise the MP unit. In extensions beyond the massive sulfide ore, sulfides occur in numerous, commonly reticulated stringer veins that extend beneath the massive ore, within the MP unit and into the underlying FB unit. In addition, sulfide minerals occur laterally along strike in the MP unit as either sulphide-rich clasts within coarse-grained beds of the MPS, or as fine-grained disseminated grains and sulphide-rich veins. Fine-grained disseminated sulfide minerals also occur locally in the basal part of the Hangingwall Andesite unit that overlies the sulfide-rich facies in the MP unit. In addition, down dip of, and peripheral to the main ore lens, sulphide-rich clasts (up to 2 cm) occur within the dacite breccia and conglomerate facies. The amount of sulfide-rich clasts is variable but generally low. In drillcore the maximum quantity observed is about 5 vol. %.

The majority of the sulfide-rich clasts are pyrite.

The ore zones are shown on the isometric cross-sections (Fig. 6.1) which show the ore zone in greater detail than seen on the stratigraphic cross-sections (Figs 4.3 and 4.4).

6.2.1 Geometry and distribution

The sulfide-rich facies that makes up the Jaguar orebody is a lens shaped accumulation of polymetallic sulfide ore. The main accumulation of massive sulfide ore lies between 55900N and 56200N. It has a dip extent of roughly the same dimension (~300 m). The top of the massive sulfide lens is about 300m beneath the current land surface, at a mine RL of approximately 4200 m. The lens is underlain by an aureole of blebby or disseminated, and/or stringer mineralisation that extends up to 150 m laterally within the MP unit and locally at least 80 m into the footwall. The true thickness of the massive sulfide lens is estimated to achieve a maximum width of approximately 15 m. The interpretation from logging suggests that the massive sulfide lens reaches a maximum thickness on section 56000 N. More commonly it has a thickness of about nine to five metres, thinning towards the margins.

The breccias with sulfide-rich clasts occur within the Mineralised Package unit, down dip of the main sulfide lens on sections 55900 N to 56100 N. As previously described in the Chapter 3, the overall geometry of these breccias is wedge shaped, the bedding is mainly chaotic and overall they show normal grading. Within the breccias the distribution of sulfide-rich clasts is not mappable and the total volume does not exceed 5%. The geometry of these breccias with respect to the main ore lens is somewhat problematic. In drillhole TBD0242 on section 56100 N, a sulfide clast bearing breccia lies above a zone of massive sulfide, and this whole intersection appears downthrown in relation to the massive sulfide lens in drillhole TBD0242W which is 50 m higher in the same section (Fig. 4.4). A similar relationship is present on the other sections. These apparent anomalies are likely to be the result of growth faulting and associated tectonic instability. The relationship is further complicated by the presence of dolerite sills and small dolerite apophyses.

The orebody is split by younger dolerite sills that are sub-parallel to the stratigraphy. The sills display sharp, locally discordant chilled margins. Along the strike of the ore, these sills pass from the footwall to the orebody on section 55850N, splitting the orebody into separate lenses on sections 56100N and 56150N, and to above the massive sulfide (in the upper part of the orebody) on section 56200N (Fig. 6.1). The bisection of the original massive sulfide lens by the dolerite sill has essentially isolated the section of the orebody on 56200N (intersected by drillholes TBD0209 and TBD0243) and prevented it from experiencing the intensity of deformation observed throughout the rest of the orebody. This in turn has preserved the primary textures observed in this zone (discussed below) which are obliterated in other sections of the orebody.

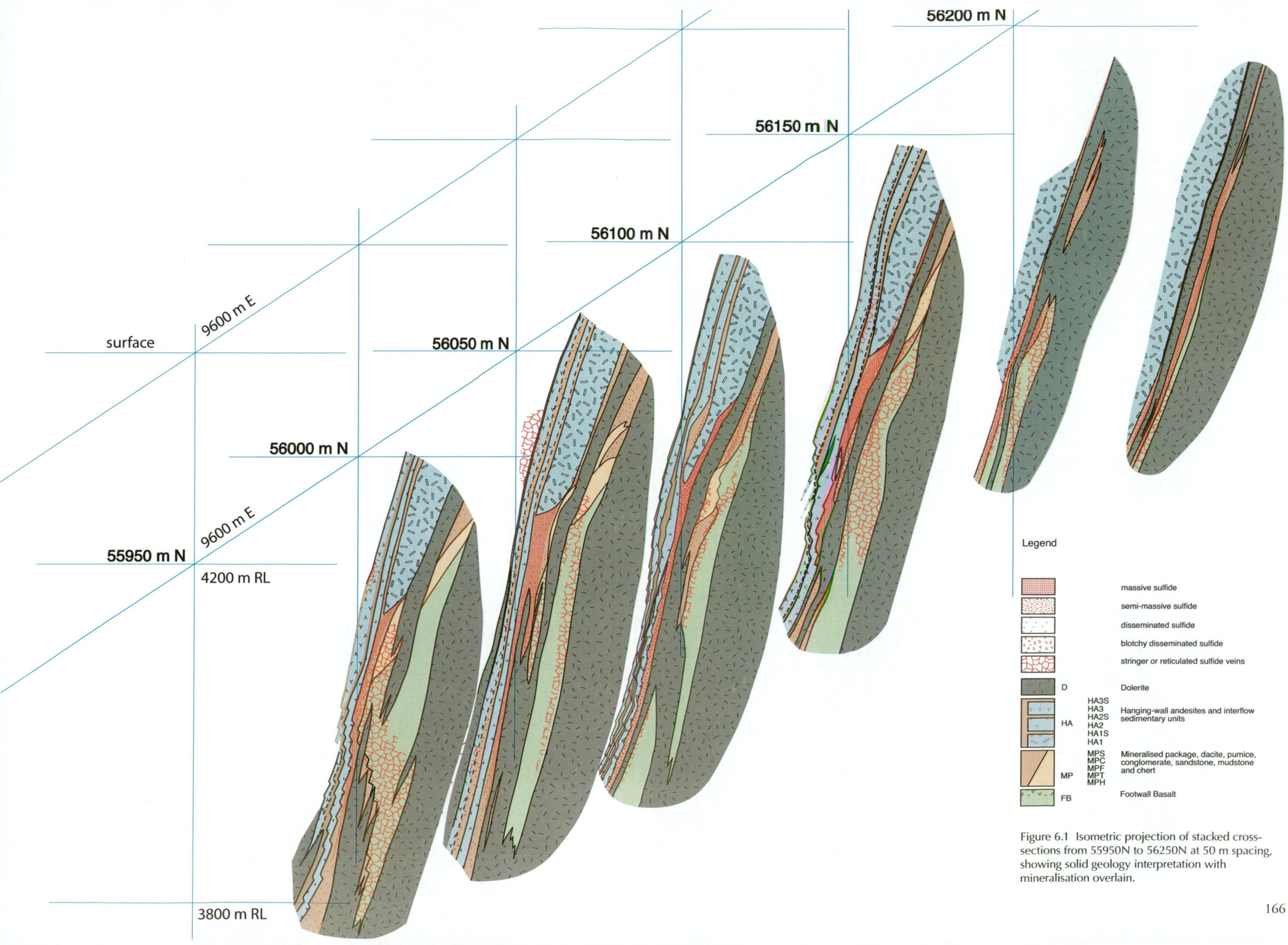

Figure 6.1 Isometric projection of stacked cross-sections from 55950N to 56250N at 50 m spacing, showing solid geology interpretation with mineralisation overlain.

6.2.2 Massive sulfide

The main massive sulfide ore type comprises pyrrhotite, pyrite and sphalerite in variable amounts. Locally, zones are rich in chalcopyrite and in rare zones magnetite is the dominant component. Zones rich in chalcopyrite appear to occur more commonly towards the base of the ore lens. The massive sulfide mineralisation occurs as three main types: massive or unbanded ore (Fig. 6.2a), banded ore (Fig. 6.2b) and durchbewegung ore (Fig. 6.2c). These types are all defined from hand-specimen ore samples and all three types are observed to grade into each other (Figs 6.2d and 6.2e). The percentage of each ore type is variable among the drillcores logged and in any one intersection one type may dominate. As drillcore is the only source of information, and only a selection of the drillholes were logged, interpretation by extrapolation of zones between drillholes is not meaningful at the scale of the individual ore-types, it is not possible to know the geometry i.e. the extent or continuity of these ore-type zones. The global resource for the massive ore is 1.37 Mt @ % 3.54 Cu, 11.45 % Zn, 0.74 % Pb, 126 g/t Ag (Jabiru Metals, pers comm 2009).

Massive ore

This ore type is massive in the sense that there is no preferred fabric orientation or banding apparent at the hand-specimen scale. It may be mono- or polymineralic, it may have an irregular, blebby or patchy texture, it may be dominated by pyrite, pyrrhotite, chalcopyrite or magnetite (Figs 6.3a and 6.3b), and it may comprise greater than 90 vol. % ore minerals or comprise as little as 50 vol. % of disseminated or blebby sulfide (Figs. 6.3c). These zones may be a part of a greater banded ore-type, in which the bands are thick (>30 cm) to the point of being unrecognisable in core logging.

Banded ore

In this thesis the banded ore is defined as massive sulphide with a banded or sub-parallel macrostructure of the ore minerals that is apparent at the hand-specimen scale, having band widths from millimetres to centimetres. It does not refer the fabric of the host lithology, which may show obvious primary bedding features as recorded in several lithofacies of the MP unit. The banded ore most commonly comprises alternating bands of pyrite, sphalerite and pyrrhotite; some pyrite bands are brecciated and incoherent. Less commonly narrow chalcopyrite-rich bands occur.

Durchbewegung ore

'Durchbewegung' is a term introduced to the English literature for deformation by Vokes (1969) after the usage in German by Ramdohr (1960). He described durchbewegung as a progression of processes involving disruption, separation, kneading, milling, and rotational movement of competent silicate rock and competent ore minerals within an incompetent sulfide matrix. Vokes (1969) indicated that the resultant rock would include

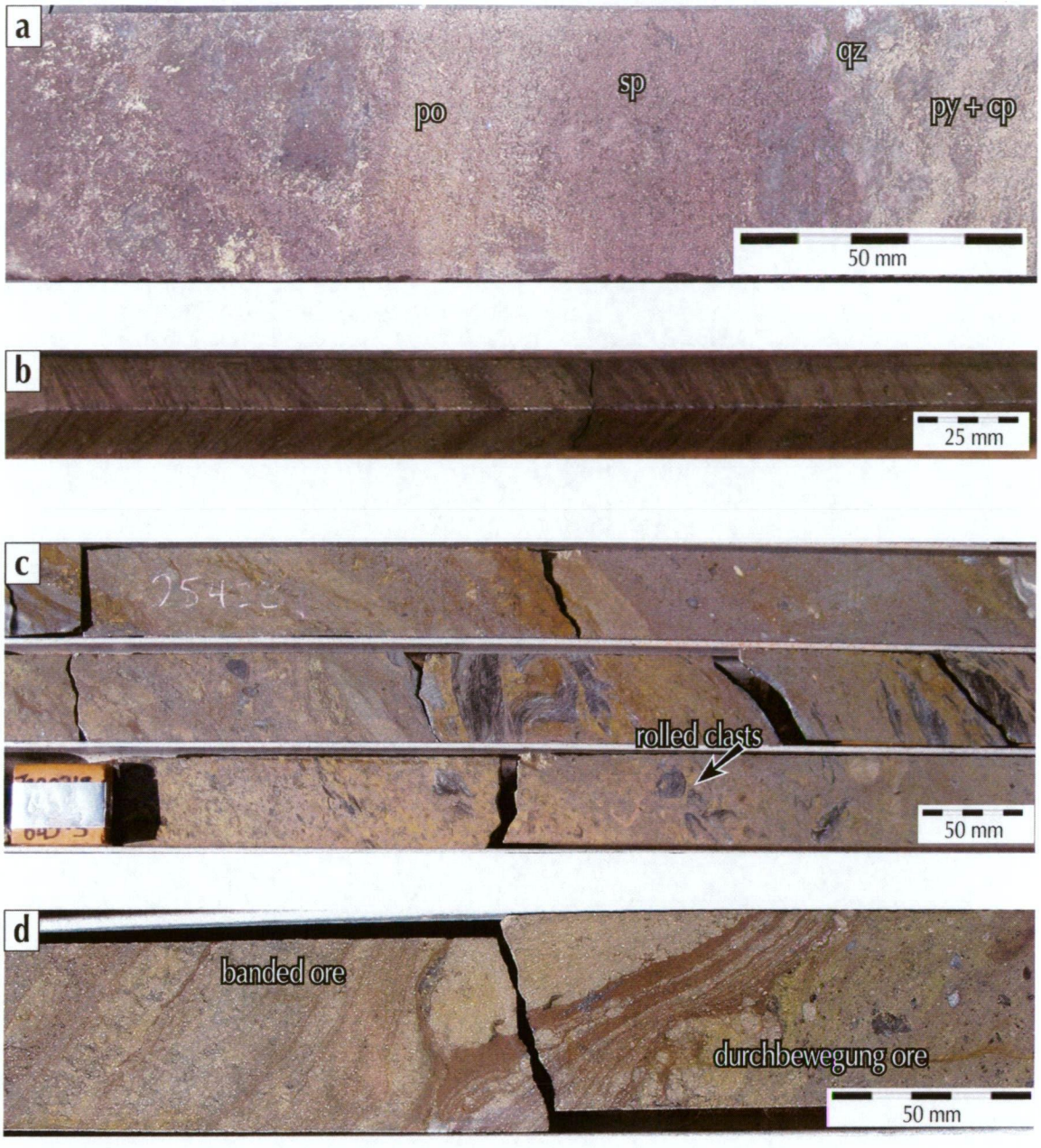

Explanation of annotations for photos and captions. The top is to the left in all core photos.

Ore minerals		Gangue minerals		Lithofacies	
py	pyrite	am	amphibole (tremolite-actinolite)	bas	basalt
cp	chalcopyrite	bt	biotite	bls	black shale
po	pyrrhotite	cb	carbonate	dac	dacite
sp	sphalerite	ch	chlorite	mds	mudstone
mt	magnetite	pl	plagioclase	cht	chert
ga	galena	pr	prenhite		
ap	arsenopyrite	qz	quartz	Other	
te	tetrahedrite/tennantite	se	sericite	ppl	plane polarised light
ge	geochronite	ti	titanite	rl	reflected light
		zo	zoesite/epidote	xp	crossed-polarised light

Figure 6.2 Massive sulfide ore types: a) massive or unbanded ore, with sphalerite, pyrrhotite and pyrite with chalcopyrite in quartz gangue, TBB0256 449.3 m; b) banded ore with narrow bands (<1–10 mm) of sphalerite, pyrite and pyrrhotite, TBD0235 472.8 m; c) durchbewegung ore with rolled and deformed gangue and pyrite clasts, TBD0218 645.3 m; d) single piece of core showing change from banded ore to durchbewegung ore, TBD0219b 542.8 m.

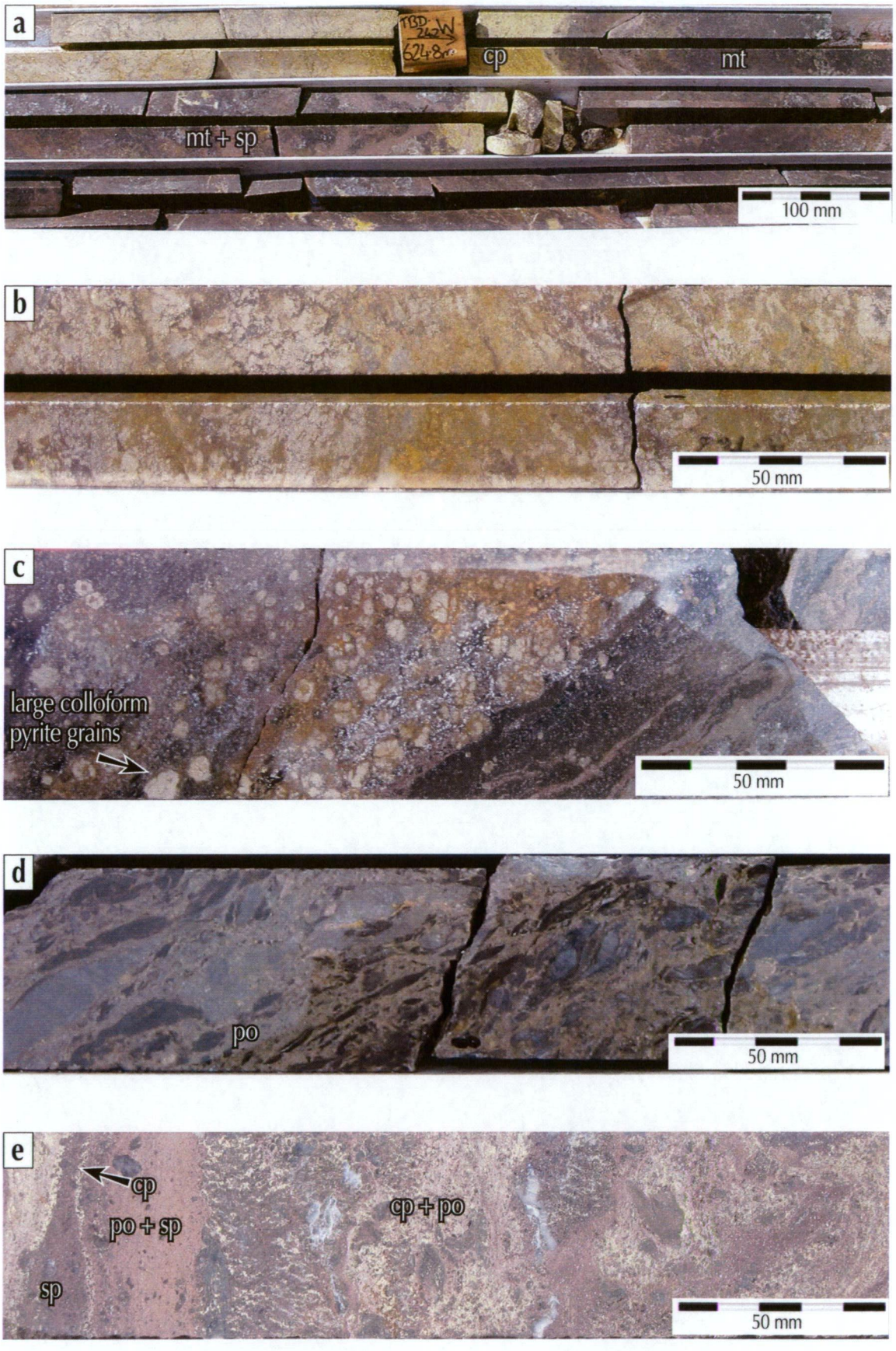

Figure 6.3 Massive sulfide ore types continued: a) massive ore, massive chalcopyrite sharply grades to massive magnetite with patches of sphalerite and rare chalcopyrite, TBD0242w 624.8 m; b) massive ore, patchy pyrite and pyrrhotite with minor sphalerite, TBD0209 536.7 m; c) massive ore with a blebby appearance, comprising colloform pyrite grains (up to 8 mm) among sphalerite, fine-grained pyrite and quartz gangue, TBD0256 472.4 m; d) durchbewegung ore dominated by pyrrhotite, domains showing different clast orientations are apparent, clasts comprise mudstone (black shale) and quartz, TBD0208 602.2 m; e) durchbewegung ore showing bands defined by different mixes of sulfides, TBD0256 449.6 m.

rootless fragments and rounded clasts of competent components studded throughout an incompetent matrix. He suggested that the overall process and the structure so formed was "very characteristic if, not unique, for sulfide deposits and ... met with very seldom in silicate or even carbonate rocks" (Vokes, 1969). Marshall and Gilligan (1987) classified durchbewegung as an internal feature of ore deposits, as distinct from piercement structures, which are external. They went on to redefine durchbewegung structure as a mixture, of secondary tectonic origin, composed of angular to rounded clasts of one or more competent materials in a matrix of predominantly different less competent material. In classic durchbewegung ore, the clasts may range from large blocks down to single crystals, may be contorted and disoriented, and may comprise silicate rocks and/or gangue and ore minerals (such as pyrite and magnetite); the matrix typically consists of one or more sulfides (such as galena, chalcopyrite, and pyrrhotite) (Marshall and Gilligan, 1989).

At Jaguar the durchbewegung ore is commonly dominated by a matrix of pyrrhotite (Fig. 6.3d), but locally sphalerite, and more rarely chalcopyrite also occur (Fig. 6.3e) as the dominant matrix sulfide. The clasts may be other sulfides or gangue and can comprise quartz, black shale, prehnite, chlorite-rich, pyrite or sphalerite (Figs 6.4a to 6.4g). In some bands dominated by sphalerite, the sphalerite comprises a tightly packed aggregate of rounded grains (Fig. 6.4g) which are interpreted as milled clasts. The clasts in the durchbewegung ore may be angular, subrounded or rounded, they may have internal strike slip features (Fig. 6.4h) or they may be rolled spiral accumulations (Figs 6.5a & 6.5b). Around some clasts, fibrous quartz has grown in the pressure shadows (Fig. 6.5c), and chalcopyrite appears to have preferentially moved into pressure shadows between clasts (Fig. 6.5d). The durchbewegung zones commonly show internal banding that creates sub-parallel to anastomosing fabrics (Figs 6.5e to 6.5h).

The presence of durchbewegung ore is common at the upper contact of the massive ore lens and it also occurs within the body of the massive ore. However, the distribution of the durchbewegung ore has not been mapped because of the limitations imposed by selective core logging.

Contacts

The upper contact of the massive sulfide lens is commonly sharp and generally deformed, with a pyrrhotite-dominated durchbewegung band generally underlying a band of contorted and deformed graphitic black shale with quartz veins (Figs 6.6a and 6.6b). This durchbewegung band is commonly narrow (10 - 30 cm) but locally reaches >1 m. An exception to this is the upper contact of the massive sulfide in drillhole TBD0243 on section 56200N, where the massive sulfide is conformably overlain by, and grades upwards into, narrow beds of laminated chert and finely-bedded sulfide-rich sediment (Fig. 6.6c). As discussed earlier, this part of the orebody is isolated from the major portion of the orebody

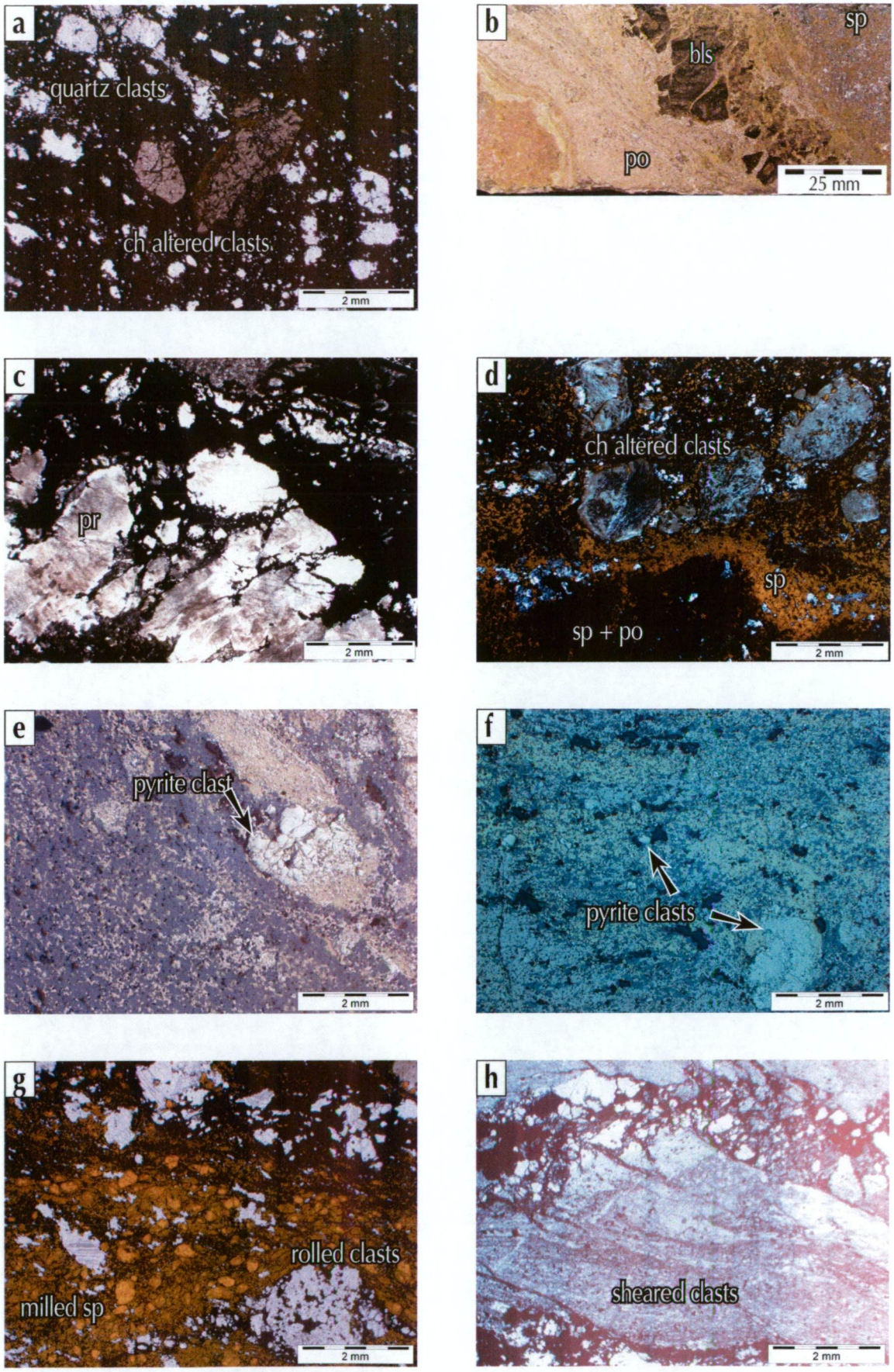

Figure 6.4 Durchbewegung clasts: a) quartz clasts and chlorite altered clasts in a matrix dominated by pyrrhotite, samp. 700410, ppl; b) brittle-fractured black mudstone clasts in banded durchbewegung ore, samp. 700413; c) clasts of prehnite, fractured but optically continuous (strained), samp. 700399, ppl; d) chlorite altered clasts, some showing rotated textures indicating crystallisation continued during deformation, in matrix dominated by chalcopyrite, with banded sphalerite and sphalerite plus pyrrhotite at bottom, samp. 700429, ppl; e) fractured colloform pyrite grains in banded durchbewegung ore, samp. 700113, rl; f) rolled and milled clasts of colloform pyrite, samp. 700426, rl; g) mixed clasts, some rolled clasted in durchbewegung band of milled sphalerite grains, samp. 7004169, ppl; h) sheared clasts, indicating simple strike-slip shearing, samp. 700411, ppl.

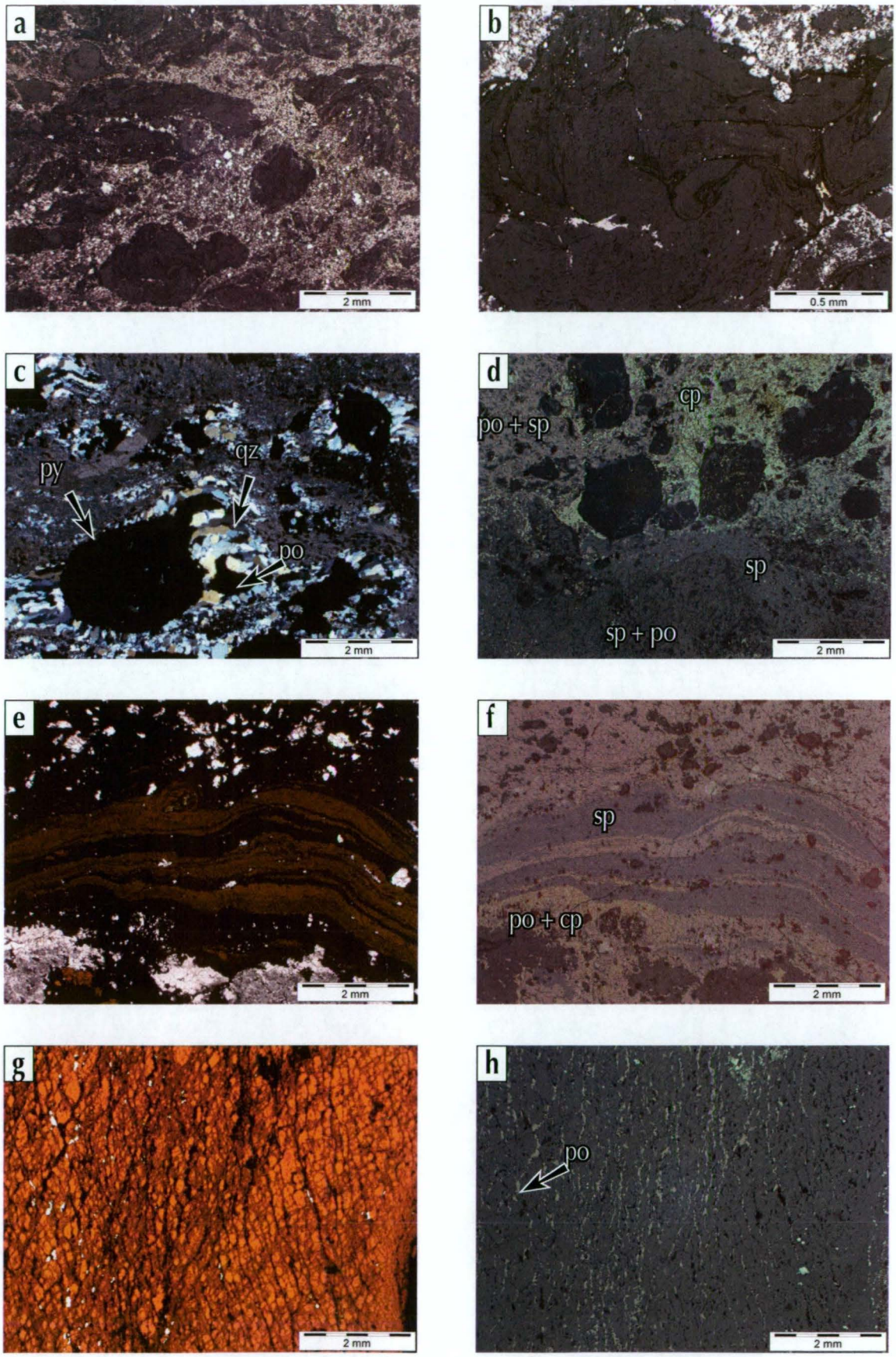

Figure 6.5 Durchbewegung texture: a) durchbewegung ore showing spiral formation of some clasts, samp. 700399, rl; b) close-up of clast showing rolled, spiral texture, samp. 700399, rl; c) quartz growing in pressure shadows around colloform pyrite in a gangue dominated band in durchbewegung ore, changes in long axis orientation demonstrate growth continued throughout deformation , samp. 700397, xp; d) clasts, some showing rotated textures indicating crystallisation continued during deformation, in matrix dominated by chalcopyrite around the clasts, with banded sphalerite and sphalerite plus pyrrhotite at bottom, samp. 700429, rl; e) and f) banded and duchbewegung ore, the spalerite rich bands have fewer clasts of gangue, samp. 700413, ppl and rl; g) and h) within a durchbewegung band, grains of sphalerite with pyrrhotite along grain boundary display an anastomosing shear pattern, samp. 700433, ppl and rl.

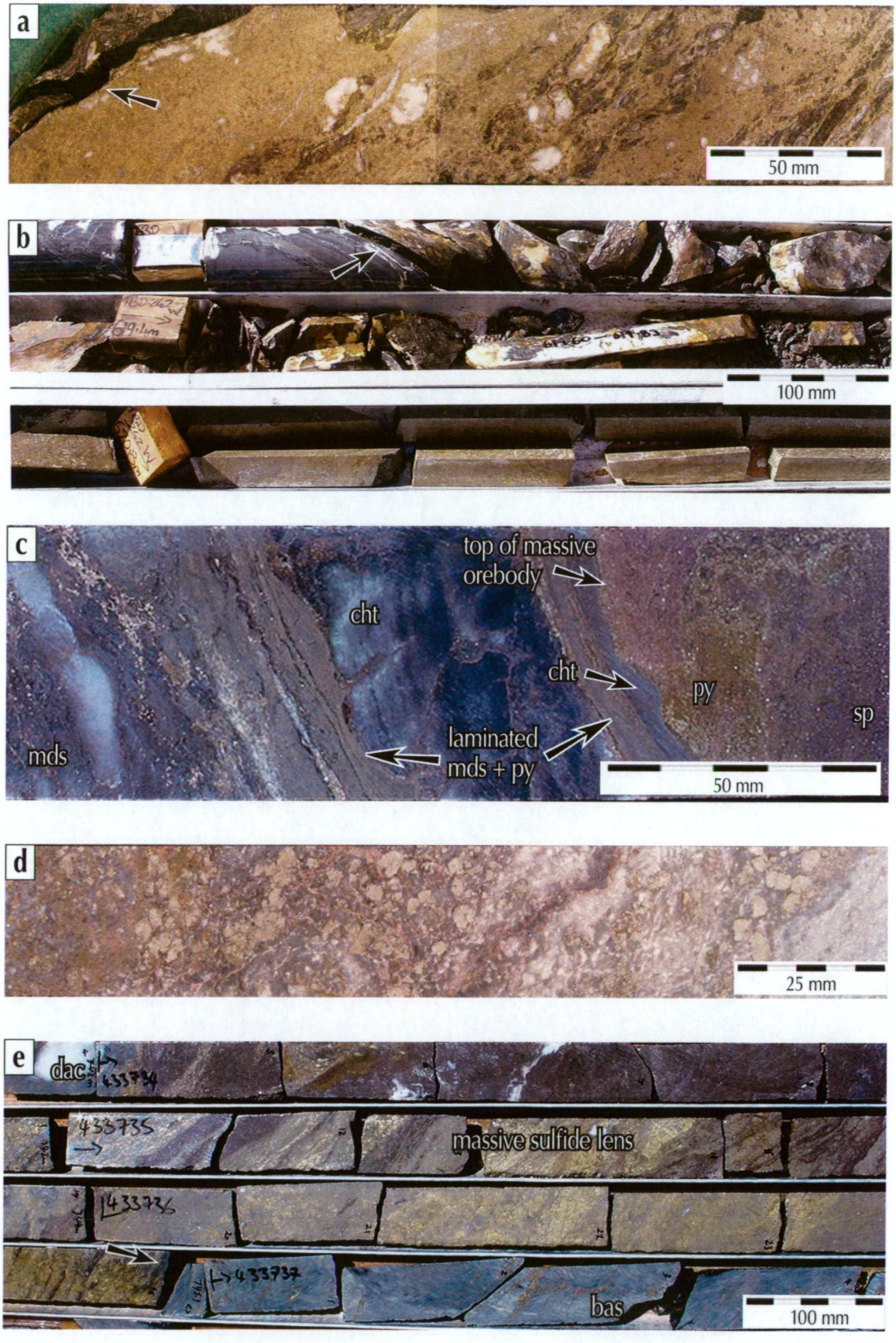

Figure 6.6 Contacts: a) upper contact of massive sulfide between pyrrhotite dominated durchbewegung ore and contorted black shale, TBD0239; b) upper contact of massive sulfide lens between durchbewegung ore and mudstone, durchbewegung ore grades downwards into massive ore, TBD0242w; c) sharp upper contact of massive sulfide between undeformed massive ore and chert, TBD0243; d) gradational contact at the base of massive sulfide into blebby, disseminated sulfide in pumice-rich breccia, which in turn overlies chert, TBD0256; e) sharp contact at base of massive sulfide lens between banded ore and stringer ore, 05TBDD003.

and appears to provide a least-deformed window into the original orebody textures.

The lower contacts of the massive sulfide lens can be sharp or gradational. In many of the logged holes the lower contact of the massive ore is sharp against a fine grained margin of a dolerite sill. In other places the massive sulphide grades into either blebby or disseminated sulfide or sulfide veins hosted by pumice-rich breccia facies (Fig. 6.6d), banded chert or volcanic mudstone facies. These contacts are commonly rich in sphalerite and or pyrite. The lower contact of massive sulfide can also sharply grade to vein or stringer mineralisation (Fig. 6.6e).

6.2.3 *Stringer veins*

The major zone of stringer vein mineralisation underlies and interdigitates with the massive sulfide lens. However, some zones of stringer mineralisation do occur in the Hangingwall Andesite unit and are also described here. The contacts between the massive sulfide and stringer mineralisation are commonly gradational but locally sharp contacts occur. The true dimensions of the main stringer zone remain unknown, obscured by the presence of dolerite sills in both the footwall and lower ore zones (Fig. 6.1). The global resource for the stringer ore is 84,000 t @ 5.24 % Cu, 1.05 % Zn, 0.06 % Pb, 30 g/t Ag (Jabiru Metals, pers comm 2009).

Within the Mineralised Package unit, stringer veins occur underlying and laterally adjacent to the lower massive sulfide in the dacite and dacite breccia facies, and the chert, pumice-rich and conglomerate facies . Most commonly, stringer veins occur in the Footwall Basalt unit, underlying the massive sulfide lens within the coherent, breccia and conglomerate basalt facies. More rarely, they occur locally in some areas of the hangingwall above the orebody.

Two styles of stringer mineralisation occur: 1) chalcopyrite-rich stringer which comprises a series of short (10–30 cm) disconnected veins commonly associated with intense, pervasive chlorite alteration and 2) a reticulated network (or stockwork) of narrow (<1 cm) veins and associated selvage alteration. Where the two styles are adjacent, they commonly have gradational contacts.

The chalcopyrite-rich stringer zones underlie the massive sulfide ore, and have lesser amounts of pyrite, pyrrhotite and sphalerite. The associated gangue minerals in the vein are quartz, sericite, carbonate and epidote/zoesite., and the veins are associated with intense, pervasive chlorite alteration, commonly to the level where all original rock texture has been obliterated. The zones with the most intense and pervasive chlorite alteration commonly have short, irregular, thick (5–30 mm wide by 10–30 cm long) chalcopyrite rich veins (Figs 6.7a, 6.7b, 6.7c and 6.7d).

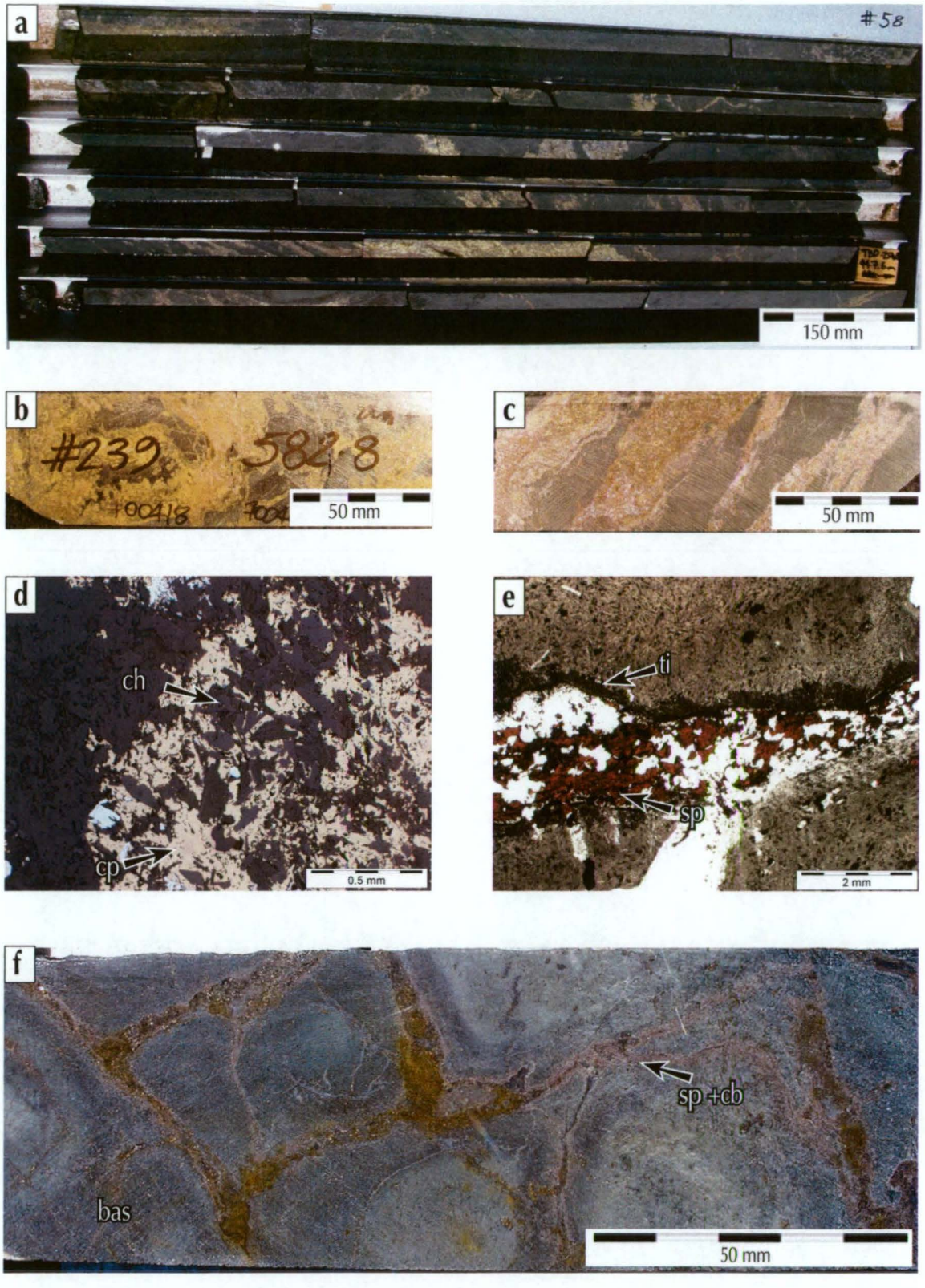

Figure 6.7 Stringer veins: a) Chalcopyrite-pyrite stringer veins in intense, pervasive chlorite alteration in Footwall Basalt, TBD0254 446 m; b) Chalcopyrite-pyrite veins in chlorite gangue in Footwall Basalt TBD0239 582.8 m; c) Chalcopyrite-pyrite-carbonate-quartz veins in chlorite in Footwall Basalt TBD0239 463.5 m; d) chalcopyrite-chlorite intergrowth in stringer vein, samp. 700418, rl; e) stringer vein in Footwall Basalt, sphalerite-quartz-carbonated cetre with titanite and zoesite along selvages, samp. 700276, ppl; f) reticulated pyrite-spalerite-carbonate veins in altered Footwall Basalt, TBD0235 517 m.

The zones of reticulated stringer mineralisation (Figs 6.7e and 6.7f) comprise narrow sulfide veins (1–8 mm) associated with a selvage (1 mm – 5 cm) style alteration. The sulfides may consist of pyrite, pyrrhotite, sphalerite or more rarely chalcopyrite, or a mixture of these minerals. The selvage style alteration, commonly comprising a mixture of quartz, carbonate and pyrite, envelops the sulfide vein, bleaching (or darkening) the rock, can result in a pseudo-brecciation texture, in which the kernels of this network are relatively unaltered. Only very rarely is this style of stringer veining associated with pervasive chlorite alteration. Deeper in the footwall, weak stringer zones of narrow (<1 cm wide), reticulated veins, comprising pyrite-sphalerite-carbonate veins, are locally developed.

The stringer zones developed in the hangingwall are not intimately associated with the massive sulfide. They occur locally and are associated dominantly with the volcaniclastic facies within the Hangingwall Andesite (HA) unit. They do extend into the adjacent coherent facies. These zones are at approximately the same position, between 4100 and 4250 m RL, although not at the same stratigraphic level (Fig. 6.1). They occur on sections 55950 N to 56100 N, and have a dip extent up to 50 m, as seen on cross-section 56000 N. If they do correlate along strike it must be related to a cross-fracture as relationships are not obvious. They occur above the termination of the HA1 sub-volcanic lava, and where the HA unit is thickest. On section 55950N there is a zone within the top of the HA3 lava and the overlying HA3S. Another zone occurs in the HA3S and extends into the lowest unit of the Hangingwall Basalt. Stringer veins also occur at the top of the HA2 lava and the HA2S overlying on sections 56050N and 56100N. These zones of stringer veins commonly comprise reticulated networks of millimetre-thick, veins of pyrite-sphalerite-carbonate with minor pyrrhotite and rare chalcopyrite. These particular veins are commonly associated with a weak, patchy carbonate alteration of the wallrock and local disseminated sulfide-carbonate blebs (Figs 6.7e and 6.7f).

6.2.4 *Breccias containing sulfide-rich clasts*

Breccias with sulfide-rich clasts occur peripheral and down dip to the main massive sulfide ore lens and are part of the MCP unit. They occur on sections 55900 N to 56100 N. The overall geometry of these breccias is wedge shaped, the bedding is typically chaotic and overall shows normal grading. The distribution of sulfide-rich clasts is not mappable and the total volume was not observed to exceed 5%. The clasts vary from sub-angular to sub-rounded, and range in size from millimetres to less than two centimetres. The alteration within these breccias is variably low-intensity, patchy to pervasive mixtures that may include sericite, carbonate, quartz and chlorite. The sulfide-rich clasts are not associated with any increase in alteration. In the drillholes logged this material never attained near ore-grade.

6.3 Ore minerals and mesoscopic to microscopic textures

The majority of the ore minerals examined were subject to varied amounts of strain. Commonly the Jaguar ore has been deformed and or recrystallised. Within parts of the Jaguar orebody, the two most competent opaque minerals, pyrite and magnetite, and arsenopyrite where present, have retained some primary, (pre-deformation and pre-regional metamorphic) textures but commonly show evidence of cataclastic deformation. Chalcopyrite, sphalerite, pyrrhotite and galena all have deformed and recrystallised more readily than magnetite and pyrite and at Jaguar; most primary textures have been destroyed in these minerals.

6.3.1 Metamorphism and deformation of sulfides: a brief review

Vokes (1969), Gilligan and Marshall (1987), Gilligan and Marshall (1993) and Craig and Vokes (1993) reviewed the metamorphism of pyrite and pyrite ores. The high thermal stability of pyrite (742°C; Kullerud and Yoder, 1959), combined with its high physical strength means pyrite can survive all but the highest grades of metamorphism (Vokes, 1969). Magnetite and arsenopyrite are also high-strength minerals and can display similar cataclastic behaviour to pyrite (Pedersen, 1980; Frater, 1985a) whereas chalcopyrite, sphalerite, pyrrhotite and galena all deform and recrystallise more readily than magnetite and pyrite, and therefore most primary texture is destroyed in the former minerals.

Brittle deformation in pyrite is common where pyrite is dominant or where pyrite euhedra are forced against one another (Graf and Skinner, 1970; Gilligan and Marshall, 1987). Cox (1987) notes that in low- to medium-grade metamorphic environments pyrite has deformed by pull apart across intra-granular extension fractures, and that these fractures can be filled by silicates, carbonates or sulfides. As metamorphic grade increases, the pyrite fabric becomes coarser, because of a tendency to recrystallise (Vokes, 1969; Mookherjee, 1976). This can include the development of porphryblastic, poikiloblastic and helicitic structures (Rickard and Zweifel, 1975; Mookherjee, 1976).

The recrystallisation manifests as development of polycrystalline aggregates. In annealed polycrystalline aggregates, all grains will adjust their shapes to minimise the total area of interface subject to the requirements of interfacial energies and space filling. Thus all boundaries must be interfaces with no voids permitted. When an aggregate of grains has adjusted itself in this way, its structure may be said to have matured and the configuration is similar to foam. The development of such mature structures in solids is part of the process known as annealing (Stanton, 1972). In foam textures the majority of grains meet in threes along lines, and this point is known as a triple junction. If the three grains are not the same mineral then the dihedral (interfacial) angles at the triple junction will not

be equal. Where sulfide ores have been annealed the grain shapes are characterised by reproducible dihedral angles attributed to characteristic interfacial boundary energies. The presence and quantity of other sulfides or gangue will determine the deviation from 120° dihedral angles (Stanton, 1964 and 1972).

6.3.2 Mineralogy

The dominant minerals of the ore are pyrite, pyrrhotite, sphalerite and chalcopyrite. Locally magnetite comprises a major ore component. Galena and arsenopyrite are present as minor phases and trace amounts of tetrahedrite-tennantite and geochronite have also been identified. Photomicrographs showing the diversity in relationships and textural forms of the ore minerals are located in the following sections on ore textures. The major gangue minerals are quartz, chlorite, albite, calcite, sericite (white mica) with lesser amounts of titanite, biotite, epidote-zoesite, tremolite-actinolite and rare prehnite.

Pyrite

Pyrite occurs in the massive sulfide ore and in the stringer vein mineralisation. Disseminated pyrite is common in bedded intervals within, and adjacent to massive sulfide ore, or stringer veins. In the FB and lower part of the MP the pyrite is typically disseminated within strongly chlorite altered wallrock. These pyrite grains (up to 8 mm) are euhedral to anhedral to coloform blebs. In the upper part of the MP the pyrite is typically disseminated in weakly altered (sericite, carbonate or chlorite) wallrock and the grains have similar form. Above the massive sulfide very fine (5–15 micron) euhedral grains appear parallel to bedding along with larger, (1–8 x 0.5–2 mm) bedding parallel crustiform pyrite nodules.

In the massive sulfide ores, pyrite occurs in a variety of textural forms: euhedral, skeleton-shaped fishbone, dendritic, crustiform, nodular, and colloform.

Pyrrhotite

Pyrrhotite is ubiquitous throughout the orebody and locally is the main sulfide in the durchbewegung ore. It commonly occurs as polycrystalline aggregates or as scattered grains. It also occurs along grain boundaries within massive sphalerite and infills fractures and cataclastic pull-aparts in pyrite. Disseminations of lath-like bladed grains and interlocking networks of tabular grains from 0.1–0.2 mm occur in bedded facies, whereas larger isolated blades (0.15–0.3 x 1–1.8 mm) are associated with colloform pyrite within laminated chert layers in the upper and lower zones of the massive sulfide.

Sphalerite

Sphalerite occurs in the massive sulfide ore, in the stringer veins and as fine-grained,

disseminated euhedral grains (0.01–0.04 mm). The euhedral grains are disseminated in altered wall rock which occurs in pockets within the lower zones of the massive sulfide. The sphalerite varies in colour from a honey brown to a deep red in transmitted light, but any textural relationship to colour is not apparent. It most commonly occurs as polycrystalline aggregates. In the massive sulfide ores, it occurs in durchbewegung bands in association with pyrrhotite. The grain form in these bands varies from rounded grains to recrystallised foam-textured polycrystalline aggregates. It also occurs as infill in skeleton-shaped and colloform pyrite grains. In the stringer veins it occurs as polycrystalline aggregates or euhedral grains scattered among quartz.

Chalcopyrite

Chalcopyrite occurs within the massive sulfide as polycrystalline aggregates and scattered irregular grains (<0.2 mm). It occurs in fractures and in the interstices of skeleton-shaped pyrite grains, along the grain boundaries of sphalerite, and very rarely along lattice plains within individual sphalerite grains. It also occurs in pressure shadows around pyrite grains and gangue clasts in the durchbewegung ore.

Magnetite

Magnetite is not widespread in the core logged and observed occurrences were limited to drillholes intersecting section 56100N. Where it does occur it can comprise a major component of the ore. In drillhole TBD0242W magnetite occurs in massive form in intervals up to 40 cm wide. It also occurs intergrown with chalcopyrite and/or sphalerite as polycrystalline aggregates in similar width intervals. The massive magnetite is made of granular (0.04–0.1 mm), commonly inclusion-rich (spongy) and bladed, skeletal textural forms (0.01–0.05 x 0.1–0.4 mm). These textural types locally transition and coalesce. Magnetite also occurs as isolated subhedral or as botryoidal grains in the nucleus of colloform pyrite grains.

Galena

Galena is an accessory occurrence in massive or banded sphalerite, in association with pyrrhotite, where it occurs along grain boundaries or as rims around rounded sphalerite grains. Galena also occurs as fill in interstices of skeleton-shaped pyrite grains, commonly in association with chalcopyrite. It also occurs locally in association with chalcopyrite inclusions in layers within colloform pyrite.

Arsenopyrite

Arsenopyrite occurs as disseminated euhedral grains that range from 0.02–0.2 mm. Although arsenopyrite is present in only trace abundance it is observed in several localities, commonly within sedimentary facies at the lateral margins of the massive sulfide lens. It also occurs immediately above the ore in conformable sediments overlying the ore in the

undeformed zone on section 56200N. It is most commonly associated with pyrrhotite but is also associated with galena and sphalerite.

Tetrahedrite-tennantite

Tetrahedrite-tennantite always occurs in association with galena and commonly sphalerite, pyrrhotite and arsenopyrite. It most commonly occurs as irregular shaped grains within polycrystalline aggregates of galena, tetrahedrite-tennantite, sphalerite and pyrrhotite, plus euhedral arsenopyrite. It is also associated with galena and pyrrhotite in sphalerite bands in durchbewegung ore. The grain size reaches up to 0.04 mm.

Geochronite

Geochronite always occurs in association with galena, arsenopyrite and commonly sphalerite and pyrrhotite. Where it occurs it is commonly irregular shaped grains within polycrystalline aggregates. The grain size reaches 0.1 mm.

Quartz - silica - chert

The quartz grains in massive, durchbewegung and vein sulfide are typically coarse-grained ranging up to 0.1 mm. Most commonly quartz grains are equant and anhedral (Fig 6.8a) but sutured grain boundaries occur in places. Where quartz occurs in pressure shadows around durchbewegung clasts it is typically fibrous and shows deformation lamellae that follows the deformation foliation. (Fig 6.5c).

The use of 'chert' in this thesis always implies primary silica, that formed on the sea-floor. The now recrystallised chert always comprises equant, anhedral grains that may range in size from 0.02 to 0.15 mm. Commonly it exhibits a grain size layering.

Chlorite

Chlorite is the main gangue mineral in the stringer zone and the lower massive sulfide zone. It can be intense and pervasive, or patchy and selective, and can display sharp alteration fronts. Chlorite occurs in two main forms, as granular interlocking mosaics or as euhedral and fibrous mosaics. Distinct birefringent colours (purple-blue and brown) and patterns indicate two varieties of chlorite. Chlorite commonly occurs with carbonate and titanite and is locally intergrown with or overprints biotite. (Figs 6.8b, 6.8c, 6.8d, 6.8e, 6.8f, 6.9a, 6.9b, 6.9c and 6.9d).

Carbonate

Carbonate alteration is widespread. Like chlorite it can vary between an intense and pervasive distribution, to patchy and selective, and is commonly associated with chlorite and or sericite. It is a common component in the stringer veins (Figs 6.8a, 6.8g, 6.8h, 6.9a and 6.9d).

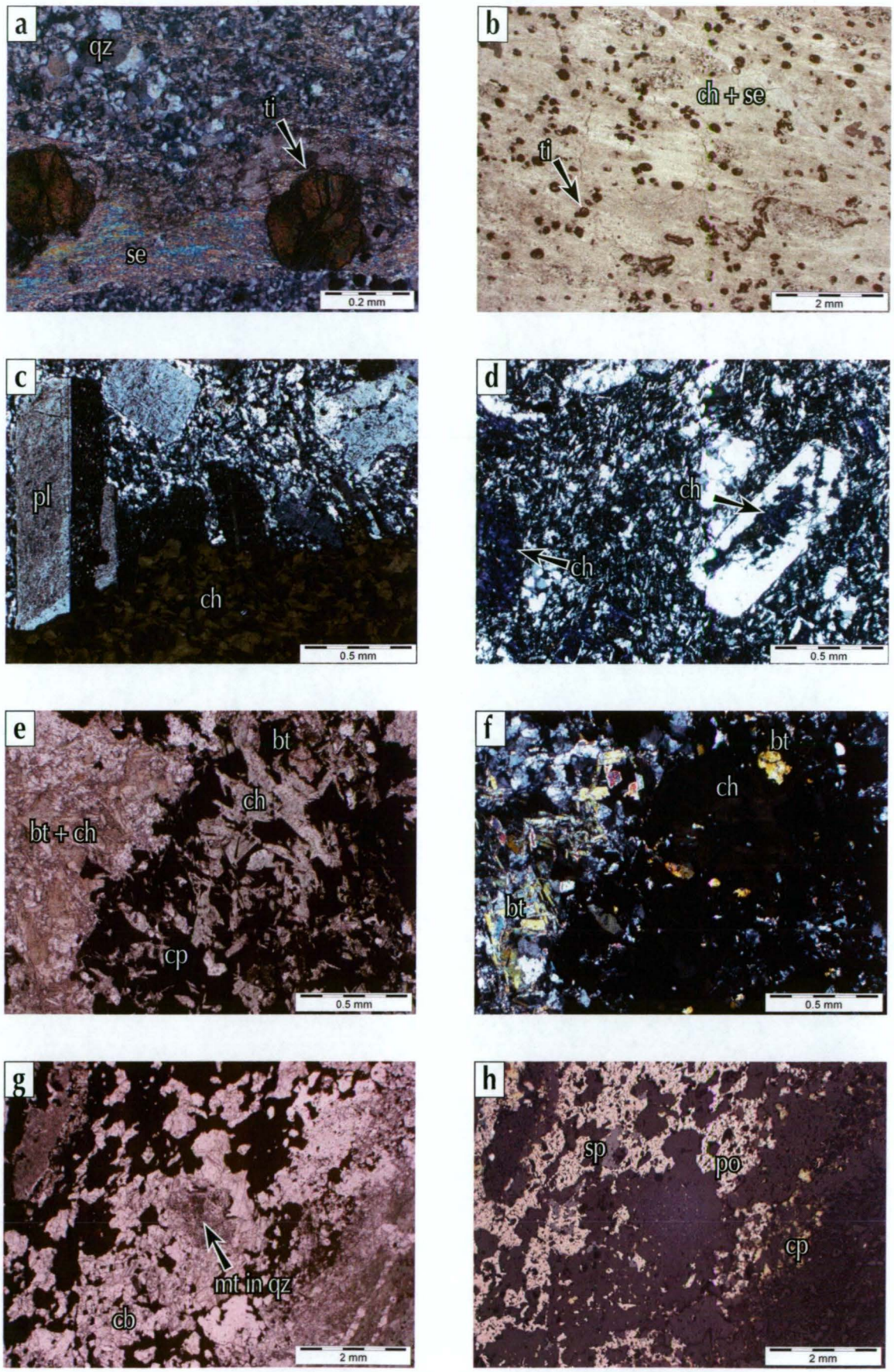

Figure 6.8 Gangue minerals: a) sericite-titanite alteration in chert, samp. 7000013, xp; b) chlorite-sericite-titanite alteration, samp. 7000195, ppl; c) chlorite alteration front in coherent dacite, samp. 7000179, xp; d) blue birefringent chlorite replacing plagioclase in altered dacite in MP, samp.700180 xp; e) and f) chalcopyrite-chlorite in stringer vein with selvage biotite-chlorite-carbonate in basalt breccia, (see also Fig 6.7d) samp. 7000418, ppl and xp; g) and h) pyrrhotite-chalcopyrite-carbonate stringer vein with bleb of quartz with very fine-grained magnetite bipyramidal grains, in chloritised basalt breccia, samp. 7000416, ppl and rl.

Sericite (fine white mica)

Sericite is ubiquitous throughout the alteration, and shows a wide range in intensity. It commonly occurs as fine-grained cryptocrystalline intergrowths with quartz, and in association with other abundant gangue minerals i.e. quartz, carbonate, chlorite and titanite. (Figs 6.8a, 6.8b and 6.9d). Less common are zones where there is sub-parallel development of fibrous grains, that possibly developed in response to deformation.

Biotite

Although not a major gangue mineral, biotite is in places associated with either chlorite or carbonate. Locally within durchbewegung bands deformed blades of biotite occur intergrown with chalcopyrite or more rarely sphalerite (Figs 6.8d, 6.8e, 6.8f, 6.9a, and 6.9b).

Amphibole (tremolite-actinolite)

Rare euhedral prisms (0.05–0.15 mm) occur most commonly associated with annealed chalcopyrite (Figs 6.9e and 6.9f) within the durchbewegung ore.

Zoesite - epidote

Euhedral zoesite grains are associated predominantly with stringer veins, developed predominantly along the selvages that locally extend into the wall rock. They also occur as rare clusters of gangue within massive sulfide. They do not occur in areas with strongly developed durchbewegung fabric. (Figs 6.9g and 6.9h).

Prehnite

Large grains (0.5–2 mm) of prehnite are observed in a single, coarse-grained occurrence in gangue in a narrow band of durchbewegung ore (Fig. 6.4c).

Titanite and other Ti rich minerals

Titanite is ubiquitous throughout the deposit, commonly associated with chlorite. It occurs commonly as scattered anhedral grains (0.05–0.2 mm) in altered wallrock. These grains can display radial growth and commonly are nucleated on diamond-rhomb shaped cores. Isolated diamond-shaped euhedra occur and in places titanite is concentrated along stylolites, within sericite-chlorite alteration. These stylolites most likely represent alteration fronts resulting from fluid–rock interaction processes. In addition titanite grains locally concentrate in patches along selvages of stringer veins (Figs 6.8a, 6.8b, 6.9b and 6.9d).

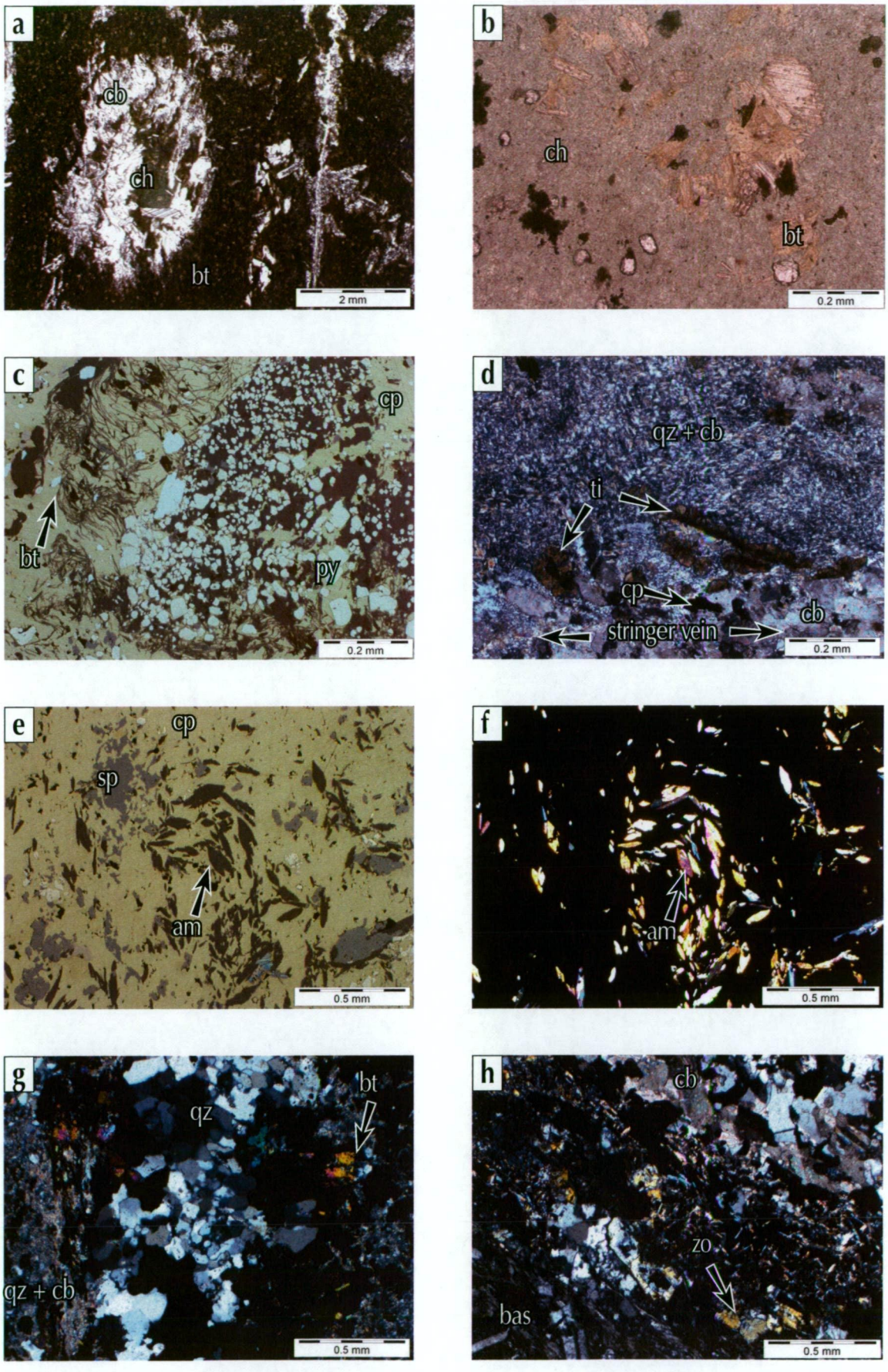

Figure 6.9 Gangue minerals continued: a) biotite-carbonate-chlorite alteration in altered dacite, samp. 700369, ppl; b) chlorite-biotite alteration in basalt breccia, samp. 700406, ppl; c) durchbewegung ore, chalcopyrite with biotite needles, rare sphalerite plus pyrrhotite and idiomorphic pyrite, samp. 700427, rl; d) titanite in chlorite-sericite-biotite groundmass adjacent to carbonate stringer vein, samp. 700417, xp; e) and f) durchbewegung ore, massive chalcopyrite around a contorted swirl of euhedral tremolite-actinolite grains, samp. 700415, rl and xp; g) transect across stringer vein in mudstone, chlorite-biotite selvage alteration, samp. 700008, xp; h) zoesite in stringer sulfide vein in basalt breccia, samp. 700113, xp.

6.3.2 Primary textures (pre-deformation)

Well preserved primary textures occur at the northern end of the massive orebody in drillholes TBD0243 and TBD0209 on section 56200N. In TBD0243 the top of the massive sulfide (Fig. 6.10a) shows primary colloform textures, in a chert-pyrite intergrowth which grades upwards into a narrow band of chert and then to graphitic mudstone with disseminated fine-grained, euhedral, zoned pyrite grains, plus crustiform nodules (Fig. 6.10b). Primary textures in sulfides are also observed in some stringer veins and within zones of disseminated or blebby sulfides (in volcaniclastic facies at the lateral peripheries to massive ore, and beneath massive ore at the base of the Mineralised Package unit (MP) within the Laminated MP (MPS), the Pumiceous MP (MPP) and basal chert (MPH) units).

Bladed grains

In places, both pyrrhotite and magnetite occur in bladed form. Long bladed grains (0.15–0.3 x 1–1.8 mm) of pyrrhotite (Figs 6.11a, 6.11b and 6.11c) coexist with undeformed colloform pyrite-chert intergrowths towards the top of the MP. Bladed, or lozenge-shaped pyrrhotite grains (<0.4 mm) also occur among chert gangue (Figs 6.11d) towards the base of the massive sulfide lens in TBD0209. Many of these grains are slightly prism shaped, with one end slightly wider than the other. Pyrrhotite also occurs as crudely aligned fine-grained (0.05–0.2 mm) scattered tabular grains or more rarely as an interlocking network, within chlorite–biotite-altered fine-grained mudstone (MPS) (Figs 6.11e).

Rare instances of bladed pyrite (Figs 6.11f) grains occur among spongy pyrrhotite and quartz in stringer veins in the footwall basalt. The blades of pyrite are more wedge-shaped than the pyrrhotite bladed grains.

Randomly oriented blades of magnetite, in places showing a 'boxwork' texture occur among chert gangue in association with chalcopyrite, pyrrhotite and pyrite (Figs 6.11g and 6.11h).

Colloform

Colloform texture, sometimes referred to as botryoidal or reniform depending on scale (e.g., Ramdohr, 1980) is common in pyrite grains at Jaguar (Figs 6.12a, 6.12b and 6.12c), although most instances show some evidence of later cataclastic fracture or breakup. Towards the top of the massive sulfide body in drilholes TBD0243 and TBD0209, colloform intergrowths of pyrite and chert (Figs 6.11a, 6.11b, 6.11c and 6.12c) are locally preserved with no overprinting deformation textures. Locally, cockade texture overgrowth occurs on the rims of some colloform grains (Fig. 6.12d). Extended sub-parallel bands of rhythmic colloform pyrite are less common (Fig. 6.12e). Within some colloform pyrite grains, rare zoned bands of chalcopyrite and galena (Figs 6.12c and 6.12d) or sphalerite

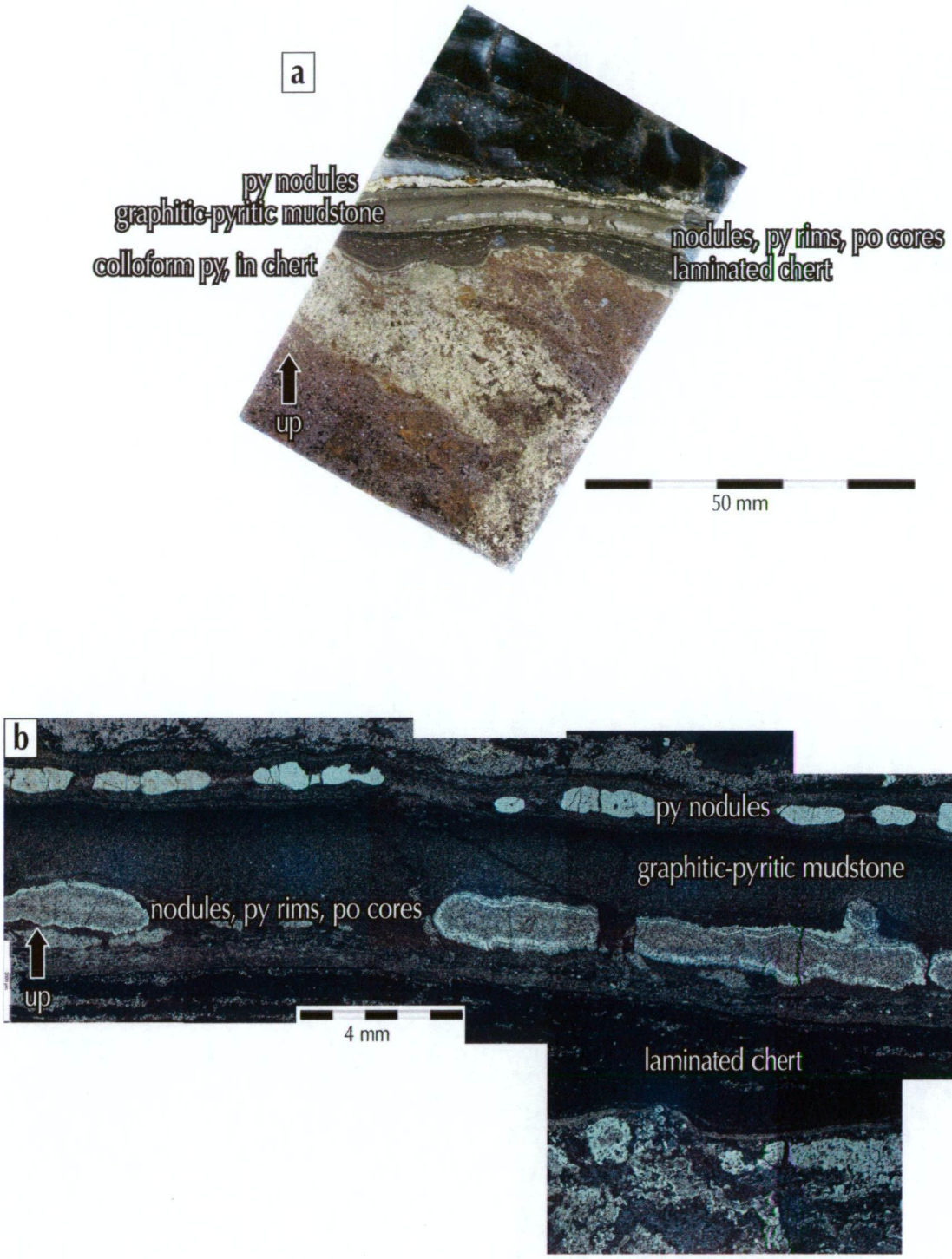

Figure 6.10 Undeformed top of ore lens: a) top of massive sulfide, patches of sphalerite and colloform pyrite overlain by laminated chert then by laminated, graphitic-pyritic mudstone with pyrite-pyrrhotite nodules, in turn overlain by weakly brecciated laminated chert, TBD0243 579.2 m, scan of polished section; b) microscopic detail of same interval, colloform pyrite overlain by laminated chert, overlain by laminated, pyritic mudstone with pyrite-pyrrhotite nodules, TBD0243 579.2 m, composite photomicrograph, rl.

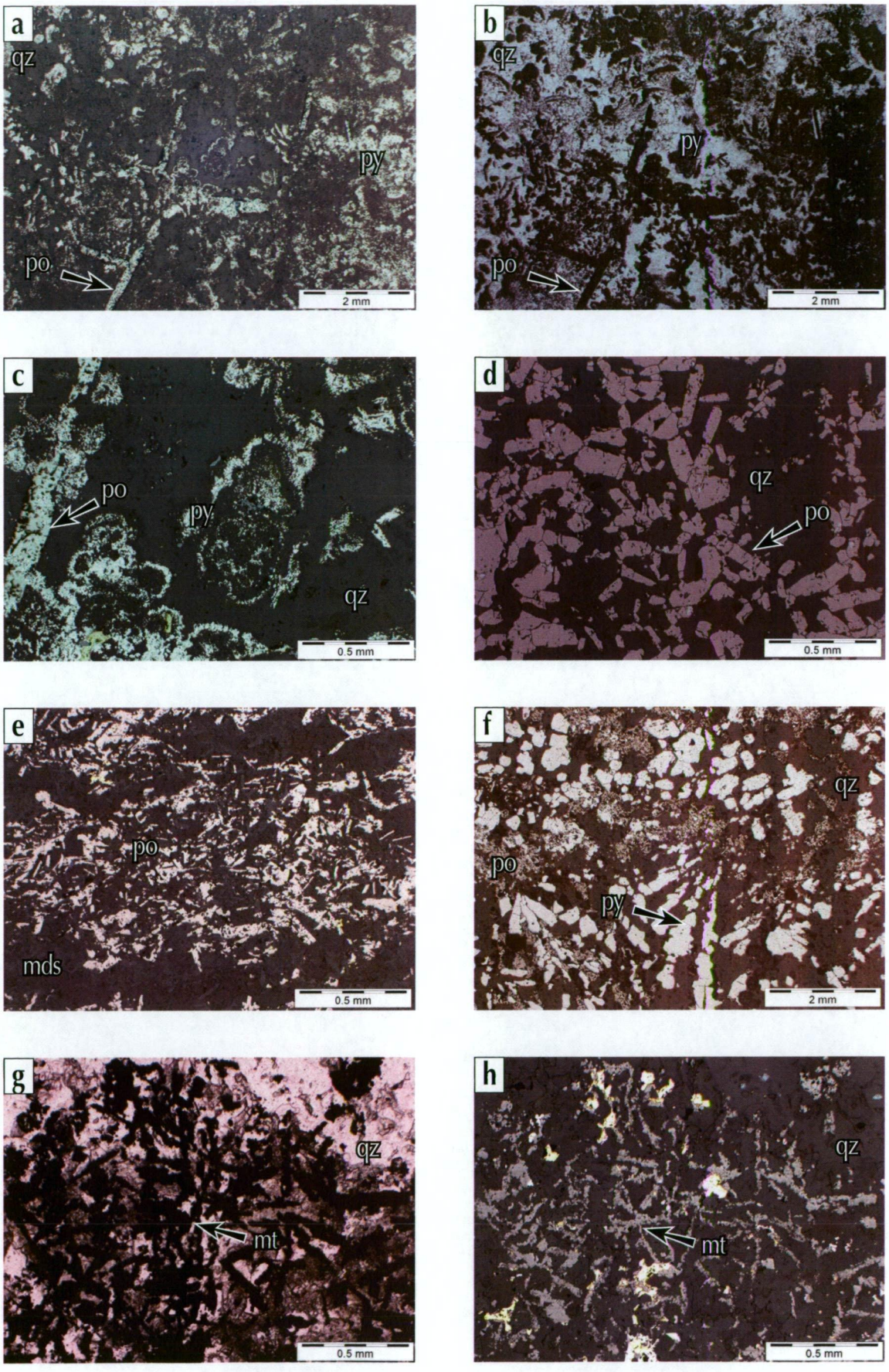

Figure 6.11 Primary ore textures - bladed grains: a) and b) bladed pyrrhotite among colloform intergrowth of chert and pyrite, samp. 700431, rl and ppl; c) close up of bladed pyrrhotite among colloform pyrite grains, samp. 700431, ppl; d) laths of pyrrhotite, that have a slight taper, in chert beneath massive sulfide ore, samp. 700388, rl; e) fine laths of pyrrhotite, disseminated in chloritised mudstone close to top of the MP, samp. 700443, rl; f) tapered blades of pyrite in a radial form, plus seived pyrrhotite and quartz in stringer vein in basalt beneath the massive sulfide, samp. 700417, rl; g) and h) skeletal laths of magnetite, plus minor chalcopyrite in chert matrix, samp. 700428, ppl and rl.

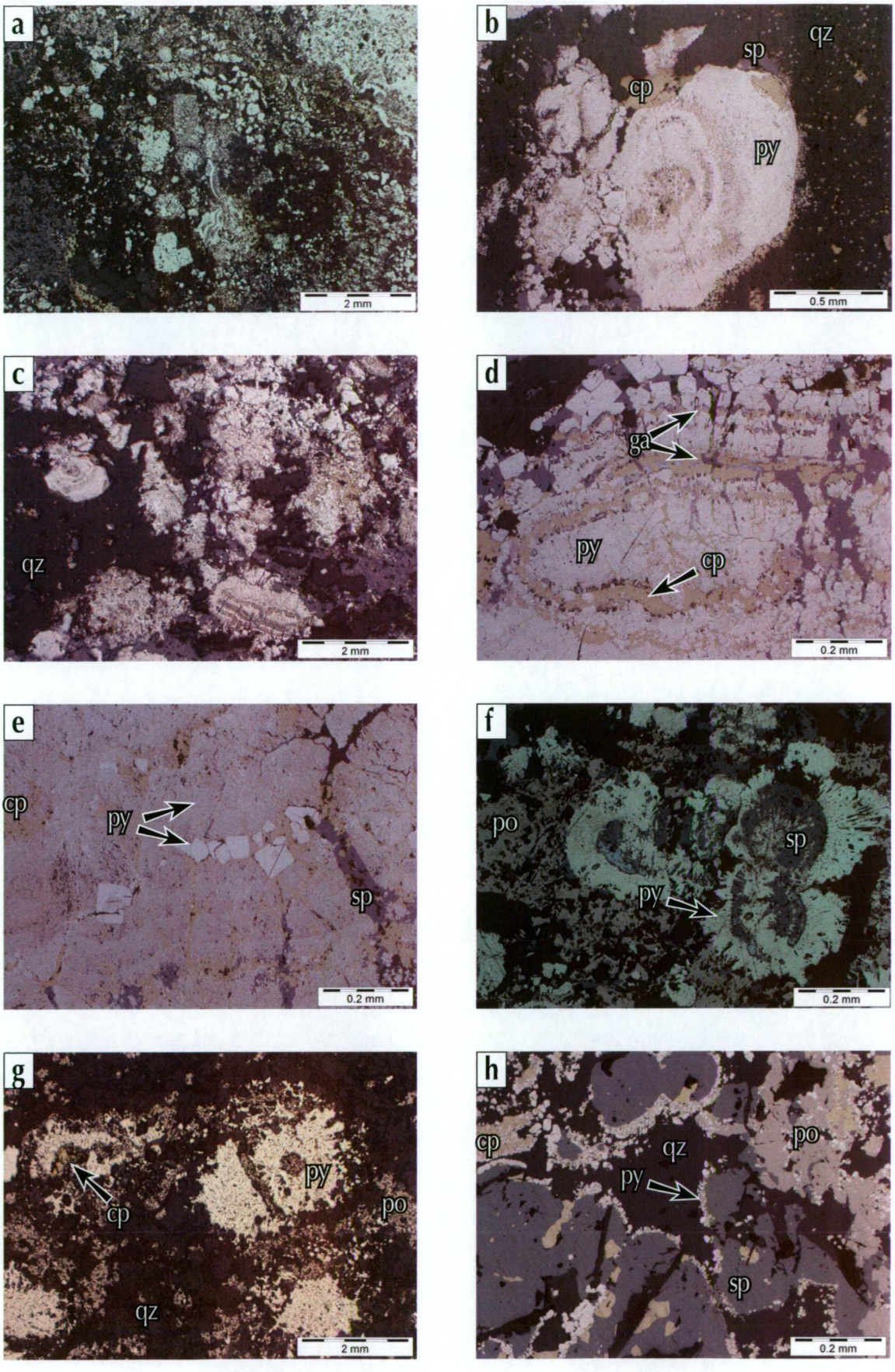

Figure 6.12 Primary textures - colloform grains: a) colloform grains and bands among chert at the very top of the massive sulfide body, an enlargment of the samples in Fig. 6.10, samp. 700473, rl; b) colloform pyrite grain, with chalcopyrite-rich bands, free growing in chert, samp. 700385, rl; c) samp. 700385, rl; d) colloform pyrite with cockade bands of chalcopyrite and galena, samp. 700385, rl; e) colloform banding in pyrite, overgrown with porphryblastic pyrite, samp. 700464, rl; f) colloform sphalerite overgrown with colloform pyrite, among pyrrhotite and quartz gangue, samp. 700473, rl; g) blebby sulfide beneath grades to massive ore, recrystallised coloform pyrite grains among pyrrhotite, rare chalcopyrite and quartz, samp. 700446, rl; h) botryoidal sphalerite with cockade pyrite rims, among pyrrhotite and chalcopyrite, samp. 700435, rl.

(Fig. 6.12f) occur. In the lower part of the orebody in TBD0256 (section 56100 N) zones of 'blebby' (up to 8 mm) sulfides occur in the volcanic breccia and sandstone facies (Figs. 6.12g, 6.3c and 6.6d). These 'blebs' are large colloform pyrite grains.

In places, clusters of botryoidal sphalerite with cockade pyrite rims (Fig. 6.12h) coexist with colloform pyrite. In addition, sphalerite occurs as central cores within colloform pyrite (Fig. 6.13a).

Although limited in extent, small colloform grains of magnetite coexist with subhedral magnetite grains in a chert gangue (Fig. 6.13b) where locally, central cores of magnetite are rimmed with colloform pyrite (Fig. 6.13c).

Nodular

Nodular pyrite grains (up to 1 x 4 mm) occur in beds immediately above the massive sulfide lens. Some grains have pyrrhotite centres and with crustiform pyrite rims. The nodules show radial and crustiform, or concentric growth structures with distortions in the surrounding bedding (Figs 6.10a, 6.10b, 6.13d and 6.13e). Some nodules are 'split' and appear to have been separated with minimal disturbance of the surrounding material.

Dendritic

Dendritic or feathery pyrite, ending in a chrysanthemum-like form (e.g., Ramdohr, 1980), occurs as composite grains among the chalcopyrite - pyrite intergrowth (Figs 6.13f and 6.13g). This texture is only observed in the zone of chalcopyrite-rich stringer veins in the strongly chlorite-altered Footwall Basalt.

Euhedral grains

Pyrite and arsenopyrite, along with rarer sphalerite and magnetite, can occur as euhedral grains. Magnetite euhedra occur among sphalerite in association with spongy, botryoidal magnetite and pyrrhotite (Fig. 6.14a), and as isolated cubic grains in chert (Fig. 6.14b). A rare occurrence of very small euhedral magnetite grains (<0.03 mm) is confined to a quartz aggregate within the centre of a carbonate dominated stringer vein (Figs 6.8g and 6.14c).

Diamond-shaped arsenopyrite euhedra (Figs 6.14d and 6.14e) occur locally as disseminated grains in laminated mudstone on the peripheries of the massive sulfide lens. They are rare in massive sulfide ore, and where present are always at the margins, where locally they are zoned (Fig. 6.14f). Euhedral, very fine-grained pyrite (<0.01 mm) is common within the laminated mudstone that overlies the orebody (Figs 6.14g). Pyrite euhedra also occur within the laminated facies lateral to, and beneath, the orebody.

Towards the base of the massive sulfide lens, disseminated and euhedral very fine-grained sphalerite grains (Figs 6.15a and 6.15b) occur in laminated chert. More rarely, they occur in laminated facies towards the top of the orebody.

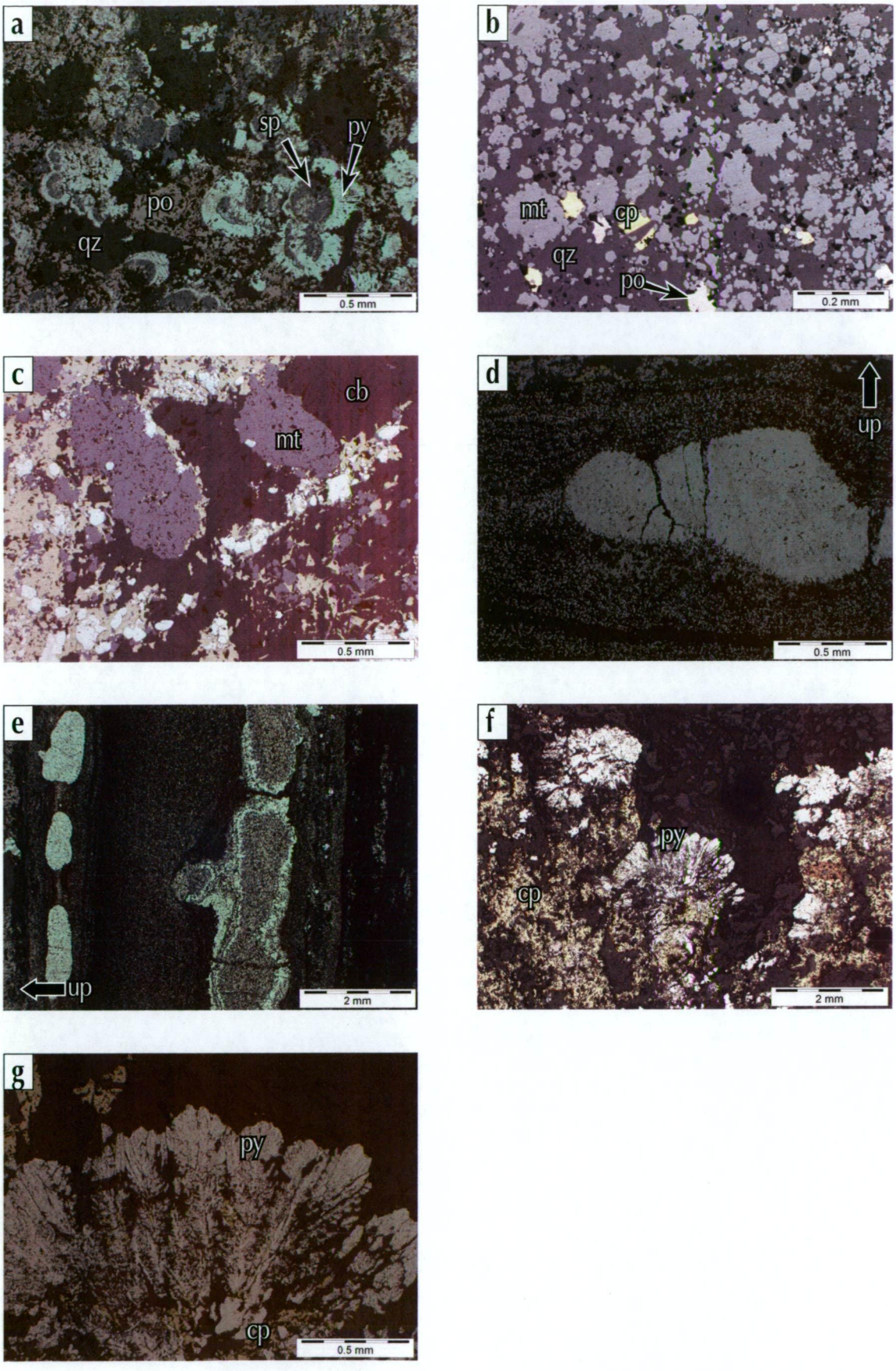

Figure 6.13 Primary textures - colloform grains continued: a) botryoidal, layered sphalerite and pyrite grains among pyrrhotite and chert at top of orebody, samp. 700473, rl; b) colloform clasts of magnetite among quartz gangue, minor chalcopyrite and pyrrhotite, samp. 700472, rl; c) spongy colloform magnetite grains plus chalcopyrite and pyrite among carbonate gangue, samp. 700471, rl; d) pyrite nodule in laminated pyritic mudstone, showing distortions in bedding around nodule, samp. 700473, rl; e) multiple pyrite-pyrrhotite nodule in laminated pyritic mudstone, showing distortions in bedding around nodule, samp. 700473, rl; f) feathery, dendritic pyrite, ending in a chrysanthemum-like form among chalcopyrite and quartz and trace pyrrhotite in stringer vein, samp. 700418, rl; g) close up of feathery, dendritic pyrite, ending in a chrysanthemum-like form, samp. 700418, rl.

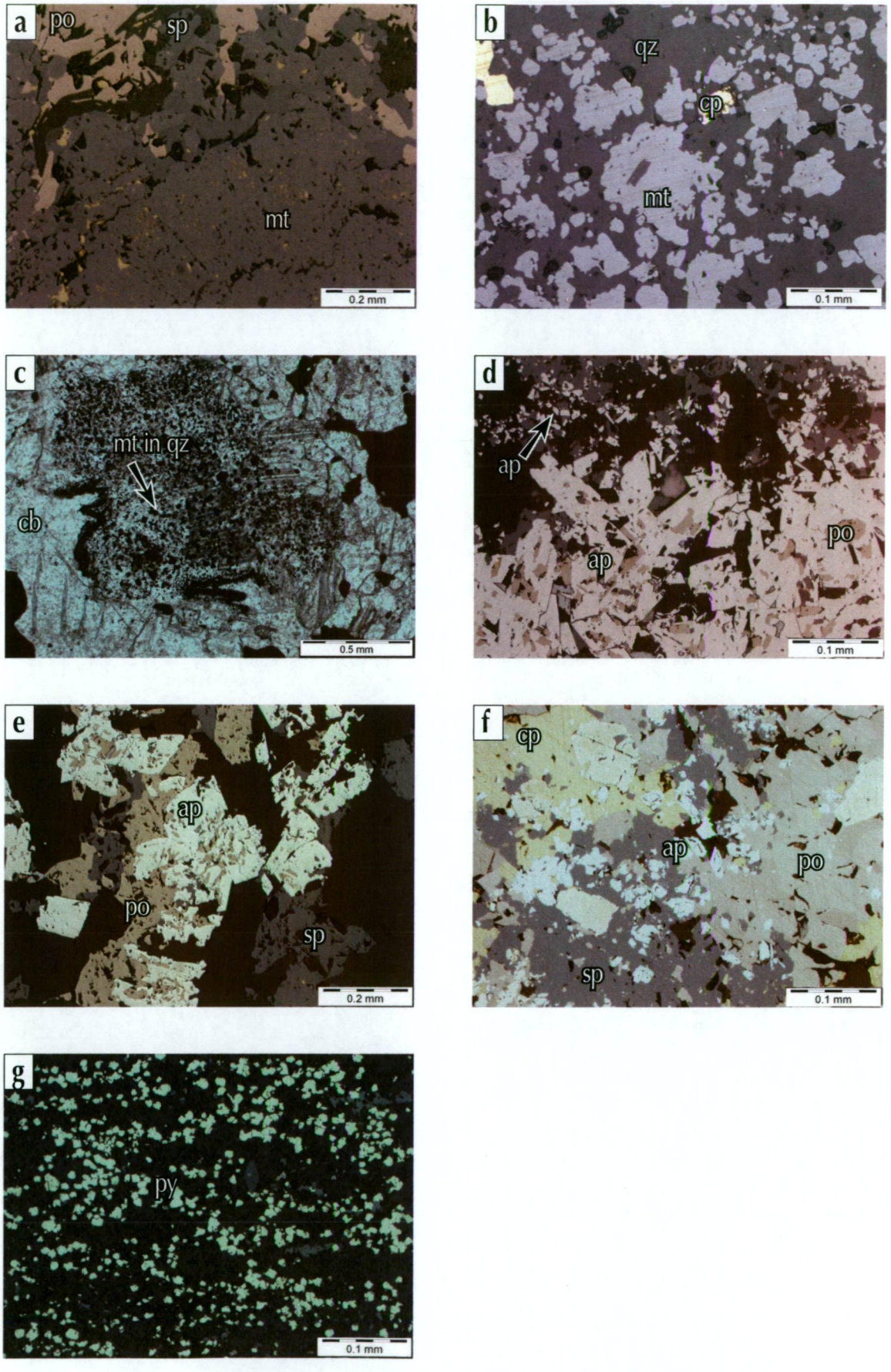

Figure 6.14 Primary textures - euhedral grains: a) magnetite euhedra among sphalerite grains in association with spongy, botryoidal magnetite (sieved with chalcopyrite), samp. 700429, rl; b) colloform and euhedral magnetite grains in chert gangue, samp. 700472, rl; c) center of stringer vein with euhedral magnetite in quartz surrounded by carbonate, samp. 700416, ppl; d) two grain size populations of diamond arsenopyrite euhedral grains, samp. 700372, rl; e) diamond arsenopyrite grains with associated sphalerite and pyrrhotite, samp. 700372, rl; f) zoned, diamond arsenopyrite grains in polycrystalline aggregate of sphalerite, pyrrhotite and chalcopyrite, samp. 700426, rl; g) fine-grained pyrite euhedra, disseminated in mudstone, cms above top of massive sulfide orebody, samp. 700430, rl.

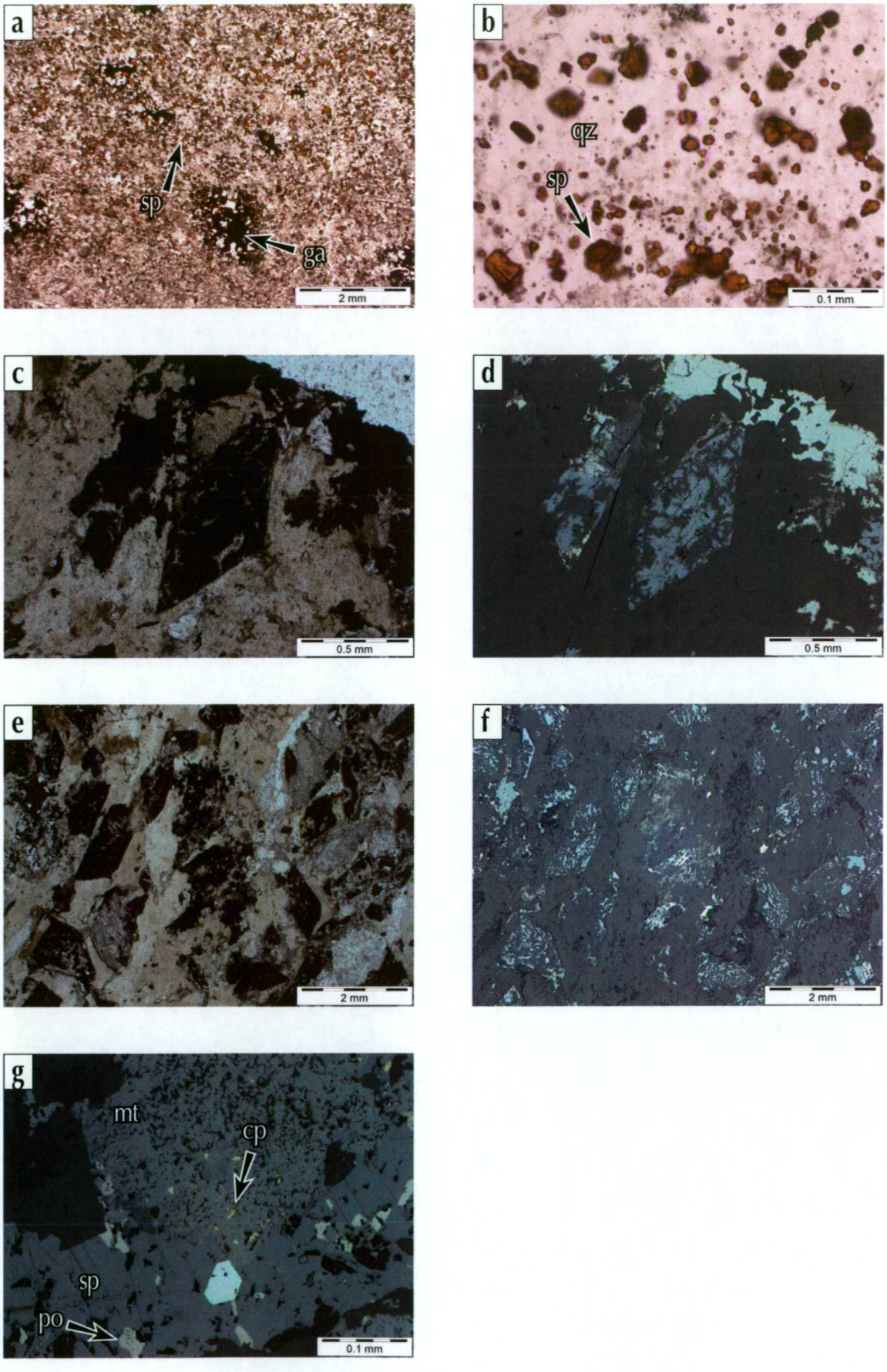

Figure 6.15 Primary textures - euhedral grains continued: a) sphalerite disseminated among quartz, dark clots are galena, samp. 700444, ppl; b) close up of previous sample, sphalerite crystals in quartz gangue, samp. 700444, ppl; c) and d) large relict rhombs, now replaced with mix of Ti-minerals and sulfides, samp. 700383, ppl and rl; e) and f) large relict rhombs, now replaced with mix of Ti-minerals and sulfides, samp. 700383, ppl and rl; g) large spheroidal spongy magnetite grain, seived with chalcopyrite, sphalerite in lower half of slide, samp. 700428, rl.

In a single occurrance within a coarse-grained volcaniclastic facies in the upper part of the massive sulfide lens in drillhole TBD0209, relict, large (2 mm), euhedral diamond and rhomb shaped grain-shapes are preserved. Although the textural form is preserved, the original mineral has been replaced with a mixture of ore and gangue minerals, specifically TiO_2 minerals (titanite, anatase or rutile), pyrrhotite, chalcopyrite and carbonate and quartz. The original mineral remains unknown but it may have been siderite or another carbonate. The shape is also characteristic of arsenopyrite but this particular occurrence is coarser grained than any of the other Jaguar arsenopyrite occurrences (Figs 6.15c, 6.15d, 6.15e and 6.15f).

Sieved

Sieved or spongy textured grains are most common amongst magnetite and pyrrhotite. Magnetite is commonly sieved with chalcopyrite (Fig. 6.15g), rarely sphalerite or quartz, whereas pyrrhotite is sieved most commonly with pyrite or quartz gangue (Fig. 6.15h). It is most likely that sieved pyrrhotite is not primary.

Sulfide clasts

Small 'lithic' clasts of massive sulfide (commonly pyrite) occur as lithics within the volcanic breccia, sandstone, and conglomerate facies of the Mineralised Package. Distribution and abundance are erratic, but they become more abundant with increasing proximity to massive sulfide. The clasts are commonly sub-rounded to sub-angular and vary in size from <1 to ~ 25 mm. They are not associated with any apparent increase in alteration intensity. Their form, association and distribution among the other clasts within the breccias indicates that at least some, if not the majority of them, are primary clasts. The source of the clasts is likely to have been a contemporaneously forming sulfide body. Rare clasts, generally in those units close to ore, show rimmed sulfide overgrowth around a sub-angular core.

Discussion

Bladed (acicular and tabular) grains of pyrrhotite occur throughout the host sequence in siltstone, sandstone and breccia, and range from 0.05–2 mm. The textural relationships between the pyrrhotite laths and the colloform chert-pyrite indicate that the timing of the lath-forming phase and the chert formation was contemporaneous, but pyrrhotite may have replaced the original lath mineral. The laths do not have a pointed termination like a hematite crystal but a more blunted end like a sulfate and are may be replacive of an earlier phase, i.e. a preserved primary texture. The crystals have an orthorhombic form, consistent with pseudomorphic replacement of barite or anhydrite. However, morphologically these crystals are similar to the interlocking networks of tabular pyrrhotite which form a substrate for encrustation by the earliest pyrite, described from the Juan de Fuca Ridge (Davis et al., 1987). Paradis et al. (1988) described pyrrhotite replacing anhydrite, and pyrrhotite

occurring as small laths disseminated in silica gangue, a description that sounds similar to the texture seen at Jaguar. If this is the case, then at least some of the pyrrhotite formed pre-deformation. Ixer (1990) described fine-grained pyrrhotite laths, which had been largely altered to pyrite and marcasite, which had been precipitated from 'black smoke'.

The majority of colloform grains are spheroidal and reniform, radiating out from a core, indicating growth patterns are directed outwards away from a nucleus rather than inwards, filling a pore space. Not all grains are symmetrical; some have grown preferentially in one hemisphere suggesting there was some restriction that impeded free growth in all directions (e.g., Fig. 6.12b). No textures other than those seen in stringer veins appear to have grown inward.

Dendritic, bladed, skeletal, and fibrous textures are typical of early, rapid crystal growth (e.g Lebedev,1967; Mullin, 1993). They may develop in open space or within a medium and probably require a higher degree of supersaturation (Rimstidt, 1997). The dendritic or feathery-shaped pyrite that occurs in the stringer zones is the product of rapid crystallisation, with growing pyrite having nucleated around a 'feather spine'. Ramdohr (1980) considered these feathery chrysanthemum-like forms to be uncommon, but added a note that due to their two-dimensional nature, that even where present, they would only be seen sometimes.

Granular magnetite is typical of magnetite formed by slow and unimpeded growth whereas skeletal and inclusion-rich magnetite are characteristic of rapidly deposited magnetite (Ramdohr, 1980). Frater (1983, 1985a) interpteted similar skeletal-shaped magnetite grains among the massive granular magnetite in the Gossan Hill deposit to indicate replacement of primary hematite by magnetite later in the evolution of the deposit. However, Sharpe and Gemmell (2002) considered that the skeletal and inclusion-rich magnetite textures at Gossan Hill represented rapid precipitation of magnetite (e.g., Wedekind, 1990) They thought this because the skeletal and inclusion-rich magnetite grains had a spongy to 'boxwork' texture due to intergrowths with ankerite-siderite, and that common inclusions of magnetite in ankerite-siderite grains supported their synchronous formation. The magnetite at Jaguar (in granular, sieved (inclusion-rich) and sleletal forms) is interpreted as a primary mineral, rather than as a replacement mineral.

The fine-grained euhedral pyrite that is disseminated in the mudstone above, and lateral to the massive sulfide orebody, is possibly 'exhalative' and to have precipitated from hydrothermal fluid that exhaled into the sea (e.g., Franklin et al., 1981; Solomon and Kin Zaw, 1997). A similar origin is proposed for the less common, fine-grained euhedral sphalerite that occurs disseminated in mudstone and chert windows, towards the base of the orebody.

The split and parted nodules show that the pyrite must have grown subsurface, possibly as an FeS-gel (e.g. Duhig et al., 1992; Grenne and Slack, 2005) of some sort, that likely contracted during diagenesis.

The source of the sulfide clasts in breccia, conglomerate and sandstone facies that are lateral to, and down-dip of the massive sulfide orebody, is likely to be the orebody itself. Whether they were generated by a collapse (or part collapse) of a sulfide-chimney forming mound on the seafloor, or from an orebody forming sub-surface, that was exposed by growth-fault triggered tectonic instability, is not known, and cannot be determined from the clasts. Debris flows generated by this collapse would have then incorporated the sulfide and mixed it with the volcaniclastic material. (e.g., Mt Read Volcanics: Gibson, 1991).

Chimney fragments occur in many VHMS orebodies and this supports the concept of seafloor mound growth by chimney collapse and subsequent incorporation into the mound. However, despite careful observation of sulfide-carrying drillcore, no chimneys or chimney fragments were recognised anywhere in the study area. It is possible that these features are present at a larger scale and not recognisable in drillcore.

6.3.3 Replacement textures (micro and macro scale) - pre and post deformation

The most common replacement texture observed at Jaguar are in chalcopyrite which has variably replaced cataclastically fractured pyrite. The chalcopyrite has replaced the pyrite along and outward from the intra-pyrite fractures (Fig. 6.16a).

Caries and atoll textures

Caries texture is not common at Jaguar but in rare occurrences chalcopyrite has replaced pyrite (Fig. 6.16a). Arsenopyrite grains, (although not common in the deposit) commonly show a combination of caries and atoll textures where pyrrhotite (Fig. 6.16b) plus rare galena (Fig. 6.16c) or sphalerite have replaced arsenopyrite.

Skeleton-shaped

Skeleton-shaped[1] pyrite is ubiquitous within the massive sulfide lens at Jaguar. These pyrite grains commonly have fishbone to cross-shaped skeleton textures with interstices filled by chalcopyrite (Fig. 6.16d) and less commonly sphalerite (Fig. 6.16e) or galena (Fig. 6.16f). Nearly all of these occurrences are part- or semi-spherical. Skeleton-shaped grains are a common textural form for pyrite (e.g., Ramdohr, 1980) and suggest replacement of the pyrite by the other sulfide.

1 Skeleton-shaped (e.g., Ramdohr, 1980). This term is used to distinguish this texture from skeletal texture. Skeletal is used in this thesis to describe a primary grain shape and skeleton-shaped is used to describe a texture in which the framework, or skeleton of the grain remains, and the interstices are replaced by another mineral (Ramdohr, 1980). This texture is also sometimes called fishbone texture in the literature.

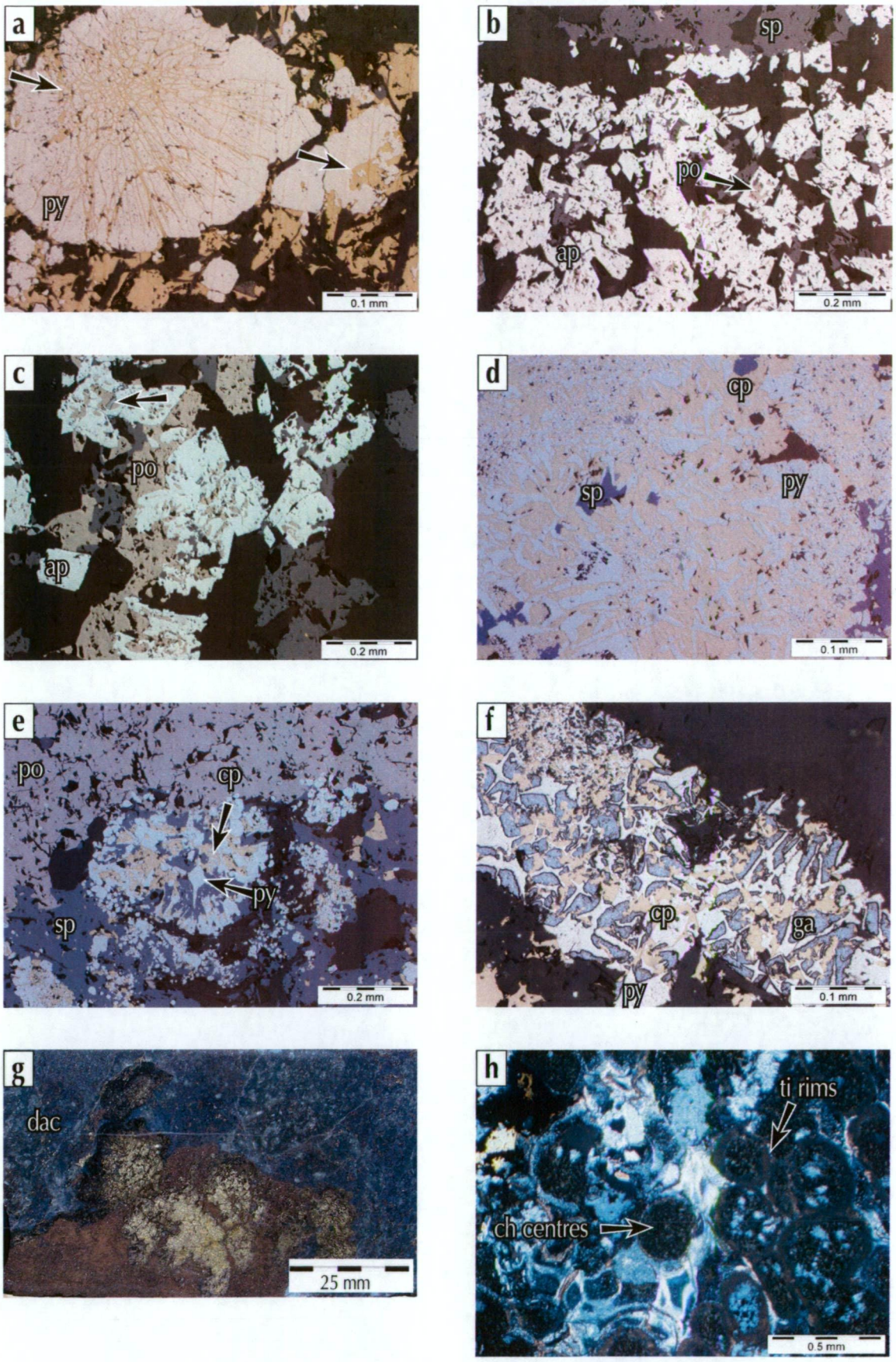

Figure 6.16 Replacement textures: a) large pyrite grain shows chalcopyrite that replaced pyrite along and between cataclastic fractures, a smaller pyrite grain in the lower right corner shows a good example of caries texture, samp. 700477 rl; b) caries texture in arsenopyrite grains, pyrrhotite has replaced arsenopyrite, samp. 700372 rl; c) caries texture in arsenopyrite grains, pyrrhotite and rare galena have replaced arsenopyrite, samp. 700372 rl; d) skeleton-shape pyrite with the interstices replaced by chalcopyrite, samp. 700442 rl; e) skeleton-shape pyrite with the interstices replaced by spalerite and chalcopyrite, samp. 700464 rl; f) skeleton-shape pyrite with the interstices replaced by galena and chalcopyrite, samp. 700385 rl; g) sphalerite and chalcopyrite have replaced coherent dacite, TBD0256 ~448.2 m, core; h) spherulites in basalt replaced by chlorite with titanite rims, samp. 700449, xp.

Replacement fronts

Within the dacite, sulfide replacement fronts occur on macro (Fig. 6.16g) and micro-scales (Fig. 6.16h). These fronts commonly have sharp, lobate or irregular boundaries. On a deposit scale, gradational replacement fronts occur on the lateral and lower margins of the orebody and are characterised by progressively increasing abundance of sulfide and intensity of alteration towards the ore.

Other

In the lower part of the Mineralised Package unit, spherulites in the dacite facies have been replaced in places with chlorite and carbonate gangue minerals, or with sulfides. Within the stringer zone, in the basalt breccia facies in the Footwall Basalt, spherulites and variolites are replaced by chlorite (Fig. 6.16h). In rare instances pyrite and chalcopyrite also appear to have partially replaced spherulites.

Discussion

It is likely that caries and atoll replacement textures are not common because deformation and recrystallisation have destroyed primary textures in sulfide aggregates. However, isolated or semi-isolated grains of the moderately hard sulfides – arsenopyrite and pyrite – have not been ductilely deformed and therefore preserve caries textures.

The ubiquitous presence of skeleton-shaped replacement texture in pyrite is much more common than caries texture. This may reflect that most of the primary pyrite grains were colloform growths rather than euhedral crystals.

Replacement of spherulites in the Dacite MP and in the Footwall Basalt indicates that sub-seafloor replacement did occur. The occurrences in the footwall are not necessarily good evidence that the whole orebody was formed in this way as replacement commonly occurs in the footwall under seafloor deposits (e.g., Kuroko: Eldridge et al., 1983; Mattabi: Morton and Franklin., 1987).

6.3.4 Textures produced by brittle behaviour during deformation

Where pyrite has deformed it has commonly failed in a brittle manner evidenced by cataclastic fracture and breccia of pyrite grains. Large colloform grains locally display fracture sets, and minor brecciation, attributed here to cataclastic failure during shearing (Fig. 6.17a). Fracture patterns vary from internal orthogonal fractures (Figs 6.17b and 6.17c), to random (Fig. 6.17d) and to radiating (Fig. 6.16a) fracture sets. The radiating fracture sets may have orthogonally fractured centres. Zones of massive sulfide dominated by colloform pyrite aggregates commonly show a fractured and imbricated texture, and

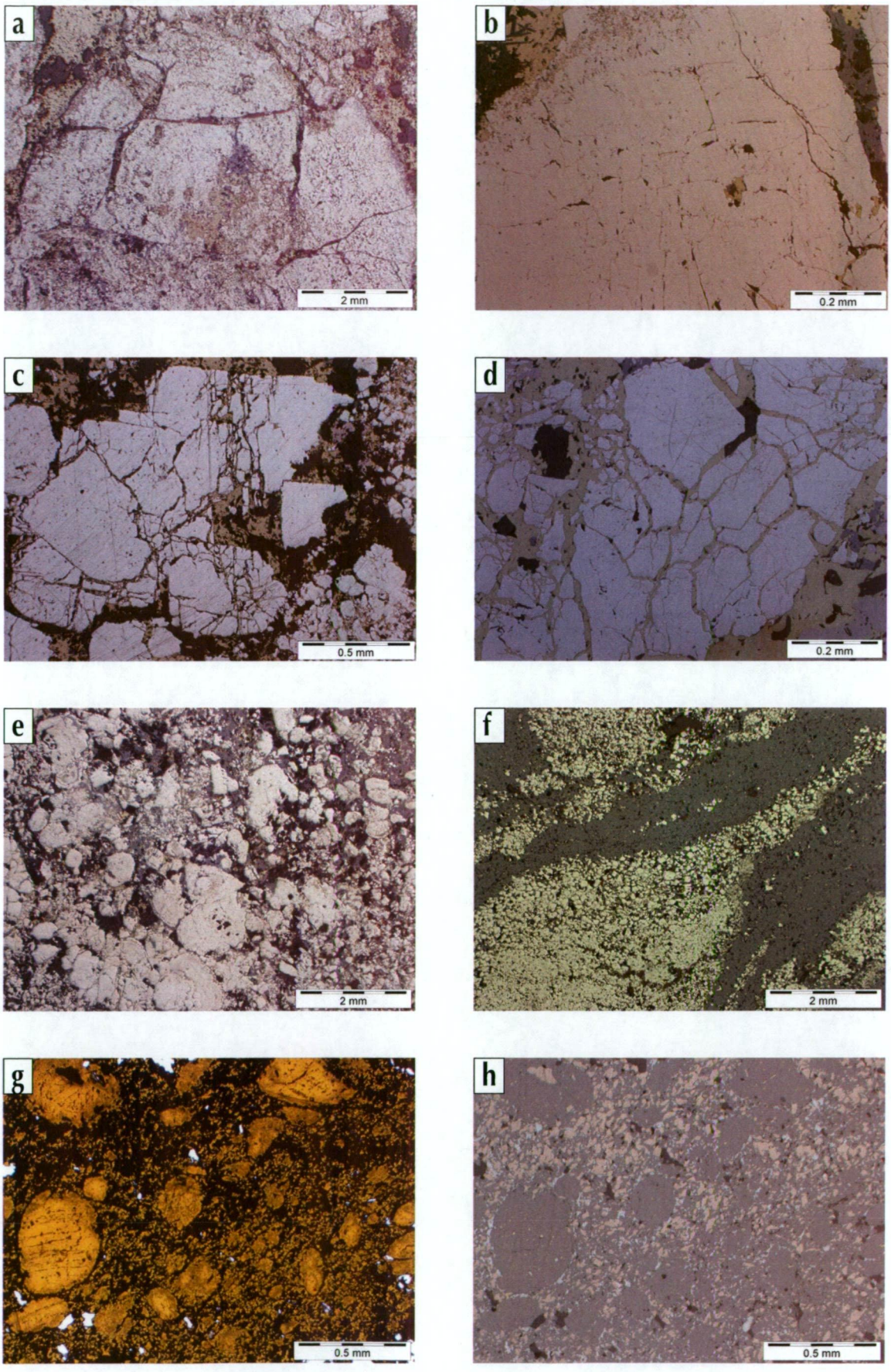

Figure 6.17 Brittle deformation: a) colloform pyrite grain, showing cataclastic fracture and minor breccia, samp. 700464, rl; b) orthogonal fracture in pyrite grain, samp. 700477, rl; c) orthogonal plus irregular fractures in pyrite grains, samp. 700477, rl; d) irregular cataclastic fracture in pyrite grain, samp. 700415, rl; e) some milling and partial imbrication of colloform pyrite grains, samp. 700387. rl; f) total cataclastic breccia of pyrite grains and fragments, manifested as a train among more ductile sphalerite grains, samp. 700414, rl; g) and h) sphalerite grains that were milled and rounded during cataclastic deformation, surrounded by a matrix of more ductile galena and pyrrhotite, samp. 700469, ppl and rl.

evidence that grains were ground together (Fig. 6.17e).

Where brecciated, pyrite grain fragments comprise trains (Fig. 6.17f), where these fragments are commonly surrounded by sulfides (chalcopyrite, pyrrhotite) which have deformed by ductile deformation. Where total failure of the pyrite grains occurred, macroscopically the pyrite appears to have 'flowed' in zones several millimetres wide. However, examination of polished sections reveals the cataclastic nature of the pyrite grains. The matrix in these zones comprises sphalerite, pyrrhotite and chalcopyrite in varying amounts.

Arsenopyrite, although not common in the deposit, also exhibited brittle behaviour. The deformation typically manifests as fractured grains or aggregates.

Some of the sphalerite bands in the durchbewegung ore comprise poorly sorted, tightly packed, sub- to well-rounded grains of sphalerite (Figs 6.17g and 6.17h). Where this is the case the intergranular matrix is dominated by galena and pyrrhotite.

Magnetite, typically a high-strength mineral that can display similar cataclastic behaviour to pyrite (Pederson, 1980; Frater, 1985), does not display obvious brittle fracture textures at Jaguar. This may be a function of its limited occurence, because in the rare examples where magnetite was incorporated in durchbewegung zones, the magnetite grains had been dragged into trains in a similar manner to pyrite.

Discussion

The orthogonal fractures observed in pyrite may be crystallographically controlled (e.g. Graf and Skinner, 1970), and indicate an original crystal grain aggregate, whereas the radiating fracture sets, which occur most commonly in spheroidal grains, may follow the grain boundaries developed during primary colloform growth. This mix of primary and secondary growth boundaries may have helped to influence clast shapes during durchbewegung development.

Zones comprising rounded grains of sphalerite in a galena-pyrrhotite matrix durchbewegung ore, are most likely to have formed by milling and grinding where the sphalerite has locally behaved in a brittle, rather than a ductile manner during cataclastic deformation. The poor sorting and close packing of the grains support this interpretation. Gilligan and Marshall (1987) noted that sphalerite aggregates in a galena matrix may show evidence of brittle deformation, and ascribed this to partitioning of strain into highly ductile galena, whereas the sphalerite, because it is unable to deform ductilely at a comparable strain rate, fails brittlely.

6.3.5 *Textures produced by ductile behaviour during deformation*

Where there is interconnectivity of sulfide grains, nearly all sulfides (excluding pyrite and arsenopyrite) show evidence of ductile flow deformation. This is expressed as mineral banding that is commonly observed within the massive sulfide at micro to meso scales. In most instances the bands are the result of deformation; rarely, the nature of mineral banding is equivocal. In most bands the sulfides appear to have been recrystallised post-deformation because the grains are not elongated and they show normal triple-point junctions which do not form during ductile flow.

Where pyrite occurs within these shear zones and has boudinaged, or has failed cataclastically, prominent fine fractures perpendicular to the banding are filled with other sulfides, most commonly chalcopyrite, locally with pyrrhotite and in rare instances with galena. Chalcopyrite is most commonly remobilised into brecciated pyrite grains (Figs 6.18a and 6.18b) within durchbewegung bands. Relicts of colloform pyrite (undeformed or fractured) may remain within these ductile bands. Where clasts of gangue occur within the bands, the typical durchbewegung texture is developed through a process of sulfide flow and clast fracturing and milling (Figs 6.18c and 6.18d). In a pyrrhotite band between lithic clasts, pyrrhotite has flowed into orthogonal fractures in pyrite (Fig. 6.18e). Pressure shadows have developed between some clasts, and chalcopyrite is the dominant sulfide in these shadows (Figs 6.18g and 6.18h).

There were no occurrences regognised of magnetite or arsenopyrite showing ductile behaviour.

Discussion

The textural evidence for ductile deformation is expressed as intergranular structures, flattened and/or elongate coherent grains and circumstantial evidence of foliations and lineations as defined by grain aggregates (Gilligan and Marshall, 1987). However, these are commonly overprinted by annealing recrystallisation and grain growth in sulfides.

The interconnected pyrrhotite grains are typically anhedral, as are grains of galena, chalcopyrite and most sphalerite. Rarely do any grains in polymetallic aggregates retain any elongation. However, remobilisation is indicated by mineral banding, the occurrence of pyrrhotite as a fracture fill of pyrite and its presence as the major component of the sulfide matrix to the durchbewegung ore. That pyrrhotite has flowed into the fractures within pyrite grains, is evidence that the pyrrhotite was present during deformation, and not introduced later.

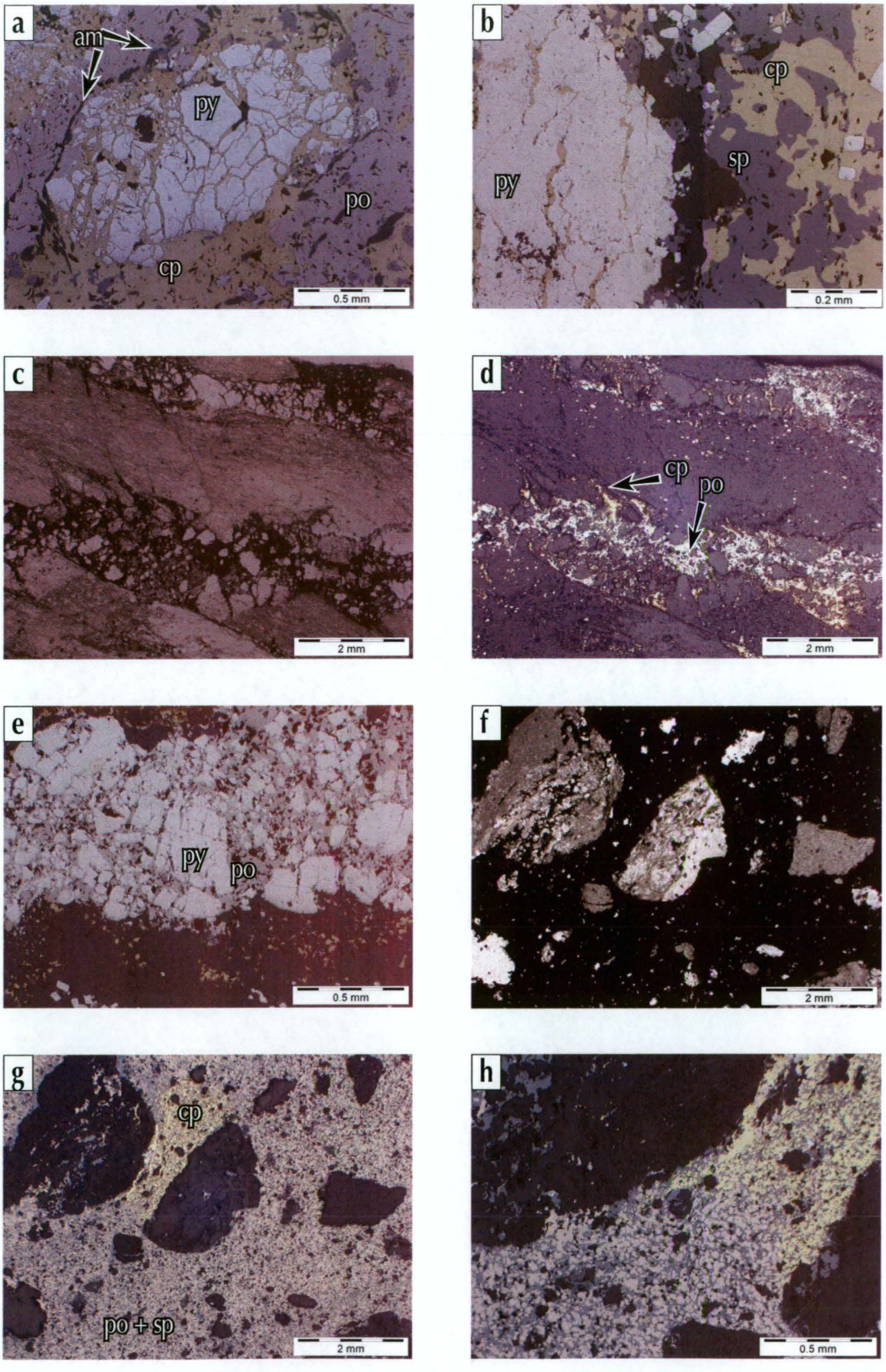

Figure 6.18 Ductile deformation textures: a) chalcopyrite remobilised into fractures in cataclastically deformed pyrite, samp. 700415, rl; b) chalcopyrite remobilised into fractures in cataclastically deformed pyrite, samp. 700385, rl; c) an d) chalcopyrite and prrhotite remobilised into fractures in cataclastically deformed host rock, chalcopyrite has moved to the cusp of piercement structures, samp. 700411, ppl and rl; e) pyrrhotite remobilised into fractures in cataclastically deformed pyrite, samp. 700411, rl; f) and g) durchbewegung ore with a variety of clast types with chalcopyrite in pressure shadow between grains samp. 700384, ppl and rl; h) close up of chalcopyrite in pressure shadow, samp.700384, rl.

6.3.6 Equilibrium recrystallisation textures

Within the durchbewegung bands – formed by a combination of brittle and ductile behaviour during deformation – much of the sulfide mass shows evidence of recrystallisation and annealing, evidenced by well developed foam textures that are consistent with achievement of textural equilibrium. Even when present as clasts in the deformed sulfide ores, this generally excludes the pyrite, magnetite and arsenopyrite, which commonly retain their primary texture. Galena, chalcopyrite and pyrrhotite always appear to have recrystallised, whereas sphalerite in some durchbewegung bands may retain the rounded textural form created by milling during cataclasis. Ramdohr (1980) remarked that in nature, the medium soft to moderately hard minerals (galena to pyrrhotite) recrystallise very easily, whereas the soft and very hard minerals (pyrite, ilmenite, magnetite and arsenopyrite) recrystallise less easily or not at all.

Foam-like polycrystalline aggregates of sulfides (e.g., Stanton, 1972) are well developed, with the triple-point junction dihedral-angles being dependent on the minerals present. A foam of an annealed durchbewegung band of pyrrhotite and sphalerite (Figs 6.19a and 6.19b) shows near-equal dihedral angles in comparison to a polycrystalline aggregate foam of chalcopyrite and sphalerite (Fig. 6.19c) which produces a smaller chalcopyrite dihedral angle value. A polycrystalline aggregate of galena–pyrrhotite–sphalerite (Fig. 6.19d) shows a range of dihedral angles.

Two rare minerals, tetrahedrite-tennantite (Fig. 6.19e) and geochronite (Fig. 6.19f), also occur as minor phases in polycrystalline aggregates of distinct composition.

In the rare occurrences where grains of pyrite within durchbewegung bands have been annealed, the resulting polycrystalline aggregates display the large dihedral angle value of pyrite in chalcopyrite (Fig. 6.19g), and pyrite in sphalerite (Fig. 6.19h). Locally some pyrite occurs as coarse euhedral porphryblasts, where they overprint primary colloform-banded pyrite (Fig. 6.12e). Such porphyroblasts provide evidence for static grain growth during deformation and metamorphism (Craig and Vokes, 1993). Among other sulfides, recrystallised euhedral pyrite occurs in trains (Fig. 6.17f) or among a matrix of sphalerite and galena, with minor pyrrhotite and chalcopyrite (Fig. 6.20a). Craig and Vokes (1993) noted that pyrite within a significant to dominant amount of other sulfides, typically recrystallises to euhedral grains.

In single sphalerite grains, chalcopyrite blebs occur along lattice boundaries (Fig. 6.20b) forming a typical exsolution fabric (e.g., Barton and Bethke, 1987). In massive annealed sphalerite, which behaved as a single phase aggregate, chalcopyrite and pyrrhotite blebs occur along the grain boundaries (Figs 6.5g, 6.5h, 6.20c and 6.20d).

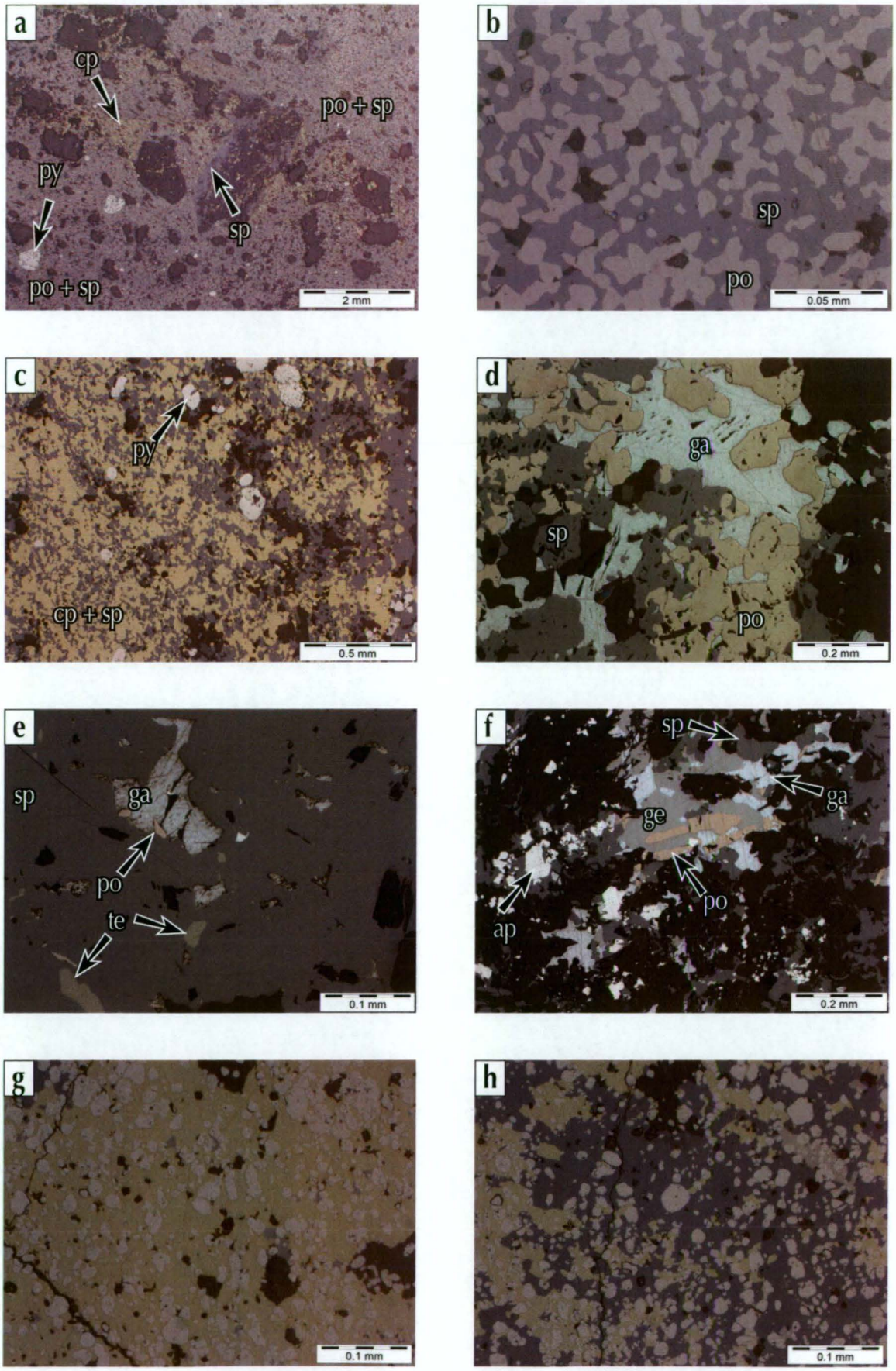

Figure 6.19 Recrystallisation textures: a) recrystallised durchbewegung massive sulfide. samp. 700410, rl; b) a close up of (a) showing the intergranular relationship and dihedral angles between sphalerite and pyrrhotite. samp. 700410, rl; c) recrystallised chalcopyrite and sphalerite intergrowth with local idomorphic pyrite grains, and rare pyrrhotite plus quartz gangue. samp. 700456, rl; d) pyrrhotite, sphalerite and galena plus quartz gangue. samp. 700372, rl; e) a polycrystalline aggregate comprising sphalerite, galena and tetrahedrite-tennantite (and pyrrhotite) showing a range of dihedral angles. samp. 700431; f) galena, geochronite and pyrrhotite arsenopyrite. samp. 700193, rl; g) recrystallised ore, idiomorphic pyrite in a matrix of chalcopyrite, plus minor sphalerite. samp. 700442, rl; h) recrystallised ore, idiomorphic pyrite in a recrystallised matrix of sphalerite, chalcopyrite and rare pyrrhotite. samp. 7004442, rl.

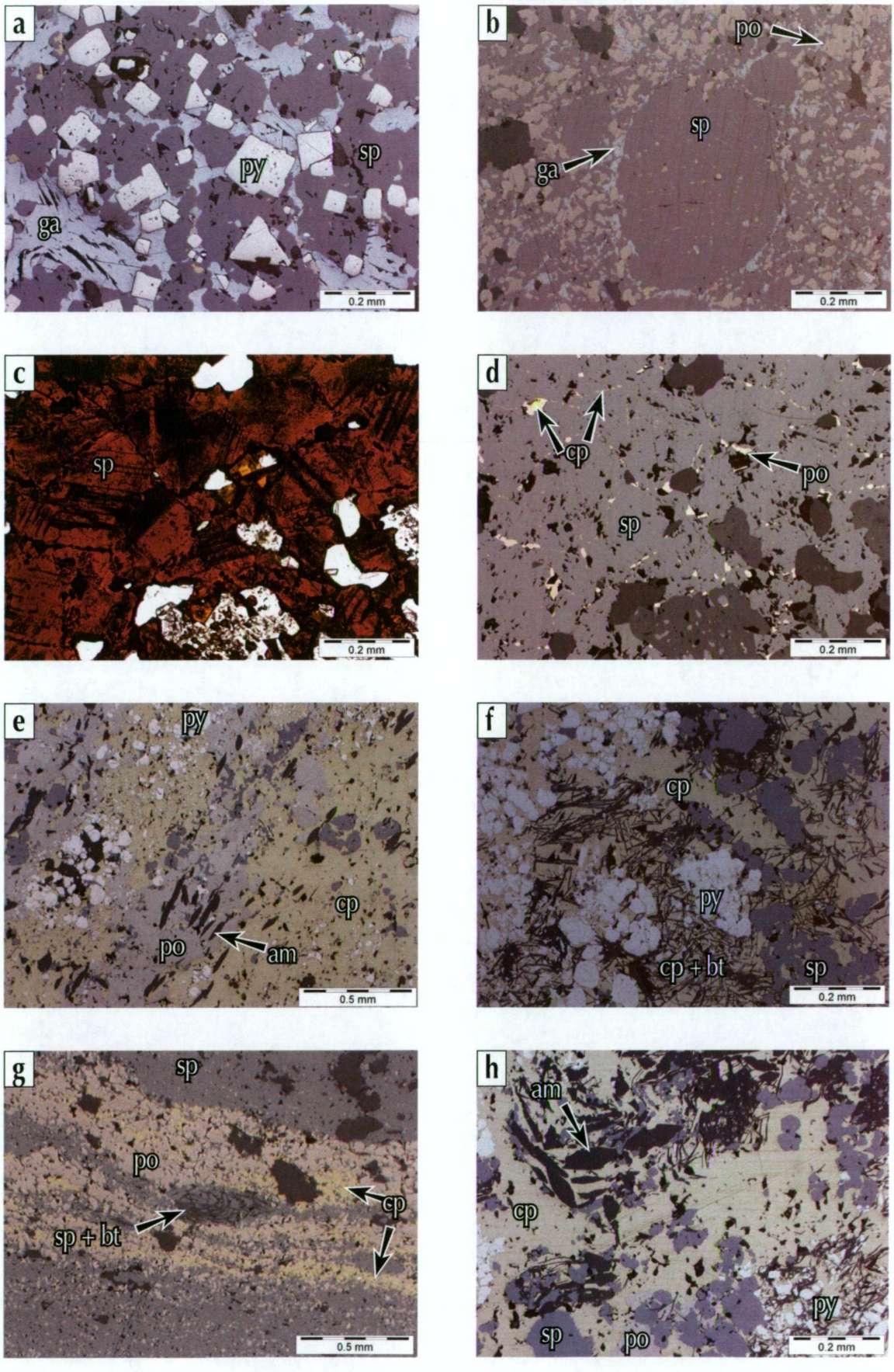

Figure 6.20 Recrystallisation textures - continued: a) porphryblasts of pyrite in matrix of galena and sphalerite, curved cleavage traces in galena, samp. 700385, rl; b) chalcopyrite exsolved along lattice planes in sphalerite, galena and pyrrhotite interstitial to sphalerite grains, samp. 700469, rl; c) and d) tightly packed, recrystallised sphalerite with chalcopyrite and pyrrhotite along grain boundaries, samp. 700453, ppl and rl; e) samp. 700415, rl; f) curved needles of biotite intergrown with chalcopyrite, among sphalerite, pyrrhotite and pyrite, samp. 700471, rl; g) durchbewegung bands, chalcopyrite in pressure shadows around clasts, clast in centre is a grain of rotated sphalerite and biotite, samp. 700469, rl; h) curved needles of biotite intergrown with chalcopyrite, among sphalerite, pyrrhotite and pyrite samp. 700471, rl.

The intergrowth of spiky retrograde chlorite-biotite needles in pyrrhotite and/or chalcopyrite (Figs 6.9c, 6.20e and 6.20f) and rarely sphalerite, showed that there was continued mobility of pyrrhotite and chalcopyrite until late in the structural and metamorphic evolution. The curved trails of crystals and curved needles provide evidence of concurrent growth (Figs 6.9e and 6.20g), although recrystallisation has destroyed the grain shape evidence in the sulfide minerals, the original mineral partitioning remains and the silicate minerals retain the crystal forms developed during deformation.

Discussion

Galena, chalcopyrite and pyrrhotite at Jaguar almost always show evidence of recrystallisation. Although much of the sphalerite has recrysallised in foam-structure intergrowths, there are many occurrences where the sphalerite grains have retained the rounded, grain shape that formed as a result of cataclastic milling rather than ductile behaviour. Typically here the interstices between the sphalerite grains are typically filled with recrystallised pyrrhotite and galena. When compared to modern seafloor deposits, such as those of the Guaymas Basin (ubiquitous pyrrhotite grains <0.01-2.5 mm, sphalerite <0.01-0.2 mm, very rare pyrite 0.01-0.4: Peter and Scott, 1988) or the SuSu Knolls (eastern Manus basin, Papua New Guinea: pyrite <0.01- 0.12 mm, chalcopyrite <0.2 mm: Hrischeva et al., 2007) the grain size at Jaguar indicates that recrystallisation of the sulfide ore probably resulted in an ore with a slight increase in average grain size and a decrease in the range of the grain size. That is, the lower grain-size limit has increased five to ten times, whereas the upper grain-size limit has only increased between one and two times.

Most, but not all pyrite grains, retain some evidence of primary texture, although some show recrystallisation features. In pyrite-rich massive sulfide zones, recrystallisation and grain growth during metamorphism led to impingement of pyrite grain boundaries and the development of annealed mosaic textures with near 120° triple junctions in well developed foam-like textures. Arsenopyrite and magnetite do not show convincing evidence of recrystallisation.

The rotated inclusions of euhedral tremolite-actinolite, and biotite trails record rotation within these durchbewegung zones and indicate that shearing took place at peak metamorphic conditions (e.g. Sulitjelma: Cook et al., 1993). The intergrowth of spiky chlorite and/or biotite needles in recrystallised pyrrhotite and/or chalcopyrite, where the foam-structure of the polycrystalline aggregate has triple-points of about 120°, indicates that there was no ongoing strain. This suggests that recrystallisation continued until late in the structural and metamorphic evolution after physical deformation had ceased (e.g.,Stanton, 1972). The segregation of the sulfides, i.e. chalcopyrite in pressure shadows, also suggests that recrystallisation is likely to have occurred after deformation. This is also supported by the unstrained nature of the foam-like recrystallisation textures which retain dihedral angles developed in a no-strain state.

6.4 Implications

In unmetamorphosed VHMS deposits (e.g., Sulfur Springs - Veancombe, et al., 1995; Ruttan - Barrie et al., 2003; Hellyer - McArthur and Dronseika, 1990; Solomon and Gaspar, 2001) it is common to see retained primary opaque-mineral textures. In Jaguar, despite middle greenschist-facies regional metamorphism and local deformation, some primary textures are retained. However, in most areas the opaque mineral textures are modified, indeed obliterated, by an array of alteration and deformation processes that probably commenced with late hydrothermal adjustment and continued through burial, contact and regional metamorphism and concomitant shearing. The variability of deformation textures between the ore types is due to their contrasting rheological properties, which in turn is constrained by their mineralogy and pre-existing textures (Gilligan and Marshall, 1987).

6.4.1 Deformation History

Mineral banding is commonly observed in the sulfides and in most examples is the result of deformation. In polished thin section it is apparent that banding in the banded ore is tectonic and is a clast-poor variety of the durchbewegung ore. Bands are a mixture of brittle/cataclastic and ductile features that are commonly overprinted by recrystallisation/ annealing.

The most deformed ore has a pronounced durchbewegung texture. These zones formed as a result of contrasting rheological behaviour among the various sulfides and silicates when subjected to shearing under greenschist conditions. Where there was interconnectivity of sulfide grains, nearly all sulfides (excluding pyrite) deformed ductilely. The fabric and structure of the sulfide ore indicate that pyrite was the least ductile sulfide during metamorphism and deformation, followed by arsenopyrite, sphalerite, pyrrhotite and chalcopyrite, with galena being the most ductile. The presence of chalcopyrite in pressure shadows and as filling fractures in pyrite are usually interpreted as fluid-state remobilisation, and, therefore, pressure solution-segregation of chalcopyrite from the mixed sulfide matrix (Gilligan and Marshall, 1987).

Zones of apparently (mesoscopically) ductile pyrite are actually composed of resistant grains of pyrite that were entrained in ductile shear assemblages of more ductile minerals and have pressure shadows or exhibit evidence of rolling and accretion. Rare entrainment of magnetite among the more ductile sulfides also occurs in durchbewegung bands. Where pyrite or arsenopyrite are common, they display cataclastic fracture and breccia where the grains were forced against one another, whereas, chalcopyrite, sphalerite, pyrrhotite and galena all deformed and recrystallised more readily than magnetite and pyrite (Vokes,

1969; Gilligan and Marshal, 1987; Marshall and Gilligan, 1993). Therefore, most primary textures are destroyed in the softer minerals.

The exception to this at Jaguar appears to be the pyrrhotite blades that are found in the cherts in association with the colloform pyrite. This blade textured pyrrhotite, which has poor grain interconectivity, appears to be isolated from the effects of ductile deformation. Most interconnected sphalerite shows evidence of ductile deformation, with some exceptions where sphalerite grains appear to have behaved brittlely, and were milled and rounded during cataclastic flow. Isolated sphalerite grains show no evidence of ductile behaviour. The variation in the behaviour of sulfides over short distances suggests that the strain was not uniform.

Rotated inclusions of euhedral tremolite-actinolite, and biotite trails, indicates that the durchbewegung shearing and synchronous recrystallisation took place at peak metamorphic conditions. The intergrowth of spiky chlorite and/or biotite needles in pyrrhotite and/or chalcopyrite, indicates that mobility of pyrrhotite and chalcopyrite continued until late in the structural and metamorphic evolution.

The dihedral/interfacial angles that aproximate 120° between like sulfide grains in polycrystalline aggregates indicate that recrystallisation and annealing postdated the deformation. In addition, most of the recognised replacement textures appear to be post-deformation, another indication that high temperature metamorphic conditions persisted post deformation. The slight increase in grain size, when compared to grain sizes in modern seafloor deposits (undeformed and unmetamorphosed) and isolated, porphryblasts of euhedral pyrite grains also supports the interpretation that high temperature metamorphic conditions extended annealing times.

6.4.2 Paragenesis

The deformation and subsequent recrystallisation of the more ductile sulfide minerals, and the consequent destruction of textures meant that a primary sulfide mineral paragenesis could not be confidently constructed. However, careful analysis of the few primary textures and the grain-forms produced during replacement, deformation and recrystallisation allow reconstruction of a partial sulfide paragenesis as illustrated in Table 6.1.

Table 6.1. Paragenesis and timing of the dominant textures

Mineral	textural style	primary	deformation	recrystallisation syn-shear	recrystallisation post-shear
pyrite	colloform/botryoidal	x			
	skeletal/bladed/euhedral	x			
	stringer veins	x			
	cataclastic milling/fracture		x		
	annealed foam aggregates		x		x
	fishbone/skeleton				x
magnetite	colloform/seived	x			
	euhedral/skeletal/bladed	x			
arsenopyrite	euhedral	x			
	cataclastic milling/fracture		x		
chalcopyrite	replaced in fishbone pyrite	x			
	stringer veins	x			
	annealed foam aggregates		x	x	x
	pressure shadows		x	x	x
sphalerite	replaced in fishbone py	x		x	x
	cataclastic milling/fracture		x		
	annealed foam aggregates		x		x
galena	replaced in fishbone pyrite	x			x
	annealed foam aggregates		x		x
pyrrhotite	skeletal/bladed/euhedral	x			
	stringer veins	x			
	annealed foam aggregates		x	x	x
chlorite		x	x	x	
titanite		x			
sericite		x		x	
zoesite/epidote	stringer veins	x			
quartz		x	x	x	
carbonate		x	x		
biotite			x	x	
amphibole			x	x	

6.4.3 Formation: seafloor vs. sub-seafloor replacement

Exhalation and sub-seafloor replacement are both important processes in the formation of VHMS deposits (e.g., Eldridge et al., 1983; Ohmoto et al., 1983; Lydon 1988; Humphris et al., 1995; Doyle and Allen, 2003). In undeformed ores the products formed during these processess can be distinguished using textural and facies contraints (e.g., Doyle and Huston, 1999; Doyle and Allen, 2003) whereas in deformed ores it can be difficult to determine the exact processes involved.

Although the Jaguar massive sulfide orebody is deformed and commonly recrystallised with most primary features destroyed, the low-strain window does provide information about primary textures. When this information is combined with what is known about the host lithofacies and succession, it is possible draw some conclusions about the formation of the orebody.

The literature on VHMS deposits emphasises exhalative formation on the seafloor by endogenic growth of a sulfide mound, or by accumulation of sulfides precipitated from exhaling hydrothermal fluids (e.g., Solomon and Walshe, 1979; Ohmoto and Skinner, 1983; Lydon, 1988; Large, 1992; Solomon and Gaspar, 2001). Studies of modern sulfide mounds and the structure of chimneys (e.g., Goldfarb et al., 1983; Paradis et al., 1988; Petersen et al., 2000), and the texture and metal zonation in ancient deposits (e.g., Large, 1977; Eldridge et al., 1983; Lydon, 1984; Galley et al., 2005), all highlighted the importance of sulfide accumulation by open space filling and replacement within the sulfide mound. Increasing evidence suggests that these processes extend into the sub-seafloor environment, and that some VHMS deposits form largely by replacement of sub-seafloor lithofacies (e.g., Kerr and Mason, 1990; Kerr and Gibson, 1993; Bodon and Valenta, 1995; Morant, 1995; Doyle and Huston, 1999). Furthermore, separate lenses or segments of a single deposit may form by different processes and both sub-seafloor replacement and seafloor accumulation may be involved in a single deposit (Sangster, 1972; Large, 1977; Solomon and Walshe, 1979; Eldridge et al., 1983; Vivallo, 1985; Galley et al., 1993; Gibson and Kerr, 1993; Humphris et al., 1995).

Sharpe and Gemmell (2001) described six criteria for the recognition of exhalative sulfide deposition in VHMS environments: (i) sulfide breccia facies; (ii) sulfide clasts; (iii) chimney fragments; (iv) hydrothermal chert or chert-iron facies (e.g., Kalogeropoulous and Scott, 1983; Peter and Goodfellow, 1996; Doyle, 1997); (v) primary open-space sulfide textures (Eldridge et al., 1983); and (vi) bedded sulfide facies. In addition, the formation of sulfides at the seafloor is typically associated with a hiatus represented by a stratigraphic break (e.g., Morton et al., 1991; Kerr and Gibson, 1993).

Doyle and Allen (2003) varied these criteria and used the following criteria to distinguish seafloor ore: (i) sedimentary clastic sulfide textures; (ii) sulfide chimney textures; (iii) exhalite at the ore horizon; (iv) fossil tubeworms and bivalves; (v) facies characteristics indicating slow accumulation rate of the host rocks, and/or occurrence of VHMS ores between units of rapid emplacement rate; and (vi) an asymmetric alteration pattern of strong footwall alteration and weaker hanging wall alteration. Criteria i–iv are diagnostic of seafloor sulfide formation, whereas v and vi suggest seafloor deposition but are not diagnostic.

Doyle and Allen (2003) suggested that sub-seafloor sulfide replacement may be inferred from the occurrence of the following: (i) mineralized intervals are enclosed within rapidly emplaced volcanic or sedimentary facies (lavas, intrusions, subaqueous mass-flow deposits, pyroclastic fallout); (ii) relics of the host facies occur within the mineral deposit; (iii) replacement fronts occur between the mineral deposit and the host lithofacies; (iv) the mineral deposit is discordant to bedding; and (v) strong hydrothermal alteration continues into the hangingwall without an abrupt break in intensity. Criteria i–iii are diagnostic of replacement, whereas criteria iv and v may suggest replacement but alone are not diagnostic. Because clastic sulfide ores contain accessory rock fragments collected by the parent sediment gravity flow(s) during transport, criteria ii can only be applied to massive, semi-massive, disseminated or vein style deposits, and not to clastic ores.

The Jaguar sulfide body is here considered against the criteria of Doyle and Allen (2003) to assess its environment of formation.

Bedforms

The Jaguar sulfide ore does not have preserved examples of sedimentary structures, such as sulfide breccias or intercalations of laminated and fragmental ore. However, in lateral volcanic breccia facies, there are small clasts of massive sulphide. Such clasts could be sourced as accidental lithics in volcaniclastic mass-flow deposits (e.g., Mt Read Volcanics: Gibson, 1991). Mass flows can erode several metres into the substrate and may be triggered by local uplift resulting from seismic activity associated with growth faults. As both seafloor and shallow sub-seafloor sulfide deposits can be eroded, this criteria is not definitive either way.

Exhalites

At Jaguar an exhalite layer of hydrothermal chert occurs at the base of the Mineralised Package, and commonly underlies the massive sulfide lens. It represents a hiatus after emplacement of the Footwall Basalt. In addition, rare narrow (<2 cm) discontinuous layers of chert appear in the upper MP, and in the single occurrence where the top of the orebody is undeformed, intermittent, narrow bands of laminated chert overlie massive sulphide. The extent is unknown but there is no apparent widespread exhalite horizon at or above the top of the orebody, beyond the orebody margins. In comparison, the bedded tetsusekiei overlying the Kuroko deposits (Japan) is discontinuous and usually covers an area about twice that of the ore (Kalgeropoloulos and Scott, 1983). At Hellyer (Tasmania) the massive sulfide ore lens is overlain by a discontinuous barite-sulfide layer, and a more restricted silica-sulfide cap (McArthur and Dronseika, 1990; McArthur, 1996) This criteria is not conclusive but does indicate that the hydrothermal system reached the seafloor.

Rate of emplacement of host facies

The Jaguar orebody is hosted by coherent dacite, dacite breccia, pumice-rich breccia, polymictic conglomerate and volcanic sandstone facies; these are all rapid emplacement facies. These facies overlie hydrothermal chert and are overlain by laminated mudstone, which are both slowly deposited ambient or chemical sediment types. A positive for this criteria is consistent with a replacement, sub-seafloor deposit.

Replacement fronts

Two types of replacement fronts occur in the Jaguar orebody. Sharp fronts occur in the dacite facies, where a change from sulfide ore to altered dacite is marked with a lobate shape. This style occurs in drillholes TBD0256, 05TBDD003 and 05TBDD020. Gradational replacement fronts are common, and are characterised by disseminated or blebby sulfide which progressively increase in abundance towards ore. In addition, some sulfide clasts in the polymictic conglomerate facies have developed pyrite overgrowths where they are in close proximity to the orebody. Confirmation of the presence of this criteria favours a replacement, sub-seafloor origin for at least part of the ore.

Relationship with the enclosing lithofacies

No comment can be made on whether the ore lens is concordant or discordant to the enclosing lithofacies, because extrapolation using drillcore would not be reliable enough to be conclusive. Therefore this criteria cannot be assessed.

Alteration style

The Jaguar deposit has asymmetric alteration that extends into the footwall, hangingwall and laterally into adjacent facies. The footwall is dominated by intense, pervasive chlorite and the hangingwall by weak to moderate, pervasive pyritic-sericitic alteration. This criteria is a weak positive for a replacement, sub-seafloor deposit.

Chimneys

No chimney fragments or chimney-like structures were observed in any of the drillcore logged. A negative for this criteria is not conclusive as preservation potential is poor.

Sulfide textures

The Jaguar deposit has preserved open-space growth textures such as colloform and botryoidal forms, rare cockade and some network textures. Many of these textures indicate radial outward growth from a central nucleus rather than infill of a defined pore space. Gradational contacts between blebby (large isolated colloform sulfide grains), and massive ore are common and suggest that the sulfide-rich ores have formed by almost complete replacement of host rock by sulfide. This criteria is not definitive either way.

Table 6.2. Interpretation of environment of the Jaguar deposit

Characteristics	Presence at Jaguar
Deposit style	massive sulfide lenses
Immediate host lithofacies	coherent dacite, dacite breccia, pumice-rich breccia, polymictic conglomerate, laminated volcanic mudstone
Precursor facies within mineral deposit	✓
Rapidly emplaced facies	✓
Replacement Fronts	✓
Discordance between ore and host rocks	not known
Hangingwall alteration	weak
Sulfide bearing clasts	✓ (can be sourced during scouring by mass flow of seafloor or sub-seafloor deposit)
Chimneys or chimney-like features	no, not diagnostic
Exhalite at top of orebody	✓ (is very narrow, discontinuous and limited in lateral extent)
Bedded sulfide	± (above the deposit)
Interpreted environment	sub-seafloor ± seafloor

Conclusion

The Jaguar deposit ticks the three criteria (Doyle and Allen, 2003) considered diagnostic of a replacement sulfide deposit (Table 6.2), but also has some features that indicate that some seafloor formation may have occurred. The preferred interpretation is that most ore formed by invasion of the glassy dacite and associated volcaniclastic facies before encountering the seafloor.


volcanic
et
al
deposits
Jaguar
Volcanic
Chapter
Fig
time
lava
breccias
sulfide
formation
within
mudstone
Abitibi
facies
deposit
mantle
MP
andesite
water
study
major
probably
felsic
may
along
depth
geochemical
growth
evidence
seafloor
rocks
chert
extension
interpreted
suggested
zones
footwall
rhyolite
VHMS
belt
upper
basalt
volcanism
development
greenstone
associated
hydrothermal
lavas
breccia
succession
faults
hyaloclastite
exploration
margins
events
scale
still
stratigraphy
dome
hiatus
geodynamic
environment
global
However
Thurston
occur
magma
clasts
host
deposition
followed
units
magmas
flows
part
cn
Zn
single
stress
iron
change
area
e.g.
Archean
dacite
massive
formed
pillow
likely
considered
exposed
endowment
low
regional
rare
basin
arc
new
Ayer
values
instability
regime
carapace
long
although
lower
top
early
source
times
activity
mineralisation
FW
sedimentation
stratigraphic
lithofacies
limited
dominated
crust
several
Barley
setting
Yilgarn
unit
sediment
described
Ga
significant
complex
volcaniclastic
layers
form
domes
Bore
extensional
local
also
eruption
similar
Teutonic
crisis
Cu
comparison
eruptive
developed
erupted
episodes
HA

7. EVOLUTION OF THE JAGUAR DEPOSIT AND ITS HOSTROCKS

7.1 Introduction

This chapter summarises the evolution of the Jaguar deposit. After setting the geodynamic context (with emphasis on comparison to the Abitibi terrain, Canada), the evolution of the volcanic pile, and the syngenetic development of the massive sulfide deposit, is described. A lot of new work in the Abitibi (e.g. Ayer et al., 2002; Ayer et al., 2005; Mercier-Langevin et al., 2007a, 2007b; Dinel et al., 2008; Finamore et al., 2008; Hathway et al., 2008; Thurston et al., 2008; Pearson and Daigneault, 2009; Stott and Mueller, 2009; Wyman and Kerrich, 2009) has driven rethinking of Archean tectonics and this in turn has stirred thoughts on the related metallogenous terrains. The Abitibi is of particular importance as it is the most richly endowed VHMS terrain in the world.

In section 7.5 the Jaguar deposit is compared with other VHMS deposits using several criteria. Comparisons are made only with other Archean districts or deposits; this is justified by the changes across time in the global heat-flow regime, and the uncertainty this creates.

7.2 Tectonic setting and geodynamic significance

7.2.1 Global geodynamic significance

The Neoarchean Jaguar succession (c. 2.69 Ga) was laid down during a period of Earth history characterised by massive reworking of pre-existing continental crust (Condie, 1995, 2000; Rey et al., 2003; Wyman, 2003; Barley et al., 2005). The model proposed by Condie (2000) for this event, suggested that the collapse of a subducted slab through the 660 km seismic discontinuity, and mantle convection changing from layered to whole mantle, culminated in the aggregation of the first supercontinent. He further suggested that during this super-event the mantle may have become well mixed, thus expunging geochemical evidence for enriched mantle sources.

Rey et al. (2003) described this event as the 2.75-2.65 Ga 'global crisis'. These authors proposed a model to explain the amplitude and timing of a global thermal anomaly, that is required to account for the Superior Province (Canada) and the Yilgarn Craton (Australia) volcanism, and which involved a global re-arrangement of convection cells in the deep mantle and formation of multiple mantle plumes. They elaborate: "The greenstones emplaced at the surface and the plumes that spread in the thermal boundary layer contributed to heat the crust from both above and below. This produced massive crustal

partial-melting that reached its climax c. 40 m.y. after the emplacement of the plumes and associated greenstone cover rocks. In turn, this led to gravitational instabilities in the crust, as dense greenstone cover rocks progressively sank into the thermally softened crust and, granite domes rose in response. The extraction of heat-producing elements toward the upper part of the crust has contributed to the cooling and stabilisation of the cratons. This succession of events, which is not incompatible with plate-tectonic processes, may have profoundly changed the nature of the crust exposed at the surface and could explain the contrasting geochemical signatures of Archaean and post-Archaean shales."

Barley et al. (2005), focussing on the linkages between global tectonics, changing sea levels and environmental conditions described the period between c. 2.72 to 2.65 Ga as "the most prodigious period of generation and preservation of juvenile continental crust recorded in Earth history during a plume breakout accompanied by high sea levels."

7.2.2 *Global and craton scale events during the 'global crisis'*

The Abitibi greenstone belt is of particular interest when making comparisons as it is the most extensive (Fig. 7.1) Archean terrain formed during the 'global crisis' and because of

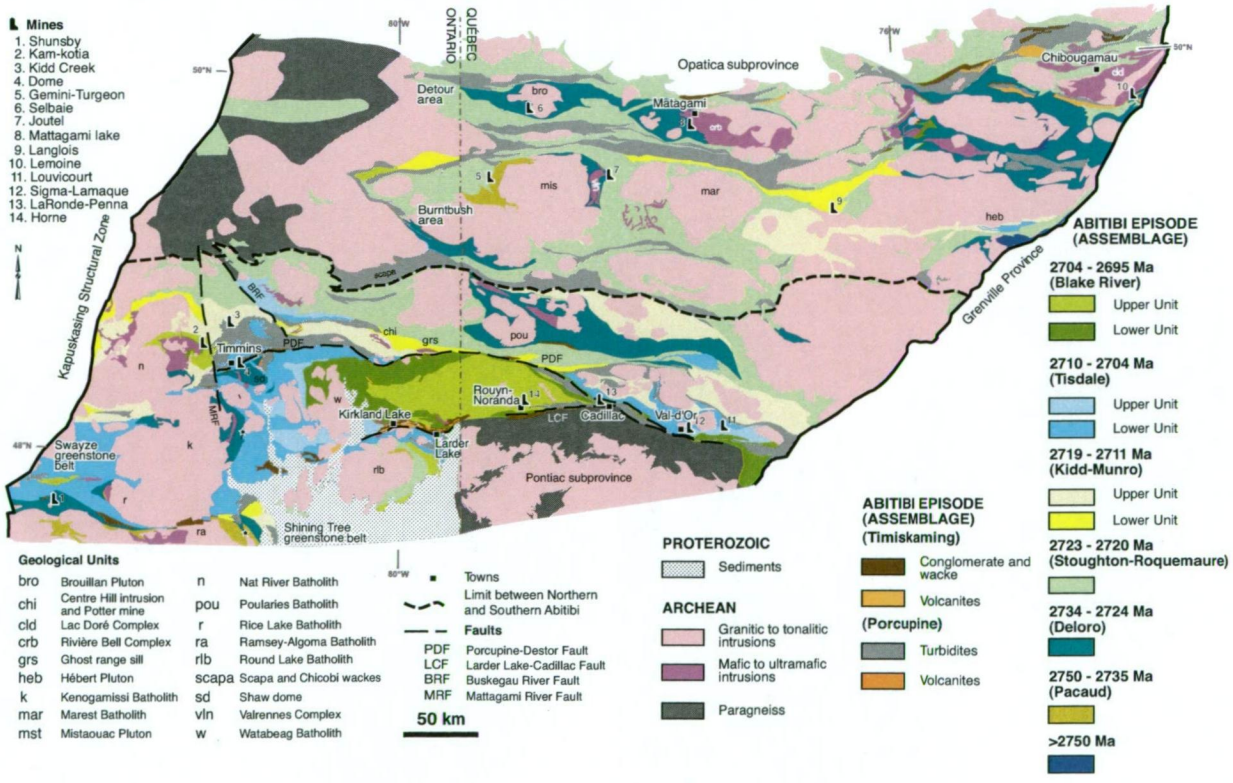

Figure 7.1 Stratigraphic map of the Abitibi greenstone belt. The geology of the southern Abitibi greenstone belt is from Thuston et al. (2008) is based on Ayer et al. (2005) and the Québec portion on Goutier and Melançon (2007). Abbreviations and acronyms used on the map are listed.

its fabulous mineral endowment. The western part of the southern Abitibi greenstone belt contains some of the world's largest copper-zinc and gold deposits and significant amounts of nickel-copper-platinum group element (PGE) (Ayer et al., 2005). The evolutionary history of the southern Abitibi extends from 2750 to 2660 Ma, a span of 90 m.y., and includes volcanism, sedimentation and plutonism. Despite the Abitibi being one of the most intensely studied greenstone belts in the world, the mantle processes associated with its volcanism remain poorly understood, despite numerous detailed studies of its volcano-sedimentary successions (Wyman, 2003). Using Nb-Zr-Y systematics ,Wyman (2003) divided the Abitibi volcanic suites into two main trends. One trend comprised the Kidd-Munro Assemblage and Malartic Block and corresponded to mixtures of interpreted strongly depleted plume asthenosphere and adakitic melts. A shared trace element signature of these volcanic successions confirmed that they are parts of a single autochthonous supracrustal assemblage. The second trend, consisting of the younger Kamiskotia Assemblage and the Blake River Group[1], is interpreted to relate to crustal extension episodes within an Abitibi island arc. Trace element plots are consistent with their derivation from mantle plume-related asthenosphere. The trends require a slab melt origin for the adakitic magmas rather than origin by internal differentiation of underplated mafic crust.

At the same general time as these events in the Abitibi, in the eastern Yilgarn Craton, arc and back-arc basin associations (c. 2.78 to 2.72 Ga) were followed by coeval, deep–marine, mantle–plume derived, tholeiite–komatiite and tholeiite–calc-alkaline arc associations (2.72 to 2.70 Ga) (Barley et al., 1998). This was followed by episodic deep-water volcaniclastic sedimentation, layered mafic–ultramafic sills and regional emplacement of granitoids (2.70 to 2.66 Ga).

The regional geodynamic synthesis for the central Eastern Goldfields Superterrane (Fig. 2.5) (Blewett and Czarnota, 2007) places the deposition of the Jaguar succession (at c. 2.69 Ga) during a period of arc building, in an east-northeasterly directed extension-dominated regime. Regionally the first significant contraction terminated the volcanism, with shortening orientated east-northeast, perpendicular to the grain of the earlier extensional orogen. This was followed by significant granite doming accompanied by the development of high-strain shear zones around the major granite-dome margins.

7.2.3 *Local scale*

The geodynamic setting of the Gindalbie Domain is uncertain. Brown et al. (2002) in a

1 The Blake River Group (2704–2695 Ma) is considered age-equivalent to the Teutonic Bore volcanic complex (2.69 Ga: Nelson, 1995) (which contains the Jaguar succession). Interestingly the lithology and chemistry of the Blake River Group (mafic to felsic volcanic, tholeiitic and calcalkalic: Ayer et al., 2005) is also similar to the Jaguar succession.

study on the Melita volcanic complex suggested that the compositional range, eruptive style, abundance of thick mass flow deposits, and association with late mafic sill complexes demonstrated by the igneous rocks was typical of intra-arc-rift settings such as the Sumisu Rift, Isu-Bonin arc, Japan, whereas the bimodal basalt-rhyolite volcanism was characteristic of active rifting in a marginal arc. Ongoing geochemical work (Dickins, UWA PhD project), involving Sm-Nd isotope analysis of rocks from the Teutonic Bore volcanic complex, suggest that these rocks are typical of products of renewed extension. Dickins et al. (2006) suggested that in terms of the tectonostratigraphic architecture of the Gindalbie Domain, the HFSE-enriched volcanic rocks are probably the result of magmatism associated with a convecting mantle that had been enriched by melting of a previously subducted slab.

Dickins et al. (2006) suggests that the setting of the Gindalbie Domain is extensional, possibly an early back-arc basin environment (indicated by the compositional range, eruptive style, subduction signature) that has had an interaction with a mantle plume.

7.3 Building the local pile

7.3.1 The footwall forms

The Footwall (FW) was laid down during a period of extension that is interpreted to have been regional in extent. The FW is dominated by a succession of subaqueous, coherent lavas, with associated volcaniclastic facies. There are essentially no sedimentary lithofacies and only minimal reworking of the volcanic breccias is evident. The limited exposure of the footwall units and their contacts, means the relationships between the FW units are not tightly constrained.

The lack of sedimentation in the eruptive sequence could have several causes: (1) the sequence may have been erupted semi-continuously, with no hiatus between eruptive events therefore allowing very little time for any ambient sedimentation to accumulate; (2) sediment input may have been very restricted, perhaps implicating a deep marine environment far from any emergent volcanic edifices; or (3) a combination of these alternatives.

The depth of water is poorly constrained. The dominant volcanic facies – pillow lavas with hyaloclastite breccia carapaces – occurs today over a wide range of water depths. The minimal reworking in the hyaloclastite breccias indicates that the depth is likely to have been below storm wave base (i.e. >200 m) (e.g., Cas and Wright, 1991; Mueller et al., 1994).

The FW and the MP Dacite (MPD) volcanic units appear to be chemically related and are considered likely to be differentiation products from the same magma chamber. These

lavas, all stratigraphically beneath the massive sulfide mineralisation, show trends consistent with a constantly fractionating source. The DFA, FA, FB and MPD[1] show near-identical trends and slopes in the chondrite-normalised REE and BABB-normalised multielement spidergrams. The range of [La/Sm]cn and [La/Yb]cn values reflect the sub-parallel slopes of the trend lines and have a weak negative slope; they share similar Zr/Nb values, and similar enrichment and depletion anomalies in other elements, excepting Eu.

The depositional environment is likely to have been a deep marine basin, with a subdued but irregular topography caused by building of local volcanic edifices. Relief within the basin could only have been in the order of several tens of metres.

A series of isometric block diagrams show a schematic development of the footwall (Fig. 7.2). Following the emplacement of the basal andesite unit (DFA), the FR rhyolite was extruded as a dome complex comprising coherent and breccia facies. The FA, a coherent andesite lava with a hyaloclastite breccia top (Fig. 7.2a) was likely coeval with the still growing rhyolite dome, but the relationships are unclear. Conformably, and directly overlying the andesite breccia, are the pillow basalts and associated hyaloclastite breccias of the lower FB (Fig. 7.2b). These early basalt lavas were lower than the summit of the rhyolite dome, as shown by the presence of intercalated rhyolite breccias. The rhyolite breccias are interpreted as having formed from debris flows that originated on the dome, which probably were the result of collapse of unstable dome carapace breccias, or runout of unstable talus following seismic events associated with tectonic instability or growth faults (Fig. 7.2c).

The continued eruption of pillow lavas and their associated volcanic breccias eventually covered the rhyolite dome. This culminated in a seafloor with an irregular topography where unstable mounds of pillow basalts were surrounded by talus aprons of basalt breccia and conglomerate (Fig. 7.2d). These aprons were formed as a result of both autoclastic processes and local collapse due to tectonic and/or gravitational instability.

7.3.2 *The beginning of the mineralised package*

The MP is a complex package of lithofacies dominated by volcaniclastic facies associated with the coherent dacite facies as described in Chapter 3. A series of isometric block diagrams showing a highly schematic development of the MP are shown in Figure 7.3.

At the onset of MP times, a hiatus in the volcanic activity after the eruption of the FB lead to the deposition of a thin (av. 30–40 cms) mantle of banded hydrothermal chert (MPH) deposited over the irregular upper surface of the FB (Fig. 7.3a). This volcanic hiatus,

1 A single sample of the MPD (Fig. 5.13d) shows enrichment in the HREE, not reflected in any other sample.

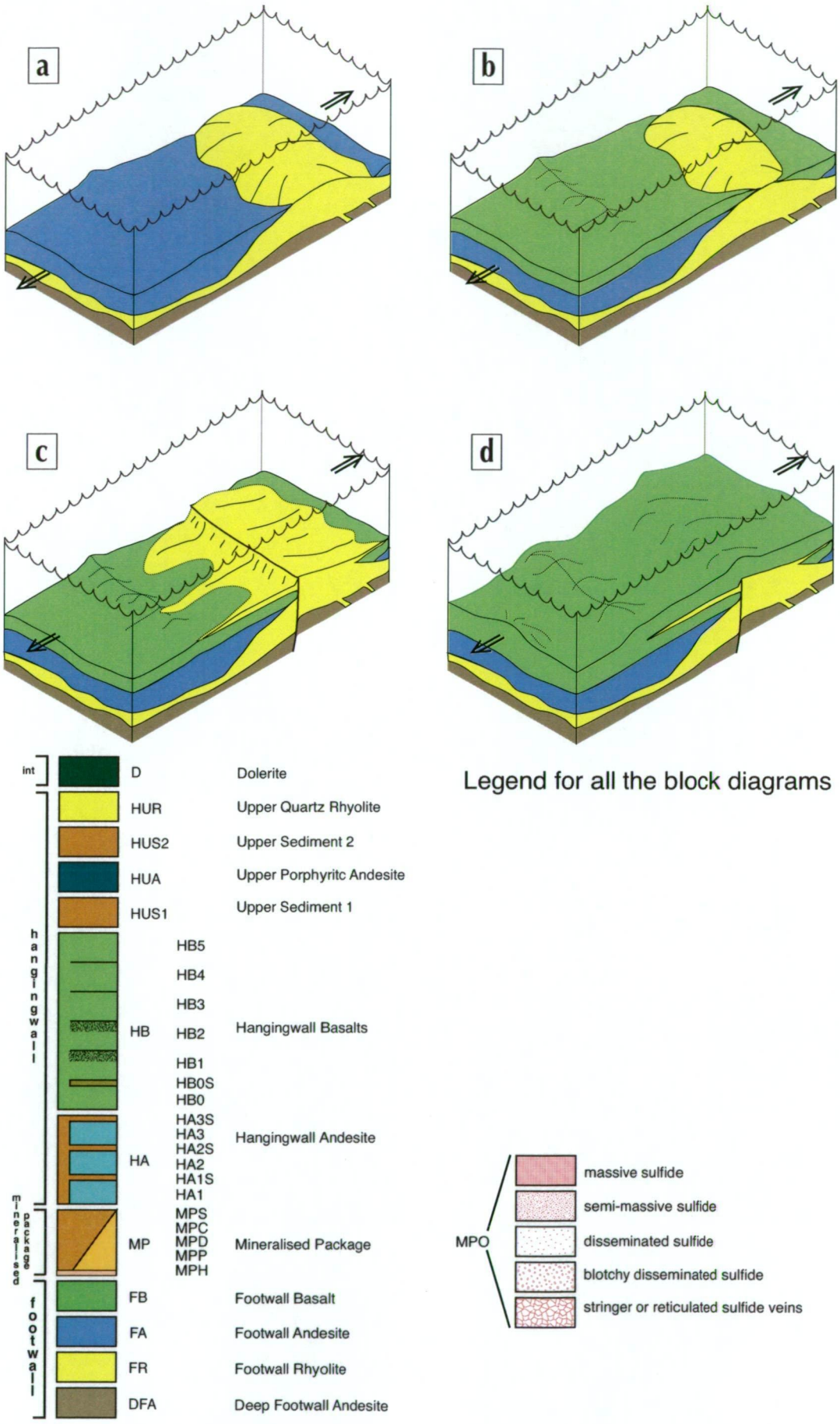

Figure 7.2 Series of isometric block diagrams showing a highly schematic development of the footwall: a) the FA erupts and partially covers the FF dome complex; b) the early FB lavas are erupted; c) extension causes growth faulting and spall from the dome spreads as debris flows; d) the final FB lavas and associated volcaniclastic facies result in a topographically uneven seafloor. [Figure is not to scale, and narrow units are vertically exaggerated to better show the process].

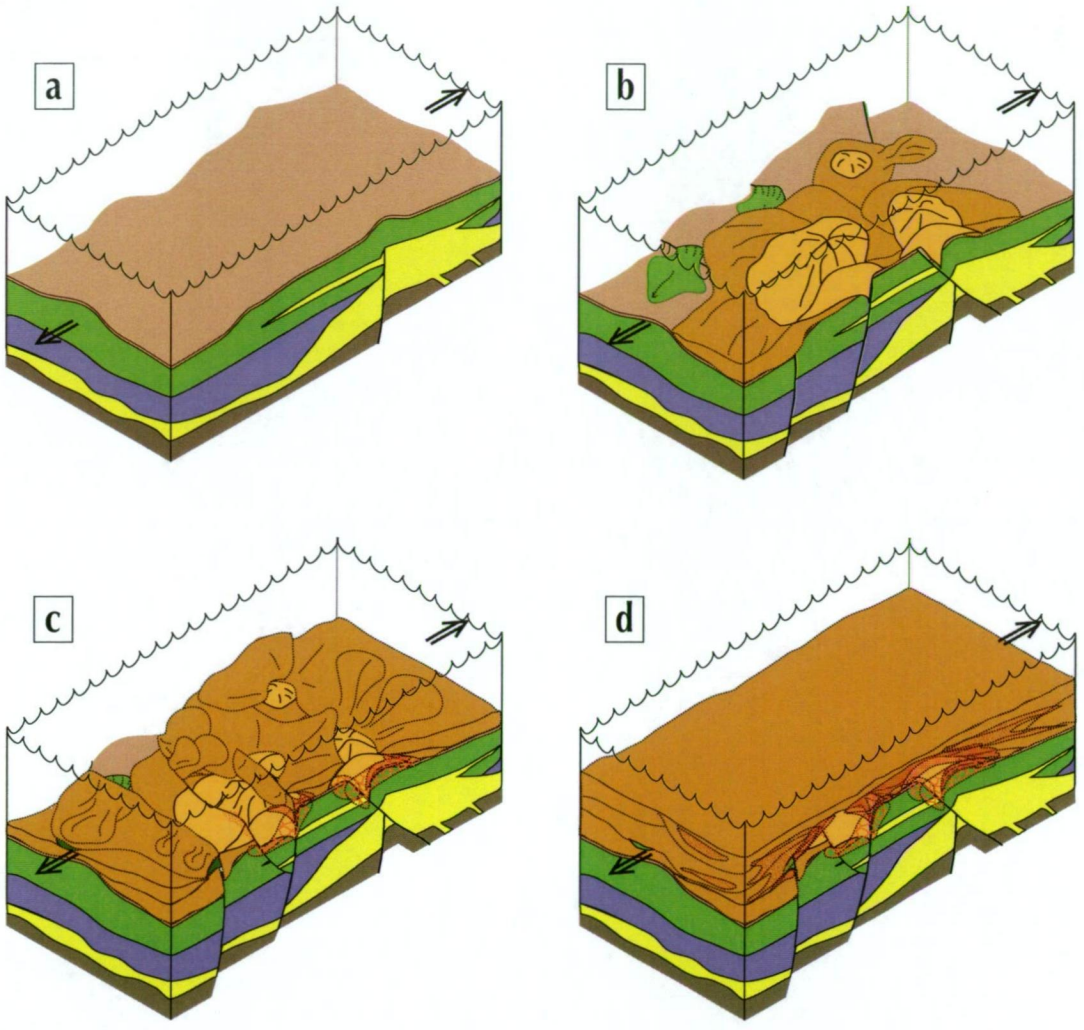

Figure 7.3 Series of isometric block diagrams showing a highly schematic development of the MP: a) a thin mantle of hydrothermal chert covers the uneven seafloor; b) dacite domes erupted contemporaneously with growth faults (possible eruption conduits), vesiculated pumiceous carapace broke apart after quench fragmentation and produced pumice-rich breccia debris flows, plus more distal pumice fallout, growth faulting exposed the underlying basalt breccias at the top of the FB; c) growth faulting continued, debris flow and fallout deposits formed and the hydrothermal sulfide body precipitated; d) at the end of MP times the seafloor showed little topographic elevation. See Figure 7.2 for the legend. [Figure is not to scale, and narrow units are vertically exaggerated to better show the process and fault positions are schematic].

apparently free of epiclastic input, allowed accumulation of the chert on the sea floor as an exhalative precipitate. This implies that a lower temperature hydrothermal system was developing in the footwall and that virtually no external sediment input was occurring at this time. Local seismic events, associated with ongoing regional extension and and development of local growth faults resulted in plastic deformation of the chert while it was still in a gel state. The length of time for chert deposition is not known. It was probably not prolonged, but was long enough for consolidation to a state able to support the weight of new sediment (commonly, pumice-rich granule breccia facies).

Immediately after the formation of the chert, the MPD was erupted onto the seafloor as the last phase of the fractionated products of the magma chamber that sourced all the FW magmas (as shown in Chapter 5). This eruption was concomitant with an increased

tectonic instability and the local development of growth fault scarps probably exposed the underlying basalt breccias. Growing small domes of dacite produced pumiceous and vesiculating carapace breccias. The pumice produced in these early stages of the eruption most likely formed by non-explosive quench fragmentation of the pumiceous dacite lava or dome carapace (eg., Allen and McPhie, 2009). This process also produced debris flows that originated in the carapace breccia and during transport these incorporated clasts of the still plastic chert (Chapter 4.4.7) among the volcaniclastic dacite fragments, and more rarely, basalt breccia clasts that had been exposed by local fault scarps (Fig. 7.3b). Pumiceous mass-flow deposits are a particularly common site for economic sulfide deposits (Doyle and Allen, 2003) as the originally highly porous, permeable, water saturated and glassy nature of these lithofacies makes them very favourable host rocks for contemporaneous mineralisation.

Away from the dacite domes, pumice granules settled to the seafloor, to rest either overlying the chert, or directly on to areas of the slump-exposed basalt breccia. The wedge shape of many of the breccia and conglomerate lenses supports the interpretation that active growth faults were contemporaneous with deposition. As deposition of the MP continued, dacite dome activity reduced and the last dacite magmas were probably erupted as cryptodomes within the unconsolidated volcanic breccias.

Throughout this activity the seafloor topography was irregular and constantly changing.

The sulfide body forms

The polymetallic sulfide orebody was formed in this environment. Sulfide growth was syn-volcanic and is interpreted to have been predominantly beneath the seafloor (Fig. 7.3c). The location of the massive sulfide deposit within the MP indicates that the underlying hydrothermal system had evolved to higher temperature.

Some VHMS deposits, especially those hosted by coherent flows are underlain by a focussed alteration pipe (Franklin et al., 1981, Franklin et al., 2005) interpreted to be the source of the high temperature hydrothermal fluids (e.g., Noranda Camp: Gibson and Watkinson, 1990; Bathurst Camp: Goodfellow et al., 2003; Hellyer: Gemmell and Large, 1992; Solomon and Gaspar, 2001; Kuroko: Eldridge et al., 1983). This is not the case at Jaguar. Other deposits, especially those hosted in volcaniclastic rocks (e.g., Scuddles: Ashley et al., 1988; Woodlawn: McKay and Hazeldene, 1987; Filon Norte: Tornos, 1998; Gibson and Kerr, 1993; Franklin et al., 2005) do not possess a distinct pipe structure. At Jaguar there is no obvious single conduit that demonstrates a constrained focus for the discharging hydrothermal fluids. The ascending hydrothermal fluids were probably focused at depth by these syn-volcanic growth faults and/or volcanic vent structures, but lost focus and were dispersed within the porous volcaniclastic facies that dominated the near- sea floor environment of the FB and MP (e.g., Matsuki: Kuroda, 1983; Mt Morgan: Taube, 1986).

Continued extension and resulting seismic activity caused instability along growth faults, exposed the developing sulfide body, and provided sulfide clasts to mass flows, which formed the surrounding breccias and conglomerates. The run-out distance of these conglomerates is not known, but considering the limited relief it is probably in the region of hundreds of metres rather than thousands (e.g., Kano, 1996; Busby et al., 2003). These clasts support other evidence that the sulfide body was formed contemporaneously with deposition of the MP.

The water depth at the time of mineralisation is difficult to determine but geological data are consistent with formation below storm-wave base (>200 m) (e.g., Cas and Wright, 1991; Mueller et al., 1994).

The upper part of the Mineralised Package is dominated by laminated mudstone and sandstone lithofacies of the MPS sub-unit. They are interpreted to have been derived (Chapter 3) by fallout of felsic shards and sand sized particles (including individual crystals) which were most likely elutriated during 1) debris flows; or 2) tectonic instability. All of these activities would have resulted in the finer grained particles being mixed into the water column and moved about by both water and weak gravity flow currents before settling out of suspension to form the bedded layers of the MPS.

By the end of MP times (Fig. 7.3d), only fallout ambient sedimentation was occurring. Magmatism had ceased, as had major high-temperature hydrothermal activity. The seafloor now showed little topographic elevation. The sedimentation rate was very slow; weak low-temperature hydrothermal activity persisted, manifested as small layers (< 2 cm) of hydrothermal iron-bearing chert (e.g., Kalogeropoulos and Scott, 1983; Davidson et al., 2001; Grenne and Slack, 2003) among mudstone laminae and uncommon beds of black graphitic shale. Some of the chert layers show evidence of maturation cracks, an indication that they formed at the water - seafloor interface. Sulfide is present as disseminated, fine-grained pyrite grains within mudstone laminae and may have precipitated from buoyant fluids or have grown in-situ.

As the laminated mudstone at the top of the MP shows no evidence of widespread silicified 'hardground', the overall time that this unit was exposed to what many workers considered were silica-rich Archean waters (Krapez et al., 2003; Mercer-Langevin et al., 2007a) was not long. In addition, where parts of the overlying HA1 andesite lava burrowed shallowly into this mudstone, peperite is locally developed, an indication that the material was still semi-unconsolidated.

7.3.3 The early hanging wall

The onset of HW times was signalled by the eruption of new magma, with a different chemistry to the FW lavas, which together indicated that a major change occurred at the end of MP times. As discussed in Chapter 5, the HA lavas were more LILE enriched and more HREE depleted than the FW magmas, and successive HA lavas also showed increased Ti/Zr values.

The HA1 lava flowed over, and along its southern extremity burrowed shallowly into, the slowly accumulating ambient sediment at the top the MP (Fig. 7.4a). The HA1 lava has the form of a low aspect coulee, and although twice the thickness of the HA2 and HA3 lavas, it is more areally restricted than these lavas. Deposition of intercalated laminated volcanic mudstone and sandstone (HA1S) followed emplacement of the HA1 (Fig. 7.4b).

HA2 erupted onto the seafloor and partially burrowed into the unconsolidated sediments of HA1S that made up the sea floor at the time (Fig. 7.4c) with peperites forming along the upper and lower margins. Ambient sedimentation continued and the HA2S mudstone and black shale were laid down conformably over the limited occurrences of HA2 hyaloclastite carapace-breccias. Extension-generated growth faulting continued (Fig. 7.3d) probably as a response to far-field extensional tectonics.

HA3, the last andesite, was then erupted on to the seafloor, in parts as a pillow lava and otherwise as a massive lava with a hyaloclastite breccia carapace. The lower contacts of HA3 are in places peperitic or otherwise conformably overlaid the mudstone, whereas the upper contact is marked by a hyaloclastite breccia carapace overlying massive or pillowed andesite (Fig. 7.4e). HA3 was then passively overlain by laminated mudstone and black shale (HA3S), which signaled the end of the calc-alkaline magmas of the HA (Fig. 7.4f). The HA is thickest and best developed in the area between 56100 N and 56250 N and the vent source was probably close to this area. The geometry of the HA unit suggests that throughout the formation of the HA there was continual, gradual subsidence, most likely the result of extension generated growth faulting which was more pronounced in the south of the study area.

Next, the massive outpouring (180 m thick) of tholeiitic basalt magma of the HB indicates another new pulse of magma, together with a change in chemical composition and magmatic affinity compared to the previous HA magma (Chapter 5). In overview, the eruption of massive volumes of tholeiite is a signature of renewed extension (e.g., Smellie, 1995).

These HB lavas, are interpreted (Chapter 4) to have formed by a voluminous outpouring of tholeiitic basalt in five major episodes. An initial lava, HB0 was of low volume and limited extent (Fig. 7.5a). HB0 appears to have been restricted to the southern, down-dip area and

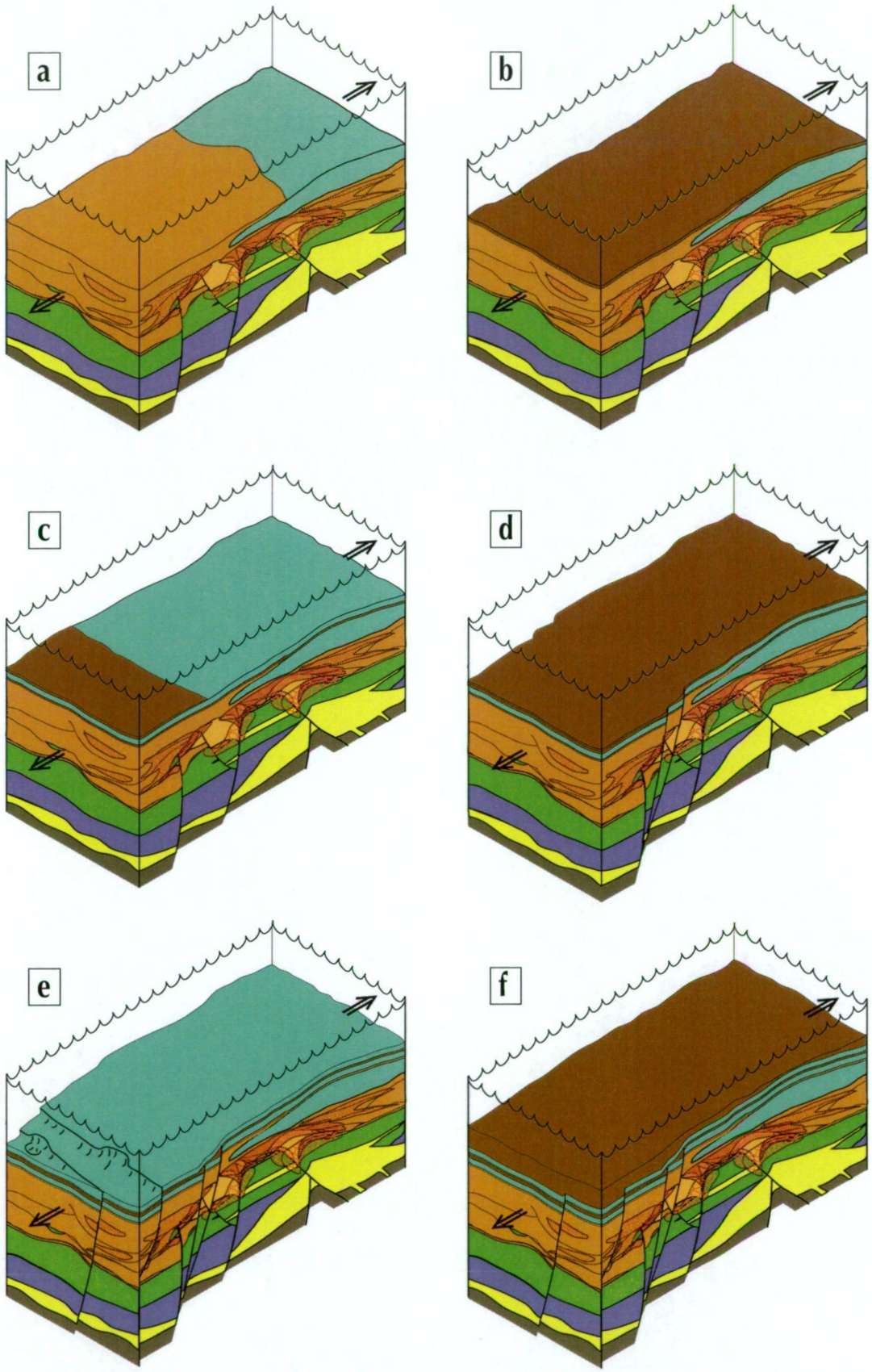

Figure 7.4 Series of isometric block diagrams showing a highly schematic development of the HA: a) the HA1 lava partially burrows into the upper mudstone units of the MP; b) the HA1S unit is deposited across the seafloor; c) the HA2 lava flows over and in places burrows beneath the HA1S; d) deposition of the HA2S mudstone plus idealised growth faulting; e) eruption of the HA3 lava, in places pillowed and with a hyaloclastic carapace plus idealised growth faulting; f) deposition of the HA3S mudstone. See Figure 7.2 for the legend. [Figure is not to scale, and narrow units are vertically exaggerated to better show the process].

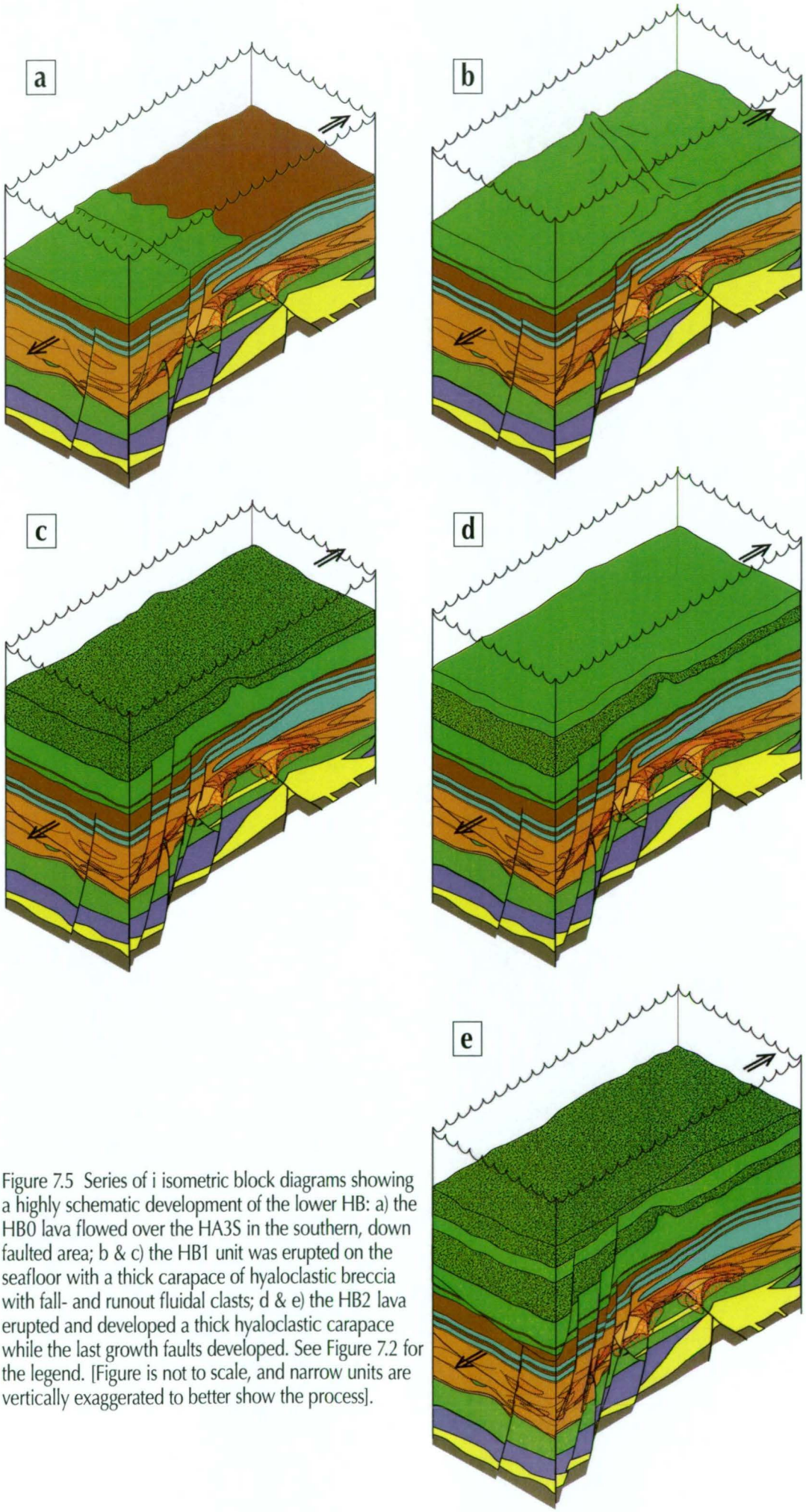

Figure 7.5 Series of i isometric block diagrams showing a highly schematic development of the lower HB: a) the HB0 lava flowed over the HA3S in the southern, down faulted area; b & c) the HB1 unit was erupted on the seafloor with a thick carapace of hyaloclastic breccia with fall- and runout fluidal clasts; d & e) the HB2 lava erupted and developed a thick hyaloclastic carapace while the last growth faults developed. See Figure 7.2 for the legend. [Figure is not to scale, and narrow units are vertically exaggerated to better show the process].

the likelihood is that due to continued subsidence this was a topographic low at the time of formation. The HB1 lava which followed is the thickest of the HB eruptive episodes and its increased thickness wedge and shape to the south (Figs 7.5b and 7.5c) indicates the influence of a southerly depocentre.

The HB1 and HB2 eruptive episodes were marked by pillow lavas with extensive development of hyaloclastite breccia carapaces, including a widespread fluidal-clast breccia facies, associated with vigorous fountaining vents. This fountain deposit indicates a maximum water depth of about 3000 m (Chapter 3.4.9). Subsidence appeared to continue in the southern area during the eruption of the HB2 lava (Figs 7.5d and 7.5e) and marked the end of the expression of major extension. In overview, it is apparent that the main hangingwall extension, based on a thickness change (Fig. 7.4a-c) likely re-activated fault structures that were active in MP times. However, the ore-related MP-time fault zones did not reactivate and remained in the footwall of the zone of reactivation extension. Furthermore, the lack of alteration along these zones suggests that fluid discharge did not continue post-Jaguar above the ore area.

At about the time of the eruption of the HB3 lava the stress regime appears to have changed from extensional to compressional (Fig. 7.6a). The D sills were emplaced coeval with the comagmatic (Chapter 5.3.3 and 5.4.1) HB3 to HB5 lavas at stratigraphic levels up to HB2 (Fig. 7.6c). The interpreted stress regime switch to compression meant that melts more readily propagated sub-parallel to layering rather than erupting. This is also reflected in the upper three units (HB3, HB4 and HB5) being progressively less extensive in volume, with only minor carapace breccias in comparison to HB1 and HB2. During the HB outpouring, there was minimal deposition of sediment with only rare occurrences of black mudstone occurring in peperite along the base of some lava flows. This setting contrasts with some sites of silling on the modern seafloor, that occur in thick accumulations of sediment deposited in a zone of extension. At oceanic sediment-covered rift zones, magmatic activity is manifested mostly as sill-sediment complexes along the rift axis. Because of the low density and rigidity of water-saturated sediments, basaltic magmas reach a point of neutral buoyancy at which they flow laterally, forming sill complexes several kilometres in length (Einsele, 1982; Einsele, 1985). This is not the case at Jaguar. Examples of well-studied sedimented spreading ridges include Middle Valley on the Juan de Fuca Ridge (Davis and Villanger, 1992; Goodfellow and Franklin, 1993) Teagle and Alt, 2004) and the Guaymas Basin (Gulf of California: Koski et al., 1988; Peter and Shanks, 1992). In summary the key contrast is that at modern sedimented ridges, sill complexes form under extension within the sediment package, due to density differences between sediment and basalt substrates (Einsele, 1985), but at Jaguar the fact that silling occurred within volcanic substrate (no density difference) implies a change from extensional to compressional stress regime.

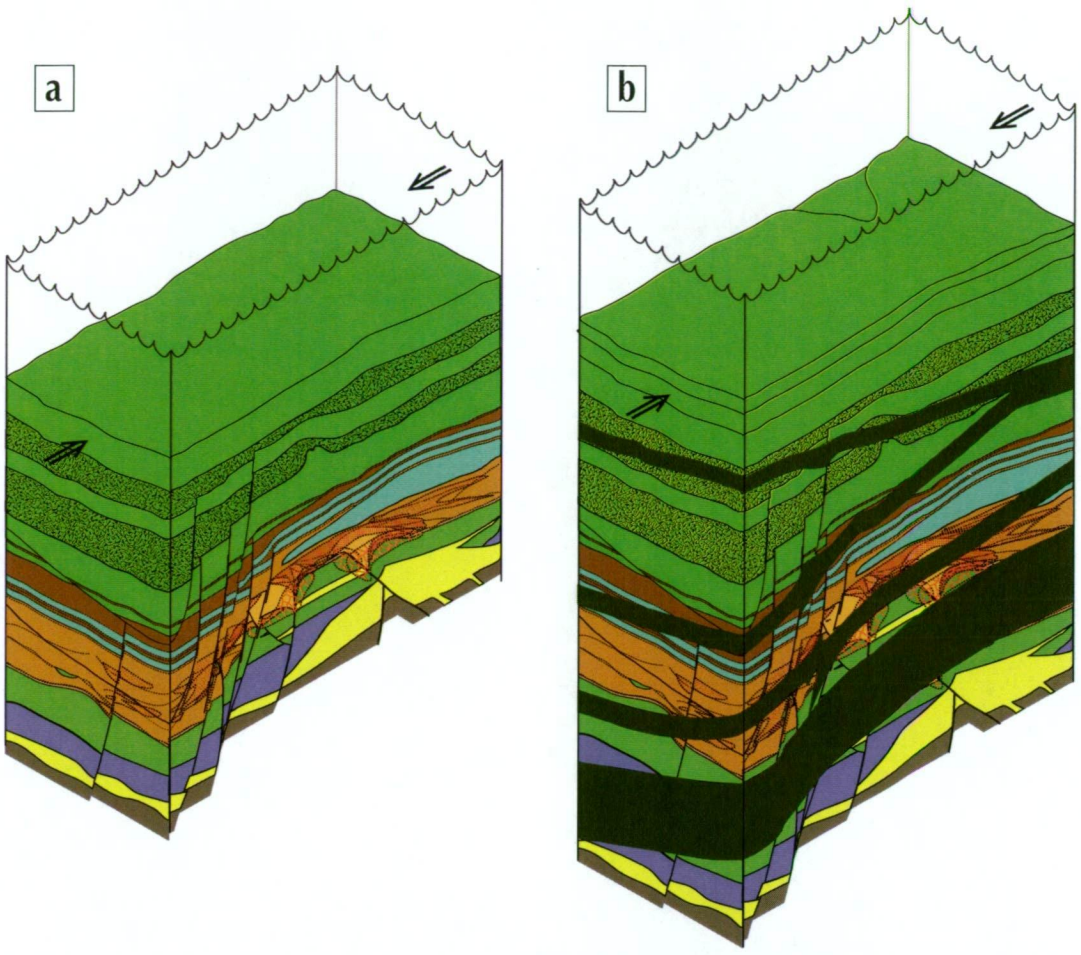

Figure 7.6 Series of isometric block diagrams showing a highly schematic development of the upper HB: a) the HB3 lava erupts in a changed stress regime; b) the D sills intrude as the HB4 and HB5 lavas erupt, the sills add up 150 to 200 m to the succession. See Figure 7.2 for the legend. [Figure is not to scale, and narrow units are vertically exaggerated to better show the process].

There is no evidence for fault reversal (i.e. normal faulting changed to reverse motion) during this stress field inversion although this can be an important effect of sustained compression (e.g., Cloetingh et al., 1988; Ziegler et al., 1995). This reversal may not have happened because the steep normal faults were 'stitched' by the sills.

7.3.4 The late hanging wall

After the cessation of the voluminous outflow that generated the hangingwall basalts, a long volcanic hiatus is evidenced by an accumulation of sediments (HUS1) that were initially dominated by mudstone with rare gravel-sized beds. However, as with the earlier mudstones in the MP, there is no evidence of prolonged exposure to silica-rich water that would have resulted in silicified 'hardground' for very long (Chapter 7.3.2). A short time interval is further supported by the peperitic margins on apophyses from the overlying andesite body, which indicate that the upper mudstone layers were unconsolidated at the time of the andesite intrusion.

This hiatus was followed by the eruption of the HUA, a with coherent andesite and associated autoclastic and volcaniclastic facies. Andesite apophyses also extended into the HUS1 unit below. The peperite margins attest to the semi-consolidated nature of the underlying mudstone at the time of the eruption. The composition of this andesite is similar to the HA andesites, but it is more felsic and more calc-alkaline than the HA suggesting that it was a more evolved and fractionated part of the same source magma (Chapter 5.4.1 and Table 5.13).

Following another volcanic hiatus (deposition of the HUS2 mudstone dominated unit) the HUR, a quartz-phyric rhyolite unit, was erupted. The top of this unit is nor seen so it is not known if the rhyolite was extrusive or intrusive (Fig. 7.7). By the end of Hangingwall times it is certain if a mafic and an intermediate felsic source were both contributing to the development of the HW overall. It is not known how these sources interacted at depth or indeed if they did interact.

7.3.5 Discussion

All the sedimentary younging evidence seen at Jaguar (graded bedding, flame structures, load casts) unequivocally youngs to the west, indicating that no major folds are present. The lateral continuity of almost all Jaguar units, and the lack of repetition of sequence, indicates that to date no subtle thrust ramp repetitions have been identified, giving confidence that the observed succession is stratigraphically intact.

There was no structural analysis undertaken for Jaguar, and although syn-volcanic growth faults have been inferred during the construction of the Jaguar succession, no judgement can be made on whether the extension occurred within a cauldron or within a wider, less focused extensional basin, because the scale of observations are too small. However, the regional tectonics for this period indicate it was a time of regional extension (Blewett and Czarnota, 2007).

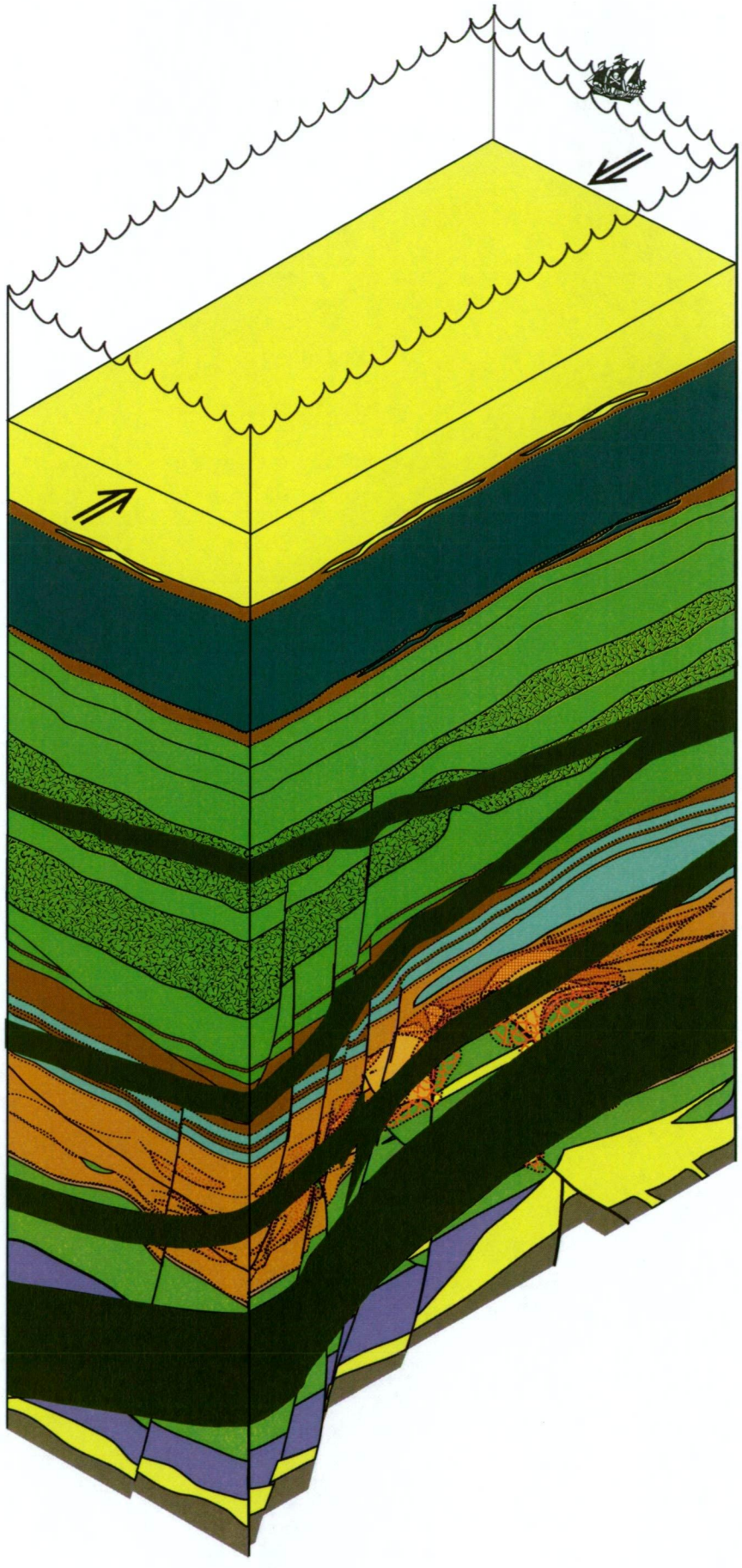

Figure 7.7 An isometric block diagrams showing a highly schematic complete succession for Jaguar. See Figure 7.2 for the legend. [Figure is not to scale, and narrow units are vertically exaggerated to better show the process].

7.4 Post-Lithification Evolution

That the Jaguar succession has been deformed is manifest in the durchebewgung textures and other high-strain features present in ductile sulfides (Chapter 6.2.2 and 6.3.5) and the rare graphite layers. The extent of tectonic disruption of the stratigraphy caused by deformation is unknown, but it must be measurable based on the extent of strain; this awaits the discovery of appropriate marker features. However, it has to be stated that apart from local manifestations, the majority of the primary rock fabric is undeformed. The essential requirements for the development of durchbewegung fabric are suitable competency contrasts and time for sufficient deformation to accrue and partition between components (Marshall and Gilligan, 1989). Locally at Jaguar there are also narrow (<5 m) zones of brittle deformation where jigsaw-fit to rotated breccias (quartz-carbonate cement, and essentially unaltered wall-rock fragments) occur, and very rare, narrow (<20 cm) zones of fault-gouge. However, there is no evidence that there was significant movement along these structures, and such zones were not correlateable hole to hole. These are interpreted to have formed post lithification. In essence the deformation of the succession is not interpreted to be significant enough to have influenced the stratigraphic reconstruction.

Regional metamorphism has affected the rocks and the grade appears to be mid - upper Greenschist facies.

7.5 Comparison of the Jaguar host succession with global VHMS systems in Archean settings

At craton scale, the Abitibi belt in the Canadian Superior Province and the Eastern Goldfields Superterrane in the eastern Yilgarn Craton are Earth's largest and most intensely mineralised greenstone belts. Although the Abitibi is frequently compared to the eastern Yilgarn gold deposit endowment, the richness of VHMS endowment of the former contrasts starkly with their scarcity in the latter.

Models of greenstone belt development are crucial for exploration and the establishment of a chronologically constrained, greenstone belt stratigraphy in the Abitibi (Ayer et al., 2002; Thurston, 2002; Ayer et al., 2005; Mercier-Langevin et al., 2007a, 2007b; Finamore et al., 2008; Hathway et al., 2008; Thurston et al., 2008; Stott and Mueller, 2009) documented seven discrete volcanic episodes and indicated that the greenstone belt developed autochthonously. Of particular interest are the implications of autochthonous development for syngenetic mineralisation exploration.

It appears that 1- to 350-m-thick, 'sedimentary interface zones' occur at the top of each of the seven volcanic episodes. Intraformation gaps of short duration (a volcanic hiatus) also occur in some units. These zones provide evidence for the existence of depositional gaps

in the development of the Abitibi greenstone belt. The duration of the gaps between the seven groups varies between 2 and 27 m.y.. Thurston et al. (2008) described four types of sedimentary interface zone: (1) units with pronounced lateral thickness variation, from several tens of metres of carbonate-facies iron formation and/or iron formation breccia and/or conglomerate, to a few metres of oxide-facies iron formation, (the latter are interpreted herein to represent condensed sections); (2) oxide-facies iron formation and felsic tuff with chert replacement of upper parts of depositional units, which is interpreted as possibly representing diagenetic replacement; (3) graphitic argillite units intercalated with volcanic rocks at geochemical transitions; and (4) chert breccia and/or iron formation conglomerate units.

Within each of the seven groups the distribution of VHMS mineralisation indirectly identifies volcanic centres (Thurston et al., 2008), the distribution of which does not display any discernible trend within or between the major units. Within each group, the VHMS deposits occur at one or several stratigraphic levels that represent hiatuses at the formation and/or member level.

A similar stratigraphy for the eastern Yilgarn Craton has not been proposed, and current geodynamic models for Eastern Goldfields Superterrane (Blewett and Czarnota, 2007; Krapez and Barley, 2008), Barley et al., 2008; Krapez et al., 2008) suggest allochthonous development by terrane accretion, which by its nature could preclude the development of a unified regional stratigraphy. Nevertheless, terrane-wide chronostratigraphic mapping and detailed chemistry is required to determine if discrete volcanic episodes that have a similar character to those of the Abitibi can be identified.

Favourable horizon concept

For many years, exploration emphasis classically depended upon tracking a single 'time equivalent' or 'favourable horizon', now refered to as a 'stratigraphic interval' (Franklin et al. 1981; Gibson et al., 1999; Franklin et al., 2005) in any one belt or camp. This related to the fact that in a given belt or camp, the link between clusters of VHMS deposits is the seafloor position, in some districts defined by a distinctive, distal, hydrothermally-derived, chemical sediment layer commonly described as an exhalite (e.g., Ridler, 1971; Large, 1977; Spry et al., 2000). While this is the case in many instances, this focus on 'exhalites' may have resulted in other prospective hiatuses having been inadequately explored because in other districts this 'gap' may be represented by a change in volcanic composition or affinity (Franklin et al., 2005).

Recent work has emphasised the importance of 'sedimentary interface zones' and/or 'geochemical discontinuities' (e.g., Hathway et al., 2008; Thurston et al., 2008). They may not be as obvious as a distinctive lateral-marker exhalite, but they are of equal significance.

Volcanic centre or convection cell centre, and ore location

The question of whether the spacing and/or size of VHMS deposits is related to volcanic centres (e.g., Mt Read volcanics: Gifkins and McPhie, 1999) or convection cell (hydrothermal cell) centres (e.g., Panorama: Brauhart et al., 2000; Iberian Pyrite Belt; Solomon et al., 1987) has long been argued.

Huston et al. (1996) argued that hydrothermal cell size is a major control on the size of resultant VHMS deposits and that the hydrothermal cell size increases with increasing depth of emplacement of the subvolcanic intrusion. Brauhart et al. (1998) described the relatively shallow emplacement of the subvolcanic intrusion at Panorama[1] and concluded that a large heat source beneath a thin volcanic pile could initiate more intense hydrothermal circulation, thus leading to more clearly defined discharge zones. They further suggested that such intense circulation of fluid through a thin volcanic pile could explain the contrast between semiconformable alteration zonation at Panorama and that documented in other VHMS districts. Brauhart et al. (2000) developed a three-stage model for the evolution of the Panorama VHMS hydrothermal system using oxygen isotope mapping. They described it as; a) the development of low temperature, randomly located and shallow convection cells after the intrusion of the outer- phase granite; b) the continued development of the hydrothermal system with stable, deeper and higher temperature, seawater- dominated convection cells in the volcanic pile and separate convection of magmatic fluids in the granite; and c) the descent of the seawater- dominated cells into the outer-phase granite as the inner-phase granite is intruded.

Carr et al. (2008) investigated the size and spacing of VHMS deposits in the Matagami district, Abitibi greenstone belt, by calculating zinc transport across the seafloor, first above sills of simple geometry then above the Bell River Complex. They concluded that a simple and reasonable dependence of permeability and temperature localises hydrothermal upwelling and produces a spatial pattern and range of vented fluid volumes similar to that found in VHMS districts.

Schwarz-Schampera et al. (2010) described 12 VHMS deposits in the Murchison greenstone belt, South Africa which form the 'Cu-Zn line'. These deposits are closely associated with quartz porphyritic rhyolite domes, developed during the early stages of highly evolved felsic volcanism. They described a distinct equidistance of 7 to 14 km between the single deposits and considered that the locations largely represent the original sites of formation, as the deposits are associated with high-temperature upflow zones in their footwalls. Chemical exhalite horizons are virtually absent. They concluded that the ore-forming processes were short-lived periods of hydrothermal activity and higher temperature

1 Panorama is an exceptionally well exposed Pilbara craton succession, that includes a regional syn-volcanic intrusive basement.

upflow that likely coincided with discrete magmatic events. In effect they are suggesting that in this instance the convection cells are spaced on the volcanic centres (which may in turn be linked to sub surface sills/plutons).

Chemical evidence for true magmatic input is used by some workers to indicate that at least some centres must sit right above an intrusion. These appear to mainly be more oxidised and lie on submarine arcs, and are best exemplified by the Brothers seamount and about 50 -like systems (de Ronde et al., 2005).

With the recent discovery of the Bentley deposit (Jabiru Metals, 2009), a spacing of about 4.5 km is evident between the Teutonic Bore mine, the Jaguar mine and the Bentley deposit. But studies of these sites are required to determine how, and if they relate to volcanic centres.

Fertility concept

Since the initial development of the 'fertility concept' (Lesher et al., 1986) based on rhyolite geochemistry, and the identification of so-called 'fertile' and 'barren' rock suites (as discussed in Chapter 5.1.3), some explorers in Archean terrains have used this discriminant to exclude some volcanic suites and concentrate their exploration in suites considered most prospective. A study on the recently discovered world–class LaRonde Penna deposit (Mercier-Langevin et al., 2007b) shows that Archean HREE-depleted and high Th, transitional to calc-alkaline dacites, rhyodacites, and rhyolites, referred to as FI and FII type, can be important hosts for VHMS and Au-rich VHMS, and F1 suites may be as prospective as the other rhyolite-type bearing sequences. This research effectively invalidated the original fertility thesis and a comparative study (Gaboury and Pearson, 2008) suggested that a combination of rhyolite geochemistry, volcanic facies, and style of the mineralisation may be more meaningfully applied in exploration than rhyolite type alone.

This leads to the conclusion that a lot of ground considered unprospective since the late 1980's on the basis of its rhyolite geochemistry could now be regarded as under-explored for VHMS deposits. The Jaguar tholeiitic to calc-alkaline, dacite and rhyolite, has been assessed and classified as FII and FIIIA type (Chapter 5, Figs 5.9d and 5.9e).

7.5.1 Comparison of time equivalent VHMS sequences

It may be interesting to compare age equivalent volcanic episodes around the world with the Jaguar succession, on the basis that similar events are now recognised to have occurred synchronously during the 'global crisis' (Rey et al., 2003; Barley et al., 2005) i.e. from ~2.72 to 2.65 Ga.

In the Abitibi greenstone belt, Superior province, Canada, the 2704 to 2695 Ma volcanic

episode (Upper Blake River assemblage) is concentrated in the Rouyn-Noranda camp and the Kamiskotia area to the west of Timmins township (Thurston et al., 2008). In the Rouyn-Noranda camp, VHMS mineralised volcanic hiatuses occur at several stratigraphic levels (Gibson and Watkinson, 1990). In the Kamiskotia volcanic complex, which hosts the Jameland, Kam-Kotia and Can. Jamieson deposits, the mineralisation occurs in a restricted (< 150 m) stratigraphic interval that is broadly correlative between deposits. All deposits are associated with a bimodal sequence of tholeiitic basalts and rhyolite. The deposits from these areas contain in the region of 250 Mt @ 1.2% Cu, 1.5% Zn, 4.5 g/t Au and 25 g/t Ag (this total excludes the gold-only deposits, e.g. Horne No 5).

In the Yilgarn craton, the 2.69 Ga Teutonic Bore volcanic complex in the Gindalbie Domain hosts the Teutonic Bore, Jaguar and Bentley deposits in a suite that ranges from basalt to andesite to dacite to rhyolite. Although the deposits do not appear to be at the same volcanic hiatus, they do occur in a restricted (< 200 m) stratigraphic interval, at a deposit spacing of about 4.5 km. The total endowment of these three deposits is about 5 Mt of ore with grades in the region of 3.5% Cu, 11% Zn, 0.5% Pb and 120 g/t Ag.

The endowment of these two areas could hardly be more different. Despite having formed during the ~2.72 to 2.65 Ga 'global crisis' (Rey et al., 2003; Barley et al., 2005) there appears no basis for comparison between them, other than that the deposits in each area cluster within narrow (< 200m stratigraphic intervals). Perhaps understandably, mineralised Archean basins during the 'global crisis' were as diverse as those back-arc basins today that have been found to contain venting hydrothermal systems.

7.5.2 Comparison of the Jaguar sequence discontinuities to in other Archean VHMS terrain examples

At Jaguar, the discontinuous, thin, graphite-rich mudstone beds at the top of the MP unit, represent a volcanic hiatus which is also a geochemical discontinuity (Chapter 5). In the footwall magmas the [La/Sm]cn and [La/Yb]cn values reflect weak negative, sub-parallel slopes of the trend lines, whereas in the immediate hangingwall the magmas have [La/Sm] cn and [La/Yb]cn values that indicate REE patterns with much steeper, negative slopes and lower Zr/Nb values than the footwall.

Within the Kidd-Munro assemblage, graphitic horizons (Ayer et al., 2005) are also indicative of a volcanic hiatus, sometimes located between two geochemical types of volcanism. Thurston et al. (2008) described these as geochemical discontinuities within the volcanic stratigraphy and they are interpreted to represent a hiatus, with very low rates of sedimentation in a basinal setting. They further suggested that graphitic horizons of this type are probably more directly related to volcanism and form very direct targets similar

to the exhalite units of the Rouyn-Noranda camp. However, distribution of the argillites is discontinuous and not traceable at a regional scale.

The Jaguar discontinuity would be at member level if comparison was to be made to the Abitibi study. It is not known if the Jaguar mudstone (MPS) is traceable beyond the confines of the study area, although this could potentially be evaluated using electromagnetic surveys. The geochemical discontinuity certainly should be identifiable, enabling tracing of this interval along the belt.

The Murchison greenstone belt, Limpopo Province, Kaapvaal craton, South Africa, contains the largest VHMS district in Southern Africa (Schwarz-Schampera et al., 2010). The deposits developed during initial phases of highly evolved felsic volcanism between 2,974.8± 3.6 and 2,963.2± 6.4 Ma. The so-called Cu–Zn line is host to 12 deposits of massive sulfide mineralization including: Maranda J, LCZ, Romotshidi, Mon Desir, Solomons, and Mashawa and the total endowment is about 3 Mt of very high grade Zn, subordinate Cu, and variable Pb and Au ore. Within the felsic volcanic sequences that host the "Cu–Zn line", the associated VHMS deposits occur on preferred lithological horizons. The "Cu–Zn line" forms a poorly defined, discontinuous, package about 500-m wide that is characterised by variably altered volcaniclastic sedimentary rocks and effusive felsic flows. Chemical exhalite horizons are virtually absent, and sulfide was precipitated within thin layers of felsic volcaniclastic rocks closely associated with quartz porphyritic rhyolite domes (Schwarz-Schampera et al., 2010). Thus in this belt the deposits do not represent either a volcanic hiatus or a geochemical discontinuity.

7.5.3 Comparison of Jaguar with the worldclass Kidd Creek deposit

Kidd Creek, one the worlds largest Cu-Zn deposits, (149 Mt @ 2.31% Cu, 0.225 Pb, 6.18% Zn 0.01g/t Au, 87g/t Ag: Franklin et al., 2005) occurs within the 2719 to 2711 Ma volcanic episode of the Kidd-Munro assemblage (Thurston et al., 2008)(Fig. 7.1). Despite the vast difference in (or perhaps because of) the metal endowment between the deposits it is interesting to compare them, but a comparison is also stimulated by the fact that some researchers have considered the presence of HFSE–rich volcanics in both belts to be potentially metallogically significant (Messenger, 2000).

In detail, the world–class Kidd Creek deposit occurs at the top of a rhyolitic succession overlying basal komatiites. The strongly bimodal mine sequence consists of komatiitic flows, high silica rhyolites, basalt and gabbros (Hannington et al., 1999). Mudstone and argillaceous units overlie the Kidd Creek deposit but are confined to the sub-basin that hosts the massive sulfide (Walker et al., 1975). Argillaceous units also occur through the upper part of the 2717 to 2711 Ma volcanic episode, reflecting additional hiatuses in

volcanism. However, distribution of the argillites is discontinuous and not traceable at a regional scale (Thuston et al., 2008).

The rhyolites at Kidd Creek are classified as FIII rhyolites (Lesher et al., 1986), and characterised by elevated HFSE concentrations and constant Hf–Th–Ta ratios (Schandl et al., 1999). Prior et al. (1999) compared the REE and HFSE geochemistry of the rhyolites with examples from known tectonic settings. They showed that they have a close geochemical affinity to the felsic igneous products of anomalous midocean ridge spreading centres such as the axial rifts zones of Iceland, the Galapagos spreading centre and the mid-Atlantic ridge at 45°N. Other similarities they noted included fissure–controlled eruptions, incompatible element–enriched tholeiitic basalts, lack of terriginous sedimentation, absence of a continental chemical component in igneous rocks, and the presence of Mg–rich volcanic rocks. An alternative to this was proposed by Wyman et al. (1999) who suggested an arc–like setting as indicated by the presence of distinctive low–Ti basalts, interpreted as melts transitional between subduction– and plume–related magmas.

This is in contrast to the Jaguar succession, which is definitely not bimodal and includes at least four andesite units (DFA, FA, HA, HUA). In addition the Jaguar felsic rocks lie within the FII and FIII clasifications of Lesher et al. (1986). The suggested tectonic setting for Jaguar is a back–arc basin and the presence of andesite precludes oceanic ridge spreading centres. Furthermore there are no Mg–rich volcanic rocks in the footwall, and there is a strong subduction chemical component in the igneous rocks. Jaguar does share the presence of fissure–controlled eruptions, incompatible element–enriched tholeiitic basalts and lack of terriginous sedimentation.

7.5.4 Implications for mineral exploration around Jaguar

The exploration implications of the volcanic hiatuses and correlative conformities for massive sulfide orebodies are predicated on recognition of, and the ability to correlate, potentially mineralised packages. The basis for correlation are the sedimentary interface zones and/or geochemical discontinuities, which may have coincided with episodes of hydrothermal activity that gave rise to VHMS mineralisation somewhere along their length.

The discontinuous graphitic black shale horizon that occurs at the top of the MPS can be equated to the geochemical discontinuity in an exploration sense. Although this horizon may not be regionaly or even locally geologically mappable, it may be mappable by electromagnetic geophysical methods. However, the use of lithogeochemistry to identify the geochemical discontinuity is a guaranteed way to locate the Mineralised Package unit.

Other discontinuities were recognised and these also need to be considered as explorable

horizons. However, until they are proven to host ore they are lower priority but should be chemically assessed for distal signs of VHMS activity.

On the validity of the use of the 'fertility concept' (Lesher et al., 1986) in targeting certain types of rhyolites, the conclusions (this thesis; Mercier-Langevin et al., 2007a, 2007b; Gaboury and Pearson, 2008) suggest that this is not a worthwhile exercise as all rhyolite types are now known to host major deposits. It further suggests that areas discounted specifically because of their unfavourable rhyolite geochemistry should be reassessed.

It is interesting to consider whether the recognition of a compressive phase that choked off extrusive extensional mafic activity has exploration implications. Compressive episodes can be considered as opportunities to build up reservoirs of heated metal-rich fluid which then vents following renewed extension. If this is the case at Jaguar, then following deposition of the MP, extension was renewed with the emplacement of hot mafic melts. The system was then compressed, presenting a possible opportunity for more ore somewhere in the succeeding stratigraphy.

As Jaguar is interpreted to have been formed largely as a sub-seafloor replacement deposit, it follows that any of the units beneath this horizon may be host to replacement-style massive sulfide mineralisation if they are suitable hosts, that is, of a highly porous, permeable, water saturated and/or glassy nature (e.g., Doyle and Allen, 2003) as these lithofacies are very favourable host rocks for contemporaneous mineralisation. Therefore mineralisation contemporaneous with Jaguar may not be confined to the exact same stratigraphic position.

7.6 Conclusions

Relationship to Teutonic Bore

Being at deposit scale, the lateral extent of the study area is quite small (~ 1600 m). As this distance is only slightly greater than one quarter of the distance between the Teutonic Bore and Jaguar deposits, the question has to be asked – how widely applicable is the stratigraphy? The distance between Jaguar and Teutonic Bore is about 4.5 km with negligible surface outcrop and limited drilling between the two deposits. What has been shown, is that the succession described at/(relative to) Jaguar is compositionally different from the succession described at/(relative to) Teutonic Bore (Greig, 1984; Hallberg and Thompson, 1985) making confident stratigraphic correlation between the two deposits difficult. However, by comparing the description of the Teutonic Bore stratigraphy with the succession described in this study for Jaguar, it is suggested that the Jaguar deposit lies at a higher stratigraphic level than Teutonic Bore.

Conclusions from global comparisons

The Jaguar deposit was formed during the Neoarchean 'global crisis' at a local hiatus and geochemical discontinuity. Unlike some other Archean deposits there is no oxide-facies iron deposit at this break. Like many other VHMS camps there is a regular spacing between deposits which may relate to eruptive centres. Other VHMS camps that formed during the 'global crisis' are dissimilar in lithology and endowment suggesting diversity existed in the Archean, as it does now in basins hosting venting hydrothermal systems.

Jaguar does not have a lot in common with the world-class Kidd Creek deposit. Kidd Creek occurs in a strongly bimodal sequence, whereas Jaguar abounds in andesites. The Kidd Creek rhyolites are classified as FIII type, whereas at Jaguar the felsic rocks are classified as FII and FIII types.

Setting of Jaguar

The tectonic setting is interpreted to have been an extensional environment, adjacent to a subduction zone, but not close to an emergent arc. Within it the Jaguar succession was dominated by proximal lithofacies generated by effusive eruptions and shallow intrusions; lavas; domes; cryptodomes and syn-volcanic sills; and their associated volcaniclastic facies which collectively define a submarine volcanic environment with no external terrigenous input. In this restricted basin, which was distal to large faults and steep topography, near-continuous volcanism continued through several cycles, as signified by geochemical discontinuities. The most important of these discontinuities is the Mineralised Package unit and host to the Jaguar massive sulfide.

The facies model for the volcanic environment of the Jaguar massive sulfide deposit is a lava dome complex, with aprons of mass–flow emplaced, resedimented autoclastic breccia–sandstone facies derived from either over-steepening of lava or dome carapaces and margins, or tectonically triggered through seismic activity caused by extensionally stimulated lystric/ block faulting. The massive sulfide ore formed by invasion of the volcaniclastic facies and glassy-dacite before encountering the seafloor and is predominantly replacement-style ore.

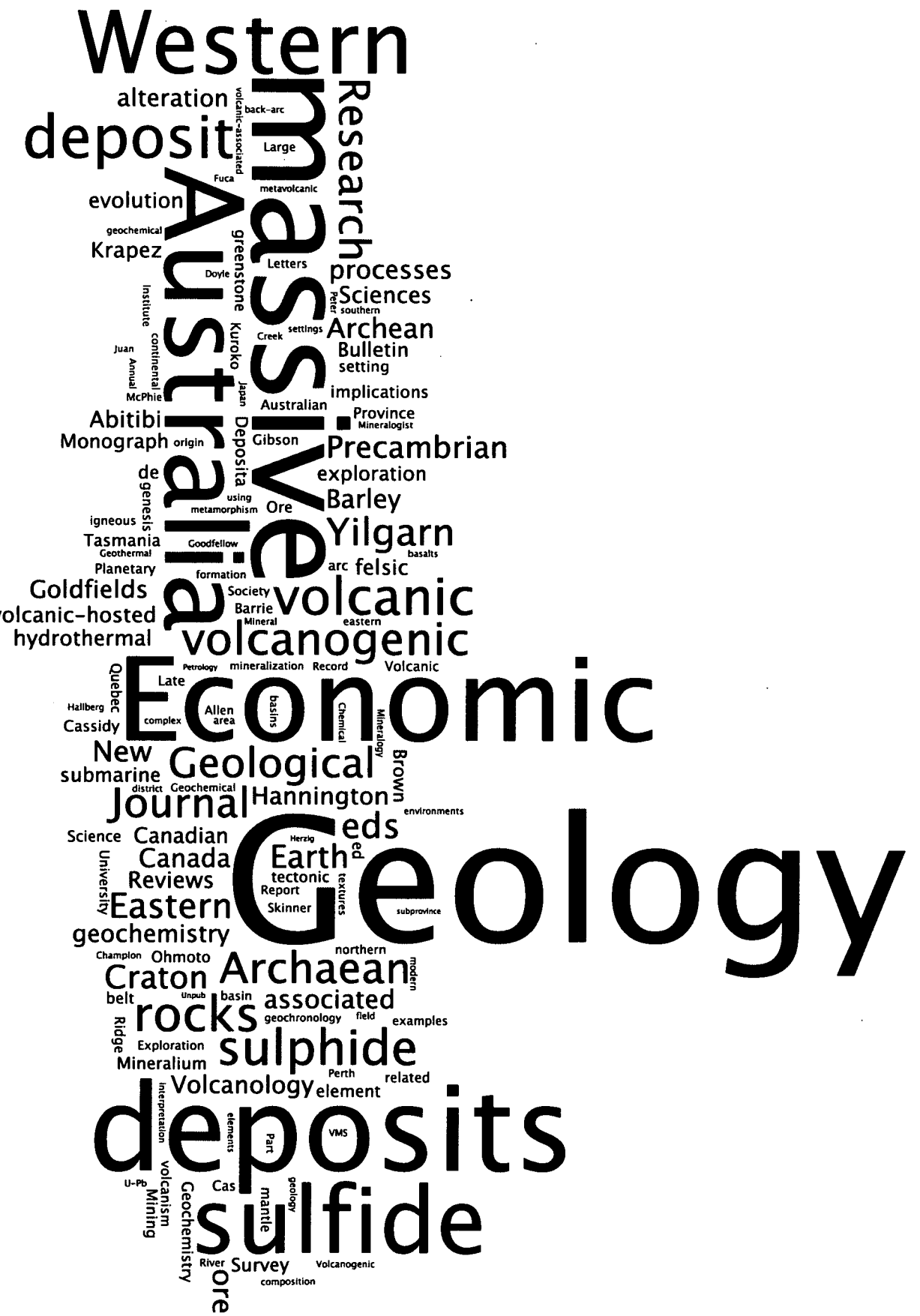
Western
Australian
Massive
Research
alteration
deposit
volcanic-associated
back-arc
Large
Fuca
metavolcanic
evolution
geochemical
Krapez
greenstone
Letters
processes
Doyle
Sciences
Peter
southern
Archean
Kuroko
Creek
settings
Bulletin
Juan
Annual
continental
Institute
setting
McPhie
Japan
implications
Australian
Province
Mineralogist
Abitibi
Deposita
Gibson
Precambrian
Monograph
origin
exploration
de
genesis
using
metamorphism
Ore
Barley
igneous
Yilgarn
Tasmania
Goodfellow
basalts
Geothermal
Planetary
formation
arc
felsic
Goldfields
Society
volcanic
volcanic-hosted
Barrie
Mineral
eastern
hydrothermal
volcanogenic
Petrology
mineralization
Record
Volcanic
Economic
Late
Quebec
Hallberg
Allen
area
basins
Chemical
Mineralogy
Cassidy
complex
New
Geological
Brown
submarine
district
Geochemical
Journal
Hannington
environments
Herzig
Science
Canadian
eds
Canada
Earth
ed
Reviews
tectonic
Report
textures
University
Eastern
Skinner
subprovince
Geology
geochemistry
northern
Champion
Ohmoto
Archaean
Craton
modern
belt
Unpub
basin
associated
rocks
geochronology
field
examples
Ridge
Exploration
sulphide
Mineralium
Perth
related
Volcanology
element
deposits
interpretation
elements
Part
VMS
U-Pb
volcanism
Cas
Mining
Geochemistry
mantle
geology
sulfide
River
Survey
Volcanogenic
ore
composition

8. REFERENCES

Allen, R. L., Weihed, P., and Svenson, S., 1996, Setting of Zn-Cu-Au-Ag massive sulphide deposits in the evolution and facies architecture of a 1.9Ga marine volcanic arc, Skellefte District, Sweden: Economic Geology, v. 91, p. 1022-1053.

Allen, S. R., and McPhie, J., 2009, Products of neptunian eruptions: Geology, v. 37, p. 639-642.

Alt, J. C., 1999, Hydrothermal alteration and mineralization of oceanic crust: mineralogy, geochemistry, and processes, in Barrie C.T. & Hannington M.D., eds, Volcanic-associated massive sulfide deposits: processes and examples in modern and ancient settings: Reviews in Economic Geology, v. 8, p. 133-155.

Anand, R. R., and Cornelius, M., 2004, Vegetation and soil expression of the Jaguar base metal deposit, Yilgarn Craton: CRC LEME Monograph, Regolith 2004.

Anders, E., and Grevesse, N., 1989, Abundances of the elements: Meteoritic and solar: Geochimica et Cosmochimica Acta, v. 53, p. 197-214.

Appelgate, B., and Embley, R. W., 1992, Submarine tumuli and inflated tube-fed lava flows on Axial Volcano, Juan de Fuca Ridge: Bulletin of Volcanology, v. 54, p. 447-458.

Archibald, N. J., Bettenay, L. F., Binns, R. A., Groves, D. I., and Gunthorpe, R. J., 1978, The evolution of Archaean greenstone terrains, Eastern Goldfields Province, Western Australia: Precambrian Research, v. 6, p. 103-131.

Ashley, P. M., Dudley, R. J., Lesh, R. H., Marr, J. M., and Ryall, A. W., 1988, The Scuddles Cu-Zn prospect, an Archaean volcanogenic massive sulphide deposit, Golden Grove district Western Australia.: Economic Geology, v. 83, p. 918-951.

Ayer, J., Amelin, Y., Corfu, F., Kamo, S., Ketchum, J., Kwok, K., and Trowell, N., 2002, Evolution of the southern Abitibi greenstone belt based on U-Pb geochronology: autochthonous volcanic construction followed by plutonism, regional deformation and sedimentation: Precambrian Research, v. 115, p. 63-95.

Ayer, J. A., Thurston, P. C., Bateman, R., Dubé, B., Gibson, H. L., Hamilton, M. A., Hathway, B., Hocker, S. M., Houlé, M. G., Hudak, G., Ispolatov, V. O., Lafrance, B., Lesher, C. M., MacDonald, P. J., Péloquin, A. S., Piercey, S. J., Reed, L. E., and Thompson, P. H., 2005, Overview of results from the Greenstone Architecture Project: Discover Abitibi Initiative; , Open File Report 6154, Ontario Geological Survey, p. 146.

Barley, M. E., Bekker, A., and Krapez, B., 2005, Late Archean to Early Paleoproterozoic global tectonics, environmental change and the rise of atmospheric oxygen: Earth and Planetary Science Letters, v. 238, p. 156-171.

Barley, M. E., Brown, S. J. A., Krapez, B., and Cas, R. A. F., 2002, Tectonostratigraphic analysis of the Eastern Yilgarn Craton: an improved geological framework for exploration in Archaean terranes, P437A Final Report (unpublished), AMIRA.

Barley, M. E., Brown, S. J. A., Krapez, B., and Cas, R. A. F., 2002, Tectonostratigraphic analysis of the Eastern Yilgarn Craton: an improved geological framework for exploration in Archaean terranes; Chap 3 Felsic Volcanics, P437A final report (unpublished), AMIRA.

Barley, M. E., Brown, S. J. A., Krapez, B., and Kositcin, N., 2008, Physical volcanology and geochemistry of a Late Archaean volcanic arc: Kurnalpi and Gindalbie Terranes, Eastern Goldfields Superterrane, Western Australia: Precambrian Research, v. 161, p. 53-76.

Barley, M. E., Krapez, B., Brown, S. J. A., Hand, J., and Cas, R. A. F., 1998, Mineralised volcanic and sedimentary successions in the Eastern Goldfields Province, Rep. P437, AMIRA.

Barley, M. E., Krapez, B., Groves, D. I., and Kerrich, R., 1998, The Late Archaean bonanza: metallogenic and environmental consequences of the interaction between mantle plumes, lithospheric tectonics and global cyclicity.: Precambrian Research, v. 91, p. 65-90.

Barrett, T. J., and MacLean, W. H., 1994, Chemostratigraphy and hydrothermal alteration in exploration for VHMS deposits in greenstones and younger volcanic rocks: Short Course Notes - Geological Association of Canada, v. 11, p. 433-467.

Barrett, T. J., and MacLean, W. H., 1999, Volcanic sequences, lithogeochemistry, and hydrothermal alteration in some bimodal volcanic-associated massive sulfide systems, in Barrie C.T. & Hannington M.D., eds, Volcanic-associated massive sulfide deposits: processes and examples in modern and ancient settings: Reviews in Economic Geology, v. 8, p. 101-131.

Barrie, C., Taylor, C., and Ames, D., 2005, Geology and metal contents of the Ruttan volcanogenic massive sulfide deposit, northern Manitoba, Canada: Mineralium Deposita, v. 39, p. 795-812.

Barrie, C. T., and Hannington, M. D., 1999, Classification of volcanic-associated massive sulfide deposits based on host-rock composition, in Barrie C.T. & Hannington M.D., eds, Volcanic-associated massive sulfide deposits: processes and examples in modern and ancient settings: Reviews in Economic Geology, v. 8, p. 1-11.

Barrie, C. T., Ludden, J. N., and Green, T. H., 1993, Geochemistry of volcanic rocks associated with Cu-Zn and Ni-Cu deposits in the Abitibi Subprovince: Economic Geology, v. 88, p. 1341-1358.

Barton, P. B., Jr., and Bethke, P. M., 1987, Chalcopyrite disease in sphalerite: pathology and epidemiology: American Mineralogist, v. 72, p. 451-467.

Batiza, R., and White, J. D. L., 2000, Submarine lavas and hyaloclastite, in Sigurdsson, H., Houghton, B. F., McNutt, S. R., Rymer, H., and Stix, J., eds., Encyclopedia of volcanoes, Academic Press, San Diego, CA, United States (USA), p. 361-381.

Belford, S. M., Davidson, G. J., McPhie, J., and Large, R. R., 2010, The stratigraphic succession at the Jaguar VHMS deposit [abs]: 5th International Archean Symposium, Perth, in press.

Blewett, R. S., and Czarnota, K., 2007, Tectonostratigraphic architecture and uplift history of the Eastern Yilgarn Craton, Record 2007/15, Geoscience Australia, p. 114.

Bodon, S. B., and Valenta, R. K., 1995, Primary and tectonic features of the Currawong Zn-Cu-Pb(-Au) massive sulfide deposit, Benambra, Victoria; implications for ore genesis, Economic Geology, 90, p. 1694-1721.

Brauhart, C. W., Groves, D. I., and Morant, P., 1998, Regional alteration systems associated with volcanogenic massive sulfide mineralisation at Panorama, Pilbara, Western Australia.: Economic Geology, v. 93, p. 292-302.

Brauhart, C. W., Huston, D. L., and Andrew, A. S., 2000, Oxygen isotope mapping in the Panorama VMS district, Pilbara Craton, Western Australia: applications to estimating temperatures of alteration and to exploration.: Mineralium Deposita, v. 35, p. 727-740.

Brown, S. J. A., Barley, M. E., Krapez, B., and Cas, R. A. F., 2002, The late Archaean Melita Complex, Eastern Goldfields, Western Australia; shallow submarine bimodal volcanism in a rifted arc environment: Journal of Volcanology and Geothermal Research, v. 115, p. 303-327.

Brown, S. J. A., Krapez, B., Beresford, S. W., Cassidy, K. F., Champion, D. C., Barley, M. E., and Cas, R. A. F., 2001, Archaean volcanic and sedimentary environments of the Eastern Goldfields Province, Western Australia; a field guide, 2001/13: Perth, Geological Survey of Western Australia, p. 66.

Busby, C. J., Kessel, L., Schulz, K., Foose, M., and Slack, J., 2003, Volcanic setting of the Ordovician Bald Mountain Massive Sulfide Deposit, Northern Maine, in Goodfellow, W., S.R.McCutcheon, and Peter, J. M., eds., Massive Sulfide Deposits of the Bathurst Mining Camp, New Brunswick and Northern Maine, Economic Geology Monograph 11, p. 219-244.

Busby-Spera, C. J., and White, J. D. L., 1987, Variation in peperite textures associated with differing host-sediment properties: Bulletin of Volcanology, v. 49, p. 765-776.

Cabanis, B., and Lecolle, M., 1989, The La/10-Y/15-Nb/8 diagram: a tool for discriminating volcanic series and evidencing continental crust magmatic mixtures and/or contamination: Comptes Rendus - Academie des Sciences, Serie II, v. 309, p. 2023-2029.

Carr, M., 2007, Igpet 2007 software.

Carr, P. M., Cathles, L. M., III, and Barrie, C. T., 2008, On the size and spacing of volcanogenic massive sulfide deposits within a district with application to the Matagami District, Quebec: Economic Geology, v. 103, p. 1395-1409.

Cas, R. A. F., 1992, Submarine volcanism: eruption styles, products, and relevance to understanding the host rock secessions to volcanic-hosted massive sulphide deposits.: Economic Geology, v. 87, p. 511-524.

Cas, R. A. F., Allen, R. L., Bull, S. W., Clifford, B. A., and Wright, J. V., 1990,

Subaqueous, rhyolitic dome-top tuff cones: a model based on the Devonian Bunga Beds, southeastern Australia and a modern analogue: Bulletin of Volcanology, v. 52, p. 159-174.

Cas, R. A. F., and Wright, J. V., 1987, Volcanic successions: London, Allen & Unwin, 529 p.

Cas, R. A. F., and Wright, J. V., 1991, Subaqueous pyroclastic flows and ignimbrites: an assessment.: Bulletin of Volcanology, v. 53, p. 357-380.

Cassidy, K. F., 2004, Geological evolution of the eastern Yilgarn Craton (EYC) and terrane, domain and fault system nomenclature, in Blewett, R. S., and Hitchman, A. P., eds., Final Report, Geological models of the eastern Yilgarn Craton, Project Y2, AMIRA.

Cassidy, K. F., Champion, D. C., Fletcher, I. R., Dunphy, J. M., Black, L. P., and Claoue-Long, J. C., 2002, Geochronological constraints on the Leonora-Laverton transect area, north eastern Yilgarn Craton, Geology, geochronology and geophysics of the north eastern Yilgarn Craton, with an emphasis on the Leonora-Laverton transect area; proceedings of papers presented at an industry workshop, Australian Geological Survey Organisation, p. 37-58.

Cassidy, K. F., Champion, D. C., Krapez, B., Barley, M. E., Brown, S. J. A., Blewett, R. S., Groenewald, P. B., and Tyler, I. M., 2006, A revised geological framework for the Yilgarn Craton, Western Australia, Record 2006/8, Western Australia Geological Survey, p. 8.

Champion, D. C., and Cassidy, K. F., 2002, Granites in the Leonora-Laverton transect area, north eastern Yilgarn, in Cassidy, K. F., ed., Geology, geochronology and geophysics of the north eastern Yilgarn Craton, with an emphasis on the Leonora-Laverton transect area, Geoscience Australia, p. 13-35.

Champion, D. C., and Sheraton, J. W., 1997, Geochemistry and Nd isotope systematics of Archaean granites of the Eastern Goldfields, Yilgarn Craton, Australia: implications for crustal growth processes: Precambrian Research, v. 83, p. 109-132.

Cloetingh, S., 1988, Intraplate stresses; a new element in basin analysis, in Kleinspehn, K. L., and Paola, C., eds., New perspectives in basin analysis, Springer-Verlag, New York, NY, p. 205-230.

Cole, J. W., 1990, Structural control and origin of volcanism in the Taupo volcanic zone, New Zealand: Bulletin of Volcanology, v. 52, p. 445-459.

Condie, K. C., 1995, Episodic ages of greenstones - a key to mantle dynamics: Geophysical Research Letters, v. 22, p. 2215-2218.

Condie, K. C., 2000, Episodic continental growth models: afterthoughts and extensions: Tectonophysics, v. 322, p. 153-162.

Condie, K. C., 2008, Did the character of subduction change at the end of the Archean? Constraints from convergent-margin granitoids: Geology, v. 36, p. 611-614.

Cook, N. J., Halls, C., and Boyle, A. P., 1993, Deformation and metamorphism of massive sulphides at Sulitjelma, Norway: Mineralogical Magazine, v. 57, p. 67-81.

Cox, K. G., Bell, J. D., and Pankhurst, R. J., 1979, The interpretation of igneous rocks: London, Allen and Unwin.

Cox, S. F., 1987, Flow mechanisms in sulphide minerals: Ore Geology Reviews, v. 2, p. 133-171.

Craig, J. R., and Vokes, F. M., 1993, The metamorphism of pyrite and pyritic ores; an overview: Mineralogical Magazine, v. 57, p. 3-18.

Crawford, A. J., Beccaluva, L., and Serri, G., 1981, Tectono-magmatic evolution of the West Philippine-Mariana region and the origin of boninites: Earth and Planetary Science Letters, v. 54, p. 346-356.

Crowe, D. E., Nelson, S. W., Brown, P. E., Shanks, W. C., and Valley, J. W., 1992, Geology and geochemistry of volcanogenic massive sulphide deposits and related igneous rocks, Prince William Sound, south-central Alaska: Economic Geology, v. 87, p. 1722-1746.

Crozier, S. J., 1999, Palaeovolcanology, palaeogeography and palaeoenvironmental reconstruction of the Archaean Spring Well Volcanic Complex, Western Australia: Unpub. B.Sc (Hons) thesis.

Davidson, G. J., Stolz, A. J., and Eggins, S. M., 2001, Geochemical anatomy of silica iron exhalites: Evidence for hydrothermal oxyanion cycling in response to vent fluid redox and thermal evolution (Mt. Windsor Subprovince, Australia). Economic Geology, v. 96, p. 1201-1226.

Davis, E. E., Goodfellow, W. D., Bornhold, B. D., Adshead, J., Blaise, B., Villinger, H., and Le Cheminant, G. M., 1987, Massive sulphides in a sedimented rift valley, northern Juan de Fuca Ridge: Earth and Planetary Science Letters, v. 82, p. 49-61.

Davis, E. E., and Viilinger, H., 1992, Tectonic and thermal structure of the Middle Valley sedimented rift, northern Juan de Fuca Ridge: Ocean Drilling Program Proceedings: Initial Reports, v. 139, p. 9-41.

de Ronde, C. E. J., Hannington, M. D., Stoffers, P., Wright, I. C., Ditchburn, R. G., Reyes, A. G., Baker, E. T., Massoth, G. J., Lupton, J. E., Walker, S. L., Greene, R. R., Soong, C. W. R., Ishibashi, J., Lebon, G. T., Bray, C. J., and Resing, J. A., 2005, Evolution of a submarine magmatic-hydrothermal system; Brothers Volcano, southern Kermadec Arc, New Zealand: Economic Geology, v. 100, p. 1097-1133.

De Rosen-Spence, A. F., Provost, G., Dimroth, E., Gochnauer, K., and Owen, V., 1980, Archean subaqueous felsic flows, Rouyn-Noranda, Quebec, Canada, and their Quaternary equivalents: Precambrian Research, v. 12, p. 43-77.

Dickins, C. A., Barley, M. E., and Cassidy, K. F., 2004, Late Archaean mineralised high-field-strengthelement (HFSE) enriched igneous rocks in the Gindalbie Terrane, Eastern

Yilgarn Craton, Western Australia [abs]: Predictive mineral discovery CRC Conference Barossa Valley 1-3 June 2004, 2004, p. 27-30.

Dickins, C. A., Cassidy, K. F., and Barley, M. E., 2006, Evolution of Late Archean HFSE-enriched igneous rocks of the Gindalbie Domain, Eastern Yilgarn Craton, Western Australia: Geochimica et Cosmochimica Acta, v. 70, p. A140.

Dickins, C. A., Cassidy, K. F., and Barley, M. E., 2006, Geochemistry and evolution of the HFSE-enriched igneous rocks of the Gindalbie Domain, Eastern Yilgarn Craton, Western Australia [abs]: Montreal 2006, Montreal, Canada, 2006.

Dinel, E., Fowler, A. D., Ayer, J., Still, A., Tylee, K., and Barr, E., 2008, Lithogeochemical and stratigraphic controls on gold mineralization within the metavolcanic rocks of the Hoyle Pond Mine, Timmins, Ontario: Economic Geology, v. 103, p. 1341-1363.

Doyle, M., 1997, A Cambro-Ordovician submarine volcanic succession hosting massive sulfide mineralisation: Mount Windsor subprovince, Queensland: Unpub. PhD thesis, University of Tasmania, 242 p.

Doyle, M., and Huston, D. H., 1999, The subsea-floor replacement origin of the Ordovician High-Reward volcanic-associated massive sulfide deposit, Mount Windsor subprovince, Australia.: Economic Geology, v. 94, p. 825-843.

Doyle, M. G., and Allen, R., 2003, Subsea-floor replacement in volcanic-hosted massive sulfide deposits: Ore Geology Reviews, v. 23, p. 183-222.

Doyle, M. G., and Allen, R., 2004, Subsea-floor replacement in volcanic-hosted massive sulfide deposits; features, styles and volcanic settings: Abstracts - Geological Society of Australia, v. 73, p. 69.

Dube, B., Mercier-Langevin, P., Hannington, M., Lafrance, B., Gosselin, G., and Gosselin, P., 2007, The LaRonde Penna world-class Au-rich volcanogenic massive sulfide deposit, Abitibi, Quebec: Mineralogy and geochemistry of alteration and implications for genesis and exploration: Economic Geology, v. 102, p. 633-666.

Duhig, N. C., Stolz, J., Davidson, G. J., and Large, R. R., 1992, Cambrian microbiol and silica gel textures in silica iron exhalites from the Mount Windsor volcanic belt, Australia: their petrography, chemistry and origin.: Economic Geology, v. 87, p. 764-784.

Einsele, G., 1982, Mechanism of sill intrusion into soft sediment and expulsion of pore water: Initial Reports of the Deep Sea Drilling Project, v. 64, p. 1169-1176.

Einsele, G., 1985, Basaltic sill-sediment complexes in young spreading centers: Genesis and significance: Geology, v. 13, p. 249-252.

Eldridge, C. S., Barton, P. B., Jr., and Ohmoto, H., 1983, Mineral textures and their bearing on formation of the kuroko orebodies, in Ohmoto, H., and Skinner, B. J., eds., The Kuroko and related volcanogenic massive sulfide deposits, Economic Geology Monograph 5, p. 241-281.

Ellis, P., 2004, Geology and mineralisation of the Jaguar copper-zinc deposit, Western Australia, in McConachy, T. F., and McInnes, B. I. A., eds., Copper-zinc massive sulphide deposits in Western Australia, CSIRO, p. 39-46.

Eriksson, K. A., Krapez, B., and Fralick, P. W., 1994, Sedimentology of Archean greenstone belts; signatures of tectonic evolution: Earth-Science Reviews, v. 37, p. 1-88.

Finamore, S. M., Gibson, H. L., and Thurston, P. C., 2008, Archean synvolcanic intrusions and volcanogenic massive sulfide at the Genex mine, Kamiskotia Area, Timmins, Ontario: Economic Geology, v. 103, p. 1203-1218.

Finlow-Bates, T., and Stumpfl, E. F., 1981, The behaviour of so-called immobile elements in hydrothermally altered rocks associated with volcanogenic submarine-exhalative ore deposits: Mineralium Deposita, v. 16, p. 319-328.

Fisher, R. V., and Schmincke, H. U., 1984, Pyroclastic Rocks: Berlin, Springer-Verlag, 472 p.

Fisher, R. V., and Schmincke, H. U., 1994, Volcaniclastic sediment transport and deposition, in Pye, K., ed., Sediment transport and depositional processes: Edinburgh, Blackwell Scientific Publications.

Floyd, P. A., and Winchester, J. A., 1978, Identification and discrimination of altered and metamorphosed volcanic rocks using immobile elements: Chemical Geology, v. 21, p. 291-306.

Fouquet, Y., Von Stackelberg, U., Charlou, J. L., Donval, J. P., Erzinger, J., Foucher, J. P., Herzig, P., Mühe, R., Soakai, S., Wiedicke, M., and Whitechurch, H., 1991, Hydrothermal activity and metallogenesis in the Lau back-arc basin: Nature, v. 349, p. 778-781.

Fouquet, Y., von Stackelberg, U., Charlou, J. L., Erzinger, J., Herzig, P. M., Muhe, R., and Wiedicke, M., 1993, Metallogenesis in back-arc environments: The Lau basin example.: Economic Geology, v. 88, p. 2154-2181.

Francheteau, J., Needham, H. D., Choukroune, P., Juteau, T., Seguret, M., Ballard, R. D., Fox, P. J., Normark, W., Carranza, A., Cordoba, D., Guerrero, J., Rangin, C., Bougault, H., Cambon, P., and Hekinian, R., 1979, Massive deep-sea sulphide ore deposits discovered on the East Pacific Rise: Nature, v. 277, p. 523-528.

Franklin, J. M., Gibson, H. L., Jonasson, I. R., and Galley, A. G., 2005, Volcanogenic massive sulfide deposits, in Hedenquist, J. W., Thompson, J. F. H., Goldfarb, R. J., and Richards, J. P., eds., Economic Geology; One hundredth anniversary volume, 1905-2005, Economic Geology, p. 523-560.

Franklin, J. M., Lydon, J. W., and Sangster, D. F., 1981, Volcanic- associated massive sulphide deposits: Economic Geology, v. 75th Aniversary Volume, p. 485-627.

Frater, K. M., 1983, Geology of the Golden Grove prospect, Western Australia: a volcanogenic massive sulphide-magnetite deposit.: Economic Geology, v. 78, p. 875-919.

Frater, K. M., 1985a, Mineralization at the Golden Grove Cu-Zn deposit, Western Australia; I, Premetamorphic textures of the opaque minerals: Canadian Journal of Earth Sciences = Revue Canadienne des Sciences de la Terre, v. 22, p. 1-14.

Frater, K. M., 1985b, Mineralization at the Golden Grove Cu-Zn deposit, Western Australia; II, Deformation textures of the opaque minerals: Canadian Journal of Earth Sciences = Revue Canadienne des Sciences de la Terre, v. 22, p. 15-26.

Gaboury, D., and Pearson, V., 2008, Rhyolite geochemical signatures and association with volcanogenic massive sulfide deposits; examples from the Abitibi Belt, Canada: Economic Geology, v. 103, p. 1531-1562.

Galley, A., Hannington, M., and Jonasson, I., 2005, Volcanogenic massive sulphide deposits, in Goodfellow, W., ed., Mineral deposits of Canada: a synthesis of major deposit-types, district metallogeny, the evolution of geological provinces, and exploration methods, Geological Association of Canada, Mineral Deposits Division, 5, p. 141-161.

Galley, A. G., 1993, Characteristics of semi-conformable alteration zones associated with volcanogenic massive sulphide districts, in: Hoffman E.L. and Moore D.W., eds, Deep exploration using lithogeochemistry.: Journal of Geochemical Exploration, v. 48, p. 175-199.

Gee, A. M. M., and Swager, C., 2008, Preface: Precambrian Research, v. 161, p. 1-4.

Gee, R. D., Baxter, J. L., Wilde, S. A., and Williams, I. R., 1981, Crustal development in the Archaean Yilgarn Block, Western Australia [abs]: 2nd International Archaean Symposium, Perth, 1981, Geol. Soc. Aust. Spec Publ. no. 7, p. 43-56.

Gemmell, J. B., and Herrmann, W., 2001, A special issue devoted to alteration associated with volcanic-hosted massive sulfide deposits, and its exploration significance; preface: Economic Geology, v. 96, p. 909-912.

Gemmell, J. B., and Large, R. R., 1992, Stringer alteration system and alteration zones underlying the Hellyer and Que River volcanic-hosted massive sulphide deposit, Tasmania, Australia.: Economic Geology, v. 87, p. 620-649.

Gibson, 1991, The geology of the Mount Read Volcanics in the Antony Road-Newton Creek area, western Tasmania: Unpub. B.Sc. (Hons) thesis, University of Tasmania.

Gibson, H. L., Morton, R. L., and Hudak, G. J., 1999, Submarine volcanic processes, deposits, and environments favourable for the location of volcanic-associated massive sulfide deposits, in Barrie C.T. & Hannington M.D., eds, Volcanic-associated massive sulfide deposits: processes and examples in modern and ancient settings: Reviews in Economic Geology, v. 8, p. 13-51.

Gibson, H. L., and Kerr, D. J., 1993, Giant volcanic-associated massive sulfide deposits: with emphasis on Archean deposits, in Whiting B.H, Hodgsen C.V, & Mason R., eds, Giant ore deposits,: Economic Geology, v. SP-2, p. 319-348.

Gibson, H. L., and Watkinson, D. H., 1990, Volcanogenic massive sulphide deposits of the Noranda cauldron and shield volcano, Quebec: Special Volume - Canadian Institute of Mining and Metallurgy, v. 43, p. 119-132.

Gifkins, C., Herrmann, W., and Large, R., 2005, Altered volcanic rocks: a guide to description and interpretation, CODES, Univ. Tas., 275 p.

Gifkins, C., and McPhie, J., 1999, Understanding ancient submarine silicic volcanism in western Tasmania; the host rocks to massive sulphide and gold deposits, AustralianJournal of Mining, Tasmanian Mineral Exploration and Investment conference '99: Hobart.

Giles, C. W., 1982, The geology and geochemistry of the Archaean Spring Well felsic volcanic complex, Western Australia: Journal of the Geological Society of Australia, v. 29, p. 205-220.

Giles, C. W., and Hallberg, J. A., 1982, The genesis of the Archaean Welcome Well volcanic complex, Western Australia: Contributions to Mineralogy and Petrology, v. 80, p. 307-318.

Gilligan, L. B., and Marshall, B., 1987, Textural evidence for remobilization in metamorphic environments: Ore Geology Reviews, v. 2, p. 205-229.

Goldfarb, M. S., Converse, D. R., Holland, H. D., and Edmond, J. M., 1983, The genesis of hot spring deposits on the East Pacific Rise, 21°N, in Ohmoto, H., and Skinner, B. J., eds., The Kuroko and related volcanogenic massive sulfide deposits, Economic Geology Monograph 5, p. 184–197.

Goodfellow, W. D., and Franklin, J. M., 1993, Geology, mineralogy and chemistry of sediment hosted clastic massive sulfides in shallow cores, Middle Valley, northern Juan de Fuca Ridge.: Economic Geology, v. 88, p. 2037-2068.

Goodfellow, W. D., McCutcheon, S. R., and Peter, J. M., 2003, Massive sulfide deposits of the Bathurst mining camp, New Brunswick, and northern Maine; introduction and summary of findings: Economic Geology Monographs, v. 11, p. 1-16.

Gorton, M. P., and Schandl, E. S., 2000, From continents to island arcs; a geochemical index of tectonic setting for arc-related and within-plate felsic to intermediate volcanic rocks: Canadian Mineralogist, v. 38, p. 1065-1073.

Goscombe, B., Blewett, R., Czarnota, K., Maas, R., and Groenewald, B., 2007, Broad thermo-barometric evolution of the Eastern Goldfields Superterrane: Proceedings of Geoconferences (WA) Inc Kalgoorlie '07 Conference, Kalgoorlie, WA, 2007, p. 33-38.

Goutier, J., and Melançon, M., 2007, Compilation géologique de la Sousprovince de l'Abitibi (version préliminaire), Ministère des Ressources naturelles et de la Faune du Québec.

Graf, J. L., Jr., and Skinner, B. J., 1970, Strength and deformation of pyrite and pyrrhotite: Economic Geology, v. 65, p. 206-215.

GreatGoldMines, 2007, Annual Report: Perth, Great Gold Mines

Greig, D. D., 1984, Geology of the Teutonic Bore massive sulphide deposit, Western Australia: Australasian Institute of Mining and Metallurgy, v. Proceedings 289, p. 147-156.

Grenne, T., and Slack, J. F., 2003, Bedded jaspers of the Ordovician Lokken Ophiolite, Norway; seafloor deposition and diagenetic maturation of hydrothermal plume-derived silica-iron gels: Mineralium Deposita, v. 38, p. 625-639.

Grenne, T., and Slack, J. F., 2005, Geochemistry of jasper beds from the Ordovician Lokken Ophiolite, Norway: Origin of proximal and distal siliceous exhalites: Economic Geology, v. 100, p. 1511-1527.

Groenewald, P. B., Doyle, M. G., Brown, S. J. A., and Barnes, S. J., 2006, Stratigraphy and physical volcanology of the Archean Kurnalpi Terrane, Yilgarn Craton - a field guide, Record 2006/11, Western Australia Geological Survey, p. 25.

Hallberg, J. A., 1984, A geochemical aid to igneous rock type identification in deeply weathered terrain: Journal of Geochemical Exploration, v. 20, p. 1-8.

Hallberg, J. A., 1985, Geology and mineral deposits of the Leonora - Laverton area, northeastern Yilgarn Block, Western Australia: Carlisle, West. Aust., Australia, Hesperian Press.

Hallberg, J. A., Ahmat, A. L., Morris, P. A., and Witt, W. K., 1993, An overview of felsic volcanism within the Eastern goldfields province, Western Australia. [abs], Record 1993.54, AGSO, p. 29-32.

Hallberg, J. A., and Giles, C. W., 1986, Archaean felsic volcanism in the northeastern Yilgarn Block, Western Australia: Australian Journal of Earth Sciences, v. 33, p. 413-427.

Hallberg, J. A., and Thompson, J. F. H., 1985, Geologic setting of the Teutonic Bore massive sulfide deposit, Archean Yilgarn Block, Western Australia: Economic Geology, v. 80, p. 1953-1964.

Hammond, R. L., and Nisbet, B. W., 1992, Towards a structural and tectonic framework for the central Norseman-Wiluna greenstone belt, Western Australia, in Glover, J. E., and Ho, S. E., eds., The Archaean; terrains, processes and metallogeny; proceedings volume for the Third international Archaean symposium, 22, Geology Department and Extension Service, University of Western Australia, p. 39-49.

Hannington, M. D., Jonasson, I. R., Herzig, P. M., and Petersen, S., 1995, Physical and chemical processes of seafloor mineralization at mid-ocean ridges: Geophysical Monograph, v. 91, p. 115-157.

Hannington, M. D., Kjarsgaard, I. M., Galley, A. G., and Taylor, B., 2003, Mineral-chemical studies of metamorphosed hydrothermal alteration in the Kristineberg volcanogenic massive sulfide district, Sweden: Mineralium Deposita, v. 38, p. 423-442.

Hannington, M. D., Santaguida, F., Kjarsgaard, I. M., and Cathles, L. M., 2003, Regional-scale hydrothermal alteration in the Central Blake River Group, western Abitibi subprovince, Canada: implications for VMS prospectivity: Mineralium Deposita, v. 8, p. 393-516.

Hanson, R. E., 1991, Quenching and hydroclastic disruption of andesitic to rhyolitic intrusions in a submarine island-arc sequence, northern Sierra Nevada, California: Geological Society of America Bulletin, v. 103, p. 804-816.

Harrison, T. M., Blichert-Toft, J., Muller, W., Albarede, F., Holden, P., and Mojzsis, S. J., 2005, Heterogeneous Hadean Hafnium: Evidence of continental crust at 4.4 to 4.5 Ga: Science, v. 310, p. 1947-1950.

Hart, T. R., Gibson, H. L., and Lesher, C. M., 2004, Trace element geochemistry and petrogenesis of felsic volcanic rocks associated with volcanogenic massive Cu-Zn-Pb sulfide deposits: Economic Geology, v. 99, p. 1003-1013.

Hathway, B., Hudak, G., and Hamilton, M. A., 2008, Geologic setting of volcanic-associated massive sulfide deposits in the Kamiskotia area, Abitibi Subprovince, Canada: Economic Geology, v. 103, p. 1185-1202.

Hawkesworth, C. J., Gallagher, K., Hergt, J. M., and McDermott, F., 1993, Mantle and slab contributions in arc magmas: Annual Review of Earth and Planetary Sciences, v. 21, p. 175-204.

Hawkesworth, C. J., Turner, S. P., McDermott, F., Peate, D. W., and van Calsteren, P., 1997, U-Th isotopes in arc magmas; implications for element transfer from the subducted crust: Science, v. 276, p. 551-555.

Head, J. W., and Wilson, L., 2003, Deep submarine pyroclastic eruptions: theory and predicted landforms and deposits: Journal of Volcanology and Geothermal Research, v. 121, p. 155-193.

Herrington, R., Maslennikov, V., Zaykov, V., Seravkin, I., Kosarev, A., Buschmann, B., Orgeval, J.-J., Holland, N., Tesalina, S., Nimis, P., and Armstrong, R., 2005, Classification of VMS deposits; lessons from the Uralides: Ore Geology Reviews, v. 27, p. 203-237.

Hrischeva, E., Scott, S. D., and Weston, R., 2007, Metalliferous sediments associated with presently forming volcanogenic massive sulfides; the SuSu Knolls hydrothermal field, eastern Manus Basin, Papua New Guinea: Economic Geology, v. 102, p. 55-73.

Humphris, S. E., Herzig, P. M., Millar, D. J., Alt, J. C., Becker, K., Brown, D., Brugman, G., Chiba, H., Fouquet, Y., Gemmel, B., Guerin, G., Hannington, M. D., Holm, N. G., Honnorez, J., Iturrino, G. J., Knott, R., Ludwig, R., Nakamura, K., Petersen, S., Reysenbach, A. L., Rona, P. A., Smith, S., Strutz, A. A., Tivey, M. K., and Zhao, X., 1995, The internal structure of an active seafloor massive sulphide deposit.: Nature, v. 377, p. 713-716.

Huston, D. L., Taylor, B. E., Bleeker, W., and Watanabe, D. H., 1996, Productivity of volcanic-hosted massive sulphide districts: New constraints from the d18O of quartz phenocrysts in cogenetic rocks.: Geology, v. 24, p. 459-462.

Hutchison, R. W., 1973, Volcanogenic sulfide deposits and their metallogenic significance: Economic Geology, v. 68, p. 1223-1246.

Ixer, R. A. R. A., 1990, Atlas of opaque and ore minerals in their associations: New York, Van Nostrand Reinhold.

JabiruMetals, 2006, Annual Report: Perth, Jabiru Metals.

JabiruMetals, 2009, Annual Report: Perth, Jabiru Metals.

Kalogeropoulos, S. I., and Scott, S. D., 1983, Mineralogy and geochemistry of tuffaceous exhalites (Tetsusekiei) of the Fukazawa Mine, Horuroku District, Japan, in Ohmoto, H., and Skinner, B. J., eds., The Kuroko and related volcanogenic massive sulfide deposits, Economic Geology Monograph 5, p. 412-432.

Kano, K., 1996, A Miocene coarse volcaniclastic mass-flow deposit in the Shimane Peninsula, SW Japan: product of a deep submarine eruption?: Bulletin of Volcanology, v. 58, p. 131-143.

Kerr, D. J., and Mason, R., 1990, A re-appraisal of the geology and ore deposits of the Horne Mine complex at Rouyn-Noranda, Quebec: Special Volume - Canadian Institute of Mining and Metallurgy, v. 43, p. 153-165.

Kerr, D. J., and Gibson, H. L., 1993, A comparison of the Horne volcanogenic massive sulfide deposit and the intracauldron deposits of the mine sequence, Noranda, Quebec: Economic Geology, v. 88, p. 1419-1442.

Kokelaar, B. P., 1982, Fluidization of wet sediments during the emplacement and cooling of various igneous bodies: Journal of the Geological Society, v. 139, p. 21-33.

Kokelaar, B. P., Bevins, R. E., and Roach, R. A., 1985, Submarine silicic volcanism and associated sedimentary and tectonic processes, Ramsey Island, SW Wales: Journal of the Geological Society, v. 142, p. 591-613.

Kositcin, N., Brown, S. J. A., Barley, M. E., Krapez, B., Cassidy, K. F., and Champion, D. C., 2008, SHRIMP U-Pb zircon age constraints on the Late Archaean tectonostratigraphic architecture of the Eastern Goldfields Superterrane, Yilgarn Craton, Western Australia: Precambrian Research, v. 161, p. 5-33.

Koski, R. A., Shanks, W. C., Bohrson, W. A., and Oscarson, R. L., 1988, The composition of massive sulfide deposits from the sediment-covered floor of Escanaba Trough, Gorda Ridge; implications for depositional processes: Canadian Mineralogist, v. 26, p. 655-673.

Krapez, B., and Barley, M. E., 2008, Late Archaean synorogenic basins of the Eastern Goldfields Superterrane, Yilgarn Craton, Western Australia. Part III: Signatures of tectonic escape in an arc-continent collision zone: Precambrian Research, v. 161, p. 183-199.

Krapez, B., Barley, M. E., and Brown, S. J. A., 2008, Late Archaean synorogenic basins of the Eastern Goldfields Superterrane, Yilgarn Craton, Western Australia. Part I: Kalgoorlie and Gindalbie Terranes: Precambrian Research, v. 161, p. 135-153.

Krapez, B. E., Barley, M. E., and Pickard, A. L., 2003, Hydrothermal and resedimented origins of the precursor sediments to banded iron formation: sedimentological evidence from the Early Palaeoproterozoic Brockman Supersequence of Western Australia: Sedimentology, v. 50, p. 979-1011.

Kullerud, G., and Yoder, H. S., 1959, Pyrite stability in the Fe-S system: Economic Geology, v. 54, p. 533-572.

Kuroda, H., 1983, Geological characteristics and formation environment of the Furutobe and Matsuki Kuroko deposits, Akita Prefecture, northeast Japan, in Ohmoto, H., and Skinner, B. J., eds., The Kuroko and related volcanogenic massive sulfide deposits, Economic Geology Monograph 5, p. 149-166.

Langmuir, C., Bezos, A., Escrig, S., and Parman, S. W., 2006, Hydrous mantle melting at ridges and back-arc basins: Geochimica et Cosmochimica Acta, v. 70, p. A341.

Large, R. R., 1977, Chemical evolution and zonation of massive sulphide deposits in volcanic terrains.: Economic Geology, v. 72, p. 549-572.

Large, R. R., 1992, A special issue devoted to Australian volcanic-hosted massive sulfide (VHMS) deposits and their volcanic environment. Preface.: Economic Geology, v. 87, p. 469-470.

Large, R. R., 1992, Australian volcanic-hosted massive sulfide deposits: features, styles and genetic models.: Economic Geology, v. 87, p. 471-510.

Large, R. R., McPhie, J., Gemmell, J. B., Herrmann, W., and Davidson, G. J., 2001, The spectrum of ore deposit types, volcanic environments, alteration halos and related exploration vectors in submarine volcanic successions: Some examples from Australia.: Economic Geology, v. 96, p. 913 - 938.

Le Maitre, R. W., Bateman, P., Dudek, A., Keller, J., Lemeyre, J., Le Bas, M. J., Sabine, P. A., Schmid, R., Sorensen, H., Streckeisen, A., Wooley, A. R., and Zanettin, B., 1989, A classification of igneous rocks and glossary of terms: Oxford, United Kingdom, Blackwell Sci. Publ., 193 p.

Lebedev, L. M., 1967, Metacolloids in endogenic deposits: New York, Plenum Press, 298 p.

Lehnert, K., Su, Y., Langmuir, C. H., Sarbas, B., and Nohl, U., 2000, A global geochemical database structure for rocks: Geochem. Geophys. Geosyst., v. 1, p. 1-14.

Lentz, D. R., 1998, Petrogenetic evolution of felsic volcanic sequences associated with Phanerozoic volcanic-hosted massive sulfide systems: The role of extensional dynamics.: Ore Geology Reviews, v. 12, p. 289-327.

Lesher, C. M., and Campbell, I. H., 1987, Trace element geochemistry of ore associated, and barren felsic metavolcanic rocks in the Superior Province Canada. Reply: Canadian Journal of Earth Sciences, v. 24, p. 1500-1501.

Lesher, C. M., and Campbell, I. H., 1990, Trace element geochemistry of ore associated, and barren felsic metavolcanic rocks associated with massive polymetallic base metal deposits, Research School, Earth Sciences. Annual Report, Australian National University, p. 69.

Lesher, C. M., Goodwin, A. M., Cambell, I. H., and Gordon, M. P., 1986, Trace-element geochemistry of ore-associated and barren, felsic metavolcanic rocks in the Superior Province: Canadian Journal of Earth Sciences, v. 23, p. 222-237.

Lowe, D., 1976, Grain flow and grain flow deposits: Journal of Sedimentary Petrology, v. 46, p. 188-199.

Lowe, D., 1982, Sediment gravity flows: II Depositional models with special reference to the deposits of high-density turbidity currents: Journal of Sedimentary Petrology, v. 52, p. 279-297.

Lydon, J. W., 1984, Volcanogenic massive sulphide deposits. Part 1: a descriptive model: Geoscience Canada, v. 11, p. 195-202.

Lydon, J. W., 1988, Volcanogenic massive sulphide deposits. Part 2: genetic models: Geoscience Canada, v. 15, p. 43-65.

Macdonald, G. A., 1972, Volcanoes: New Jersey, Prentice Hall.

MacGeehan, P. J., and MacLean, W. H., 1980, Tholeiitic basalt-rhyolite magmatism and massive sulphide deposits at Matagami, Quebec.: Nature, v. 283, p. 153-157.

MacLean, W. H., and Barrett, T. J., 1993, Lithogeochemical techniques using immobile elements: Journal of Geochemical Exploration, v. 48, p. 109-133.

Marsaglia, K. M., 1995, Interarc and backarc basins, in Busby, C. J., and Ingersoll, R. V., eds., Tectonics of Sedimentary Basins: Oxford, Blackwell Science, p. 299-329.

Marshall, B., and Gilligan, L. B., 1987, An introduction to remobilization: Information from ore-body geometry and experimental considerations: Ore Geology Reviews, v. 2, p. 87-131.

Marshall, B., and Gilligan, L. B., 1989, Durchbewegung structure, piercement cusps, and piercement veins in massive sulfide deposits; formation and interpretation: Economic Geology, v. 84, p. 2311-2319.

Marshall, B., and Gilligan, L. B., 1993, Remobilization, syn-tectonic processes and massive sulphide deposits: Ore Geology Reviews, v. 8, p. 39-64.

Marston, R. J., 1979, Copper mineralization in Western Australia.: Perth, Geological Survey of Western Australia, 208 p.

McArthur, G., 1996, Textural evolution of the Hellyer massive sulfide deposit.: Unpub. PhD thesis, University of Tasmania.

McArthur, G. J., and Dronseika, E. V., 1990, Que River and Hellyer zinc-lead-silver deposits, in Hughes, F. E., ed., Geology of the Mineral Deposits of Australia and Papua New Guinea (Monograph Series, No. 14), II: Parkville, Victoria, Australasian Institute of Mining and Metallurgy, p. 1229-1239.

McBirney, A., 1963, Factors governing the nature of submarine volcanism: Bulletin of Volcanology, v. 26, p. 455-469.

McConachy, T. F., and McInnes, B. I. A., 2004, Copper-zinc massive sulphide deposits in Western Australia, CSIRO, p. 149.

McKay, W. J., and Hazeldene, R. K., 1987, Woodlawn Zn-Pb-Cu sulfide deposit, New South Wales, Australia: An interpretation of ore formation from field observations and metal zoning: Economic Geology, v. 82, p. 141-164.

McPhie, J., Doyle, M., and Allen, R. L., 1993, Volcanic textures. A guide to the interpretation of textures in volcanic rocks: Hobart, University of Tasmania, Centre for Ore Deposit and Exploration Studies, 198 p.

Mercier-Langevin, P., Dube, B., Hannington, M. D., Davis, D. W., Lafrance, B., and Gosselin, G., 2007a, The LaRonde Penna Au-rich volcanogenic massive sulfide deposit, Abitibi Greenstone Belt, Quebec: Part I. Geology and geochronology: Economic Geology, v. 102, p. 585-609.

Mercier-Langevin, P., Dube, B., Hannington, M. D., Richer-Lafleche, M., and Gosselin, G., 2007b, The LaRonde Penna Au-rich volcanogenic massive sulfide deposit, Abitibi Greenstone Belt, Quebec: Part II. Lithogeochemistry and paleotectonic setting: Economic Geology, v. 102, p. 611-631.

Meschede, M., 1986, A method of discriminating between different types of mid-ocean ridge basalts and continental tholeiites with the Nb-Zr-Y diagram: Chemical Geology, v. 56, p. 207-218.

Messenger, P. R., 2000, Geochemistry of the Yandal belt metavolcanic rocks, Eastern Goldfields Province, Western Australia: Australian Journal of Earth Sciences, v. 47, p. 1015-1028.

Mookherjee, A., 1976, Ores and metamorphism; temporal and genetic relationships, in Wolf, K. H., ed., Handbook of strata-bound and stratiform ore deposits; I, Principles and general studies; Vol. 4, Tectonics and metamorphism.

Morant, P., 1995, The Panorama Zn-Cu VMS deposits, Western Australia.: Australian Institute of Geoscientists, v. Recent Developments in Base Metal Geology and Exploration, Bulletin 16, p. 75-86.

Morris, P. A., 1998, Archaean felsic volcanism in parts of the Eastern Goldfields region, Western Australia, Rep 55, Geological Survey of Western Australia, p. 80.

Morris, P. A., and Witt, W. K., 1997, Geochemistry and tectonic setting of two contrasting Archaean felsic volcanic associations in the Eastern Goldfields, Western Australia: Precambrian Research, v. 83, p. 83-107.

Morton, R. L., Walker, J. S., Hudak, G. J., and Franklin, J. M., 1991, The early development of an Archean submarine Caldera complex with emphasis on the Mattabi massive sulphide deposit: Economic Geology, v. 86, p. 1002-1011.

Mueller, W., Chown, E. R., and Potvin, R., 1994, Substorm wave base felsic hydroclastic deposits in the Archean Lac des Vents volcanic complex, Abitibi belt, Canada: Journal of Volcanology and Geothermal Research, v. 60, p. 273-300.

Mulholland, I. R., Cowden, A., Hay, I. P., Ion, J. C., and Greenaway, A. L., 1998, Nimbus silver-zinc deposit, Geology of Australian and Papua New Guinean mineral deposits, Monograph 22, Australasian Institute of Mining and Metallurgy, p. 273-277.

Mullin, J. W., 1993, Crystallization: Oxford, Butterworth-Heinemann, 527 p.

Nakamura, N., 1974, Positive cerium anomaly and two types of lunar samples: Geochemical Journal, v. 8, p. 67-74.

Nelson, D. R., 1995, Compilation of SHRIMP U-Pb zircon geochronology data, 1994, Record 1995/3, Western Australia Geological Survey.

Nelson, D. R., 1996, Compilation of SHRIMP U-Pb zircon geochronology data, 1995, Record 1996/5, Western Australia Geological Survey.

Nelson, D. R., 1997, Evolution of the Archaean granite-greenstone terranes of the Eastern Goldfields, Western Australia: SHRIMP U-Pb zircon constraints: Precambrian Research, v. 83, p. 57-81.

Nelson, D. R., 1997, Compilation of SHRIMP U-Pb zircon geochronology data, 1996, Record 1997/2, Western Australia Geological Survey.

Neuendorf, K. K. E., Mehl, J. P. J., and Jackson, J. A., 2005, Glossary of Geology (5th edition), American Geological Institute, 779 p.

Nickel, E. H., 1984, The mineralogy and geochemistry of the weathering profile of the Teutonic Bore Cu-Pb-Zn-Ag sulphide deposit: Journal of Geochemical Exploration, v. 22, p. 239-264.

Nimis, P., Zaykov, V. V., Omenetto, P., Melekestseva, I. Y., Tesalina, S. G., and Orgeval, J. J., 2008, Peculiarities of some mafic-ultramafic- and ultramafic-hosted massive sulfide deposits from the Main Uralian Fault Zone, southern Urals: Ore Geology Reviews, v. 33, p. 49-69.

Offler, R., and Whitford, D. J., 1992, Wall rock alteration and metamorphism of a volcanogenic massive sulphide deposit at Que River, Tasmania: petrology and mineralogy: Economic Geology, v. 87, p. 686-705.

Ohmoto, H., 1983, Geologic setting of the Kuroko deposits, Japan, Part I: geologic history of the Green Tuff region, in Ohmoto, H., and Skinner, B. J., eds., The Kuroko and related volcanogenic massive sulfide deposits, Economic Geology Monograph 5, p. 39-54.

Ohmoto, H., Mizukami, M., Drummond, S. E., Eldridge, C. S., Pisutha-Arnond, V., and Lenagh, T. C., 1983, Chemical processes of kuroko formation, in Ohmoto, H., and Skinner, B. J., eds., The Kuroko and related volcanogenic massive sulfide deposits, Economic Geology Monograph 5, p. 570-604.

Ohmoto, H., and Skinner, B. J., 1983, The Kuroko and related volcanogenic massive sulfide deposits., Economic Geology Monograph 5, 604 p.

Painter, M. G. M., Groenewald, P. B., and McCabe, M., 2003, East Yilgarn Geoscience Database, 1:100 000 geology of the Leonora–Laverton region, Eastern Goldfields Granite–Greenstone Terrane — an explanatory note, Rep 84, Western Australia Geological Survey, 45 p.

Paradis, S., Jonasson, I. R., Le Cheminant, G. M., and Watkinsons, D. H., 1988, Two zinc-rich chimneys from the plume site, southern Juan de Fuca Ridge: Canadian Mineralogist, v. 26, p. 637-654.

Pearce, J. A., 1983, Role of the sub-continental lithosphere in magma genesis at active continental margins, in Hawkesworth, C. J., and Norry, M. J., eds., Continental basalts and mantle xenoliths.

Pearce, J. A., 1996, A user's guide to basalt discrimination diagrams, in Wyman, D. A., ed., Trace element geochemistry of volcanic rocks: applications for massive sulphide exploration, 12. Short Course Notes - Geological Association of Canada, p. 79-113.

Pearce, J. A., and Cann, J. R., 1973, Tectonic setting of basic volcanic rocks determined using trace element analysis: Earth and Planetary Science Letters, v. 19, p. 290-300.

Pearce, J. A., and Norry, M. J., 1979, Petrogenetic implications of Ti, Zr, Y, and Nb variations in volcanic rocks: Contributions to Mineralogy and Petrology, v. 69, p. 33-47.

Pearce, J. A., and Peate, D. W., 1995, Tectonic implications of the composition of volcanic arc magmas: Annual Review of Earth and Planetary Sciences, v. 23, p. 251-285.

Pearson, V., and Daigneault, R., 2009, An Archean megacaldera complex: The Blake River Group, Abitibi greenstone belt: Precambrian Research, v. 168, p. 66-82.

Pedersen, F. D., 1980, Remobilization of the massive sulfide ore of the Black Angel Mine, central West Greenland: Economic Geology, v. 75, p. 1022-1041.

Peter, J. M., and Goodfellow, W. D., 1996, Mineralogy, bulk and rare earth element geochemistry of massive sulphide-associated hydrothermal, Bathurst Mining Camp, New Brunswick.: Canadian Journal of Earth Sciences, v. 33, p. 252-283.

Peter, J. M., and Scott, S. D., 1988, Mineralogy, composition, and fluid inclusion microthermometry of sea-floor hydrothermal deposits in the southern trough of Guaymas Basin, Gulf of California: Canadian Mineralogist, v. 26, p. 567-587.

Peter, J. M., and Shanks, W. C., 1992, Sulfur, carbon, and oxygen isotope variations in submarine hydrothermal deposits of Guaymas Basin, Gulf of California, USA: Geochimica et Cosmochimica Acta, v. 56, p. 2025-2040.

Petersen, S., Herzig, P. M., and Hannington, M. D., 2000, Third dimension of a presently forming VMS deposit; TAG hydrothermal mound, Mid-Atlantic Ridge, 26N: Mineralium Deposita, v. 35, p. 233-259.

Pichler, H., 1965, Acid hyaloclastites: Bulletin of Volcanology, v. 28, p. 293-310.

Piercey, S. J., Chaloux, E. C., Peloquin, A. S., Hamilton, M. A., and Creaser, R. A., 2008, Synvolcanic and younger plutonic rocks from the Blake River Group: Implications for regional metallogenesis: Economic Geology, v. 103, p. 1243-1268.

Pouclet, A., and Bellon, H., 1992, Geochemistry and isotopic composition of volcanic rocks from the Yamato Basin; Hole 794D, Sea of Japan: Proceedings of the Ocean Drilling Program, Scientific Results, v. 127-128, p. 779-789.

Ramdohr, P., 1960, Die Erzmineralien und ihre Verwachsungen, ed. 3: Berlin, Akademie-Verlag.

Ramdohr, P., 1980, The ore minerals and their intergrowths: Oxford, Pergamon Press, 1207 p.

Relvas, J. M. R. S., Barriga, F. J. A. S., Ferreira, A., Noiva, P. C., Pacheco, N., and Barriga, G., 2006, Hydrothermal alteration and mineralization in the Neves-Corvo volcanic-hosted massive sulfide deposit, Portugal; I, Geology, mineralogy, and geochemistry: Economic Geology, v. 101, p. 753-790.

Rey, P. F., Philippot, P., and Thebaud, N., 2003, Contribution of mantle plumes, crustal thickening and greenstone blanketing to the 2.75-2.65 Ga global crisis: Precambrian Research, v. 127, p. 43-60.

Rickard, D. T., and Zweifel, H., 1975, Genesis of Precambrian sulfide ores, Skellefte district, Sweden: Economic Geology, v. 70, p. 255-274.

Ridge, J. D., 1973, Volcanic exhalations and ore deposition in the vicinity of the sea floor: Mineralium Deposita, v. 8, p. 332-348.

Ridler, R. H., 1971, Analysis of Archean volcanic basins in the Canadian Shield using the exhalite concept: Canadian Mining and Metallurgical Bulletin, v. 64, p. 20.

Rimstidt, J. D., 1997, Gangue mineral transport and deposition, in Barnes, H. L., ed., Geochemistry of hydrothermal ore deposits, 3rd ed: New York, Wiley, p. 487–515.

Rollinson, H., 2007a, When did plate tectonics begin?: Geology Today, v. 23, p. 186-191.

Rollinson, H., 2007b, Early Earth systems : a geochemical approach, Blackwell Publishing.

Rollinson, H. R., 1993, Using geochemical data; evaluation, presentation, interpretation: Harlow, United Kingdom, Longman Scientific & Technical.

Ross, C. S., and Smith, R. L., 1955, Water and other volatiles in volcanic glasses: American Mineralogist, v. 40, p. 1071-1089.

Schandl, E. S., and Gorton, M. P., 2002, Application of high field strength elements to discriminate tectonic settings in VMS environments: Economic Geology, v. 97, p. 629-642.

Schwarz-Schampera, U., Terblanche, H., and Oberthür, T., 2010, Volcanic-hosted massive sulfide deposits in the Murchison greenstone belt, South Africa: Mineralium Deposita, v. 45, p. 113-145.

Sharpe, R., and Gemmell, J. B., 2001, Alteration characteristics of the Archean Golden Grove Formation at the Gossan Hill Deposit, Western Australia; induration as a focusing mechanism for mineralizing hydrothermal fluids: Economic Geology, v. 96, p. 1239-1262.

Sharpe, R., and Gemmell, J. B., 2002, The Archean Cu-Zn magnetite-rich Gossan Hill volcanic-hosted massive sulfide deposit, Western Australia; genesis of a multistage hydrothermal system: Economic Geology, v. 97, p. 517-539.

Simpson, K., and McPhie, J., 2001, Fluidal-clast breccia generated by submarine fire fountaining, Trooper Creek Formation, Queensland, Australia: Journal of Volcanology and Geothermal Research, v. 109, p. 339-355.

Sinton, J. M., Ford, L. L., Chappell, B., and McCulloch, M. T., 2003, Magma genesis and mantle heterogeneity in the manus back-arc basin, Papua New Guinea: J. Petrology, v. 44, p. 159-195.

Sinton, J. M., and Fryer, P., 1987, Mariana Trough lavas from 18°N: implications for the origin of back arc basin basalts: Jour. Geophys. Res, v. 92, p. 12782-12802.

Skilling, I. P., White, J. D. L., and McPhie, J., 2002, Peperite: a review of magma-sediment mingling: Journal of Volcanology and Geothermal Research, v. 114, p. 1-17.

Smellie, J. L., 1995, Volcanism associated with extension at consuming plate margins: London, Geological Society.

Smith, T. L., and Batiza, R., 1989, New field and laboratory evidence for the origin of hyaloclastite flows on seamount summits: Bulletin of Volcanology, v. 51, p. 96-114.

Solomon, M., 1976, Volcanic massive sulphide and their host rocks - a review and an explanation, in K.H., W., ed., Handbook of Stratabound and stratiform ore deposits, Elsevier, p. 21-50.

Solomon, M., and Gaspar, O. C., 2001, Textures of the Hellyer volcanic-hosted massive sulfide deposit, Tasmania; the aging of a sulfide sediment on the sea floor: Economic Geology v. 96, p. 1513-1534.

Solomon, M., and Walshe, J. L., 1979, The formation of massive sulfide deposits on the sea floors: Economic Geology, v. 74, p. 797-813.

Solomon, M., Walshe, J. L., and Eastoe, C. J., 1987, Experiments on convection and their relevence to the genesis of massive sulphide deposits.: Australian Journal of Earth Sciences, v. 34, p. 311-323.

Solomon, M., and Zaw, K., 1997, Formation on the sea floor of the Hellyer volcanogenic massive sulfide deposit: Economic Geology, v. 92, p. 686-695.

Spry, P. G., Peter, J. M., and Slack, J. F., 2000, Meta-exhalites as exploration guides to ore: Reviews in Economic Geology, v. 11, p. 163-201.

Stanton, R. L., 1964, Mineral interfaces in stratiform ores: Trans Inst. Min. & Met., B., v. 696, p. 45-79.

Stanton, R. L., 1972, Ore petrology: New York, McGraw-Hill.

Stern, R. J., 2005, Evidence from ophiolites, blueschists, and ultrahigh-pressure metamorphic terranes that the modern episode of subduction tectonics began in Neoproterozoic time: Geology, v. 33, p. 557–560.

Stern, R. J., Lin, P.-N., Morris, J. D., Jackson, M. C., Fryer, P., Bloomer, S. H., and Ito, E., 1990, Enriched back-arc basin basalts from the northern Mariana Trough: implications for the magmatic evolution of back-arc basins: Earth and Planetary Science Letters, v. 100, p. 210-225.

Stott, G., and Mueller, W., 2009, Superior Province: The nature and evolution of the Archean continental lithosphere: Precambrian Research, v. 168, p. 1-3.

Sun, S. S., and McDonough, W. F., 1989, Chemical and isotopic systematics of oceanic basalts; implications for mantle composition and processes: Geological Society Special Publications, v. 42, p. 313-345.

Swager, C. P., 1997, Tectono-stratigraphy of late Archaean greenstone terranes in the southern Eastern Goldfields, Western Australia: Precambrian Research, v. 83, p. 11-42.

Swager, C. P., Witt, W. K., Griffin, T. J., Ahmat, A. L., Hunter, W. M., McGoldrick, P. J., and Wyche, S., 1992, Late Archaean granite–greenstones of the Kalgoorlie Terrane, Yilgarn Craton, Western Australia, in Glover, J. E., and Ho, S. E., eds., The Archaean: terrains, processes and metallogeny, The University of Western Australia, Geology Department and University Extension, Publication no. 22, p. 107–122.

Syme, E. C., and Bailes, A. H., 1993, Stratigraphic and tectonic setting of Early Proterozoic volcanogenic massive sulphide deposits, Flin Flon, Manitoba: Economic Geology, v. 88, p. 566-589.

Taube, A., 1986, The Mount Morgan gold-copper mine and environment, Queensland; a volcanogenic massive sulfide deposit associated with penecontemporaneous faulting: Economic Geology, v. 81, p. 1322-1340.

Taylor, B., and Martinez, F., 2003, Back-arc basin basalt systematics: Earth and Planetary Science Letters, v. 210, p. 481-497.

Teagle, D. A. H., and Alt, J. C., 2004, Hydrothermal alteration of basalts beneath the Bent Hill massive sulfide deposit, Middle Valley, Juan de Fuca Ridge: Economic Geology, v. 99, p. 561-584.

Thurston, P. C., 2002, Autochthonous development of Superior Province greenstone belts?: Precambrian Research, v. 115, p. 11-36.

Thurston, P. C., Ayer, J. A., Goutier, J., and Hamilton, M. A., 2008, Depositional gaps in Abitibi greenstone belt stratigraphy: A key to exploration for syngenetic mineralization: Economic Geology, v. 103, p. 1097-1134.

Tornos, F., Gonzalez Clavijo, E., and Spiro, B., 1998, The Filon Norte orebody (Tharsis, Iberian pyrite belt); a proximal low-temperature shale-hosted massive sulphide in a thin-skinned tectonic belt: Mineralium Deposita, v. 33, p. 150-169.

Vaasjoki, M., 1985, The Teutonic Bore deposits, Western Australia; a lead isotope study of an ore and its gossan: Mineralium Deposita, v. 20, p. 266-270.

Vearncombe, S., Barley, M. E., Groves, D. I., McNaughton, N. J., Mikucki, E. J., and Vearncombe, J. R., 1995, 3.26 Ga black smoker-type mineralization in the Strelley Belt, Pilbara Craton, Western Australia: Journal of the Geological Society of London, v. 152, p. 587-590.

Vivallo, W., 1985, The geology and genesis of the Proterozoic massive sulfide deposit at Garpenberg, central Sweden: Economic Geology, v. 80, p. 17-32.

Vokes, F. M., 1969, A review of the metamorphism of sulphide deposits: Earth-Science Reviews, v. 5, p. 99-143.

Walker, R. R., Matulich, A., Amos, A. C., Watkins, J. J., and Mannard, G. W., 1975, The geology of the Kidd Creek mine: Economic Geology, v. 70, p. 80-89.

Wang, Y., Qin, K., Tan, Y., and Hou, Z., 2000, The Derni Cu-Co massive sulfide deposit, Qinghai province, China: Ultramafic volcanic-hosted submarine-exhalative minerralisation: Exploration and Mining Geology, v. 9, p. 253-264.

Wedekind, M. R., 1990, Geology and geochemistry of the Warrego Au-Cu-Bi mine, Tennant Creek, Northern Territory, Australia: Unpub. PhD thesis, University of Tasmania, 380 p.

Whitford, D. J., and Ashley, P. M., 1992, The Scuddles volcanic-hosted massive sulfide deposit, Western Australia: Geochemistry of the host rocks and evaluation of lithochemistry for exploration: Economic Geology, v. 87, p. 873-888.

Whitford, D. J., and Cameron, M. A., 1987, Trace element geochemistry of ore associated, and barren felsic metavolcanic rocks in the Superior Province Canada. Discussion:: Canadian Journal of Earth Sciences, v. 24, p. 1498-1500.

Whitford, D. J., McPherson, W. P. A., and Wallace, D. B., 1989, Geochemistry of the host rocks of the volcanogenic massive sulphide deposit at Que River, Tasmania: Economic Geology, v. 84, p. 1-21.

Wilson, L., and Head, J. W., III, 1981, Ascent and eruption of basaltic magma on the Earth and Moon: Journal of Geophysical Research, v. 86, p. 2971-3001.

Winchester, J. A., and Floyd, P. A., 1977, Geochemical discrimination of different magma series and their differentiation products using immobile elements: Chemical Geology, v. 20, p. 325-343.

Witt, W. K., 1994, Geology of the Melita 1:100,000 sheet, Western Australia, Expl. Notes., Geol Surv. West Aust.

Wood, D. A., 1980, The application of a ThHfTa diagram to problems of tectonomagmatic classification and to establishing the nature of crustal contamination of basaltic lavas of the British Tertiary Volcanic Province: Earth and Planetary Science Letters, v. 50, p. 11-30.

Wyman, D., and Kerrich, R., 2009, Plume and arc magmatism in the Abitibi subprovince: Implications for the origin of Archean continental lithospheric mantle: Precambrian Research, v. 168, p. 4-22.

Wyman, D. A., 2003, Upper mantle processes beneath the 2.7 Ga Abitibi Belt, Canada; a trace element perspective: Precambrian Research, v. 127, p. 143-165.

Wyman, D. A., Bleeker, W., and Kerrich, R., 1999, A 2.7 Ga komatiite, low Ti tholeiite, arc tholeiite transition, and inferred proto-arc geodynamic setting of the Kidd Creek deposit: evidence from precise trace element data., in Hannington, M. D., Barrie, C. T., and Bleeker, W., eds., The giant Kidd Creek volcanogenic massive sulfide deposit, Western Abitibi subprovince, Canada, Economic Geology Monograph 10, p. 511-528.

Yamagishi, H., 1987, Studies on the Neogene subaqueous lavas and hyaloclastites in southwest Hokkaido: Report of the Geological Survey of Hokkaido, v. 59, p. 55-117.

Yamagishi, H., 1991, Morphological features of Miocene submarine coherent lavas from the "Green Tuff" basins: examples from basaltic and andesitic rocks from the Shimokita Peninsula, northern Japan: Bulletin of Volcanology, v. 53, p. 173-181.

Yamagishi, H., and Dimroth, E., 1985, A comparison of Miocene and Archaean rhyolite hyaloclastites: evidence for a hot and fluid rhyolite lava: Journal of Volcanology and Geothermal Research, v. 23, p. 337-355.

Ziegler, P. A., Cloetingh, S., and van Wees, J-D., 1995, Dynamics of intra-plate compressional deformation; the Alpine Foreland and other examples: Tectonophysics, v. 252, p. 7-59.

APPENDICES

All appendices are stored digitally on CD stored at the back of the volume.